

UNIVERSITY OF
BIRMINGHAM

EFFECTS OF CREEP AND OXIDATION INTERACTION ON HIGH TEMPERATURE CRACK GROWTH BEHAVIOUR OF NICKEL BASED SUPERALLOYS

Joseph Charles Fisk

A thesis submitted to

The University of Birmingham

For the degree of

DOCTOR OF PHILOSOPHY

Department of Metallurgy and Materials

School of Engineering and Physical Sciences

University of Birmingham

UNIVERSITY OF
BIRMINGHAM

University of Birmingham Research Archive

e-theses repository

This unpublished thesis/dissertation is copyright of the author and/or third parties. The intellectual property rights of the author or third parties in respect of this work are as defined by The Copyright Designs and Patents Act 1988 or as modified by any successor legislation.

Any use made of information contained in this thesis/dissertation must be in accordance with that legislation and must be properly acknowledged. Further distribution or reproduction in any format is prohibited without the permission of the copyright holder.

Abstract

A complete and comprehensive understanding of dwell crack growth behaviour is required for two compressor and turbine disc alloys, Udimet 720Li and RR1000, both having a fine grain microstructure. The effect of temperature, dwell time and dwell load has been studied in air and vacuum along with detailed fractographic and microstructural analysis to understand the relevant contributions of oxidation, creep and microstructure.

The data agrees well with those gathered on similar alloys, indicating that crack growth rates according to high temperature dwell loading are significantly higher than those associated with otherwise similar baseline loading conditions; provided the tests are carried out in air rather than in a vacuum. Crack growth rates are shown to increase with increasing dwell time and temperature; indicating that the phenomena are condition specific. Furthermore, data in this programme of research also indicates that finer grained microstructures are associated with faster high temperature dwell crack growth rates when compared with otherwise similarly tested coarser grained microstructures.

These increases in crack growth rates are associated with a full or partial mechanism change from predominantly transgranular (for high temperature baseline loading) to predominantly intergranular (for high temperature dwell loading) crack growth; again, provided that the tests are carried out in laboratory air.

The increase in crack growth rates and the associated change in mechanism are thought to be induced by time-dependent environmental factors. It is postulated that at high temperatures, given enough time at high loads; oxygen will diffuse preferentially along grain boundaries ahead of a crack tip and cause the formation of oxides such as NiO and Cr_2O_3. These oxides are brittle, and will crack readily. Hence the crack propagates along grain boundaries and at faster rates.

The volume expansion associated with the formation of such oxides is catered for by two main factors: stress at the crack tip and the associated accumulation of plastic strain around the crack tip which occurs as a result of creep. The phenomena are therefore thought to be dependent upon testing (or operating) conditions and the microstructure of the material in the following ways:

High temperatures and longer dwell times increase the extent to which diffusion of oxygen may occur along grain boundaries ahead of a crack tip; hence both with increase crack growth rates associated with high temperature dwell loading. Higher stresses cause the accumulation of more profound creep strain at the crack tip, which accommodates greater volumes of oxide formation and promote the diffusion of oxygen along grain boundaries; hence will also increase the extent to which damage occurs ahead of a crack tip and therefore will cause a more profound increase in crack growth rates.

(These concepts are only true up to a critical thickness for the formation of oxides ahead of a crack tip; and so long as the oxides are actually cracking. Oxide formation is parabolic, hence

as the thickness of the oxide increases, the rate at which it forms decreases. Furthermore, as they become more dense they become more difficult to break. Therefore, if thick, dense, stable oxides form and are not easily cracked, high temperature dwell crack growth rates may decrease.)

Furthermore, a finer grain size may also allow for a larger amount of plastic strain accumulation at the crack tip, which in turn might encourage the cracking of oxides ahead of a crack at lower stresses, or earlier on (in terms of time) during the hold period at maximum load. Therefore a finer grain sized microstructure might be more susceptible to high temperature environmentally induced damage ahead of a dwell crack tip.

In terms of microstructure, primary γ' precipitate size and morphology is also thought to have an effect: The bonds between primary γ' particles, and between primary γ' and the γ matrix in which they reside are shown to form low energy paths for fatigue cracks to propagate since they are observed to break even during high temperature high frequency loading (1Hz or baseline loading) under regimes dominated by cycle-dependent fatigue. It is therefore thought that, given the required conditions, it is the breaking of these bonds which promote "true" intergranular cracking (along the γ grain boundaries). Hence, microstructures comprising smaller primary γ' precipitates (and hence larger amounts of primary γ' boundary material) might be less susceptible to intergranular damage. This is shown by the data in that high temperature dwell crack growth rates are slower in these microstructures when compared with otherwise similarly tested material with larger average primary γ' precipitate sizes.

The study has been extended to determine the effect of an overload segment in the load waveform, the rationale being that this type of waveform more accurately models real loading cycles on engines in service. In support with extensive modelling carried out within Rolls-Royce plc. in order to understand the stress state ahead of the crack tip and its relaxation over dwell time, the effect of overload factor, test temperature and dwell time has also been examined empirically.

In good agreement with the findings of others, crack growth rates according to overload cycling are shown to propagate significantly slower when compared with crack growth rates according to (otherwise similar) dwell-only loading, or static loads; even at high temperature and in an oxidising environment.

A good agreement between modelled predictions and experimental results has been achieved, indicating that the retardation of crack growth rates is mainly affected by mechanical factors. Both empirical and analytical data conclude that high temperature crack growth rates are further reduced or retarded with decreasing temperature, increasing overload factor and decreasing dwell time. This is due, in part, to the introduction and evolution of a complex beneficial residual stress state ahead of the crack tip immediately upon partial unloading from the overload segment. In essence, crack tip stresses unload preferentially (as seen in finite element analysis) and gradually relax back to those normally associated with dwell-only loading as a function of high temperature creep during the subsequent dwell time. Therefore the phenomenon is shown to be a function of dwell time, nominal background stress, temperature and microstructure.

A further contribution to the retardation of dwell crack growth rates may be the accumulation of creep strain at the crack tip which might cause it to become blunted to some extent. This is evident in the "settling up" and "settling down" behaviour shown in crack growth resistance curves which comprise baseline, dwell and overload waveforms applied to each test piece. When switching from baseline to dwell loading, crack growth rates increase as discussed above; nevertheless immediately on switching they begin relatively fast and settle down to more stable, linear Paris law crack growth across a definite period of crack length. Crack fronts pertaining to baseline loading where cycle-dependent fatigue dominates (in terms of mechanism) are thought to be relatively sharp and hence this settling down behaviour may occur due to the blunting of crack tip fronts during dwell loading; where time-dependent phenomena such as creep become competing mechanisms.

Further analysis focuses on the understanding of failure mechanisms, by experimenting with novel, complex overload waveforms (such as the "unload" and "reload" waveform). This programme also involves extensive modelling work carried out within Rolls-Royce plc. to determine the extent to which models and empirical data agree and to further understand the phenomenon of overload crack growth rate retardation.

Dedication

To my wife, Hannah.

Acknowledgements

A great deal of thanks are owed to Professor Paul Bowen and Dr. Hang Yue Li at The University of Birmingham for their extensive academic, technical and personal support. Their expertise, experience and enthusiasm were inspirational.

Thanks are also owed to Mr. David Price for his technical and personal support. He made the often laborious lab work a great deal of fun. Neil Stephens is also thanked for his training and for preliminary results, which ultimately have paved the way for this thesis.

Professor Paul Bowen's Fracture and Fatigue Research Group is a formidable and friendly one. Special thanks go to Andrew Seymour, Danial Khoshkhou, Santiago Flores-Torres, James Rosser, Samuel Cruchley, Sophie Reynolds, Craig Knaggs, Jonathan Boukhobza, Christopher Simpson, Matthew Dear, Suyang Yu, and Jifueng Sun. Their friendship has made the last four years extremely enjoyable and their technical and academic support has been influential and greatly appreciated. Special thanks also go to Jenny Henderson for her continued personal support.

Technical and professional support has been greatly appreciated from Mr. Steve Williams and Dr. Lik-Beng Lim from within Rolls-Royce plc.

Undergraduate students Junnan Jiang and Angharad Griffiths are specially thanked for their support and contribution during the final stages of thesis preparation.

I am owed a huge debt of thanks to Graham Newton for tirelessly proof reading large sections of this thesis for spelling and grammatical errors. Any significant errors which are still left behind are entirely his fault.

Special thanks also go to my parents, Philip and Linda Fisk for their on-going love and support.

Finally special thanks also go to my wife Hannah. Her support has been a great source of comfort and motivation. Without her I am sure this thesis would never have been completed.

One final addendum is that I would like thank my three month old son Solomon for his contribution. My hope is that those a little more familiar with the subject will not find my *Discussion* as hilarious as he did when it was read to him.

Contents

ABSTRACT ..... **I**

DEDICATION ..... **VI**

ACKNOWLEDGEMENTS ..... **VII**

1. INTRODUCTION **1**

1.1 THE JET ENGINE 2

1.2 BUSINESS CONTEXT 6

2. LITERATURE REVIEW **9**

2.1 HIGH PRESSURE COMPRESSOR AND TURBINE DISCS 10

2.2 NICKEL BASED SUPERALLOYS 16

2.2.1 Microstructure *17*

2.2.2 Effects of Alloying Elements *20*

2.2.3 Processing *21*

2.2.4 A Short History of Disc Alloy Development *24*

2.2.5 Udimet 720Li *25*

2.2.6 RR1000 ..... *27*

2.3 FRACTURE AND FATIGUE 30

2.3.1 Introduction *30*

2.3.2 Linear Elastic Fracture Mechanics *30*

2.3.3 Fatigue *34*

2.3.4 Crack Tip Stress States *39*

2.4 DWELL CRACK GROWTH 43

2.4.1 Environmental Effects *46*

2.4.2 Creep Effects *56*

2.4.3 Linear Superposition Lifing Methodologies *64*

2.5 ANALYTICAL TECHNIQUES 70

2.5.1 Introduction to Finite Element Analysis *70*

2.5.2 Modelling Variations in Stress and Strain *71*

2.5.3 Crystal Plasticity Modelling *81*

2.6 EFFECT OF OVERLOAD 83

2.6.1 Introduction *83*

2.6.2 Theoretical Modelling *87*

2.6.3 Preliminary Testing *92*

3. METHODOLOGY 95

3.1 MATERIAL 96

3.2 MECHANICAL TESTING 99

3.2.1 Introduction *99*

3.2.2 Test Rig Set-Up *102*

3.2.3 Testing Procedure *106*

3.2.4 Data Analysis *113*

3.2.5 Summary of Testing Conditions *125*

3.3 SCANNING ELECTRON MICROSCOPY 140

3.3.1 Fractography *140*

3.3.2 Metallography *140*

3.4 MODELLING 150

3.4.1 Model Implementation *150*

3.4.2 Data Analysis *162*

3.4.3 Validity of Modelled Crack Tip Geometry *164*

3.4.4 Further Considerations on the Use of Finite Element Models *166*

4. RESULTS 169

4.1 MECHANICAL TESTING 170

4.1.1 Introduction *170*

4.1.2 Effect of Dwell *170*

4.1.3 Effect of Overload *175*

4.1.4 Influence of Microstructure *178*

4.1.5 Effect of Changing the Waveform *181*

4.1.6 Time-Dependent ΔK_{th} *181*

4.1.7 Summary *184*

4.2 SCANNING ELECTRON MICROSCOPY 191

4.2.1 Fractography *191*

4.2.2 Metallography *212*

4.3 MODELLING 244

4.3.1 Introduction *244*

4.3.2 Incubation Time *247*

4.3.3 Crossing Time *256*

4.3.4 Experimentally Derived Incubation Time *274*

5 DISCUSSION 279

5.1 DWELL CRACK GROWTH BEHAVIOUR 280

5.1.1 Introduction *280*

5.1.2 Fatigue, Creep and Oxidation *281*

5.2 INFLUENCE OF MICROSTRUCTURE 286

5.2.1 Crack Growth Mechanisms *286*

5.2.2 Influence of Primary γ' Morphology *288*

5.2.3 Influence of Grain Size *291*

5.2.4 Differences in RR1000 Test Pieces *294*

5.3 EFFECT OF OVERLOAD 297

5.3.1 Introduction *297*

5.3.2 Crack Tip Plasticity *297*

5.3.3 Crack Growth Mechanisms *302*

5.3.4 Fatigue, Creep and Oxidation *306*

5.3.5 Crack Tip Blunting *307*

5.3.6 Influence of Microstructure *309*

5.3.7 Time at Overload *312*

5.3.8 Implication of Data *314*

5.3.9 Summary *316*

5.4 TIME-DEPENDENT ΔK_{TH} 318

5.4.1 Introduction *318*

5.4.2 Crack Growth Mechanisms *318*

5.4.3 Effect of Dwell Period *320*

5.4.4 Influence of Microstructure *321*

5.4.5 Effect of Testing Procedure *323*

5.5 TRANSIENT CRACK GROWTH BEHAVIOUR 324

5.5.1 Introduction *324*

5.5.2 Oxygen Induced Damage Zone *325*

5.5.3 Crack Tip Blunting *328*

5.5.4 Summary *330*

6 CONCLUSIONS 333

7 FURTHER WORK 339

7.1 CONTINUATION OF TESTING PROGRAMME 340

7.2 CRACK GROWTH WITHIN ONE CYCLE 341

7.3 INTERRUPTED TESTS 342

7.4 THE EFFECT OF DWELL AT OVERLOAD 343

7.5 THE EFFECT OF BI-THERMAL LOADING 344

7.6 OVERLOAD CRACK GROWTH RETARDATION IN INERTIA WELDS 345

7.7 UNDERSTANDING FAILURES IN MODELLING CODES 346

APPENDICES 347

APPENDIX I GLOSSARY OF COMMON TERMS 348

APPENDIX II LIST OF FIGURES 351

APPENDIX III LIST OF TABLES 396

APPENDIX IV TEST PIECE DRAWINGS 399

APPENDIX V VALIDITY OF ASSUMPTIONS 401

Crack Length Calculations *401*

Geometric Shape Factor *414*

Model Geometry and Resolution *416*

APPENDIX VI CRACK GROWTH RESISTANCE CURVES 424

Udimet 720Li *424*

RR1000 ..... *446*

APPENDIX VII FRACTOGRAPHY 465

Udimet 720Li *466*

RR1000 ..... *573*

8 REFERENCES 629

1. Introduction

1.1 The Jet Engine

Current trends for jet engine design are to improve efficiency by reducing weight and increasing Turbine Entry Temperature (TET). These drives put huge demands upon the components of the jet engine and the materials involved. The stress systems are dynamic, which means that materials utilised must have excellent fatigue properties and must retain these properties at elevated temperatures. For this reason, superalloys are used extensively in the jet engine.

The engine works by sucking a large volume of air through the front, low pressure fan. This air is compressed, mixed with fuel and combusted, which causes a huge increase in pressure. The mixture is allowed to expand through the nozzle at the rear, exiting the engine at a significantly higher velocity than the intake, and therefore at a greater momentum [1]. This is conserved by a change in momentum of the engine (and therefore the aeroplane) and results in the application of thrust to the aeroplane.

A cutaway diagram of the Rolls-Royce Trent 800 turbofan engine is presented in Figure 1-1 including pressure and temperature plots to show that the high pressure compressor and turbine regions represent the most demanding sections of the engine.

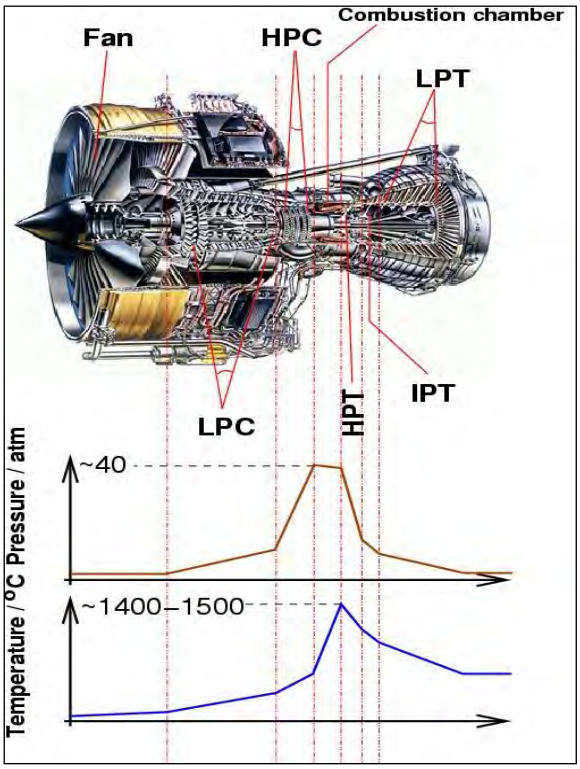


Figure 1-1: Cut away of a Trent 800 series engine showing: low, intermediate, and high pressure compressor stages; the combustion stage; and the low, intermediate, and high pressure turbine stages, with relative temperatures and pressures [2].

Furthermore, the temperature, pressure and therefore associated component stress states vary as a function of time throughout any given flight cycle. A graph plotting turbine entry temperature (TET) against time for a typical civil aerospace flight cycle is presented in Figure 1-2. Associated stress states experienced by components of the jet engine usually vary similarly with TET and as such, stress-time plots for high pressure compressor or turbine discs (for example) throughout a flight cycle would look similar in shape to TET-time plots.

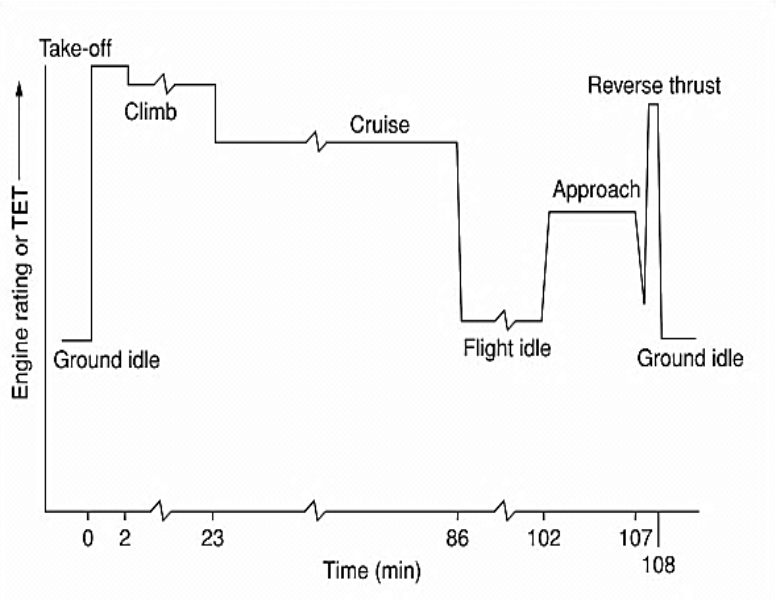


Figure 1-2: Variation of the turbine entry temperature (TET) and associated stress states of various components as a function of time for a typical flight cycle of a civil aircraft [1].

Most empirical and analytical modelling carried out to understand the response of a component to such temperature and stress variations during in-service operation seek to represent the "take-off" and "climb" segments of the waveform above by a single application of high load at high temperatures for periods of two minutes to one hour. The process involves unloading to a minimum load and reloading back to a maximum in between each hold period, thereby defining a "cycle". The analysis essentially mimics in-service conditions on test pieces of material in a laboratory or by using analytical software. Such careful analysis is required since these stages represent the most damaging part of the cycle for many components.

The analysis is referred to as *dwell crack propagation* and is reported in great detail in subsequent sections. Essentially, crack growth rates are found to comprise a cycle-dependent

component (which has a da/dN term) due simply to the loading and unloading of high temperature stresses; and a linearly superimposed time-dependent crack growth component (a da/dt term) pertaining to extended hold periods at maximum load. Cycle-dependent crack growth involves the evolution and progression of a small region of plasticity ahead of a crack tip, and time-dependent crack growth comprises both oxygen induced damage zones and creep affected regions ahead of the crack tip, both of which are time-dependent phenomena.

Dwell crack propagation therefore involves interaction between complex and involved phenomena, and analysis pertaining to current generations of nickel superalloys for compressor and turbine disc applications remains lacking. Further investigation and understanding is thus required.

Crucially however, current dwell models within Rolls-Royce plc fail to incorporate the effect of partial unloading from take-off segments to slightly reduced climb stress states. Hence, in order to ensure that methodologies which seek to define the fatigue life of critical components subjected to these types of loading waveforms are appropriate, empirical and analytical understanding of these effects is required.

This programme involves work on high pressure compressor and turbine disc components of the engine. Such components experience large, cyclic stresses and elevated temperatures. Currently, nickel based superalloys are used for this particular application and two alloys (Udimet 720Li and RR1000) are studied in this programme. High pressure compressor discs are “Critical Group A” engine components, the failure of which would have a catastrophic

effect on the engine. They are therefore parts whose failure would cause danger to human life, and as such it is extremely important to ensure that in-service failure is designed against.

Furthermore, the key requirements (with regard to mechanical properties) vary across the section of the disc since different regions of the disc are subject to different loading conditions. Therefore, it is beneficial to have a coarse grained microstructure at the rim, where high temperature creep resistance is required and a finer grain sized microstructure at the disc bore where higher strength and greater fatigue crack growth resistance are required. This gives rise to a "dual microstructure" disc [3, 4], and this programme involves work on fine-grained versions of these alloys.

1.2 Business Context

The project aims to improve lifing methodologies by using experimental data to model real life flight cycles. Crack growth data will be generated for various conditions and will be used to model the total life of the engine components which will in turn be used to calculate inspection intervals. Empirical mechanical testing data will be combined with stress analysing finite element modelling to better understand modes of failure. Linear superposition models of creep and fatigue interactions are currently inaccurate and unnecessarily conservative. Inspection and maintenance costs can be cut significantly if better lifing methodologies can be confidently created.

Secondly, as previously stated; jet engine efficiency is improved by increasing the TET. The efficiency of the engine, η is defined as the ratio of input heat energy to the work output which is based upon an idealised model, the Carnot cycle:

$$\eta = \frac{W}{Q_{\text{in}}} = 1 - \frac{T_2}{T_1}$$ ..... Equation 1

Where W is work output in Joules, Q is the input heat in Joules, T_1 and T_2 are the input and output temperature in Kelvin respectively [5].

It follows that by increasing the turbine entry temperature (TET), T_1, the overall engine efficiency will also increase as more thermo to mechanical energy conversion can take place [6]. The demand for an increased TET is one of the main driving forces for development of superalloy discs.

It therefore follows that materials with excellent high temperature capabilities must be designed and fully understood, for it is only with the development of such materials that engines could operate under higher TETs. Current work has been to test nickel disc material behaviour at temperatures up to 675˚C. Fuel consumption and associated costs can be cut by improving understanding of fatigue behaviour at such temperatures.

2. Literature Review

2.1 High Pressure Compressor and Turbine Discs

The jet engine comprises a shaft which drives a series of discs which are in turn connected to a series of blades. It is the job of the discs to transfer rotational force from the shaft to the compressor blades (or vice-versa in the turbine), and to hold the blades in place. The stresses and temperatures experienced by the discs reach a maximum in the compressor section of the engine, where the air / fuel mixture is at its highest pressure and temperature. At the front end of the engine, the fan blades are large which means that the discs have a small rim radius but large geometries in the engine axial direction. In the compressor section the blades are much smaller which necessitates a large rim radius for the discs.

The high pressure sections represent the most demanding conditions in terms of stress and temperature in which these components operate. Discs need to be designed to survive not only the mechanical stresses but those arising from temperature gradients. Therefore compressor discs must be manufactured using materials with excellent high temperature mechanical properties, including good resistance to fatigue crack initiation and propagation, and good creep resistance.

It is also important for design and lifing engineers to have a good understanding of the types of stresses and temperatures which may be induced in service. The centrifugal load on the disc is proportional to the mass, radius and the square of the angular velocity. A rotating disc will attempt to “grow” under this force and as such both circumferential (hoop) and radial stresses are induced. These stresses have complex relationships with respect to radius and

appropriate geometries must be chosen to minimise both types of stresses, taking in to account the various conditions of the compressor sections.

It is also important to understand the way in which thermal energy can induce stresses in the disc sections. Thermal stress components will increase the total hoop stress at the bore but decrease its magnitude at the rim. A thermal radial component is also induced which increases the total radial stress at the rim. It should also be noted that high temperatures in the high pressure discs will result in creep deformation and growth of the disc; and it is important to ensure that this deformation does not allow blade tip rubbing and damage. Typically a limit of 0.1% strain is set [7].

It is also extremely important to take in to consideration the various types of stress raisers which exist within the geometry of a disc. These include the root section, the shank neck and the rim section. Crucially, these also include any defects present which may occur as a result of handling damage or in-service operation, including and especially fatigue crack growth which may propagate from surface damage regions or sub-surface initiation sites. The design specifications for most components include geometric discontinuities such as holes, keyways, notches or other changes in cross section. Since stress is equal to force divided by area, where a force is concentrated over a smaller area, the resultant stresses will be higher and therefore require further correction and analysis within a lifing model. This issue is particularly important in both the low and high pressure sections of the jet engine, as the turbine blades connect to the discs via a dovetail joint. To take the dovetail joint root as an example, the contact stresses here are extremely high and require careful analysis.

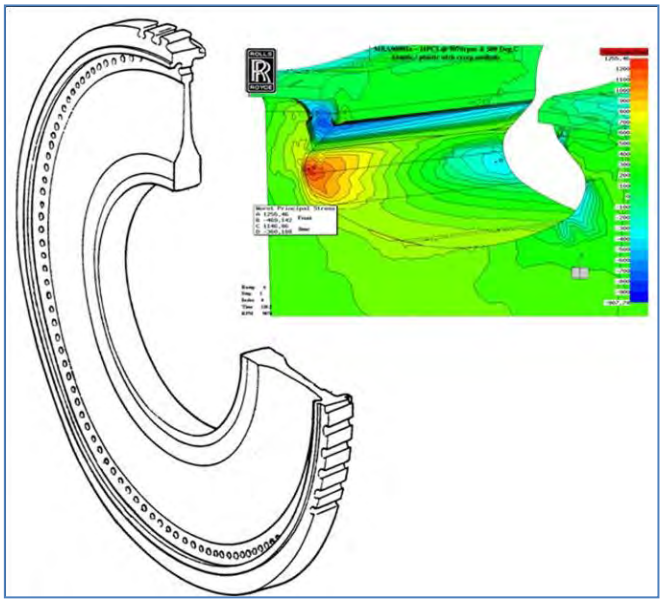


Figure 2-1: Stress contours shown around a dovetail rim feature [7].

Fatigue properties are therefore sensitive to a number of surface conditions, including roughness and surface finish. Clearly the presence of a crack will have a detrimental effect on fatigue performance, and poor surface finish has the same effect and for the same reasons. Small scratches, dents or surface cracks act as stress concentrations and have a profound effect on fatigue life, since they provide crack initiation sites. Therefore, fatigue performance is improved dramatically by carefully machining a component to an extremely high standard. However, problems arise within a lifing methodology when plane sided laboratory specimens for total life testing are polished to a higher standard than is possible to achieve with in-service components, and therefore correction factors should be applied when using total life laboratory data to life such components.

Another way to improve fatigue life with surface treatment is to purposefully introduce residual compressive stresses in to the surface of the material. Shot peening is an example of this type of practice, and involves bombarding a component with small, hard spheres of material. The surface layers will deform plastically and hence a residual stress is induced on the surface of the material. This stress acts as an imposed compressive mean, which reduces the tensile phase of the nominal fatigue cycle, which greatly improves the fatigue life of the material. It must be remembered however, that compressive residual stresses on the surface are compensated for by tensile stresses within the component. The technique only improves fatigue life if the main crack initiation sites are likely to be on the surface. For example, if the material is known to contain brittle intermetallics which might cause fatigue crack initiation beneath the surface and throughout the material, shot peening is likely to encourage the initiation of such cracks within the component.

The maximum in-service stresses and temperatures experienced by high pressure compressor and turbine nickel disc components are around 500 – 700 MPa and 600 – 700°C respectively. For some military applications the conditions are even more extreme. Therefore empirical mechanical testing and analytical modelling undertaken by this programme will concentrate between those conditions, in order to gain a better understanding of how these materials behave in service.

As discussed previously, these components are described as “critical” in that their failure would result in potential harm to human safety. The failure of a disc or blade in any section of the jet engine while it is in service is likely to cause catastrophic damage to the engine and

possibly the aircraft itself. Rolls-Royce plc. has an excellent track record in terms of safety and one of the reasons for this is that they employ highly stringent statistical and safety factors. The general standard is that there must be no greater risk than one disc failure per 2 x 10^6 flight hours [7].

As with many other aspects of lifing methodologies, this type of analysis is carried out mathematically. Firstly, the data obtained is assumed to be distributed on a log-normal basis, and a probability density function is defined:

$$f(x)\frac{1}{\sigma\sqrt{2\pi}}EXP\left[-\frac{1}{2}\left(\frac{x-\bar{x}}{\sigma}\right)^2\right] \quad \text{..... Equation 2}$$

This generates a normal uniform distribution, from which a mean and standard deviation can be calculated. A declared safe life is calculated by applying these statistically derived factors to data which has been obtained by testing, and is applied within European and worldwide specifications.

Furthermore, discs are required to "demonstrate adequate burst strength to protect the system in the event of an overspeed" [8]. Typical engines in service can, for various reasons, be required to run at up to 122% of their maximum designed capacity, and disc rupture must be

prevented in such an event. In such circumstances high tensile strength becomes a key requirement, alongside high temperature fatigue crack growth resistance.

Conventional disc alloy design and development has relied upon the assumption that materials properties are constant with respect to time during high temperature cyclic loading in-service conditions. Current disc alloys have therefore been designed within stress and temperature regimes which assume the effects of in-service time-dependent creep and oxidation phenomena are insignificant. These assumptions are now widely reported to have been erroneous and hence greater understanding of conventional alloy response to time-dependent phenomena such as creep and oxidation interactions during in-service high temperature high stress states is now both crucial and critical.

2.2 Nickel Based Superalloys

Superalloys are materials which retain their mechanical properties at elevated temperatures, "often in excess of 0.7 of the absolute melting temperature" [9]. In order to create a material with these characteristics one must carefully select a base-metal, and the choice is limited. Titanium alloys are desirable since they have a low density and hence superior specific properties. Nevertheless their poor resistance to oxidation at temperatures above 700°C render them unsuitable for high pressure compressor and high pressure turbine applications. High-strength ferritic steels are another desirable option, since they have significantly lower economic impact. However, for modern high temperature applications nickel is (to date) the only viable option.

Nickel has a melting point of 1453°C, and a reasonably low density (8.88 kg m^{-3}). Its crystal structure is face-centred cubic (fcc), which makes it capable of being highly alloyed (in solid solution as well as for strengthening second phase precipitates). It has a relatively low coefficient of thermal expansion (13.3 x 10^{-6} K^{-1}), which minimises thermal stresses in components used at high temperatures. It has a relatively high thermal conductivity (~60 W/mK) which enables components to cool quickly, both from in-service temperature states and from processing and heat treatments. It has relatively good resistance to environmental degradation due to oxidation when alloyed with chromium or aluminium, a crucial requirement since high pressure compressor and turbine discs operate in high temperature, oxidising environments. Finally, it is also relatively abundant in supply and hence has acceptable cost.

The primary drive for Ni-based superalloy development has conventionally centred on improving and developing mechanical properties. Recent trends however have been to improve resistance to oxidation, as TETs continue to rise. This brings new challenges since alloy design for oxidation resistance is generally detrimental to high temperature mechanical properties.

2.2.1 Microstructure

A Ni-based superalloy consists of nickel alloyed with aluminium or titanium to give a two phase microstructure – a gamma (γ) unordered face centre cubic matrix with gamma prime (γ') ordered fcc precipitates. γ' exists in three forms, primary, secondary and tertiary (defined by how and when they form). Primary γ' forms first (at higher temperatures) and forms on grain boundaries of the γ phase. Primary γ' therefore pins grain boundaries upon cooling from heat treatment, preventing grain growth and refining grain size whilst also contributing to grain boundary strengthening [10]. Further intragranular γ' precipitates on cooling and exhibits a bimodal distribution in particle size. In modern superalloys such as RR1000, γ' particles between 90-200 nm are typically defined as secondary γ', and particles of < 90 nm are defined as tertiary γ' [11]. Secondary and tertiary γ' precipitates are therefore much smaller and more finely dispersed when compared with primary γ' precipitates. It is the secondary and tertiary γ' precipitates which give the material excellent mechanical properties at elevated temperatures.

The γ' phase is essentially an ordered $Ni_3(Al,Ti)$ fcc structure with nickel atoms at the faces of the fcc unit cell, and aluminium or titanium atoms at the corners (Figure 2-2). The nickel γ phase is also fcc in structure, and is almost totally coherent with the γ' phase. γ' displays a strong degree of chemical order since the Ni-Al bonds are preferred rather than Ni-Ni or Al-Al bonds in the crystal structure.

Plastic deformation occurs by defect or dislocation movement; hence the resistance of a crystal structure to such movement represents the macroscopic material resistance to plastic deformation. The γ fcc system has 12 slip systems upon which deformation can occur: the {111} planes, and the <110> directions. Furthermore the matrix becomes easier to deform with increasing temperature since the dislocations can move non-conservatively out of their slip planes, a phenomenon known as dislocation creep by climb.

Generally, there are three types of crystallographic defects: planar, line and point defects. At high stresses these defects must move through the γ' precipitates. Since the crystal structure of γ' is ordered, the movement of a planar defect through the crystal must disorder (or "anti-order") the crystal structure, creating what is known as an anti-phase boundary (APB). An APB comprises of a series of like atoms aligned. This is associated with a substantial energy penalty [1] and hence requires a large amount of stress. It therefore gives the material excellent strength (and associated) properties. Reed notes that such defects must move through γ' in pairs, on the {111} plane, "anti-ordering" and reordering and these are known as "super dislocations" [1].

At further elevated temperatures cross slipping is activated. Here slip occurs on the {010} plane, which requires even greater stresses. Hence yield strength actually increases as temperature increases, until a critical temperature is reached [12], when the rate at which dislocations are able to diffuse (due to the high temperatures) exceeds the rate at which they are blocked.

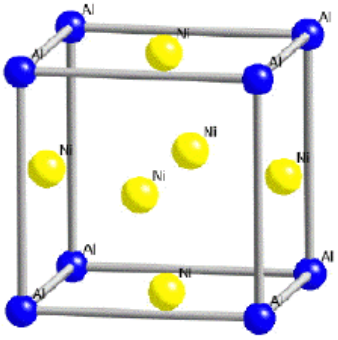


Figure 2-2: The unit cell showing the crystal structure of γ' [9].

A number of other phases are also formed in nickel superalloys and particularly during service ageing. The most common of which is the topologically close packed (TCP) sigma (σ) phase which comprises a complex crystal structure giving plate like microstructures. These phases therefore reduce rupture strength and ductility [13] and hence particular alloying elements are introduced to limit their formation (discussed below).

2.2.2 Effects of Alloying Elements

Computational alloy design has, in recent developments, allowed for relatively informative predictions and a good understanding of the effect of individual alloying elements. Nevertheless an empirical approach has been successful in determining more general effects:

- Cobalt reduces the solubility of both Al and Ti in Ni. This allows relatively high volume fractions of γ' and increases stacking fault energy. It therefore increases yield strength and creep properties. Co also reduces the temperature at which γ' goes in to solution, which allows for easier heat treatments; a consideration which is especially important when considering sub-solvus heat treatments for fine-grained microstructures.

- Chromium is added primarily to improve high temperature oxidation resistance via the formation of the stable oxide Cr_2O_3. It also provides some solid solution strengthening.

- Aluminium also provides high temperature oxidation resistance improvement since its oxide Al_2O_3 is also relatively stable. However its primary role in nickel based superalloys is the formation of γ', the principal strengthening precipitate.

- Titanium is also added to form γ', but it also forms carbides which strengthen disc alloys. Its inferior oxidation properties however have lead to the minimisation of Ti addition in current generations of nickel based superalloys.

- Refractory elements such as molybdenum, tungsten and rhenium all partition strongly to the γ phase [1, 14]. They therefore provide solid solution strengthening and carbide formation. Re has very slow diffusion rates in Ni [15] and a very high partitioning ratio from γ:γ', concentrating on the γ phase. It is the addition of around 3wt% Re which distinguishes second generation superalloys from their predecessors.

- Ta is added for solid solution hardening. It is also a refractory metal strengthener although unlike Re it partitions preferentially to the γ' phase.

- Boron, zirconium, cerium, magnesium and hafnium have all been added as grain boundary carbide formers which improve creep properties.

Table 1: Roles of various alloying additions in various Ni-based superalloys [10].

Alloying Element	**Co**	**Cr**	**Mo**	**W**	**Re**	**Ru**	**Nb**	**Al**	**Ti**	**Ta**	**Hf**	**C,B**	**Y,La**
Solid Solution Strengtheners	x	x	x	x	x	x				x			
Precipitation Strengtheners							x	x	x	x			
Oxidation Resistance		x						x			x		x
Sulphidation Resistance		x											
Carbide / Boride Formers		x	x	x					x	x	x	x	

2.2.3 Processing

High pressure compressor and turbine discs are machined from superalloy forgings. These forgings are processed by two possible routes: conventional ingot metallurgy (resulting in what is termed "cast and wrought" material) or powder metallurgy (PM) [1, 16]. Powder processing enables the production of a more highly alloyed material, and it produces material

with a more uniform and tightly controlled microstructure. Nevertheless it is a more expensive process and hence its application is limited.

2.2.3.1 Cast and Wrought

The conventional cast-and-wrought process of manufacturing turbine disc components is typically applied in the fabrication of alloys with relatively low levels of alloying elements. This method involves the thermal-mechanical working of material produced by three melting stages: vacuum induction melting (VIM), electro-slag remelting (ESR) and vacuum arc remelting (VAR) [1, 17]. This combination of processes is also known as triple melting, which is required to refine superalloys by removing impurities. These melting processes are followed by annealing to improve the homogeneity of the material. Finally, the billet is thermal-mechanically worked before being forged into the desired disc shape [1].

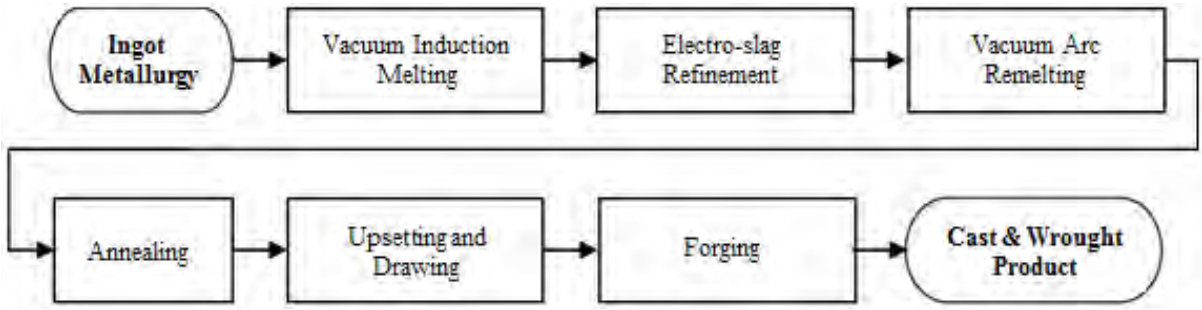


Figure 2-3: Conventional ingot metallurgy processing route.

The drawbacks to this processing method are those inherent in any casting process, namely chemical segregation and porosity. Hence this route is unsuitable for processing materials which are highly alloyed (such as RR1000).

2.2.3.2 Powder Metallurgy

Powder metallurgy is a considerably more complex and involved process and hence incurs greater cost. Nevertheless this cost is balanced by the manufacture of high integrity alloys with significantly lower concentrations of inclusions, porosity defects and therefore with superior and more consistent mechanical properties.

VIM is followed by remelting and inert gas atomisation to produce an uncontaminated metallic powder. This powder is then sieved in order to remove any inclusions or segregations which may have been introduced in processing thus far. This clean powder is then consolidated, degassed and sealed. Heat and pressure are then applied to the powder by hot isostatic pressing (HIP) and the metal powder is extruded before being forged into shape.

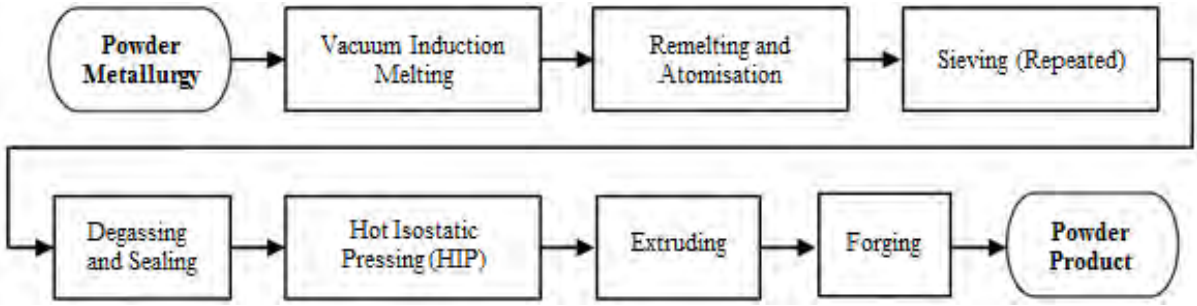


Figure 2-4: Powder metallurgy processing route.

The PM process produces strong alloys with homogeneous microstructures and uniform properties throughout due to the elimination of macrosegregation and the development of a fine grain size [1, 17, 18]. The drawbacks however are the increased cost and the time consuming nature of the process.

2.2.4 A Short History of Disc Alloy Development

For jet engines designed and developed in the 1950's, turbine entry temperatures were relatively low. Hence the requirements for turbine and compressor disc components could be met by forged steel alloys. Such components were relatively easy to manufacture and thus had lower economic impact than their modern counterparts. Nevertheless their strength and fatigue resistance were appropriate for the conditions in which they were required to operate, and the alloys were extensively used at temperatures up to 450°C. These alloys typically consisted of a ferritic, 12% chromium composition, and a typical example might be FV535 which was in wide operation in Rolls-Royce Avon engines [8].

By the 1960's however, turbine entry temperatures and therefore associated engine efficiency and capacity had increased due to the development of Ni-Fe systems such as Inconel 718 and Nim 901 [8]. The austenitic crystal structure of the alloys were stabilised due to higher Ni weight percentages and so had superior and more stable properties at elevated temperatures.

Finally, with the development of the first generation of Ni-based superalloys such as Waspaloy and Rene 95 the high strength γ / γ' microstructure systems were discovered and both gave excellent strength and fatigue crack growth resistance at temperatures up to 600°C. Subsequent alloy design has focussed on increasing the concentration of γ' forming elements such as Al, Ti and Ta, and refractory elements such as Mo, W and Ta.

Chemical compositions for a selection of typical conventional turbine disc alloys are presented in Table 2 (from [8]):

Table 2: Nominal chemical compositions for a range of conventional turbine disc alloys, weight %.

Alloy	Ni	Fe	Co	Cr	Mo	W	Ta	Al	Ti	Nb	Zr	Hf	C	B
FV535	1	Bal	5.0 to 7.0	9.8 to 11.2	0.5 to 1.0	--	--	--	--	--	--	--	0.05 to 0.12	--
Nim901	40.0 to 45.0	Bal	1.0	11.0 to 14.0	5.0 to 6.5	--	--	0.35	2.8 to 3.1	--	--	--	0.1	--
IN718	Bal	19.0	0.4	18	3	--	--	0.5	1.0	5	--	--	0.03	0.003
Astroloy	Bal	--	17.0	15.0	5.3	--	--	4.0	3.5	--	--	--	0.06	0.03
Waspalloy	Bal	--	13.5	19.6	4.3	--	--	1.37	2.95	--	0.06	--	0.019	0.0063
Rene95	Bal	--	8.0	13.0	3.5	3.5	--	3.5	2.5	--	--	--	0.06	0.01

2.2.5 Udimet 720Li

Udimet 720Li (low interstitial) is a high strength nickel based superalloy currently in service for compressor and turbine disc applications. It is adapted from the original U720 composition and has reduced chromium, carbon and boron content compared to its predecessor [19]. It has been in service for many years and hence there is a wide database of fatigue behaviour for the alloy. The material is available in cast and wrought or powder processed forms, the former being preferred for fine-grain, reduced cost applications. This in turn means that it is difficult to precisely control microstructure. For this reason a large

distribution of grain size and γ' size is observed which gives the material varied mechanical and environmental properties.

The reduced chromium content avoids σ phase formation so that mechanical properties are less likely to degrade during high temperature service. The reduced carbon and boron content enables secondary melting techniques to be used for ingot conversion prior to forging, avoiding the need for costly powder processing [11].

The typical heat treatment used for fine-grained Udimet 720Li is a sub-solvus solution heat treatment at 1080-1100°C to eliminate the presence of γ grains whilst keeping γ' out of solution. On cooling to 650°C the unsolutioned γ' prevents γ-grain growth by the action of Zener pinning [20]. A two stage ageing treatment is then carried out, first at 650°C for 24 hours then at 760°C for 16 hours. The result is a fine grain size of between 10 -12 μm with γ' decorating the grain boundaries [11].

This fine-grained material is tested in the current programme. Table 3 (Section 3.1) gives nominal chemical composition limits. Presented in Figure 2-5 is an example micrograph to show the microstructure of fine grained Udimet 720Li as etched by Kalling's reagent.

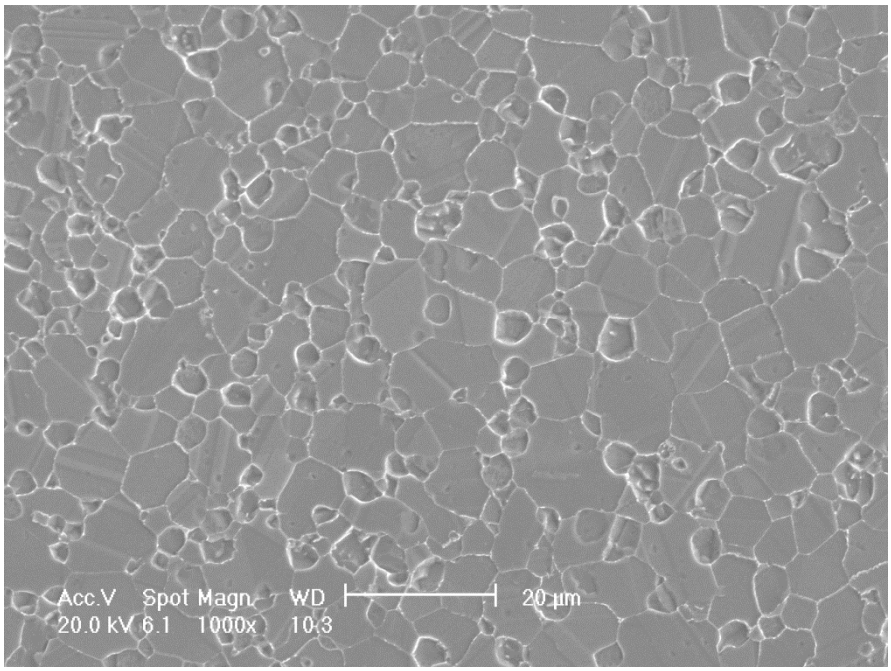


Figure 2-5: Example micrograph showing γ grains and primary γ' precipitates in a typical fine-grained Udimet 720Li microstructure, etched using Kalling's reagent.

2.2.6 RR1000

RR1000 is a "new generation" superalloy which has been developed by Rolls-Royce plc. for use in their latest Trent 1000 engines, and indeed in subsequent engine designs. The significant difference between RR1000 and preceding generations of Ni-base superalloys is the powder processing route used to process the alloy. Powder processing enables the production of a finer grained and more consistent microstructure.

Furthermore, powder processing naturally minimises chemical segregation during processing which enables the material to be more heavily alloyed [1]. This enabled the development of a less dense material, with increased temperature capabilities [18].

Table 4 in section 3.1 gives a full list of alloying elements. RR1000 has been developed to carefully balance strength with fatigue crack growth resistance [18]. Aluminium and titanium have been alloyed to give a 45% weight fraction of γ'. Tantalum is used to give strength, but limited to 2.15 weight % in order to maximise fatigue crack growth resistance. 15 weight % chromium gives oxidation resistance. Small levels of boron, carbon and zirconium improve high temperature creep properties [18]. Various carbide formers are used for grain boundary strengthening, including hafnium.

The typical grain size of fine-grained RR1000 is 5 – 9 μm which is considerably finer than Udimet 720Li (10 – 30 μm) and with considerably less variation. This reduces variation in the fatigue life of the alloy, which improves confidence in lifing methodologies generated from fatigue data calculations. A micrograph detailing typical γ grain and primary γ' precipitate morphologies is presented in Figure 2-6.

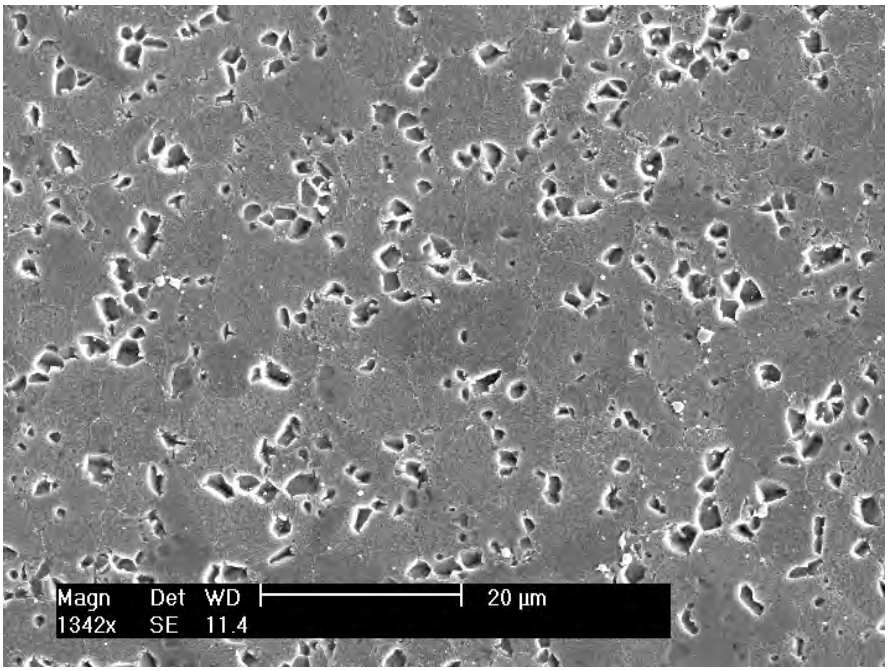


Figure 2-6: Example micrograph showing γ grains and primary γ' precipitates in a typical fine-grained RR1000 microstructure, etched using Kalling's reagent. Note the finer grain size and primary γ' precipitate sizes, and the subtle differences in morphologies when compared with cast and wrought fine-grained Udimet 720Li.

2.3 Fracture and Fatigue

2.3.1 Introduction

Fracture by fatigue occurs when a material is subject to a cyclic stress. "A metal subject to a repetitive or fluctuating stress will fail at a stress much lower than that required to cause fracture on a single application of load" [21]. This phenomenon occurs because although nominal design stresses throughout a given engineering component are likely to be well below those which would cause the material to yield, localised stresses around a notch, defect or fatigue crack can be extremely high. In such circumstances general yield is unlikely to occur, but a small amount of highly localised plastic deformation can occur around a notch or scratch or ahead of a fatigue crack tip. It follows therefore that precise understanding of how these cracks grow through a material during service is extremely important, especially for safety critical components such as high pressure compressor and turbine discs in the jet engine.

2.3.2 Linear Elastic Fracture Mechanics

The presence of a defect, either a pre-existing crack from a manufacturing process or a metallurgical inclusion, can significantly reduce the life of a component or structure by providing a large enough stress intensity to initiate a fatigue crack. Once a fatigue crack begins to propagate, the useful life of the component is consequently dependent on the rate at which the fatigue crack will propagate through the alloy [22]. Generally speaking there are two types of fatigue problems: those whose total life relate to a number of cycles above 10^4

and those whose total life to failure occurs over a shorter number of cycles. Problems described by the former are said to be High Cycle Fatigue (HCF) problems and are particularly relevant for low stress, high frequency applications such as vibration effects on components; for example the shaft of the jet engine. Components which are more highly stressed according to a lower frequency of cycling and which fail under a comparatively lower number of cycles are said to be Low Cycle Fatigue (LCF) problems. Such conditions are experienced by Ni-discs in the jet engine and as such any analysis or prediction of component life uses an LCF approach.

It is very important to model how fatigue cracks will propagate through a component, based on a comprehensive understanding, in order to ensure safe use across its in-service "life". One approach especially relevant to safety critical components is that of damage tolerance. Damage tolerance design begins by accepting that a component may contain a defect or defects such as scratches (from handling or processing damage for example) or metallurgical flaws such as inclusions or cracks for example. Non-destructive testing techniques (NDTs) are used to inspect components for the presence of such defects. If they are not found they are nevertheless assumed to be present as having length a_0, defined by the detection limit of the applied NDT method. It is assumed that these defects are present where stresses are a maximum and that they are oriented to cause the maximum amount of damage (i.e. the worst case scenario). A lifing approach then seeks to define a critical crack length a_{crit} (which would cause failure) and an associated number of applied cycles which would cause the crack to grow from a_0 to a_{crit}: i.e. the number of cycles to failure (N_f).

It is therefore necessary to model the extent to which stress, crack length and associated crack geometries induce damage around a crack tip. The parameter known as the linear elastic stress intensity factor, K, is used in fracture mechanics to describe the severity of the local stress state surrounding a crack. In a large, semi-infinite specimen subjected to a uniform tensile stress, the relationship can be approximated by:

$K = Y.\sigma_{applied}(\pi.a)^{1/2}$ ..... Equation 3

Where *K* is the linear elastic stress intensity factor, *Y* is a dimensionless shape factor of the crack, ranging from 0.6 for a semi-circular (thumbnail) contained crack, to 1.12 for a through thickness edge crack, $\sigma_{applied}$ is the applied nominal stress (MPa) and *a* is the crack length (m) [23]. Hence K has units of MPa√m.

Fracture toughness, K_{IC} is the critical value of K at failure which would cause fast fracture and can be established as a material property independent of the test piece size. 'I' refers to mode I crack opening, where a tensile stress is applied normal to the crack surfaces, mode I is the most significant case of crack opening. K_{IC} is determined experimentally by applying a load to a fatigue pre-cracked sample and measuring the crack length at which failure occurred. Hence:

$K_{IC} = Y.\sigma_{applied}(\pi.a_{crit})^{1/2}$ ..... Equation 4

Plane strain conditions are required to limit the local plasticity at the crack tip and to ensure that K_{IC} is test piece size independent. Plane strain conditions prevail when one of the three dimensions of the test piece or component is considerably larger when compared with the other two dimensions. Since strain is equal to the change in length divided by the original length, strain in the plane of the maximum dimension will be close to zero (since the "original length" is close to infinity). Hence the conditions are such that strain only has a value in two of the three dimensional planes. The influence that crack tip stress state has upon plastic zone sizes and geometry is discussed in section 2.3.4; here however it is important to highlight that plane stress conditions prevail near the free surfaces of the test piece. An appropriate test piece width must therefore be employed, in order to ensure that the sample contains a large amount of plane strain tested material with respect to plane stress conditions towards the outer surfaces. This is enforced by applying the following inequality:

$$B \geq 2.5\left(\frac{K_{1c}apparent}{\sigma_y}\right)^2 \quad \text{..... Equation 5}$$

Where B is the test piece width, and K_{IC} apparent is the apparent (tested) value of the fracture toughness of the material. If this inequality is fulfilled, then the K_{IC} apparent becomes the final K_{IC} value. This keeps the system in plane strain, and should give a load trace (against time or displacement) which is linear to failure.

2.3.3 Fatigue

In the 1960s Paris [24] postulated that the *range* of stress intensity factor, ΔK might characterise sub-critical crack growth under fatigue loading in the same way that K characterised critical or fast fracture. After testing a number of different alloys and plotting their crack growth rates against the linear elastic stress intensity factor range on log-log scales, a linear relationship between the two was realised [24]. This is described by the Paris relationship:

$$\frac{da}{dN} = A.\Delta K^m \quad \text{..... Equation 6}$$

Where A and m are empirically derived material constants, and N is the number of cycles.

The number of cycles to failure N_f for a component with a crack of a certain known size can then be predicted by finding the final size which causes fast fracture using Equation 4. Separation of the variables "a" and N and substitution of the range of stress intensity by the equivalent equation in terms of stress range and crack size gives:

$$\frac{da}{dN} = A.\Delta K^m = A(Y\Delta\sigma\sqrt{\pi a})^m \quad \text{..... Equation 7}$$

$$\therefore \int_0^{Nf} dN = \int_{a_0}^{a_1} \frac{da}{AY^m\Delta\sigma^m(\pi a)^{m/2}} \quad \text{..... Equation 8}$$

This approach can be used to predict the growth rate of a fatigue crack and is usually treated as independent of cyclic frequency and cyclic waveform. That is to say, the cyclic stress intensity ΔK exceeds a threshold stress intensity ΔK_{th}, shown in Figure 2-7.

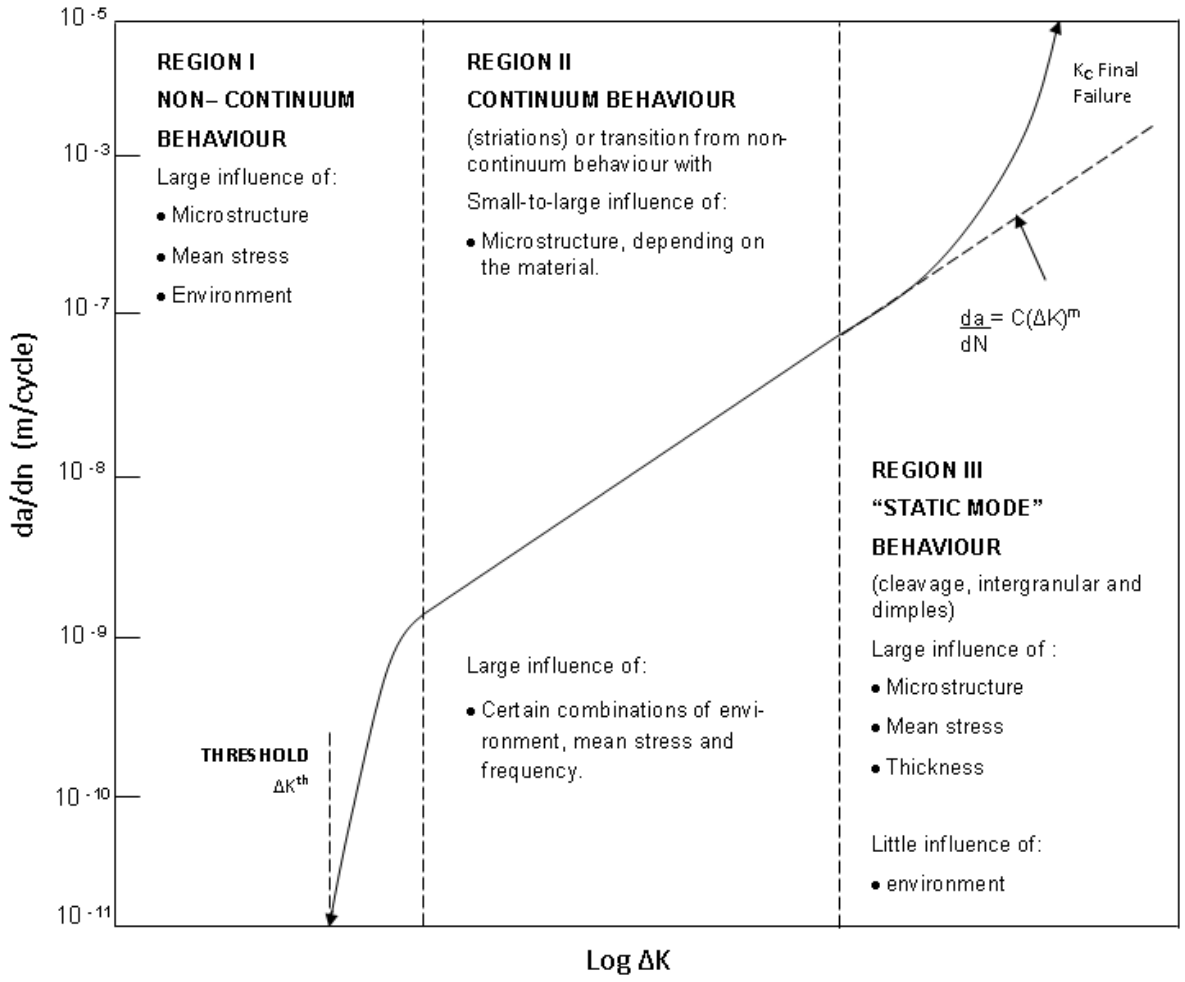


Figure 2-7: Schematic showing the three different regions of fatigue crack growth. Region 1 describes threshold behaviour; region 2, linear Paris law growth; region 3 Fast growth to failure [23].

As highlighted, the graph shows three stages. Region 1 represents near threshold crack growth, which is important for crack initiation understanding (initiation from either a plane sided sample or component, or further initiation from an already present fatigue crack).

Region 3 is largely unimportant for design since crack growth rates are very high, unstable and difficult to predict. Region 2 represents a linear log-log relationship between crack growth rate and ΔK and hence can be used to determine models to predict crack growth behaviour.

Fluctuating stress may occur over a controlled stress cycle, which can be modelled in many different ways. One example of a stress wave form is "trapezoidal" where stress is increased from a minimum to a maximum over a period of one second, held at maximum stress for a given time (known as the "dwell time"), reduced from maximum to minimum over a period of one second, and held at a minimum stress for a period of one second. An "R" ratio is defined as the minimum stress divided by the maximum stress.

This type of stress cycle is a simple model to represent in-service component stress states experienced by high pressure compressor or turbine Ni-discs, where dwell times represent "take-off" and "climb" or the long cruising periods (shown in Figure 1-2), during which disc components experience a high stress. It is necessary to compare and understand how the material behaves when it is subject to varying stress cycles, and dwell periods of up to 3,600 seconds are currently of interest to Rolls-Royce plc. Furthermore it is also important to compare dwell crack growth behaviour with that observed when there is very little time at peak load, since this loading isolates the "cycle-dependent" or fatigue-only component of crack growth (discussed below). For this reason, a trapezoidal stress cycle with a 1 second dwell time is known as "baseline" loading.

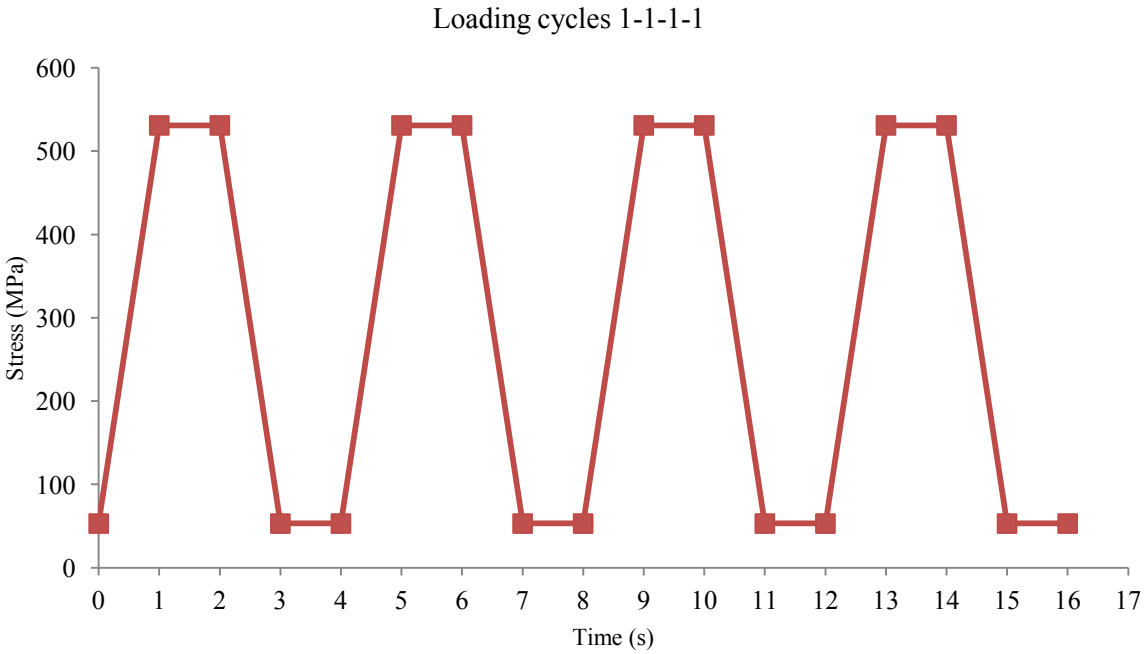


Figure 2-8: Baseline loading cycles with a hold time of 1 second and an R ratio of 0.1

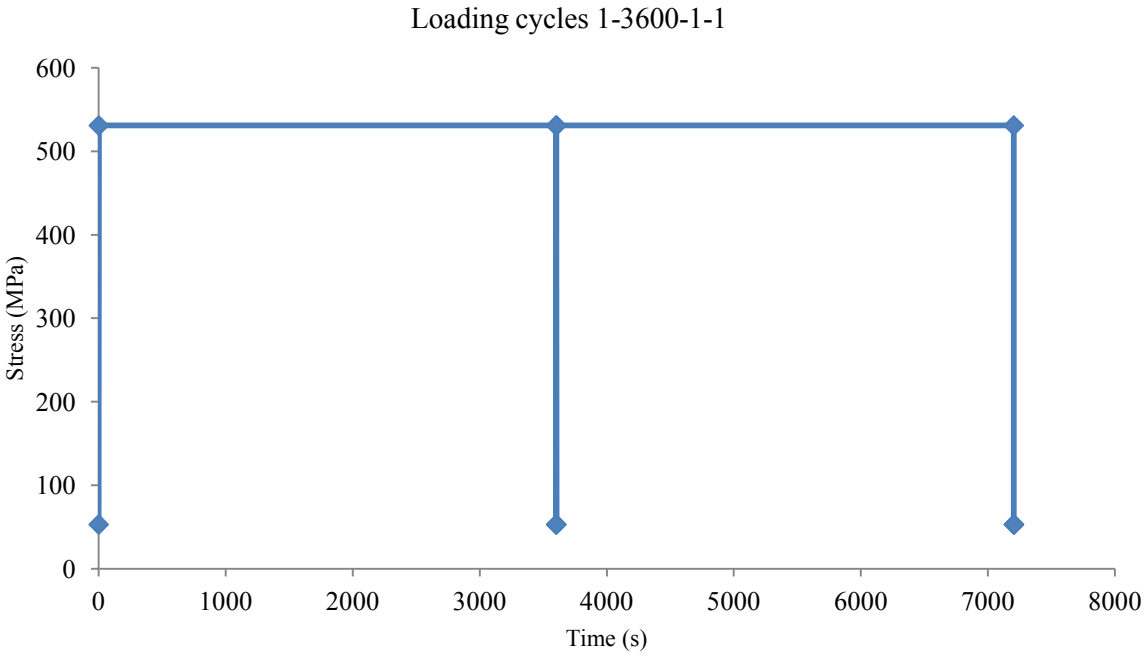


Figure 2-9: Dwell cycles with a hold time of 3,600 seconds and an R ratio of 0.1

Stress cycles such as those represented above can be modelled by using test piece samples of material and a tensile testing rig. A constant amplitude force-controlled waveform is applied to a corner notched test piece, from which a fatigue crack will grow as a result of cyclic loading. It is possible to continuously measure the length of a crack as it propagates through a test piece using the direct current potential drop (d.c.p.d) technique (explained in section 3.2).

Crack growth data obtained in this way can be used to generate crack growth resistance curves where the empirically observed crack growth rate (with respect to number of cycles) is plotted against ΔK on a log-log scale.

It is important to highlight at this stage that linear, Paris law crack growth behaviour is associated with cycle-dependent high frequency (or baseline) loading. Crack growth rates according to high temperature dwell loading comprise several interacting and competing mechanisms and as such, extrapolation in terms of Paris material components is complex and must be made with care. A detailed account of the way in which this understanding may be generated and interpreted is presented in section 2.4.3; "Linear Superposition Lifing Methodologies."

2.3.4 Crack Tip Stress States

Irwin [25] developed a method for estimating the idealised (circular) size of the plastic zone ahead of the crack tip using the stress intensity factor K. Equating the yield stress to the stress perpendicular to the crack tip and solving for the radius gives the expression:

$$r_y = \frac{1}{2\pi}\left(\frac{K}{\sigma_{ys}}\right)^2 \quad \text{..... Equation 9}$$

Where r_y is the radius of the idealised plastic zone ahead of the crack tip, K is the stress intensity factor and σ_{ys} is the yield stress of the material. In plane strain conditions, the triaxial stress state suppresses crack tip plasticity and as such is approximated by an altered version of Equation 9:

$$r_y = \frac{1}{6\pi}\left(\frac{K}{\sigma_{ys}}\right)^2 \quad \text{..... Equation 10}$$

Presented in Figure 2-10 is a schematic model of the plastic zone around a crack tip, including descriptions and expressions for associated stress states.

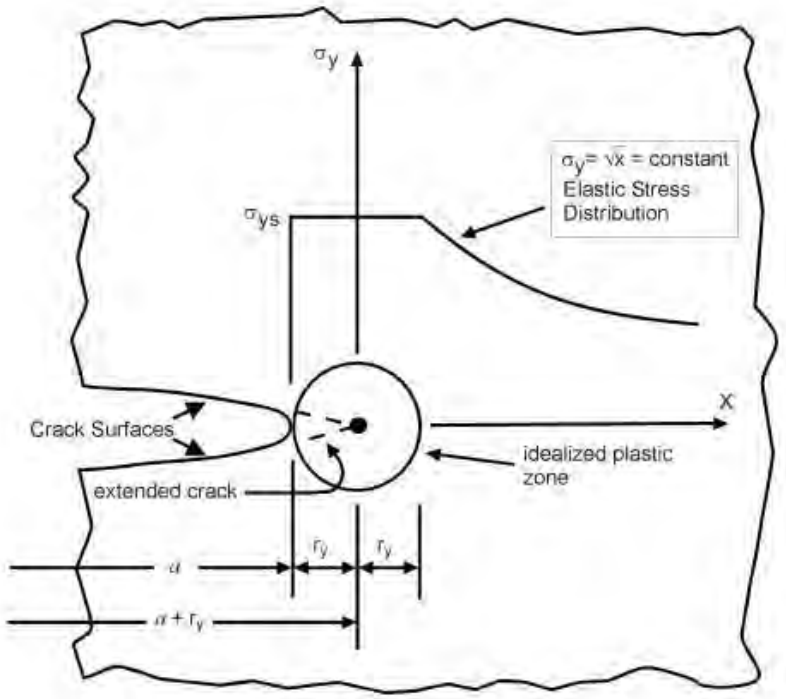


Figure 2-10: Schematic yield model for idealised restricted crack tip plastic deformation and associated stress states [26].

As discussed above, if the extent of the plastic zone size ahead of the crack tip is small with respect to test piece, material or component geometry then a plane strain linear elastic fracture mechanics approach is appropriate. The approach is applicable to most structural problems within the aerospace industry since the "extent of yielding is contained within a small region of the crack tip" in most cases [26].

Ewalds [23] went on to discuss several factors which might influence plastic zone size. The most significant of which is that plastic zone size is strongly dependent on whether plane stress or plane strain conditions prevail (as shown by the approximations above). Larger plasticity occurs under plane stress conditions (which prevail at or near free surfaces of test pieces or components) and smaller plasticity is associated with plane strain conditions. This is represented graphically by Elwads:

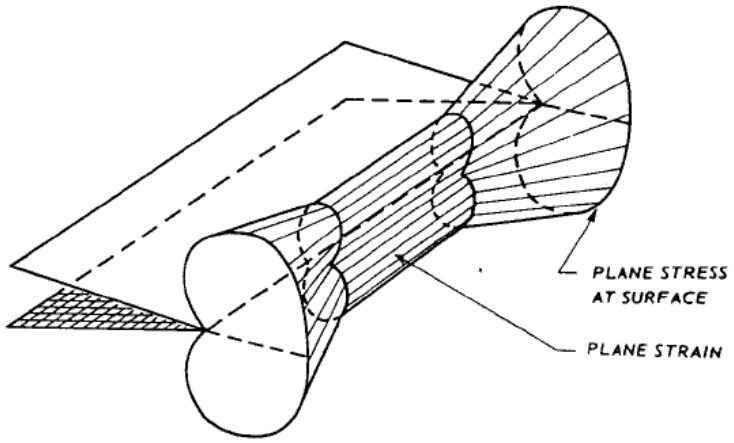


Figure 2-11: Showing plastic zone size for a through-thickness edge crack [23].

Crompton and Martin [27] report that crack tip plastic zone sizes are also a function of temperature, cyclic load frequency and stress intensity factor, K. They discuss complex ways in which crack tip stresses can relax due to the accumulation of creep strain at the crack tip which can cause crack tip blunting, which in turn causes a reduction in plastic zone size as a result.

Luo and Bowen [28] report in studies on crack propagation rates of Udimet 720 that the size of the plastic zone ahead of a crack tip can have a critical effect on the rate and associated mechanism by which a fatigue crack will propagate. They propose that if the associated plastic zone sizes are smaller than a single grain of material and hence are contained within one single crystallographic system; crack paths will be faceted since crack propagation is restricted to a single slip system. If the plastic deformation spans several grains however, it follows that the plastic zone size spans across different slip systems active within adjacent grains and hence planar crack growth occurs. Similar concepts are also confirmed in Udimet 720Li reported by Pang and Reed [29].

2.4 Dwell Crack Growth

A fatigue crack will generally propagate through a material by one of two mechanisms: most commonly straight through the grains (transgranular crack growth) or, under certain conditions along grain boundaries (intergranular crack growth). The way in which an alloy will behave under baseline loading, following a 4 stage trapezoidal loading pattern of 1-1-1-1 seconds, is already well understood: under baseline loading at temperatures of around 650^{o}C, Ni-based superalloys have usually been shown to fracture in the transgranular mode. This can, with care, be interpreted as indicating that a cyclic stress controlled fracture mechanism is dominant.

Under otherwise similar conditions, in air and at temperature, longer dwell periods at maximum load will cause an increase in crack growth rates when compared with baseline loading (often by many orders of magnitude), as a function of dwell period, for many Ni-based superalloys. Furthermore this increase in crack growth rate is usually associated with a full or partial mechanism change from transgranular (baseline) to intergranular (dwell) crack growth.

G. Onofrio's investigations [30, 31] into the fatigue crack growth rate of Udimet 720Li highlights the contribution of the dwell period in a fatigue cycle to the crack growth rate. Five different wave forms were tested at 700^{o}C; long loading and unloading ramp, 30 second dwell, 120 second dwell and a balance cycle. The dwell wave forms (1-120-1-1 and 1-30-1-1) resulted in a crack growth rates roughly an order of magnitude higher than those

observed during long loading testing for the stress intensity factor range investigated (Figure 2-12). Fractography showed complete intergranular fatigue crack growth morphologies during dwell crack growth [31].

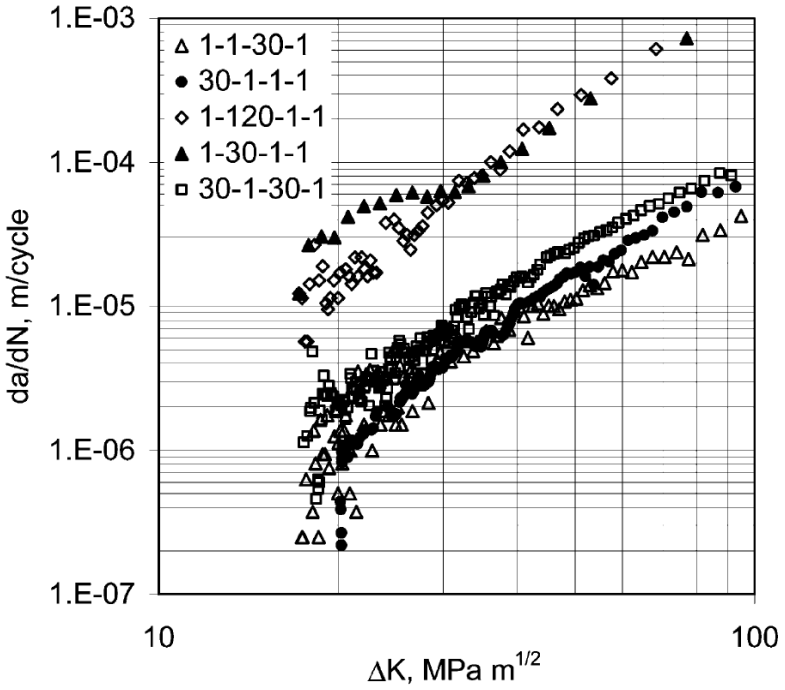


Figure 2-12: Fatigue crack growth rate curves showing the influence of wave shape. R=0.1, 700°C [31].

Since these phenomena are introduced only when time at peak load is increased to a dwell period, crack growth under this regime is often denoted "time-dependent" in that crack growth rates and morphologies are no longer dominated by cyclic fatigue but rather by effects which vary as a function of time at peak load. Time-dependent components of fatigue crack growth are discussed in detail in subsequent sections.

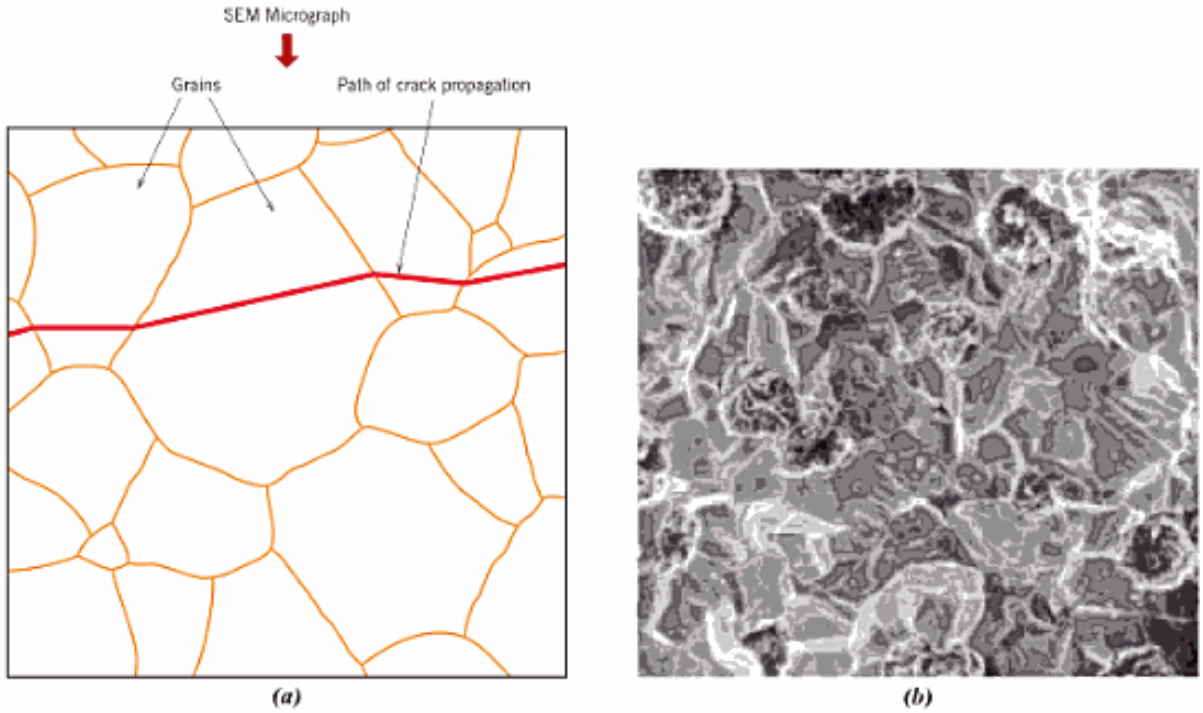


Figure 2-13: (a) Schematic cross-section profile displaying crack propagation through the interior of grains for transgranular fracture.

(b) SEM image showing a transgranular fracture surface [32].

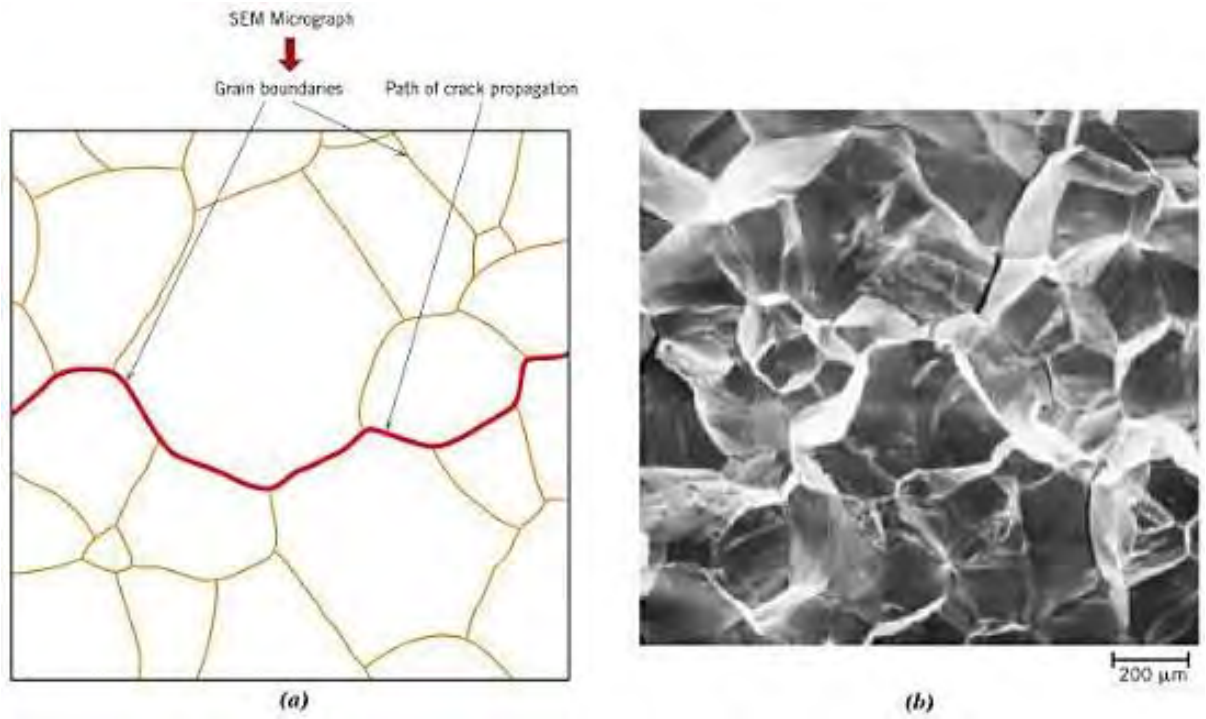


Figure 2-14: (a) Schematic cross-section profile displaying crack propagation along grain boundaries for intergranular fracture.

(b) SEM image showing an intergranular fracture surface [32].

2.4.1 Environmental Effects

2.4.1.1 Stress Assisted Grain Boundary Oxidation (SAGBO)

The first significant evidence to suggest that high temperature dwell crack growth damage is caused primarily by oxygen effects was produced by Coffin [33] in 1973, in his pioneering work "Fatigue at Elevated Temperatures". He compared fatigue crack growth rates measured in air with those in a vacuum for stainless steel alloy A286, noting that those associated with a vacuum were orders of magnitude lower than those in air. Onofrio developed these ideas for Ni-based superalloys [30, 31, 34, 35] and suggests that the increase in crack growth rates due to dwell loading in air occurs as a result of the mechanism change from transgranular

(baseline loading) to intergranular (dwell loading). He reports that this mechanism change is caused by environmental degradation due to the combination of high stress and high temperatures which facilitates the (time-dependent) ingress of oxygen by grain boundary diffusion. This may cause grain boundary oxidation and subsequent embrittlement, a mechanism that has been termed "Stress Assisted Grain Boundary Oxidation" or SAGBO [36, 37].

Pure nickel has relatively poor resistance to oxidation but when alloyed with chromium the more stable Chromia (Cr_2O_3) can form. The oxide formation depends upon the partial pressure of oxygen, and at atmospheric pressure Cr_2O_3 initially forms relatively slowly, which allows the formation of less stable oxides from less noble elements such as Ni to form first. Therefore time is needed for the Cr_2O_3 layer to reach the required thickness for it to be fully protective (Andrieu, studying alloy IN718 [38]). Furthermore whether passive or otherwise, these oxide wedges are extremely brittle, and thus are susceptible to cracking as a result of cyclic loading. Hence fatigue cracks as a result of dwell loading propagate more rapidly than those under baseline loading and along grain boundaries.

Oxides have higher specific volumes than their pure metal cousins; their formation therefore induces some crack tip opening. The SAGBO mechanism suggests that this volume expansion is permitted due to high stresses over long dwell periods. Upon unloading and subsequent reloading, these oxides crack; revealing fresh material from which new oxide then forms (at the grain boundaries); and the process continues. Thus the crack propagates along grain boundaries to give the observed intergranular crack growth morphologies. Discussion

of stress assisted grain boundary oxidation must involve careful analysis of both oxidation phenomena and crack tip stress states.

In a study on Ni-based superalloy Inconel 718, Woodford [39] reports that further to metal oxide formation, several other oxidation mechanisms are confirmed ahead of a crack which is subject to sustained loads at high temperature. He writes; “three distinct processes of intergranular embrittlement involving oxidation reactions have been confirmed” [39]. These processes involve the formation of intergranular sulphides, the oxidation of carbides and, as reported above; the formation of metal oxides. In all three cases oxidation occurs preferentially along grain boundaries (as low energy paths for oxygen diffusion), and results in the embrittlement and subsequent local decohesion of grain boundaries under stress.

Knowles [40] and Turan [41] have studied these effects in RR1000 and Turan reports that; “observations of the crack tips of interrupted (dwell) tests have revealed oxidation at the crack tip [41]” which occurs along grain boundaries. Both reports suggest that the two-phase oxide formation model suggested by Andrieu [38] is appropriate, but that it is localised to the crack tip region.

Both reports also suggest that the mechanism is highly dependent upon microstructural factors. Molins [42] found that improved static and dwell crack growth resistance at high temperatures comes as a result of an enhanced capability to relax stresses at the crack tip, following a study on Ni-based superalloy Inconel 718. This capability is attributed to decreased resistance to creep behaviour which in turn can be attributed to microstructural

factors such as grain size, grain boundary modifications and γ' morphology. Creep behaviour of alloys and the dependence upon microstructural factors are discussed in section 2.4.2.

Furthermore, Knowles [40] highlights that materials with greater volume fractions of the chromium-rich sigma phase (which precipitate along grain boundaries) will cause a decrease in dwell crack growth resistance. This is because the grain boundary material is therefore likely to contain reduced amounts of chromium in solid solution and hence have a greater susceptibility to the formation of detrimental oxides. He suggests that "chromium depletion is likely to retard the formation of Cr_2O_3 while having little effect of the formation of NiO" [40]. Hence non protective oxides form faster and at greater depths ahead of the crack tip, resulting in a reduction of crack growth resistance for sustained and high temperature dwell loading.

2.4.1.2 Dynamic Embrittlement

"Oxygen induced environmental fracture does not necessarily require the formation of oxides" [36]. An alternative mechanism to explain the faster rates and intergranular mechanism at these temperatures may be that the diffusion of oxygen in to the grain boundaries under the influence of tensile stress lowers the cohesion of the atomic bonds. These will eventually break under tensile stress, and thus the crack propagates along grain boundaries and at accelerated rates. Both the diffusion of oxygen and decohesion of the atomic bonds are time-dependent; hence the failure mechanism becomes dominant only when time at peak load is increased to a dwell time. This mechanism is known as "Dynamic

Embrittlement" where the driving forces for grain boundary diffusion are the tensile stress acting ahead of the crack tip, the increased diffusivity from high temperatures, and the oxygen concentration gradient.

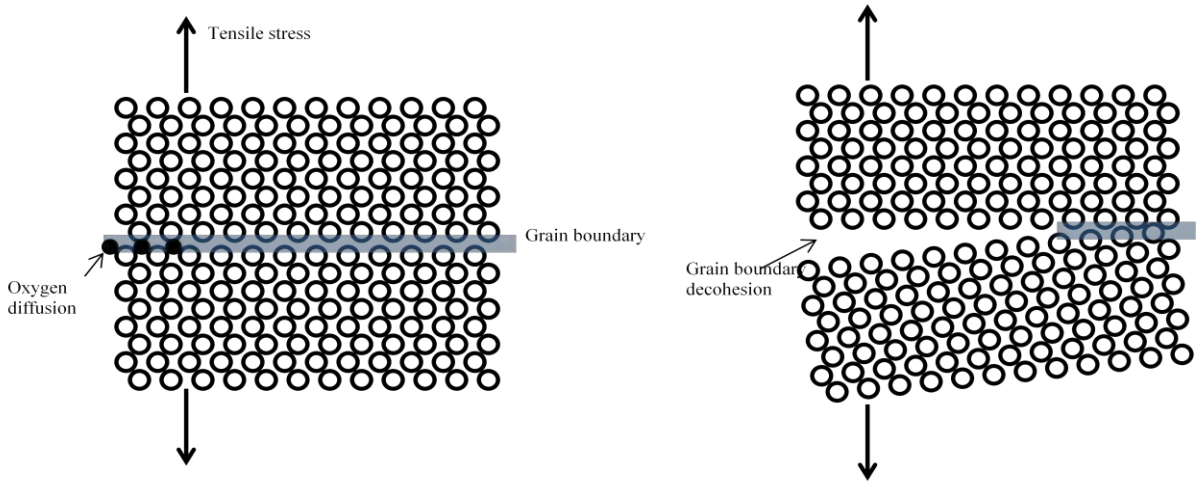


Figure 2-15: Schematic diagram to show the dynamic embrittlement mechanism, from [43].

There are two main distinctions between SAGBO and dynamic embrittlement; the role of stress and the depth of oxygen penetration. The SAGBO mechanism as previously discussed suggests that stress assists in allowing for the volume expansion associated with oxide formation, in essence allowing for and encouraging the formation of oxides. Alternatively, the dynamic embrittlement mechanism suggests that stress assists the diffusion of oxygen in to the grain boundaries and causes grain boundary decohesion.

Further to this distinction; upon first inspection; the bulk oxide formation in SAGBO necessitates the assumption that atomic diffusion of oxygen occurs on the micrometer scale; orders of magnitude higher than those suggested by extrapolating diffusion coefficients for

nickel alloy bulk material. The dynamic embrittlement mechanism suggests that oxygen diffusion is only required on the nanometre scale, which suggests that it may be more scientifically robust.

The issue of oxygen diffusion depth is discussed by McMahon [44] who comments on Ma and Chang's 2003 study on Alloy 783 [45]. Ma and Chang report "damage zones" ahead of a high temperature sustained loading crack tip of around 200 μm which they analyse by applying fast cycles to a test piece immediately after sustained loading and measuring the distance over which the crack grows at relatively high speed before it stabilises to rates normally associated with fast cycle loading.[1] Ma and Chang ascribe the phenomena to stress assisted grain boundary oxidation ahead of the dwell crack tip which McMahon contests as requiring a diffusion range which is too deep. He writes that a more appropriate method to describe the phenomena is dynamic embrittlement since it requires far shorter oxygen diffusion depths.

Ma and Chang reply to McMahon's comments [46] by agreeing that bulk oxide formation on such a scale and depth would be unlikely but that the observed damage zone occurs as a result of selective oxygen attack which causes the crack to propagate along "fingers" or "microcracks"; the extent of which may indeed occur over large distances. These findings are discussed in the light of data gathered in this programme in section 5.5.2.

[1] The method by which oxygen induced damage zones ahead of a dwell crack tip can be measured is also discussed in detail in subsequent sections, using data gathered from this programme.

A third, more subtle distinction between SAGBO and dynamic embrittlement can also be made; namely that oxide formation (suggested by SAGBO) is an irreversible process, while oxygen may diffuse in and back out of grain boundaries if they do not form oxides (suggested by dynamic embrittlement). This phenomenon is explored by Pfaendtner [36, 47] who carried out static load tests in an air filled vacuum chamber which was used to pump down to a vacuum during the testing procedure. The hypothesis was that if crack growth rates slowed immediately on pumping down to a vacuum it could be suggested that the embrittlement process was indeed reversible and therefore not caused by oxides. He found that the crack growth could be "switched on or off very quickly" by introducing or completely removing oxygen from the testing environment.

While the exact mechanism by which oxygen induced damage occurs ahead of a crack tip is still under contest, it is true that oxides *are* observed ahead of a crack tip for specific alloys under specific testing conditions.

Ma and Chang [46] suggest in their reply to McMahon's comments [44] on their original paper [45] that "time-dependent fatigue crack growth at elevated temperatures should be ascribed to stress accelerated grain boundary oxygen embrittlement [46]" – a term which encompasses and fits all of the empirical data reviewed. The term was first used by Lyons [48] who studied these effects on a range of aerospace alloys. The term more eloquently, accurately and appropriately describes the more general mechanisms.

Further to this discussion, and more recently, Evans [49] and Kitaguchi [50] present strong evidence for the formation of oxides such as CoO, NiO, Cr_2O_3, TiO_2 and Al_2O_3 ahead of a crack tip during high temperature sustained load and dwell cracking in RR1000. Both reports indicate that despite the difficulties in terms of precise understanding of the nature and extent of their formation, the conditions under which these components operate do indeed provide a mechanism for these oxides to form. Kitaguchi [50] shows that Nickel and Cobalt oxides form in layers along grain boundary intrusions around 1.5 μm ahead of a fast-growing crack tip (~6 μm s^{-1}). Underlying layers of (protective) Chromia and Alumina are also reported; and Kitaguchi notes that "the layering of oxides within the intrusion followed the expected thermodynamic sequence" [50].

Crucially therefore a link between oxide formation and nominal dwell time (in terms of testing or in-service operation) can be made and used to predict crack growth rates. The rate of oxide formation follows a parabolic relationship; which means that after a given period of time formation of further oxide becomes very slow. Furthermore, if protective layers of oxides such as Chromia and Alumina are formed along the grain boundaries, this will further reduce the rate of oxide formation in these regions. In order for any further oxide formation to occur, the oxides must therefore break or crack; revealing fresh material. This usually occurs either due to the accumulation of creep strain at the crack tip during the dwell time, or upon unloading to the minimum load and reloading back to the maximum (beginning the next stress cycle). Thus high temperature dwell-type stress cycles are shown to be extremely damaging; and crack growth rates pertaining to such conditions are shown to be a function of dwell time, temperature, crack tip stress and microstructure.

Whether by SAGBO or dynamic embrittlement, it is clear that oxygen has a deleterious effect on the fatigue crack growth resistance of these materials when time at peak load is increased to a dwell time. Gayda [51] and Andrieu [38, 42] showed generally that the intergranular crack growth mechanism is driven by environmental factors by comparing dwell crack growth results and fracture surfaces generated in air with those in a vacuum for Astralloy and alloy IN718 respectively. Similar work has also been carried out as part of this programme on RR1000 and the conclusions are similar: fracture surface morphologies are transgranular in a vacuum and crack growth rates are relatively slow when compared with those as a result of similar conditions repeated in air, even at temperature and under dwell conditions. These early conclusions are displayed graphically in crack growth resistance curves by Onofrio [30].

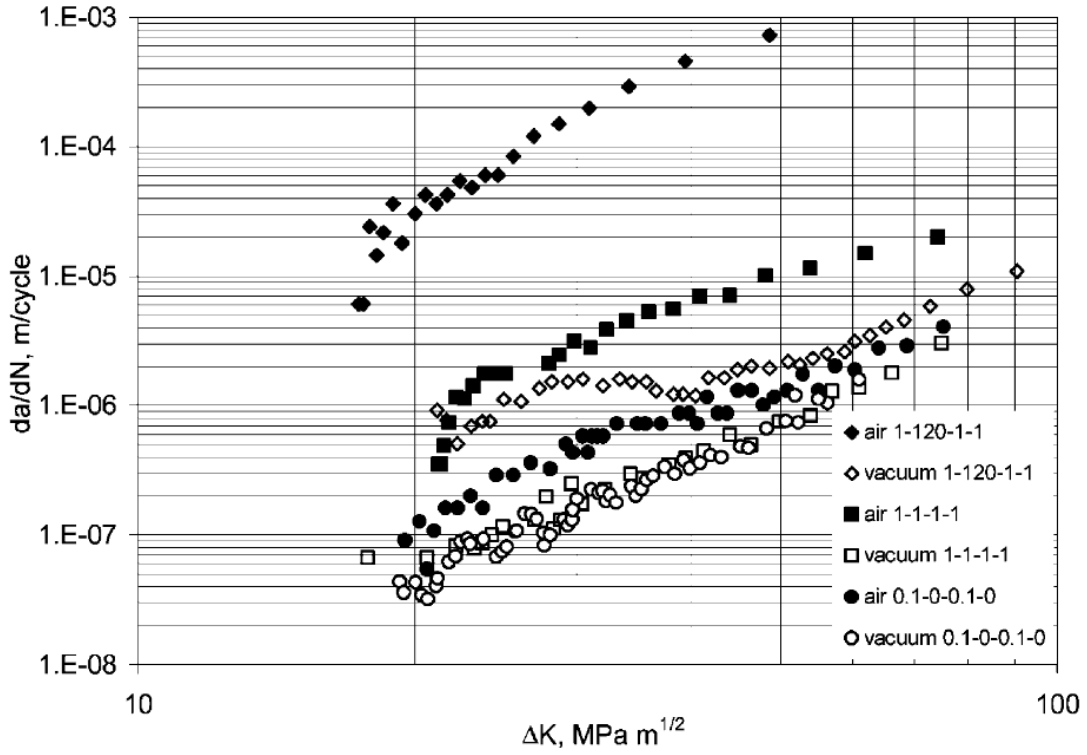


Figure 2-16: Showing Onofrio's work in the influence of loading waveform and environment on fatigue crack growths in a Ni-based superalloy [30].

Assuming that the increase in crack growth rates and associated mechanism change as a result of switching from baseline to dwell loading is dependent, at least in part, on oxygen effects, it follows that factors such as temperature, oxygen partial pressure, time at maximum load, and microstructure will affect this behaviour. An increase in temperature provides more energy for oxygen diffusion for example, and a longer period at maximum load will provide more time for this diffusion to occur. Hence it may be that both variables increase crack growth rates since they allow oxygen to penetrate deeper into the material ahead of the crack tip during each cycle.

It is also likely that oxygen diffusion and subsequent embrittlement is highly selective; and hence strongly dependent upon microstructural characteristics such as grain size, grain orientation, and γ' size, distribution and morphology. Woodford [39] considers attempts to reduce the sensitivity of an alloy to time-dependent oxygen induced crack propagation by increasing chromium content for example; and by careful control of microstructure by heat treating and controlled cooling processes. The effect of microstructure on fatigue crack propagation is also reported by Pang and Reed for Udimet 720Li [29]. Most significantly they found that an increase in grain size gives "benefits in terms of overall fatigue lifetime" [29]. This is explained in part by the fact that materials with a larger grain size will contain a smaller specific amount of grain boundary material, and hence have superior resistance to high temperature oxygen induced intergranular crack growth.

In order to ensure that Rolls-Royce in-house lifing methodologies are safe and accurate and that they are not unnecessarily conservative; a thorough, empirical analysis and understanding of the effect of dwell time, test temperature and microstructure on crack growth rates for fine-grained Udimet 720Li and RR1000 is required.

2.4.2 Creep Effects

Creep is also a time-dependent failure mechanism which competes alongside cyclic and oxygen effects to form the total failure mechanism by which a fatigue crack propagates. Creep is the slow deformation of materials subject to long periods of high stress. The deformation can occur at loads lower than the yield strength of the material and is known to

be more severe in components which are exposed to stresses under high temperatures. Creep is an irreversible deformation mode where final failure occurs by micro void coalescence and grain boundary cracking. Before this final failure, deformation occurs by atomic diffusion, hence at high temperatures the phenomenon is more profound as these conditions cause "greater mobility of dislocations by climb" [21]. Since creep is a diffusion controlled process it follows that it will occur in a time-dependent manner, in a similar way to oxidation effects; it only becomes a competing factor (in terms of low cycle fatigue crack growth rates) when time at peak load is increased to a dwell period. Since dislocations can be pinned by grain boundaries, and given that grain boundaries themselves deform at high-temperature due to creep, it follows that the process is also heavily dependent upon microstructural factors such as grain size and (in the case of Ni-based superalloys such as Udimet 720Li and RR1000) γ' content. Similarly to environmental (oxidation) effects, creep rate also varies according to temperature, as discussed above. A typical creep curve for a metal is given in Figure 2-17:

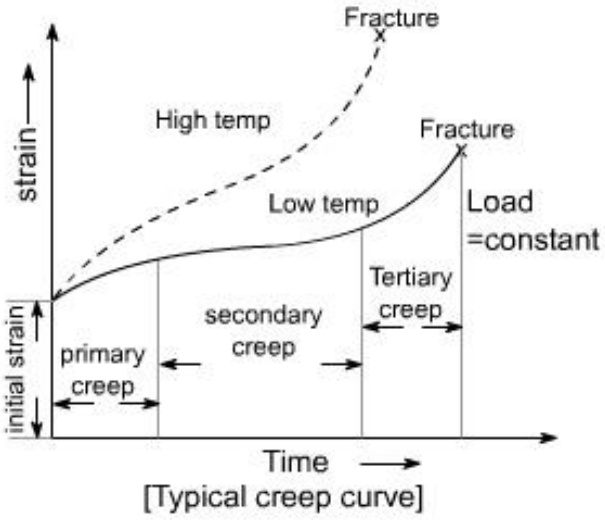


Figure 2-17: A stress-time graph to show typical metal creep behaviour [52], from [53].

Andrade, in 1910 [53] first considered the constant-stress creep curve as a superposition of two separate creep processes; transient creep, where creep rate decreases with time; and viscous creep, where creep rate increases linearly with time. These are superimposed upon an initial "sudden strain" which results from the initial application of load. Andrade went on to derive an empirical relationship for the constant-stress creep deformation curve above including each of these components:

$$\varepsilon = \varepsilon_0 \left(1 + \beta t^{\frac{1}{3}}\right) e^{kt} \quad \text{..... Equation 11}$$

Where ε is the strain, ε_0 is the instantaneous strain and t, β and k are constants.

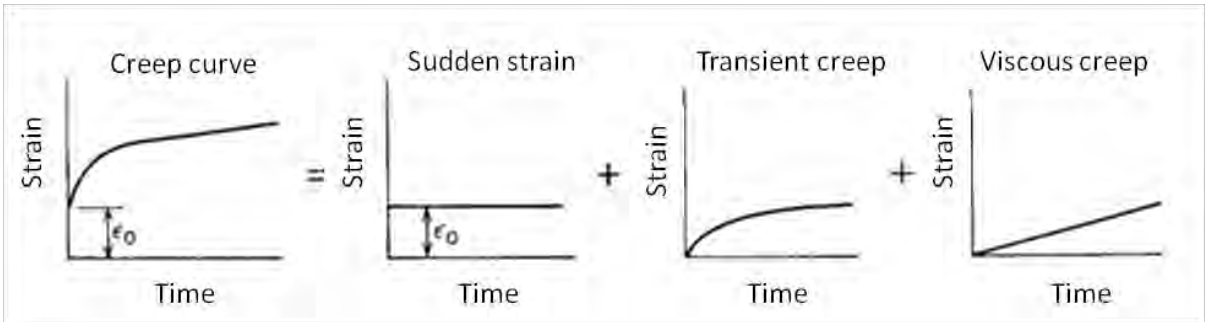


Figure 2-18: Showing Andrade's first analysis of the components of the constant-stress creep curve [21], from [53].

Furthermore, the curve shows three stages of creep, primary, secondary and tertiary. Primary creep is a region of decreasing strain rate with time which is usually because of work hardening (i.e. dislocation-dislocation interactions) hence it represents a region of transient creep. Secondary creep is a period of nearly constant strain rate, which occurs when there is a balance between the rate of work hardening and the recovery process (i.e. dislocation-dislocation annihilation and reorganisation into sub-grains). Tertiary creep is especially pronounced under constant load tests, where (as the cross section of the test piece becomes increasingly small) the material stresses increase rapidly towards the end of the test. This relationship occurs because of external necking, or more usually because of internal damage, and is followed by final fracture.

The typical creep curve for metals will vary in shape as a function of stress. It should be noted that these effects are especially important to consider in aerospace applications since stress varies greatly as a function of time for a number of critical components. Typically components such as Ni-discs are subjected to stresses which follow a cyclic pattern with time and as such stress and strain curves will form hysteresis loops depending upon creep

behaviour such as work hardening effects. Furthermore, the shape of the typical creep curve will vary as a function of temperature; a further consideration which is especially important in aerospace applications. A methodology for the analytical representation of fatigue crack tip stresses as a function of creep is detailed in section 3.4.1. It works in part by considering and applying the effects of stress and temperature, shown in Figure 2-19:

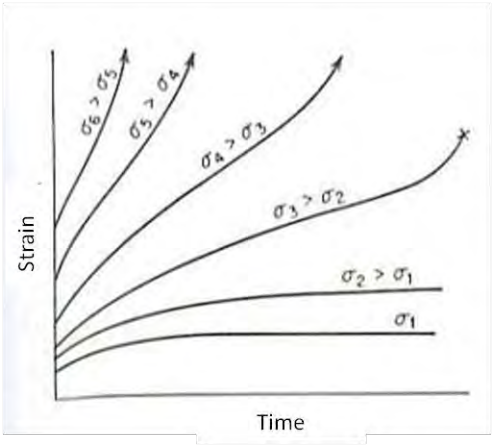


Figure 2-19: Showing the effect of stress on constant-stress creep deformation curves for metals [21].

2.4.2.1 Dislocation Creep:

At high stresses, creep is controlled by dislocation movement. Screw dislocations can cross slip, and edge dislocations must climb, hence vacancy diffusion is required. It takes time for vacancies to diffuse and therefore is a time-dependent mechanism.

Modelling gives the following relationship for minimum creep rate:

$$\dot{\varepsilon}_{ss} \approx B\sigma^{n} e^{-\left(\frac{Q}{kT}\right)}$$

Modelling also shows that n ranges from about 3 to 8 in metals, with 5 most common.

2.4.2.2 Diffusion Creep:

There are two forms of diffusion controlled creep, and these become the controlling mechanisms at high temperatures. Both variations are concerned with stress driven atomic diffusion. Herring-Nabarro creep [54, 55] considers lattice diffusion through grains, which dominates at higher temperatures, and Coble [56] creep considers diffusion along grain boundaries.

For Herring-Nabarro:

$$\dot{\varepsilon}_{ss} \propto \frac{\sigma D_v}{Td^2}$$

Where D_v is the lattice diffusion coefficient and d is the grain size.

For Coble:

$$\dot{\varepsilon}_{ss} \propto \frac{\sigma D_g b}{Td^3}$$

Where D_g is the grain boundary coefficient.

There are no theoretical models which enable the calculation of accurate predictions. Rather, assumptions rely upon experimental data (and relationships derived from experimentation)

and extrapolation of information. However, extrapolation is inherently easier and more reliable with straight line relationships and these relationships are not linear. It is possible to use log relationships of time to rupture and of stress versus minimum creep rate, but for extrapolation of data it is necessary to develop time-temperature compensated parameters. It is also very important to ensure that no microstructural changes will occur over the extrapolation period.

2.4.2.3 Grain Boundary Sliding

Polycrystalline materials, such as those evaluated in this programme of work can also deform by grain-boundary sliding. Here, grains move relative to each other in the direction of the grain boundary as result of prolonged high stresses at high temperatures. Two models to describe the phenomenon have been suggested; the most common considers "sliding along the grain boundary as a bulk movement of the two grains" [21], the second suggests that deformation occurs over a small distance penetrating into one grain away from the sliding boundary. Furthermore, the mechanism is complex and discontinuous with time; hence exact models and precise understanding are lacking. Nevertheless it is important to consider grain boundary sliding as a function of creep since it can influence time-dependent intergranular fatigue cracking phenomena detailed above.

2.4.2.4 Creep and Fatigue

Hall et al [57] identified and defined two extreme modes of creep behaviour; "creep ductile" and "creep brittle". Creep ductile crack growth rates and mechanisms are so labelled because

they are relatively slow when compared with the rate of enlargement of the creep zone. This leads to an accumulation of creep strain in the cracked body. Creep brittle behaviour occurs when crack growth rates are faster than the expansion in size of the creep zone associated with cyclic stress loading. Although the behaviour is described as "brittle" it is usually associated with intergranular cavitation creep fracture; more accurately described as a ductile mechanism. Nevertheless the distinction is important since it is only for creep brittle materials that the regime is appropriately approximated by linear elastic fracture mechanics and the parameter K, the stress intensity factor. High strength creep resistant Ni-based materials such as Udimet 720Li and RR1000 are best described as "creep brittle" since crack growth rates are indeed faster than the growth and expansion of the plastic zone ahead of the crack tip; hence a linear elastic fracture mechanics approach is indeed appropriate for such materials. Knowles and Skelton [58, 59] confirmed that the stress intensity factor K (described above) normalises crack growth rates over a range of a/W ratios. Nevertheless the suitability of K to describe crack growth rates in Ni-based superalloys for disc applications has been carefully contested by researchers who sought to investigate further effects of creep at the crack tip:

G. Onofrio et al [30] suggested that for Udimet 720Li, in a vacuum at 700°C, under long dwell periods crack growth rates can be lower than those associated with baseline (cyclic fatigue dependent) crack growth, and that the failure mechanism is partially intergranular. Previous work in this programme confirmed similar conclusions for RR1000 at 650°C. This suggests that crack tip blunting may occur as a result of creep which causes the retardation of crack growth rates, when the oxidation component is removed. Onofrio [31] on observing

variations between crack growth rates for similarly tested specimens suggested that the introduction of a dwell time could lead to creep related damage and that this would "significantly increase the extent of plasticity at the crack tip." It is suggested that the linear elastic fracture mechanics approach detailed above is therefore limited in modelling such behaviour. This further suggests that it is the combination of oxidation and creep that causes the reduced dwell crack growth resistance of fine-grained Udimet 720Li and RR1000 at these temperatures.

2.4.3 Linear Superposition Lifing Methodologies

Given the above discussion it follows that crack growth pertaining to dwell cycling will involve the development and evolution of three types of affected zones ahead of the crack tip. Namely; a zone of plasticity as a function of the yield stress and stress intensity factor as described by Irwin; a creep affected zone as a function of time, temperature, stress intensity factor and alloy creep properties; and an oxygen induced damage zone as a function of diffusivity of oxygen, time and temperature. These damage zones are represented graphically in Figure 2-20:

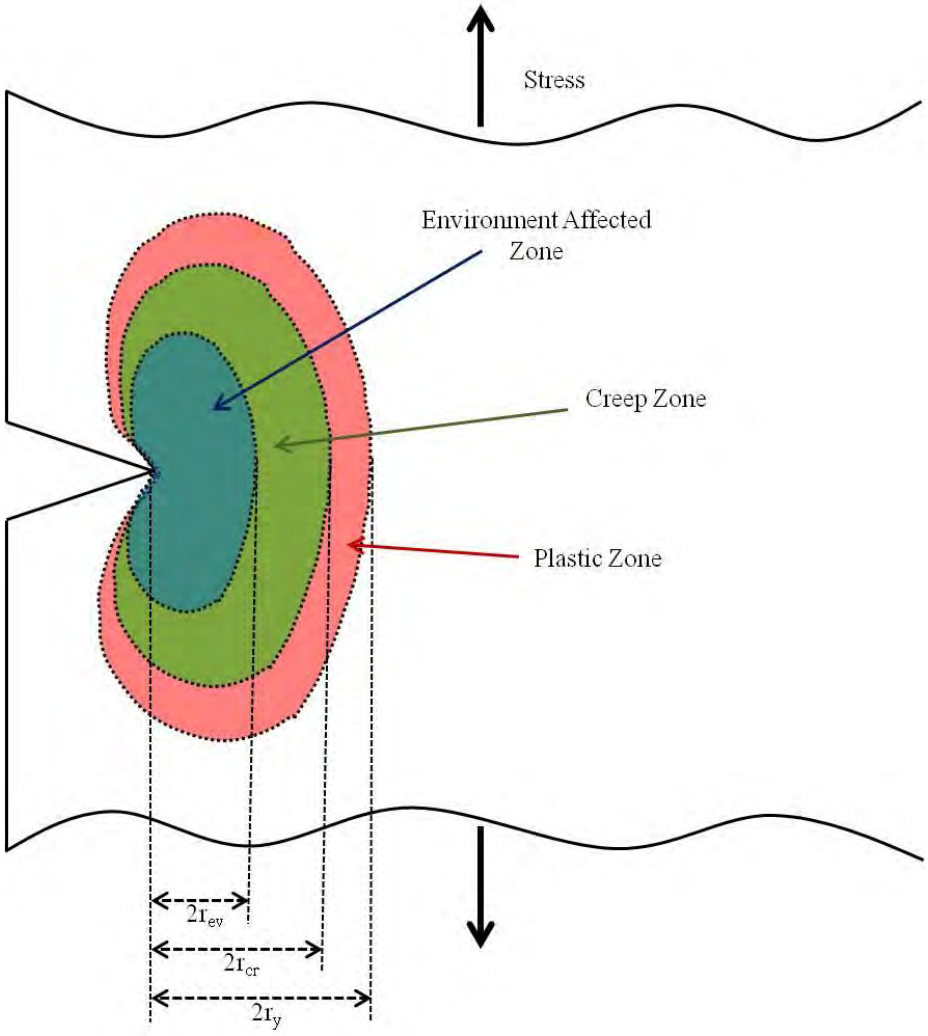


Figure 2-20: Schematic showing various damage zones ahead of a crack tip in the dwell regime, from [60].

Where;

$2r_y \propto \left(\frac{K}{\sigma_{ys}}\right)^2$ ..... Equation 12

$2r_{cr} \propto K^2(EBt)^{\frac{2}{(n-1)}}$ ..... Equation 13

$2r_{ev} \propto \sqrt{Dt}$ ..... Equation 14

Knowles and Skelton [58, 59] sought to include time-dependent oxidation and creep affected dwell crack growth mechanisms in crack growth rate calculations, in order to improve confidence in lifing methodologies and models. They found that a simple linear summation of cyclic fatigue crack growth and sustained load crack growth rate data gave good predictions of total dwell crack growth rates. These findings have been confirmed by Knowles and others, and have been developed within Rolls-Royce plc. in to what is termed a "TiDI" model: a "**Ti**me-**D**ependent and **I**ndependent" linear superposition of crack growth rates. Here, cyclic dependent crack growth rates are considered to interact synergistically with time-dependent cracking in the following way:

$\left(\frac{da}{dN}\right)_{Total} = \left(\frac{da}{dN}\right)_{Ind} + \int_{Cycle}\left(\frac{da}{dT}\right)_{Dep}$ ..... Equation 15

The total crack growth rate then becomes:

$\left(\frac{da}{dN}\right)_{Total} = \left(\frac{da}{dN}\right)_{SAR/D/305} + \int_{Cycle} \mathrm{D'(K)^n}$ ..... Equation 16

Where D' is the introduced time-dependent crack growth rate parameter. The subscript SAR/D/305 refers to the Safety Alert Report which contains analysis carried out to understand the effect of out of phase peak stresses and temperatures; as occurs in real life flight cycles. The work is reported in Rolls-Royce in-house technical report number

DHC210697 and recommended that the mean of the crack growth rates calculated at the temperature at which the peak tensile stress occurs, and the peak temperature in the cycle should be used in fracture mechanics based integrity assessments. For nickel alloys:

$$\left(\frac{da}{dN}\right)_{SAR/D/305} = \left\{C_{T_{max}} \times (\Delta K_{eff})^{n_{T_{max}}} + C_{T_{\sigma max}} \times (\Delta K_{eff})^{n_{T_{\sigma max}}}\right\} \times \frac{1}{2} \text{ ..... Equation 17}$$

Where C and n are taken from coefficients for the Paris crack growth law for baseline loading for the alloy in question. These are available for a range of alloys and temperatures from Rolls-Royce plc. in-house materials database, COMMIT. ΔK_{eff} is calculated from maximum and minimum values of the stress intensity factor in the loading cycle using the Walker equation:

$$\Delta K_{eff} = (K_{max} - K_{min}) \times \left(1 - \frac{K_{max}}{K_{min}}\right)^{m-1} \text{ ..... Equation 18}$$

The time-dependent crack growth rate parameter D' is described by the following Arrhenius equation:

$$D' = A \times exp\left(\frac{-B}{T}\right) \text{ ..... Equation 19}$$

Where T is the temperature in Kelvin and A and B are obtained experimentally. For isothermal tests (where the effects of SAR/D/305 can be neglected) and for a trapezoidal

loading cycle with a hold time of t_{hold} seconds and symmetrical loading of ramps over t_{ramp} seconds; the overall time-dependent crack growth rate through the cycle is then described as:

$$\left(\frac{da}{dN}\right)_{Dep} = D' \times \left(\Delta K_{eff}\right)^n \times \left\{t_{hold} + \frac{2\times t_{ramp}}{n+1}\right\} \text{ ..... Equation 20}$$

Therefore the combined time independent and dependent crack growth rate becomes:

$$\left(\frac{da}{dN}\right)_{total} = C \times \left(\Delta K_{eff}\right)^n + D' \times \left(\Delta K_{eff}\right)^n \times \left\{t_{hold} + \frac{2\times t_{ramp}}{n+1}\right\} \text{ ..... Equation 21}$$

Using the above equation optimum values of D' are obtained at each temperature from experimental crack growth data for a range of dwell periods, including static loading. An optimum fit for D' is then used to determine A and B from Equation 19.

Nevertheless, the method described above suffers from a number of shortcomings. Firstly, it assumes that the introduction of a dwell period causes an increase in crack growth rates when compared with baseline loading by a constant factor for all stress intensity factor values. In terms of the Paris law, this means that the slope of log da/dN Vs log ΔK (i.e. the parameter *n*) is not affected by dwell. The assumption is indeed reasonable for a wide range of fatigue crack growth data but nevertheless may require further investigation.

Most significantly however, in predicting overall in-service crack growth rates it assumes a simple dwell loading cycle rather than a more accurate representation of in-service stress

states which includes unloading from a maximum load to the dwell load as a result of switching from “take-off” to “climb” associated engine capacity. The effect of partial unloading from an overload to a dwell load is reported in great detail in subsequent chapters but here it is important to highlight that linear superposition models may be unnecessarily conservative and hence inappropriate for use in a lifing methodology which seeks to optimise engine performance. Whether or not this is the case it is certainly true that it fails to accurately represent in-service stress states and as such further analysis is required.

2.5 Analytical Techniques

2.5.1 Introduction to Finite Element Analysis

Following the discussion of lifing methodologies within Rolls-Royce plc. it follows that techniques to fully understand in-service stress states must be employed in order to add confidence and understanding to such criteria.

One approach is that of Finite Element Analysis. The approach involves the generation of a two or three dimensional geometric model which comprises a series of nodes which define "elements" in a mesh arrangement. Modelling software then runs numerical analyses at each of these nodes using mathematical techniques involving material data such as strength, creep and plasticity properties over a fictitious nominal condition (stress and temperature) history defined by the user. The analysis essentially provides a mechanism to understand or predict stress (and associated) states throughout a component or test piece as a function of operating conditions. One of the most powerful tools of such an approach is that it highlights the location and magnitude of the maximum principle stresses of a given component under service conditions. It also enables the careful modelling of a defect under such stress states and as such can be used to add confidence to life predictions which seek to model worst-case scenarios.

It is important to highlight that the technique is sensitive to "mesh size". As described, the geometric mesh is defined as a series of individual nodes which represent finite locations at which analysing techniques and codes are applied. If, for example the mesh is created using

too small a number of elements then analysis will be unreliable and unpredictable. This is because the physical distance between calculations is too large to accurately extrapolate outputs across from one element to its neighbour. A mesh which is too fine however can render simulations impractical in terms of run time and in terms of the size of the data generated in associated results files. Therefore a compromise must be made between the two and is usually found by running analyses at various mesh sizes and plotting one particular output (maximum Von Mises stress for example) against mesh size. The largest mesh size (i.e. the smallest number of elements) at which the solution converges is generally then applied as the appropriate stress analysing methodology.

Rolls-Royce plc. adopts such an approach and has a long history of technical experience pertaining to finite element analysis. Crucially, analysis which seeks to represent in-service conditions must be capable of modelling the effects of high temperature stress systems. Furthermore, fluid flow analysis and understanding the behaviour of dynamic moving parts is also essential. Therefore the company have developed their own in-house modelling software package and associated materials database known as SC03 (in its third version): capable of high temperature stress analysis along with dynamic solid and fluid simulation.

2.5.2 Modelling Variations in Stress and Strain

For a complete analytical understanding of the way in which a component will behave under fluctuating stress states it is important to comprehensively include understanding of the evolution of stress-strain hysteresis loops mentioned in section 2.4.2 which occur as a result

of creep, plasticity and hardening effects. The condition at which stress and strain stabilise will relate directly to the number of cycles to failure for a given component, hence accurate lifing methodologies must include numerical descriptions of:

1) A yield criterion defining the stress state at which plastic deformation initiates
2) A hardening criterion to describe the effect of work hardening
3) A flow rule which relates elastic and inelastic strain rates with stress and strain states

A yield criterion is used to represent three dimensional (multi-axial) stress states experienced by components in service. Various criteria are used to incorporate the effect of different loading directions in a single parameter, creating an "effective" stress or strain (σ_{eff} or ε_{eff}) as a function of the three orthogonal principal stresses in the multi-axially loaded structure (σ_1, σ_2, σ_3 where $\sigma_1 > \sigma_2 > \sigma_3$).

The most widely accepted method is the Von Mises relationship [61], alluded to above:

$$\sigma_{eff} = \left(\frac{1}{\sqrt{2}}\right)[(\sigma_1 - \sigma_2)^2 + (\sigma_2 - \sigma_3)^2 + (\sigma_3 - \sigma_1)^2]^{\frac{1}{2}} \quad \text{..... Equation 22}$$

Yield in the structure is said to occur when $\sigma_{eff} = \sigma_{ys}$ where σ_{ys} is the monotonic yield stress in a simple tensile test.

For plane stress conditions, where $\sigma_2 = 0$, the Von Mises criterion reduces to the form:

$\sigma_{eff}{}^2 = \sigma_1{}^2 + \sigma_3{}^2 - \sigma_1\sigma_3$..... Equation 23

An alternative multi-axial yield criterion is the Tresca [62] or maximum shear stress criterion (τ_{max}):

$\tau_{max} = \frac{(\sigma_1 - \sigma_3)}{2}$..... Equation 24

Where yield is said to occur when $\tau_{max} = \tau_{ys}$ and τ_{ys} is the shear yield stress in a monotonic tensile test, $\tau_{ys} = \sigma_{ys}/2$

The plane stress Von Mises criterion can be represented on a Mohr's circle as an ellipse with a major semi-axis of $\sqrt{2}.\sigma_{eff}$ and a minor semi-axis of $\sqrt{(2/3)}.\sigma_{eff}$

The yield surface represented by this is presented in Figure 2-21, along with the hexagonal yield surface based upon application of the Tresca yield criterion. Combinations of co-ordinates for σ_1 and σ_3 which lie within the ellipse or hexagon will not result in yield but rather elastic deformation. Any combination of co-ordinates however which lie outside the bounding ellipse will cause plastic deformation.

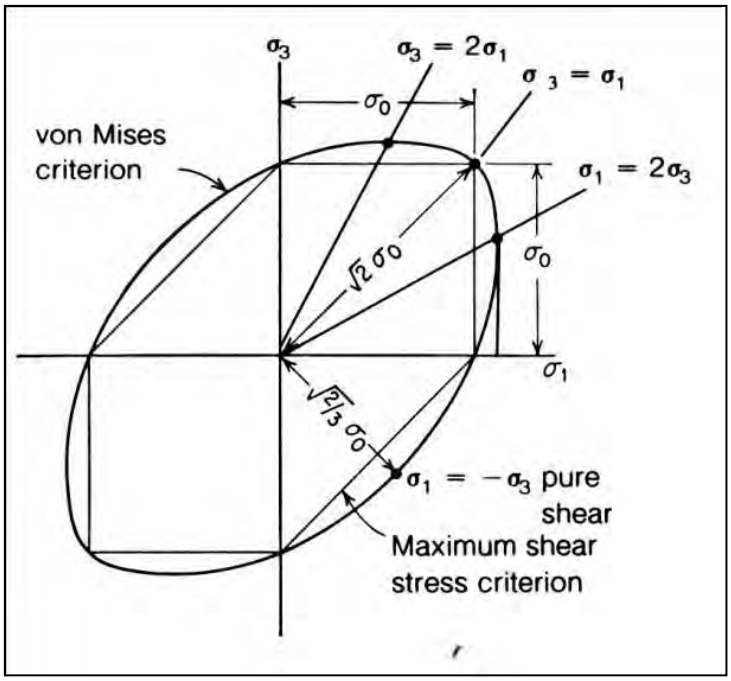


Figure 2-21: Yield surfaces under bi-axial (plane stress) loading conditions defined by Von Mises and Tresca yielding criteria, from [61] and [62].

A hardening criterion is then employed to capture the way in which the initial yield surface moves and changes as strain hardening occurs as a result of dislocation-dislocation interaction as plastic deformation proceeds. Various approaches have been suggested; the oldest and simplest of which is that of isotropic hardening.

Isotropic hardening approaches assume that the initial yield surface represented by Figure 2-21 expands uniformly and that the origin of the yield surface remains fixed. Essentially the method assumes that material will harden uniformly in all directions, which is an over simplification; especially in cases where fluctuating stress states include a superimposed mean or where minimum stresses are compressive.

To overcome some of these disadvantages the yield surface must be modelled as moving through the stress axes. One approach is that of kinematic hardening, a method which has been developed to better represent in-service material hardening behaviour. Nevertheless the shape and size of the represented yield surface is held constant, allowing hardening effects in the direction of applied stress but ignoring any effects in other stress directions. Clearly therefore a method for numerical representation of both isotropic and kinematic hardening effects is required if meaningful stress and strain calculations are to be made.

One such approach has been suggested by Mroz [63] and developed extensively within Rolls-Royce plc. Mroz sought to characterise non-linear hardening behaviour by proposing a multi-yield surface model. Each layer is defined as having an individual hardening modulus and as such finite definitions of hardening behaviour can be numerically represented as the material plastically deforms. Consider a simple circular plot of plane stress σ_1 and σ_2 conditions:

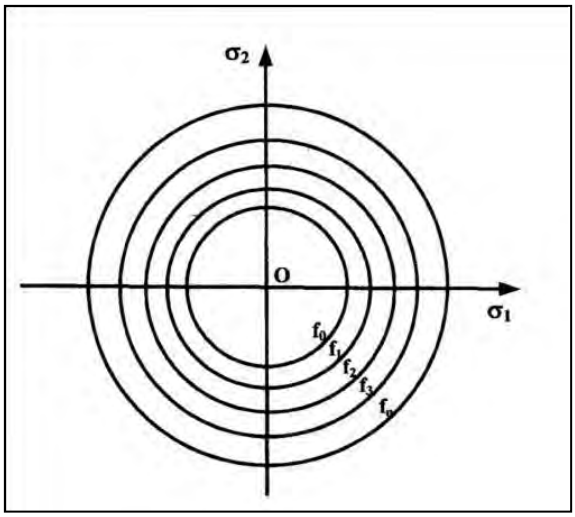


Figure 2-22: Multi-yield surfaces suggested by Mroz.

The circle labelled f_0 represents initial elastic behaviour, i.e. the initial yield surface. Should stress be applied in the σ_1 direction such that it causes the material to yield in that direction; an appropriate hardening modulus will be applied to accurately represent such transformation across the axis. Once deformation reaches the boundary f_1 however; a new hardening modulus relating to this particular amount of plastic deformation will be applied. Hence the region between each circle is associated with its own particular numerical representation of hardening behaviour.

The transformation of multi-yield layers during a simple loading, unloading and reverse loading sequence of stress in the σ_1 direction is represented by Mroz in Figure 2-23. Solid lines denote active surfaces and dotted lines inactive surfaces. Starting at the origin, σ_1 increases elastically until it reaches f_1 where initial yield occurs. As described above, plastic

deformation is then represented by a particular hardening modulus as stress moves through the region f_1 to f_2, after which a new hardening modulus is applied and the process continues.

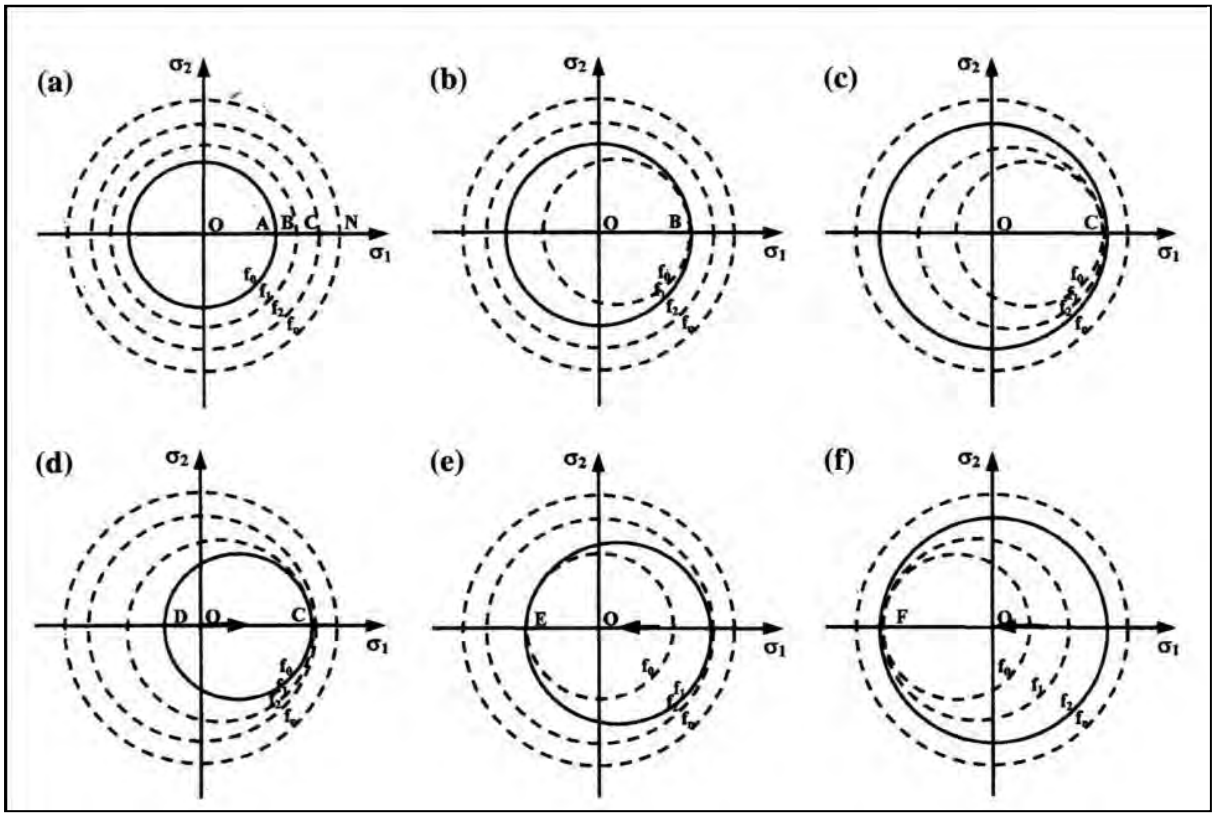


Figure 2-23: Showing evolution of multi-yield surfaces as represented by Mroz hardening criteria [63].

Yield and hardening criteria must also include numerical representations of the way in which plastic and elastic flow defines stress and strain components. Within an elastic regime this is described by Hooke's law. However in plasticity the relationship is considerably more complex, especially because the level of plasticity will be a function of the entire loading history. This complexity is represented by small increments of strain throughout the loading history and the total amount of strain is determined by integration.

Several approaches to define this total strain have been made. Levy-Mises approaches relate stress and plastic strain increments using "flow rules" (detailed below). Prandtl and Reuss [64] developed these approaches and sought to relate stresses with combined elastic and plastic strains. Hence the approach is more relevant to situations which involve small amounts of plastic strain such as fracture toughness problems faced in the aerospace industry.

Levy-Mises equations begin with the Von-Mises effective stress relationship in Equation 18. It can be adapted to represent an effective strain:

$$\varepsilon_{eff} = \left(\frac{\sqrt{2}}{3}\right)[(\varepsilon_1 - \varepsilon_2)^2 + (\varepsilon_2 - \varepsilon_3)^2 + (\varepsilon_3 - \varepsilon_1)^2]^{\frac{1}{2}} \text{ ..... Equation 25}$$

The strain increments (dε) can then be represented:

$$d\varepsilon_{eff} = \left(\frac{\sqrt{2}}{3}\right)[(d\varepsilon_1 - d\varepsilon_2)^2 + (d\varepsilon_2 - d\varepsilon_3)^2 + (d\varepsilon_3 - d\varepsilon_1)^2]^{\frac{1}{2}} \text{ ..... Equation 26}$$

Levy-Mises approaches also take in to consideration the fact that yielding and plasticity does not involve the total stress but rather the "deviatoric stress" obtained by subtracting the hydrostatic stress from each of the principal stresses. For σ_1 therefore:

$$\sigma_1' = \sigma_1 - \sigma_h \text{ ..... Equation 27}$$

Where:

$\sigma_h = \frac{\sigma_1+\sigma_2+\sigma_3}{3}$ ..... Equation 28

Assuming therefore that during plastic deformation the total volume of material remains constant, Levy-Mises equations can be derived:

$$d\varepsilon_1 = \left(\frac{d\varepsilon_{eff}}{\sigma_{eff}}\right)\left[\sigma_1 - \frac{(\sigma_2+\sigma_3)}{2}\right]$$

$$d\varepsilon_2 = \left(\frac{d\varepsilon_{eff}}{\sigma_{eff}}\right)\left[\sigma_2 - \frac{(\sigma_3+\sigma_1)}{2}\right]$$

$$d\varepsilon_3 = \left(\frac{d\varepsilon_{eff}}{\sigma_{eff}}\right)\left[\sigma_3 - \frac{(\sigma_1+\sigma_2)}{2}\right]$$ ..... Equation 29

The parameter $d\varepsilon_{eff} / \sigma_{eff}$ is shown in Figure 2-24. It is represented by a line drawn from the accumulated inelastic strain on the strain axis to the point on the stress-strain curve after the current increment of strain. In essence, it is a description of the work hardening parameter required by Mroz multi-layer yield surface criteria.

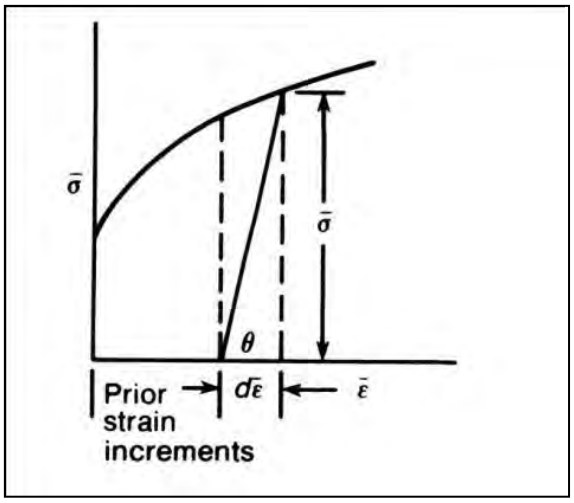


Figure 2-24: Showing the parameter $d\varepsilon_{eff} / \sigma_{eff}$ (the "hardening parameter") for Levy-Mises equations.

As discussed above, Prandtl relationships seek to include both elastic and plastic components of strain. Hence the strain increment now becomes:

$$d\varepsilon_{ij} = d\varepsilon_{ij(elastic)} + d\varepsilon_{ij(plastic)} \quad \text{..... Equation 30}$$

Where the plastic component is derived from Levy-Mises equations and where the elastic component is derived using Hooke's law (and again, by subtracting the hydrostatic component).

A full and comprehensive incorporation of yield and hardening criteria and plasticity modelling can be combined to accurately represent cyclic loading from first application to stabilisation. Such approaches are indeed adopted by Rolls-Royce plc. and are widely reported within the company.

2.5.3 Crystal Plasticity Modelling

The approaches detailed above assume that simulated material data is homogenous and isotropic and therefore constant average material properties are applied across an entire geometric model. This renders the method incapable of simulating and analysing microstructural influences such as interactions between grains as a function of oxidation and creep. First used by Taylor to simulate stress and associate conditions in single crystal materials for the aerospace industry, Crystal Plasticity FEA (CPFEA) seeks to model each individual grain as a single crystal with complex boundary conditions pertaining to interaction with neighbouring grains. It is therefore possible to simulate interactions between grains and to analyse grain boundary activity; which means that it might be possible to develop modelling simulations which include simple cyclic stress analysis with time-dependent crack growth phenomena.

The method is implemented by the generation of actual grain boundary stress and strain behaviour including analysis for grain orientation. Such empirical data can be gathered for a particular alloy under specific conditions by the use of Electron Backscatter Diffraction (EBSD) techniques which "reveals grain size, grain boundary character, grain orientation, texture and phase identity" [65]. Such empirical data can then be carefully modelled through the creation of CPFEA codes and used to predict grain size and orientation, grain plasticity and grain boundary interactions as a function of microstructure through a fictitious nominal condition-time history.

Clearly such analysis is highly complex and necessitates large amounts of computing power and data storage. For these reasons the method has not been widely employed for the analysis of dwell crack growth phenomena; nevertheless it might be possible to suggest ways in which it might be applied in future analyses.

2.6 Effect of Overload

2.6.1 Introduction

In predicting crack growth rates, the effect of introducing an overload segment to the dwell waveform is, to date, relatively unreported in the literature. Some data has been gathered on a range of structural steels [66] and on previous generations of Ni-based superalloys [6, 67], while data on Udimet 720Li and RR1000 remains lacking. Nevertheless there is much activity within Rolls-Royce plc. to understand any effect that overloading might have on crack growth rates since this waveform better represents in-service stress states. Here, the material is subject to a load which is higher than the dwell load for a defined period before unloading back down to the dwell load, after which the waveform continues as described above. Such waveforms better model in-service stress states since the engine works at maximum capacity during “take-off”, and works at slightly reduced capacity during the “climb” stage of the engine cycle, during which the aircraft reaches altitude. TET and associated stress states of various components as a function of time during a typical civil aircraft flight cycle is plotted in Figure 1-2, and shows this in-service overload waveform.

An overload factor is defined as the overload divided by the dwell load. Overload factors of between 1.05 and 1.15 are currently of interest to Rolls-Royce plc.

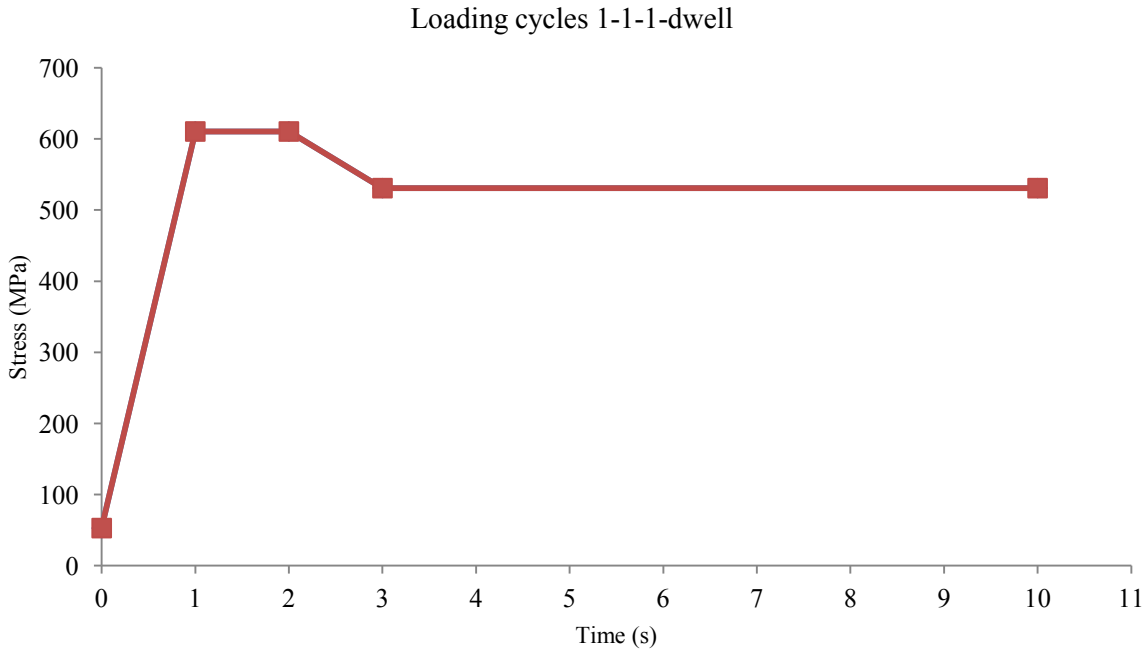


Figure 2-25: An example of an overload waveform with an overload factor of 1.15. The waveform would normally go on to hold the "dwell" load for between 120 and 3,600 seconds, before unloading over a period of 1 second and holding at the minimum load for a period of 1 second, thereby defining the "cycle".

Several sources [68-73] discuss the effect of overload and subsequent unloading on fatigue crack growth rates on a range of materials. Many of these sources report that introducing an overload in the waveform causes the reduction or retardation of crack growth rates as a function of overload factor, when compared with otherwise similar dwell loading. This may at first sound counter intuitive since greater bulk stresses usually result in greater effective crack tip stress intensity factors (K) and therefore faster crack growth rates. Nevertheless several suggestions to explain such overload retardation effects have been made.

The oldest suggestion appears to have been made by Christensen in 1959 [68] who postulated that the phenomenon may occur as a result of crack tip blunting caused by creep and

plasticity around the crack tip at these higher stresses. He postulated that a crack tip which has been blunted to some extent might therefore be better represented by a new effective stress intensity factor range. Jones, in 1973 [69], studying singe-cycle overload effects on Ti-6AL-4V titanium alloy, suggested that crack growth retardation occurred as a result of crack tip strain hardening, and also postulated that a favourable residual stress system may be introduced ahead of the crack tip upon unloading. Suresh suggested in 1983 [71] that retardation occurred as a result of crack tip branching and deflection which could lead to a decrease in the effective crack driving force (K).

Finally Elbert [72] suggested that crack growth retardation as a result of overload may occur due to plasticity induced crack tip closure. He argues that overload segments in the waveform introduce a large plastic zone in the material ahead of the crack tip. When the crack goes on to grow through this plastic zone under the application of (slightly reduced) dwell load stress states, the crack is pressed shut by a residual wake of plastic deformation around the crack flanks.

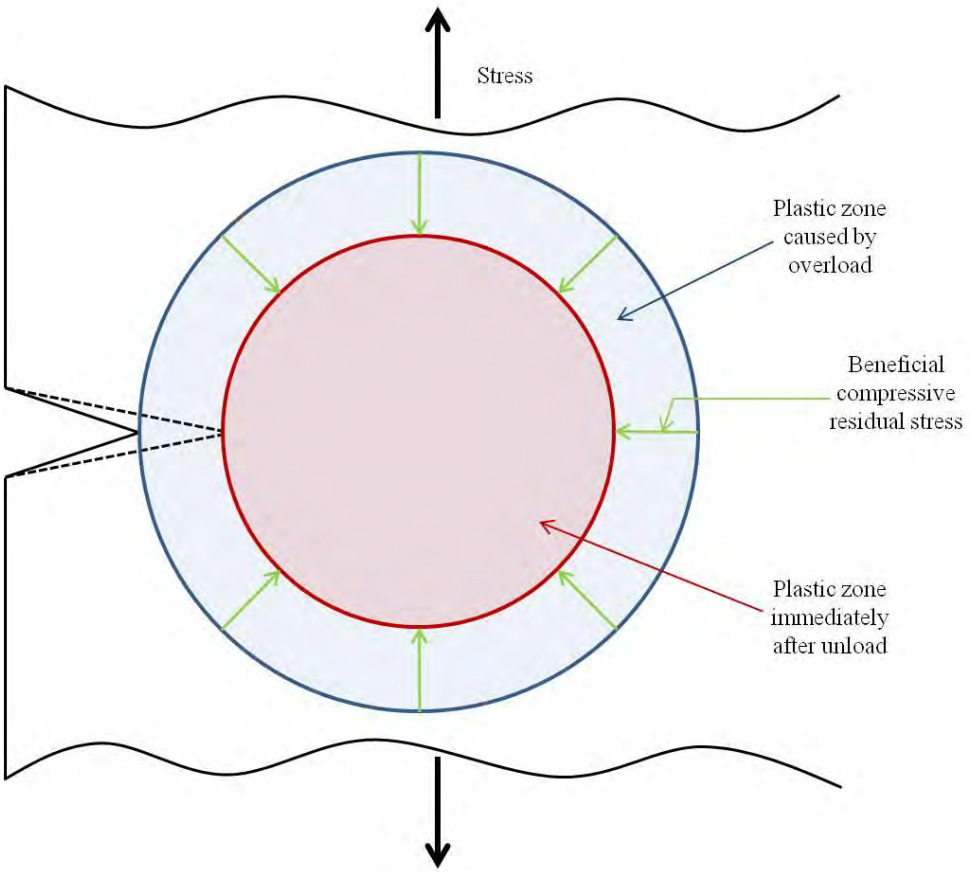


Figure 2-26: Schematic of plastic zone sizes associated with overload and subsequent dwell load stress states.

More recently, empirical evidence relating to crack growth retardation as a result of partial unloading has been presented by Kruch [67] and Pineau [6, 73] for Astroloy and Inconel 718 respectively. Both reports suggest preferential unloading of crack tip stresses as represented analytically by FEA modelling.

Whether crack growth retardation as a result of overloading in the stress-time waveform occurs by crack tip blunting, branching or as a result of the introduction of complex beneficial residual stresses ahead of the crack tip, it follows that the phenomena are likely to

be microstructural and condition specific. It is also certainly true to say that the phenomena may have significant implications in terms of in-service crack growth rate calculations and methodologies which seek to define the in-service life of components subjected to such conditions. It therefore follows that a comprehensive and complete understanding of the effect of overload retardation in Udimet 720Li and RR1000 is required in order to create accurate lifing methodologies for Ni-discs in service and to optimise their performance.

2.6.2 Theoretical Modelling

A number of models have been developed to understand and describe the effects of overload retardation on fatigue crack growth rates of materials. As discussed above, Elbert included the crack tip closure concept to explain and model crack growth rates and mechanisms. He argued that upon unloading from the overload segment, a larger portion of the subsequent tensile load was required to cause the crack to open and hence modelled a new "effective" stress [72]. Matsuoka et al [74] based their models on crack tip closure and included considerations for crack tip blunting as first suggested by Christensen [68]. Wheeler [75], in 1972, emphasised Elbert's larger plastic zone size model suggesting that the crack tip must grow beyond the larger plastic zone induced due to overloading before crack growth rates will return to the "normal" (higher) levels associated with dwell-only or static load crack growth. Sheu et al [76, 77] went on to describe a Wheeler retardation parameter as "a power function of the ratio of the present plastic zone size to the distance from the crack tip to the boarder of the plastic zone caused by the overload", described and explained in more detail below. Finally, Lu and Li [78] went on to argue that several interacting and co-existing

mechanisms would compete to result in the overall crack growth rates and mechanisms observed, such as crack tip blunting and strain hardening.

Other involved mechanisms may be those described above; namely, oxygen and creep effects as a result of sustained (dwell) load at high stresses and high temperatures in an oxidising environment. Needless to say, an analytical approach to combine all of these mechanisms would be extremely complex and rely upon vast quantities of empirical data and therefore such an approach has not been successfully attempted to date.

Generally therefore there are three methods for modelling fatigue crack growth and its retardation as a result of overload cycling: crack closure models; statistical models and crack tip plasticity models. All three methods use a linear elastic fracture mechanics approach and hence rely upon the assumption that plastic zones around the crack tip (although larger in the case of overloads) are very small with respect to the geometry of samples, materials or components.

It is worth expanding on Wheeler's model at this stage, since it most eloquently and accurately describes crack tip plasticity approaches to retardation problems. Wheeler suggested that the Paris-Erdogan law could be modified to include an empirical retardation parameter C_p:

$\frac{da}{dN} = C_p(A.\Delta K^m)$ ..... Equation 31

Where, for constant amplitude cycling, $C_p = 1$

Wheeler defines C_p as a function of the ratio of the nominal plastic zone size (caused by, for example simple dwell loading or a sustained load) to the plastic zone size produced by the introduction of an overload in the cyclic waveform. For homogenous materials, plastic zone sizes are approximated using Irwin's model described in section 2.3.2, where the monotonic *overload* plastic zone size is calculated by substituting in the stress intensity factor corresponding to the single overload segment in the waveform:

$\Delta K_{OL} = Y.(\sigma_{OL} - \sigma_{\min}).(\pi.a)^{1/2}$ ..... Equation 32

And therefore:

$r_{yOL} = \frac{1}{2\pi}\left(\frac{K_{OL}}{\sigma_{ys}}\right)^2$ ..... Equation 33

Wheeler then defines the retardation parameter C_p as:

$(C_p)_i = \left(\frac{r_{yi}}{a_p - a_i}\right)^p$ ..... Equation 34

Where a_i is the crack length at the *i*th loading cycle, r_{yi} is the plastic zone size caused by the *i*th loading cycle and a_p is the sum of the crack length at which the overload cycle was applied and the plastic zone size created by its application. The parameter p is introduced as

the Wheeler shaping component which is determined empirically as the value which best fits the data for a given material.

Wheeler therefore postulates that crack growth delay will occur while the current applied plastic zone size falls within the plastic zone which was created by previous application of an overload. When the boundary of the current applied plastic zone reaches that of the boundary associated with the overload plastic zone, crack growth retardation will stop – i.e. where $C_p = 1$. Hence at this stage, stress states have returned to those normally associated with single amplitude cyclic loading and the crack grows as normal.

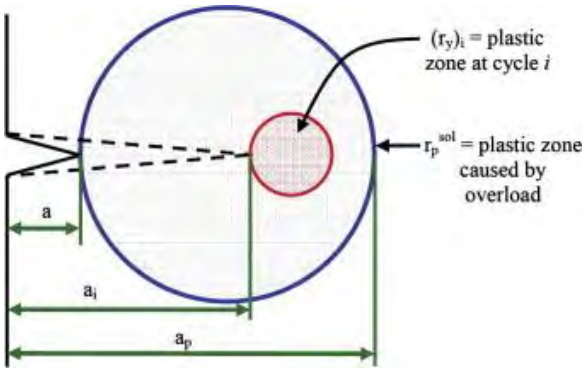


Figure 2-27: A schematic view of the plastic zones induced by nominal cycling and by the application of an overload cycle, as discussed in the Wheeler model, from [75].

Nevertheless the Wheeler model suffers from a number of shortcomings. The most significant of which is that it does not include any time-dependent oxygen or creep effects induced by previous or subsequent extended periods at maximum loads. It may be, for aerospace applications especially, that alongside complex beneficial residual stress states ahead of the crack tip; oxygen induced damage also occurs as a function of time, temperature,

stress and microstructure. Therefore any crack tip plasticity models which seek to capture overall overload and subsequent dwell crack growth rates, mechanisms and behaviour must also include understanding of time-dependent oxygen induced crack growth phenomena. Pineau [6] sought to study the effect of partial unloading on crack growth rates in Inconel 718, and reports that preferential unloading of tensile stresses immediately ahead of the crack tip could lead "to significantly reduced or even suppressed environmental effects." Hence further understanding, especially in the case of Udimet 720Li and RR1000 is crucial.

Theoretical modelling with respect to overload waveforms and their effect on crack growth rates in fine-grained Udimet 720i and RR1000 within Rolls-Royce plc. has focussed on in-depth finite element analysis (FEA) of crack tip stresses and a crack tip plasticity approach. Preliminary simulations have been carried out using various mesh sizes and crack tip geometries and it appears as though crack tip stresses are indeed unloaded preferentially as nominal loads unload from the overload segment. For example, if the nominal load is reduced by a factor of 15% from the overload to the dwell load, stresses immediately ahead of the crack tip are observed to relax much further than 15%. This is an extremely important observation since it implies that overload cycling is indeed beneficial to the overall fatigue life of the material. It implies that current lifing methodologies which assume a linear superposition of cycle-dependent and time-dependent crack growth components may be unnecessarily conservative. Hence it is important to understand and define overload and subsequent dwell crack propagation behaviour.

There is currently no method for including time-dependent oxygen effects in stress analysing modelling approaches. High temperature creep and associated crack tip stresses are the only outputs from the analysis. Nevertheless it may be possible to combine a series of modelling analyses with empirical data to better understand interacting dwell and overload crack growth retardation phenomena.

2.6.3 Preliminary Testing

Preliminary results gathered as part of this programme have indeed begun to imply that the introduction of a one second overload in the waveform can (under certain conditions) reduce or retard crack growth rates when compared with otherwise similar dwell cycling in fine-grained Udimet 720Li and RR1000. Nevertheless these observations need quantifying and indeed explaining before any current lifing predictions can be updated or improved. It is necessary to define the extent of any retardation as a function of condition (temperature, dwell load, overload factor and dwell time for example) and for each alloy. As such a comprehensive dwell and overload test matrix must be designed and implemented. Furthermore a far clearer understanding of *why* the phenomena occur is also required before any confident alterations can be made to lifing methodologies.

This particular type of testing provides a unique opportunity to study the various ways in which cycle-dependent and time-dependent failure mechanisms interact with one another during high temperature fatigue crack growth. It may be that with improved understanding of such phenomena, improvements to current lifing methodologies can be made. Such

improvements might result in higher performance engine capabilities and therefore reduced fuel and maintenance costs, while maintaining unprecedented confidence in safety.

3. Methodology

3.1 Material

Test piece samples are fine-grained Udimet 720Li and RR1000, their nominal chemical composition limits are given in Table 3 and Table 4:

Table 3: Nominal chemical composition limits (weight percent, balance Nickel) of Udimet 720Li.

Element	Cr	Co	Mo	W	Al	Ti	C	B	Zr	Ni
Weight %	16	15	3	1.25	2.5	5	0.015	0.015	0.035	Bal

Table 4: Nominal chemical composition limits (weight percent, balance Nickel) of RR1000 [79].

Element	Cr	Co	Mo	Al	Ti	Ta	Hf	Zr	C	B	Ni
Weight %	15	18.5	5	3	3.6	2	0.5	0.06	0.027	0.015	Bal

Udimet 7201Li samples from Phase One, and Phase Two, Batch One (defined and discussed in subsequent paragraphs) are machined from the remnant rim of a Trent 500 high pressure turbine disc whose serial number is LDREC13907. Test pieces from Phase Two, Batch Two were machined from a smaller disc (discussed in subsequent paragraphs). Discs were heat

treated at 1080 – 1110°C for four hours and oil quenched. Precipitation hardening (ageing) then followed at 760°C for 16 hours, which was followed by air cooling.

RR1000 samples were heat treated below the solvus temperature for γ', at 1120°C. The material is fan-assisted air cooled down to 900 – 1000°C and the (out of solution) γ' particles pin grain boundaries as they form hence refining the grain size. Material is then held at 760°C for 16 hours during which time tertiary and secondary γ' particles coarsen throughout the γ matrix.

It is important to highlight at this stage that fine-grained Udimet 720Li test pieces were provided to the programme in two phases, referred to in this report as "Phase One" and "Phase Two". Each "phase" of material was further separated in to two "batches", "Batch One" and "Batch Two". Hence four distinct groups of test pieces are distinguished:

Phase One: Batch One

Phase One: Batch Two

Phase Two: Batch One

Phase Two: Batch Two

As has already been discussed, Udimet 720Li is cast and wrought and hence has naturally more variation in terms of its microstructure. This may in turn have pronounced effects upon the mechanical properties of the alloy, and as such it is important to group together and compare and contrast crack growth resistance curves generated by Phase and Batch number,

and to relate each particular crack growth resistance curve with a set of microstructural analysis.

The material from Phase One (Batches One and Two) and from Phase Two, Batch One are all sourced from one disc and hence from material which has undergone similar heat treatment. The material from Phase Two, Batch Two however has been sourced from a different type of nickel disc; namely one for use in industrial power generation. These discs are smaller in terms of rim radius (around 300 mm when compared with 900 mm for use in aero engines). Although the nominal heat treatments are similar, material contained in these smaller discs will naturally cool from the maximum heat treatment temperatures at a faster rate. This can have a profound effect upon the microstructure of the material including and especially grain size and γ' size and distribution. Faster cooling rates usually cause the formation of smaller grains, since there is insufficient time for large grains to form. The effect of grain size on the dwell crack growth behaviour of (nominally) fine-grained Udimet 720Li is therefore analysed and discussed by comparing data gathered from each source (Batch) of material.

3.2 Mechanical Testing

3.2.1 Introduction

Documented below is a detailed step-by-step guide of the exact methodology by which test pieces were tested in this programme. The guide assumes and explains testing conditions pertaining to baseline, dwell and overload cycling; since these types of tests are the most common in this programme. Subsequent chapters (section 3.2.5) detail the exact testing conditions for each test piece across the whole testing programme.

Uniaxially loaded, constant amplitude[2] force-controlled crack growth tests are carried out on square cross section, corner notched specimens of fine-grained Udimet 720Li and RR1000. All tests are implemented according to Rolls-Royce plc. testing procedure MMM 31001 which is based on the EN Aerospace standard Pr EN 3874. Each specimen has been machined to a gauge section of 7 x 7 mm dimensions and more accurate geometrical measurements are recorded before each experiment in order to precisely calculate the stresses applied to the material. Test piece drawings are available in Appendix IV.

The tests consist of maintaining a test piece at a uniform temperature and subjecting it to a constant force-amplitude waveform. The magnitude of the applied cyclic force (and hence

[2] The term "constant amplitude" refers to the fact that the maximum and minimum applied force remains constant throughout the testing procedure, as does the superimposed mean of these forces. It is important to highlight that the overload waveform has two effective "maximum" applied forces, namely the overload load and the slightly reduced dwell load. Nevertheless these tests are also referred to as constant in amplitude since the overload and dwell load are not altered with respect to themselves or each other as the test is carried out. A distinction between ΔK calculations performed using σ_{OL} and σ_{dwell} is defined in subsequent paragraphs.

associated stress) affects the development of microscopic plastic strain within the test section, thus determining fatigue crack growth rates for a variety of conditions.

The term "force-controlled" describes the fact that servo-hydraulic tensile testing machines control the test by applying prescribed force waveforms to the sample. The R ratio is kept constant, hence ΔK increases with increasing crack length. The "test section" is defined as the region of the test piece between the blending fillets into the threaded gripping section, and is a parallel sided section 7 x 7 mm (49 mm^2) in area with a notch machined at one corner. A "cycle" is defined as the smallest section of the force-time function which is repeated periodically; hence 4 cycles are shown in Figure 2-8 and 2 in Figure 2-9.

Testing machines are verified and calibrated in accordance with relevant requirements detailed in Rolls-Royce plc. in-house testing procedure documentation. Load cells and cycle counters are calibrated to ensure accurate representation. It is also especially important to calibrate the alignment of testing fixtures since misalignment could induce unknown and therefore un-modelled bending strains in the test pieces. Testing fixtures are cooled during high temperature tests either by cooled water or mixtures of cooling fluids which ensures minimum dimension changes and reduces high temperature effects such as creep or failure by fatigue in the fixtures.

Heating devices are used to uniformly heat test pieces to a specific and carefully controlled temperature at a rate no greater than 50°C per minute. The temperature is continuously monitored during each test using calibrated thermocouples and is controlled to within +/- 2°C

of the apparent testing temperature. Where possible, a resistance furnace with three controlled zones is used. The uniformity of temperature along the test section is verified by the use of three thermocouples fixed along and around the section of a small sample of test pieces, and temperature homogeneity is confirmed.

It is important to note at this stage that during heating, temperature stresses due to expansion of the test piece volume can be induced in the sample. Therefore, during the heating process, testing machines should be set to hold the sample at a controlled load value (i.e. “Load Control”) and hence automatic adjustments of the absolute position of the actuator will automatically maintain this load despite dimension changes in the test piece. However, while inserting a test piece in to a testing rig the user should be careful to operate testing machines in “Position Control”. This is because, while the test piece remains free, the load cell associated with the top fixture is unconnected to the actuator which drives the fixture at the bottom of the rig. Hence if the load cell is asked to find and apply a certain load in kN (in “Load Control”) the actuator will accelerate downwards in a completely uncontrolled manner, looking for a tensile load which it will not find. Should testing machines be left in “Position Control” upon heating however, the fixtures will maintain their position despite any volume expansion of the test piece and hence compressive stresses will be induced in the specimen. The level of these stresses is known to cause permanent plastic deformation across the test piece (general yield) or indeed test piece fracture. Hence testing machines should be switched from “Position Control” to “Load Control” only once a test piece is correctly and completely inserted and before switching on power to the heating furnace.

3.2.2 Test Rig Set-Up

Platinum wires coated in a ceramic protective sheath are spot welded on to test pieces across the notch in order to monitor voltage as it increases with crack length. The process involves first careful attachment of p.d wires to the sample by the use of high temperature tape and high temperature ceramic rope, which ties around the wire and test piece, holding the tips of the platinum wires close to either size of the notch on the test piece. MacGregor spot welding equipment (part M1-10) is used in conjunction with a constant force weld head to apply force and current to the platinum wires across the notch of the sample, spot welding them in place. The process utilises optical microscopy techniques which are mounted on to the spot welding equipment, in order to observe the spot welding process.



Figure 3-1: Photograph showing spot welding equipment including attached optical analysis equipment and light source.

Spot welds must be made within 1 mm of the notch and within 1 mm of the edge of the test piece. It is also important to ensure that the section of the platinum wire which feeds immediately out from the spot welded region does not run flush against the test piece but rather, runs up and away from making any metal contact. This is to ensure that the potential difference across the spot weld is measured accurately.

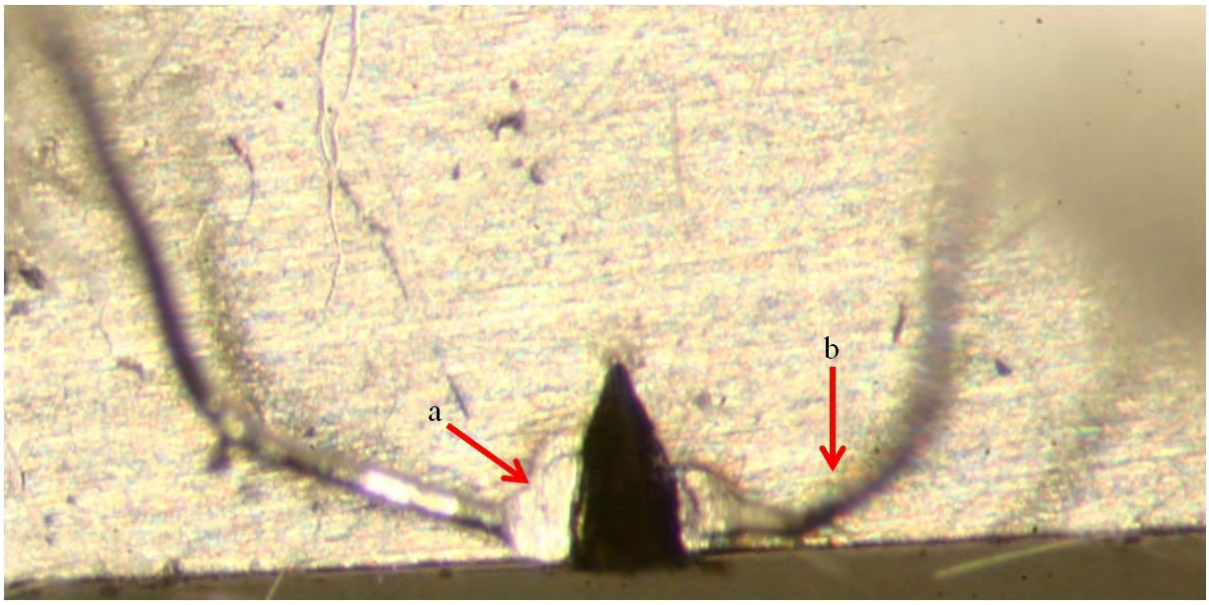


Figure 3-2: Image showing; a) the spot welded region within 1 mm of the notch and the edge of the test piece and b) the platinum wire running immediately upwards from the spot welded region rather than running flat against the test piece.

Test pieces are then carefully screwed in to fixtures and on to a testing rig. A constant current of ~7 amps is passed through the fixtures (and therefore the sample) and the circuit is isolated from earth by the use of ceramic washers around the bolts of the rig. A calibrated thermocouple is positioned such that it makes physical contact with the test piece along its gauge length, at a location close to the notch, and a furnace is clamped around the testing rig. The furnace is insulated by the use of body-soluble cladding which ensures minimal heat is

lost from the system. This reduces the amount of temperature variation during the testing procedure. As previously discussed, the test rig fixtures are water cooled in order to ensure that they themselves do not fail as a result of creep or fatigue during the test. Platinum p.d. wires feed in to a chart recorder which continuously monitors the voltage across the sample as it changes as a function of crack length.

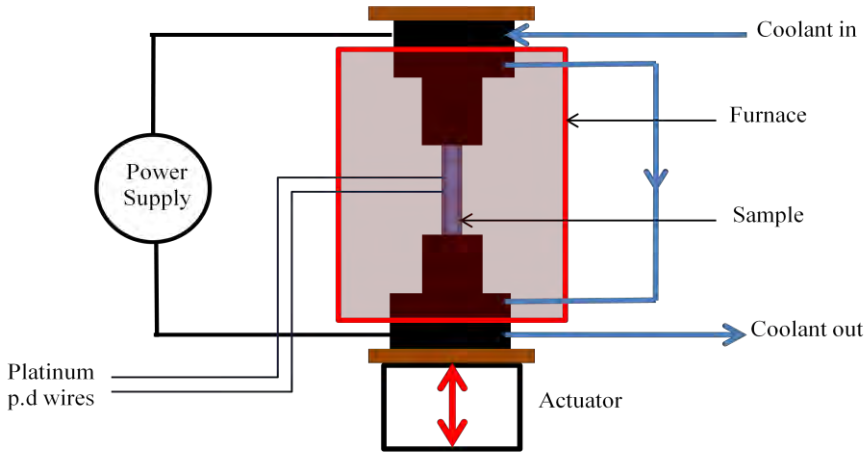


Figure 3-3: Schematic diagram of the testing rig.



Figure 3-4: Photograph showing complete testing rig including servo-hydraulic tensile testing machine, furnace and associated cooling.

The servo-hydraulic tensile testing machines used in this programme run with load cells of either 50 or 100 kN. These are calibrated down to a minimum level of 2% of the maximum (i.e down to 1 kN or 2 kN respectively). A calibrated oscilloscope is used to visualise the stress versus time waveform applied to the test piece by each testing machine in order to ensure that it follows the correct trapezoidal shape shown in Figure 2-8 and Figure 2-9 (for example), and that maximum and minimum loads are indeed those expected. Tests are carried out at temperatures ranging from 625˚C to 675˚C in laboratory air, and for comparison some conditions are repeated in a vacuum.

Crack length is continuously monitored using the potential drop technique which assumes that the electrical resistance across a specimen will increase linearly with crack growth. Crack length data obtained in this way are calibrated after each test by measuring crack length at known voltage values, a technique which is reported in greater detail in subsequent paragraphs. It is possible to measure crack length optically by taking replicas using a solvent and by pressing polymer plates against a sample. Replicas are taken at intervals and measured using an optical microscope. The method is disadvantageous however for three main reasons; that continuous crack length monitoring is not possible, that only the edge lengths of cracks are measurable and finally that it is not possible to do inside a furnace at high temperatures. A significant advantage of using the D.C.P.C technique of crack length measurement is that it naturally calculates an average crack length magnitude across the whole sample. Nevertheless crack length measurements and calibration calculations rely on two fundamental assumptions; that crack length increases linearly with voltage (p.d.) across the sample, and that crack geometries are quarter circular in shape. The appropriateness of both of these assumptions is reported in subsequent sections and their validity is discussed through analysis presented in Appendix V.

3.2.3 Testing Procedure

The main body of work in this programme involves baseline, dwell and overload cycling of fine-grained Udimet 720Li and RR1000 test pieces. First, an atomically sharp fatigue pre-crack is grown in to the material from the machined notch. The pre-cracking waveform applied is sinusoidal in shape and with a 1 Hz frequency, and pre-cracking is performed at

temperature. The procedure involves shedding the load at intervals of crack length to ensure that the plastic zone ahead of the crack tip is kept smaller than that which results from the initial peak in stress intensity. The exact procedure is documented in subsequent paragraphs.

Following pre-cracking, three different waveforms are applied to each test piece in separate sections defined by a given amount of crack growth. This procedure isolates the effect of waveform; allowing direct comparisons between each type of waveform and eliminating microstructural variation between test pieces. This particular method is also implemented for two further reasons, namely that it saves time and that it minimises any crack tunnelling.

First, baseline cycling (1-1-1-1) is applied after pre-cracking until a pre-defined crack length has been reached. Once the crack has grown to this pre-defined length under baseline loading, the load waveform is switched such that dwell cycling (1-dwell-1-1) is applied. The crack is then grown under this particular regime for a further pre-determined amount. When the crack has grown further, a series of overload cycling (1-OL-1-dwell-1-1) is applied to the test piece; again, over a pre described amount of crack growth. After overload cycling, a final segment of baseline cycling is applied to finish the test. The total crack length after the final baseline loading is grown to around half the width of the specimen:

$\frac{a}{w} = 0.5$ ..... Equation 35

Where “a” is the crack length (mm) and “w” is the thickness of the specimen (mm).

Although the total resistance of the complete circuit for each test will vary as a function of temperature (among other things), the constant current supplied to the circuit is finely altered such that at the start of each test, the potential difference across the notch (with no crack) is ~100 μV and this is referred to as "V_o" (μV). Although this value (the constant current applied to the circuit) varies according to the particular test in operation, it is usually between 7 and 8 amps. Since test pieces are 7 x 7 mm in section, a quarter circular crack which has grown to half the width of the test piece corresponds to a length of 3.5 mm. Based on previous methodologies a crack length of 3.5 mm corresponds to a potential difference value of ~1,200 μV. Baseline, dwell and overload tests are therefore carried out such that pre-cracking is completed to a length corresponding to a p.d value of ~200 μV, baseline loading then grows the crack until ~400 μV is reached, dwell loading grows the crack from ~400 μV to ~600 μV, overload cycling from ~600 μV to ~900 μV and a final segment of baseline loading from ~900 μV to ~1,200 μV. Test pieces are then allowed to cool to room temperature by switching off power to the furnace and ensuring that test machines hold samples at a small load (~2 kN) in load control (to account for the fact that they will change dimensions upon cooling). Test pieces are then broken open at room temperature using the same 1 Hz sinusoidal wave as for pre-cracking.

Table 5 documents this technique; where the above p.d values are tabulated against approximate corresponding crack lengths (in mm) and ΔK values (in MPa√m). Associated ΔK values are calculated assuming that the maximum load is 26 kN (~531 MPa on a 7 x 7 mm sample) and that the geometric shape factor Y is appropriately represented by Equation 24 (reported in subsequent sections).

Table 5: Detailing testing methodology for baseline, dwell and overload tests. Approximate p.d values, crack lengths (a) and ΔK calculations are presented; more accurate and calibrated calculations are completed after each test.

	Pre-cracking	Baseline	Dwell	Overload	Baseline
p.d (μV)	100 – 200	200 – 400	400 – 600	600 – 900	900 – 1,200
a (mm)	0.3 – 0.58	0.58 – 1.17	1.17 – 1.75	1.75 – 2.625	2.625 – 3.5
ΔK (MPa√m)	9.9 – 14.0	14.0 – 20.1	20.1 – 25.5	25.5 – 34.5	34.5 – 45.8

It is important to ensure that the plastic zone size ahead of the crack tip is minimised during pre-cracking. A "load shedding" technique is therefore applied. Here, pre-cracking begins at a high maximum load (32 kN or ~653 MPa) and is gradually reduced as the crack grows. Assuming that the potential difference across the notch while no crack is present (V_0) is ~100 μV, pre-cracking at 32 kN is used to introduce a fatigue crack from the notch until it has grown to a length which corresponds to a p.d value of ~120 μV which represents a ΔK value of 13.3MPa√m. The load is then shed down to 30 kN (or ~612.25 MPa) until a crack length corresponding to a p.d value of ~140 μV is reached. This represents ΔK values of 12.5 MPa√m at 120 μV until 13.5 MPa√m at 140 μV. A load of 28 kN (or ~571.5 MPa) is used to grow the crack to a p.d value of ~160 μV, which represents ΔK values of 12.6 MPa√m at 140 μV until 13.5 MPa√m at 160 μV. Finally the pre-crack is grown to ~200 μV using a maximum load of 26 kN which represents ΔK values of 12.5 MPa√m at 160 μV until 14.0 MPa√m at 200 μV. Hence the maximum ΔK value is not reached until finishing pre-cracking but is kept below ~13.5 MP√m during the pre-cracking process. This ensures that the plastic zone size ahead of the crack tip is minimal during pre-cracking and only grows larger during the actual test. It is especially important in the case of load shedding

techniques since each time the load is reduced; the fatigue crack should grow through the plastic zone caused by the previous application of load.

These calculations are tabulated in Table 6 including estimations for associated idealised (circular) plane stress plastic zone sizes (radii, r) assuming Irwin's model and a yield stress of around 1000MPa for fine-grained Udimet 720Li and RR1000. It should be noted that 20 μV of crack growth refers to around 58 nm, hence in each case the crack is shown to have grown through the plastic zone size caused by the previous application of load. It is important to highlight that pre-cracking is completed with an R ratio of 0.1 (where the minimum load is 10% of the maximum load). Pre-cracking is also completed at temperature (i.e. the same temperature conditions under which the test will go on to be completed).

Table 6: Detailing "load shedding" pre-cracking methodology including idealised (circular) estimations for associated plane stress plastic zone size radii (r).

Max Force (N)	**32**	**30**	**28**	**26**
Max Stress (MPa)	653	612	571	531
p.d (μV)	100 – 120	120 – 140	140 – 160	160 – 200
a (mm)	0.3 – 0.35	0.35 – 0.4	0.4 – 0.47	0.47 – 0.58
ΔK (MPa√m)	12.2[3] – 13.3	12.5 – 13.5	12.6 – 13.5	12.5 – 14.0
r (nm)	7.8 – 9.4	8.3 – 9.7	8.4 – 9.6	8.3 – 10.4

[3] This value for ΔK is estimated assuming the stress state around the machined notch represents sharp fatigue crack growth stress states (i.e. assuming the same geometric shape factor Y as for fatigue crack stress intensity factor calculations). Although this is unlikely to be the case, the value quoted above will be an overestimate (hence conservative). The actual value for ΔK at this stage would sit just above the fatigue threshold for the material since cracks begin to grow extremely slowly, as represented by pre-cracking crack growth resistance curves.

As discussed below, baseline, dwell and overload testing is only one example of the type of testing carried out in this programme. A full matrix of testing conditions in presented in section 3.2.5.

In each case, dwell loads are usually 26kN (which is ~531 MPa of nominal stress on a 7 x 7 specimen), and a small proportion are tested at 23.4 kN (a reduction of 10%). Each time the waveform is set up such that minimum loads are 10% of the dwell load, to give an R ratio of 0.1.

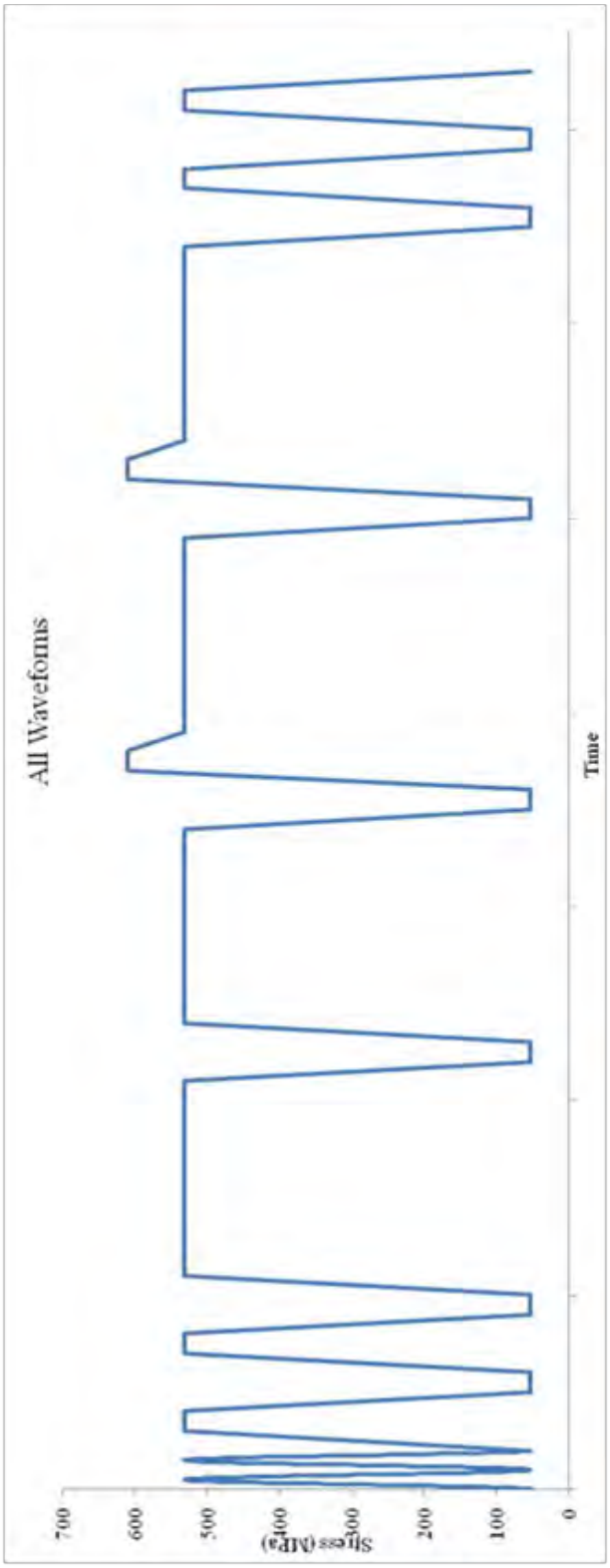


Figure 3-5: Showing all waveforms used to test each sample. From left to right: sinusoidal precracking; 1-1-1-1 baseline loading; dwell loading; overload loading and final baseline loading.

3.2.4 Data Analysis

3.2.4.1 Crack Growth Resistance Curves

Tests carried out in this way leave characteristic "stripes" on the fracture surfaces of the samples, where different loading waveforms beach-mark the sample respectively, due to different oxidation effects. The effect can be seen in Figure 3-6:

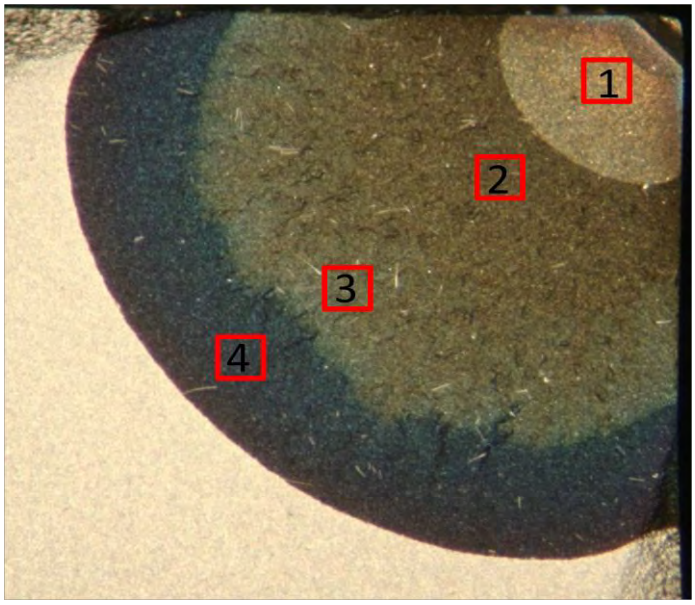


Figure 3-6: An optical image of part of the fracture surface of a sample tested using this methodology. Section one is the first baseline segment, section two is the dwell segment, section three, the overload segment and section four, the final baseline segment. The rest of the fracture surface represents room temperature 1 Hz sinusoidal cyclic fatigue crack growth. For reference, this particular example is fine-grained RR1000, tested at 625°C, with a dwell time of 1,200 seconds and an overload factor of 1.10.

Since the fracture surfaces of test pieces are beach marked at controlled and measured voltage (p.d) values, is it possible to correlate three or more points at which both crack length and p.d. is known. Crack length can be measured using image analysing software and by assuming that the crack is quarter circular in shape, as illustrated in Figure 3-7:

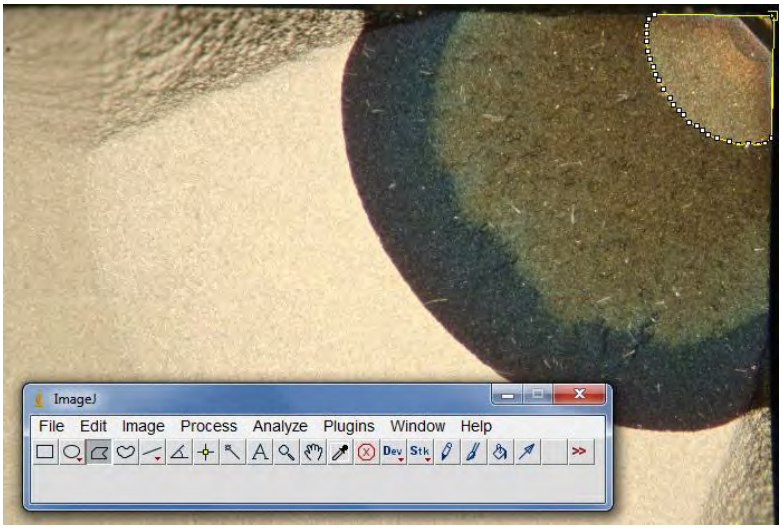


Figure 3-7: An optical image of the fracture surface with measurements for the length of the crack after the first 1-1-1-1 segment taken.

Image analysing software measures the total number of pixels which have been selected, which can be converted to area (in mm^2). This area is then multiplied by 4 to represent a total circle, and an average crack length "a" is calculated by rearranging;

$area = \pi r^2$ ..... Equation 36

Where "r" is the average crack length. Usually measurements are taken after the first baseline (1-1-1-1) segment, after the overload segment and after the last baseline segment, and a simple graph of p.d. and crack length at these three points is plotted.

It is important to highlight that this method of calculating crack length assumes that it is quarter-circular in shape. In fact the shape of the crack as it propagates through a corner

notched test piece will vary as a function of testing conditions and stress waveform type. Certain conditions tend to cause result in preferential crack growth through the middle of the sample and relatively slow crack growth along the edges, a phenomenon known as tunnelling. The effect of tunnelling is not yet well understood although it is thought to arise due to the different stress states at the edges of the cracked test piece. Nevertheless for the majority of tests carried out in this programme crack front morphologies are found to be generally quarter circular in shape. A discussion on the validity of these assumptions and analysis relating to crack shape and geometry can be found in Appendix V.

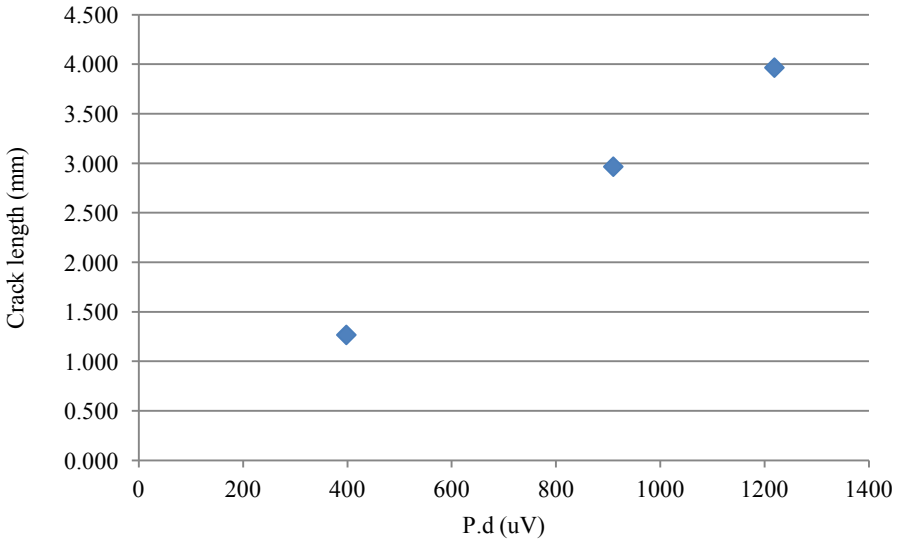


Figure 3-8: A graph of crack length against p.d. for RR1000 sample CC046.

The graph in Figure 3-8 can be used to determine an equation for crack length using:

$y = mx + c$ ..... Equation 37

Where m is the gradient of the line, c is the y intercept and y and x are p.d. values (μV) and crack lengths (mm) respectively. This enables accurate determination of crack length for a continuous range of p.d. values. It is worth highlighting that this approach always assumes a linear relationship between p.d. and crack length. A plot of these points provides a method to check whether or not this is indeed the case, giving validation to the methodology for determining crack length detailed above. In each test piece and for each condition tested crack length and p.d. were indeed found to be linearly proportional, hence the assumption is deemed to be appropriate. As previously discussed, a more detailed analysis of the relationship between p.d. and crack length and plots for each test carried out in this programme can be found in Appendix V.

Raw data is produced in the form of a chart-recorded roll of paper with a long, gradually drawn line which represents continuous measurements of the potential difference across the sample.

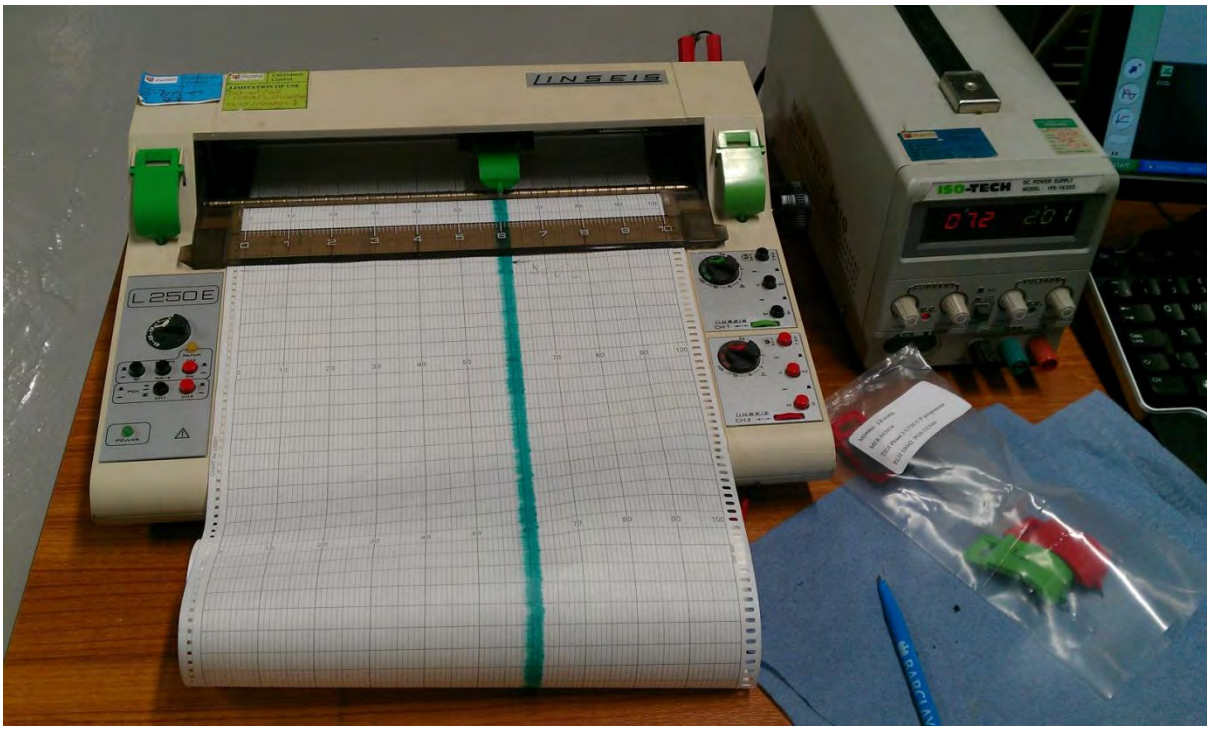


Figure 3-9: Photograph showing chart recorder continuously measuring the potential difference across the sample as a function of constant current (7.2 amps) and electrical resistance across the sample, which itself is a function of growing crack length.

This raw data is tabulated by carefully measuring the chart length (in mm) at set intervals of 10 μV (where the drawn line crosses each 10 μV line on the chart paper grid). Chart length and corresponding p.d. values are tabulated for each waveform using Microsoft Excel spread sheets. Chart length is used to calculate the number of cycles (which depends upon chart speed) and voltage is used to calculate crack length by applying the above equation;

$$y = mx + c$$

ΔK is calculated for each crack length measurement using standard linear elastic fracture mechanics:

$$\Delta K = Y\Delta\sigma\sqrt{\pi a}$$

Where Y is calculated by applying a simplified compliance function polynomial for a/W of 0 to 0.75 documented by Rolls-Royce plc. in-house procedure:

$$Y = \left(0.6799\left(\frac{a}{w}\right)\right) - \left(1.2266\left(\frac{a}{w}\right)^2\right) + \left(7.8729\left(\frac{a}{w}\right)^3\right) - \left(10.396\left(\frac{a}{w}\right)^4\right) + \left(4.714\left(\frac{a}{w}\right)^5\right)$$

..... Equation 38

The above geometric correction polynomial is used extensively within Rolls-Royce plc. to analyse data captured in this way. It is based on Pickard's original work [80] and utilised by Rolls-Royce plc. to produce relevant compliance functions for corner crack test piece geometries pertaining to quarter circular crack geometries such as those used in this programme. The capability of the polynomial to accurately represent ΔK values is well documented within the company and is discussed in Appendix V. It is important to note here however that there is a divergence in the data (compliance function versus a/W) when Pickard's original work is compared with the polynomial applied above. The reasons for this remain unclear; nevertheless the divergence is kept to below ~5% for a/W values of less than 0.6. It is therefore suggested that the simplified polynomial above is suitable only for ΔK calculations where crack lengths are below 0.6 of the total width of the sample. Hence any data captured after a crack length of 4.2 mm, or a p.d value of ~1440 μV must be disregarded.

(Furthermore, the relationship between crack length and p.d after a/w > 0.6 is not well understood.)

$\Delta\sigma$ is calculated using

$\Delta\sigma = \frac{F_1 - F_2}{A}$ ..... Equation 39

Where F_1 and F_2 are the maximum and minimum applied forces respectively (in kN) and A is the cross sectional area of the test piece (in mm^2).

da/dN is calculated by applying a differentiation of crack growth with respect to number of cycles (in mm/cycle) as the crack continuously grows, and da/dN is plotted against ΔK on a log-log scale.

It is important to note that for the overload cycle two "maximum" stresses are applied (namely, the overload load and the dwell load) and hence two ΔK values can be calculated. For comparison, data captured during the overload segments of the test is plotted alongside similarly captured data for baseline and dwell loading as ΔK_{dwell} (i.e. assuming σ_{max} = dwell load). ΔK_{full} (i.e. assuming σ_{max} = overload load) is used to determine the extent to which crack growth rates have been retarded.

This type of testing enables good comparison of crack growth rates for each different waveform since it completely isolates the effect of waveform by applying each type on one test piece. Hence microstructural variations are removed as a variable (within one test at least) and a good comparison of crack growth rates for each waveform can be made. Furthermore, generating crack growth rates pertaining to baseline and dwell loading within one test piece enables the calculation of the optimised D' parameter (in terms of Rolls-Royce plc. TiDI models), for each individual test piece. It also provides an isolated benchmark from which crack growth rates pertaining to overload cycling can be compared.

A comprehensive test matrix has been designed to determine the effect of dwell time, dwell load, overload factor, and temperature for both fine-grained Udimet 720Li and RR1000 and can be found in Table 8 to Table 13.

3.2.4.2 Defining Overload Retardation

Along with careful plotting of continuously measured and calculated da/dN versus ΔK values on a log-log scale; data is interpreted and analysed in a variety of ways. Most significantly overload crack growth data is analysed by determining the degree to which crack growth retardation has occurred as a result of introducing the overload segment to the waveform when compared with otherwise similar dwell-only cycling. A simple classification of "full retardation" (where crack growth rates have returned all the way back down to those associated with baseline), "nearly full retardation" and "partial retardation" is used to

compare the extent to which retardation has occurred. Detailed definitions of the three categories of retardation are reported in section 4.1.

Crack growth resistance curves for conditions which cause a partial retardation during the application of overload waveforms can also be used to calculate the total subsequent time (in seconds) that time-dependent crack growth has been suppressed as a result of preferential unloading of crack tip stresses due to a nominal (bulk) unload from the overload segment to the dwell load. A discussion pertaining to the mechanism by which this occurs is made in section 5.3, nevertheless presented below is a method by which the data is analysed:

Section 2.4.3 reports that linear superposition methodologies of cycle and time-dependent crack growth components are used to predict overall (total) crack growth rates in the following way:

$$\left(\frac{da}{dN}\right)_{total} = C \times \left(\Delta K_{eff}\right)^n + D' \times \left(\Delta K_{eff}\right)^n \times \left\{t_{hold} + \frac{2 \times t_{ramp}}{n+1}\right\} \quad \text{..... Equation 21}$$

A testing condition which results in the partial retardation of crack growth rates for overload cycling when compared with otherwise similar dwell cycling on the same test piece enables the calculation of a new "effective" t_{hold} for the overload segment of crack growth. The crack growth resistance curves (reported in section 4.1, Appendix VI and discussed in section 5.3) indicate that for a portion of the subsequent dwell period, after unloading from the initial overload segment, the time-dependent component of crack growth is suppressed. It follows

therefore that for overload cycling; a new "effective" t_{hold} can be calculated by rearranging the above equation and assuming that the total crack growth rate is represented by a cyclic component and a new effective time-dependent "dwell" component.

Separating Equation 21 in to its cycle and time-dependent components allows for the formation of two Equations with two unknowns (namely, C for the cycle-dependent part and D' for the time-dependent part). The known test and materials parameters are;

t_{ramp} = 1s

n is a known material constant for each alloy at a given temperature (the actual values are taken from Rolls-Royce in house material database COMMIT and given in Table 7)

da/dN is taken from baseline, dwell and overload crack growth resistance data

By substituting actual crack growth resistance data for baseline and dwell loading and rearranging the equation, values for C and D' are calculated. Finally, Equation 21 is altered such that t_{hold} is replaced with *t'*:

$$\left(\frac{da}{dN}\right)_{total} = C \times \left(\Delta K_{eff}\right)^n + D' \times \left(\Delta K_{eff}\right)^n \times \left\{t' + \frac{2 \times t_{ramp}}{n+1}\right\} \quad \text{..... Equation 40}$$

Where *da/dN* values are now substituted in from overload crack growth resistance data (from either a point or a series of points from the stable, linear part of the crack growth data) such that *t'* is the only unknown. t' is the new "effective" hold period which describes crack growth behaviour pertaining to overload cycling, as though it were normal dwell data; but

with a shorter "effective" hold period (when compared with that which was actually applied) due to the retardation of crack growth rates.

A simple subtraction of *t'* from the original total t_{dwell} gives a value for the experimentally derived "incubation time"; the effective total amount of time in seconds that time-dependent creep and oxygen induced fast crack growth has been suppressed as a result of unloading from the overload segment in the waveform.

Experimentally derived values for this incubation time allow for more quantitive descriptions (rather than simple categorisation of full or partial retardation for example) and comparisons of overload retardation behaviour for each testing condition. Furthermore, incubation times are also found for each condition tested using finite element models (section 4.3.2 and 4.3.3). Therefore, these experimentally derived values for incubation time allow for direct comparisons between experimental and analytical data; reported in section 4.3 and presented in Table 29, Table 30 and Figure 4-84.

For completeness, the parameter *n* for each alloy at each temperature tested (used in the analysis of data to determine experimentally derive incubation times) is documented in Table 7.

Table 7: The parameter *n* for each alloy at each temperature; taken from Rolls-Royce in house material database COMMIT; used to determine experimentally derived values for incubation time.

Temperature (°C)	Udimet 720Li *n*	RR1000 *n*
600	2.656	2.305
625	2.678	2.258
650	2.744	2.217
675	2.872	2.182

3.2.4.3 Creep Affected Zones and Oxygen Damage

The crack growth resistance curves generated and developed in this programme of reasearch show that transitional behaviour (in terms of crack growth rates) occurs as a result of switching the waveform from baseline to dwell loading, dwell to overload loading, and from overload to baseline loading. Crack growth rates are observed either to begin more quickly or more slowly than usual; and to stabilise (to more usual, linear crack growth) by "settling up" or "settling down" as the crack grows through fresh material. The reasons for this are discussed in section 5.5 but it is important to note here that data is analysed is such a way as to determine the length through which the crack must grow to overcome this transitional behaviour. Therefore crack growth resistance curves are used to determine the crack length at which the behaviour begins and the crack length at which growth rates stabilise by referring to individual points on the crack growth resistance curves and their associated tabulated data values for crack length "a".

A matrix of testing conditions is plotted against remarks regarding this transitional behaviour, the distance over which it occurs and (in separate tables) the degree of retardation for all conditions tested. The tabulated results also includes details about the mechanism of crack growth, reported in section 4.2.1 and discussed in detail in section 5.2.1.

3.2.5 Summary of Testing Conditions

3.2.5.1 Udimet 720Li and RR1000 Baseline and Dwell Testing

Along with baseline, dwell and overload tests, several other types of fatigue testing has been carried out in order to better understand these cyclic and time-dependent interacting failure phenomena.

Baseline and dwell fatigue tests (without an overload segment) are carried out on fine-grained Udimet 720Li and RR1000 test pieces and conditions are repeated in air and in a vacuum to isolate oxygen effects. Here, samples are pre-cracked at temperature as described above, and subsequent baseline and dwell waveforms are applied using similar methodologies. Usually a period of baseline loading is followed by dwell cycling which is then followed by a further period of dwell loading. In a number of cases this procedure is repeated (on one test piece) such that two (or more) bands of dwell loading are applied.

This methodology results in the marking of fracture surfaces with characteristic “stripes” similar to those detailed above and hence enable crack length measurements to be calibrated. As before, fatigue cracks are grown through the test pieces until a final crack length of half

the width of the specimen is measured and samples are broken open at room temperature using the same 1 Hz sine stress wave used for pre-cracking.

It is important to highlight at this stage that a number of investigations have been undertaken on all four "Batches" of fine-grained Udimet 720Li, discussed in section 3.1. Dwell and overload tests are carried out on at least one test piece from each Batch from each Phase. Full and comprehensive testing matrices which label each test piece with a series of testing conditions, and each respective Phase and Batch number are presented in Table 8, Table 9, Table 10, Table 11, Table 12 and Table 13.

3.2.5.2 Effect of Dwell at Overload

The study has been developed to explore the effect of hold period at maximum (overload) load. Time at maximum (overload) load is increased from 1 second to dwell times of 120 seconds and 600 seconds on several fine-grained Udimet 720Li and RR1000 overload tests to determine its effect on fatigue crack growth behaviour. Furthermore, these waveforms are also analysed using finite element models (section 3.4) to examine crack tip stresses pertaining to these types of loading waveforms. With the exception of an extra hold period during the maximum load segment of the overload waveforms, the empirical tests are completed using exactly the same methodology described in section 3.2.3.

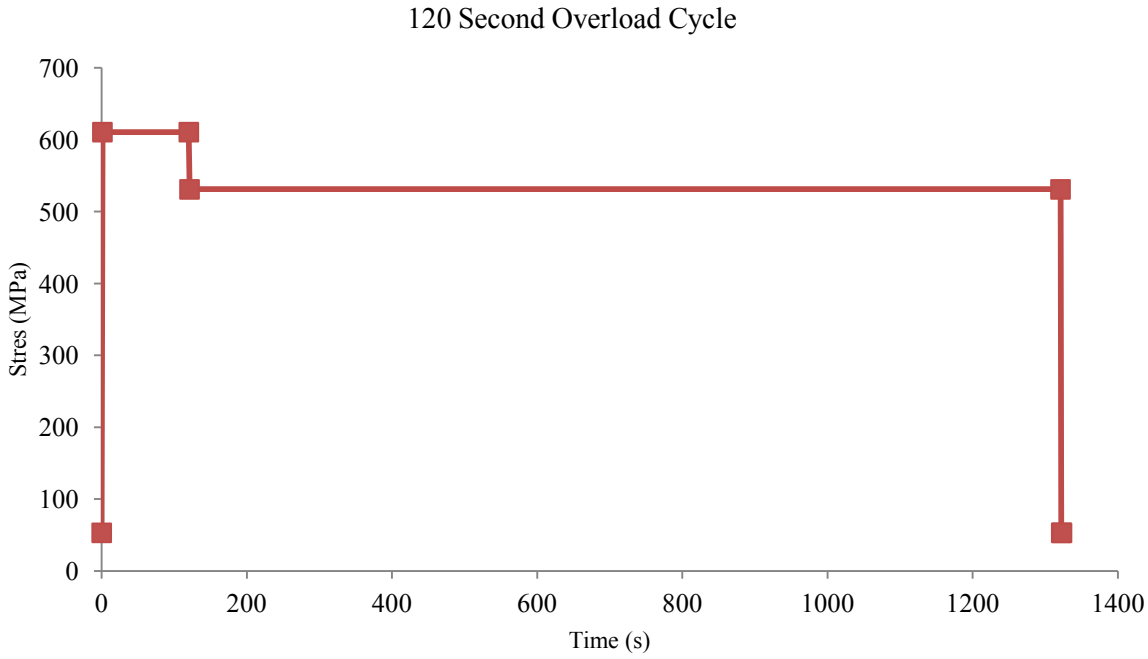


Figure 3-10: Showing the 120 second dwell at overload waveform, with an overload factor of 1.15 and a subsequent dwell time of 1,200 seconds.

The rational for performing these types of tests is that they better mimic in-service conditions experienced by high pressure compressor and turbine Ni-discs, since the engine typically works at maximum capacity (i.e. "take-off") for a period of around two minutes before entering the "climb" stage where it runs at slightly reduced capacity.

It is worth explaining why not all of the overload tests carried out in this programme are therefore run in this way, if the "two minute dwell at overload" methodology does indeed better represent in-service stress states. In general, this test programme seeks to isolate the effect of overload, or more specifically the effect of unloading from an overload segment, on otherwise typical and well-reported dwell crack growth rates and mechanisms. A hold period

of one second at the overload load is therefore used since longer periods at this level of stress would likely cause intergranular fast crack growth during the overload segment. It is indeed beneficial and necessary to explore and understand these effects but they might in some way "hide" the effect of overload, which is being studied empirically. Extrapolation of possible retardation effects can be included in already well understood two minute dwell lifing methodologies (for example) if both phenomena are properly understood.

3.2.5.3 Effect of Unloading and Reloading

Furthermore, the study has been developed to determine the effect of ramp rate and subsequent reload on the retardation effect, the rationale being that real life stress cycles are complex and involve both unloading and reloading. Tests have been carried out on two fine-grained RR1000 test pieces; under similar conditions to those described in section 3.2.3, but rather than applying nominal overload stress cycles (Figure 2-25, for example) during the third section of the test, the following stress waveforms were applied:

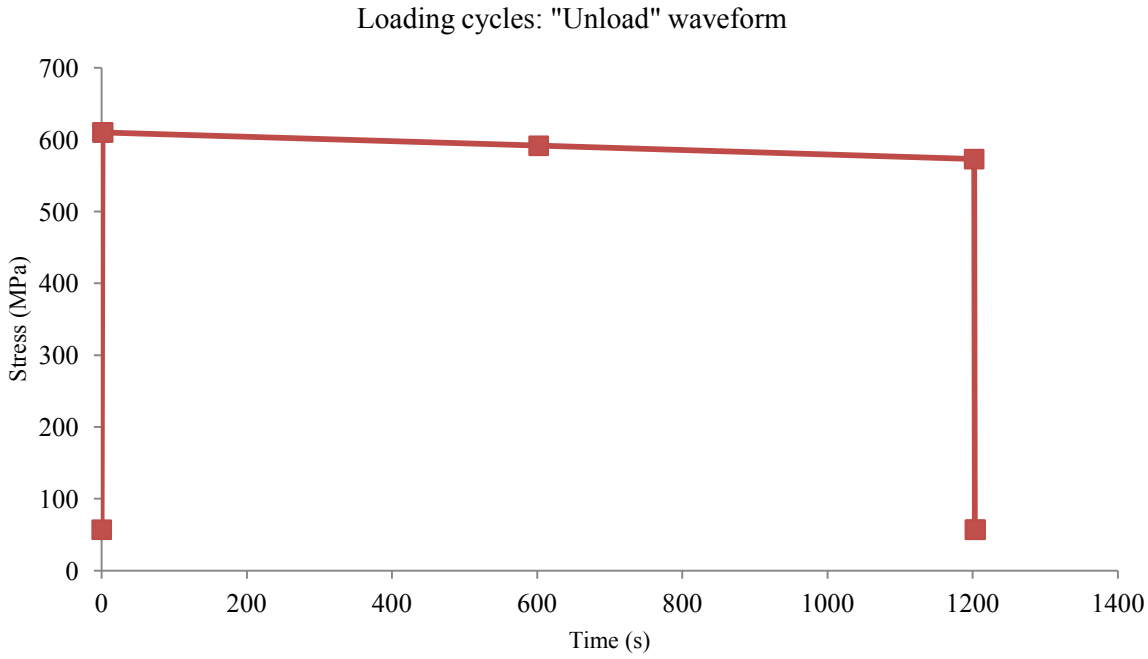


Figure 3-11: The "unloading" waveform, where the overload was gradually unloaded back down to the dwell load over the whole dwell time (1,200 seconds), rather than over a period of one second as in the previous methodology.

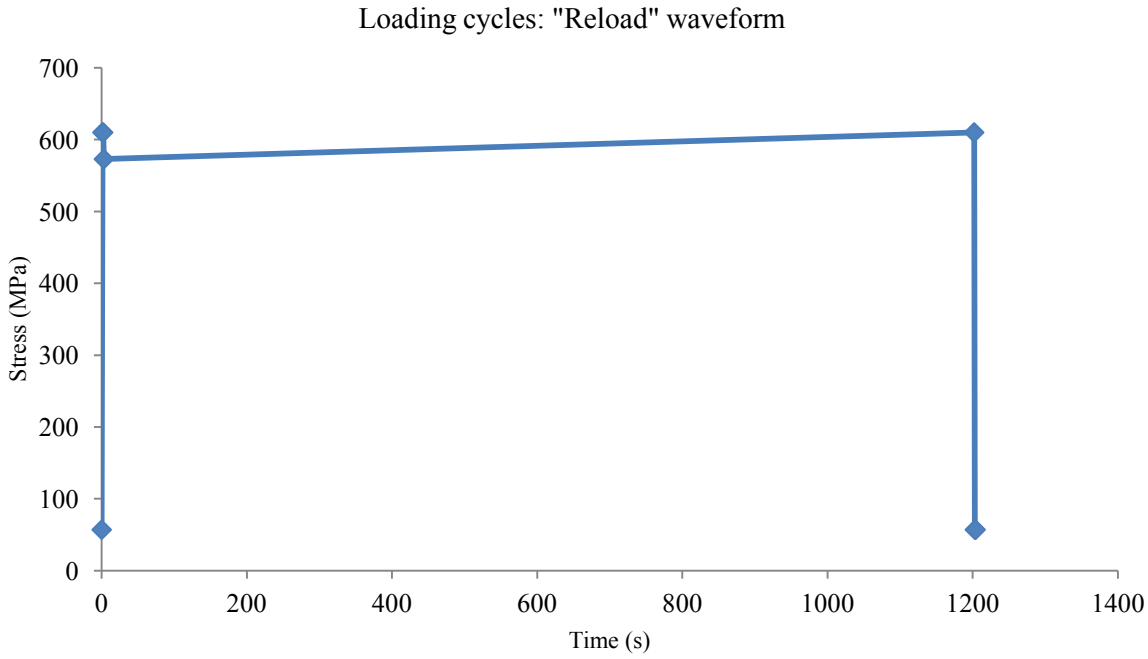


Figure 3-12: The "reloading" waveform, where after the initial one second overload, the applied stress is gradually increased back to the maximum overload over the dwell period (1,200 seconds).

3.2.5.4 Effect of Cooling Rate

In order to investigate the effect of microstructure, dwell fatigue tests on two fine-grain RR1000 samples with different cooling rates are also included in the study. RR1000 discs are cooled from above the solvus temperature at a target rate of ~1°C/s, a rate which can vary across the section of the disc from ~5 to ~0.1°C/s. These faster and slower cooling rates can cause a degree of variation in the morphology of the γ' phase, and can also have an effect on the γ grain size and morphology. This might in turn influence the mechanical properties of the material.

Completing two dwell tests under similar testing conditions but for different microstructures isolates the influence of microstructure on the dwell crack growth behaviour of the material. As with previously reported testing methodologies, test pieces are pre-cracked at temperature using a 1 Hz sine stress wave and a load shedding technique, and tested under baseline and dwell loading conditions.

3.2.5.5 Time-dependent ΔK_{th} Testing

Finally, a testing methodology has been developed to determine the stress intensity factor range threshold which would cause the onset of crack growth specifically for cycle and time-dependent (i.e. dwell) crack growth. There are two main reasons for which this type of data is sought in this programme of research. Firstly, it is important to compile a good understanding of which crack growth driving forces cause the onset of crack growth and which do not during in-service operation (i.e. under high temperature dwell loading). Furthermore, such comprehensive understanding should also include analysis pertaining to the near-threshold behaviour of crack growth, including and especially the mechanism by which cracks may grow under this regime.

The test uses a two minute (120 second) dwell period as a reference waveform since the data in the programme (Appendix VII) suggests this gives sufficient time for fully intergranular crack growth morphologies. As with previously reported methodologies, the test pieces are 7 x 7 mm corner notched specimens, and are fatigue pre-cracked at temperature using a 1 Hz sine stress wave and a load shedding technique. The pre-crack is “load shed” down to a value

near to the fatigue threshold in order to reduce the plastic zone size ahead of the crack tip to ensure that the damage is minimal before beginning time-dependent testing. Several tests have been pre-cracked down to a ΔK value of around 10 MPa$\sqrt{m}$, nevertheless further developments in the methodology sought to reduce this value further until the fatigue (cycle-dependent) threshold itself is reached. This gives an indication of the fatigue threshold value for the material which can be used to form a benchmark with which to compare the time-dependent threshold value obtained by the application of a 120 second dwell waveform.

Furthermore, it is important to determine the mechanism by which time-dependent crack growth occurs at threshold. If, for example, fracture surfaces show a transition from transgranular to intergranular crack growth as one might expect, it is essential to determine the exact crack length at which this transition occurs and to be able to relate this length back to a precise measurement for the p.d. across the test piece, and hence confirm whether or not the transition has occurred as a result of switching the waveform from sinusoidal 1 Hz pre-cracking to dwell loading. For this reason, fracture surfaces must be marked during pre-cracking according to at least one known p.d. interval, which creates a precise reference point from which crack lengths can be measured along the fracture surface. This achieved by the application of a high ΔK for a given amount of crack growth, followed immediately by the application of a much reduced ΔK (a reduction of around 25%) for a given amount of crack growth, followed immediately by the application of a high ΔK value. This sharp reduction and increase in ΔK can cause the fracture surface to be “beach-marked”, shown in Figure 3-13.

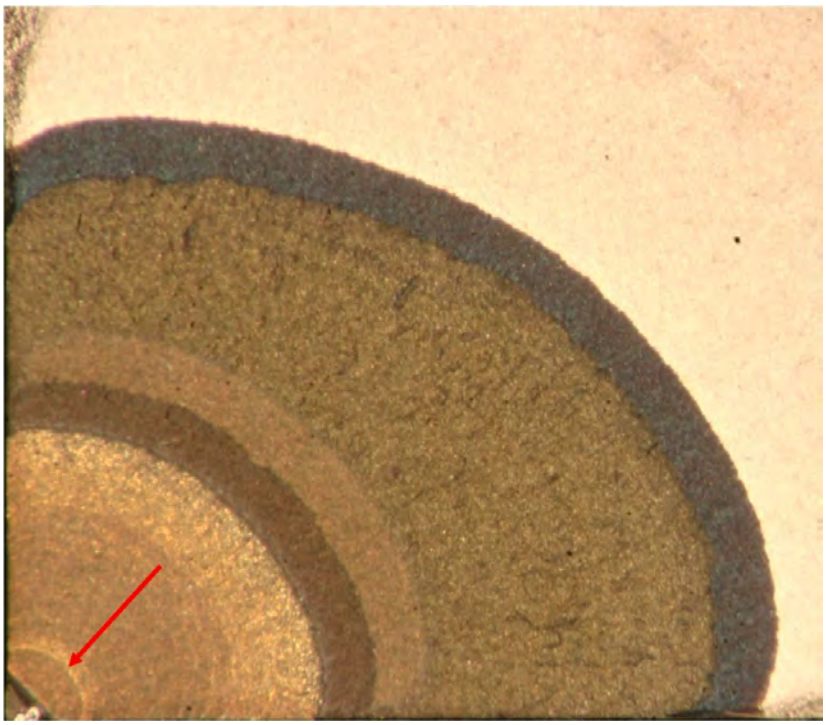


Figure 3-13: Showing a beach-marking effect on the pre-crack fracture surface of Udimet 720Li sample CC044. For reference, the sample was pre-cracked, tested for a time-dependent temperature threshold, pre-cracked again and then tested for decreasing ΔK threshold for time-dependent crack growth with a dwell period of 120 seconds and at a temperature of 650°C. The final "band" represents a final region of baseline loading.

After pre-cracking, two minute dwell periods are applied to the test piece. They are first applied at dwell loads to give a ΔK which is below the threshold value (i.e. a load which would not cause any crack growth), and they are gradually increased over time. Test pieces are left to cycle at two minute dwell periods for a total of 48 hours. If no crack growth is observed during this time; the load is increased, usually by 1 kN which correlates to an increase in ΔK of about the same value (~1 MaP√m). Once the time-dependent threshold has been reached, and the crack begins to grow, it is allowed to grow through to a length of around half the width of the specimen, in a similar way to the methods described above. A range of dwell periods and temperatures have been investigated (Table 10).

A final variation on these tests has been to experiment with testing methodology. The technique described above involves gradually increasing the applied ΔK from below the threshold value until it is reached. The 650°C, 120 second dwell test has been repeated under "decreasing ΔK" conditions where the testing begins at a ΔK value large enough to cause time-dependent crack growth (i.e. above the threshold) and gradually decreased (in a similar manner to the load shedding technique applied during pre-cracking). The rational is that these different methodologies might induce different stress states, plastic zone sizes and oxygen induced damage ahead of the crack tip and hence may affect the stress intensity factor range threshold values which are obtained. It is important to ensure that the effect of testing method is fully understood in order to validate both the methodology and the data themselves.

It is important to note that when performing decreasing ΔK_{th} tests, there are a number of valid methodologies which may be applied. One approach might be to keep the maximum load constant, and to gradually increase the R ratio by gradually increasing the minimum load (thus also reducing the effective ΔK). The approach used in this programme was to gradually decrease Δσ and keep the R ratio constant, in order to match and repeat the conditions and testing methodology discussed above for increasing ΔK threshold testing as closely as possible.

Furthermore, it should be noted that when performing these decreasing ΔK tests it is important to match up each interval (in terms of ΔK values). Therefore the load should be shed at appropriately small intervals such that a complete crack growth resistance curve can be generated.

Finally, a preliminary temperature threshold test has also been performed. Here, a test piece is pre-cracked according to the above described methodology, at a temperature of 650°C, after which the sample is allowed to cool to around 400°C. A ΔK of 25 MPa$\sqrt{m}$ is then applied to the test piece with a dwell time of 3,600 seconds at this relatively low temperature. Crack growth does not occur hence the system is below threshold. If, after 24 hours no crack growth has occurred, the load waveform (and associated ΔK value) is kept constant and the temperature is increased by 10°C (at a rate of ~2°C/hour). This procedure is repeated every 24 hours until the temperature is high enough such that time-dependent crack growth begins. This enables the investigation of the temperature threshold at which time-dependent crack growth will occur for a give ΔK, and (as with previous methodologies) the mechanism by which this crack growth occurs.

3.2.5.6 Table of Testing Conditions

A matrix of all conditions for baseline, dwell, overload, unload, reload and time-dependent threshold tests is presented in Table 8, Table 9, Table 10, Table 11, Table 12 and Table 13:

Table 8: Overview of the Udimet 720Li Phase 1 test programme.

Testpiece ID (°C)	Temperature (°C)	Environment	Loading waveform (seconds)	$P_{max}/P_{dwell}/P_{min}$ kN
CC009	650	Air	1-3,600-1-1	26/ - /2.6
CC019	650	Air	1-3,600-1-1	17-27/ - /1.7-2.7
CX023	650	Air	1-3,600-1-1	29/ - /2.9
CX027	650	Air	1-3,600-1-1	23-28/ - /2.3-2.8
CX030	650	Air	1-1-1-3,600	26/ - /2.6
CX025	650	Air	1-1-1-3,600	26/ - /2.6
CX033	650	Vacuum	1-120-1-1	26/ - /2.6
CX031	650	Vacuum	1-120-1-1	26/ - /2.6
CX034	650	Vacuum	1-3,600-1-1	26/ - /2.6
CX044	650	Air	1-120-1-3,600-1-1	27.778/25/1.25
CX046	650	Air	1-120-1-3,600-1-1	26/20.8/1.3
CX013	600	Air	1-3,600-1-1	26/ - /2.6
CX014	600	Air	1-3,600-1-1	26/ - /2.6
CX042	600	Vacuum	1-120-1-1	26/ - /2.6
CX045	600	Vacuum	1-120-1-1	26/ - /2.6
CX020	550	Air	1-3,600-1-1	26/ - /2.6
CX015	550	Air	1-3,600-1-1	26/ - /2.6
CC047	525	Air	1-3,600-1-1	26/ - /2.6

Table 9: Overview of the Udimet 720Li Phase 2 test programme.

Testpiece ID	Temperature (°C)	Dwell time (s)	Dwell Load (kN)	OLF	Remarks
CC001	600	1,200	32.5	1.15	
CC002	600	3,600	32.5	1.15	
CC003	650	3,600	26	1.15	
CC004	650	1,200	26	1.15	Invalid
CC005	600	1,200	32.5	1.05	
CC006	600	3,600	32.5	1.05	
CC007	650	1,200	26	1.15	
CC008	675	1,200	22	1.1	
CC009	625	1,200	29	1.08	
CC010	650	1,200	26	1.08	
CC011	675	3,600	22	1.13	interrupted, then used for ΔKth
CC012		3,600	24		inappropriate pre-crack
CC029	650	1,200	26	1.15	120s OL
CC032	650	1,200	26	1.15	600s OL
CC013	600	1,200	29	1.05	Batch 2
CC014	600	3,600	29	1.05	Batch 2
CC015	650	3,600	26	1.15	Batch 2
CC020	650	3,600	23.4	1.15	
CC021	600	1,200	26	1.15	Overloaded before precracking

Table 10: Overview of the Udimet 720Li ΔK_{th} test programme.

Testpiece ID	Temperature (°C)	Dwell time (s)	Remarks
CC040	650	120	
CC041	650	120	Notably different microstructure
CC044	650	120	Decreasing ΔK, also $Temp_{th}$
CC044	440-510	3,600	Const ΔK for $Temp_{th}$
CC045	650	1,200	Also 3,600
CC019	650	3,600	
CC011	650	3,600	Notably different microstructure

Table 11: Overview of the RR1000 Phase 1 test programme.

Testpiece ID (°C)	Temperature (°C)	Environment	Loading waveform (seconds)	$P_{max}/P_{dwell}/P_{min}$ kN
CC026	700	Air	1-3,600-1-1	26/ - /2.6
CC031	700	Air	1-3,600-1-1	26/ - /2.6
CC033	700	Air	Sustained load	22
CC025	675	Air	1-3,600-1-1	26/ - /2.6
CC028	675	Air	1-3,600-1-1	26/ - /2.6
CC001	650	Air	1-3,600-1-1	26/ - /2.6
CC002	650	Air	1-3,600-1-1	26/ - /2.6
CC004	650	Air	1-3,600-1-1	26/ - /2.6
CC032	650	Air	1-1-1-3,600	26/ - /2.6
CC029	650	Air	1-120-1-3,600-1-1	26/20.8/1.3
CC030	650	Vacuum	1-120-1-1/1-3,600-1-1	26/ - /2.6
CC003	600	Air	1-3,600-1-1	26/ - /2.6
CC026	600	Air	1-3,600-1-1	26/ - /2.6
CC027	550	Air	1-3,600-1-1	26/ - /2.6
CC037	550	Air	1-3,600-1-1	26/ - /2.6
CC024	525	Air	1-3,600-1-1	26/ - /2.6

Table 12: Overview of the RR1000 Phase 2 test programme.

Testpiece ID	Temperature °C	Loading waveform sec	$P_{max}/P_{dwell}/P_{min}$ kN	OLF	Remarks
CC039	600	1-1-1-3,600-1-1	29.9/26/2.6	1.15	Phase I t/p
CC042	600	1-1-1-3,600-1-1	27.3/26/2.6	1.05	Phase I t/p
CC019	600	1-1-1-1,200-1-1	29.9/26/2.6	1.15	
CC020	650	1-1-1-3,600-1-1	29.9/26/2.6	1.15	
CC021	600	1-1-1-1,200-1-1	27.3/26/2.6	1.05	
CC017	650	1-1-1-1,200-1-1	28.08/26/2.6	1.08	
CC034	675	1-1-1-1,200-1-1	25.85/23.5/2.35	1.10	
CC018	625	1-1-1-1,200-1-1	28.08/26/2.6	1.08	
CC033	650	1-1-1-1,200-1-1	29.9/26/2.6	1.15	invalid
CC045	650	1-1-1-1,200-1-1	28.08/26/2.6	1.08	Repeat CC017
CC046	650	1-1-1-1,200-1-1	29.9/26/2.6	1.15	Repeat CC033
CC047	625	1-1-1-1,200-1-1	28.08/26/2.6	1.08	Repeat CC018
CC048	650	1-1-1-3,600-1-1	29.9/26/2.6	1.15	Repeat CC020
CC049	650	1-1-1-600-1-1	28.08/26/2.6	1.08	
CC050	650	1-1-1-120-1-1	27.3/26/2.6	1.05	
CC051	650	1-1-1-300-1-1	27.3/26/2.6	1.05	
CC052	675	1-1-1-120-1-1	24.675/23.5/2.35	1.05	
CC053	675	1-1-1-600-1-2	25.38/23.5/2.35	1.08	
CC054	600	1-1-1-1,200-1-1	29.9/26/2.6	1.15	Repeat CC019
CC056	650	1-1-1,200-1-1	29.9/28.08/2.8	1.065	Unload
CC057	650	1-1-1,200-1-1	29.9/28.08/2.8	1.065	Reload

Table 13: Overview of the RR1000 cooling rate tests.

Testpiece ID	Cooling Rate (°C/s)	Temp (°C)	Dwell Time (s)	Remarks
CX001	0.1	650	3,600	5 x 5 test piece
CX005	5	650	3,600	5 x 5 test piece
CC048	Nominal (~1.4)	650	3,600	Results taken from Phase Two programme

3.3 Scanning Electron Microscopy

3.3.1 Fractography

Once the tests are completed and the final section of 1-1-1-1 baseline loading is applied to a crack length of approximately half the width of the test piece, samples are broken open at room temperature using the same 1 Hz sine wave as for pre-cracking. Jeol 6060, Phillips XL-30 and FEG S-4000 Scanning Electron Microscopes are used to examine the fracture surfaces. In all cases, electron beams are charged to 20 keV and imaging is carried out across a flat plane, with a 0^0 tilt. Fracture surfaces of all specimens are studied to determine crack growth mechanisms, and to give an indication of the grain size of the material.

A select number of samples are also sectioned across the face of the fracture surface at a 45° angle in order to more accurately quantify the extent to which intergranular and transgranular mechanisms dominate during cracking. Sectioned samples are coated in nickel-plating, mounted in conducting Bakelite using a hot mounting press and polished and etched using the methodologies described in section 3.3.2. This enables further observation and quantification of crack growth morphologies and mechanisms by studying the microstructure perpendicular to the fracture surface.

3.3.2 Metallography

In order to explore the influence of microstructure upon dwell crack growth behaviour of (nominally) fine-grained Udimet 720Li, a detailed microstructural analysis has been carried out upon samples CC009, CC015 and CX027 (each displaying three distinct behaviours

despite similar testing conditions, as reported in section 4.1 and Figure A-6 in Appendix VI). Furthermore, in the same way, microstructural analysis pertaining to fine-grained Udimet 720Li test pieces CC040 and CC045 from the time-dependent ΔK_{th} programme, and fine-grained RR1000 test pieces CX001 and CX005 from the cooling rate testing programme has also been carried out.

Samples are sectioned, mounted, polished and etched in order to carry out analysis to determine grain size and distribution, and primary γ' size and distribution. Fracture surfaces are carefully sectioned using a parallel cut 2 mm below the fracture surface of each test piece. The removed fracture surfaces are then cleaned in a beaker of acetone using an ultrasonic bath. Another parallel cut is then made a further 2 mm from each test-piece to provide a sample of material for metallographic analyses. These small pieces of material are mounted using a hot mounting press in conducting Bakelite which enables optical and SEM imaging.

Samples are polished using Struers LaboPol-5 automated polishing equipment and associated Struers polishing discs, wheels and lubricants. The methodology involves first grinding with rough sandpaper wheels and gradually using more refined textures including soft cloth and a diamond suspension lubricant, gradually polishing samples to a plane and reflective finish.



Figure 3-14: Photograph showing Struers automatic polishing equipment.

The exact methodology by which samples in this programme are polished is tabulated in Table 14.

Table 14: Detailing polishing methodology for Ni-based superalloy samples.

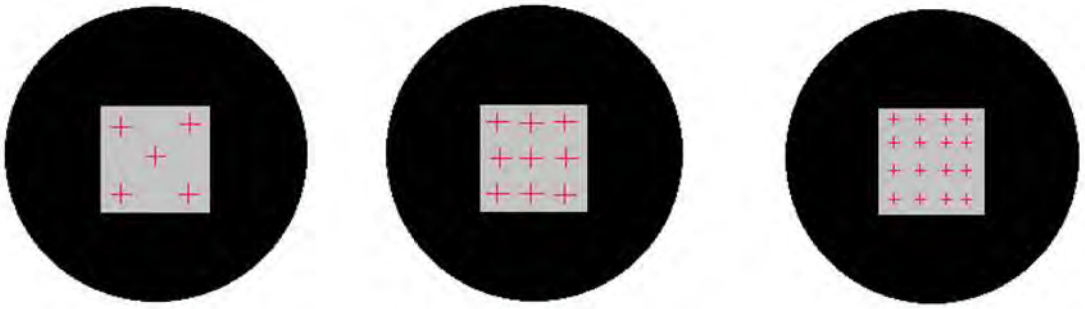
Surface	Resolution	Lubricant	Wheel Speed (RPM)	Force (kN)	Time
Piano 120		Water	330	3	Until plane
Piano 220		Water	250	3	3 mins
Allegro	9 µm	Largo	150	3.5	3 mins
Plan	6 µm	Plan	150	3	6 mins
Dac	3 µm	Dac	150	3	8 mins
Nap	1 µm	Nap	150	2.5	2 mins
Chem	OP-A	OP-A	150	1.5	2 mins

Three different etchants are used: Kallings, which attacks and dissolves γ' and highlights grain boundaries, 10% phosphoric (electrochemical etch) which etches the γ matrix to enable analysis of γ', and (for the RR1000 cooling rate test pieces), a molybdenum based γ' etch [81] (which enables clearer analysis of γ' morphology). Each sample is re-polished in between the application of different etchants. The components of each etchant used and associated etching methodologies are listed in Table 15:

Table 15: Etchant compositions and methods.

Kallings	**10% Phosphoric**	**Molybdenum γ' etch**	
10gm cupric chloride	10ml Phosphoric acid	**Part 1**	**Part 2**
50ml Hydrochloric acid	90ml H_2O	150ml H_2O	15ml HNO_3
50ml Ethanol		150ml HCL	25mlH_2O
		2.5g MoO_3	30ml Part 1
Method: 30 second swab	Method: 5 second electrochemical etch	Method: 45 second full submersion	

An Axioskop2 optical microscope is used to image the samples at varying levels of magnification in order to capture and analyse different metallographic features. Where detailed microstructural analysis is carried out; five Images are taken at 50x magnification to capture an overview of the microstructure including banded coarse and fine grain regions. 100x, 200x, 500x magnification is used to further highlight and characterise distinct features such as very fine or coarse regions in terms of grain size. The locations from which these images are taken are highlighted by the grids in Figure 3-15.



a b c

Figure 3-15: Showing the lacations from which images are taken for a; 50x magnification grid, b; 100x and 200x magnification grid and c; 500x magnification grid.

Scanning electron microscopes are also used to image each sample. The bottom left corner of each sample is located using the cross hair function. Images are taken in random locations at 1500x magnification at a working distance of 10mm using an accelerating voltage of 20keV, and a tilt of 0°. Images are taken by starting at the bottom left corner of the sample and turning the micrometer dials three full turns in one direction between images, snaking and imaging randomly across the sample as shown in Figure 3-16, in order to create a set of representative images.

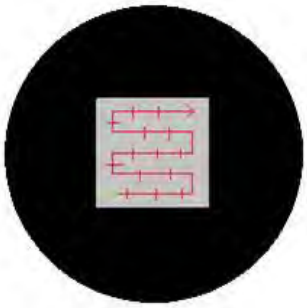
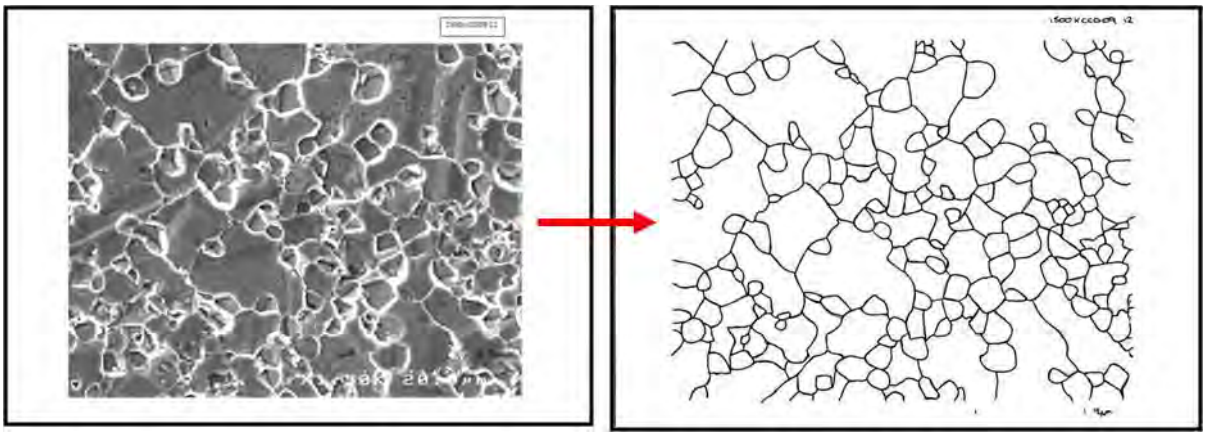


Figure 3-16: Snaked 'grid' of random SEM image locations at 1500x magnification.

Images are processed using Image-J analysing software which enables the calculation and plot of a distribution of grain size and γ' sizes. Traces of SEM images are made using translucent tracing paper and a black Staedtler non-permanent pen (nib width approx. 0.6mm). Grain boundaries and primary gamma prime boundaries are carefully traced by hand including the scale bar which was offset below the actual picture for use in calibrating the scale in ImageJ for future analysis. The traced images are then scanned and uploaded digitally, to enable analysis.



a b

Figure 3-17: a; SEM image formatted in Microsoft Word prepared for tracing, b; Scanned digital trace of the SEM image in a.

Each image is then cropped to remove the border area and scale bar. The image is then converted to binary before the 'paint bucket fill' tool (in ImageJ) is used to fill in the areas which are deduced to be primary γ' as opposed to γ grains.

Once the primary γ' precipitates are filled, the image is inverted (in terms of black and white) such that the primary γ' precipitates and grain boundaries are turned white and the grains are

turned black. Since the ImageJ software reads black particles on a white background, it is then possible to automatically analyse the area of the individual 'particles' or in this case, the grains using ImageJ's 'Analyse Particles' function.

The 'Analyse Particles' tool is used to measure particles ranging (in terms of size) from 1 um^2 to infinity. 1 um^2 is set as the lower limit in order to omit minor discrepancies in the image and discount them as being counted as grains. The particular value of 1 um^2 is specifically chosen as it is estimated that the smallest grains in the images are greater that around 1 um^2. In addition, the 'Analyse Particles' function is calibrated to exclude the grains on the extremities of the image, since they are incomplete and would skew the results.

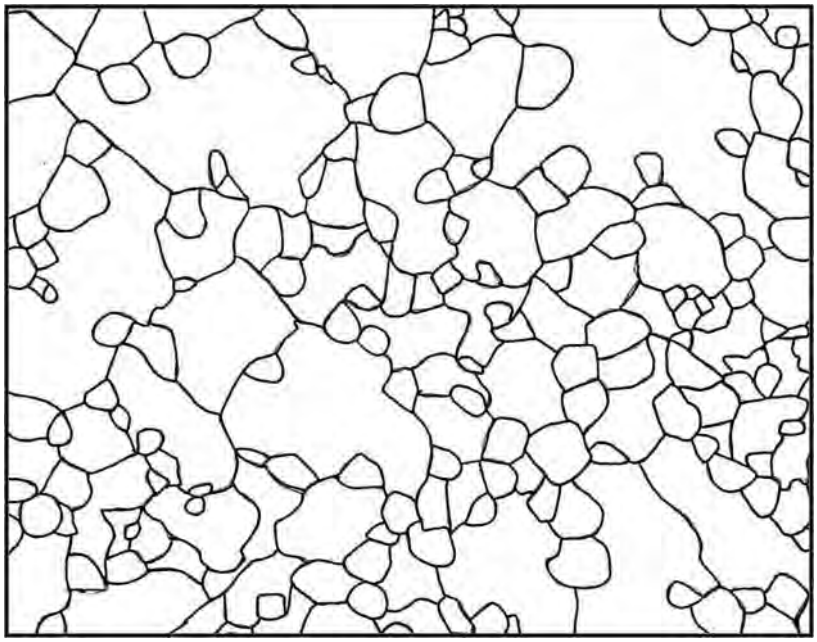


Figure 3-18: Traced and Cropped Image

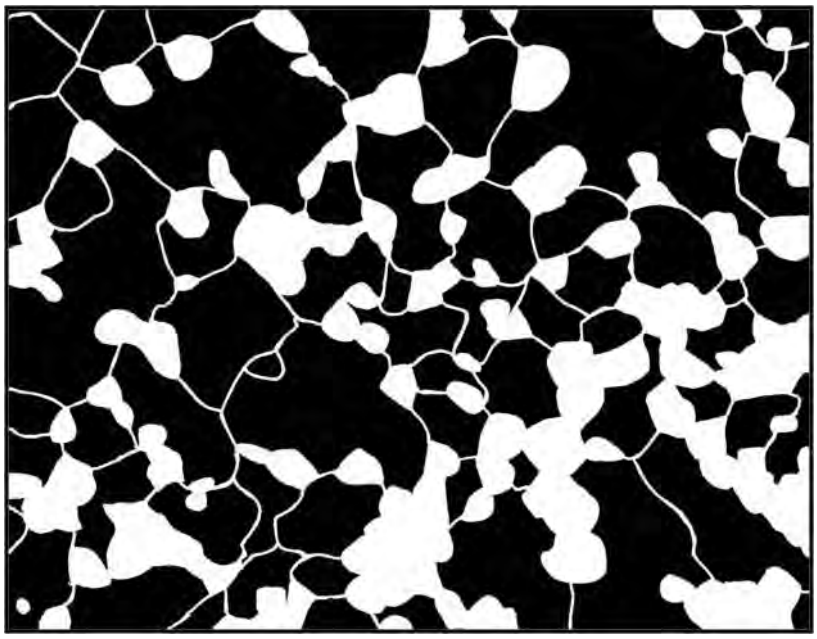


Figure 3-19: Inverted image, post gamma prime selection, used for automatic grain size analysis.

The same area measurement technique is used to analyse the size and area fraction of the primary γ' precipitates, where at the first stage, grains are painted black and the image inverted in order to show the individual primary γ' precipitates as black particles on a white background as shown in Figure 3-20.

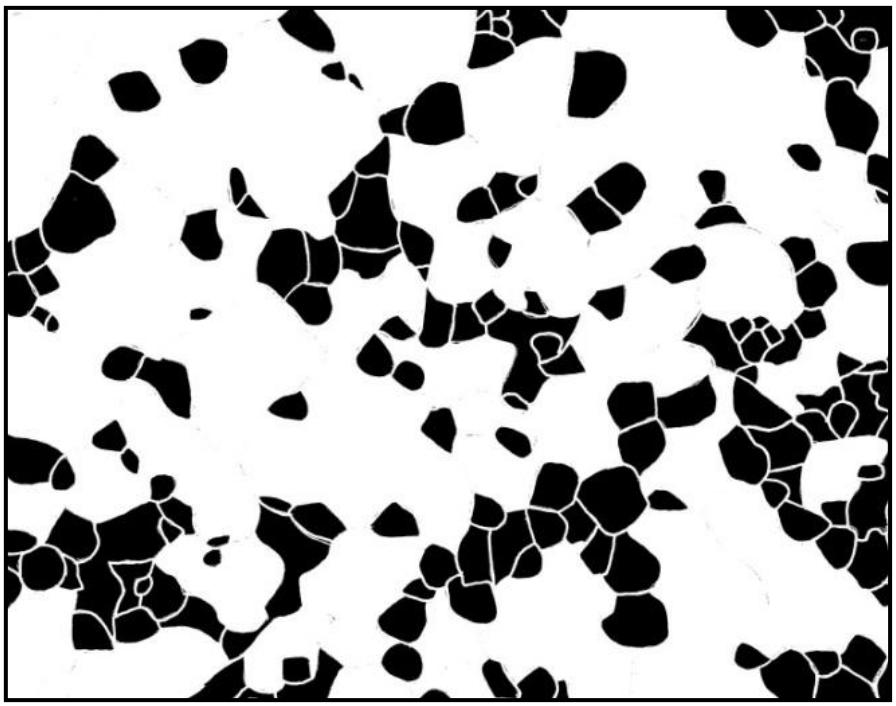


Figure 3-20: Inverted image, post grain selection, used for primary γ' analysis.

Grain size is analysed in a variety of different ways, and analysis is complicated by the fact that two-dimensional images may not accurately represent the full three-dimensional characteristics of the material. Furthermore is it important to understand and quantify any degree of bimodality in the grain size and structure, and discussions on how best to represent these phenomena are reported by Strangwood [82]. Furthermore, since Udimet 720Li is cast and wrought it may also be that the average grain size observed differs with respect to the geometry of the sectioned sample.

Nevertheless estimations and qualitative comparisons have been made using standardised techniques. The simplest approach is to determine the number of grains visible within a fixed area, and to divide this measurement by the area observed. The approach detailed above

enables a more detailed statistical approach, where the number of grains pertaining to any particular discrete range of sizes can be plotted against frequency in a histogram. ASTM standards require analysis of at least 2,000 grains of a sample of material in order for reports to be considered comprehensive. Where this has been possible it has been achieved, nevertheless slightly less stringent methods can allow careful discussion of mechanical properties and crack growth rates as a function of estimated grain size.

3.4 Modelling

3.4.1 Model Implementation

Theoretical stress analysing FEA modelling is carried out using Rolls-Royce plc. in-house modelling software package SC03, and associated material data from in-house material database "COMMIT" in order to understand crack tip stress states as a function of operating condition. A two dimensional (2D) mesh has been designed and implemented to model the geometry of the test pieces used in this programme for baseline, dwell and overload testing. The model therefore has a width of 10 mm (where the actual width of the test pieces in this plane is $\sqrt{[(7^2 + 7^2)]} \sim 10$ mm); and a small crack, represented by a modified notch of finite radius, propagating from one corner.

The crack is modelled as having a notch radius of 0.025 mm, with a fine mesh around the notch root. (The reasons for which a fatigue crack tip may been represented by a notch with finite radius is discussed in 3.4.3, and analysis pertaining to the validity of such an assumption in presented in Appendix V.) A mesh size for which solutions of outputs from analyses converge is automatically generated and balances reliable numerical convergence with the time and computer power it takes for simulations to run. The validity (convergence) of mesh sizes generated automatically by SC03 is extensively reported within Rolls-Royce plc. The mesh size described below and those used as part of this programme are found to be suitable in forming convergent results, and do so over practical and useful run times. A brief discussion on mesh size, and detailed analysis pertaining to the validity of the model geometry is presented Appendix V and discussed in some detail below.

Figure 3-21 details one example of the model geometry, loading and boundary conditions. Load is applied along the top surface, and is resisted by modelled material contact (the symmetry boundary condition, BC) along the bottom surface, except where the modified notch is modelled, along the left hand side of the underneath.

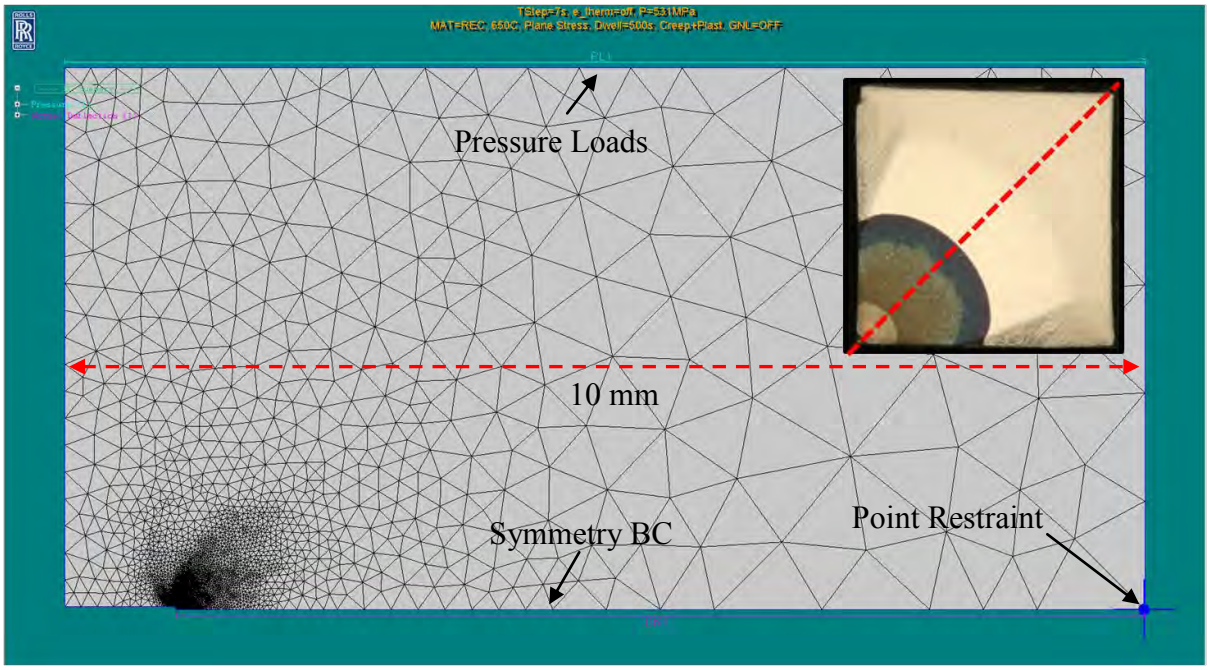


Figure 3-21: Showing an example of mesh geometry for modelling work.

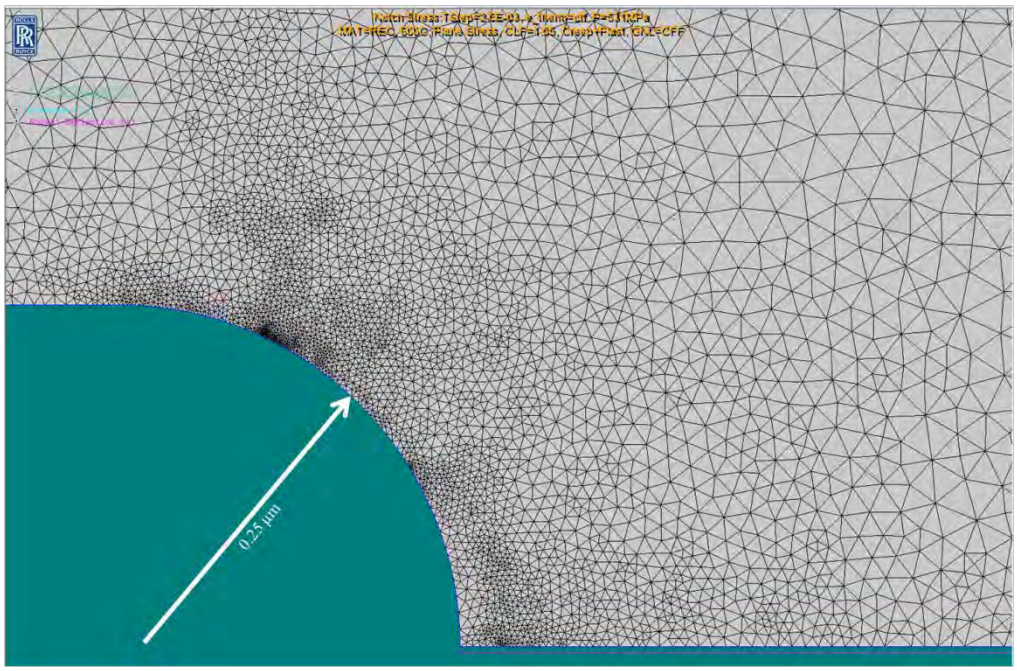


Figure 3-22: Showing the notch radius (0.25 mm) used to represent a crack. The validity of the representation is reported in Appendix V.

The environmental parameters are set up such that reference to a nominal Background Load (BL) and Temperature (TEMP) is constantly applied, and a series of "Pressure Fractions" (PF) is defined as a function of time. The pressure applied to the top surface of the mesh is therefore defined as PF*(-BL) and varies as PF does with time. Background loads of 531 MPa are investigated (as with empirical testing), and reductions of 10% (to 477.9 MPa) are also studied for some conditions. Two different crack lengths are modelled and appropriate stress intensity factors associated with each condition simulated are calculated in order to compare stress analyses with empirically derived crack growth rates and retardation phenomena. A time history is defined where BL and TEMP remain constant and PF changes with time such that dwell and overload stress waveforms may be applied to match those in Figure 2-8, Figure 2-9 and Figure 2-25.

Since the simulations do not account for any crack propagation and growth through the material it is useful only to apply one stress cycle at each condition tested and to analyse accordingly. Furthermore; simulations do not include any oxygen induced crack tip phenomena in their analyses. Rather, the model is a simple application of stress analysis approaches and seeks only to characterise crack tip stresses, strains and associated creep behaviour as a single nominal dwell or overload cycle is applied. Discussion on how the analyses may be included in dwell crack propagation linear superposition lifing methodologies and on how oxygen related phenomena may be included in stress analysis modelling is presented in section 5.3.

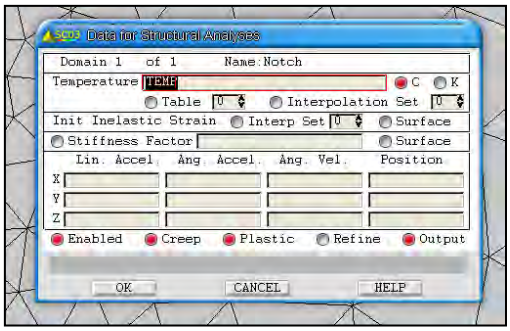


Figure 3-23: Referencing the parameter "TEMP".

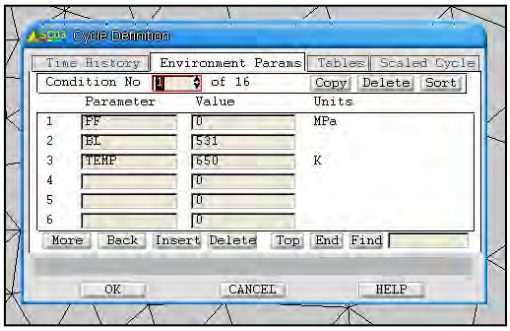


Figure 3-24: Defining BL, TEMP and PF through a range of "conditions".

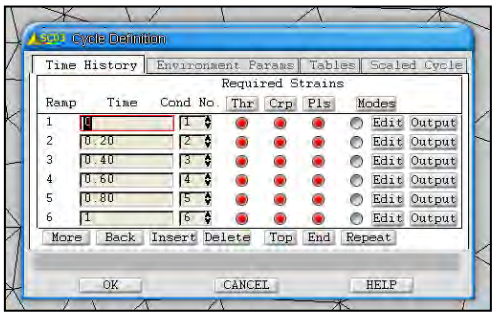


Figure 3-25: Defining a time history by assigning "time" (in seconds) to a condition number.

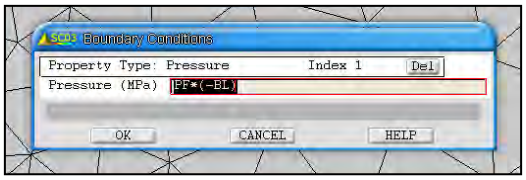


Figure 3-26: Defining the pressure load as PF*(-BL)

It is important to highlight that materials modelled in this programme display a degree of work hardening which occurs due to dislocation-dislocation interaction (among other aspects) and is described in section 2.4.2. As discussed in section 2.5.2, there are several ways in which analytical models may analyse these effects. Work carried out in this programme uses a Mroz multi-yield surface criterion, discussed in section 2.5.2.

Furthermore, creep rates and the total creep life of a given component will vary as a function of stress (Figure 2-19). It is therefore possible to model these creep effects as stresses increase by "jumping" from one creep curve to the next at a given moment in time, or at each individual stress level. A "life-fraction" approach involves movement between each creep curve by analysing the proportion of the total creep life which has been used; and moving to the associated position on subsequent creep curves. Such an approach is adopted for simulations carried out in this programme since the methodology represents more reliable and scientifically robust analyses. The method is represented graphically in Figure 3-27 which shows analysis for a typical whole flight cycle.

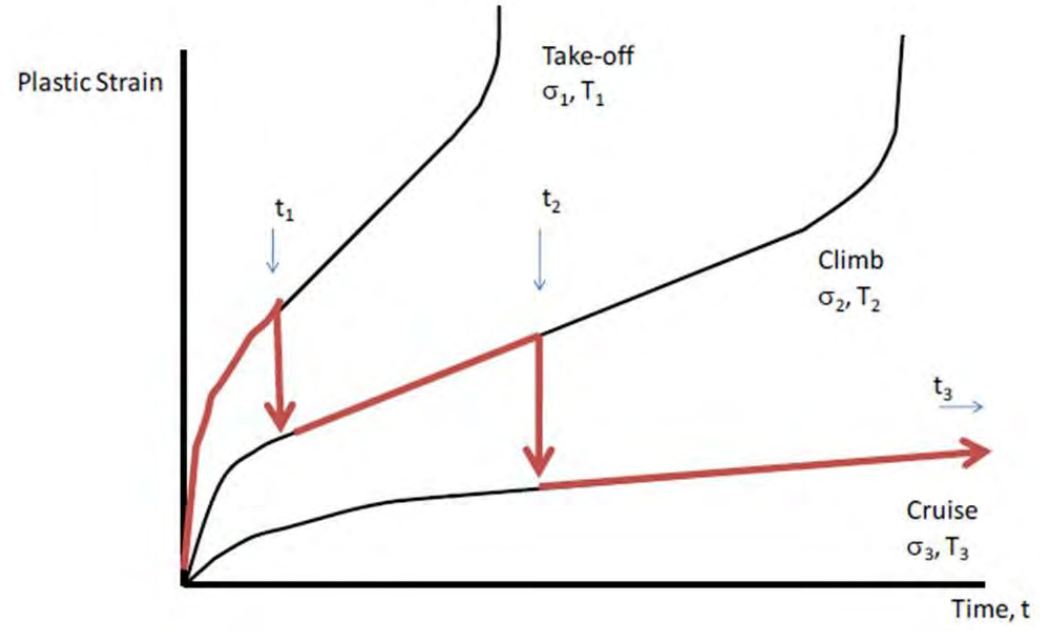


Figure 3-27: An illustration to show the way in which segmented strain is captured analytically.

Furthermore, it is possible to run each simulation according to plane strain or plane stress conditions. Each simulation used in this programme has been run according to plane stress conditions since data gathered under these conditions are shown to be more conservative in predicting crack growth retardation as a result of overload cycling. A brief discussion pertaining to the reasons for this is presented in Appendix V.

As described, a fictitious stress-time history is applied to the finite element mesh and analysed at each node at determined (input) moments in time. It is necessary to ascribe simulated moments in time with a nominal "condition" (TEMP, BL and PF), at which each calculation should be made. As described above, each "condition" refers to a constant TEMP and BL, and PF varies according to "condition".

Given that stress, creep and associated data and analyses will vary as a function of nominal applied stress over time, it follows that an appropriate number of "time steps" must be assigned to form the complete applied nominal stress / time waveform. If for example, during the up-ramp to the overload at the very beginning of the simulation the user defines PF as zero at condition 1 and time t = 0 seconds, and then condition 2 as having a PF of 1.15 (for example) at time t = 1 second in order to generate the beginning of a simple overload cycle; the simulation would involve only two analysis points. Creep data varies greatly as a function of stress especially during this stage of the creep curve; as discussed in section 2.4.2, and hence it is inappropriate to assume that smooth analyses could be made over these two conditions by applying as little as two analysis points. In actual fact, SC03 performs four calculations for each moment in time defined by the user,[4] nevertheless it is important to define an appropriate "resolution" in terms of time steps assigned to each analysis point. Typically, ramping up from zero load to the maximum overload load is suitably represented by five time steps, and the hold at overload by a further one time step. The ramp down from overload to dwell load is appropriately represented by a further single time step. After this time, the total remaining dwell period is represented most appropriately by the assignment and application of ninety time steps. For example, if the user wishes to apply a dwell period of ninety seconds, ninety time steps should be assigned a condition at one second intervals and applied. The importance of applying appropriately defined time steps along the extended dwell period is reported in Appendix V and refers to the fact that data is analysed in such a way as to render the output data sensitive to this resolution.

[4] Furthermore SC03 will automatically decrease the resolution of a particular time step if certain criteria regarding rate of change of creep, stress and strain are not met.

A typical fictitious condition history (TEMP, BL and PF) and associated time step plot is given in Table 16 and Table 17, and is represented graphically in Figure 3-28 to Figure 3-31. The cycle involves an overload factor of 1.15, a dwell period of 90 seconds, TEMP of 650°C and BL of 531 MPa.

Table 16: Assigning TEMP, BL and PF to a "condition number".

Condition Number	1	2	3	4	5	6	7
TEMP (°C)	650	650	650	650	650	650	650
BL (MPa)	531	531	531	531	531	531	531
PF	0	0.23	0.46	0.69	0.92	1.15	1

Table 17: Assigning each moment in time to a condition number.

Time (s)	Condition Number
0	1
0.2	2
0.4	3
0.6	4
0.8	5
1	6
2	6
3	7
3 – 93 in 1s steps	7
93	7

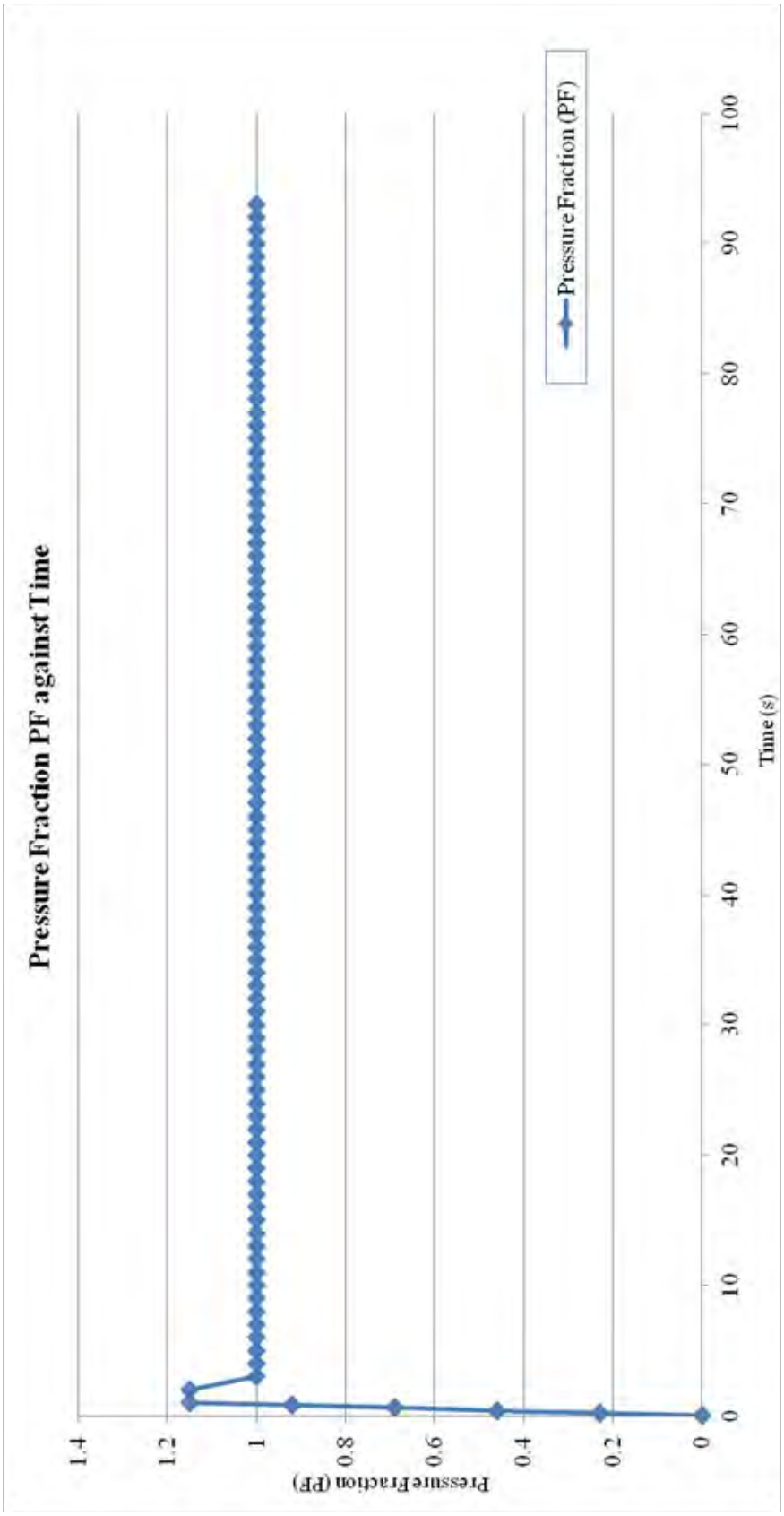


Figure 3-28: Plotting Pressure Fraction (PF) as a function of time plotted throughout its history, as referenced a total of 97 times.

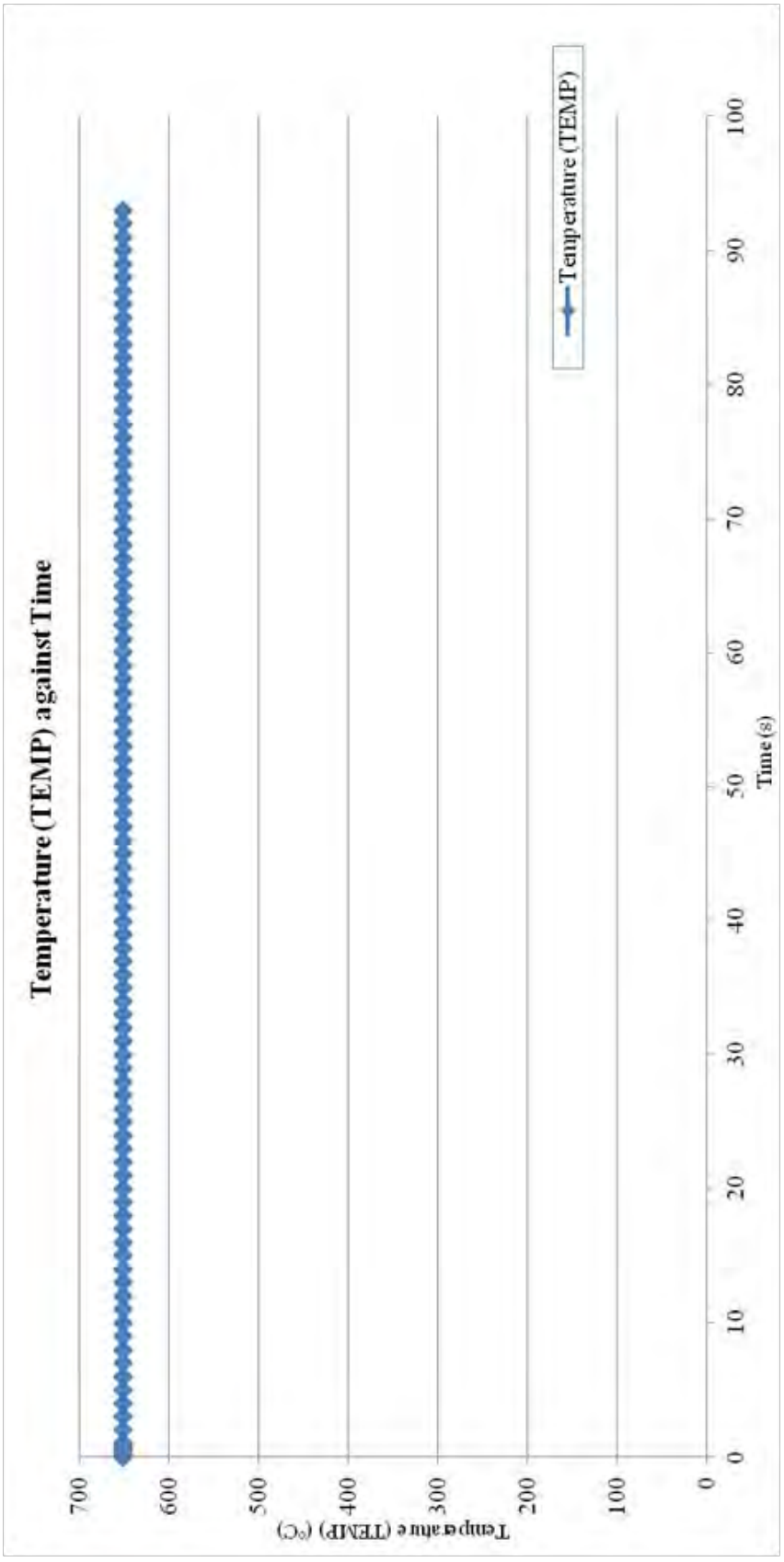


Figure 3-29 : Plotting Temperature (TEMP) as a function of time plotted throughout its history, as referenced at similar moments in time to PF above.

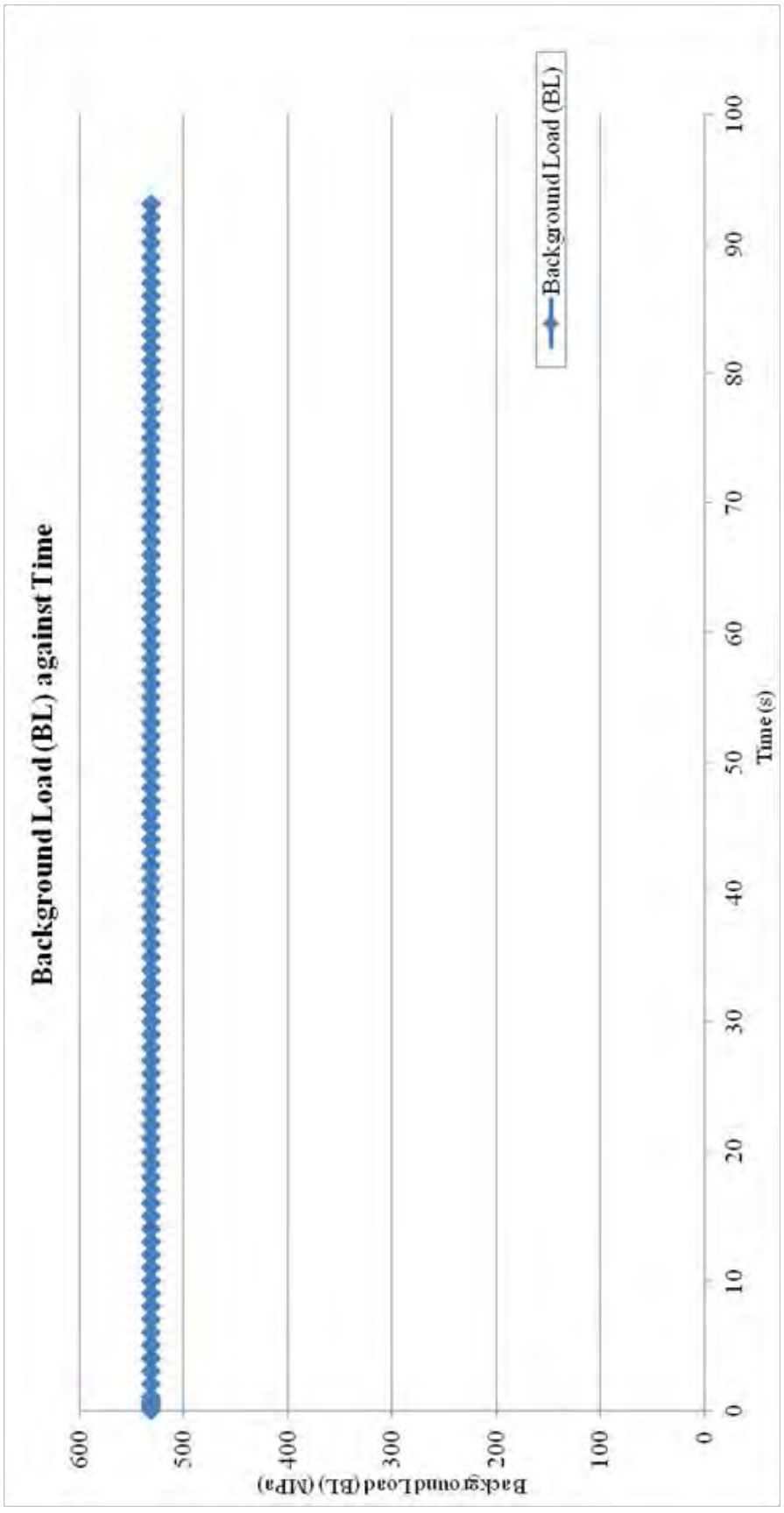


Figure 3-30: Plotting Background Load (BL) as a function of time plotted throughout its history, as referenced at similar moments in time to PF above.

Shown in Figure 3-31 are typical loading conditions as displayed by SC03, where TEMP and BL are similarly defined as above; and the applied dwell time is 6,600 seconds (hence conditions would have been applied along the dwell period at 90 separate intervals of around 70 seconds).

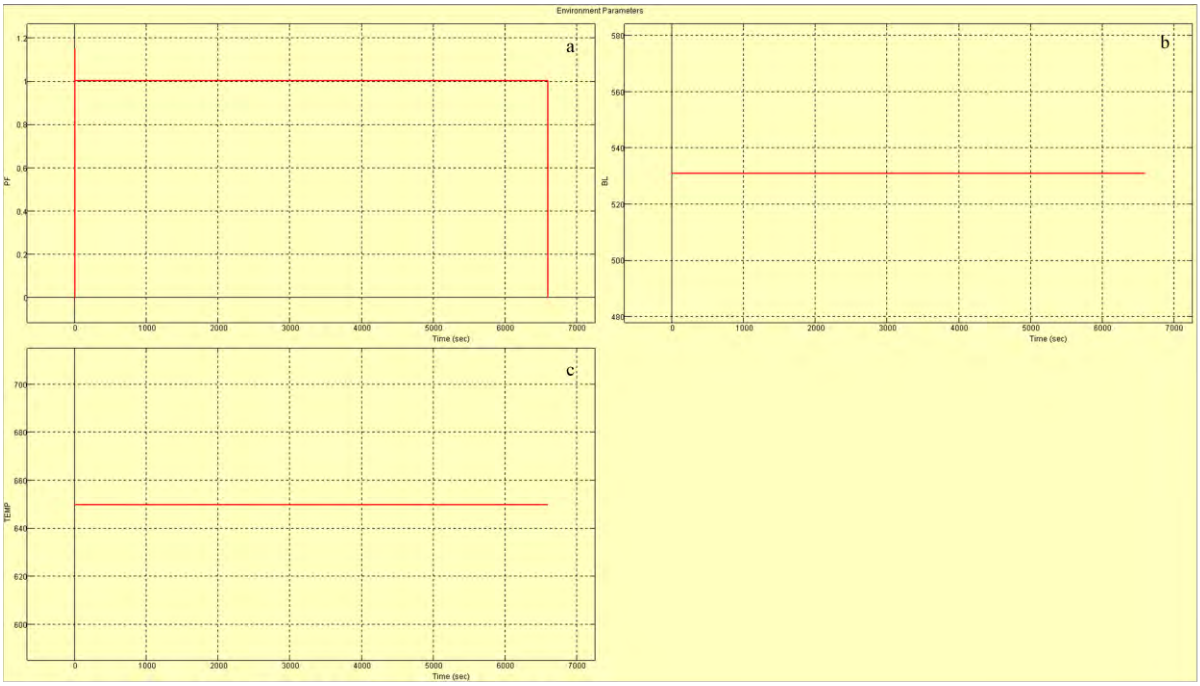


Figure 3-31: Plotting environmental parameters against time; a: PF, b: BL, c: TEMP. The example shows a typical overload waveform, with an OLF of 1.15

3.4.2 Data Analysis

Once each simulation is complete, stress and creep data is captured in several ways. Firstly, contour plots representing the stress normal to the crack tip (or notch root) (σ_{yy}) through the time history are taken in the form of screen-dumps and analysed to determine general stress states at the crack tip. Contour images are also taken in the form of inelastic creep strain

analyses. For nomenclature, in SC03, stress normal to the crack tip is referred to as “SYY”, and inelastic creep strain as “CEQI”.

Secondly, stress and creep data is plotted as a function of time for the very tip of the crack or notch (the element labelled “a” shown in Figure 3-32) in order to analyse the extent to which crack tip stresses unload from the overload, and subsequent relaxation of these stresses over time. Crack tip (or notch root) stress versus time profiles for an overload cycle are compared with those generated over the corresponding (otherwise similar) normal dwell cycle in order to determine the effect of overload on these stress states. For comparison, creep-time data is also plotted from an area ahead of the notch root deemed to represent nominal crack plane bulk material strain rates (throughout the overload cycle). The distance ahead of the notch root from which this data is gathered is defined as 1.5 x the notch radius, or 0.0375 mm ahead of the crack tip (the element labelled “b” shown in Figure 3-32). A brief discussion pertaining to the selection of this particular distance from which to gather and compare creep data is presented in Appendix V.

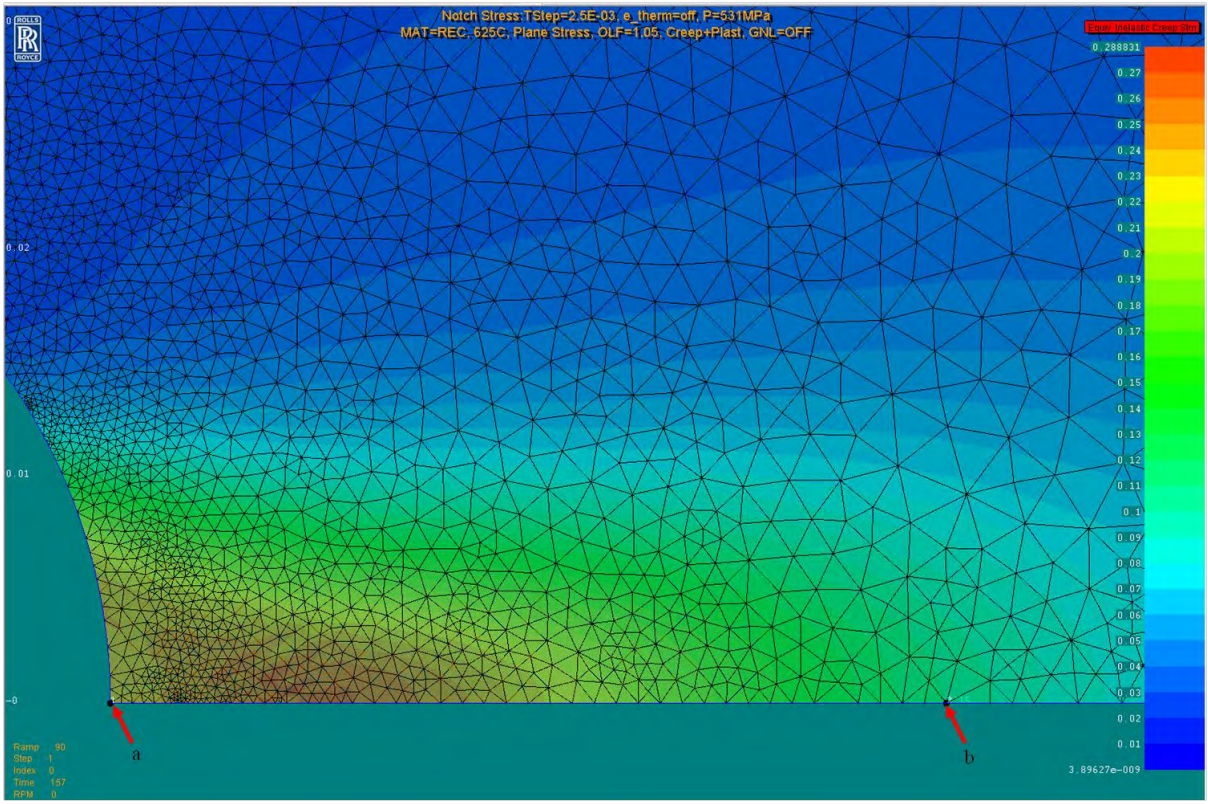


Figure 3-32: Showing the nodes from which stress and creep versus time plots were analysed; a: crack tip, b: 1.5r ahead of the crack tip. For reference the contours show inelastic creep strain normal to the crack tip (CEQI) after unloading from the dwell load at the end of the cycle.

3.4.3 Validity of Modelled Crack Tip Geometry

As discussed in section 2.3.2, a linear elastic fracture mechanics approach to a fracture toughness problem assumes that the crack tip is infinitely sharp, i.e. that it has no radius or finite width at its tip. Using the stress intensity factor parameter (K) it is possible to express a relationship between stress normal to the crack tip (under pure tensile or mode I opening) (σ_{yy}) and distance from the crack tip (x):

$$\sigma_{yy}=\frac{K}{\sqrt{(2\pi x)}} \quad \text{..... Equation 41}$$

Hence a singularity is introduced at the very tip of the crack, as x tends towards zero. In reality however, particularly under creep conditions, the crack tip is blunted to some extent. The actual size and shape of the crack tip itself will vary as a function of stress, temperature, waveform and microstructure; and its precise geometry is not widely understood or reported. Nevertheless it is reasonable to assume that σ_{yy} in the above equation would reach a maximum value capped and defined by the yield strength of the material, as a result of introduced strains from creep and plasticity around the crack tip.

Finite crack tip radii are widely applied to model these crack tip blunting effects. The work presented in this programme assumes a crack tip radius of 25 μm. The radius was chosen to compromise a balance between accurate real life representations of crack tip geometries (of which it is likely an overestimate) with the functional capability of creep and plasticity finite element codes to provide a converged numerical solution. Detailed analyses have been carried out within Rolls-Royce plc. to compare various crack tip radius values [83]. The analysis is reproduced (in part) in Appendix V.

It is important to note at this stage that although finite, the assumed notch radius remains very small with respect to the total modelled test piece size, hence the elastic stress fields relating to a "real-life" sharp fatigue crack tip in physical test pieces are likely to be similar. Therefore the model is considered to represent stress (and associated) states ahead of the crack tip in an appropriate and therefore useful way. Henceforth the terms "crack tip" and "modified notch" will be used interchangeably.

For a full report in to the development and implementation of the above detailed finite element models, readers are referred to Rolls-Royce in-house technical report DNS 160974 authored by Steve Williams and Dr. Lik-Beng Lim [83]. While the full report will not be available to those outside the Rolls-Royce partnership, the analysis which is reproduced in part in Appendix V, and indeed that which has been carried out as part of this programme, is sufficient in itself to confirm the validity and usefulness of the models implemented and data gathered.

3.4.4 Further Considerations on the Use of Finite Element Models

The above referenced document (DNS 160974) also includes detailed analysis on the effect of several variables upon overload crack growth retardation behaviour when using the models detailed above. These are:

- The effect of overload factor
- The effect of temperature
- The effect of background stress
- The effect of K
- Plane strain / plane stress differences

It is important to highlight here that data generated as part of this programme seeks to use these finite element models only to explore the first two effects detailed above, namely; the effect of overload factor and the effect of temperature. Where necessary, brief explanations

pertaining to the effects of K and background stress are reported and discussed, from the above referenced report.

4. Results

4.1 Mechanical Testing

4.1.1 Introduction

A comprehensive selection of baseline, dwell and overload crack growth resistance curves generated in this programme of research are presented in Appendix VI. A selection of representative graphs are plotted here, and their conclusions summarised in Table 18, Table 19, Table 20 and Table 21.

4.1.2 Effect of Dwell

The graphs highlight several important phenomena. Firstly, they show that when samples are tested in air, an increase in dwell time causes an increase in crack growth rates significantly when compared with crack growth rates pertaining to otherwise similar baseline loading. In general, larger dwell times and higher test temperatures result in more profound accelerated dwell crack growth rates. These phenomena are shown in fine-grained RR1000 in the representative crack growth resistance curve Figure 4-1, (below), and in the crack growth resistance curves presented in Appendix VI.

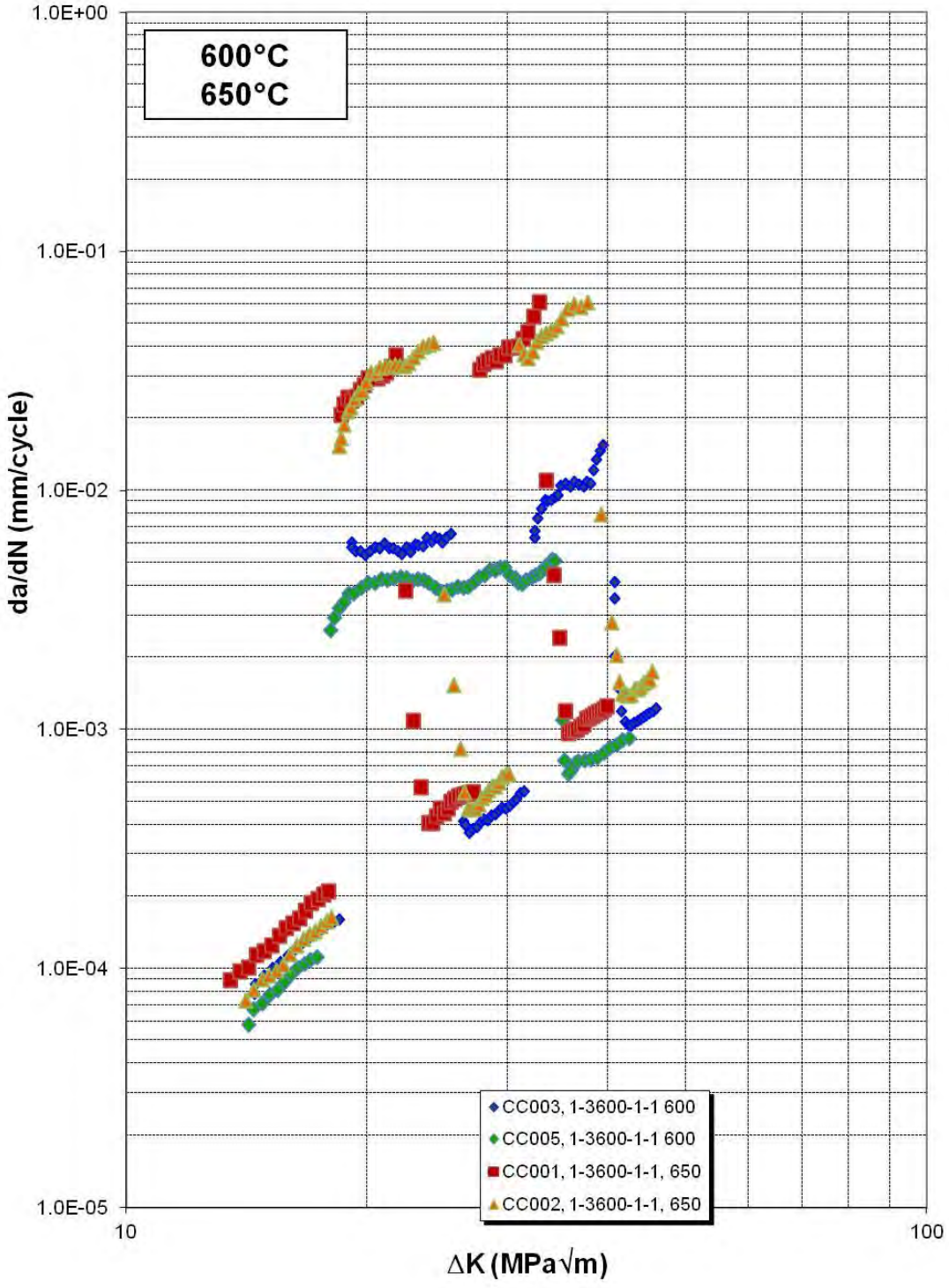


Figure 4-1: da/dN vs. ΔK curves to show a comparison in terms of baseline and dwell crack growth rates for 600°C and 650°C. Samples are fine-grained RR1000; CC003 and CC005 (600°C) and CC001 and CC002 (650°C), tested in air with a dwell load of 26kN. Note the effect of temperature and dwell period on crack growth rates.

Furthermore, the crack growth resistance curves also highlight the fact that these dwell effects are almost completely lost when conditions are repeated in a vacuum, without the presence of oxygen. In general, the introduction of a dwell time at peak load in a vacuum has little effect on crack growth rates when compared with otherwise similar baseline loading, which adds further evidence to the suggestion that accelerated dwell crack growth is dominated by environmental factors (Figure 4-2 and Figure 4-3). Figure 4-3 shows crack growth resistance data captured over a range of different dwell periods in both laboratory air and a vacuum all at 650°C.

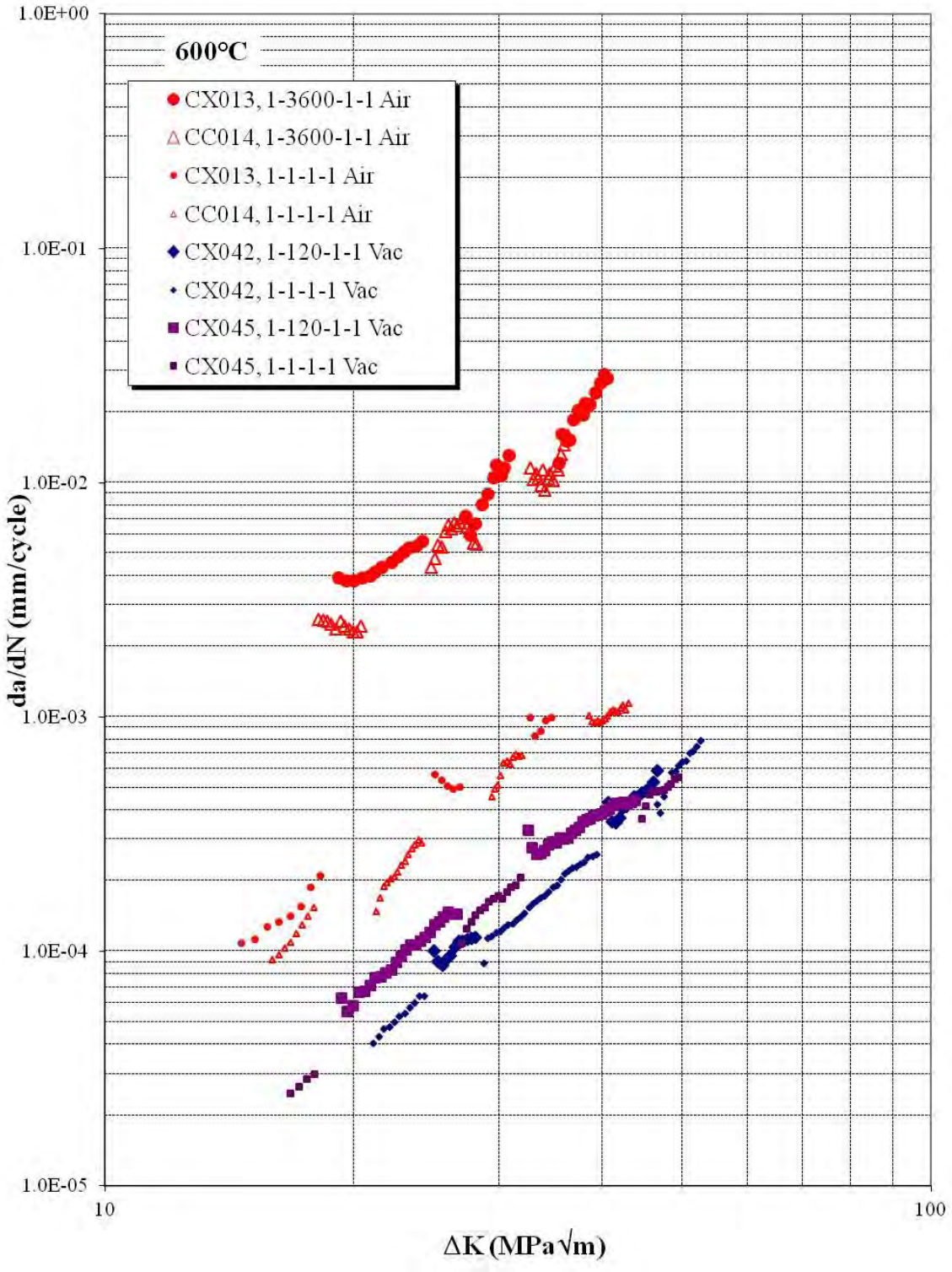


Figure 4-2: da/dN vs. ΔK curves for fine-grained Udimet 720Li samples CX013, CX014, CX042 and CX045, which were tested at 600°C, with a dwell load of 26 kN, a dwell time of 3,600s in air (CX013 and CX014) and 120s in a vacuum (CX042 and CX045). Note that dwell crack growth rates in a vacuum are similar to those associated with baseline loading.

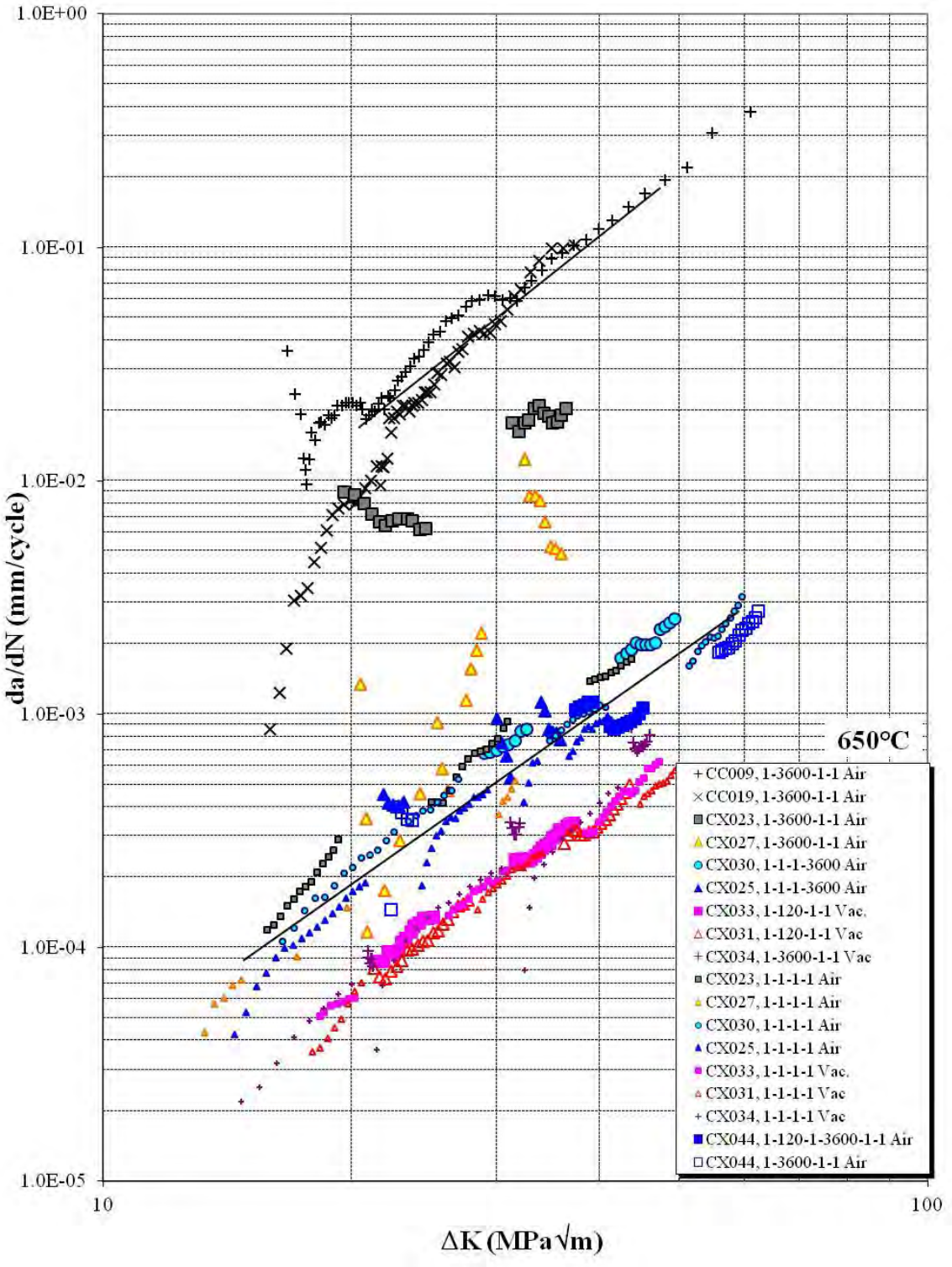


Figure 4-3: da/dN vs. ΔK curves for fine-grained Udimet 720Li samples tested at 650°C at a range of dwell periods, in air and in a vacuum.

4.1.3 Effect of Overload

Furthermore, baseline, dwell and overload testing has shown that the introduction of a one second overload before the subsequent hold time at the (slightly reduced) dwell load in the cycle can cause the reduction of crack growth rates when compared with otherwise similar dwell only cycling. For certain conditions, this retardation effect almost completely brings crack growth rates back down to those normally associated with baseline loading, i.e. cycle only fatigue. In order to fully understand this behaviour, tests have been carried out at different temperatures, with different dwell loads, various dwell times and overload factors of between 1.05 and 1.15.

Three catagories of retardation have been observed: full, nearly full, and partial. Two criteria need to be met for the tests to be evaluated as showing a full retardation:

(1) The crack growth rates from overload cycles are either equivalent to or slower than fatigue crack growth rates from (otherwise similar) baseline cycles.

(2) A predominantly transgranular fracture surface morphology has been observed.

This transformation from intergranular (dwell) to transgranular (fully retarded overload) is reported in section 4.2 and suggests that the time-dependent failure mechanism has been fully suppressed (when full retardation has occurred), and that crack growth rates and mechanisms become dominated by cyclic factors; that they are controlled purely by the fatigue process.

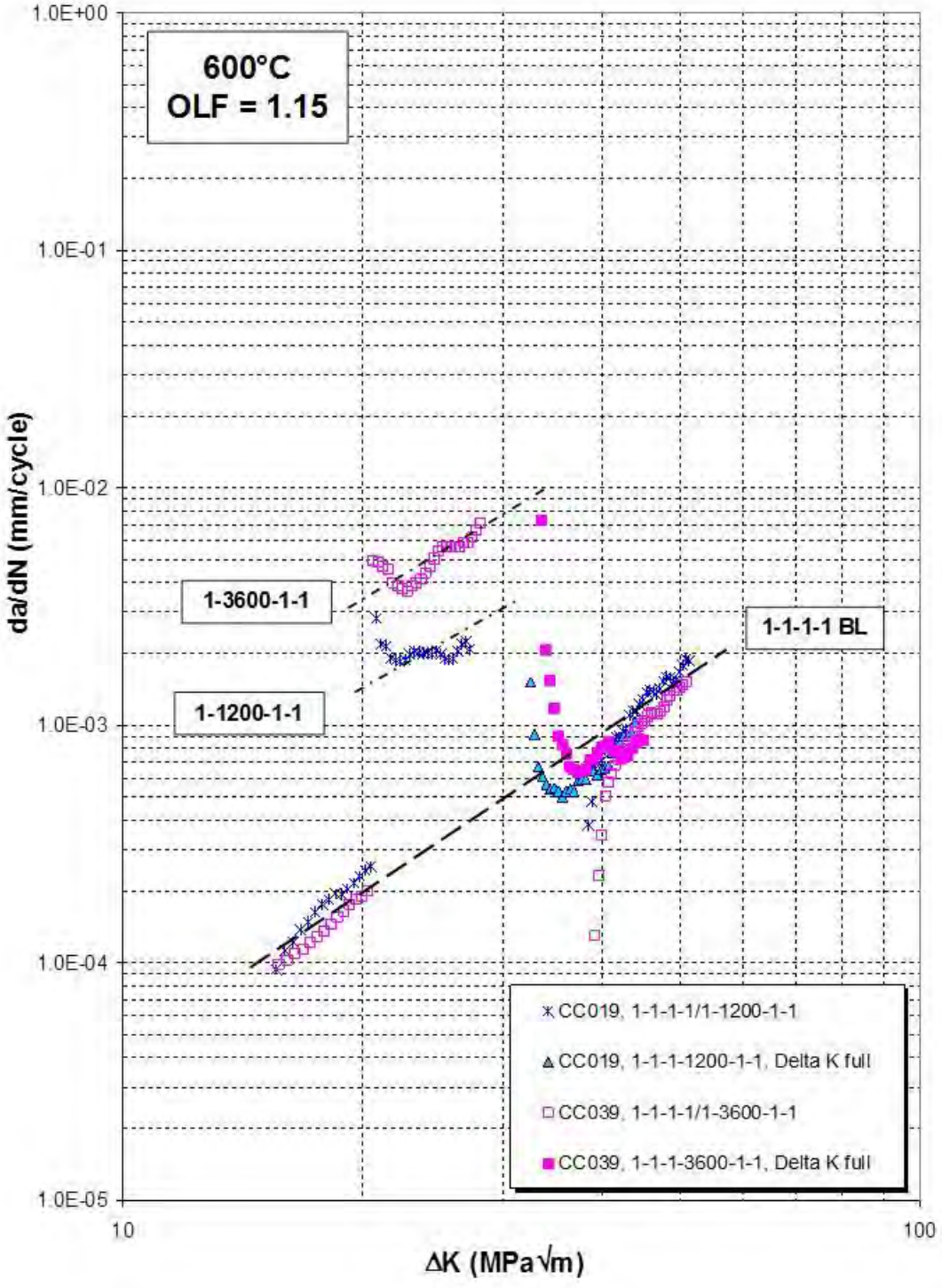


Figure 4-4: da/dN vs. ΔK curves for RR1000 samples CC019 and CC039 tested at a temperature of 600°C with an overload factor of 1.15. Note that the ΔK values are calculated using the load range between the peak overload and the minimum load (ΔK_{full}) for the overload fatigue crack growth segment. Full retardation.

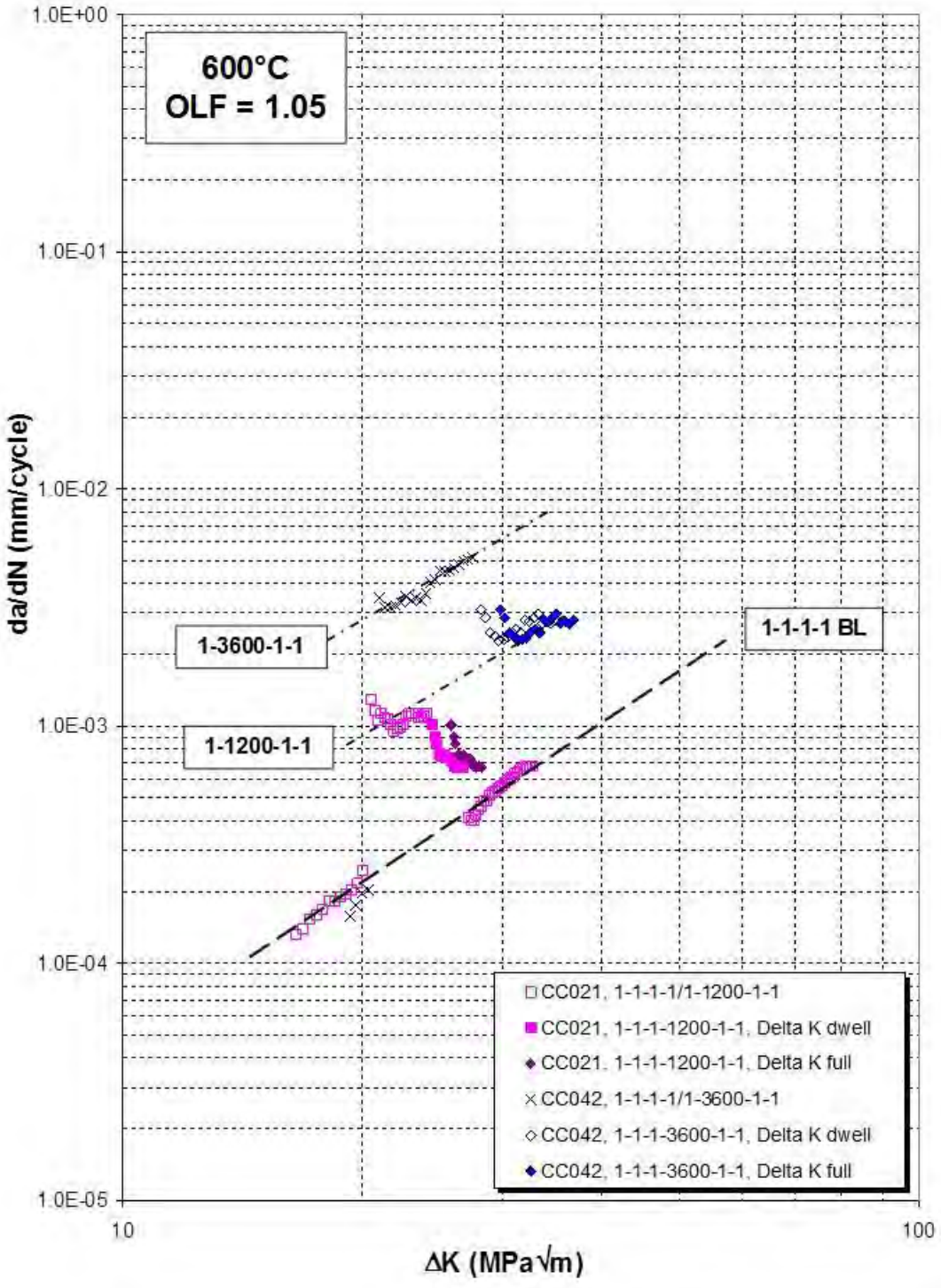


Figure 4-5: da/dN vs. ΔK curves for RR1000 samples CC021 and CC042 tested at a temperature of 600°C with an overload factor of 1.05. Partial retardation.

It should be noted that the dotted lines in Figure 4-4 and Figure 4-5 are not linear best fit lines but rather sketched estimates of how the crack growth behaviour may be simplified for ease of comparison and interpretation.

As previously stated, it is important to note that ΔK for the overload waveform can be plotted as either ΔK_{full} (taking the maximum stress as the full overload stress) or ΔK_{dwell} (taking the "maximum" stress as the dwell stress). Although it is arguable which one is more appropriate to represent the actual driving force for resultant crack growth, it is the da/dN versus ΔK_{full} plot that was used to judge whether or not a full retardation effect is achieved.

Further to "degree of retardation", the crack growth resistance data is also used to generate experimentally derived values for the incubation time (section 3.2.4.2). Incubation time is also generated analytically, and is reported in section 4.3.2. Section 4.3.4 reports on the experimentally derived values for incubation time and those values are tabulated in Table 29 and Table 30.

4.1.4 Influence of Microstructure

The graphs also confirm that for repeated test conditions, variations between samples (in terms of crack growth resistance) have been confirmed. These differences are discussed in 5.2, although at this stage it is important to highlight that the nature of retardation remains unaffected. The most significant of these observations (in terms of variation between test pieces) is that crack growth rates in Udimet 720Li from Batch Two of the Phase Two

material are significantly higher than those in other Batches of material, for the same testing conditions. These differences can be seen in the crack growth resistance curves presented in Appendix VI, although here it is highlighted that the difference relates to about 50°C of extra temperature. In other words, crack growth rates in Batch Two Phase Two material at 600°C are roughly as fast as those relating to Phase One, and Batch One of Phase Two at around 650°C (Figure 4-6). Hence Batch Two Phase Two material is worse in terms of its crack growth resistance at elevated temperature. This is related to a significant difference in terms of its microstructure which is discussed in section 5.2.

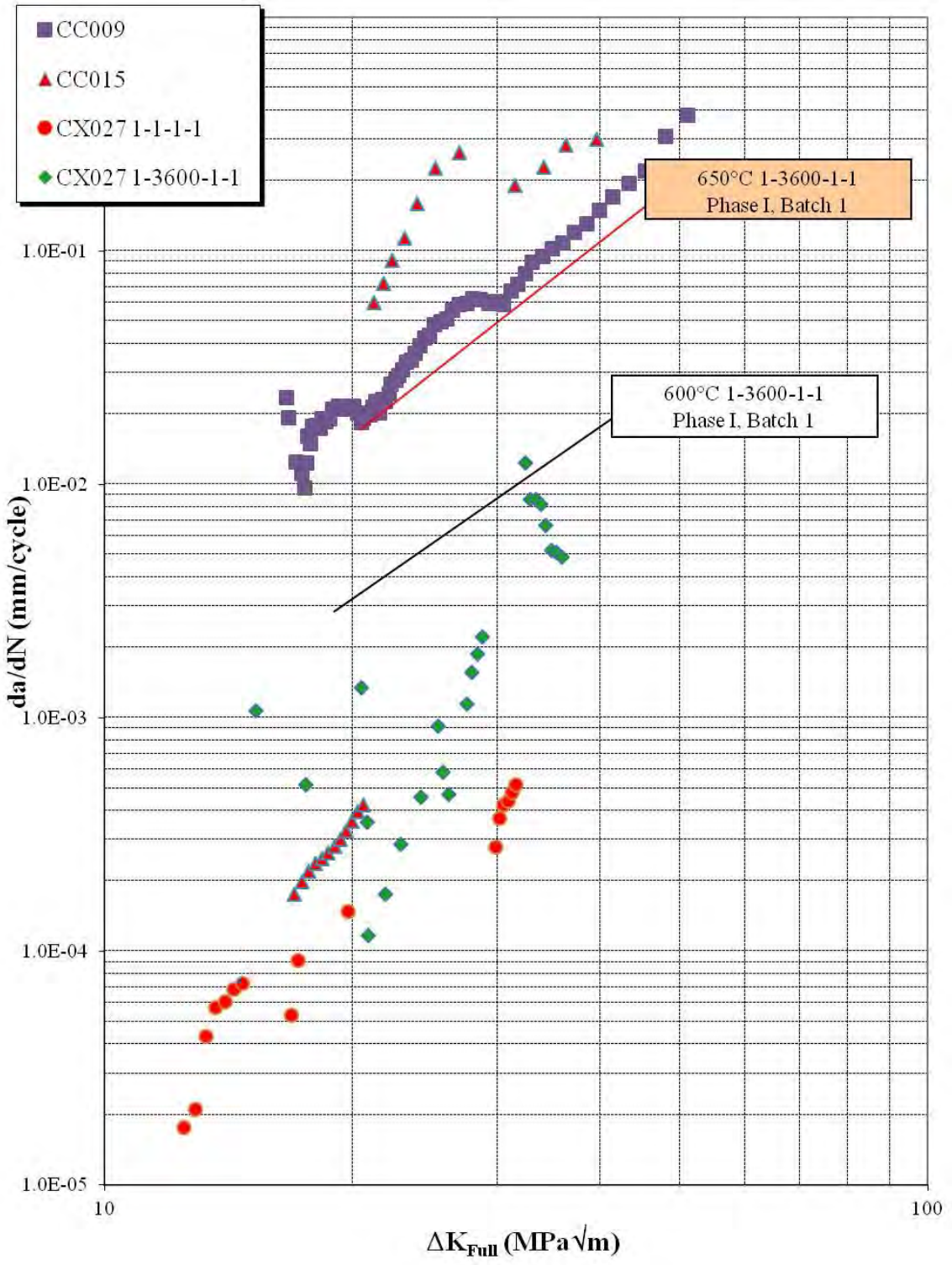


Figure 4-6: da/dN vs. ΔK curves for fine-grained Udimet 720Li samples CC009, CC015 and CX027, all tested at 650°C and with a dwell period of 3,600s, in air. Note that despite similar testing conditions crack growth rates are shown to be variable. Note also that CX027 data represents intermittent "bursts" of baseline (1-1-1-1) loading in order to encourage the crack to grow under a dwell regime.

4.1.5 Effect of Changing the Waveform

Furthermore, crack growth resistance curves also show transition regions as a result of switching between waveforms; where crack growth rates stabilise over a region of affected material to reach fresh material. In general, two types of transitional behaviour is observed: crack growth rates which begin faster than is usually observed for a given waveform and "settle down" and crack growth rates which begin slower than is usually observed for a given waveform and "settle up". The former is attributed to environmental effects ahead of the crack tip, the latter to crack tip blunting due to creep. The phenomena are discussed in detail in section 5.5.

The distance (in terms of crack growth) over which this stabilisation occurs can be estimated by measuring difference between the crack length associated with first switching the waveform and the crack length associated with complete stabilisation of crack growth rates. This distance can be used to estimate the depth of the affected zone. The type of crack growth rate stabilisation, including estimations for depths over which it occurs is tabulated for all conditions in Table 20 and Table 21.

4.1.6 Time-Dependent ΔK_{th}

Stress intensity factor threshold (ΔK_{th}) tests for time-dependent crack growth pertaining to a range of conditions are also plotted in Appendix VI. They show that, in otherwise similarly tested material, the stress intensity factor range threshold required to cause the onset of time-dependent crack growth according to dwell cycling is larger when compared with that

which is required to cause the onset of cycle-dependent, fast cycle crack growth. This can be seen in Figure 4-7.

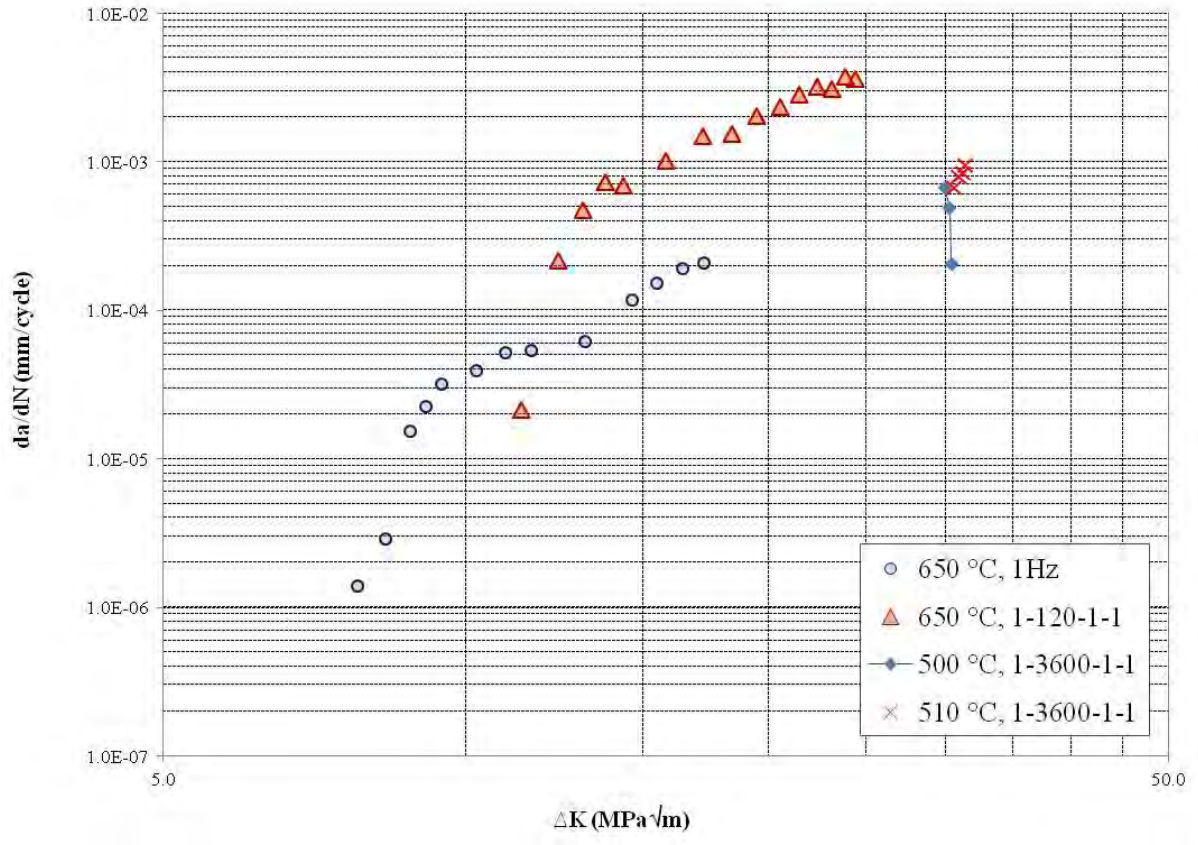


Figure 4-7: da/dN vs. ΔK graph to show the effect of a 120 second dwell period on the stress intensity factor range threshold for high temperature (650°C) crack growth when compared with 1 Hz sinusoidal loading. Note that both sets of data are gathered using the decreasing ΔK (load shedding) technique. Note also the temperature threshold data gathered on the same test piece (CC044), which was found to be ~510 °C for a ΔK of around 30MPa√m.

The data also show that in microstructurally consistent material, an increase in dwell time causes a reduction in the time-dependent threshold ΔK value which would cause the onset of dwell crack growth (Figure 4-8).

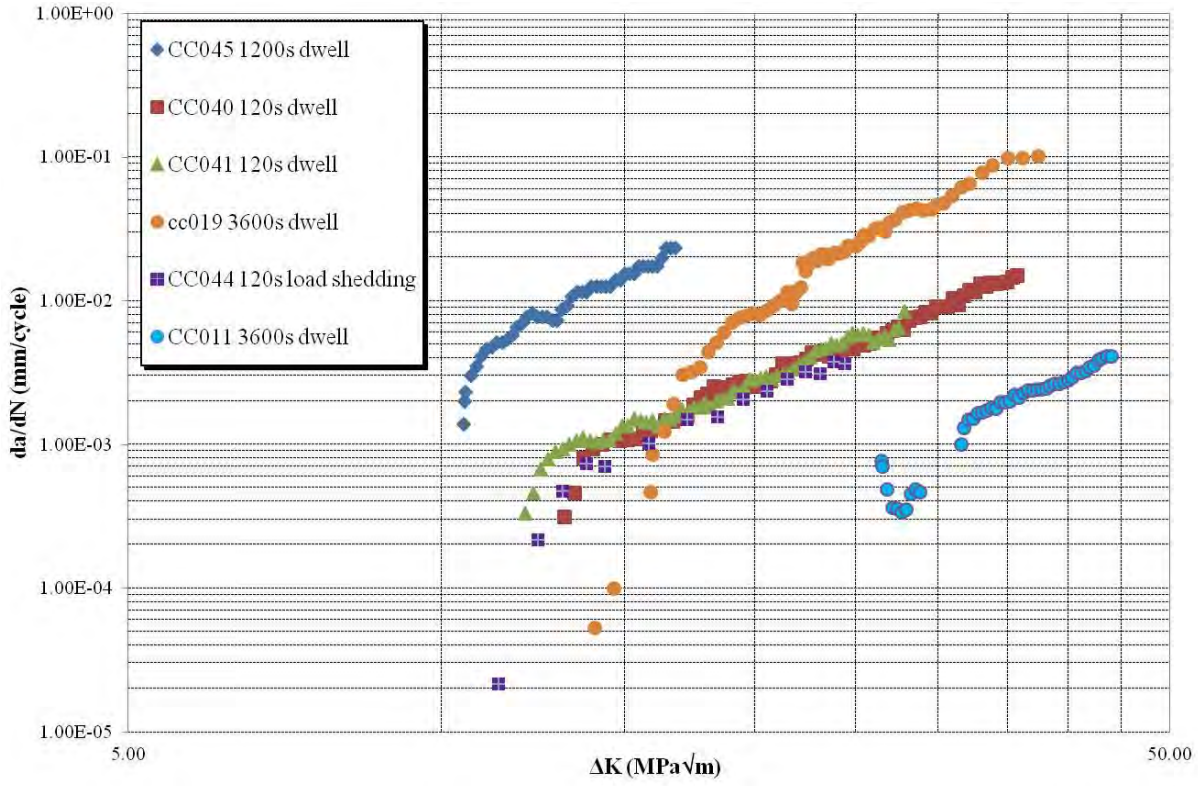


Figure 4-8: da/dN vs. ΔK graph to show comparisons for all ΔK threshold testing on Udimet 720Li sample test pieces. All tests are carried out at 650°C in laboratory air, with dwell periods of 120 or 3,600 seconds. Note that test pieces CC011 and CC045 (showing unusual results when compared with the other data presented) are found to comprise notably different microstructures.

4.1.7 Summary

Results are presented as a series of crack growth resistance curves on which several test piece conditions are compared. A full plot for each crack growth resistance curve generated on each test piece can also be found in Appendix VI. A few key results are summarised in Table 18, Table 19, Table 20 and Table 21.

A summary of results for both fine-grained Udimet 720Li and RR1000 overload programmes are displayed in Table 18 and Table 19.

Table 18: Summary of the retardation effect observed for fine-grained Udimet 720Li overload tests. Note that "Green", "Amber" and "Blue" denote "full retardation", "nearly full retardation" and "partial retardation" respectively. Note that in most cases, two bands of overload cycling have been applied to each test piece; hence coloured identifications are presented in order of results for low ΔKs and high ΔKs respectively (low/high)

600°C

t_{dwell} / OLF	120s	300s	600s	1,200s	3,600s
1.05				CC005/CC005	CC006/CC006
1.08					
1.10					
1.15			CC001/CC001		CC002/CC002

625°C

t_{dwell} / OLF	120s	300s	600s	1,200s	3,600s
1.05					
1.08				CC009/CC009	
1.10					
1.15					

650°C

t_{dwell} / OLF	120s	300s	600s	1,200s	3,600s
1.05					
1.08				CC010/CC010	
1.10					
1.15				CC007/CC007	CC003/CC003

675°C

t_{dwell} / OLF	120s	300s	600s	1,200s	3,600s
1.05					
1.08					
1.10				CC008/CC008	
1.15					

Table 19: Summary of the retardation effect observed for fine-grained RR1000 overload tests. Note that "Green", "Amber" and "Blue" denote "full retardation", "nearly full retardation" and "partial retardation" respectively.

600°C

t_{dwell} / OLF	120s	300s	600s	1,200s	3,600s
1.05				**CC021**	CC042
1.08					
1.10					
1.15				CC019	CC039

625°C

t_{dwell} / OLF	120s	300s	600s	1,200s	3,600s
1.05					
1.08					
1.10				**CC018** **CC047**	
1.15					

650°C

t_{dwell} / OLF	120s	300s	600s	1,200s	3,600s
1.05	**CC050**	**CC051**			
1.08			**CC049**	**CC017** **CC045**	
1.10					
1.15				CC046	CC020 CC048

675°C

t_{dwell} / OLF	120s	300s	600s	1,200s	3,600s
1.05	**CC052**				
1.08			**CC053**		
1.10				**CC034**	
1.15					

Note that for all conditions, some retardation is always present with the introduction of the overload segment.

Table 20: Tabulating the direction of "tails" on crack growth resistance curves as a result of switching the loading waveform, specifically for fine-grained Udimet 720Li test pieces. Shaded areas represent anomalous behaviour.

Testpiece ID	Temp (°C)	Dwell Time (s)	Overload Factor	Tailing from Dwell to Overload	Tailing from Overload to Baseline	Remarks
CC013	600	1,200	1.05	Down	Down	Ultra fine grain size
CC014	600	3,600	1.05	No tail	Down	Ultra fine grain size
CC003	650	3,600	1.15	Down	Up	
CC004	650	1,200	1.15	Down	Up	
CC007	650	1,200	1.15	Down	Up	
CC008	675	1,200	1.10	Down	Up	
CC010	650	1,200	1.08	Down	Up	
CC001	600	1,200	1.15	Down	Up	Full Retardation
CC002	600	3,600	1.15	Down	Up	Full Retardation
CC005	600	1,200	1.05	Down	Up	Partial / Full
CC006	600	3,600	1.05	Down	Up	Partial Retardation
CC009	625	1,200	1.08	Down	Up	Partial Retardation
CC029	650	1,200	1.15	Down	Up	120s Dwell at OL
CC032	650	1,200	1.15	Down	Up	600s Dwell at OL

Table 21: Tabulating the direction of "tails" on crack growth resistance curves as a result of switching the loading waveform, specifically for fine-grained RR1000 test pieces. Shaded areas represent anomalous behaviour. Where possible, an estimate for the distance over which stabilisation of crack growth rates occurs is also included.

Testpiece ID	Temp (°C)	Dwell Time (s)	Overload Factor	Tailing from Dwell to Overload	Tailing from Overload to Baseline	Remarks
CC019	600	1,200	1.15	Down	Up	Full Retardation
CC021	600	1,200	1.05	Down	No tail	Partial Retardation
CC047	625	1,200	1.08	Down ~0.2mm	Up ~0.215mm	Nearly full retardation
CC018	625	1,200	1.08	Down	Up	Nearly full retardation
CC045	650	1,200	1.08	Down ~0.25mm	Up ~0.15mm	Partial Retardation
CC046	650	1,200	1.15	Down ~0.31mm	Up ~0.2mm	Full Retardation
CC048	650	3,600	1.15	Down ~0.35mm	Up ~0.167mm	Full Retardation
CC017	650	1,200	1.08	Down		Partial Retardation
CC020	650	3,600	1.15	Down	Up	Nearly full retardation
CC034	675	1,200	1.10	Down	Down	Partial Retardation
CC035	650	3,600	1.15	Down	Up	120s Dwell at OL
CC056	650	1,200	1.065	No tail	Down	Unload
CC057	650	1,200	1.065	No tail	Down	Reload

4.2 Scanning Electron Microscopy

4.2.1 Fractography

4.2.1.1 Introduction

A full and comprehensive presentation of fractographs taken of all testing conditions for each alloy is presented in Appendix VII. Presented in subsequent paragraphs and in Table 22, Table 23, Table 24, Table 25 and Table 26 are summaries of the results, and representative trends and observations.

4.2.1.2 Effect of Dwell Period

Scanning electron microscopy confirmed that high temperature baseline loading in fine-grained Udimet 720Li and RR1000 usually resulted in a predominantly transgranular crack morphology. Fracture surfaces pertaining to high temperature dwell crack growth revealed crack paths under this regime propagated predominantly along grain boundaries in the intergranular regime, including delinenation around primary γ' particles. These observations are consistent with studies on dwell crack growth mechanisms of a range of nickel superalloys [6, 30, 31, 33, 36-41, 43, 47, 49-51, 58, 67, 84-90].

It is therefore confirmed that there is indeed a clearly observable mechanism change from relatively slow, transgranular cycle-dependent (baseline) mechanisms to fast, time-dependent intergranular mechanisms with the introduction of a hold or dwell period at maximum load in fine-grained Udimet 720Li and RR1000 in air at 525 - 675°C.

These observations are general trends however, and there are subtle exceptions. As reported in previous sections, Udimet 720Li test pieces pertaining to Batch Two of Phase Two were found to possess poorer properties in fatigue. This may be attributed to differences in microstructure (reported in section 4.2.2), the most significant of which are differences in grain size and primary γ' morphology. As reported below, primary γ' is found to have segregated during processing of the alloy, and the microstructure is characterised by regions of very fine precipitates of the primary γ' phase. Figure 4-9 and Figure 4-10 below show that these regions have affected crack paths in both baseline (Figure 4-9) and dwell (Figure 4-10) crack growth regimes. As has been suggested it is thought that crack paths will follow the boundaries between primary γ' and the γ matrix, and between neighbouring primary γ' precipitates, which for Batch Two, Phase Two material even occurs under baseline, cycle-dependent crack growth. These observations are displayed in the representative examples given below (Figure 4-9 to Figure 4-13).

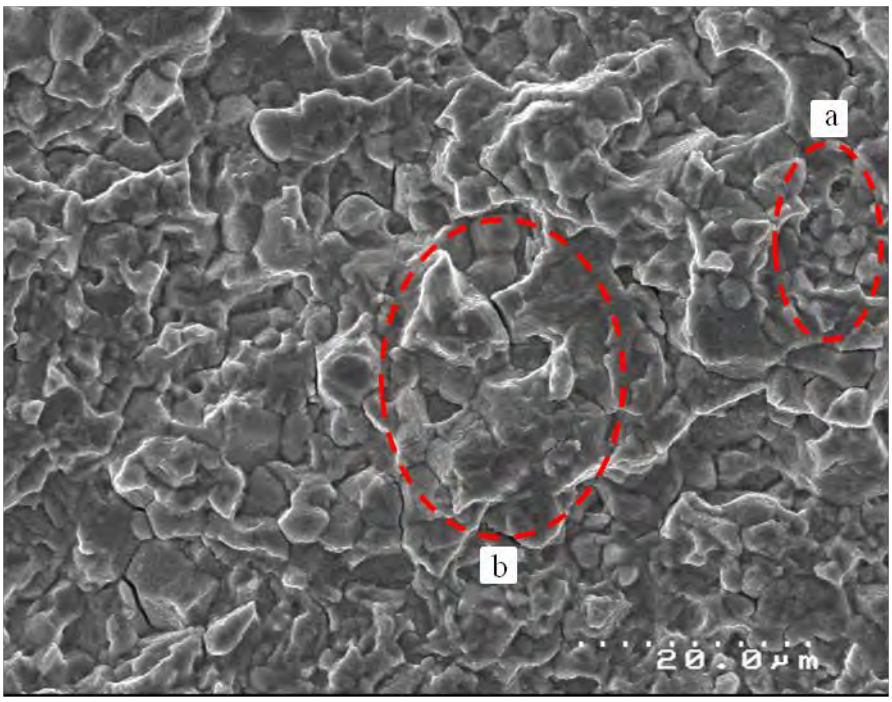


Figure 4-9: Scanning electron micrograph of fine-grained Udimet 720Li sample CC014, during the first baseline segment (ΔK~18MPa√m). The sample was tested at 600°C, and with a dwell load of 29kN. The fracture surface is predonimantly transgranular, nevertheless it can be seen from a) that crack paths have propagated around primary γ' where it has segregated in large amounts of fine precipitates. b) shows an area which contains fewer primary γ' precipitates and hence the crack appears to have propagated through the γ grains.

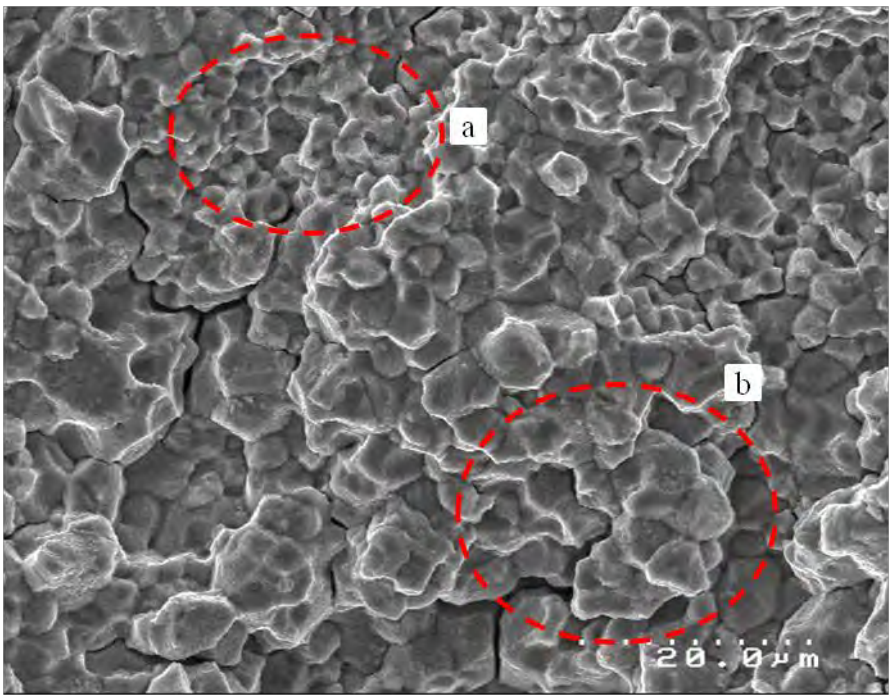


Figure 4-10: Scanning electron micrograph of fine-grained Udimet 720Li sample CC014 (as above), during the dwell segment (ΔK~22MPa√m). The fracture surface is predonimantly intergranular and shows a) segregation of fine primary γ' precipitates and b) areas of clean, faceted transgranular crack growth in regions denuded of primary γ'.

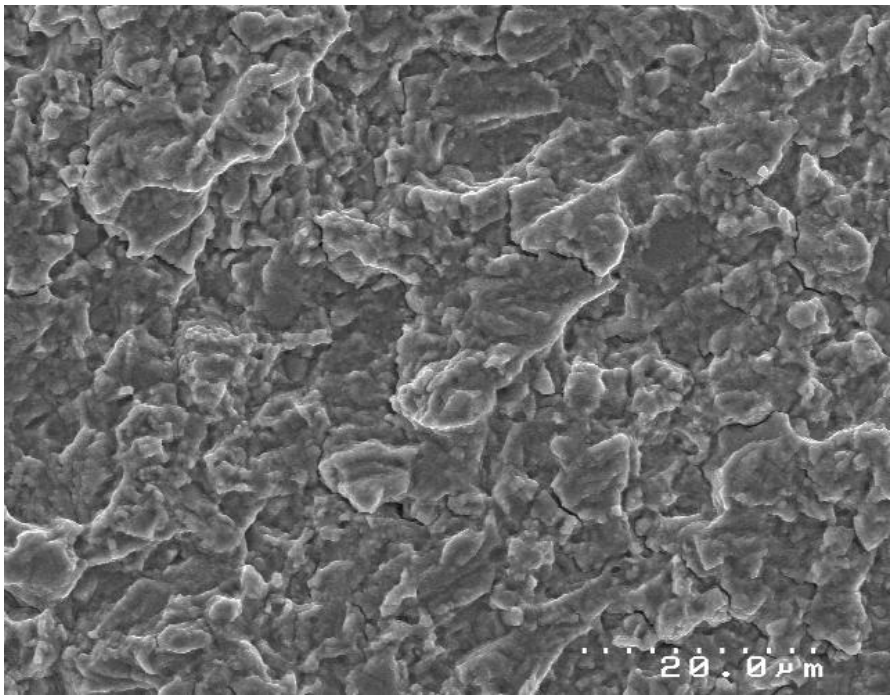


Figure 4-11: Scanning electron micrograph of fine-grained RR1000 sample CC021, during the first baseline segment (ΔK~18MPa√m). The sample was tested at 600°C, and with a dwell load of 26kN. The fracture surface is predonimantly transgranular.

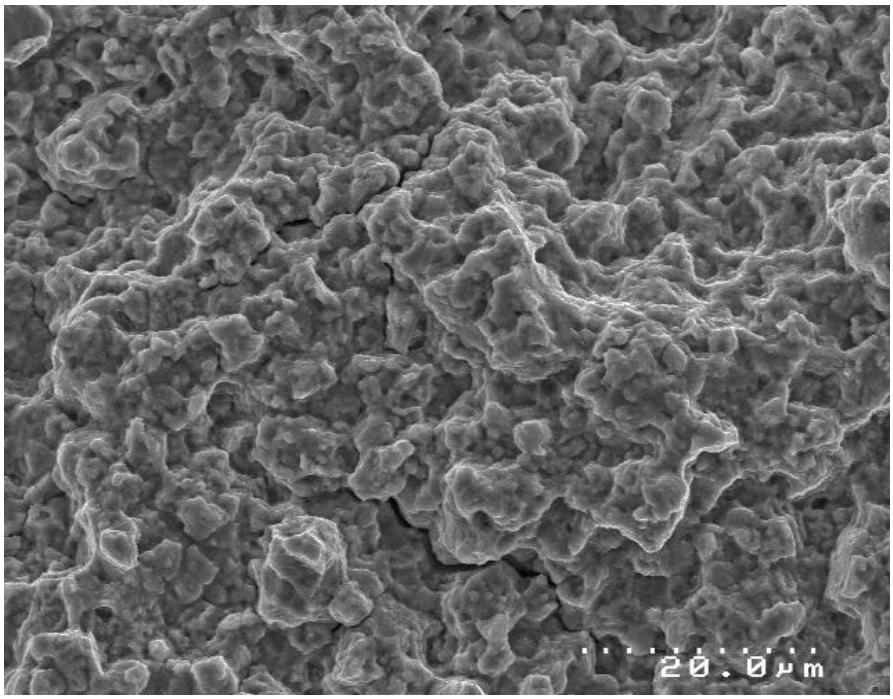


Figure 4-12: The same sample (RR1000 CC021) under dwell conditions (ΔK~22MPa√m). The test piece was tested at a dwell load of 26 kN and a dwell time of 1,200 seconds. The crack growth morphology is shown to be predominantly intergranular, with delineation of primary γ' from the γ matrix charecterising the fracture surface along with faceted intergranular grain boundary cracking.

The delineation of primary γ' from the γ matrix during dwell crack growth is shown more clearly in Udimet 720Li test pieces, and displayed in Figure 4-13.

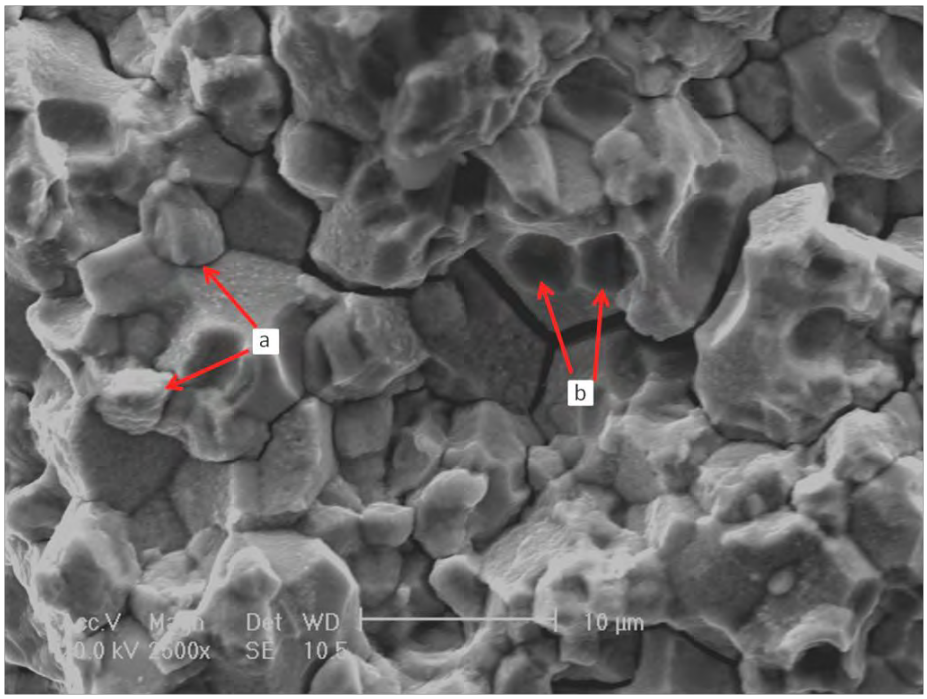


Figure 4-13: Fractograph of fine-grained Udimet 720Li test piece CC040 tested at a temperature of 650°C and with a dwell time of 120 seconds. The fracture surfaces shows where the crack path has propagated along the boundary between primary γ' and the γ matrix in which it has precipitated. The image shows a) primary γ' on the fracture surface and b) gaps in the γ matrix from which primary γ' particles have delineated.

The reasons for which primary γ' becomes segregated and an analysis on the possible effect this segregation might have upon crack growth paths and therefore crack growth resistance are discussed in section 5.2.1.

In general however, these fractographs provide further evidence to support the suggestion that oxidation affects crack growth rates, since at larger dwell periods, oxygen has more time to attack and embrittle the grain boundaries.

4.2.1.3 Effect of Overload

The difference between crack growth mechanisms pertaining to dwell and overload segments depend upon the degree to which crack growth retardation has occurred. In general, conditions which cause a full retardation are asociated with fully (or nearly full) transgranular crack growth morphologies, but conditions which cause only partial retardation show little to no difference when compared with crack growth morphologies usually asociated with dwell crack growth (i.e they are intergranular, including the effects of delineation of primary γ' from the γ matrix as discussed above). Figure 4-14 to Figure 4-18 show typical overload fracture surfaces in RR1000.

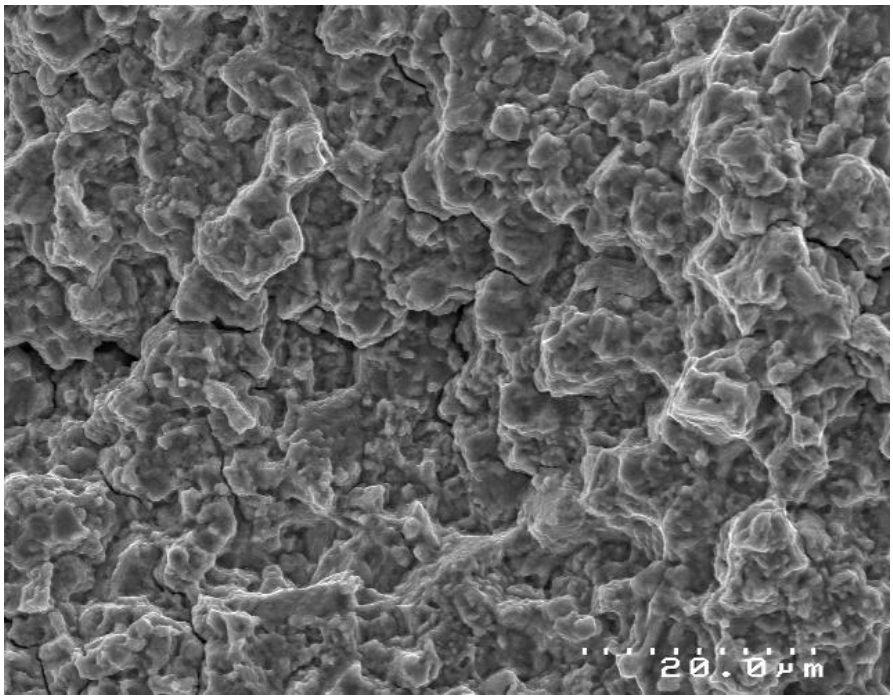


Figure 4-14: The same fine-grained RR1000 sample as shown above (CC021), during the overload segment (ΔK~34MPa√m). An overload factor of 1.05 was applied, and the amount of retardation was found to be partial. The crack growth morphology appears to be predominantly intergranular despite slower crack growth rates than those observed during dwell only loading.

Conditions for which full retardation occurred did however display more observable differences in terms of mechanisms when dwell crack paths are compared with those caused by overload cyclic waveforms.

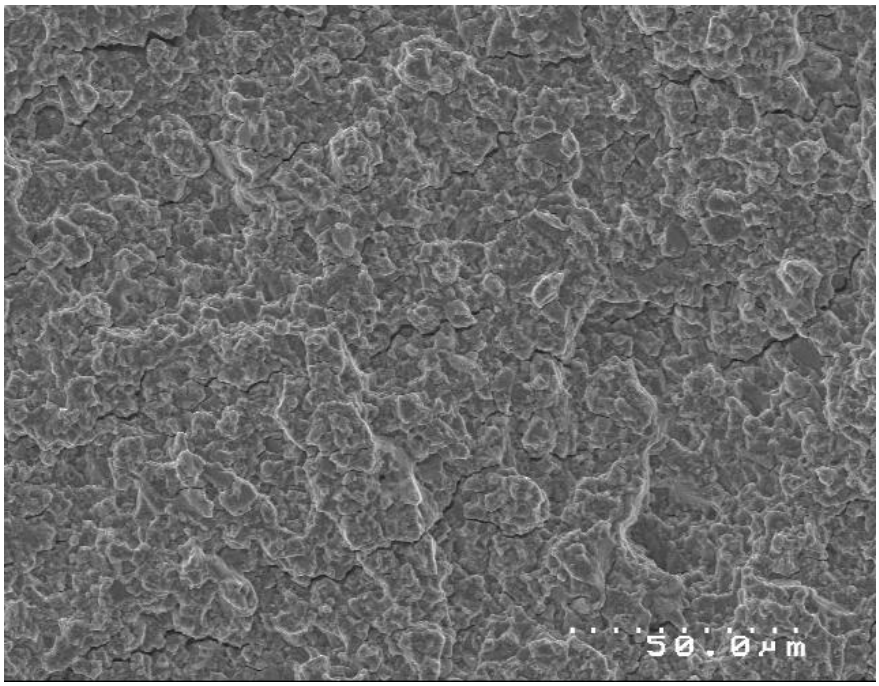


Figure 4-15: Lower magnification fractograph of RR1000 sample CC046 during overload cycling (ΔK~35MPa√m), tested at 650°C with a dwell period of 1,200 seconds and an overload factor of 1.15; conditions which caused full retardation back down to baseline crack growth rates.

Figure 4-15 suggests that for full retardation the mode of crack growth could be described as predominantly transgranular. Nevertheless, there are regions of surface roughness and intergranular crack growth, something which is observed considerably less for baseline loading at similar ΔK values.

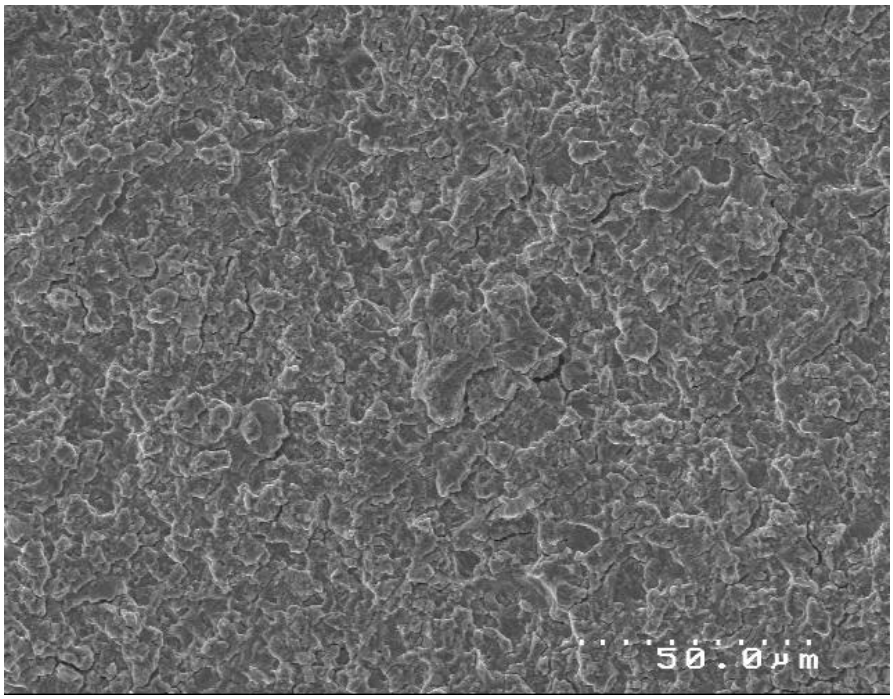
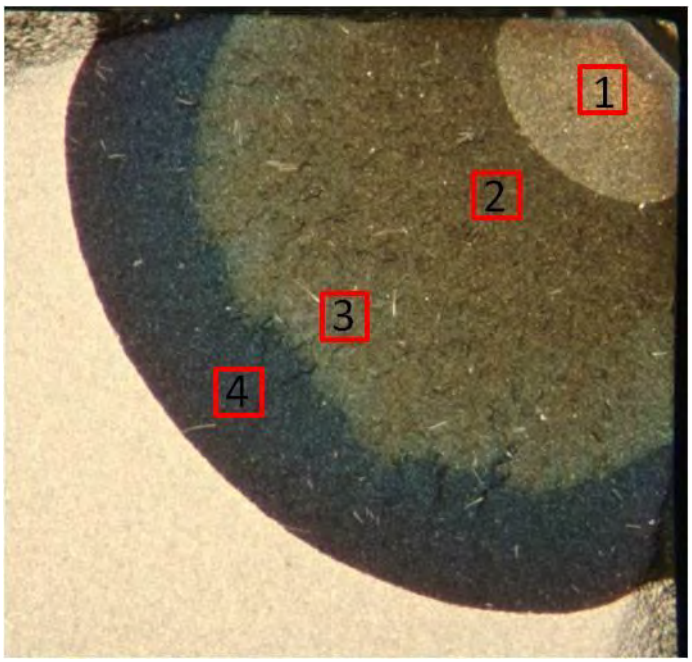
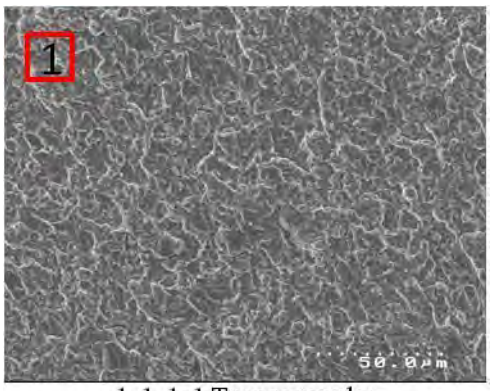
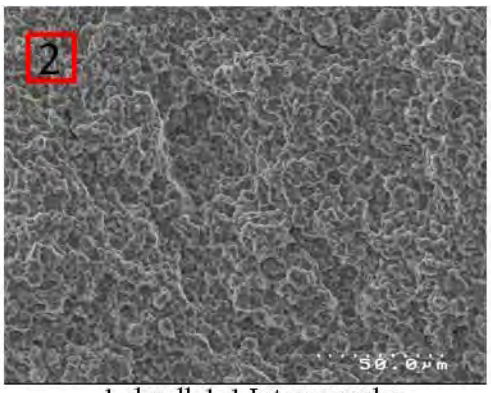


Figure 4-16: Fractograph of RR1000 sample CC046 taken of the final baseline zone (ΔK~45MPa√m), showing transgranular crack growth.

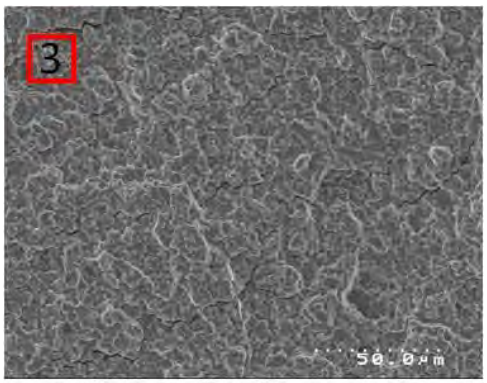




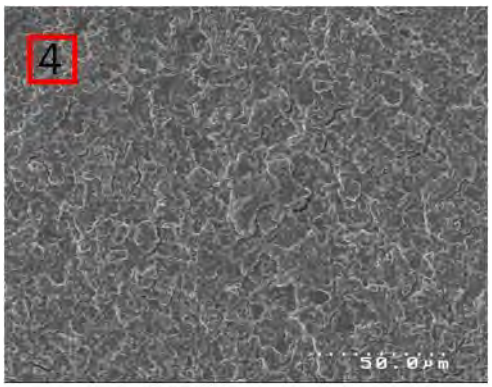
1-1-1-1 Transgranular



1-dwell-1-1 Intergranular

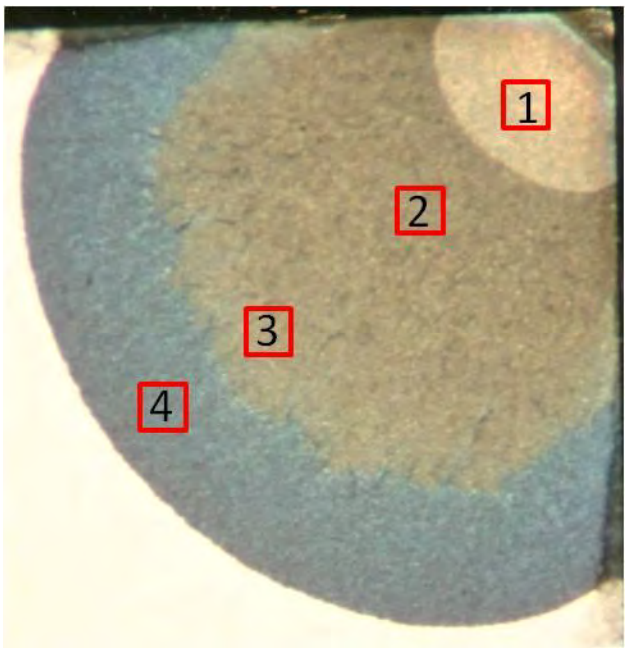


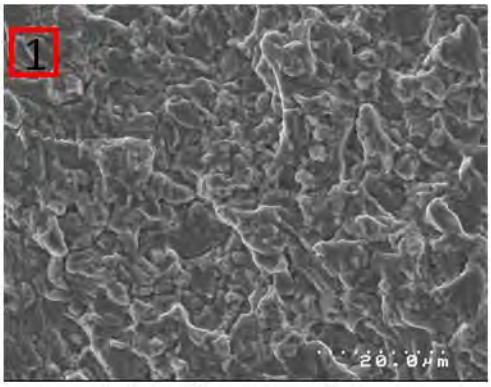
1-OL-1-dwell-1-1 Transgranular
(Full Retardation)



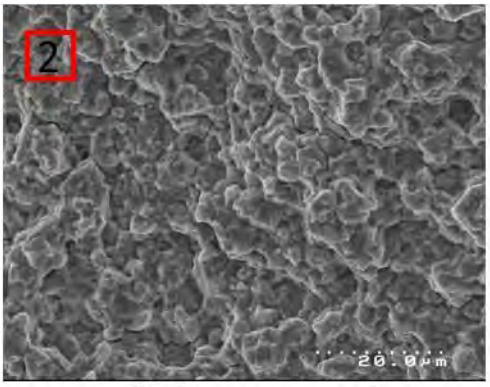
1-1-1-1 Transgranular

Figure 4-17: (Previous page) A summary of the fractography data, for fine-grained RR1000 sample CC046 – tested at 650°C, a dwell time of 1,200 seconds and an overload factor of 1.15. Full retardation was observed.

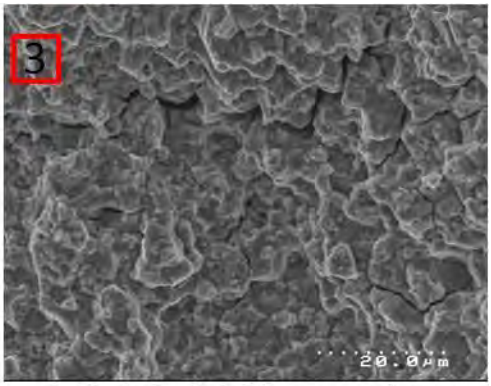




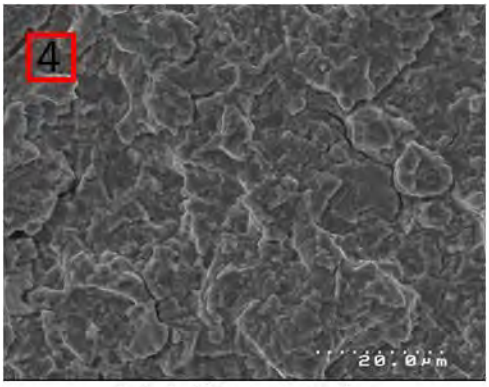
1-1-1-1 Transgranular



1-dwell-1-1 Intergranular



1-OL-1-dwell-1-1 Intergranular
(Partial Retardation)



1-1-1-1 Transgranular

Figure 4-18: (Previous page) A summary of the fractography data, for fine-grained RR1000 sample CC045 – tested at 650°C, a dwell time of 1,200 seconds and an overload factor of 1.08. Partial retardation was observed.

4.2.1.4 Time Dependent ΔK_{th}

Fractographs of fine-grained Udimet 720Li test pieces tested for the stress intensity factor range required for time-dependent crack growth (ΔK_{th}) revealed similar conclusions to those observed above; namely that crack growth according to high temperature fast-cycle fatigue usually occurs in the transgranular regime and that crack growth according to high temperature dwell cycling in air usually occurs in the intergranular regime.

More specifically, the study shows that time-dependent crack growth according to high temperature dwell cycling is predominantly intergranular even at threshold. Nevertheless for test piece CC040 a transition band was observed where the change between transgranular crack growth (due to 1 Hz sinusoidal precracking) and intergranular crack growth (according to 120 second dwell cycling) happened over a definite period of crack growth. Closer analysis reveals that at very low values of ΔK (near threshold) the crack continues to grow in the transgranular regime until sufficient driving forces to cause intergranular crack growth are applied (as the crack propagates).

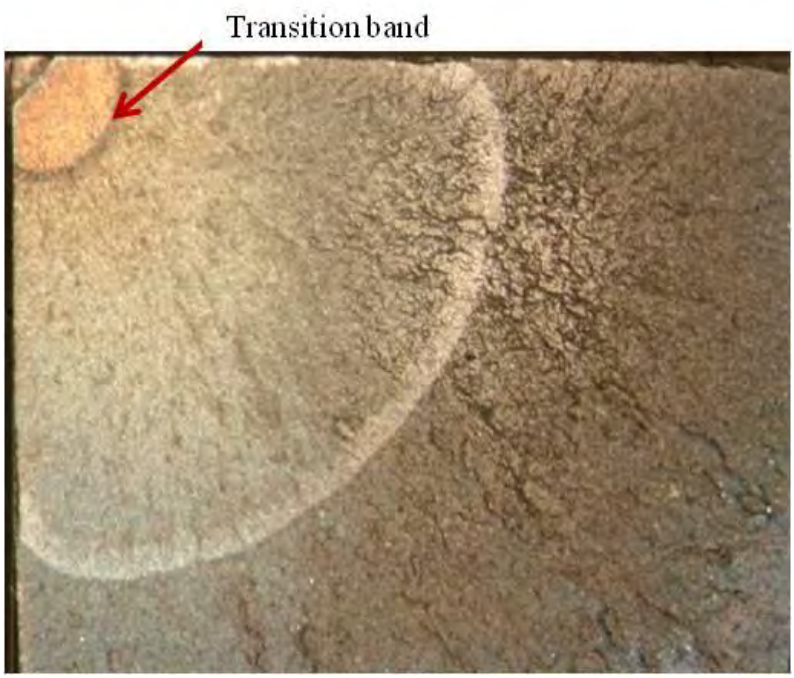


Figure 4-19: SEM image of fine-grained Udimet 720Li test piece CC040 tested for time-dependent threshold in air at 650°C with a dwell period of 120 seconds. The image shows a transition band which occurred near threshold.

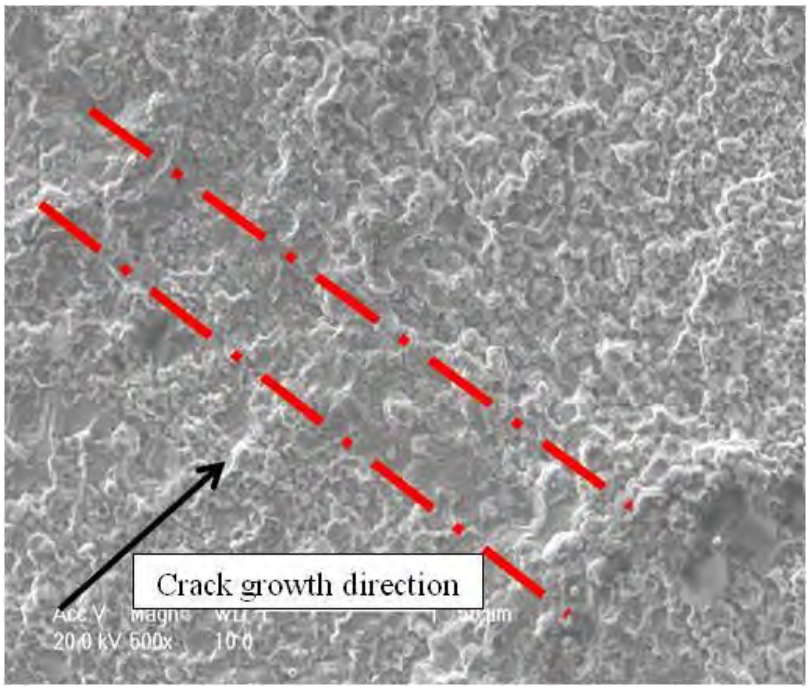


Figure 4-20: Higher magnification SEM image of the same transition band shown above.

Further analysis of crack growth mechanisms can also be made by studying SEM images taken from sectioned test pieces, looking along the face of the crack. They confirm that crack growth according to dwell cycling occurs (predominately) in the intergranular regime, and that crack growth according to fast-cycling (1-1-1-1 baseline) at high values of ΔK occurs in the transgranular. They also reveal that crack growth pertaining to fast-cycling at lower values of ΔK (~11 MPa√m) occurs according to a mixture of modes. The crack is shown to propagate through large γ grains (transgranularaly) but along the boundaries of primary γ' and the γ grains, between adjacent primary γ' boundaries; and between the boundaries between γ grains through regions of relatively fine grain sizes. These phenomena are discussed in more detail in section 5.2.1.

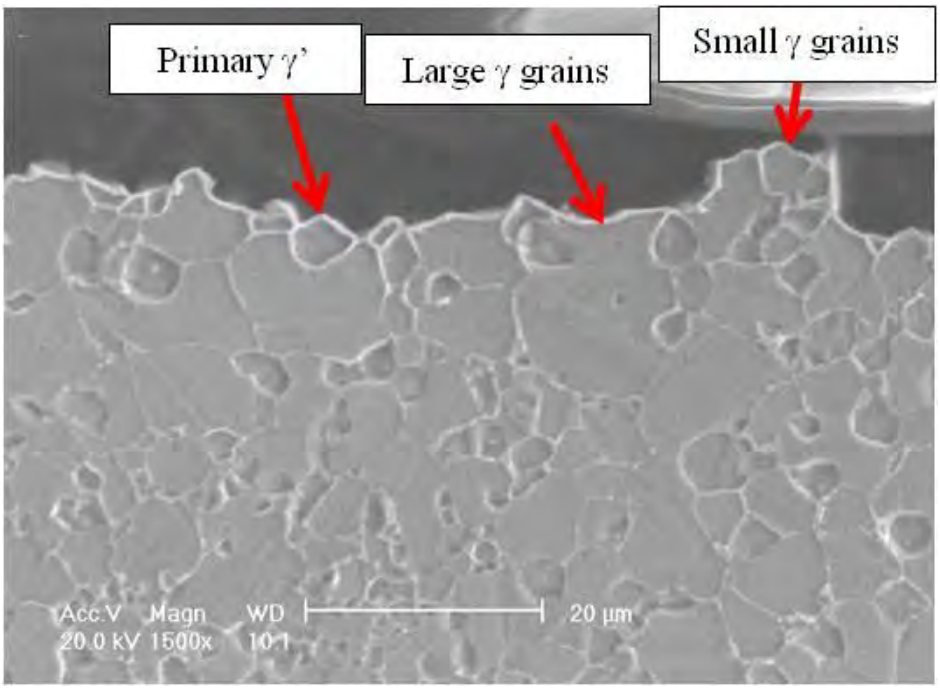


Figure 4-21: Cross section view of fine-grained Udimet 720Li test piece CC044 showing the crack profile (propagating left to right) pertaining to 1 Hz sinusoidal precracking at 650°C in air at a ΔK of ~11 MPa√m. Note the mixture of inter and transgranular crack growth.

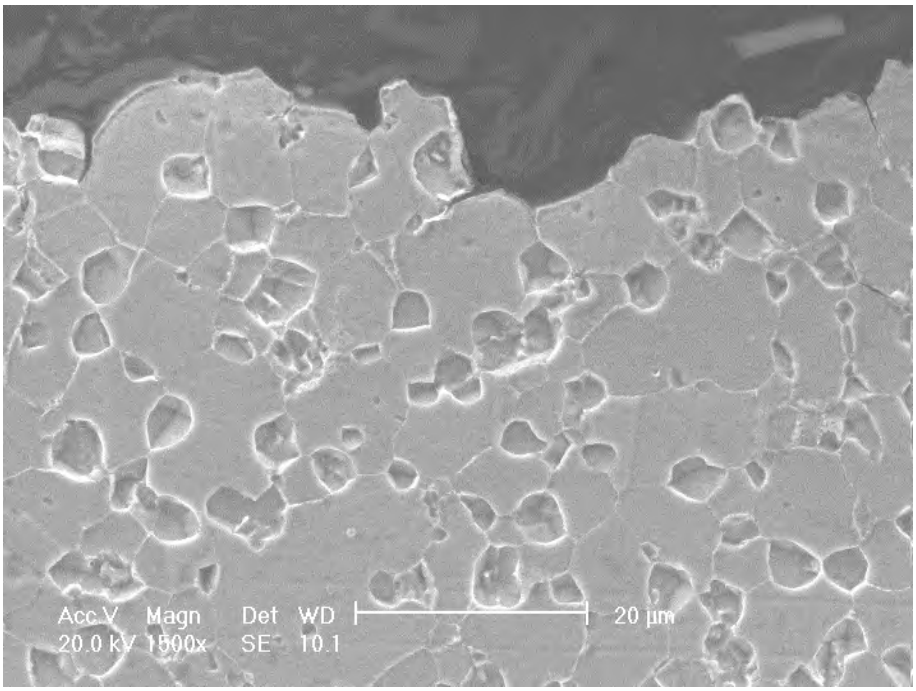


Figure 4-22: Cross section view of fine-grained Udimet 720Li test piece CC044 showing the crack profile (propagating left to right) pertaining to 120 second dwell cycling at 650°C in air at a ΔK of ~16 MPa√m. Note the intergranular mode of crack growth.

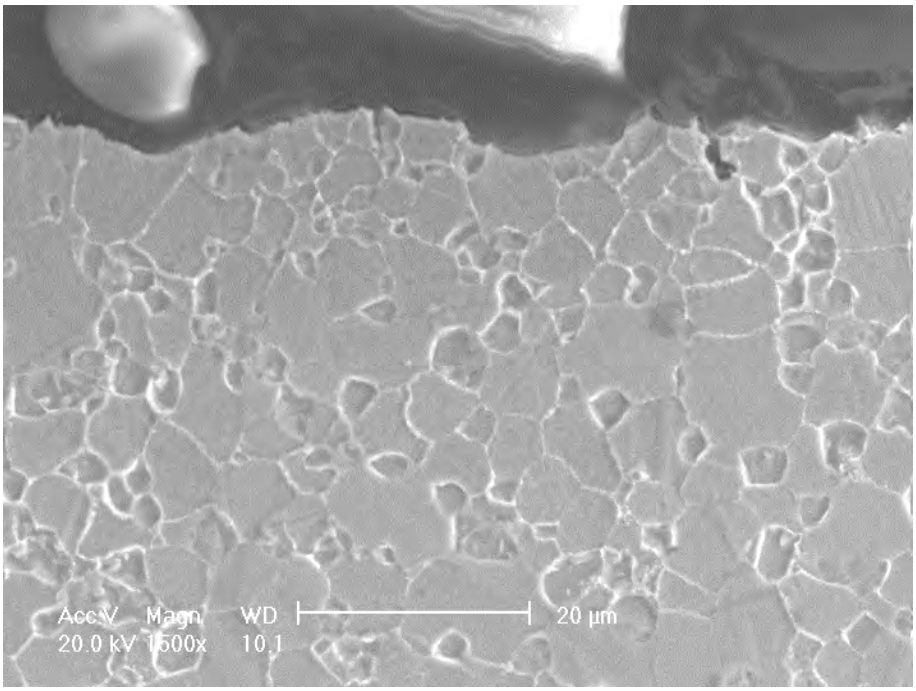


Figure 4-23: Cross section view of fine-grained Udimet 720Li test piece CC044 showing the crack profile (propagating left to right) pertaining to 1-1-1-1 baseline cycling at 650°C in air at a ΔK of ~40 MPa√m. Note the transgranular mode of crack growth.

4.2.1.5 Summary

A comprehensive selection of fractographs for all tests carried out is presented in Appendix VII. Their conclusions are summarised in Table 22, Table 23, Table 24, Table 25 and Table 26. Where possible, tabulated data is presented in the order in which their respective crack growth resistance curves are presented in Appendix VI.

Table 22: Summary of fractographic analysis for the fine-grained Udimet 720Li baseline and dwell testing programme.

Test Piece ID	Temperature (°C)	Dwell Time (s)	Predominant Mechanism Baseline	Predominant Mechanism Dwell	Remarks
CX015	550	3,600	Transgranular	Intergranular	
CC020	550	3,600	Transgranular	Intergranular	
CX013	600	3,600	Transgranular	Intergranular	
CX014	600	3,600	Transgranular	Intergranular	
CC009	650	3,600	Transgranular	Intergranular	
CC019	650	3,600	Transgranular	Intergranular	Delineation of primary γ’
CO023	650	3,600	Transgranular	Intergranular	
CX027	650	3,600	Transgranular	Intergranular	Delineation of primary γ’
CX030	650	3,600	Transgranular	Intergranular	
CX025	650	3,600	Transgranular	Mixed	Dwell at minimum load
CX031	650	120	Transgranular	Transgranular	Vacuum Test
CX034	650	3,600	Transgranular	Intergranular	Vacuum Test

Table 23: Summary of fractographic analysis for the fine-grained Udimet 720Li baseline, dwell and overload testing programme.

Test Piece ID	Temp (°C)	Dwell Time (s)	Overload Factor	Predominant Mechanism Baseline	Predominant Mechanism Dwell	Predominant Mechanism Overload	Remarks
CC013	600	1,200	1.05	Mixed	Intergranular	Intergranular	Ultra fine grain size
CC014	600	3,600	1.05	Mixed	Intergranular	Intergranular	Ultra fine grain size
CC015	650	3,600	1.15	Mixed	Intergranular	Intergranular	Ultra fine grain size
CC003	650	3,600	1.15	Transgranular	Intergranular	Intergranular	Partial Retardation
CC004	650	1,200	1.15	Mixed	Intergranular	Intergranular	Partial Retardation
CC007	650	1,200	1.15	Mixed	Intergranular	Intergranular	Partial Retardation
CC008	675	1,200	1.10	Mixed	Intergranular	Intergranular	Partial Retardation
CC010	650	1,200	1.08	Transgranular	Intergranular	Intergranular	Partial Retardation
CC001	600	1,200	1.15	Transgranular	Intergranular	Transgranular	Full Retardation
CC002	600	3,600	1.15	Transgranular	Intergranular	Transgranular	Full Retardation
CC005	600	1,200	1.05	Transgranular	Intergranular	Trans / Inter	Partial / Full
CC006	600	3,600	1.05	Transgranular	Intergranular	Intergranular	Partial Retardation
CC009	625	1,200	1.08	Transgranular	Intergranular	Intergranular	Partial Retardation
CC029	650	1,200	1.15	Transgranular	Intergranular	Intergranular	120s Dwell at OL
CC032	650	1,200	1.15	Transgranular	Intergranular	Intergranular	600s Dwell at OL

Table 24: Summary of fractographic analysis for the fine-grained Udimet 720Li time-dependent threshold testing programme.

Test Piece ID	Temp (°C)	Dwell Time (s)	Predominant Mechanism Baseline	Predominant Mechanism Threshold	Predominant Mechanism Dwell	Remarks
CC040	650	120	Transgranular	Intergranular	Intergranular	
CC041	650	120	Transgranular	Transgranular	Intergranular	
CC044	650	120	Transgranular	Intergranular	Intergranular	
CC045	650	1,200	Transgranular	Intergranular	Intergranular	

Table 25: Summary of fractographic analysis for the fine-grained RR1000 baseline and dwell testing programme.

Test Piece ID	Temperature (°C)	Dwell Time (s)	Predominant Mechanism Baseline	Predominant Mechanism Dwell	Remarks
CC003	600	3,600	Transgranular	Intergranular	
CC005	600	3,600	Transgranular	Intergranular	
CC001	650	3,600	Transgranular	Intergranular	
CC002	650	3,600	Transgranular	Intergranular	
CX001	650	3,600	Transgranular	Intergranular	Slow cooled
CX005	650	3,600	Transgranular	Intergranular	Fast cooled

Table 26: Summary of fractographic analysis for the fine-grained RR1000 baseline, dwell and overload testing programme.

Testpiece ID	Temp (°C)	Dwell Time (s)	Overload Factor	Predominant Mechanism Baseline	Predominant Mechanism Dwell	Predominant Mechanism Overload	Remarks
CC019	600	1,200	1.15	Transgranular	Intergranular	Transgranular	Full Retardation
CC021	600	1,200	1.05	Transgranular	Intergranular	Intergranular	Partial Retardation
CC042	600	3,600	1.05	Transgranular	Intergranular	Intergranular	Partial Retardation
CC047	625	1,200	1.08	Transgranular	Intergranular	Intergranular	Nearly full retardation
CC018	625	1,200	1.08	Transgranular	Intergranular	Intergranular	Nearly full retardation
CC045	650	1,200	1.08	Transgranular	Intergranular	Intergranular	Partial Retardation
CC046	650	1,200	1.15	Transgranular	Intergranular	Mixed	Full Retardation
CC048	650	3,600	1.15	Transgranular	Intergranular	Mixed	Full Retardation
CC017	650	1,200	1.08	Transgranular	Intergranular	Intergranular	Partial Retardation
CC020	650	3,600	1.15	Transgranular	Intergranular	Intergranular	Nearly full retardation
CC034	675	1,200	1.10	Transgranular	Intergranular	Intergranular	Partial Retardation
CC035	650	3,600	1.15	Transgranular	Intergranular	Intergranular	120s Dwell at OL
CC056	650	1,200	1.065	Transgranular	Intergranular	Intergranular	Unload
CC057	650	1,200	1.065	Transgranular	Intergranular	Intergranular	Reload

4.2.2 Metallography

As discussed above, detailed microstructural analysis is performed on three of the previously mechanically tested samples of (nominally) fine-grained Udimet 720Li; CC015, CC009 and CX027. The image analysis methods described above are carried out on 10 separate SEM images of CC015, 10 images of CC009 and 20 of CX027, yielding measurements for γ-grains and primary γ'-precipitates as shown below.

Furthermore, microstructural analysis of Udimet 720Li test pieces CC041 and CC045 (from the ΔK threshold investigation) are also carried out in order to analyse and understand the discrepancies in terms of high temperature dwell crack growth rates and time-dependent threshold values observed. Their results are also plotted below in separate sections.

Micrographs are also taken and presented of fine-grained RR1000 test pieces CC017, CC018, CC045 and CC047, whose mechanical properties seemed to vary despite similar testing conditions. A detailed characterisation has not been undertaken on these particular test pieces. Nevertheless the micrographs are included for reference since they show no obvious discrepancies (as in Udimet 720Li test pieces) and microstructural analysis might form part of the future work for this project. Finally, micrographs are also presented of fine-grained RR1000 test pieces CX001 and CX005 to show the effect which varying rates of cooling from the maximum heat treatment temperature can have on the microstructural characteristics of the material.

4.2.2.1 Udimet 720Li Baseline, Dwell and Overload Test Pieces

To recap: for the dwell-only investigations; sample CC015 is taken from Phase Two, Batch Two sourced material and hence is thought to comprise smaller grains due to naturally faster cooling rates from maximum heat treatment temperatures, due in turn to a smaller rim radius when compared with those pertaining to the other two samples. Furthermore, as reported in the above crack growth resistance curves; CC015 is indeed shown to possess inferior dwell crack growth resistance when compared with otherwise similarly tested material from other "Batches". To further recap; CC009 has slightly better resistance to dwell crack growth when compared with sample CC015; and CX027 displays the most resistance, in that dwell crack growth rates are slowest.

Optical Microscopy

Optical microscopy showed CC015 to exhibit a relatively uniform grain size distribution with a few, thin, darker banded regions (see below). Upon closer inspection these darker regions are confirmed to comprise areas of very fine grains and dense accumulations of fine primary γ' precipitates. An exemplary dark region can be found in Figure 4-25 which highlights a dark 'teardrop' shaped region. Images (a) to (c) are taken at increasing magnification. In Image (c) it is clear that the grain size within the dark region is finer when compared with the surrounding grains. It is also important to note that the primary γ' precipitates too are smaller and are more closely packed together in the highlighted region. The directionality of the bands may be attributed to the highly oriented forged processing route used to produce the test pieces.

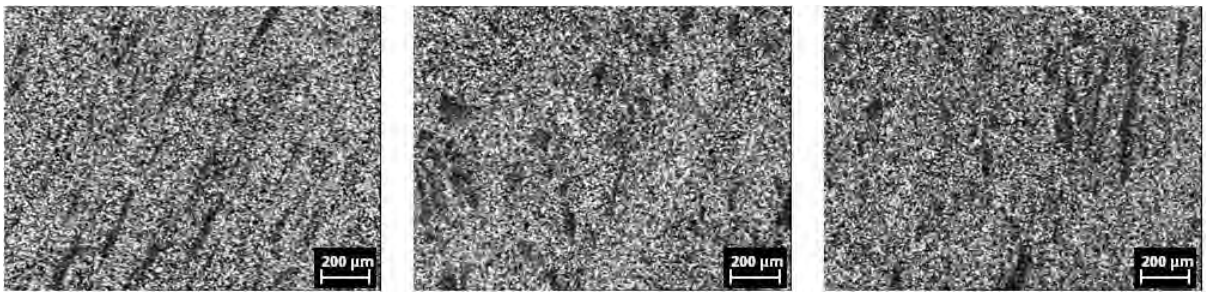
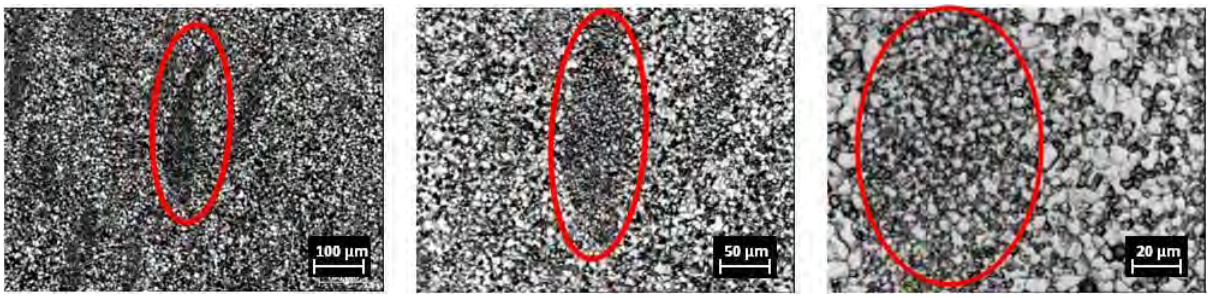


Figure 4-24: Optical micrographs taken of CC015 at 50x magnification.



a b c

Figure 4-25: Optical micrographs of 'teardrop' shaped dark region in CC015, ~350um long at a) 100x magnification, b) 200x magnification and c) 500x magnification.

Optical micrographs of CC009, shown in Figure 4-26, exhibit a higher area fraction of dense, fine grained regions than that observed in CC015.

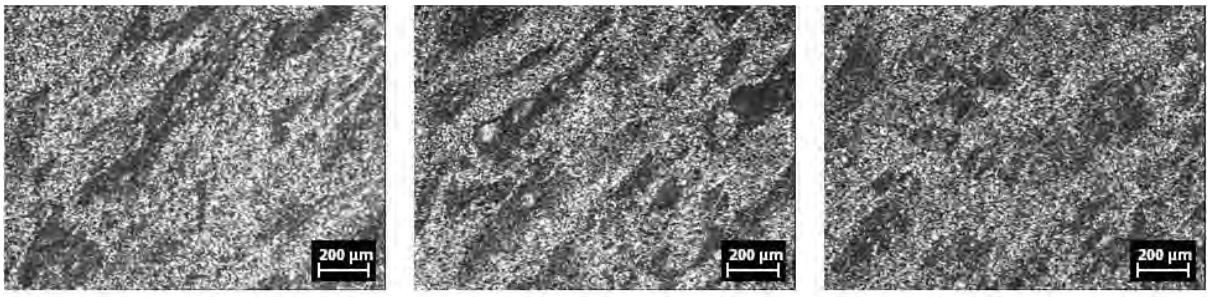


Figure 4-26: Optical micrographs of CC009 at 50x magnification.

Overview optical micrographs of CX027 taken at 50x magnification (Figure 4-27) show the sample comprises relatively uniform grain size with fewer banded regions of fine grains when compared with samples CC015 and CC009.

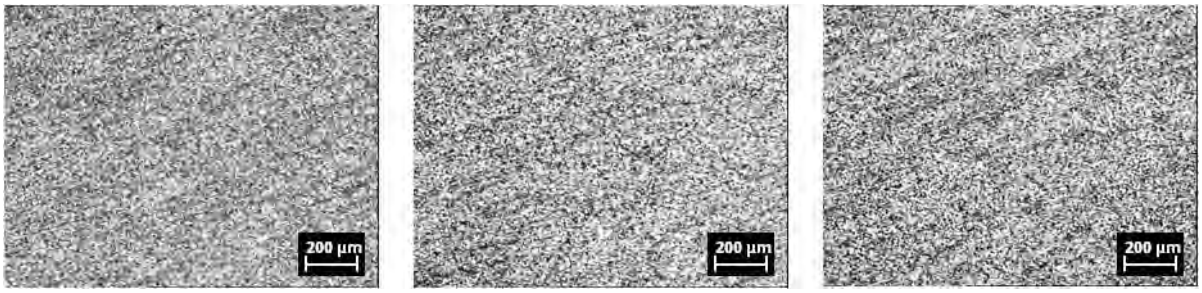


Figure 4-27: Optical micrographs of CX027 at 50x magnification.

Scanning Electron Microscopy

The bimodal grain size of CC009 observed under optical microscope is confirmed by analysis of SEM images. Figures below show a stark contrast in the difference in grain size from one image to the next within the same sample. Grains in Figure 4-28 appear to vary from 6µm - 25µm whereas Figure 4-29 comprises grains in the range of 4µm - 8µm. More noticeable is the predominance, and the relatively fine size of primary γ' in Figure 4-29. It is suggested in the literature [20] that smaller, more closely packed primary γ' precipitates lead to the formation of finer grains due to the grain boundary pinning effect of these fine and densely packed precipitates. Adjacent regions of fine and relatively coarse grains can be seen in Figure 4-30.

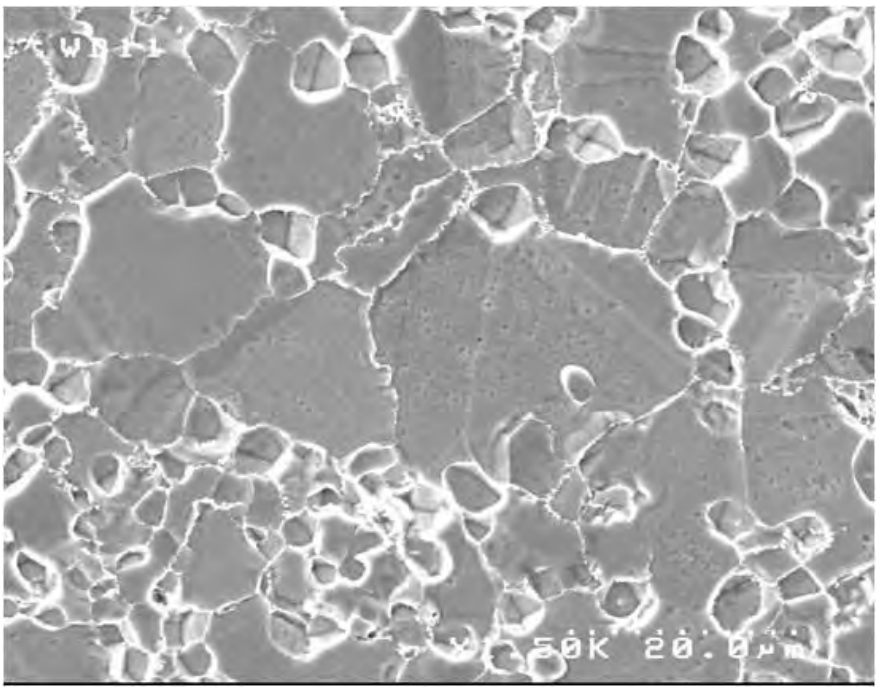


Figure 4-28: CC009, 1500x mag, 20KeV. Image shows the presence of relatively coarse grains with large primary γ' decorating the grain boundaries.

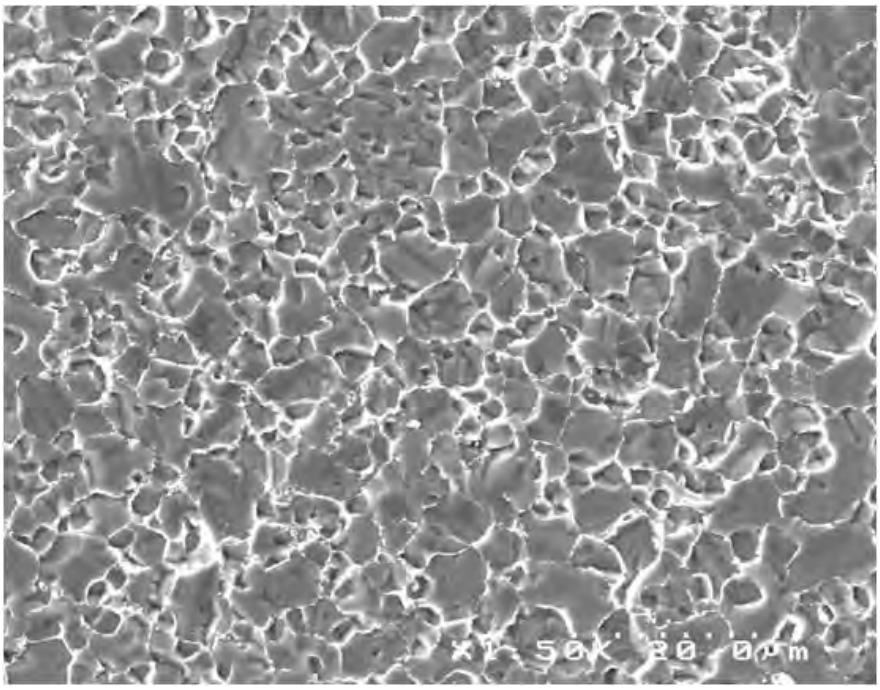


Figure 4-29: CC009, 1500x mag, 20KeV. Image shows a particularly fine grained region with small, finely dispersed primary γ' throughout.

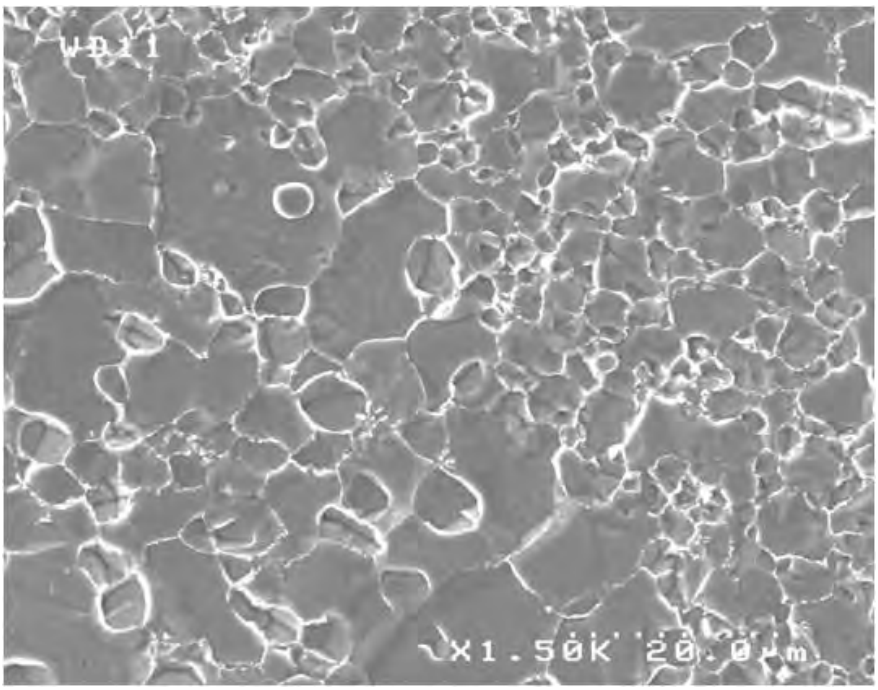


Figure 4-30: CC009, 1500x mag, 20KeV. Image shows adjacent regions of fine and relatively coarse grains at the top right and bottom left of the image respectively.

Optical micrographs above reveal that test piece CC015 has limited regions of "superfine" grains such as those observed in CC009; and this was confirmed by the SEM image analysis which showed the microstructure of CC015 to be reasonably uniform. Images Figure 4-31 and Figure 4-32 are typical of the CC015 SEM observations, showing consistently smaller grains of a limited size range. Figure 4-33 shows one of the relatively rare regions of fine grains found, towards the bottom right of the image.

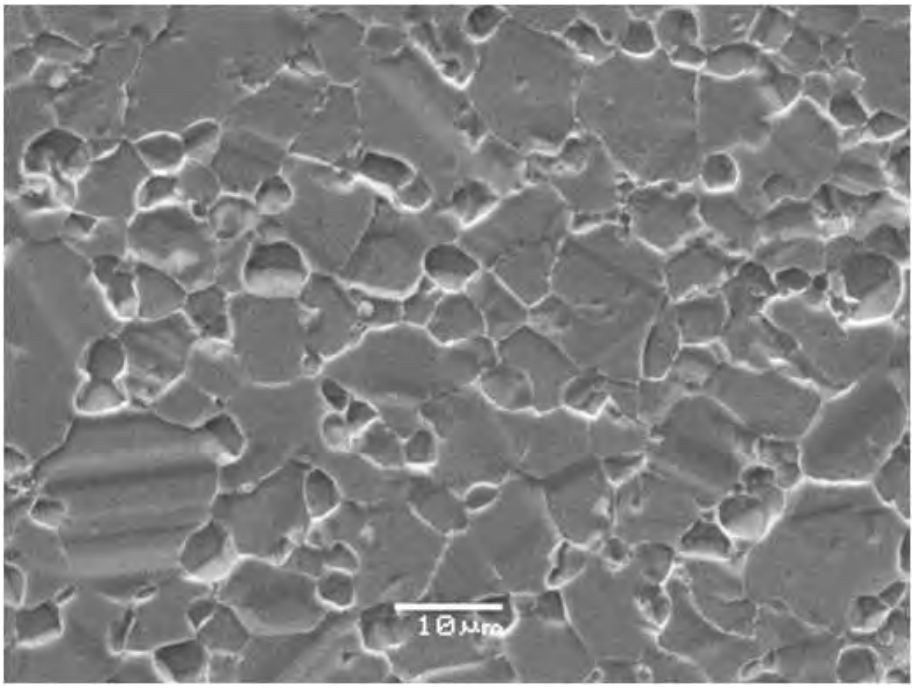


Figure 4-31: Micrograph of fine-grained Udimet 720Li sample CC015 at 1500x magnification, 20Kev. The image shows relatively uniform grain size throughout, as also displayed in Figure 4-32 (below).

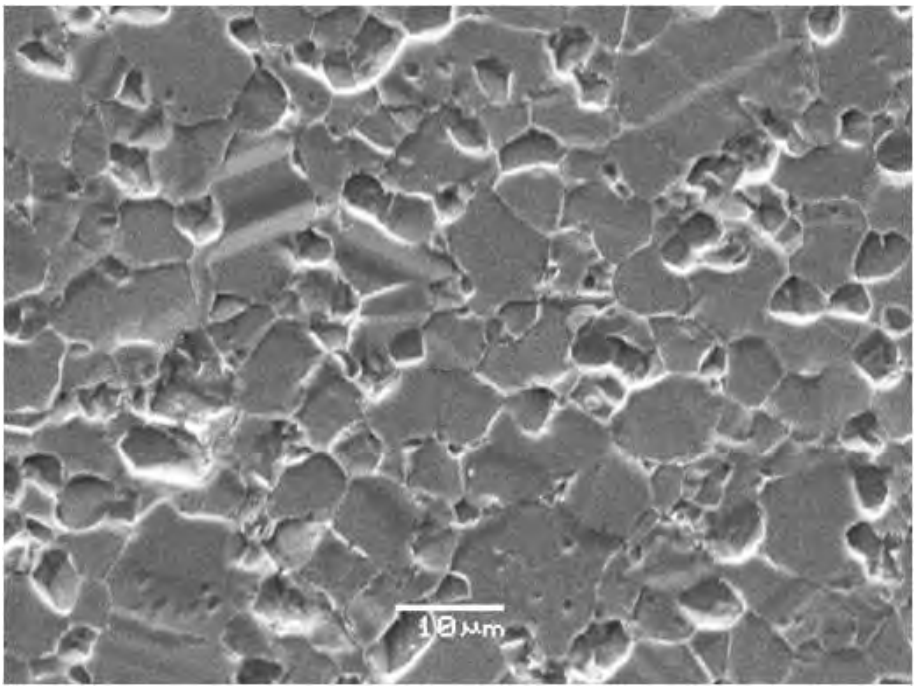


Figure 4-32: Similar micrograph to that shown above, giving an indication of the uniform nature of microstructural characteristics.

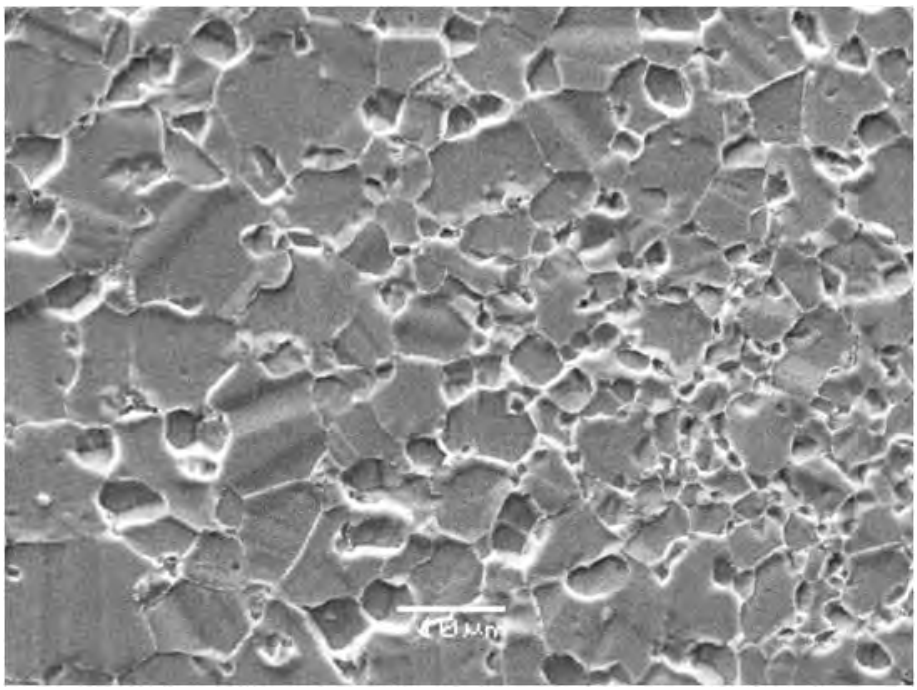


Figure 4-33: Micrograph of the same sample (CC015) under similar magnification (1500x). The image shows a region of fine grained material.

Under SEM, sample CX027 displayed a relatively uniform grain size which differed very little from image to image. These similarities can be seen in the example images presented in Figure 4-34 to Figure 4-36.

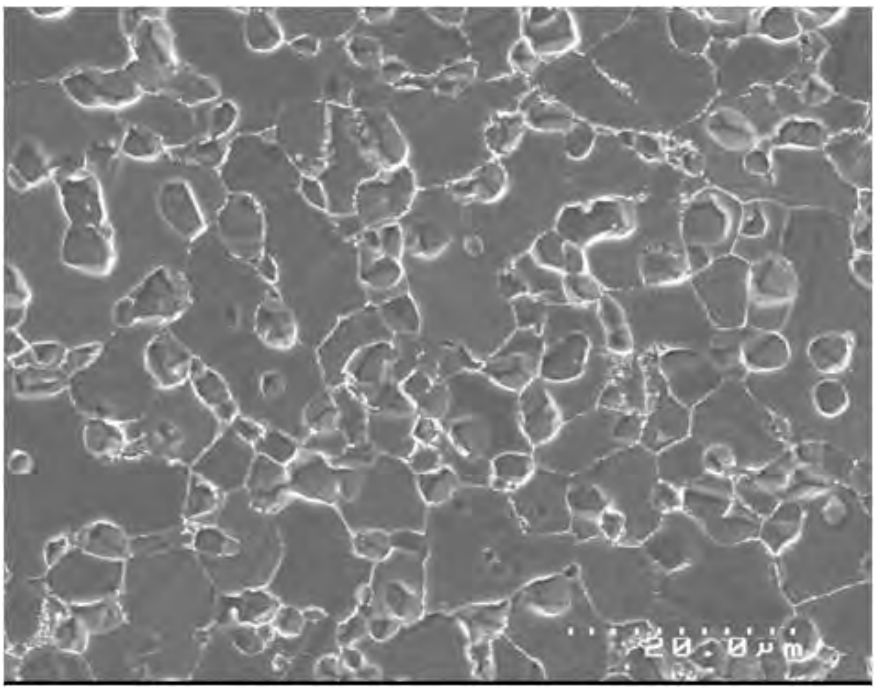


Figure 4-34: Micrograph of fine-grained Udimet 720Li sample CX027 at 1500x magnification, 20Kev.

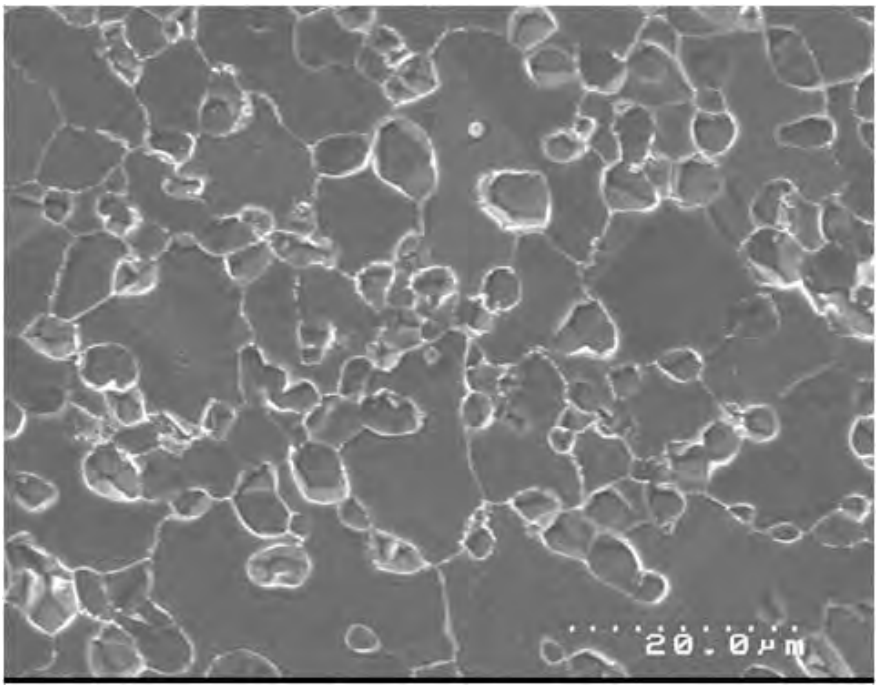


Figure 4-35: Similar micrograph of CX027 taken at a different location, showing relatively uniform microstructural characteristics.

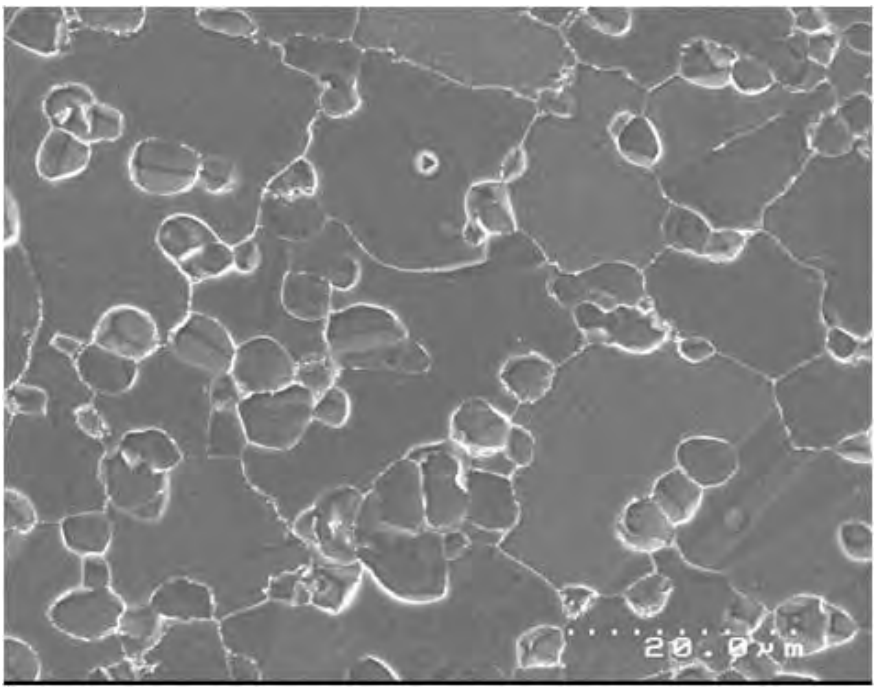


Figure 4-36: A third micrograph of CX027 taken at a different location, showing relatively uniform microstructural characteristics.

Grain Size Distributions

A summary of the average, variance and standard deviation of grain sizes found in each of the samples is presented in Table 27. CC015 comprised the smallest grains, averaging 4.2 µm. CX027 had the largest average grain size, averaging 7.4 µm. The distributions of grains found in CC015, CC009 and CX027 are shown in Figure 4-37, Figure 4-38 and Figure 4-39 respectively.

Table 27: Summarising the average grain sizes pertaining to fine-grained Udimet 720Li samples CC015, CC009 and CX027.

	CC015	CC009	CX027
Mean (μm)	4.2	5.2	7.4
Variance	4.3	9.8	15.1
Standard Dev	2.1	3.1	3.9

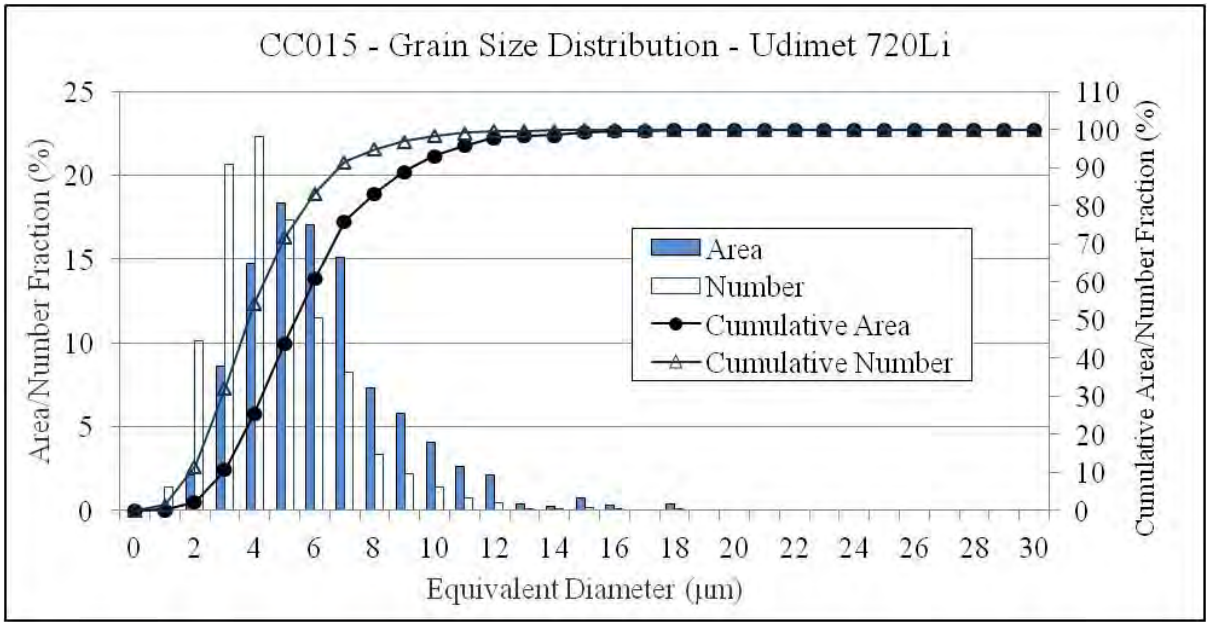


Figure 4-37: Showing the grain size distribution for fine-grained Udimet 720Li sample CC015.

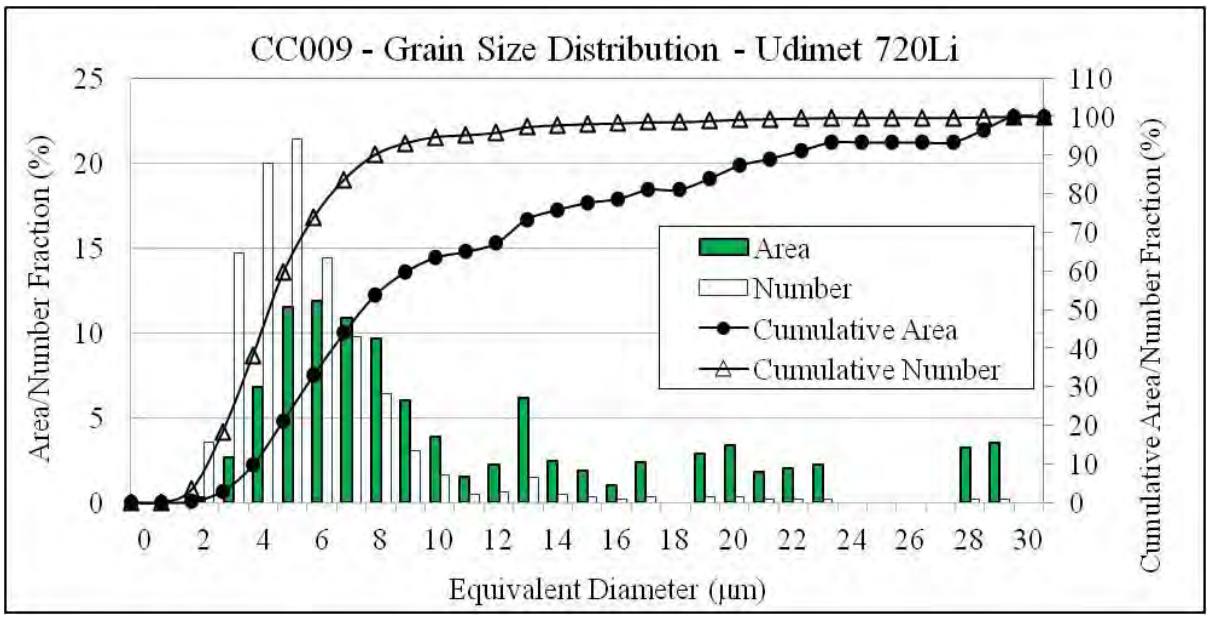


Figure 4-38: Showing the grain size distribution for fine-grained Udimet 720Li sample CC009.

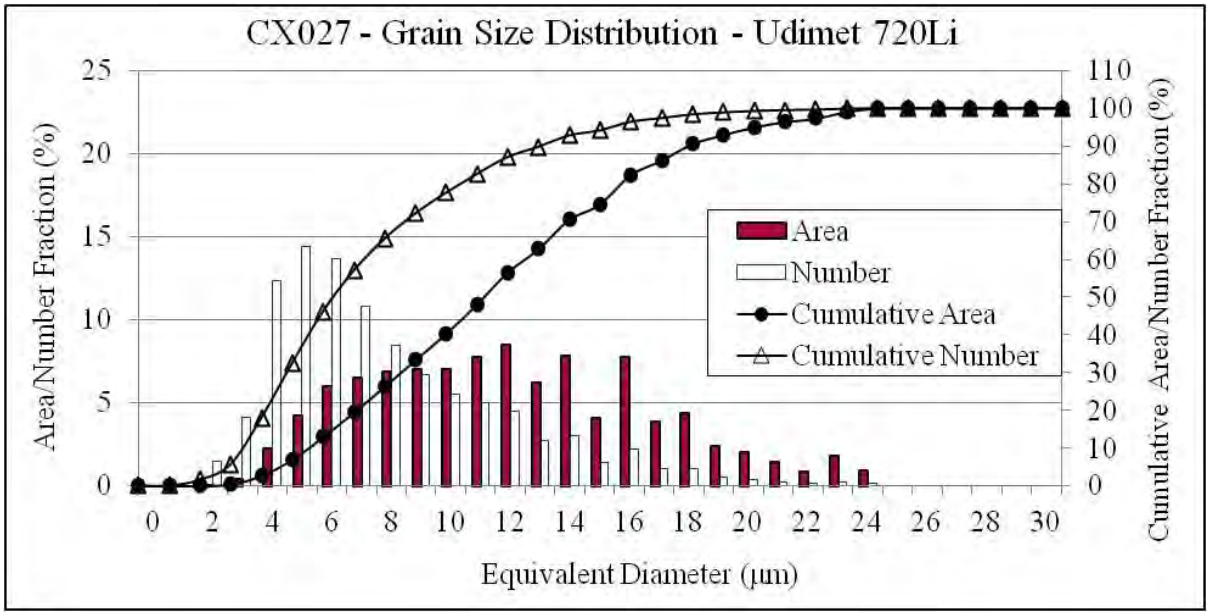


Figure 4-39: Showing the grain size distribution for fine-grained Udimet 720Li sample CX027.

Sample CC015 demonstrated the poorest resistance to fatigue crack growth during high temperature dwell cycling and was therefore thought to comprise the finest grain structure. It

follows that from the current analysis, high temperature dwell fatigue crack growth resistance of (nominally) fine-grained Udimet 720Li can be related to the mean grain size.

It can be seen that the area and number fraction distributions of grains in sample CC015 are relatively narrow and close to a normal distribution, ranging from 1 μm – 8 μm.

In contrast to the distribution of grains in CC015, sample CC009 exhibits a multimodal grain size distribution and extends to a wider range as shown in Figure 4-38.The largest grain found in sample CC015 was ~18 μm, and in CC009; ~29 μm. Grains between 18 μm and 29 μm account for 20% of the total area in CC009. The distribution of CC009 confirms previous observations on optical and SEM micrographs; that many fine grains can be found within large grained regions. The distribution of finer grains in CC009 is comparable with sample CC015. The modal grain size of CC009 is ~6 μm which is only slightly larger than that of CC015; ~5 μm.

The range of grain sizes in sample CX027 is larger than that of CC015 and smaller than CC009 and can be seen in Figure 4-39. However the difference between the area taken up by very fine grains and the area taken up by very large grains is smaller, i.e. the area occupied by 13 μm grains is comparable to the area occupied by 6 μm grains. Under optical microscopy and SEM, these appear as fairly uniform grains without clear bands of finer grains.

Primary γ' Size Distributions

Through detailed quantitative analyses on multiple traced SEM images using ImageJ software according to methodologies described, primary γ' size distributions are obtained for each of the three samples. An overview of the average sizes, variance and standard deviation can be found in Table 28.

CX027 comprised the largest primary γ' precipitates, in terms of size, with an average value of 3.1 μm and the greatest variance of 2.1. The standard deviations of each data set were comparable and this is shown by the distribution plots for each sample which are closely similar.

Table 28: Summary of the average (mean), variance and standard deviation of primary γ' values obtained.

	CC015	CC009	CX027
Mean (μm)	2.7	2.6	3.1
Variance	1.5	1.2	1.6
Standard Dev	1.2	1.1	1.3

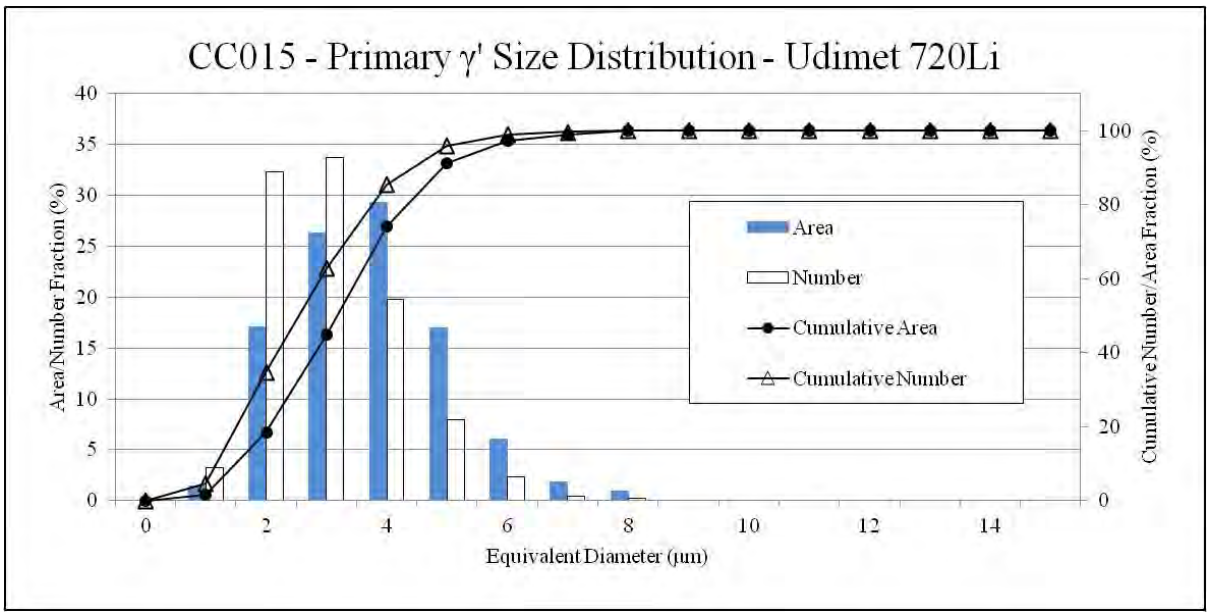


Figure 4-40: Showing the primary γ' size distribution for fine-grained Udimet 720Li sample CC015.

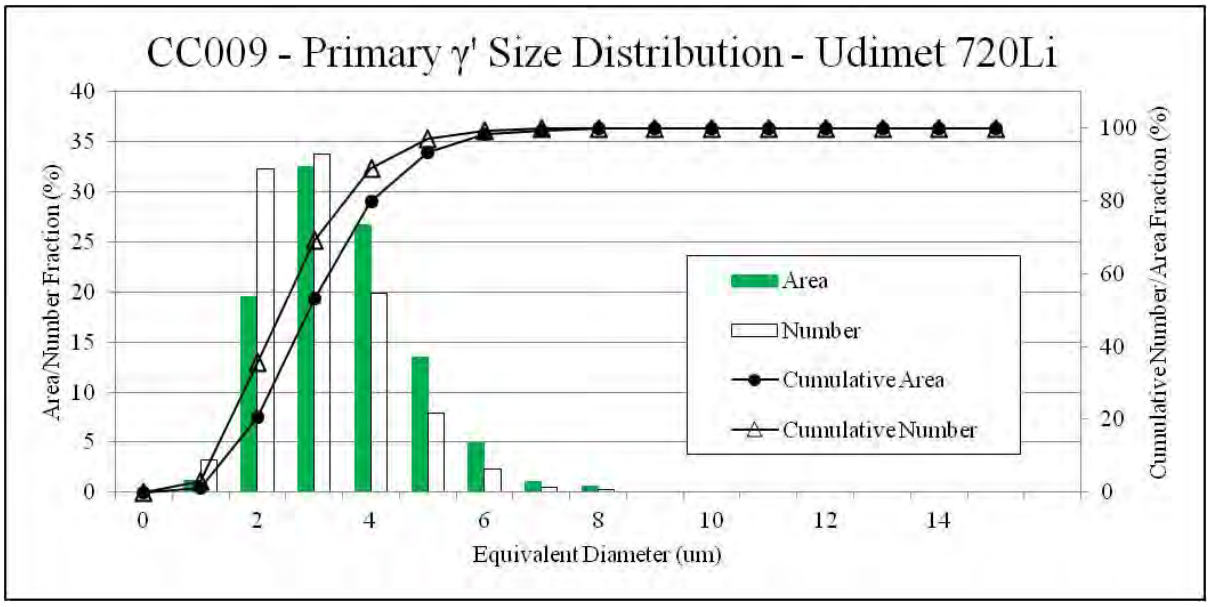


Figure 4-41: Showing the primary γ' size distribution for fine-grained Udimet 720Li sample CC009.

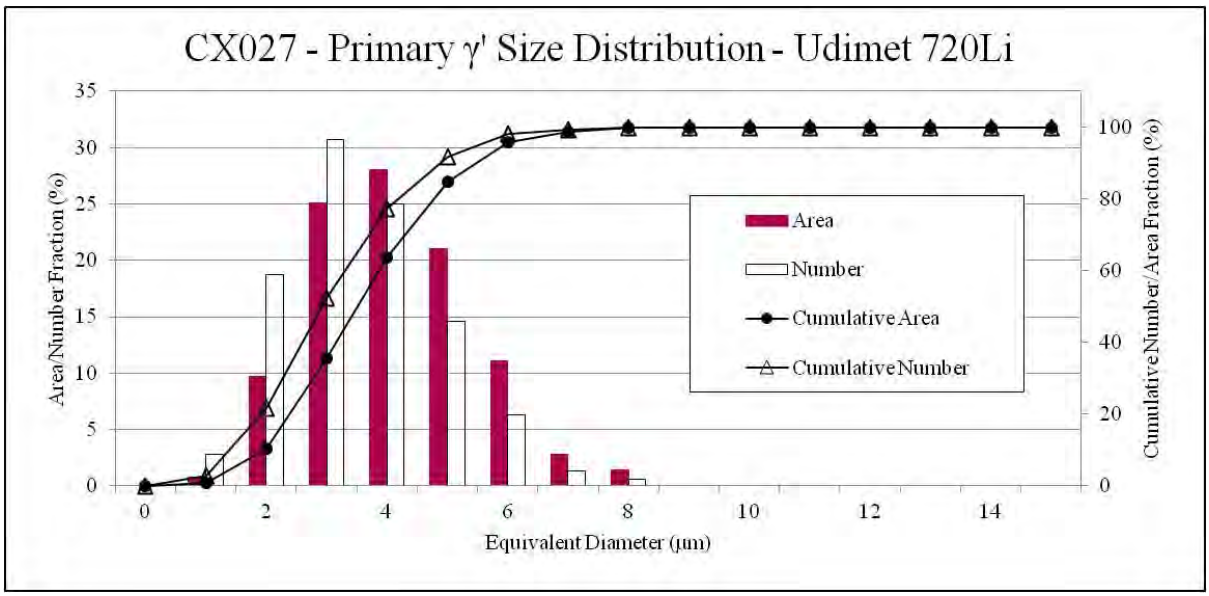


Figure 4-42: Showing the primary γ' size distribution for fine-grained Udimet 720Li sample CX027.

Area Fraction

Figure 4-43 shows that sample CC009, which exhibited the second highest high temperature dwell crack growth rate, has the largest area fraction of primary γ'. Sample CX027, the sample shown to possess the greatest high temperature dwell crack growth resistance has the second largest area fraction of primary γ'. Unpredictably, the sample exhibiting the fastest high temperature dwell crack growth rate, namely; CC015, was shown to comprise the smallest area fraction of primary γ'.

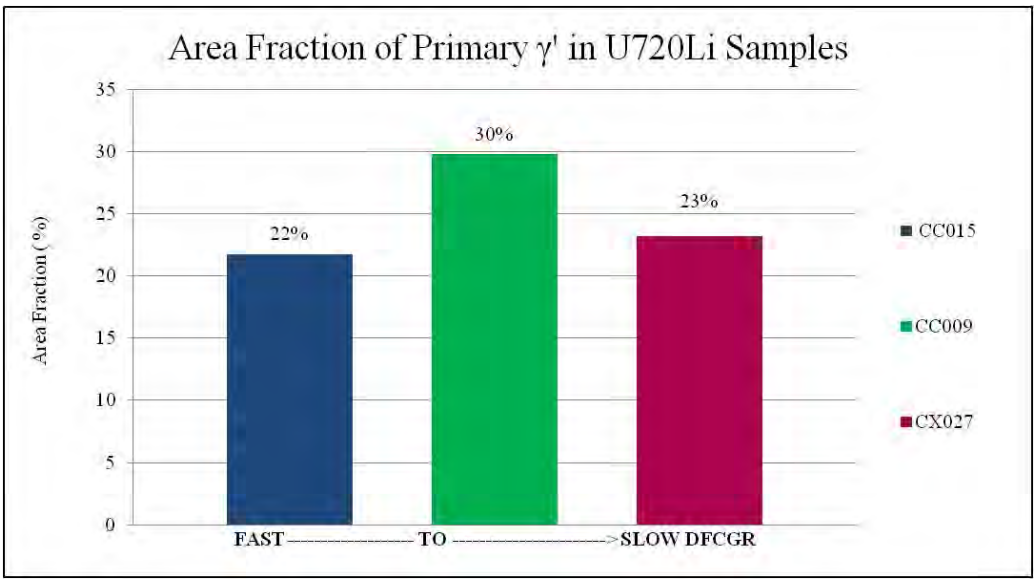


Figure 4-43: Showing the area fraction of primary γ' found in each sample.

4.2.2.2 Udimet 720Li Time-Dependent Threshold Test Pieces

A characterisation of the microstructure of three test pieces from the time-dependent threshold testing programme has also been undertaken, according to similar methodologies described above. To recap; test pieces CC040, CC041, CC044 and CC019 all displayed dwell crack growth rates (in terms of threshold and linear Paris Law behaviour) which were comparable with data gathered in other areas of this programme of research. Nevertheless test piece CC045 displayed unusual results in that dwell crack growth rates were found to be significantly higher than would otherwise have been expected. Furthermore; the value for the time-dependent threshold was observed to fall well below that which might have been predicted given the data from the programme. Therefore, a comparison between the underlying microstructure (in terms of γ grain size) of test piece CC045 and CC041 is made;

assuming that CC041 represents a “nominal” (or more normal) microstructure and predicting that CC045 might comprise significantly different microstructural characteristics.

Figure 4-44 and Figure 4-45 are a series of representative micrographs showing low and higher magnification of each test piece as etched by Kalling’s reagent.

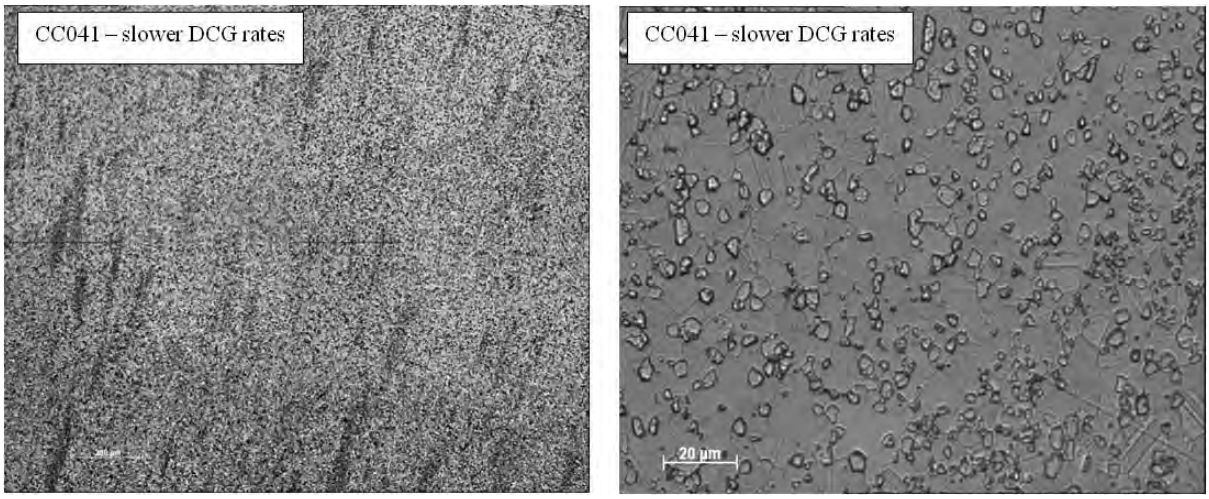


Figure 4-44: Optical micrograph of fine-grained Udimet 720Li test piece CC041 as etched by Kalling’s reagent a 100X magnification (left) and 1000X magnification (right).

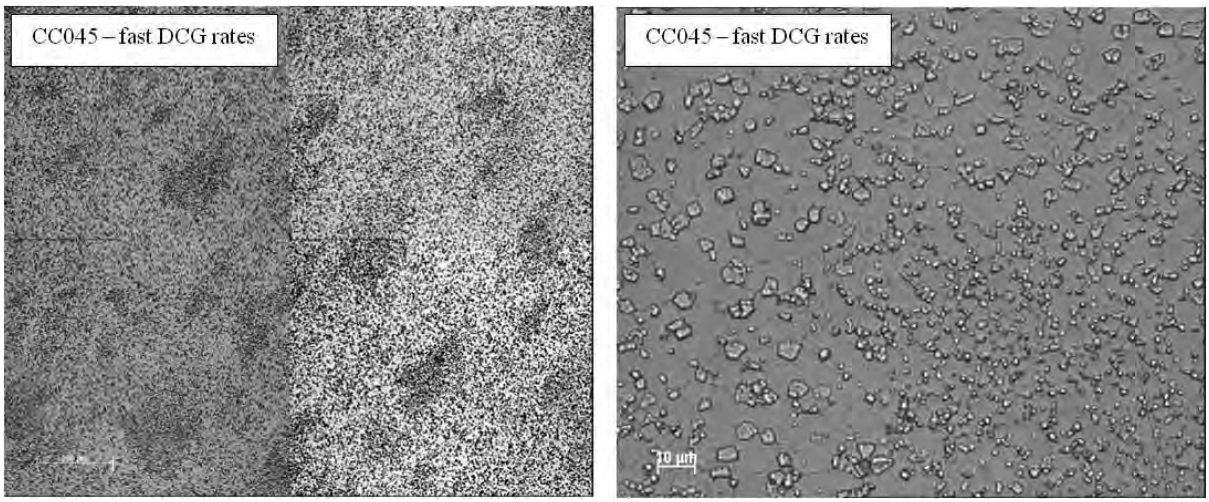


Figure 4-45: Optical micrograph of fine-grained Udimet 720Li test piece CC045 as etched by Kalling's reagent a 100X magnification (left) and 1000X magnification (right).

Higher magnification SEM images are also taken and have been analysed according to methodologies described above. They yield grain size distributions presented in Figure 4-46 and Figure 4-47.

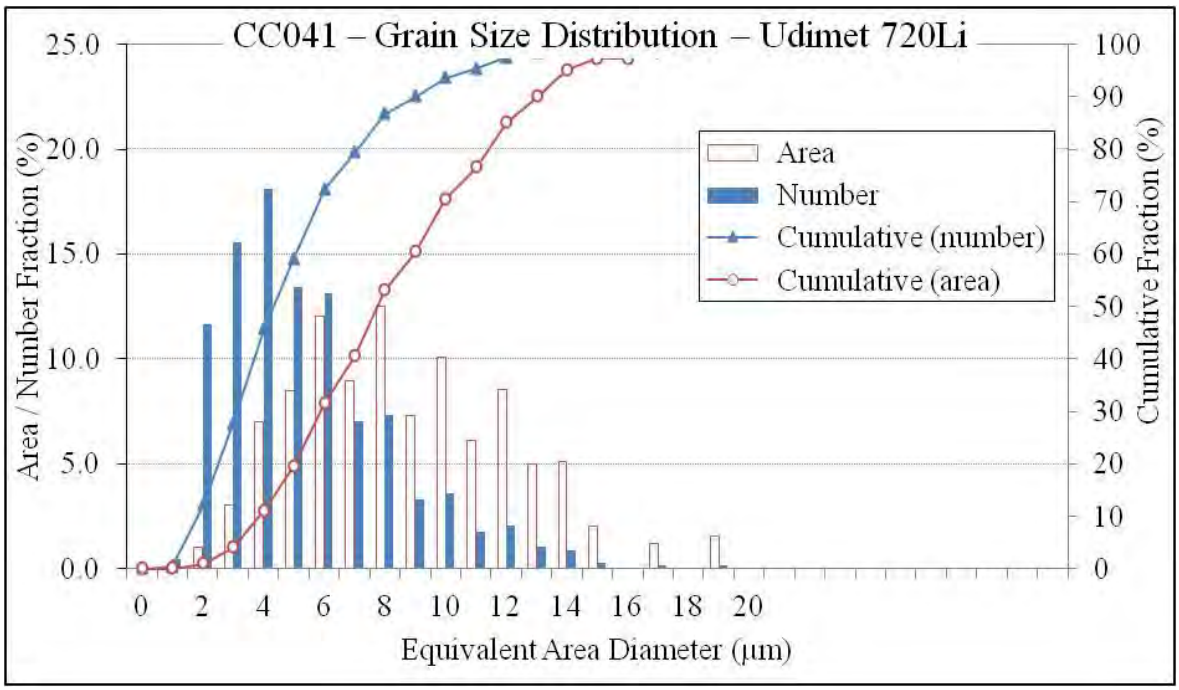


Figure 4-46: Showing the grain size distribution for fine-grained Udimet 720Li sample CC041.

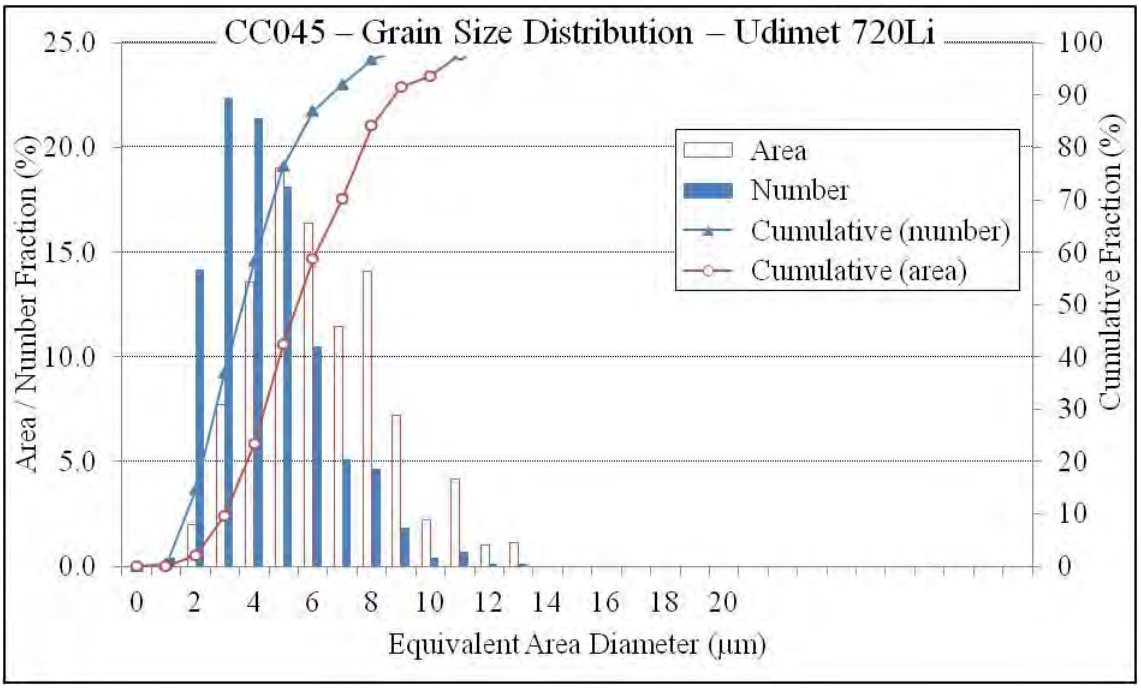


Figure 4-47: Showing the grain size distribution for fine-grained Udimet 720Li sample CC045.

The average (mean) grain size of test piece CC041 was 5.0 μm and the average grain size of test piece CC045 was 3.9 μm. Furthermore the cumulative area fraction of the grains smaller than 5 μm is 20% and 42% in test pieces CC041 and CC045 respectively. Thus the analysis indicated that test piece CC045 comprises of notably finer grains when compared with test piece CC041.

4.2.2.3 RR1000 Baseline, Dwell and Overload Test Pieces

Figure 4-48 to Figure 4-51 comprise a series of micrographs taken of RR1000 test pieces CC017, CC018, CC045 and CC047. Each of the four test pieces are tested with dwell periods of 1,200 seconds and overload factors of 1.08. CC017 and CC045 have both been tested at 650°C in laboratory air, test pieces CC018 and CC047 have both been tested at 625° (also in laboratory air). To recap: despite similar testing conditions, test piece CC017 displayed poorer crack growth resistance (according to baseline, dwell and overload cycling) when compared with CC045, and test piece CC018 displayed poorer crack growth resistance when compared with CC047. A detailed microstructural characterisation has not been undertaken; rather a presentation of four representative micrographs of each test piece, taken using Kalling's reagent (detailed in Table 15) is given in order to provide a general overview of the key microstructural features of each test piece and to draw some careful conclusions in terms of discrepancies between test pieces.

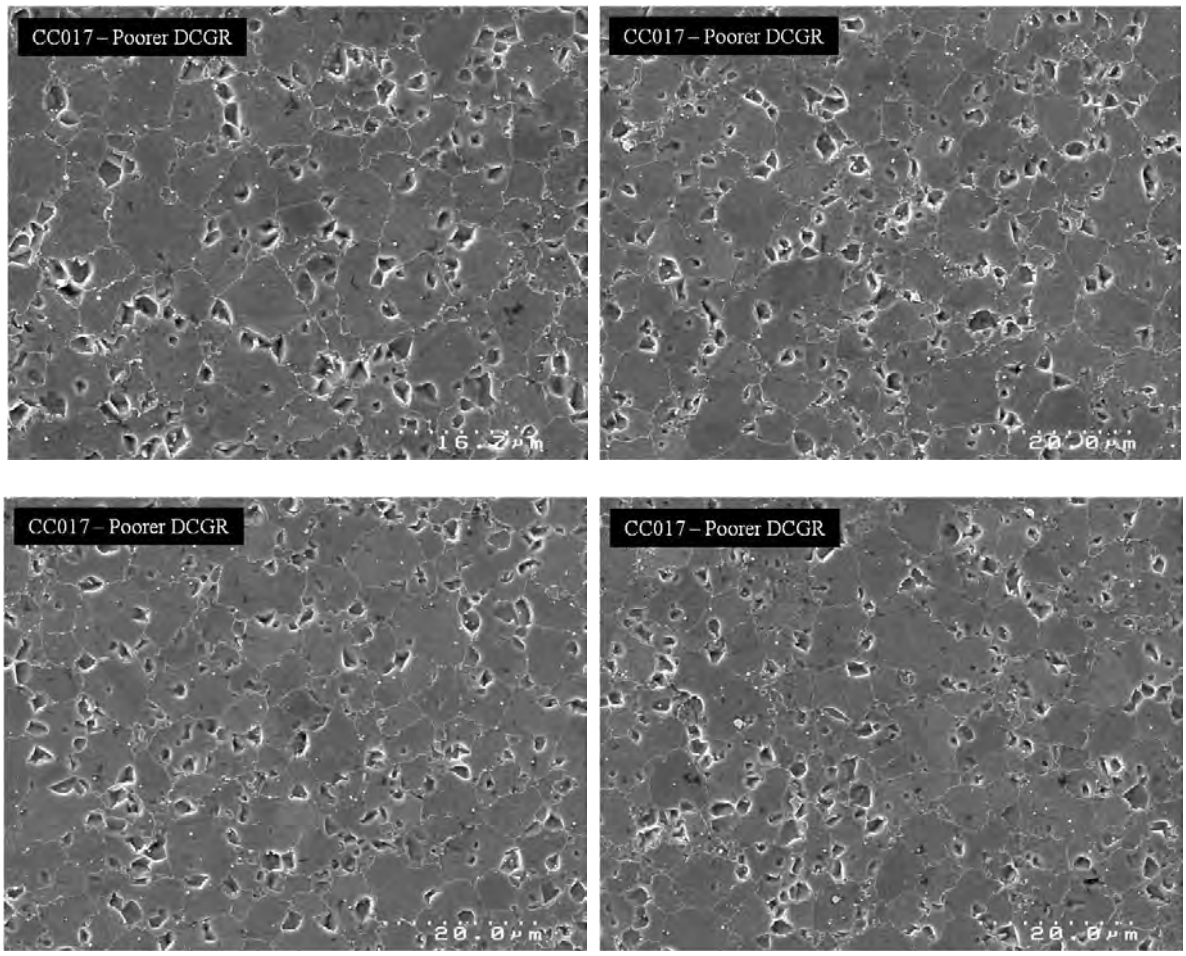


Figure 4-48: Showing four representative micrographs of sectioned test piece CC017, tested with a dwell period of 1,200 seconds, and overload factor of 1.08 and at a temperature of 650°C in laboratory air. Note that despite similar testing conditions, baseline dwell and overload crack growth rates were consistently faster in CC017 when compared with CC045 (below, Figure 4-49).

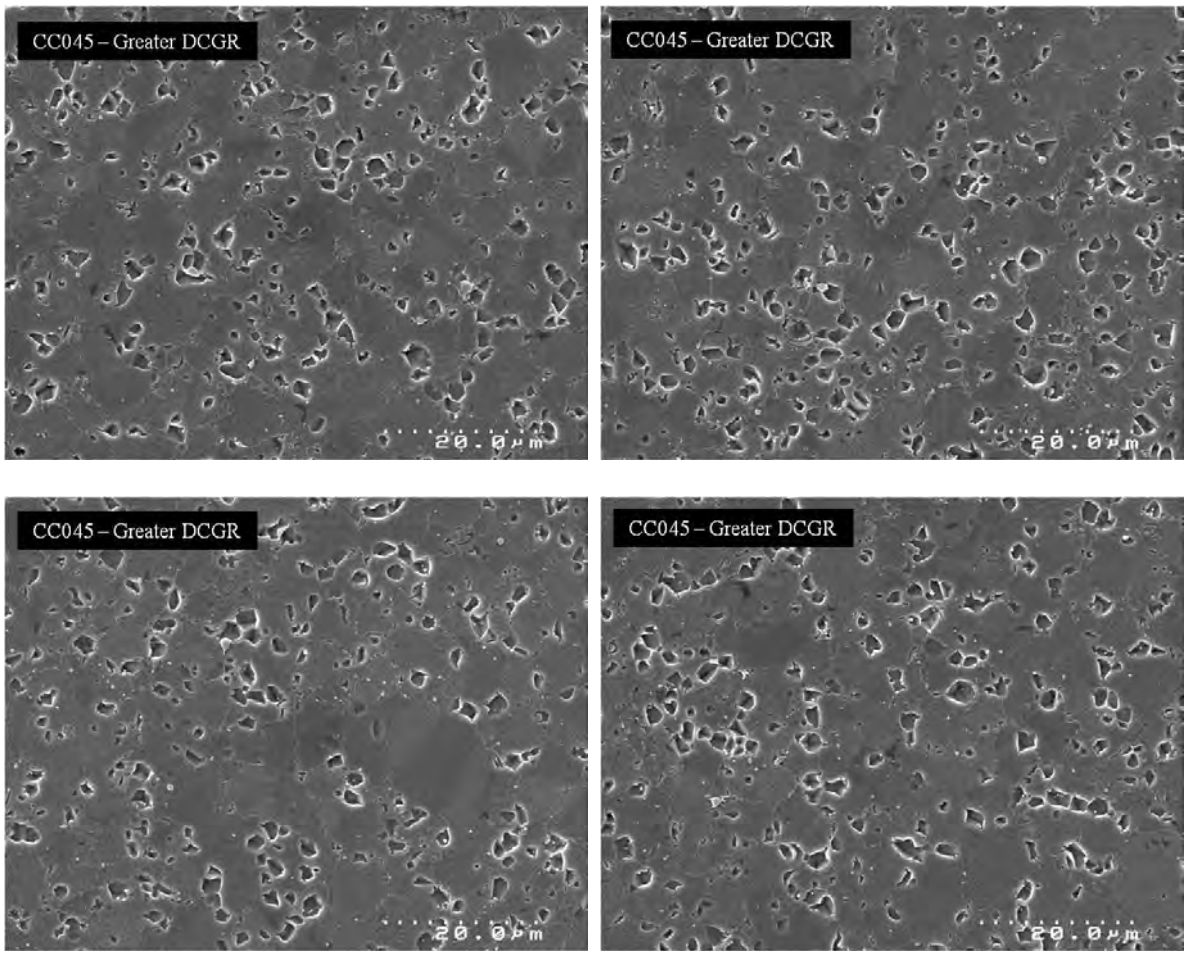


Figure 4-49: Showing four representative micrographs of sectioned test piece CC045, tested with a dwell period of 1,200 seconds, and overload factor of 1.08 and at a temperature of 650°C in laboratory air. Note that despite similar testing conditions, baseline dwell and overload crack growth rates were consistently slower in CC045 when compared with CC017 (above, Figure 4-48).

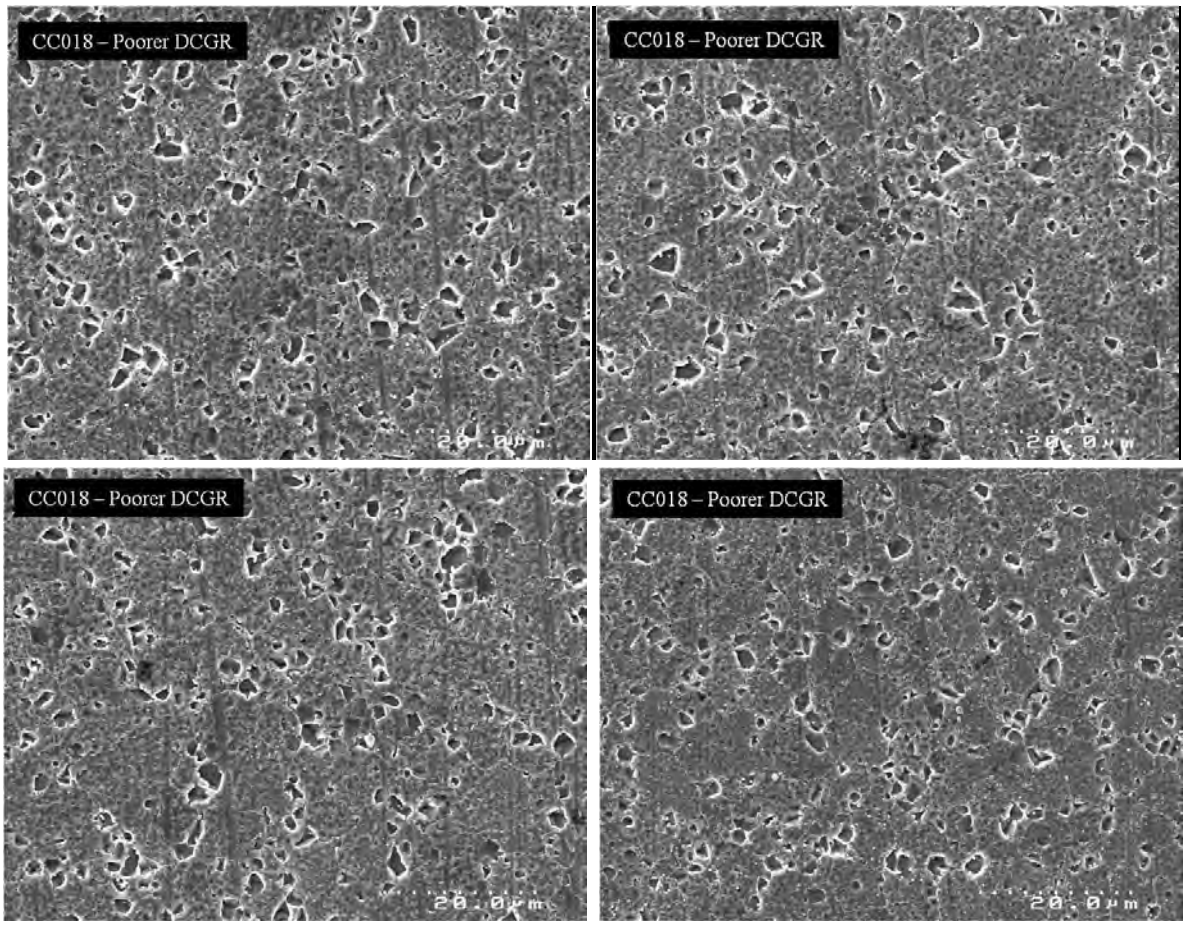


Figure 4-50: Showing four representative micrographs of sectioned test piece CC018, tested with a dwell period of 1,200 seconds, and overload factor of 1.08 and at a temperature of 625°C in laboratory air. Note that despite similar testing conditions, baseline dwell and overload crack growth rates were consistently faster in CC018 when compared with CC047 (below, Figure 4-51).

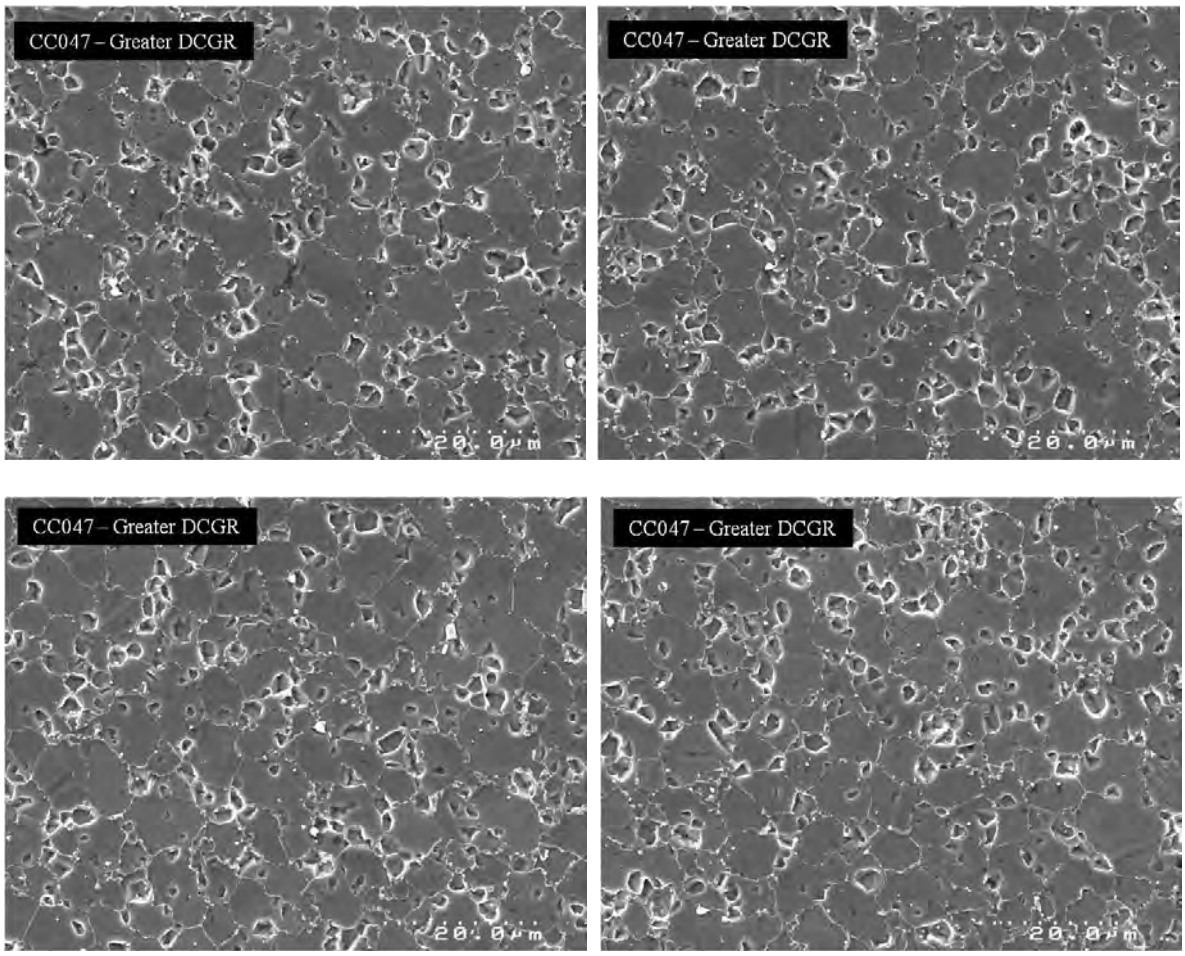


Figure 4-51: Showing four representative micrographs of sectioned test piece CC047, tested with a dwell period of 1,200 seconds, and overload factor of 1.08 and at a temperature of 625°C in laboratory air. Note that despite similar testing conditions, baseline dwell and overload crack growth rates were consistently slower in CC047 when compared with CC018 (above, Figure 4-50).

4.2.2.4 RR1000 Cooling Rate Test Pieces

Presented in Figure 4-52 through to Figure 4-63 are a series of micrographs taken of RR1000 test pieces CX001, CX005 and CC048. Test piece CX001 is slow cooled from maximum heat treatment temperatures (~0.1°C/s) and test piece CX005 is fast cooled (~5°C/s). Test piece CC048 is included for comparison since similar dwell cycles were applied during testing (a dwell time of 3,600 seconds at a temperature of 650°C in laboratory air). A detailed

microstructural characterisation has not been undertaken, rather a presentation of micrographs taken using three different etchants (detailed in Table 15) is given in order to compare the morphology of the γ' phase.

To recap; test piece CX001 (slow cooled) displayed relatively slow high temperature dwell crack growth rates, test piece CX005 (fast cooled) displayed relatively fast dwell crack growth rates and test piece CC048 (nominally intermediately cooled, in terms of cooling rate) displayed dwell crack growth rates which sat in between those associated with each other test piece.

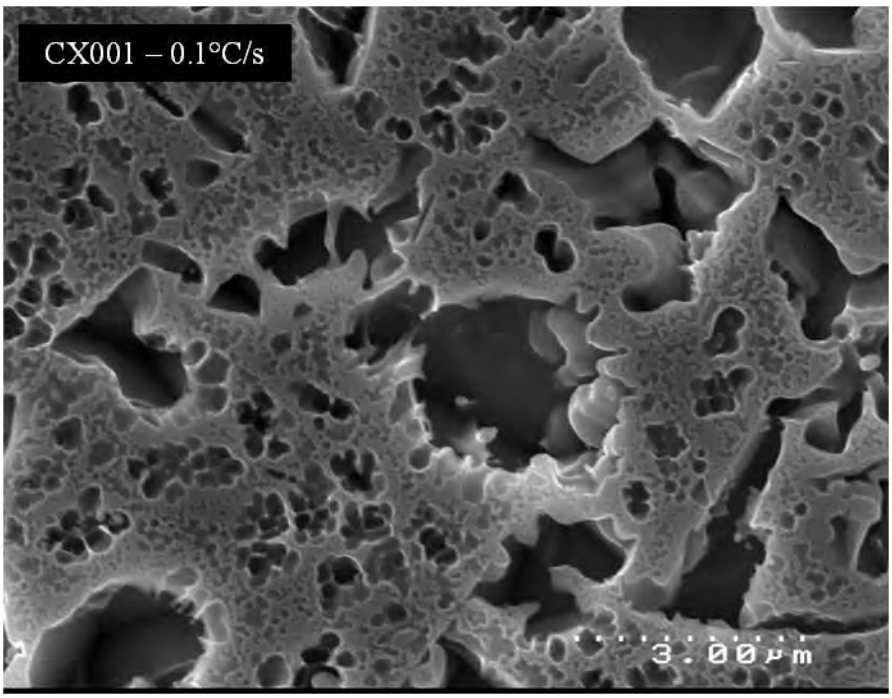


Figure 4-52: Micrograph of test piece CX001, slow cooled (at ~0.1°C/s) etched using Kalling's reagent according to methodologies detailed in Table 15.

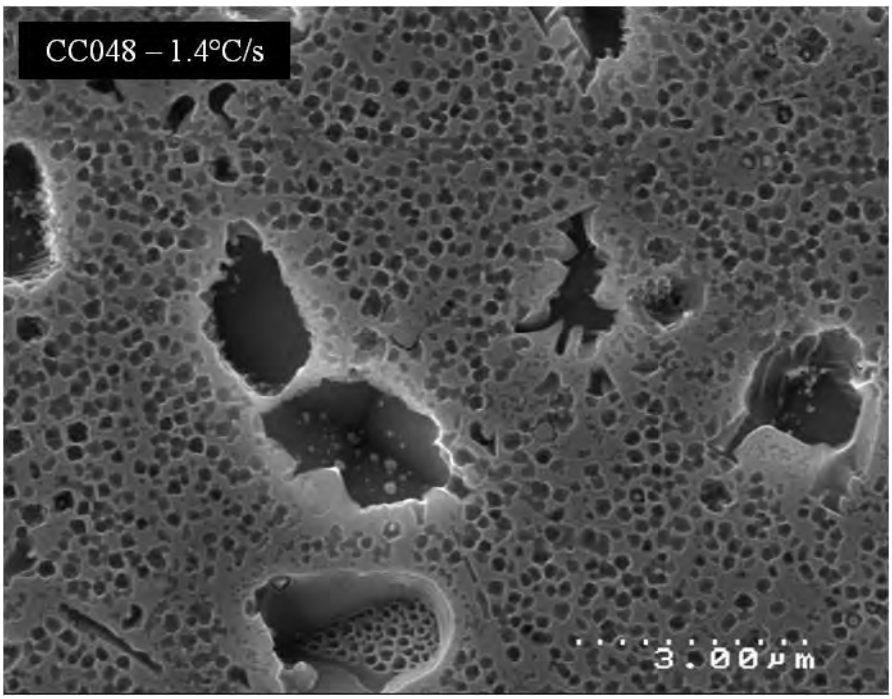


Figure 4-53: Micrograph of test piece CC048, intermediately cooled (at ~1.4°C/s) etched using Kalling's reagent according to methodologies detailed in Table 15.

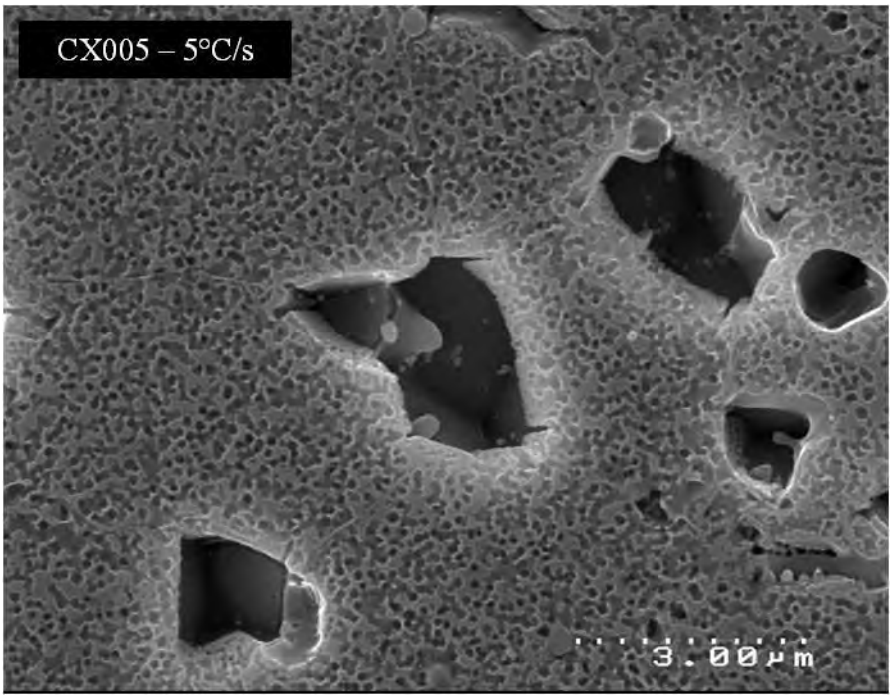


Figure 4-54: Micrograph of test piece CX005, fast cooled (at ~5°C/s) etched using Kalling's reagent according to methodologies detailed in Table 15.

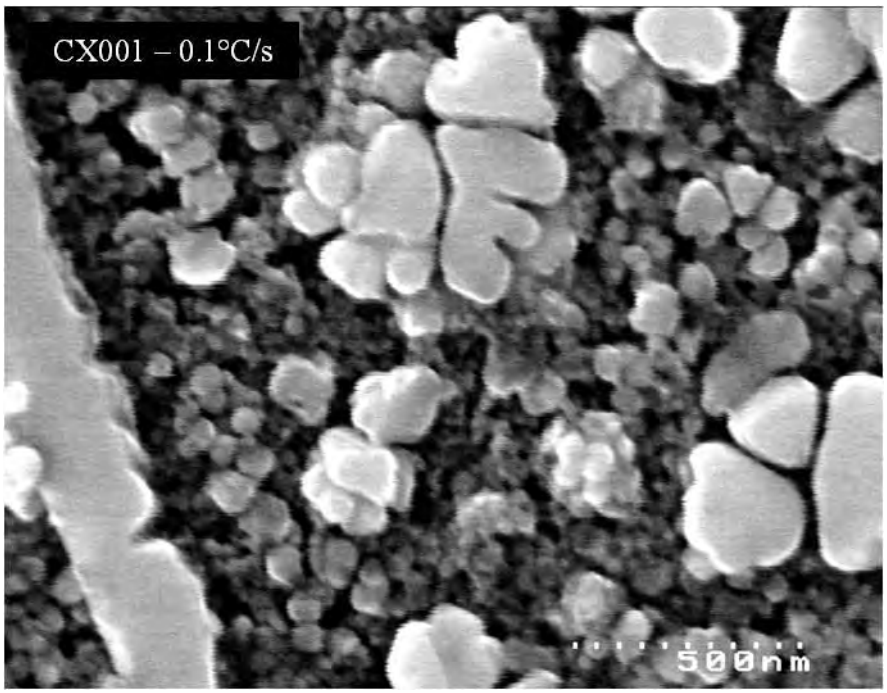


Figure 4-55: Micrograph of test piece CX001, slow cooled (at ~0.1°C/s) electro-chemically etched using 10% Phosphoric according to methodologies detailed in Table 15.

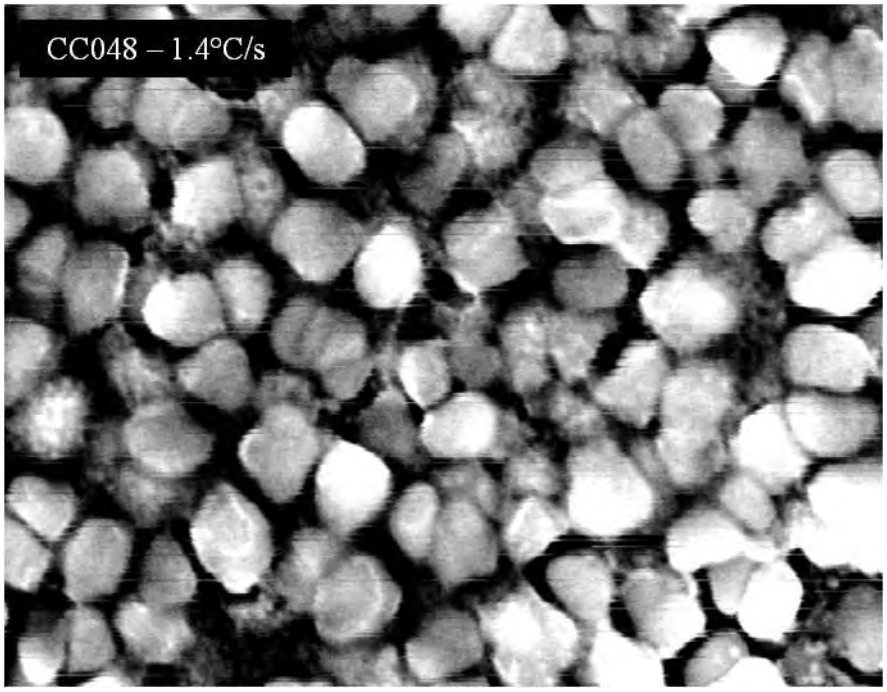


Figure 4-56: Micrograph of test piece CC048, intermediately cooled (at ~1.4°C/s) electro-chemically etched using 10% Phosphoric according to methodologies detailed in Table 15.

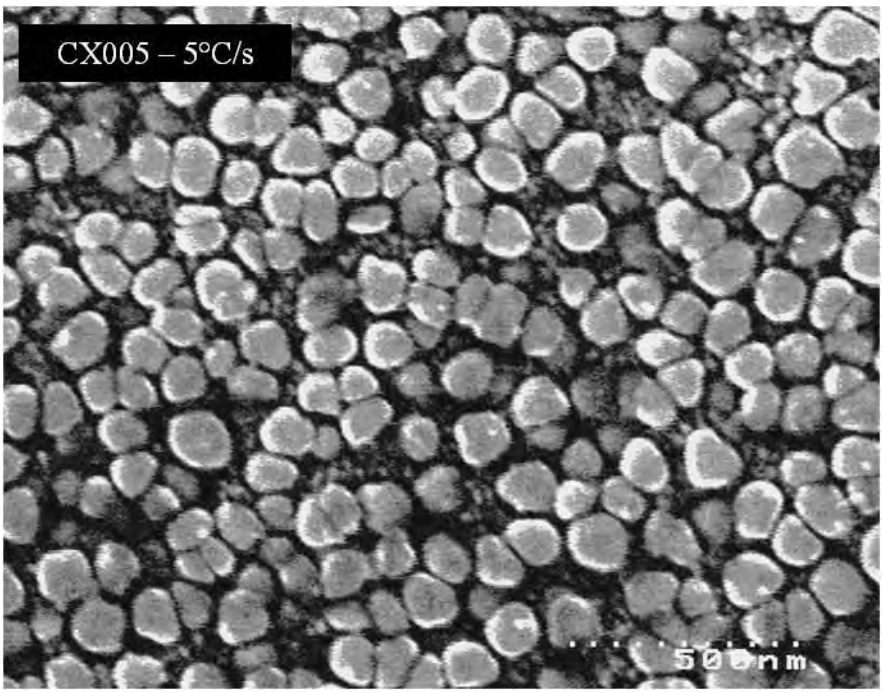


Figure 4-57: Micrograph of test piece CX005, fast cooled (at ~5°C/s) electro-chemically etched using 10% Phosphoric according to methodologies detailed in Table 15.

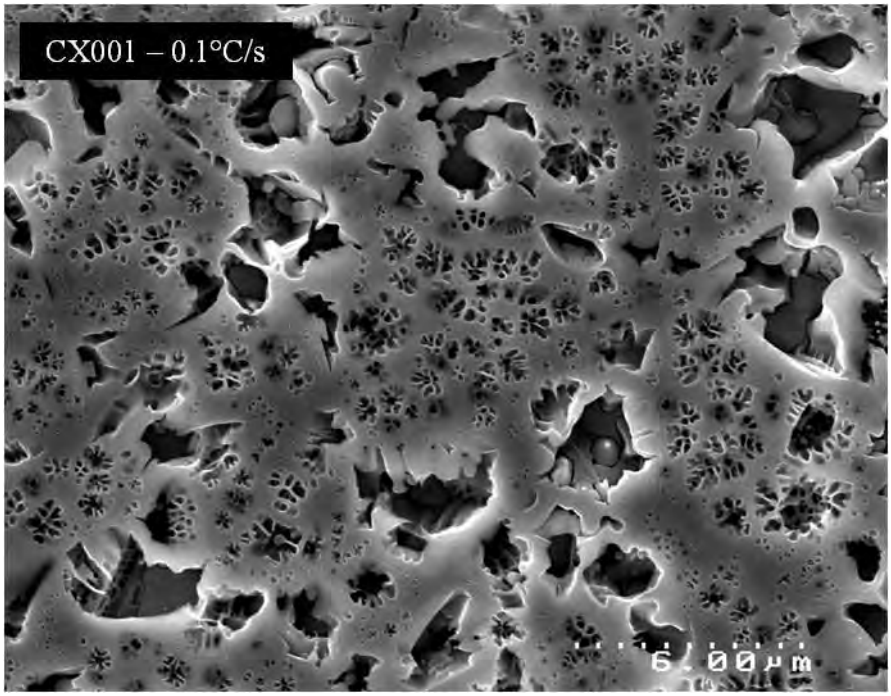


Figure 4-58: Micrograph of test piece CX001, slow cooled (at ~0.1°C/s) etched using a Molybdenum based etchant according to methodologies detailed in Table 15.

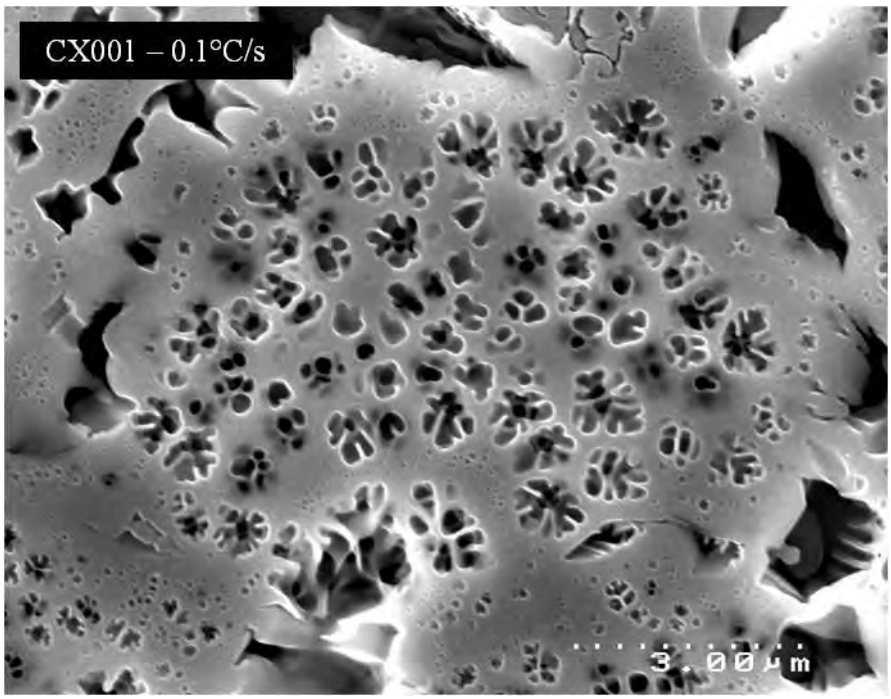


Figure 4-59: Micrograph of test piece CX001, slow cooled (at ~0.1°C/s) etched using a Molybdenum based etchant according to methodologies detailed in Table 15.

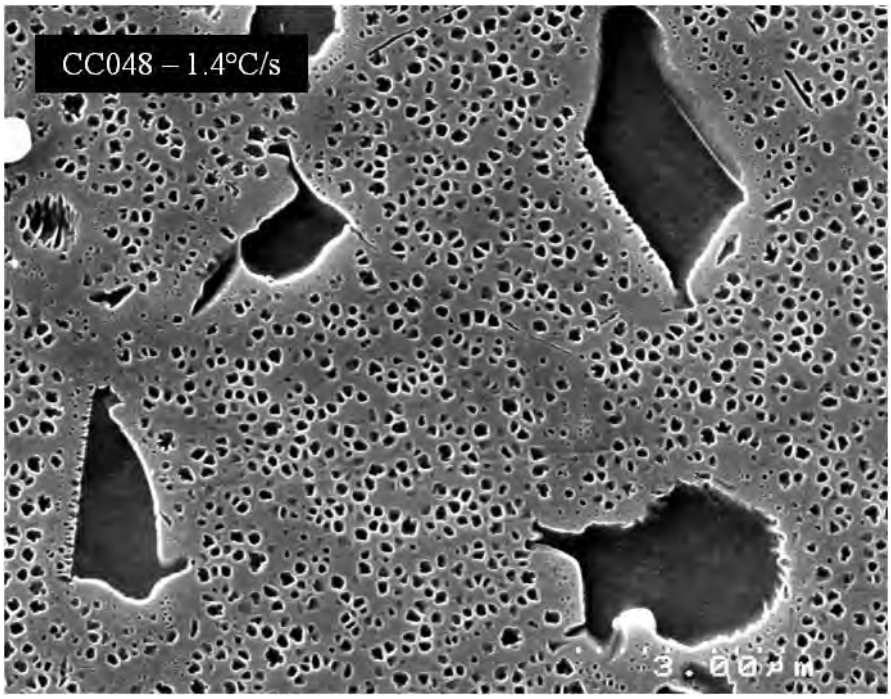


Figure 4-60: Micrograph of test piece CC048, intermediately cooled (at ~1.4°C/s) etched using a Molybdenum based etchant according to methodologies detailed in Table 15.

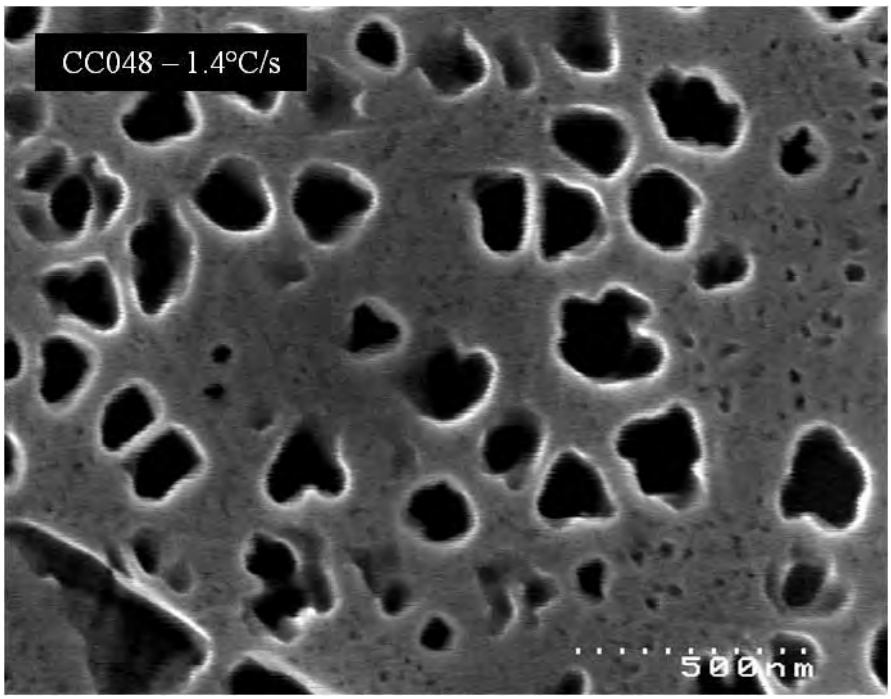


Figure 4-61: Micrograph of test piece CC048, intermediately cooled (at ~1.4°C/s) etched using a Molybdenum based etchant according to methodologies detailed in Table 15.

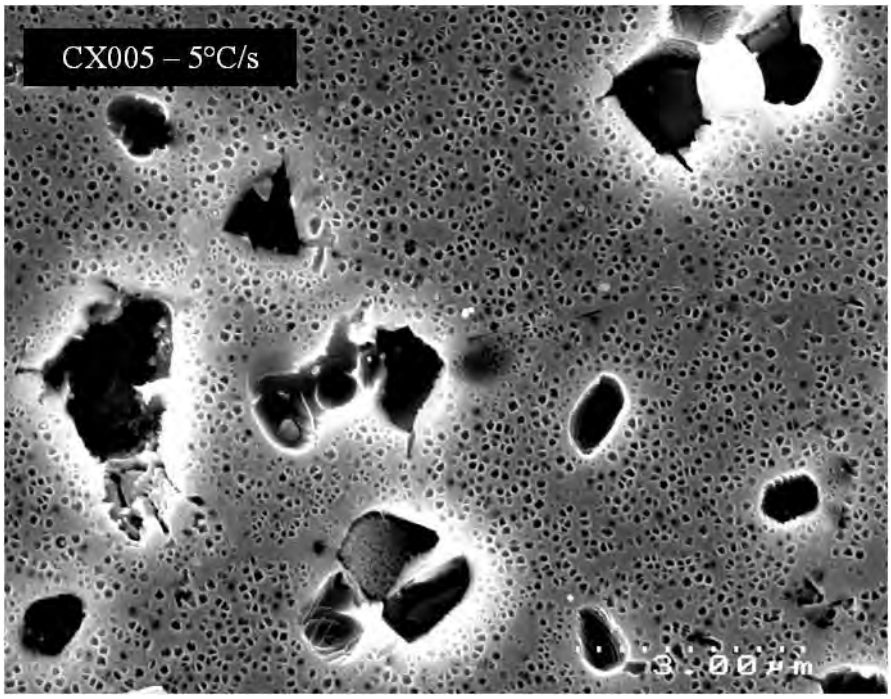


Figure 4-62: Micrograph of test piece CX005, fast cooled (at ~5°C/s) etched using a Molybdenum based etchant according to methodologies detailed in Table 15.

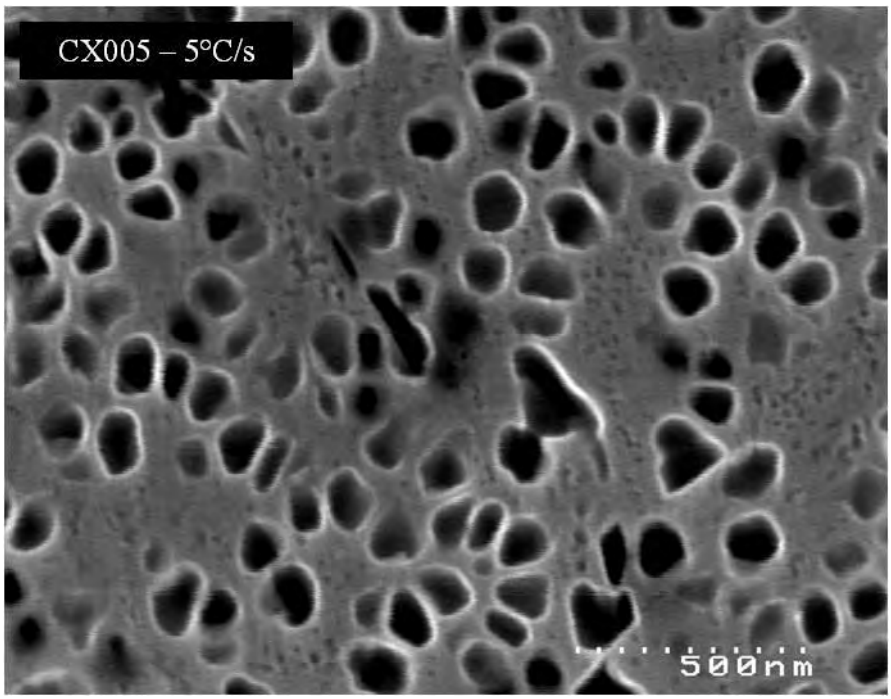


Figure 4-63: Micrograph of test piece CX005, fast cooled (at ~5°C/s) etched using a Molybdenum based etchant according to methodologies detailed in Table 15.

4.3 Modelling

4.3.1 Introduction

With regard to overload stress waveforms; modelling simulations show that crack tip stresses unload preferentially as the nominal applied stress unloads from the maximum overload load to the slightly reduced dwell load. This is best described by contour plots of stress normal to the crack face throughout one applied overload stress cycle. Presented in Figure 4-64 through to Figure 4-68 are stress (SYY) contour plots throughout a fictitious overload stress-time history applied to fine-grained Udimet 720Li (REC) at 650°C, a background load of 531 MPa, a crack length of 1.025 mm and an overload factor of 1.15.

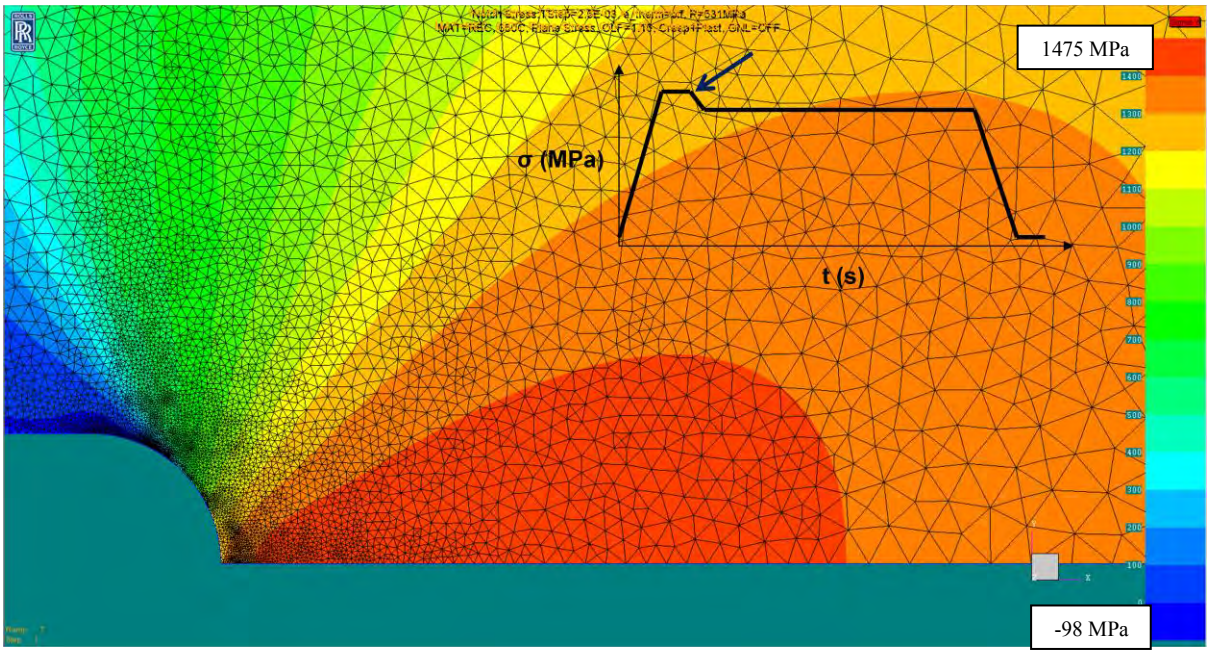


Figure 4-64: Contour plot of stress normal to the crack tip (SYY) at time t = 2, after the 1 second hold at maximum (overload) load.

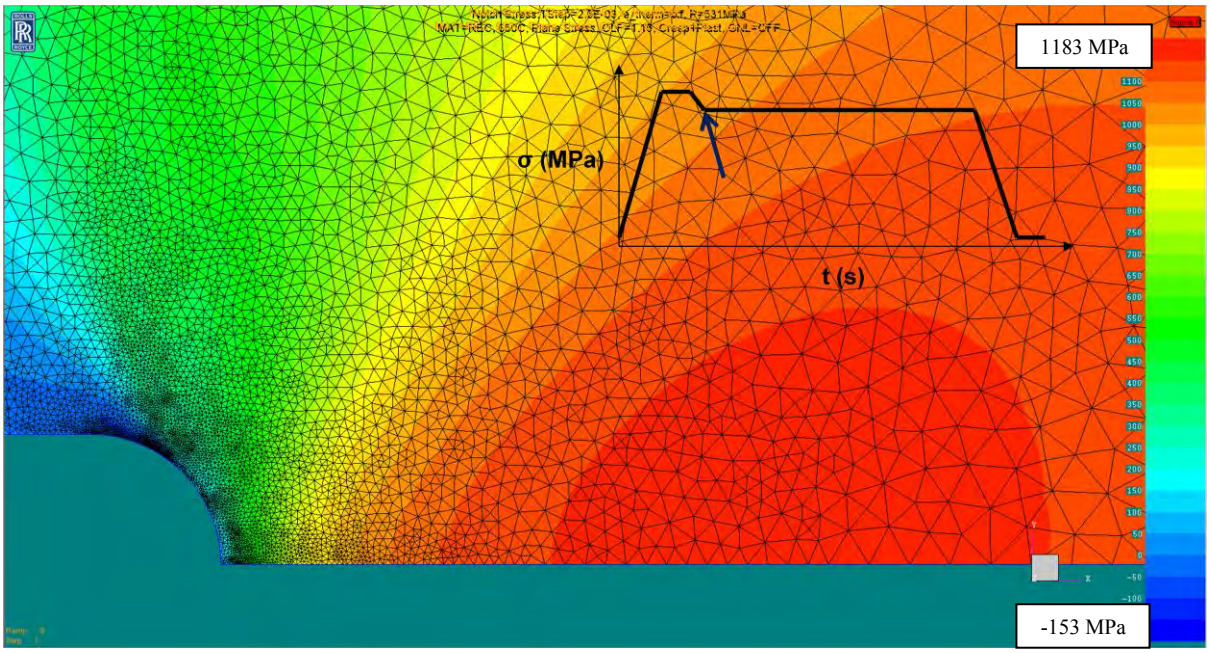


Figure 4-65: Contour plot of stress normal to the crack tip (SYY) at time t = 3, immediately after unloading from the one second hold at maximum (overload) load to the dwell load. Note stresses immediately ahead of the crack tip have unloaded preferentially.

Upon partial unloading to the dwell load (at t = 3), the stresses immediately ahead of the crack tip are much lower than the nominal stresses throughout the material; including those along the crack plane further ahead of the crack tip. In actual fact, for the conditions show in Figure 4-64 and Figure 4-65 the crack tip stresses are shown to be compressive in nature (down to below ~-150 MPa). These beneficial compressive stresses ahead of the crack tip will relax back to those normally associated with dwell loading as a function of time due to creep. For completeness; contour plots to show this relaxation are presented in Figure 4-66 and Figure 4-67 and their analysis and definition are reported in section 4.3.2.

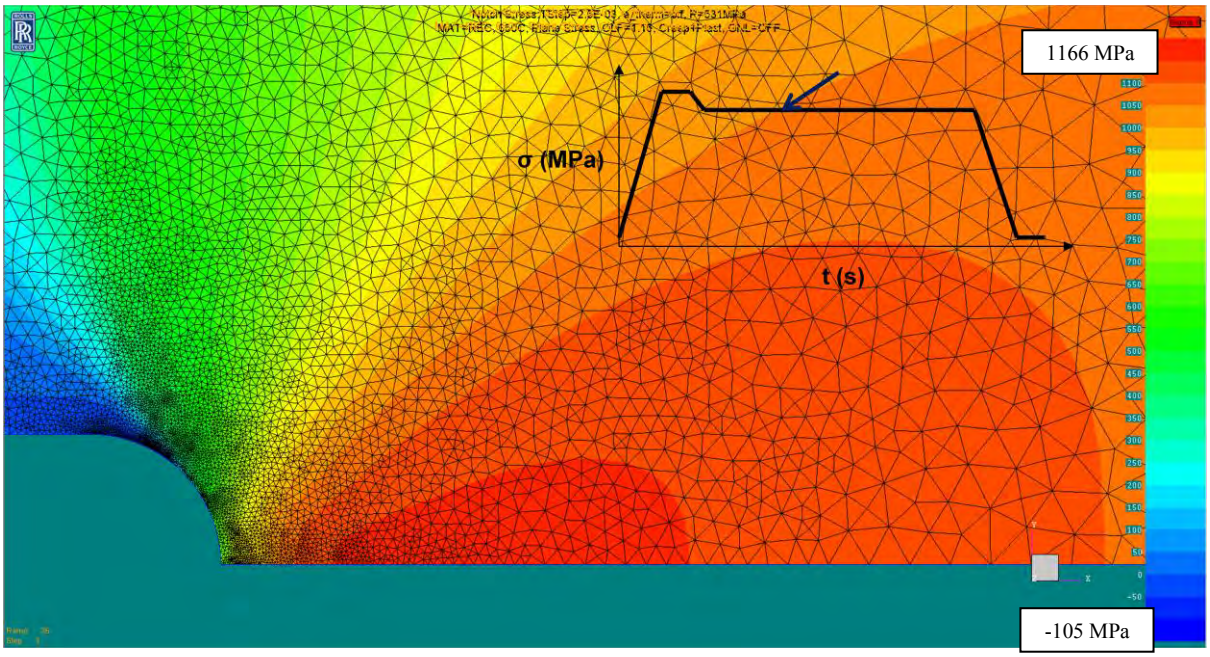


Figure 4-66: Contour plot of stress normal to the crack tip (SYY) at time t = t_{inc}/2 where t_{inc} is the incubation time (reported in section 4.3.2). Note crack tip stresses have begun to relax back to those normally associated with dwell crack tip stress states.

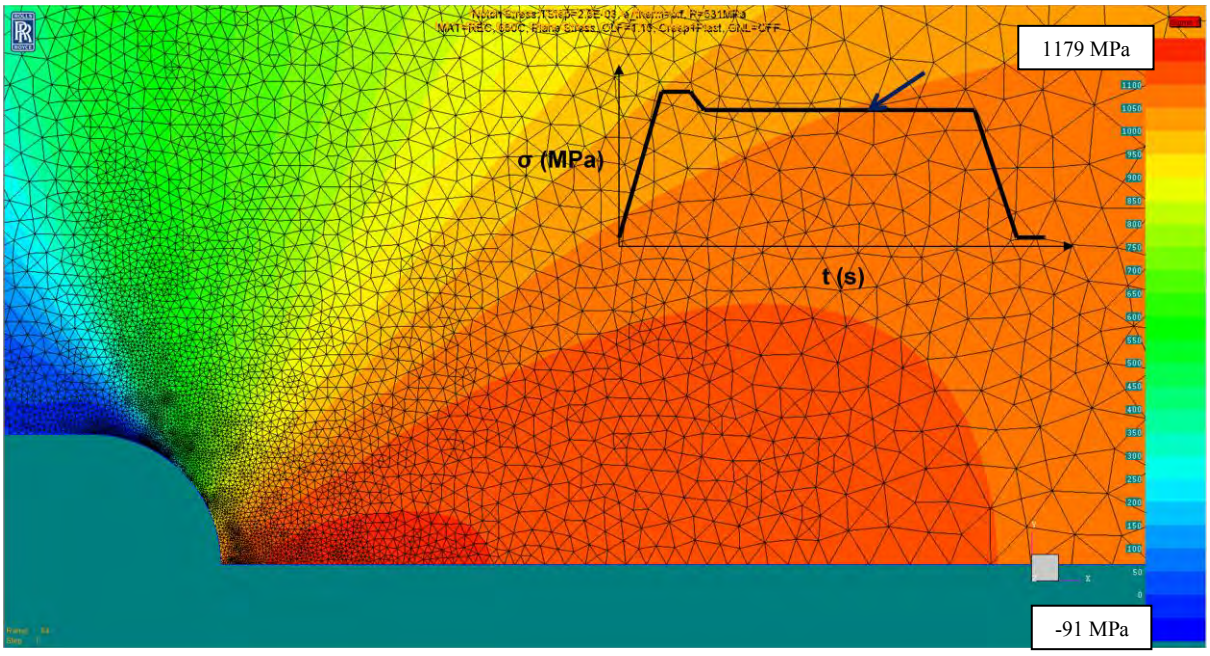


Figure 4-67: Contour plot of stress normal to the crack tip (SYY) at time t = t_{inc} where t_{inc} is the incubation time (reported in section 4.3.2). Note that at this stage, crack tip stresses are considered to be equal to those normally associated with dwell crack tip stresses (discussed below).

In analytical post processing of data to generate incubation times (reported in section 4.3.2), it is necessary to compare crack tip stress states as a function of overload cycling with those associated with normal dwell-only cycling. Therefore presented in Figure 4-68 is a contour plot to show stress normal to the crack tip for an otherwise similarly run dwell cycle simulation at time $t = t_{inc}$ for comparison with crack tip stress states at a similar moment in time with the above presented overload crack tip stress states.

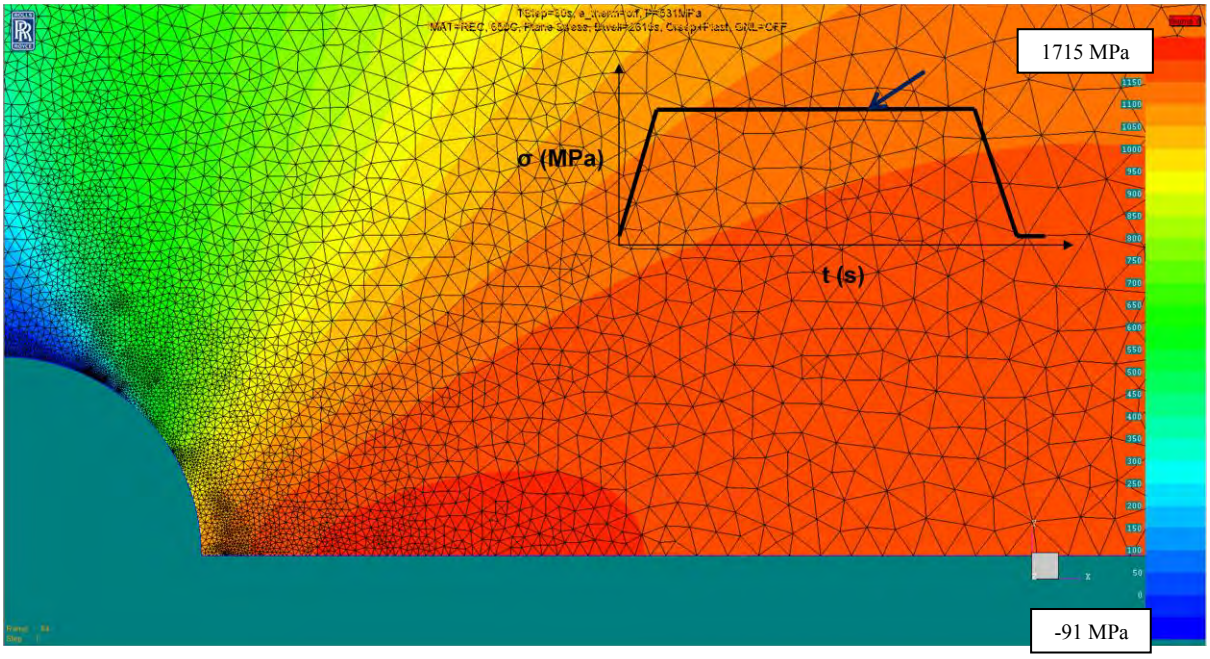


Figure 4-68: Contour plot of stress normal to the crack tip (SYY) for a dwell-only simulation at time $t = t_{inc}$ where t_{inc} is the incubation time (reported in section 4.3.2). Note crack tip stress states are comparable with those presented in Figure 4-67.

4.3.2 Incubation Time

As alluded to above, given that crack tip stresses unload preferentially to those ahead of the crack tip while nominal (bulk) applied stresses unload from the overload segment to the dwell load, it follows that they will relax back to those normally associated with dwell-only cycling

(during the subsequent dwell period) as a function of time due to creep and plasticity. Therefore stress-time plots from overload simulations are compared with those generated from normal dwell simulations in order to determine what is termed an "incubation time"; t_{inc}.

The parameter t_{inc} is defined as the first moment in time (in seconds) that the crack tip stresses from the overload cycle come to within 2% of those associated with (otherwise similar) dwell-only cycling.

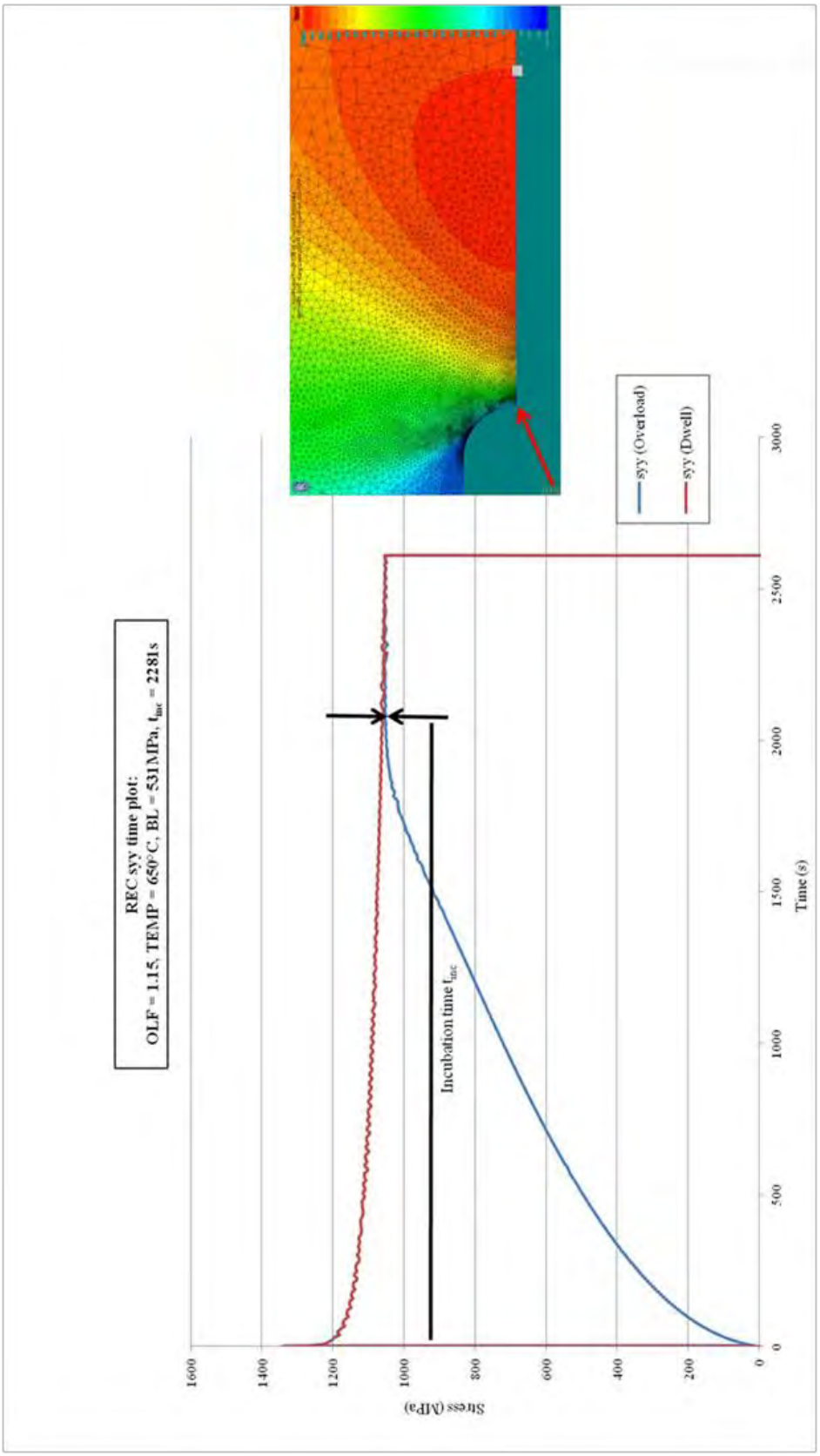


Figure 4-69: Showing dwell and overload crack tip stress as a function of time and the calculation of $t_{inc.}$

Results show that t_{inc} increases with increasing overload factor and decreasing temperature. t_{inc} is plotted against overload factor for a range of temperatures, for both fine-grained Udimet 720Li and RR1000. On linear axes the relationship between overload factor and t_{inc} is parabolic (Figure 4-70); therefore for clearer comparisons of incubation times for a range of conditions they are also plotted on log-time axes (Figure 4-71 and Figure 4-72).

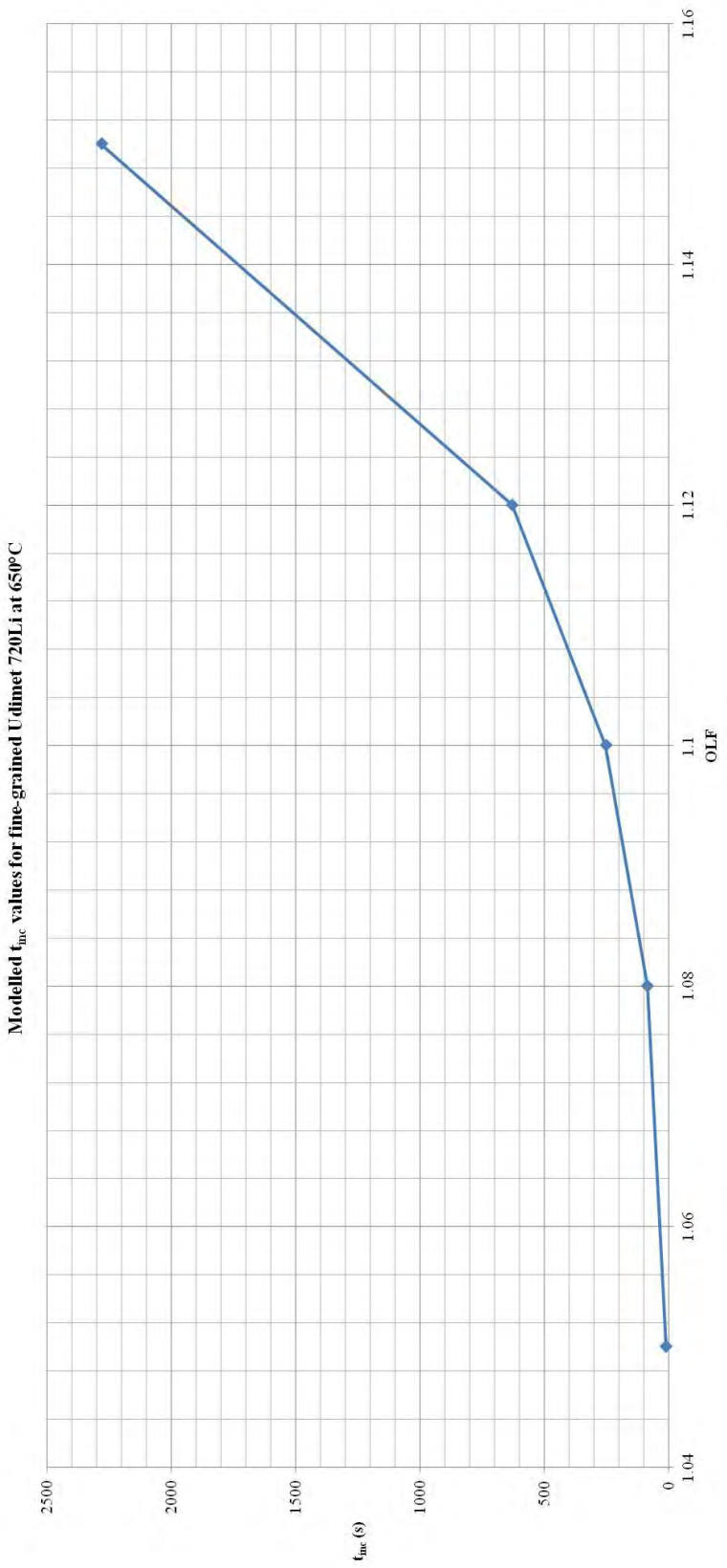


Figure 4-70: Plotting t_{inc} against overload factor for fine-grained Udimet 720Li at 650°C. Models are run with a Background Load of 531MPa and a crack length of 1.025mm which relates to a ΔK of around 18-19MPa√m.

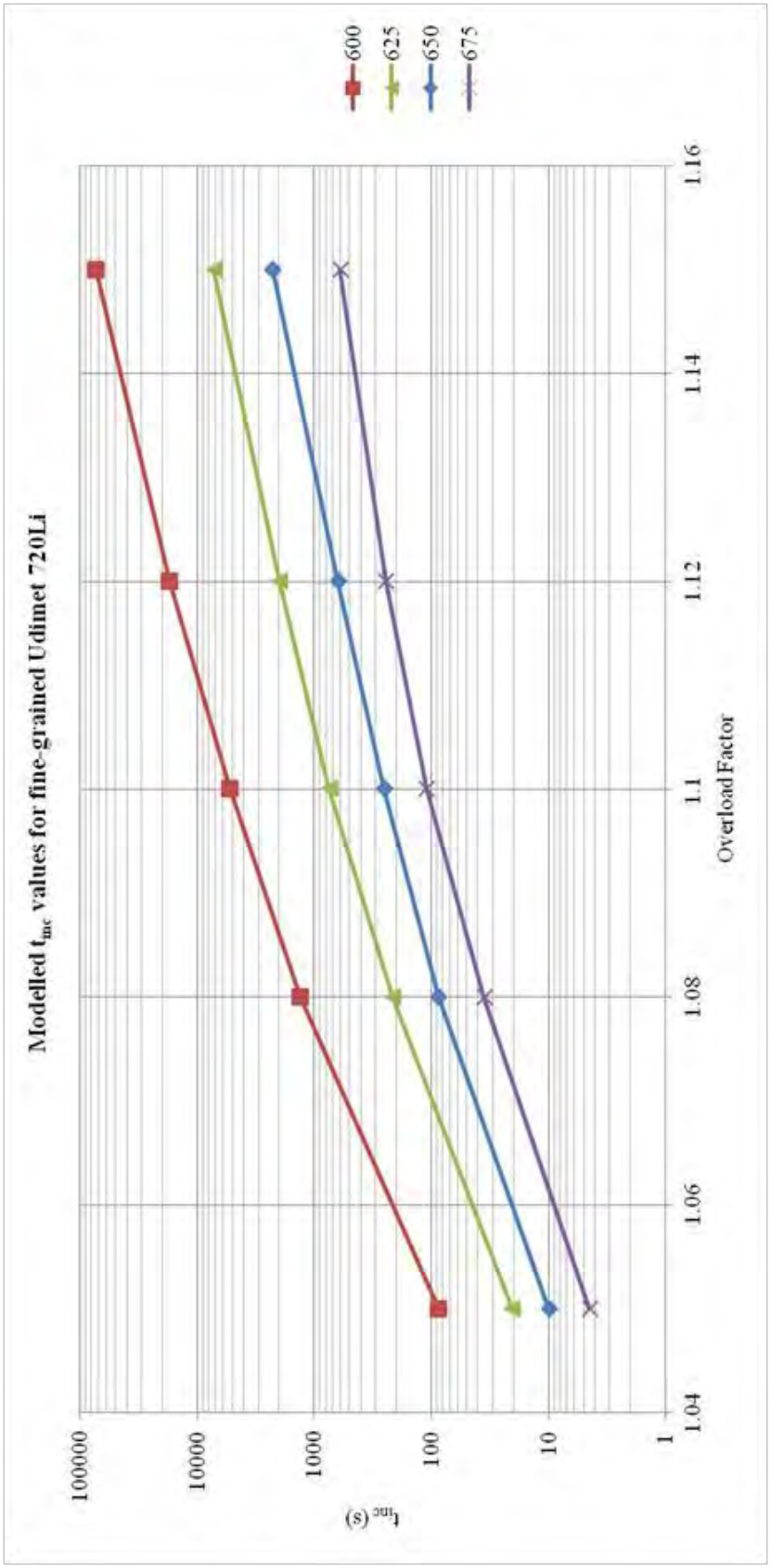


Figure 4-71: Plotting t_{inc} against overload factor for a range of temperatures, for fine-grained Udimet 720Li. Models are run with a Background Load of 531MPa and a crack length of 1.025mm which relates to a ΔK of around 18-19MPa√m.

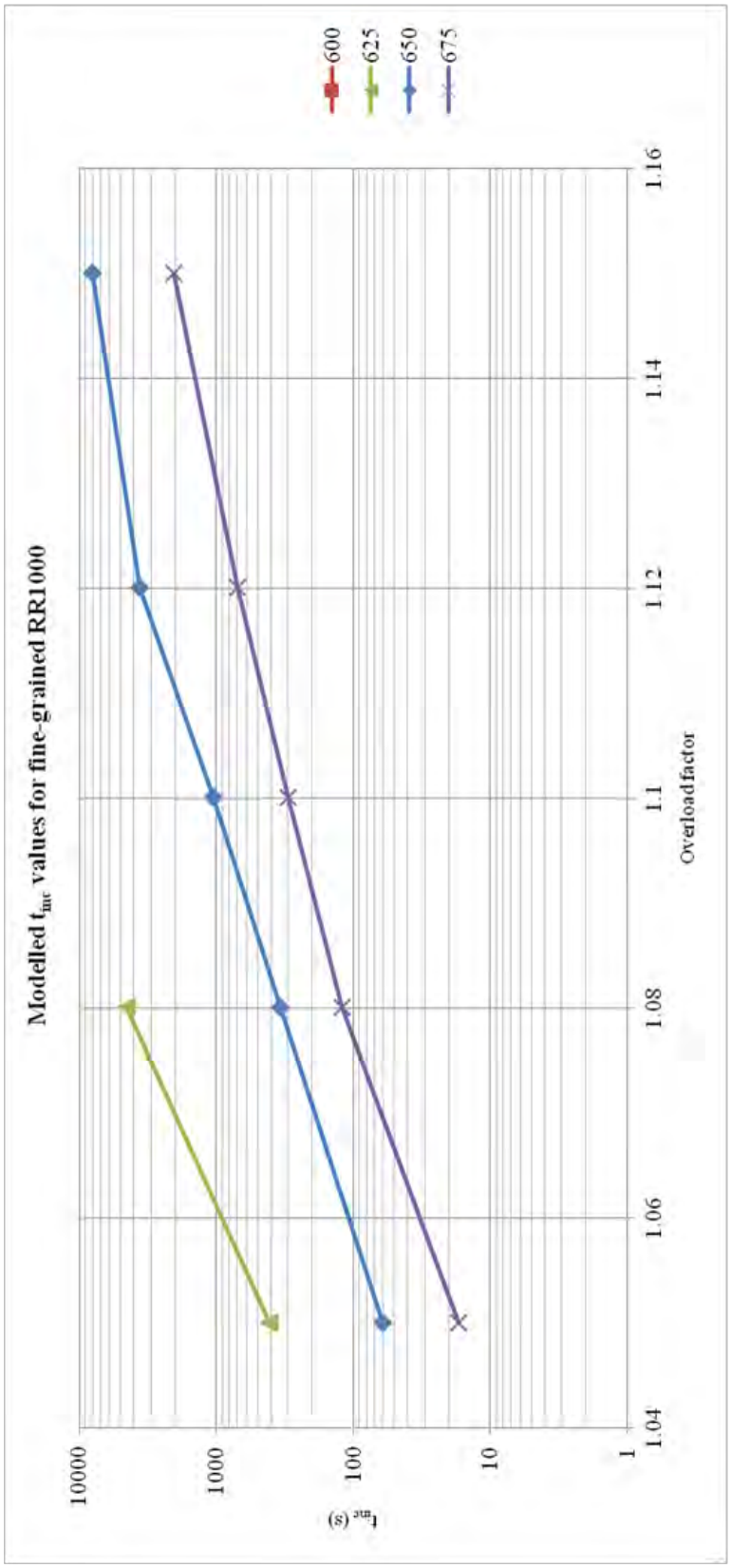


Figure 4-72: Plotting t_{inc} against overload factor for a range of temperatures, for fine-grainedRR1000. Models are run with a Background Load of 531MPa and a crack length of 1.025mm which relates to a ΔK of around 18-19MPa√m.

The gaps in Figure 4-72 represent conditions under which the finite element simulations failed to run. The reasons for which these failures occurred is unclear, and a brief discussion pertaining to the issues which may have arisen in the material database codes is made in section 5.3. At this stage it is important to highlight that failures to run occur at low temperatures and high stresses for fine-grained RR1000 (RGT) simulations occur as a result of "creep failure" in an element near to the crack tip.

The effect of overload factor on incubation time can also be assessed by plotting stress against time for a range of overload factors; including the respective normal dwell cycle crack tip stress against time plot for comparison (Figure 4-73).

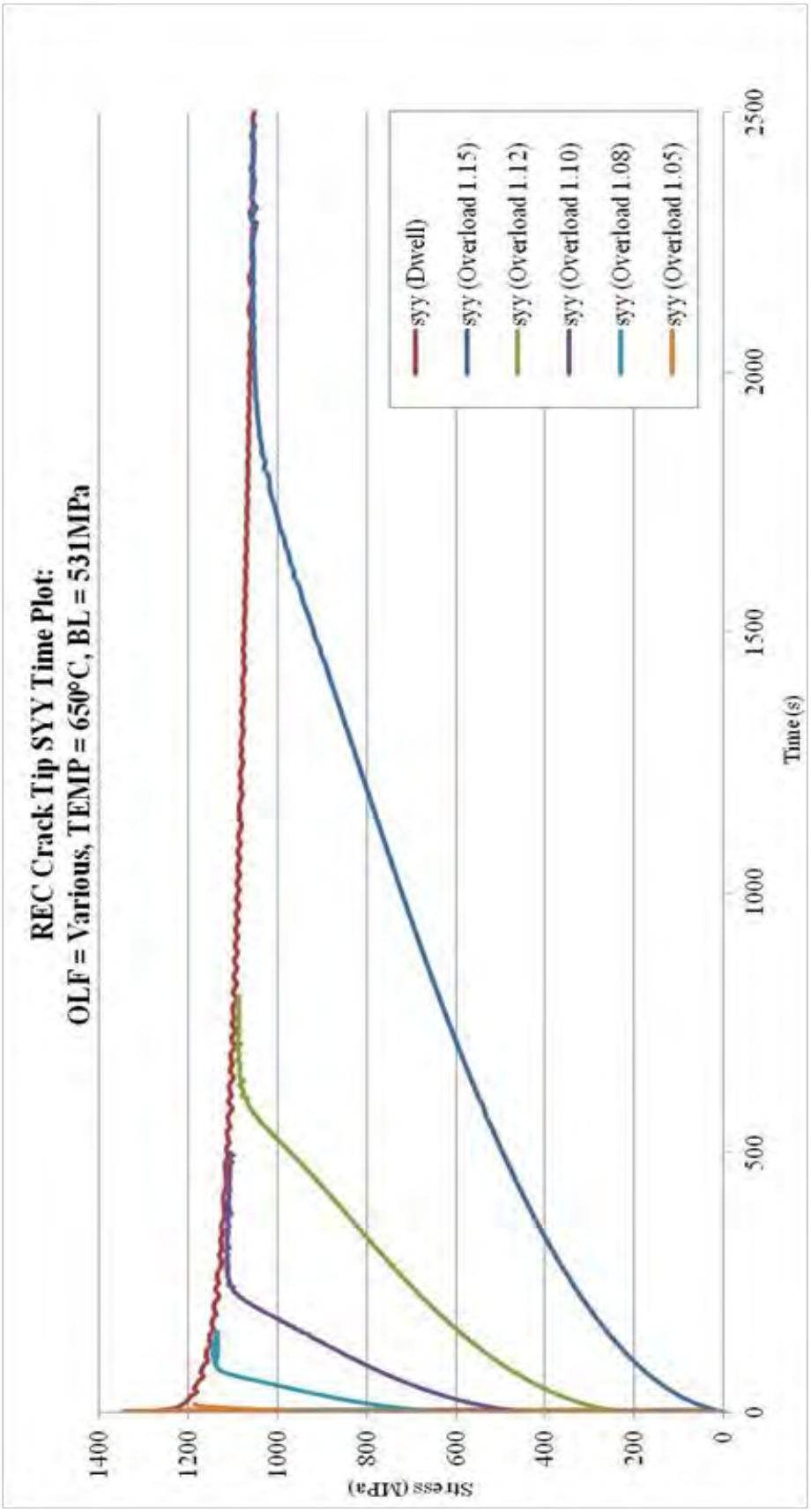


Figure 4-73: A graph of SYY against time for a range of overload factors applied to fine-grained Udimet 720Li (REC) simulations at 650°C with a background load of 531 MPa.

4.3.3 Crossing Time

A second parameter, the "crossing time" (t_x) can be defined and determined by analysing creep data. SC03 simulations can be used to plot inelastic creep strain (CEQI) as a function of time for each element. By performing a differentiation (with respect to time) on this creep data it is possible to generate a graph to show creep strain *rate* as a function of time. Creep strain rate is plotted along an x-axis of the average time point between which the differentiation was performed. A comparison of creep strain rate for the overload cycle between data collected from the element at the very tip of the crack and data collected from the element at a distance of 1.5r ahead of the crack tip enables the calculation of the "crossing time", t_x.

After unloading from the initial overload, the creep strain rate at the very crack tip is relatively low. In actual fact; it is observed to be much lower than creep strain rates ahead of the crack tip in the nominal bulk material, 1.5r ahead of the crack tip (Figure 4-76). The creep strain rate at the crack tip will gradually increase as stresses relax as a function of time, temperature, applied background load and the creep properties of the alloy.

The crossing time (t_x) is the moment in time at which creep strain rates at the crack tip "catch up" with and overtake those ahead of the crack. Hence t_x is the time it takes for creep strain rates at the crack tip to return to "normal"; where they dominate crack growth rates. It is a concept analogous to t_{inc} since it referrers to the time it takes for crack tip stresses and strains to return (creep) back to those normally associated with dwell loading. Below both t_{inc} and t_x,

crack tip stresses and strains could be thought of as "dormant" since they are well below those associated with the bulk material, a condition which is usually rare in these types of fracture mechanics problems. Under these particular conditions, crack growth rates are slow when compared with those associated with more usual waveforms (such as the dwell cycle) where crack tip stresses are high and dominate crack growth. Once t_{inc} and t_x have been reached, crack tip stresses and strains return to those normally associated with dwell crack tip stress states and begin to dominate and define crack growth once again.

The reason for which creep strain rate data at the crack tip is compared with those associated with a distance of 1.5r ahead of the crack tip is because this particular distance is deemed to represent converged solutions for stress on the crack plane ahead of the tip. A brief discussion pertaining to the appropriateness of this distance for the analysis reported below is presented in Appendix V.

Figure 4-74 and Figure 4-75 are graphs to show CEQI (inelastic creep strain) against time for the node at the crack tip and 1.5r ahead of the crack tip for a typical overload cycle. Figure 4-76 shows creep strain rate as a function of time for the two nodes. Finally, a graph is plotted of the difference between creep strain rate at the crack tip and at 1.5r ahead of the crack tip against time, to show the method by which t_x is found (Figure 4-77). When this graph crosses through zero on the time axis, the creep strain rate at the crack tip has now become faster than that at 1.5r ahead of the crack tip. Note that the time at which this crossing of the axis occurs includes three extra seconds at the beginning the cycle; where the nominal overload is applied (ramping up from 0 MPa to the overload load over a time of one second),

held for a period of one second and ramped down the dwell load (also over a period of one second). Therefore to calculate the crossing time, t_x, three seconds should be subtracted from the time at which the difference between the two creep strain rates crosses the time axis (Figure 4-77).

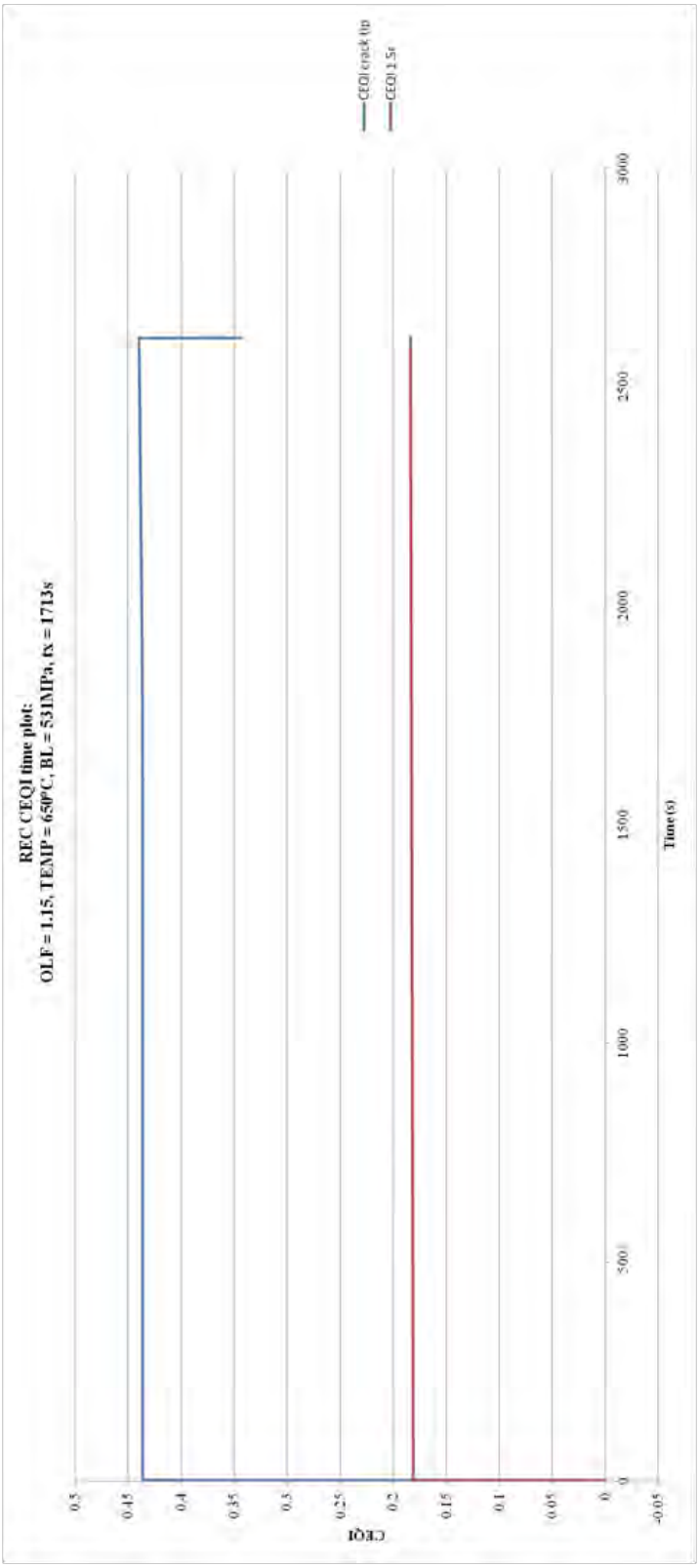


Figure 4-74: Showing inelastic creep strain (CEQI) against time for the node at the crack tip and the node 1.5r ahead of the crack tip for a typical overload cycle. For reference, the material simulated is fine-grained Udimet 720Li (REC).

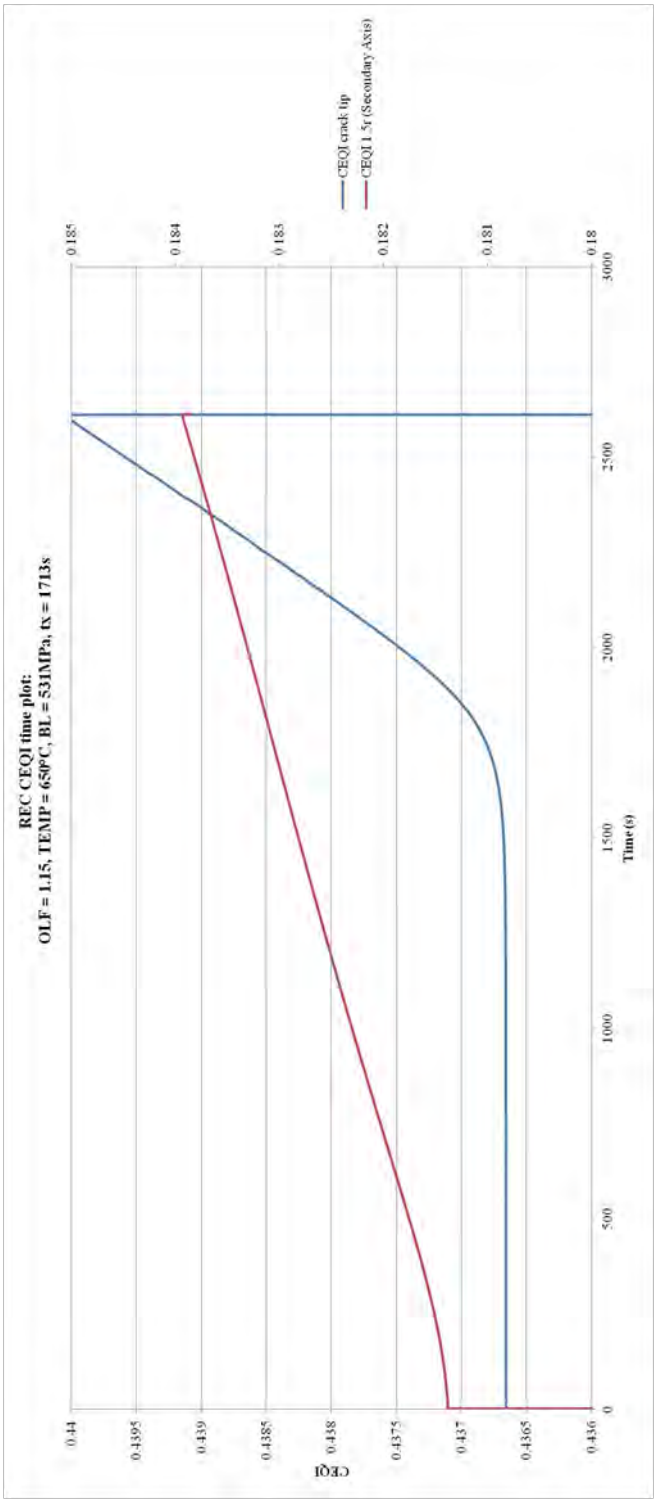


Figure 4-75: Showing the same information as Figure 4-74 (above) with higher axes resolution and the use of a secondary axis for 1.5r data.

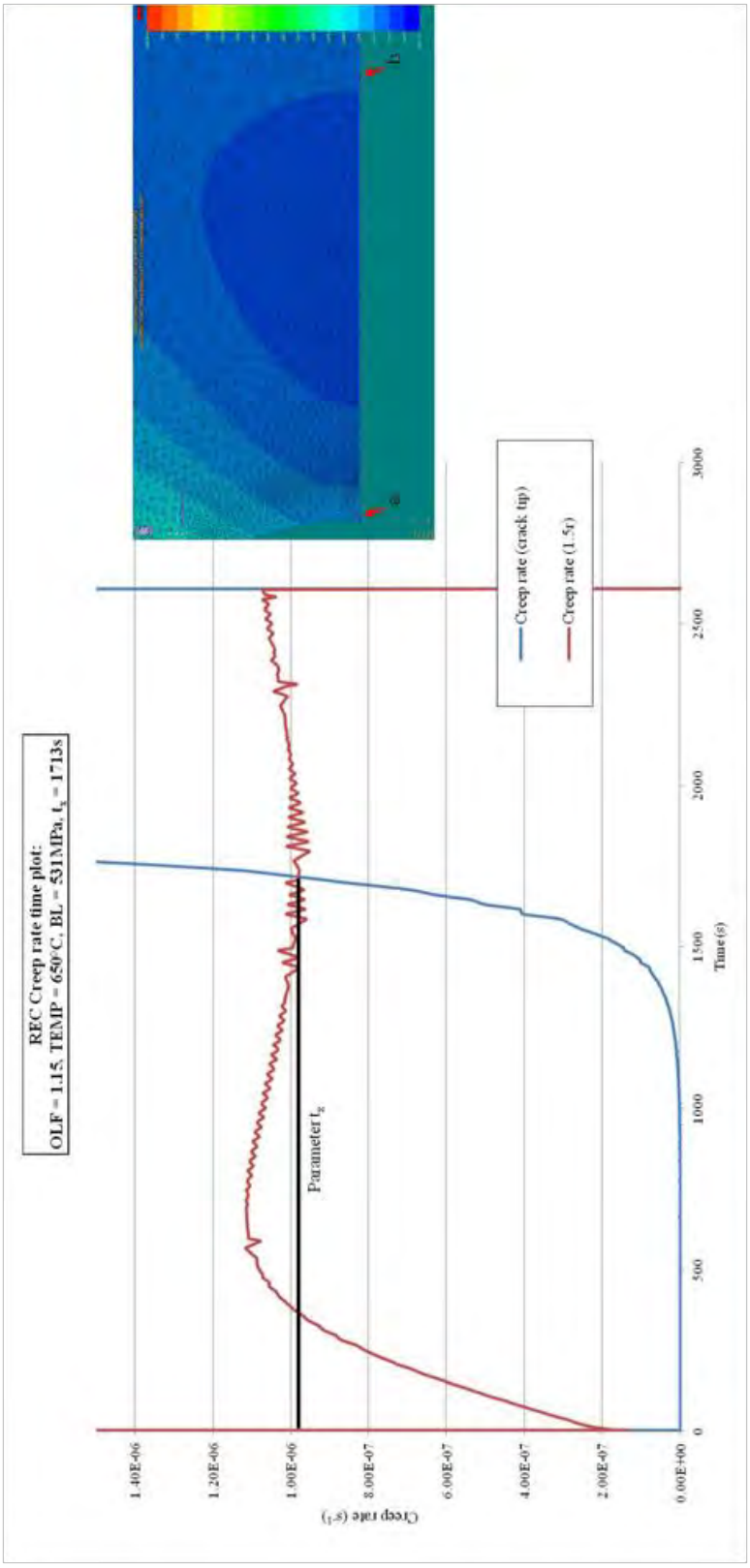


Figure 4-76: Plotting creep strain rate against time for data gathered from the crack tip and 1.5r ahead of the crack tip, for the creep data represented above in Figure 4-74, showing the calculation of parameter t_x

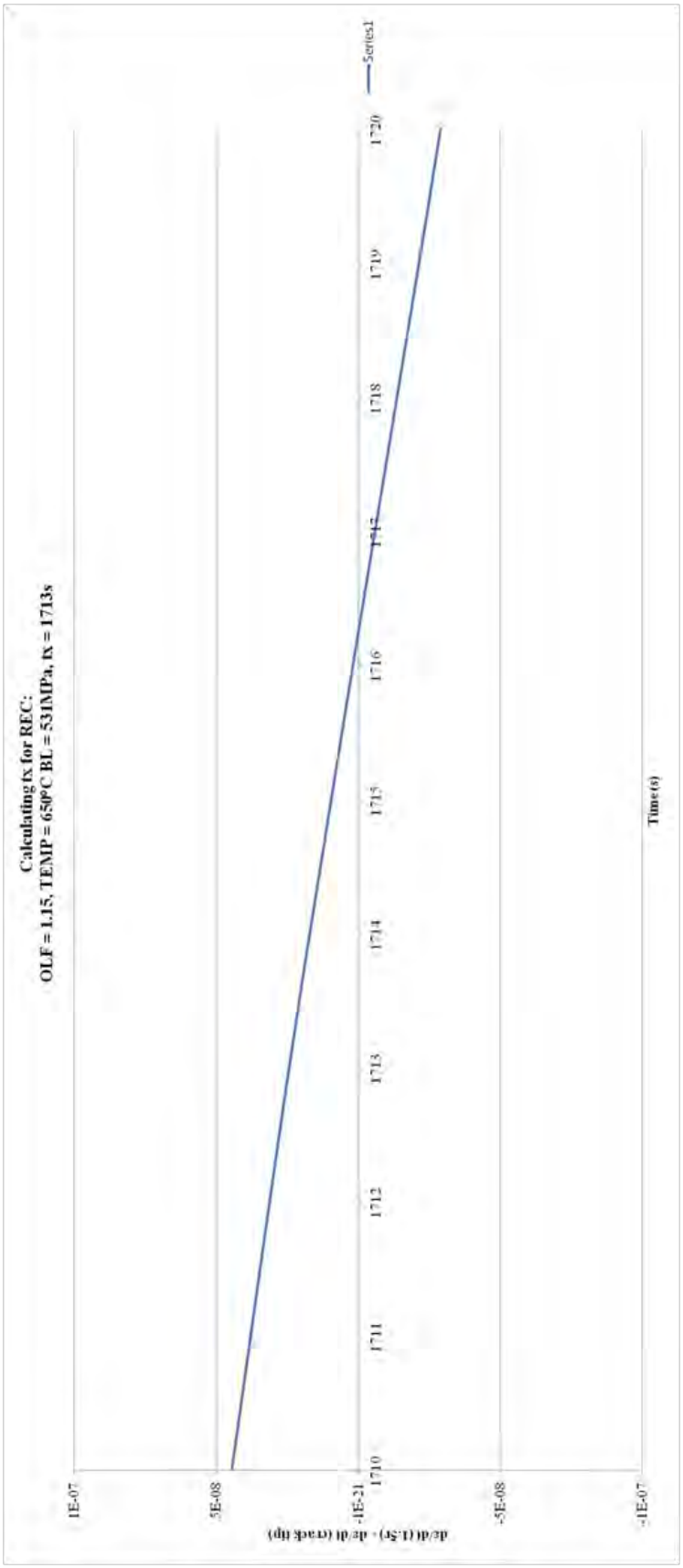


Figure 4-77: Plotting the difference between the creep strain rate at 1.5r ahead of the crack tip and the creep strain rate at the crack tip against time for a typical overload cycle. Note that t_x would actually be three seconds less than is represented by the graph.

Since the calculation of t_x involves a differentiation with respect to time, the effect of resolution (in terms of the length of time between each analysis) must be analysed. If for example the model was set to analyse and generate creep data once or twice during the subsequent dwell period it could be suggested that the resolution is too low and analysis is likely to be inaccurate. Issues pertaining to the size of the applied time steps used across simulation cycles are reported in section 3.4, and analysis to investigate the effect of time step resolution on crossing time is given in Appendix V. It is important to highlight that analysis confirmed values for t_x converged to a common point as the time step resolution reached a value such the maximum time step in between analyses was around 6% of t_x.

Therefore it is necessary to predict a value for t_x for a given condition before the simulation is run. Assume for example, for a given condition the crossing time is around 300 seconds. 6% of this time is 18 seconds; and if the user inputs time steps across the dwell time which are larger than 18 seconds, the results generated cannot be relied upon. If the user predicts for example that the crossing time might be around 3,000 seconds and therefore runs a simulation with ninety time steps along the dwell load at intervals of 180 seconds, the simulation might predict a much more reasonable t_x than previously thought (i.e. the result will be much smaller than 3,000 seconds); nevertheless the actual output t_x value from that particular simulation cannot be relied upon and the model must be re-run with a tighter resolution in terms of time steps. If on the other hand the user predicts that the for this case, the crossing time might be around 30 seconds and runs a simulation with ninety time steps across the dwell load at intervals of 1.8 seconds; the simulation will fail to capture t_x. This is because for the whole simulated dwell time the creep strain rate at the crack tip will never

"catch up" with and overtake creep strain rates ahead of the crack tip; and the model will have to be run again.

Results show that, as with incubation time t_{inc}, t_x increases with increasing overload factor and decreasing test temperature. t_x against overload factor for a range of temperatures are plotted in Figure 4-78 and Figure 4-79, for fine-grained Udimet 720Li (REC) and RR1000 (RGT) respectively.

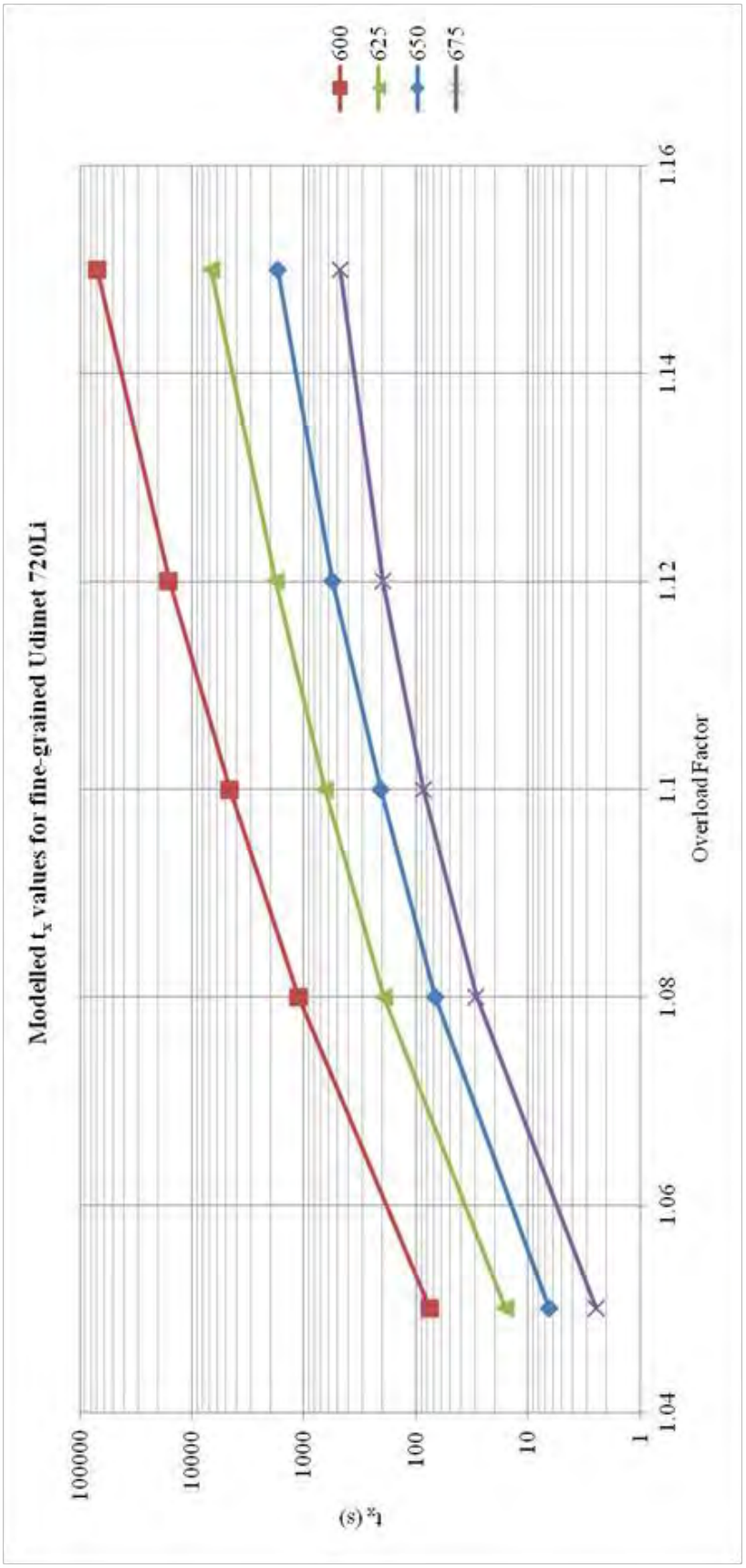


Figure 4-78: Plotting t_x against overload factor for a range of temperatures, for fine-grained Udimet 720Li. Models are run with a Background Load of 531MPa and a crack length of 1.025mm which relates to a ΔK of around 18-19MPa√m.

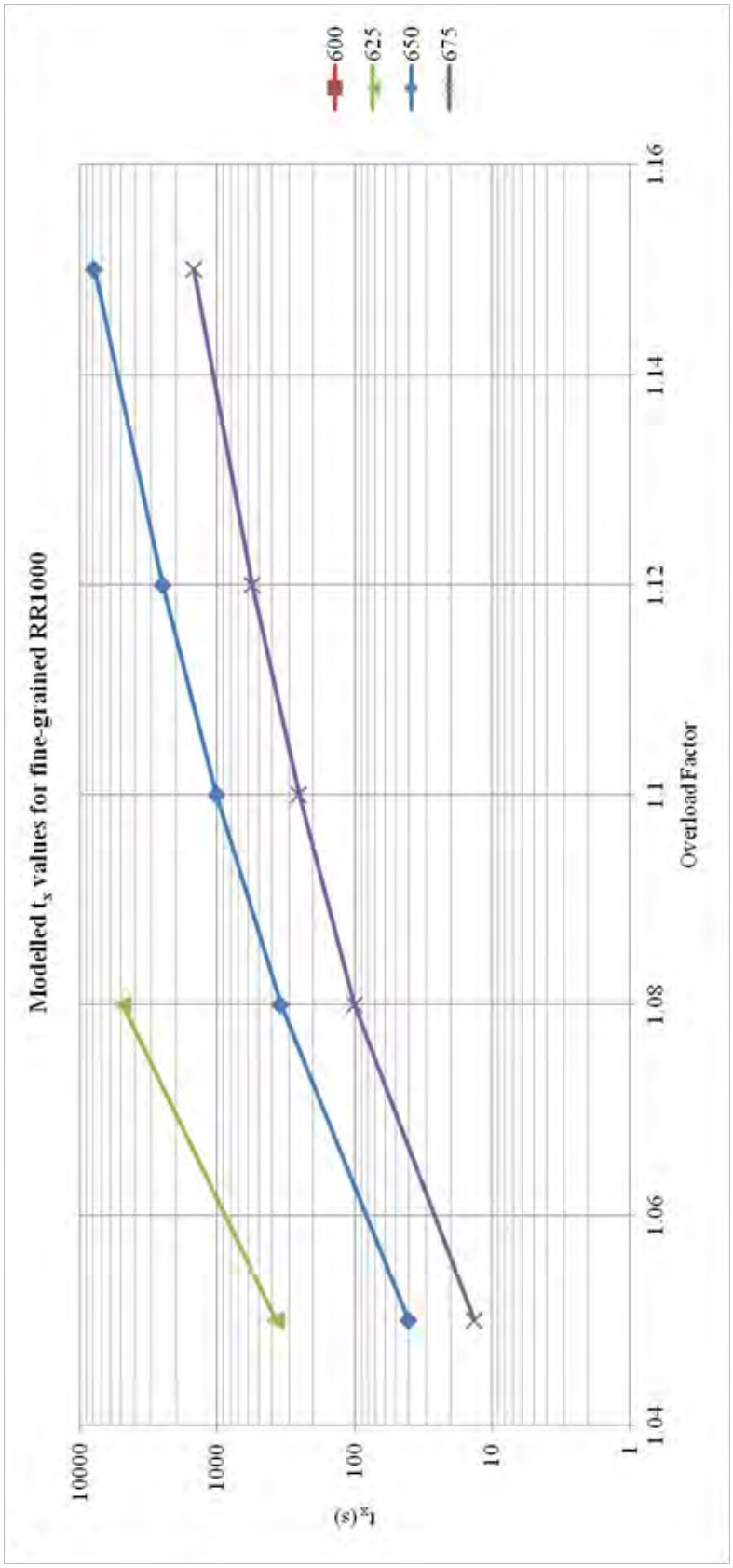


Figure 4-79: Plotting t_x against overload factor for a range of temperatures, for fine-grained RR1000. Models are run with a Background Load of 531MPa and a crack length of 1.025mm which relates to a ΔK of around 18-19MPa$\sqrt{m}$.

Similarly to the incubation time plots in Figure 4-72, the gaps in terms of crossing time values plotted above in Figure 4-79 represent conditions under which the model failed to run. As reported, simulations fail to run at high stresses and low temperatures for fine-grained RR1000 (RGT) material codes.

Results show that both incubation time and crossing time increase with increasing overload factors and with decreasing temperature. Trends also highlight that for the same conditions, both t_{inc} and t_x is larger for fine-grained RR1000 than it is for fine-grained Udimet720Li. This is represented by comparing crack tip stresses for fine-grained Udimet720Li with RR1000 through a typical overload cycle (Figure 4-80). The difference can also be seen by plotting t_x (or indeed t_{inc}) values for fine-grained Udimet 720Li and RR1000 for a range of different overload factors at a temperature of 650°C (Figure 4-81).

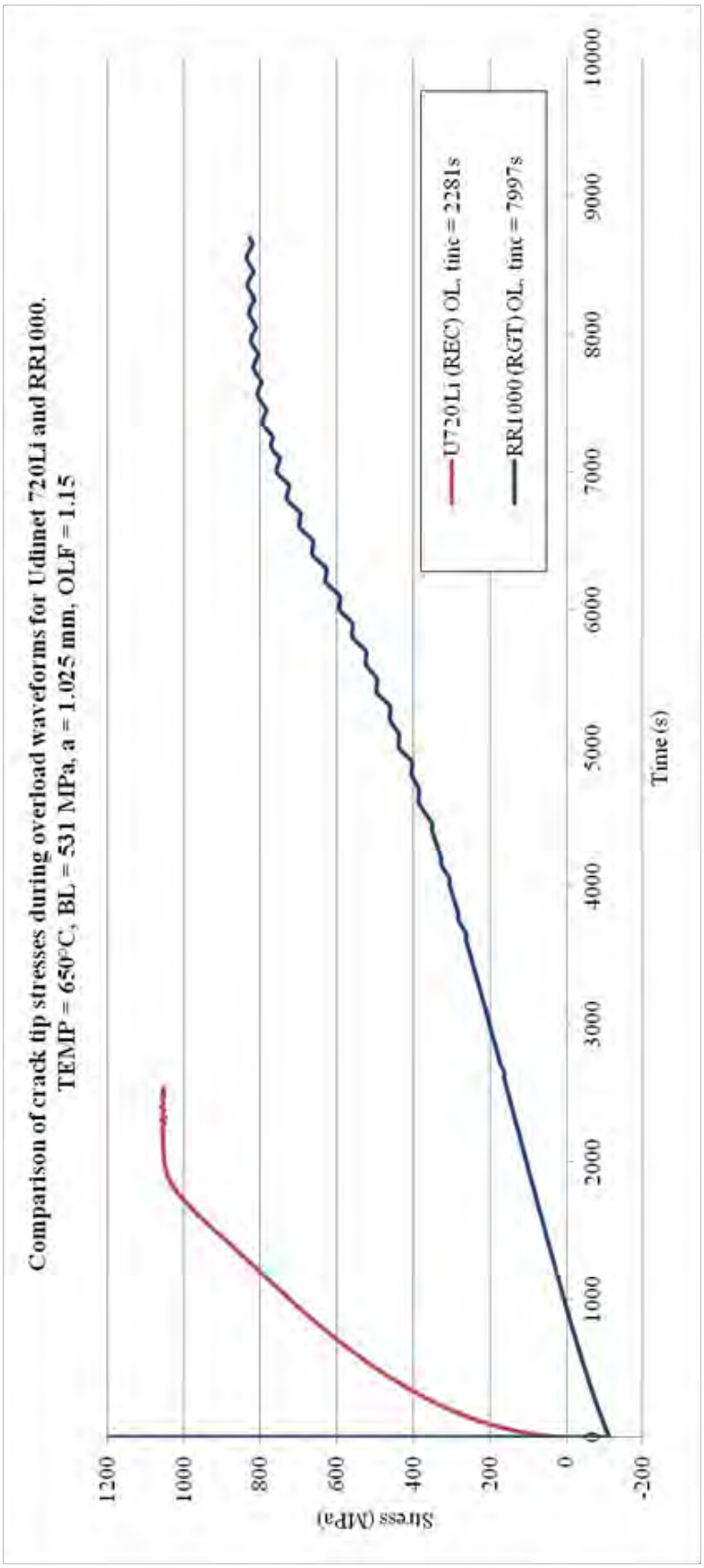


Figure 4-80: Plotting crack tip stress (SYY) against time for a typical overload waveform comparing Udimet 720Li with RR1000. Note that t_{inc} is larger for RR1000 when compared with Udimet 720Li for the same conditions.

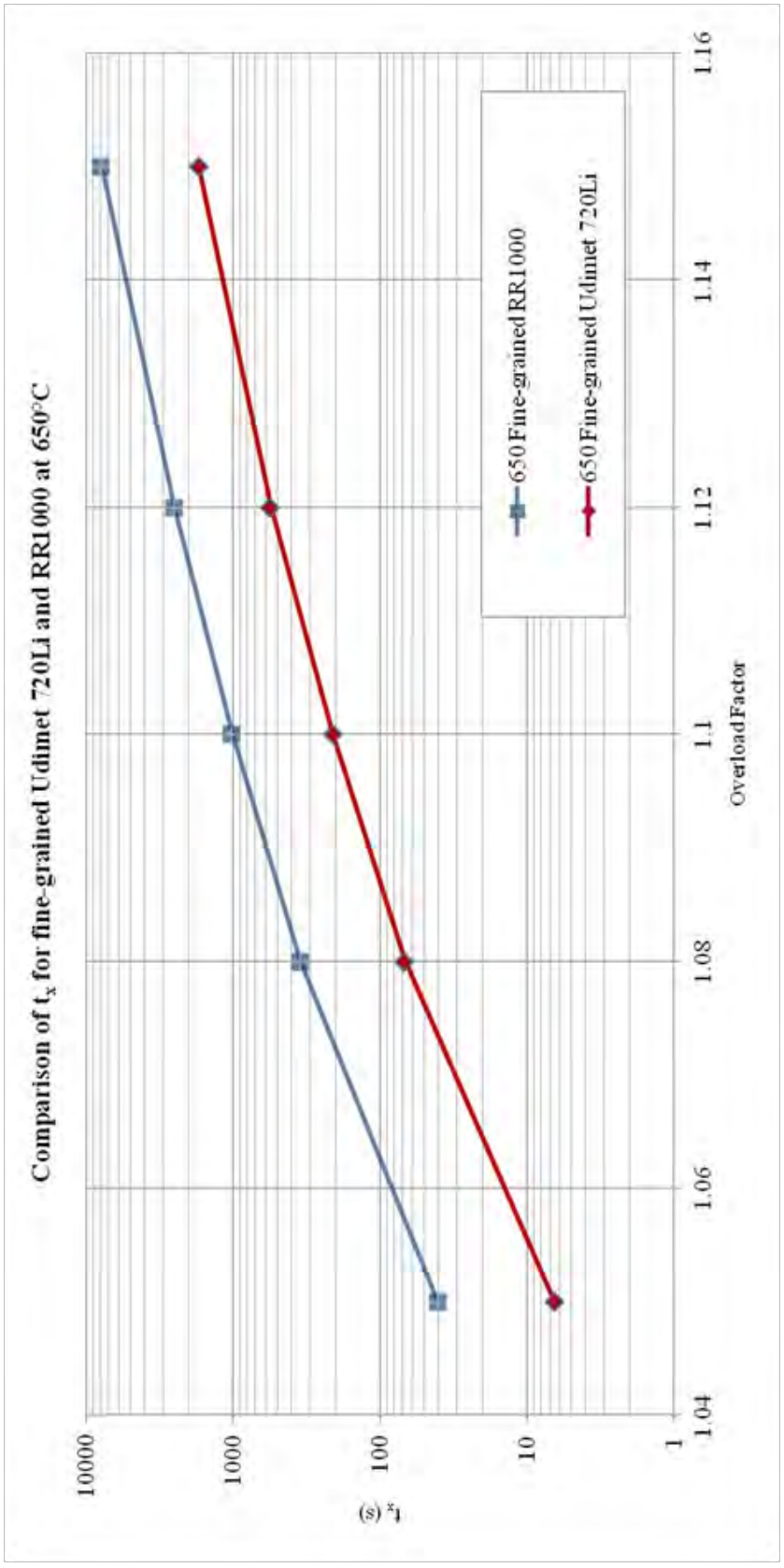


Figure 4-81: Plotting t_x against overload factor for fine-grained U720Li and RR1000 at 650°C. Models are run with a Background Load of 531MPa and a crack length of 1.025mm which relates to a ΔK of around 18-19MPa√m.

Overload waveforms reported thus far have all been applied according to a one second hold period at maximum (overload) load. As explained in section 3.2.5.2 (Effect of Dwell at Overload) this approach has been utilised in order to isolate the effect of partial unloading from the take-off to climb stages of engine operation. Nevertheless, as also explained in the above referenced section, the take-off stage of engine flight cycle (i.e. that which is represented by the application of the overload load) usually lasts for around 120 seconds. As such it is therefore important to develop the study to understand the effect of holding stresses at the maximum overload load for two minutes and to analyse stresses and creep strain rates associated with this type of loading. Therefore several conditions reported above are repeated but with the inclusion of a two minute dwell at overload.

As with previous simulations, t_{inc} and t_x are calculated using the methodologies described above, and t_x values associated with a 1 second period at overload are plotted against t_x values associated with a 120 second period at overload (and otherwise similar conditions). In each case analysed, $t_{x(2minOL)}$ is larger than $t_{x(1secOL)}$ and the difference between the two seems to vary as a function of t_x. Eight results are plotted in Figure 4-82 along with lines to represent factor differences between $t_{x(2minOL)}$ and $t_{x(1secOL)}$.

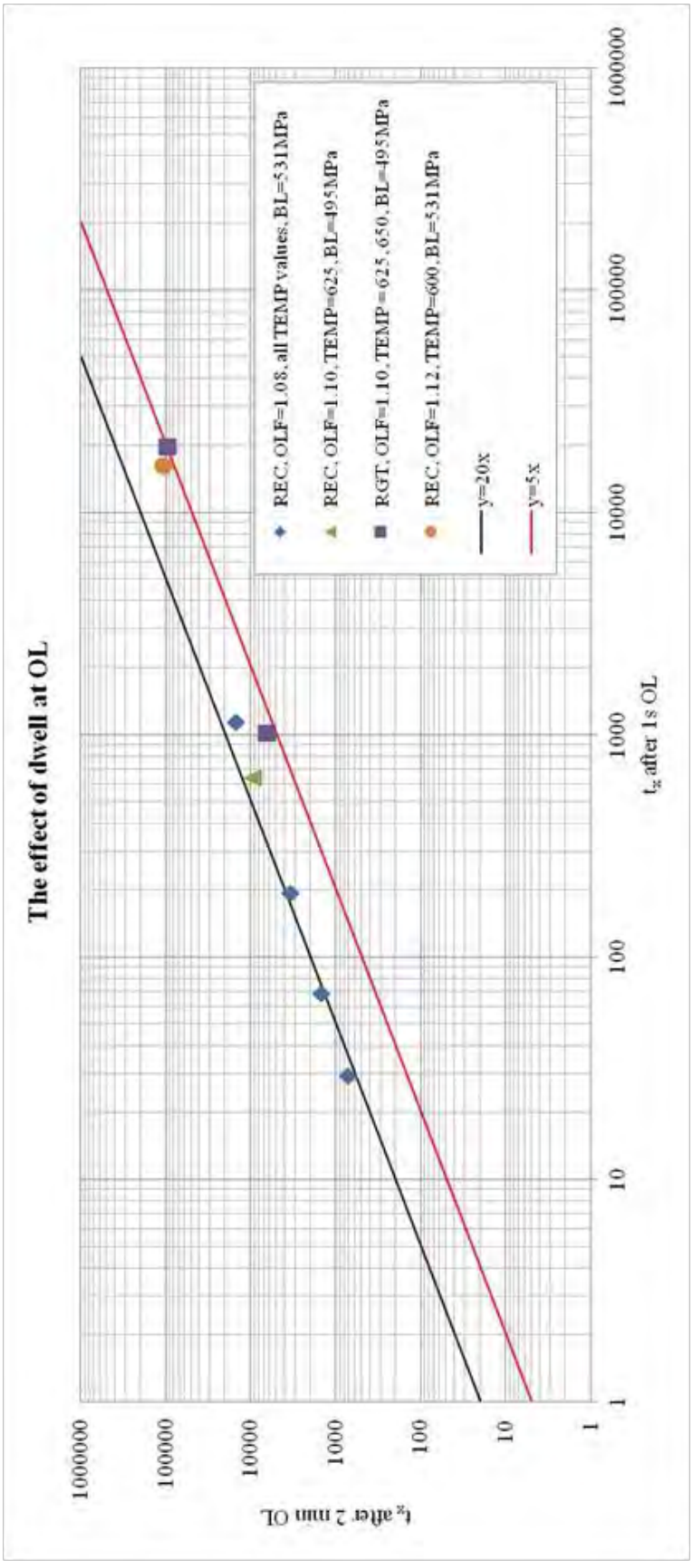


Figure 4-82: Plotting t_x after a one second period at maximum (overload) load against t_x after a two minute period at overload; for otherwise similar conditions.

Since t_{inc} and t_x are analogous to one another in terms of concept, yet they are calculated via different methods; it is useful compare the two. Results show that t_{inc} and t_x calculated for similar conditions lie close to one another which adds further validation to calculations and to each method by which those calculations are made. Such analysis provides extra validation to the model; suggesting that values for t_{inc} and t_x are reliable and useful since they are reproducible by two very different means. A graph of t_{inc} against t_x calculated for each condition is plotted in Figure 4-83.

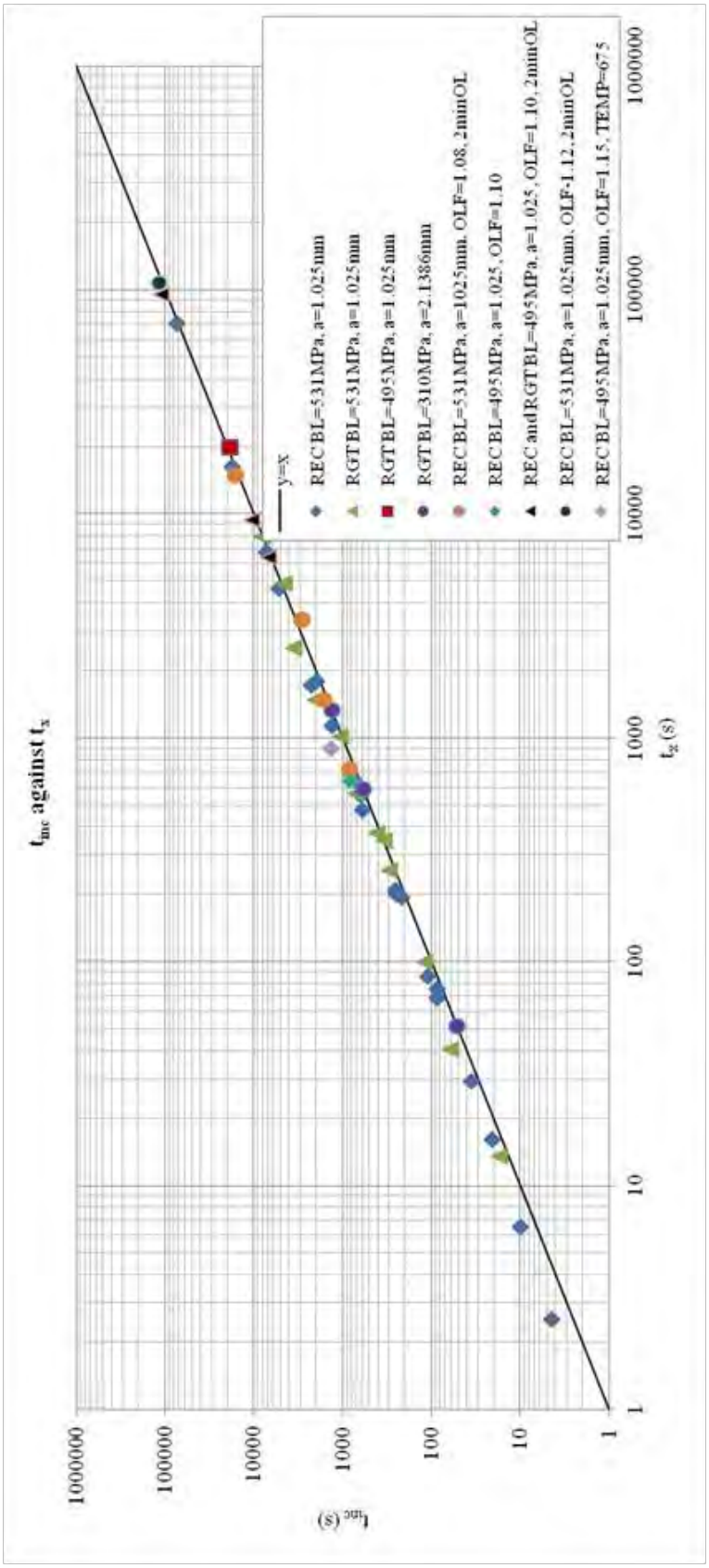


Figure 4-83: Plotting incubation time (t_{inc}) against crossing time (t_x) for all conditions analysed.

4.3.4 Experimentally Derived Incubation Time

As discussed in section 3.2.4, it is possible to use actual crack growth resistance curves where partial retardation has occurred during overload cycling (Figure A-10 for example, and several others presented throughout Appendix VI), to develop an experimentally derived value for the incubation or crossing time. In essence, the experimentally derived t_{inc} is the amount of time during the subsequent dwell period (after initial unloading from the one second overload segment) during which time-dependent crack growth has not occurred. Shown in Table 29, Table 30 and Figure 4-84 are comparisons of experimentally derived t_{inc} values with analytically derived incubation times (t_{inc}) and crossing times (t_x) calculated for similar conditions (in terms of temperature, overload factor and material).

It should be noted that the values for experimentally derived t_{inc} are averaged over a range of stress intensity factor ranges. The sensitivity of t_{inc} (whether experimentally or analytically derived) to the ΔK over which retardation occurs is not well understood and as such, comparisons should be made with care. Nevertheless, Table 29, Table 30 and Figure 4-84 do show that the general trends agree and that they are comparable with one another. Furthermore, Figure 4-84 shows that modelled predictions for t_{inc} are consistently smaller (shorter) than their respective experimentally derived values. This indicates that the modelled predictions might be conservative; i.e. that for a given temperature and overload factor the extent of retardation is slightly under predicted by finite element analysis.

Note also that the calculation of experimentally derived incubations times is only possible if the physical testing conditions are such that partial retardation has occurred. Where full retardation has occurred, the only conclusions which can be drawn are that the incubation time is larger than the subsequent dwell period applied.

Table 29: Summary and comparison of modelled t_{inc}, modelled t_x and experimentally derived t_{inc} values calculated for fine-grained Udimet 720Li (REC).

Temperature (°C)	Overload Factor	Modelled t_{inc} (s)	Modelled t_x (s)	Experimental t_{inc} (s)	Remarks
600	1.05	87	75	826	290s for Ultra-fine CC013
	1.08	1321	1125.5		
	1.10	5259	4588		
	1.12	17281	16041		
	1.15	74103	70570	>3,600	
625	1.05	20.5	16		
	1.08	217	193		
	1.10	748.5	648		
	1.12	1991.5	1773.5		
	1.15	7220	6734.5		
650	1.05	10	6.5		
	1.08	87	68	703	
	1.10	253.5	207.5		
	1.12	630.5	555		
	1.15	2281	1713	3243	
675	1.05	4.5	2.5		
	1.08	35.5	29		
	1.10	110	85.5		
	1.12	247.5	199.5		
	1.15		475		

Table 30: Summary and comparison of modelled t_{inc}, modelled t_x and experimentally derived t_{inc} values calculated for fine-grained RR1000 (RGT).

Temperature (°C)	Overload Factor	Modelled t_{inc} (s)	Modelled t_x (s)	Experimental t_{inc} (s)	Remarks
625	1.05	407	374		
	1.08	4572	4843.5		
650	1.05	60.75	40.5	116	
	1.08	338.25	346	886	
	1.10	1047	1012		
	1.12	3609.5	2498		
	1.15	7997	7847	>3,600	
675	1.05	17	13.5	102	
	1.08	124.5	99.5	525	
	1.10	298	254	798	
	1.12	697	558.5		
	1.15	2044.5	1474		

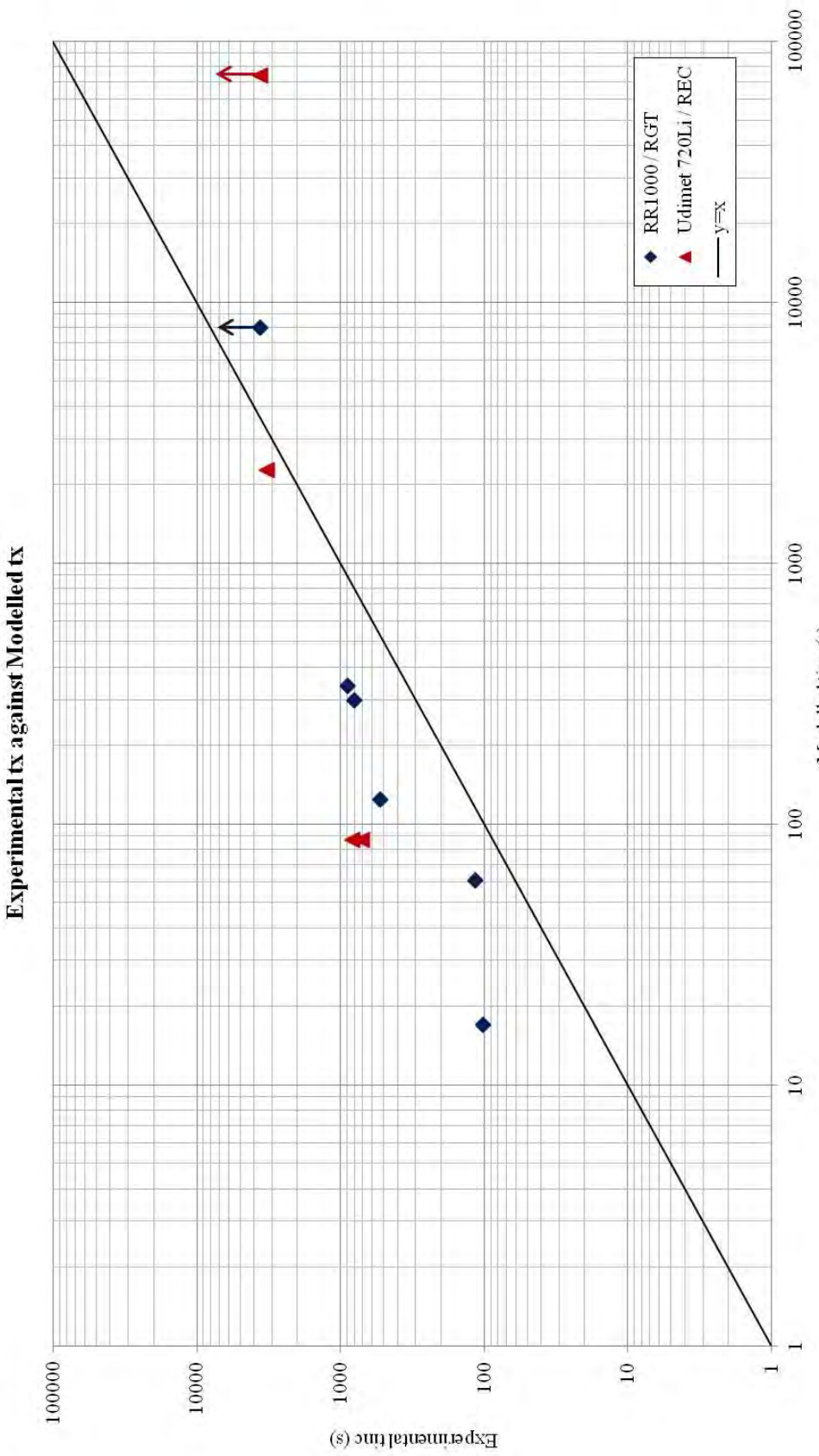


Figure 4-84: Plotting modelled t_{inc} against experimentally derived t_{inc} for all conditions analysed.

5 Discussion

5.1 Dwell Crack Growth Behaviour

5.1.1 Introduction

Baseline, dwell and overload crack growth resistance curves presented in Appendix VI show that there is indeed an increase in high temperature dwell crack growth rates when compared with those associated with otherwise similar baseline loading when tested in air. This agrees well with data gathered from other programmes on a range of alloys.

While it is not possible to infer from the graphs alone the exact mechanism by which this increase in crack growth rates is caused, it is certainly possile to make serveral other conclusions. Namely, that the phenomenon is more pronounced at longer dwell periods, higher temperatures, larger dwell loads and more generally in fine-grained Udimet 720Li when compared with similaraly tested fine-grained RR1000. This infers that dwell crack growth behaviour is condition and alloy specific. Furthermore, the phenomena are shown to be attributed to environmental attack due to the presence of oxygen since the effect is lost when conditions are repeated in a vacuum (Figure A-4, Figure A-5), agreeing with Adrieau and Pineau [6, 38, 84, 88, 91].

These results can be corroborated with fractographic analysis (Appendix VII) to confirm that an increase in crack growth rates as a result of the introduction of a dwell period is accompanied by a change in crack growth mechanism (Figure A-42 for example). With subtle exceptions, the general trend is that high temperature baseline crack growth is associated with predominantly transgranular morphologies, and high temperature dwell crack

growth is associated with predominantly intergranular crack growth morphologies, for fine-grained Udimet 720Li and RR1000. This observation is, at first, counter intuative since intergranular crack paths are associated with multiple changes of direction and as such, might require higher energies (and therefore greater stresses or crack growth driving forces) to propogate. This implies that time at peak load somehow causes the degradation of grain boundaries which makes the intergranular mechanism energetically favourable above a straight, faceted, uniform transgranular crack path.

5.1.2 Fatigue, Creep and Oxidation

Several factors imply that this degradation is caused by the ingress of oxygen due to the combination of high stresses and high temperatures. Firstly, as reported throughout Chapter 2, these conclusions have been drawn before in studies performed on similar alloys. Secondly, these conclusions can be inferred since in general, grain boundaries will oxidise before lattice material which means that grain boundaries are more susceptible to oxygen attack. Hence preferential grain boundary oxygen attack is likely at high temperatures and high stresses.

More specifically however, the effect of oxygen is investigated when high temperature dwell tests carried out in air are compared with those carried out in a vacuum. Crack growth rates in test pieces tested in a vacuum were unaffected when time at peak load was increased from one second (baseline loading) to a 120 second dwell time (Figure A-4). Furthermore; dwell crack growth morphologies in a vacuum are associated with predominantly transgranular

mechanisms, as with baseline loading, cycle-dependent crack growth (Figure A-13 and Figure A-14). Both of these findings provide strong evidence that despite high stresses, high temperatures and longer times at peak load; the increased crack growth rates usually associated with dwell loading (and associated mechanism changes) are lost when oxygen is removed.

It is important to distinguish between competing crack growth mechanisms at this stage. Loosely defined three mechanisms of failure interact and compete with one other during high temperature dwell crack growth; cycle-dependent fatigue which occurs simply as a result of loading and unloading between maximum and minimum stresses (and this component is strongly dependent upon the mean of these stresses); time-dependent inelastic creep strain and time-dependent oxygen embrittlement of grain boundaries. While the removal of oxygen from a testing environment will remove the time-dependent oxygen embrittlement component of crack growth; it does not remove the time-dependent creep component which is induced when time at peak load is increased to a long dwell time. Therefore removal of oxygen does not render the mechanism simply cycle-dependent but rather isolates fatigue and creep interactions.

Therefore it is useful to comment on subtle differences between crack growth rates and mechanisms pertaining to baseline and dwell loading in a vacuum. Generally, dwell crack growth rates in a vacuum are comparable with those associated with simple baseline loading. Nevertheless, for dwell periods of around 3,600 seconds, crack growth rates have been observed to fall down to below those normally associated with cyclic only fatigue in RR1000

(Figure A-27). Furthermore, under these conditions, crack growth mechanisms are shown to be predominantly intergranular (Figure A-75). Given that crack growth rates (in terms of cycles) are slow, and that each cycle takes one hour to complete, data is relatively scarce. Nevertheless the few observations available may indicate that a time-dependent creep component could be blunting the crack tip and slowing crack growth rates down; while also driving the crack into the intergranular regime.

Crack tip blunting as a result of creep is also discussed in section 5.5, where transient cycle-dependent crack growth occurs as a result from switching between the overload waveform and baseline loading. Crack growth rates begin relatively slowly, and stabilise by settling up (Figure A-9, for example), which is suggested to occur due to the blunting of the crack tip during dwell or overload cycling, through which a cycle-dependent fatigue crack must propagate and sharpen to reach fresh material. These examples of crack tip blunting however are suggested to have occurred alongside time-dependent oxygen embrittlement since subsequent examples involve testing in air. As such, comparisons must be made with care. Nevertheless it is possible to conclude from these observations that crack tip blunting due to the accumulation of inelastic creep strain at the crack tip during dwell loading can cause the retardation of crack growth rates when the oxidation component is removed.

Further to this, crack growth rates pertaining to dwell loading are observed to “settle down” when they are applied immediately following a period of baseline loading (this can be seen in Figure A-10, for example). This settling down behaviour is thought to occur because the crack front associated with baseline loading begins relatively sharp and is blunted to some

extent during dwell cycling for the reasons discussed above. This is further evidence to suggest the effect of crack tip blunting, and a full report of these observations is discussed in section 5.5.

Crack growth resistance curves generated by testing samples in laboratory air imply that, when oxygen is present, the increased crack growth rates and mechanism change pertaining to dwell loading is time-dependent, and that it requires high temperatures. For example, dwell crack growth rates at a dwell time of 120 seconds are slower than those observed at otherwise similarly tested dwell periods of 3,600 seconds (this can be seen in fine-grained Udimet 720Li in Figure A-23 when linear, Paris crack growth behaviour of CC019 is compared with that of CC040, 41 and 44). Furthermore, under otherwise similar loading conditions, dwell crack growth rates at temperatures of 600°C are slower than those at 650°C (seen in fine-grained RR1000 in Figure A-26).

Under high temperature baseline loading, the majority of fracture surfaces show a predominantly transgranular fracture mechanism (Figure 4-11), and under long dwell loading (120 seconds or above) at high temperatures, the mechanism becomes predominantly intergranular (Figure 4-12) (provided the tests are carried out in laboratory air). This adds further weight to the suggestion that intergranular dwell crack growth mechanisms are dominated by oxygen effects, since diffusion of oxygen in to the grain boundaries requires both time and temperature, and is indeed assisted and accelerated by both. A more detailed and comprehensive report on crack growth mechanisms is presented in section 5.2.1.

These observations are not inconsequential since high stresses, high temperatures and an oxidising environment represent the conditions in which nickel discs operate in-service. As discussed in section 2.4.3; current lifing methodologies within Rolls-Royce plc. rely upon a simple linear superposition of cycle and time-dependent crack growth components. The exact mechanism by which these components interact and compete is deeply complex and as such, linear superposition lifing methodologies may require further analysis. The models also rely upon the assumption that crack growth rates increase linearly with dwell time, an assumption which also requires analysis, careful thought and investigation in order to optimise the performance of disc alloys. Indeed it may be that simple extrapolation of linear elastic fracture mechanics is limited it terms of its capability to comprehensively model and predict dwell behaviour.

To the debate between advocates of SAGBO and Dynamic Embrittlement these conclusions have little to offer. It may be possible to suggest that bulk oxide formation is unlikely due to the fact that the depth of the "damaged zone" exceeds oxygen diffusion depths predicted by models; something which is discussed in greater detail in section 5.5. Nevertheless time-dependent oxygen effects have indeed been suggested as a competing factor in high temperature dwell crack growth in fine-grained Udimet 720Li and RR1000.

5.2 Influence of Microstructure

5.2.1 Crack Growth Mechanisms

In order to explore the influence of microstructure on time dependent dwell crack growth behaviour in these alloys, it is first important to fully understand and analyse the exact mechanisms by which a crack may propagate through the material. This report has clumped together several distinct types in to two dominating mechanisms: transgranular and intergranular crack growth. More specifically, within these two groups, six distinct ways in which a crack may propagate have been suggested by this programme of research:

1) Faceted transgranular crack growth, along the crystallographic slip planes of each grain. This is shown to occur during fast cycling (pre-cracking or baseline loading) in air or in a vacuum at low temperatures (less than ~500°C), and under relatively lower crack growth driving forces (less than ~20 MPa√m).
2) Planar transgranular crack growth; where the crack follows a more uniform or straight line through the grained structure, occurring only under high temperature fast cycling, where under these conditions more slip systems are active. This is also observed in some overloading tests, when full retardation has occurred.
3) Intergranular crack growth, where the crack propagates between γ' – γ' boundaries.
4) Intergranular crack growth, where the crack propagates between primary γ' – γ boundaries (delineation of primary γ' from the γ matrix in which it resides, as highlighted in Figure 5-1).
5) "True" intergranular crack growth, where the crack propagates along γ – γ boundaries.
6) A variation or combination of any or all of the above failure mechanisms.

Given these phenomena, and presented with fractographs pertaining to a range of testing conditions (Appendix VII), a discussion for the precise mechanism by which cracks propagate through these alloys can be made.

An example is given in Figure 5-1 showing a relatively planar, transgranular crack morphology obtained under fast cycling (baseline). The image also shows areas or regions of "intergranular" failure where either mechanism 3) or 4) (above) has formed part of the fracture surface: i.e. delineation from γ' to γ', or from γ' to the γ matrix has also occurred.

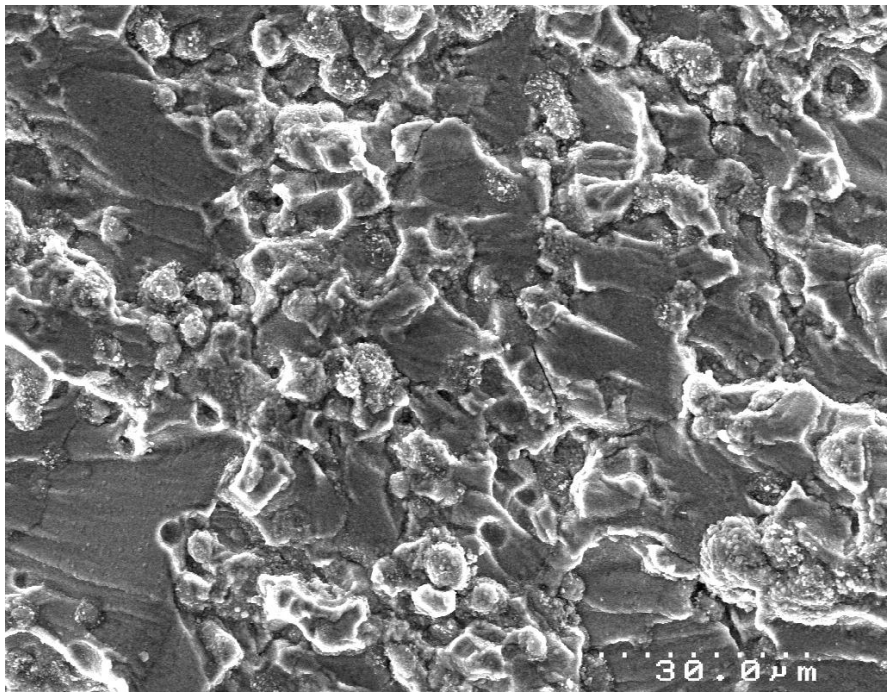


Figure 5-1: Fracture surface of fine-grained Udimet 720Li sample CX027 during high temperature (650°) baseline loading, in air. The image is taken at a ΔK of 14 MPa√m. The image shows transgranular failure of γ grains and "intergranular" failure of primary γ' precipitates.

5.2.2 Influence of Primary γ' Morphology

It is not possible to infer from the fractograph above that where primary γ' "intergranular" failure has occurred, the crack has propagated along primary γ' – γ' boundaries or along γ' – γ boundaries (i.e. by mechanism 3) or 4) from above); but it is possible to suggest from the data that any boundary which involves primary γ' is more susceptible to cracking than the γ – γ boundaries indicating that the most energetically favourable path for the crack to grow is around the boundary of the primary γ' precipitates.

This is evidence to suggest that true "intergranular" crack growth pertaining to high temperature dwell loading (along γ – γ boundaries) may be induced by this delineation of primary γ' from either its neighbours, or from the γ matrix in which it resides. Perhaps intergranular failure is deterred (either for higher temperatures, or for a longer period of time at maximum load) if less primary γ' boundary material is present in the matrix (i.e. if the primary γ' precipitates are larger in volume). This might go some way to explain why coarse grained material (both Udimet 720Li and RR1000), which comprises smaller volume fractions of primary γ' and larger average primary γ' precipitate sizes, displays greater crack growth resistance at higher temperatures when compared with their finer grained cousins. This might also provide a hypothesis to describe one effect of microstructure on the fine-grained material tested: namely that primary γ' precipitate size and morphology might influence high temperature dwell crack growth resistance by helping to induce an intergranular (γ – γ boundary) crack "earlier" (or at lower temperatures and crack growth driving forces).

Furthermore, γ grain size itself is also influenced by primary γ' volume fraction, size and distribution; and grain size is in turn known to influence both transgranular and intergranular crack growth behaviour of these alloys. In terms of time-dependent dwell (intergranular) crack growth, the understanding is that a smaller grain size provides more grain boundary material (for oxidation to occur) and a more uniform crack path (hence requiring less energy). Therefore a fine grain size is thought to be detrimental to dwell crack growth resistance in these alloys. The effect of grain size is discussed in greater detail in section 5.2.3.

As reported above, variation in terms of high temperature dwell crack growth resistance has been confirmed for several fine-grained Udimet 720Li repeated tests (Figure A-6). The analysis of these samples (CC015, CC009 and CX027) has confirmed notable differences in terms of microstructure (Figure 4-37, Figure 4-38, Figure 4-39, Figure 4-40 and Figure 4-41). It follows that for otherwise similarly repeated mechanical tests (in terms of testing conditions) any variation in crack growth rates should be attributed to these natural variations in microstructure since they provide the only variables for such experimental conclusions.

Samples of Udimet 720Li have been confirmed as having more variation in terms of grain size throughout its microstructure. This in turn can affect fatigue crack growth resistance and the creep behaviour of the alloy by mechanisms explored in section 2.4.2, and the influence of average grain size upon high temperature dwell crack growth resistance is explored in section 5.2.3. Importantly however, a sample of Udimet 720Li material has been confirmed as having a multi or bimodal grain size structure, with higher proportions of small (3-5 μm) and large (10-12 μm) grains and fewer proportions of grain sizes between these extremes

(Figure 4-38 and Figure 4-39). This is thought to occur because of the way in which primary γ' can segregate during cast and wrought processing. Large clumps of primary γ' cause the pinning of multiple grain boundaries during solution heat treating which cause the formation of a series of small grains. Areas of the γ matrix which contain fewer primary γ' precipitates however would exhibit a large grain microstructure since these regions would contain fewer grain boundary pinning particles precipitated within the matrix.

As discussed above, fracture surfaces pertaining to both dwell and overload cycling at high temperatures and in air have been shown to contain regions of crack paths where primary γ' has delineated away from the γ matrix in which they precipitate. It follows that these regions represent the lowest energy for which the crack to propagate, since they are preferred even above oxygen embrittled grain boundary material. Therefore a microstructure which contains larger regions of segregated primary γ' might give poorer resistance to crack growth propagation, since these large regions of segregated primary γ' might provide relatively large paths through which a fatigue crack could propagate at low energy.

This has indeed been confirmed to be the case. Microstructures pertaining to more profound segregation of primary γ' are characterised as having more pronounced bimodal grain size structures; and these materials do show poorer resistance to fatigue and dwell crack propagation.

5.2.3 Influence of Grain Size

The breaking of oxides along grain boundaries might occur due to the accumulation of creep strain ahead of the crack tip. The extent to which creep strain may be accumulated (and therefore the cracking of oxides ahead of a crack tip) is strongly dependent upon the grain size of the material. To clarify, this accumulation of creep strain is thought to be beneficial in that it may cause the crack tip to become blunted (explored in section 5.5.3); nevertheless it might also have a detrimental effect upon high temperature dwell crack growth resistance in the following way:

Creep deformation is achieved differently between fine and coarse grain microstructures. Fine grains are notoriously poor at resisting creep deformation since grain boundary sliding can occur more readily as there are a larger number of atoms residing in the grain boundary sites when compared with coarser grain microstructures. Thus, more heterogeneous grain boundary strain accumulation is expected in a fine grain microstructure. For bimodal grain size distributions such as the microstructures investigated and reported above, it has been confirmed that the majority of creep strain is concentrated around finer grain regions [92]. It may be that creep strain accumulation assists in the breaking of oxides formed ahead of the crack tip at an early stage (in terms of their formation). This prevents the formation of dense protective oxides (CrO_2 for example, or simply a thicker and more dense layer of NiO; both of which take longer times to form) and the occurrence of stress relaxation ahead of the crack-tip which is beneficial in resisting environmentally assisted crack growth [93].

The Ellingham diagram (Figure 5-2) indicates that at a temperature of 650°C (923K) at atmospheric partial pressure of oxygen ($p_{O2} = 10^{-1}$), it is possible for an alloy with a composition such as that of Udimet 720Li to form NiO (red), CoO (green) and CrO_2 (purple).

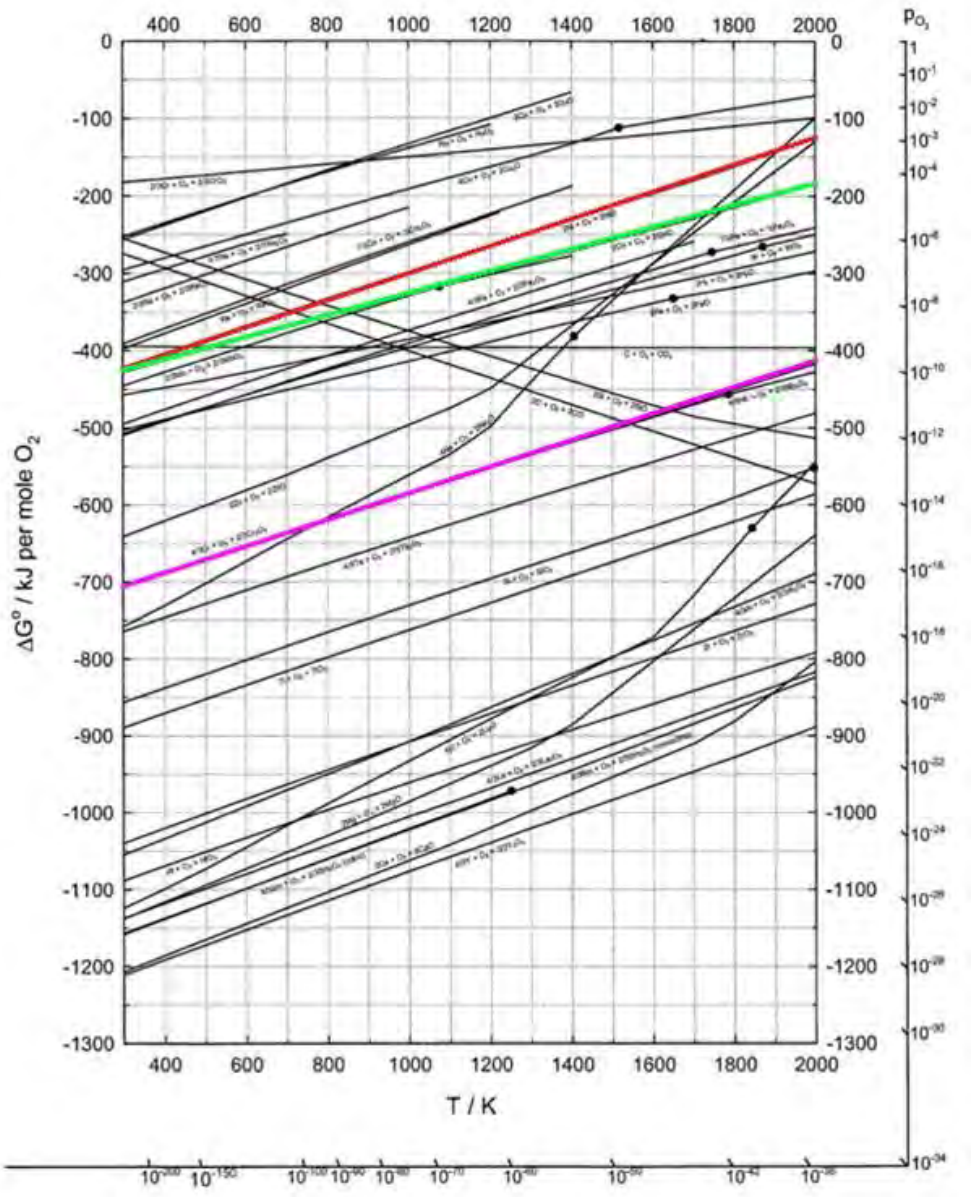


Figure 5-2: Standard free energies of formation of oxides [94].

When fresh metal is first exposed to the air, the partial pressure of oxygen allows for all three oxides to begin forming. However, as the partial pressure of oxygen decreases due to the formation of oxides, the brittle, porous NiO can no longer grow; and more stable, dense CrO_2 dominates the surface.

Therefore, in the case of the propagating crack in a fine grained test piece (CC015), there is perhaps insufficient time for the protective CrO_2 to form because before it is able to dominate and passivate the surface (offering some stress relaxation ahead of the crack tip), the brittle NiO is broken by the accumulated creep strain and the crack progresses; revealing more fresh metal on which NiO will form again. This forming and breaking of brittle nickel oxide continues and so the crack propagates intergranularly and rapidly.

In a coarser grained test piece however, it might be that the accumulation of creep strain is insufficient to break the brittle NiO and so the formation of CrO_2 begins to dominate. Chromium oxide is less porous and is expected to protect against the formation of further oxides along grain boundaries ahead of the crack tip. This in turn allows for stress relaxation ahead of the crack tip which could result in decreased high temperature dwell fatigue crack growth rates in coarser grained material, as observed in CX027.

In addition to the contribution of oxides, when large grains are present in the microstructure, it could be suggested that intergranular fatigue cracks must deviate further distances away from the mode I crack plane as it propagates. This may reduce the effectiveness of an

external mode I driving force, which could in turn improve the dwell crack growth resistance of the alloy.

5.2.4 Differences in RR1000 Test Pieces

The variation in terms of dwell crack growth resistance for fine-grained RR1000 test pieces (Figure A-32, Figure A-36 and Figure A-37) is more difficult to understand. Certainly the microstructure should be reasonably consistent due to their powder processing history. While a comprehensive microstructural characterisation has not been undertaken (and is something for future work), it is clear that there aren't any significant differences in terms of grain size or primary γ' morphology, as there are in the above discussed fine-grained Udimet 720Li test pieces (Figure 4-48, Figure 4-49, Figure 4-50 and Figure 4-51). Most significantly; obvious areas of relatively "ultra" fine grained regions are not found. To clarify; these observations are not quantitive and hence a full study is something to consider for future work.

Tests carried out on fast-cooled (5°C/s) and slow-cooled (0.1°C/s) fine-grained RR1000 reveal marked differences in dwell crack growth resistance as a function of microstructure. As in the above scenario it is first important to define the differences in microstructure which is difficult to do in these particular cases with quantitive accuracy and confidence.

Upon general inspection, it appears as though the two extreme cooling rates have a limited effect upon average grain size (Figure 4-52 through to Figure 4-63). This might be because primary γ' volume fraction dominates grain size control. Despite the differences in terms of

the rate at which the material cools, the level from which it cools is consistently below that of the solvus temperature of primary γ'. These similarities are perhaps the main controlling mechanisms (in terms of grain size) even if the grains form at different rates (and therefore form different morphologies) pertaining to the different cooling rates.

It does appear however as though there are observable differences in primary and secondary γ' size, and there are certainly marked differences in the morphology of the γ' precipitates, as a result of the cooling rate differences. In general, the average size of primary γ' decreases with increasing cooling rate; a phenomenon which occurs due to the reduced amount of time for homogenisation. A slow cooling rate also results in a material with large primary γ' precipitates with significantly less uniform morphologies, with branches, arms and facets (Figure 4-52, Figure 4-55 and Figure 4-58) rather than generally spherical geometries (Figure 4-56 and Figure 4-57 for example) (as with faster or intermediately cooled material).

In discussing the effect that these microstructural differences might have on mechanical properties, it is first important to note that (contrary to the examples discussed above) it appears to have little effect on baseline fatigue crack growth rates or mechanism (Figure A-41). This suggests that cycle-dependent fatigue only crack growth is largely independent of microstructure (at least in these cases) which adds confidence to lifing models which rely on such assumptions.

Dwell crack growth rates however are quite seriously affected; faster cooling rates (and therefore smaller γ' precipitates) relate to faster dwell crack growth rates (and hence poorer

dwell crack growth resistance). Slower cooling rates (and hence larger γ' precipitates) relate to slower dwell crack growth rates (Figure A-41).

The reasons for this may tie in with those suggested above for differences in high temperature dwell crack growth resistance of Udimet 720Li (also as a function of microstructure). It might be that primary, secondary and tertiary γ' size and morphology significantly affects the way in which creep strain is accumulated ahead of a crack tip in the material. Perhaps smaller and more uniformly shaped γ' precipitates (pertaining to faster cooling rates) assist in the accumulation of creep strain to the extent that oxides are relatively easily cracked during the application of high temperature dwell cycling; hence dwell crack growth rates are relatively fast.

The mechanism by which cracks pertaining to high temperature dwell cycling propagate through each category of material is consistently intergranular (Figure A-90 and Figure A-91) and is therefore thought to be dominated by oxygen effects. Nevertheless crack growth in material with larger and less uniformly shaped γ' precipitates might be stunted or slowed due to the accumulation of relatively smaller amounts of creep strain ahead of a crack tip. This might result in the formation of dense, protective oxides during the hold time at peak load and therefore slower high temperature dwell crack growth rates.

5.3 Effect of Overload

5.3.1 Introduction

The baseline, dwell and overload crack growth resistance curves in Appendix VI show that the introduction of an overload segment at the beginning of the dwell waveform can cause the retardation of crack growth rates when compared with those associated with otherwise similar dwell-only waveform loading. Overload factor, dwell time and temperature can have an effect on the extent to which crack growth rates are reduced during the subsequent dwell period, as shown in Table 18 and Table 19. In general, a larger overload factor and a shorter dwell time increases the amount of retardation. This suggests that the retardation effect itself is time-dependent, that under certain conditions, after a certain amount of dwell time, the retardation effect is lost. For example, an RR1000 test piece tested at 650°C with a dwell time of 1,200 seconds and an overload factor of 1.15 usually displays a full retardation effect (Figure A-35). Under similar conditions, for a longer dwell period of 3,600 seconds, the retardation effect is less pronounced (also Figure A-35). It is therefore suggested that the application of a one second overload segment has a retardation effect which lasts for a finite period of time, and that given enough dwell time, the crack will begin to grow at a faster rate towards the end of the cycle.

5.3.2 Crack Tip Plasticity

One reason for this retardation effect is that while nominal stresses unload from the overloaded segment (by 5 to 15% as tested), stresses around the crack tip unload

preferentially (Figure 4-65, section 4.3). This is thought to occur due to the evolution of complex, beneficial residual stresses just ahead of the crack tip (discussed in section 2.6), and these stresses prevent the crack from growing. They then relax over time, as a result of creep, to meet those which are normally associated with dwell loading (Figure 4-64, Figure 4-65, Figure 4-66, Figure 4-67 and Figure 4-68).

If we consider a graph of "stress" against "distance from crack tip" during a period of loading, or holding directly after a loading segment, the stresses are at a maximum immediately ahead of the crack. For atomically sharp cracks the stress is theoretically infinite at this point, however, they are "capped" by plasticity and yield ahead of the crack tip. The stresses then reduce to the nominal load further ahead of the crack. If these loads are reduced by an amount of 15% (for example), then they are reduced by significantly more in the region just ahead of the crack tip. Theoretical models and indeed empirical data from this programme seem to suggest that this reduction could put the crack tip in to compression (down to ~-150 MPa), which would stunt any further crack growth. Whether or not the stresses are negative, they are significantly less than those associated with normal dwell loading and hence cause the retardation of crack growth when compared with these waveforms.

As suggested by Elbert [72], Wheeler [75] and others, this complex beneficial stress state immediately ahead of the crack tip arises due to complex issues relating to crack tip plasticity. The application of maximum (overload) load induces a plastic zone size ahead of the crack tip which is relatively large. Upon partial unloading to dwell loads, the new

effective plastic zone size sits within the original overload plastic zone and hence the crack is pressed shut by a residual wake of plastic deformation around the crack flanks (reported in section 2.6).

This complex, benificial compressive stress state ahead of the crack tip will relax over time to more usual crack tip stress states associated with dwell loading over what is termed a relaxation time or incubation time (t_{inc}) (Figure 4-69). The incubation time depends upon temperature, overload factor, nominal dwell load and (to a degree) the microstructure of the material (Figure 4-71, Figure 4-72 and Figure 4-73; showing the effect of overload factor and temperature, Figure 4-80 and Figure 4-81; comparing the two different alloys). It is suggested that the crack stops growing immediately after unloading from the maximum overload load while the compressive stresses "relax" (as a result of high temperature creep), and then continues to grow at a normal dwell rate after this relaxation has occured. Hence, if the relaxation time is shorter than the dwell time, crack growth rates are partially retarded since for the first portion of the subsequent dwell period the crack tip stresses are small and the crack does not grow, and for the second portion of the dwell period (after the crack tip stresses have fully relaxed) the crack grows normally; in a time-dependent manner similar to usual dwell crack growth mechanisms. If however the conditions are such that the relaxation time is longer than the dwell period, the stresses at the crack tip will never fully relax within one susequent dwell cycle. Therefore the time-dependent creep and oxygen embrittlement components of the failure mechanism are almost completely lost, and the rate at which the crack grows is fully retarded back down to those associated with cyclic fatigue only.

Based on this concept, larger overloads introduce a deeper compressive residual stress, and lower temperatures delay the relaxation of these stresses ahead of the crack tip, and consequently both give larger retardation effects. This is illustrated both by the empirical data and analytical methods. General trends in the empirical data show that for otherwise similar conditions the retardation effect is more pronounced at higher overload factors (Table 18 and Table 19). They also show that for otherwise similar conditions the retardation effect is more pronounced as temperature decreases. A third trend shows that for the same conditions, fine-grained RR1000 displays greater retardation effects when compared with similarly tested fine-grained Udimet720Li.

These three observations are also captured by the analytical data which show both incubation time, t_{inc} and crossing time, t_x increases with overload factor and with decreasing temperature (Figure 4-71, Figure 4-72, Figure 4-78 and Figure 4-79). The models also show that for the same conditions t_{inc} and t_x are larger (longer) for fine-grained RR1000 (RGT) than they are for fine-grained Udimet 720Li (REC) (Figure 4-80 and Figure 4-81).

It is important to highlight that "degree of retardation" (full, nearly full and partial) and indeed the experimentally derived value of incubation time; in terms of empirical data analysis is in some way analogous to t_{inc} and t_x, which are generated analytically. For test conditions which resulted in partial retardation effects it follows that the empirical incubation time is below the subsequent dwell period. It is therefore possible to use crack growth resistance curves to estimate empirically derived values for incubation time using techniques discussed in section 3.4. Nevertheless a simple comparison of experimentally derived

incubation times and those generated analytically must be performed with care. As reported in Appendix V, real life crack tip stresses are shown to have been modelled reasonably accurately despite the limitations of using a finite radius notch root. Although a real fatigue crack is atomically sharp, stresses around the crack tip are not infinite since they are associated with creep strains which allow stresses to reach a maximum as a function of the yield stress of the material. These maximum stresses are shown to have been modelled well by finite radius notch mesh geometries used in this programme, as reported in section 3.4.3 and Appendix V. However, it is important to note that modelled t_{inc} and t_x values are generated by running simulations at ΔK values lower than those associated with dwell and overload fatigue tests carried out empirically. (The reasons for this are discussed in subsequent paragraphs). The effect of ΔK on the retardation effect is not fully understood and as such empirical and analytical incubation times should be compared with one another with caution.

Nevertheless, general trends can be compared with confident conclusions. As previously discussed these general trends between empirical and analytical methods agree: that degree of retardation, t_{inc} and t_x all increase with increasing overload factor and decreasing temperature. Experimental and analytical incubation times are plotted against one another in Figure 4-84, which shows not only that the trends agree but that analytical data is consistently conservative with respect to empirical data. These factors adds confidence to both sets of analyses (empirical and theoretical), and implies that the testing methodology is capable of modelling and representing analytical techniques and indeed vice versa. The agreement adds

confidence to lifing methodologies within Rolls-Royce plc. which rely on empirical and analytical data alike to understand retardation phenomena.

It is also important to highlight the areas of concern in terms of analytical data. Firstly, simulations failed to run under certain conditions. These were usually associated with fine-grained RR1000 modelled under high loads and low temperatures. SC03 referred to the failure event as a "creep failure" implying that under such conditions the material would have fractured as a result of creep. The conditions represent the gaps which are left in Figure 4-72 and Figure 4-79. Clearly the material does not fail under such conditions since empirical testing is carried out at similar temperatures and with even greater stresses (and hence larger ΔK values). A comprehensive understanding as to why these failures occur is therefore required and might be something to explore in future work. Nevertheless the general trends (that t_{inc} and t_x increase with increasing overload factor and decreasing temperature) are still observed and agree well with models run on fine-grained Udimet 720Li and indeed with empirical data.

5.3.3 Crack Growth Mechanisms

The stress unloading and subsequent relaxation model fits well with fractographic analysis too. It follows that if the conditions are such that full retardation back to cycle-dependent crack growth occurs during the overload segment, the crack will grow transgranularly in a similar way to baseline loading (Figure 4-15). This is because the stresses at the crack tip never relax back to those high enough to allow for oxygen embrittlement during the

subsequent dwell period after unloading from the overload. The crack therefore only ever grows as a result of unloading down to the minimum load and loading back up to the maximum (i.e. cycle only fatigue). It follows also that if only partial retardation has occurred, crack growth morphologies will be intergranular (Figure 4-14). This is because crack tip stresses have fully relaxed at some point during the subsequent dwell period back to those normally associated with dwell loading, after which, time-dependent oxygen induced embrittlement will begin to influence crack growth rates and mechanisms. These mechanisms are known to cause intergranular failure due to the diffusion of oxygen along grain boundaries ahead of the crack tip due to high stresses (now that they have fully relaxed back) and high temperatures. A summary of these observations is presented in Table 23 and Table 26; which confirm the conclusions made above.

These observations rely upon simple analysis of fractographs assuming that embrittlement is sensitive to the crack tip stress state, and that cycle-dependent failure occurs by purely transgranular mechanisms and that time-dependent oxidation dominated failure occurs purely by intergranular mechanisms. While the fracture surfaces are indeed dominated by these respective mechanisms, there are subtleties in terms of the observations which require explanation. For example, the vast majority of what have been labelled “intergranular” dwell and partially retarded overload crack growth fractographs do not show large regions of clean grain boundary facets, as illustrated in Figure 2-14 (as an example of intergranular failure). Instead fracture surfaces appear rough and almost ductile in places. There are several points to make about these observations. First, that when these fracture surfaces are compared with those associated with high temperature baseline, cycle-dependent crack growth morphologies

there are very obvious differences (Figure 4-12 cf Figure 4-11). This highlights the fact that there has indeed been a fundamental change in the predominant mechanism even if it is not observed to be complete.

Secondly, the crack path and therefore fracture surface is likely to be heavily influenced by primary γ' precipitates. It may be that while γ grain boundaries are vulnerable to oxygen embrittlement, so too are the boundaries between primary γ' and γ, and indeed those between neighbouring primary γ' precipitates. Hence delineation of these boundaries involving primary γ' may occur and thus form part of the crack growth mechanism and morphology. It is suggested that fractographs in Appendix VII which do show quite clear faceted intergranular crack growth comprise examples of primary γ' segregation, and hence in the regions where it is in short supply crack morphologies are far neater in intergranular appearance. Regions which do not appear clearly faceted are likely to represent delineation of primary γ' from the matrix rather than simple intergranular (γ – γ) crack growth.

Since RR1000 is powder processed and hence has finer and more uniformly distributed primary γ' (not confirmed in this programme of research but from Reed [1]) these regions are themselves finely distributed among otherwise faceted intergranular crack growth morphologies. It is true that examples of clean, faceted intergranular crack growth morphologies are observed on Udimet 720Li test piece fractographs and not on those generated by testing fine-grained RR1000, which adds confidence to these discussions. Furthermore, both alloys (Udimet 720Li and RR1000) are explored in their fine-grained

versions in this programme; hence primary γ' precipitates are within the same order of magnitude in terms of size as the γ grains themselves.

As discussed in previous sections, primary γ' is known to pin grain boundaries during solution heat treatment. Therefore segregation of primary γ' (resulting from segregation of alloying elements) is likely to cause a degree of bimodality in terms of the distribution of grain sizes. Given that primary γ' segregation is thought to effect crack growth rates it follows that a trend between "degree of bimodality" and crack growth resistance might be found. While fine-grained microstructures are thought to possess inherently good fatigue properties, it might be that a microstructure with a slightly larger average grain size could possess superior dwell crack growth resistance if the grain size is more uniform (and hence primary γ' is shown to have been more uniformly distributed throughout the γ matrix). A full discussion on these issues is presented in section 5.2.

Empirical descriptions of crack growth mechanisms are inherently complex. Nevertheless for the reasons discussed above, a comprehensive and critical analysis of crack growth mechanism is required. This analysis has been undertaken by the sectioning of fracture surfaces and by careful observation of their morphologies from a side profile (a comprehensive study of this kind has not been undertaken, but rather a representative few to show the difference between baseline and dwell crack growth mechanisms). The conclusions from these images (Figure 4-21, Figure 4-22 and Figure 4-23) agree with those made from studies using conventional fractographs, in that they also highlight a clear distinction between baseline cycle-dependent crack growth and time-dependent dwell crack growth

morphologies. It is difficult to suggest from them that (for intergranular dwell crack growth) the surface (i.e. the crack path) represents grain boundaries across the sample (therefore proving that the crack had propagated in the intergranular regime). Nevertheless, assuming that grain size and shape is relatively uniform it could certainly be inferred.

5.3.4 Fatigue, Creep and Oxidation

It is important to note that the retardation phenomena discussed above highlight the significance of crack tip stress states and plasticity on time-dependent dwell crack growth phenomena. Without stress, or rather, while crack tip stresses are low, it appears as though environmental degradation is severly limited. Hence the data agree well with those gathered in previous programmes and for different alloys to suggest that both SAGBO and dynamic embrittlement are stress driven phenomena.

The method by which analytical incubation time, t_{inc} is calculated assumes that crack tip stresses must reach those associated with dwell crack tip stress states before time-dependent accelerated dwell crack growth can occur. Hence for the duration of the incubation time it is assumed that the crack is stunted (or stopped althogether) in terms of its propagation through material. Nevertheless, there may be a threshold value (in terms of crack tip stresses and associated K values) which would cause the onset of time-dependent, accelerated dwell crack growth which are below those normally associated with dwell loading at simulated and tested ΔK values. These are further reasons to suggest that comparison between emprically derived "incubations times" and those generated analytically should be compared with caution. Time-

dependent dwell crack growth threshold values and the influence of test temperature and dwell time are discussed in section 5.4.

The results also highlight the importance of creep resistance for these applications. Good creep resistance delays the relaxation of crack tip stresses and hence increases the retardation effect. This is highlighted by comparing modelled t_{inc} values and empirical retardation effects observed in fine-grained Udimet 720Li with those observed in fine-grained RR1000. The optimisation of fatigue resistance (by decreasing grain size for example) may result in a decrease in creep resistance; which in turn may have a detrimental effect to overal performance when subjected to overload waveforms.

5.3.5 Crack Tip Blunting

There is a further trade-off however in that materials with low creep resistance can display a high degree of fatigue crack tip blunting; a phenomenon observed in this programme and discussed in more detail in section 5.5.3. Crack tip blunting as a result of creep and plasticity is suggested as an explaination of the transient behaviour in terms of crack growth rates upon switching between loading waveforms. It may be that the "settling down" of dwell crack growth rates immediately following a period of baseline loading (Figure A-10 for example) occurs due to the fact that crack tip fronts associated with baseline cycling are relatviely sharp and become blunted as time-dependent crack growth occurs when dwell cycling is applied. The rate at which crack growth becomes stable is still relatively high of course, because the dominant mechanism under these conditions becomes that of oxygen induced

grain boudary embrittlement. Nevetheless it seems as though dwell crack growth rates comprise a crack tip blunting component which has a measureable effect in terms of the overall crack growth rate; and that this effect is positive in that it slows the crack down to some extent.

It might be that crack growth fronts pertaining to overload cycling become blunted to an even further extent when compared with otherwise similar dwell cycling (due to higher bulk stresses in the overload segment) and that crack tip blunting becomes part of the mechanism by which crack growth rates are retarded during overload cycling. This is evidenced by the "settling down" behaviour of crack growth rates pertaining to overload cycling immediately following a period of dwell cycling (this is also highlighted in Figure A-10; although almost every crack growth resistance curve presented throughout Appendix VI which contains overload data shows similar behaviour). The effect of crack tip blunting during overload cycling is further evidenced by the fact that crack growth rates pertaining to baseline loading immediately following a period of overload crack growth begin much slower than usual, and stabilise by "settling up" (Figure A-9 shows two clear examples of this). This provides evidence that the crack tip might have become blunted to some extent during overload cycling, and is sharpened by the application of baseline loading.

A further observation is made by considering the crack growth resistance curve in Figure A-15, which shows the effect of switching the waveform from baseline loading to overload cycling. This particular transition rules out the effect of an oxygen induced damage zone ahead of the crack tip since it is unlikely to have formed during baseline loading.

Nevertheless overload crack growth rates are observed to have "settled down", begining much faster and stabilised by slowing down. This isolates the crack tip blunting effect; confirming the phenomena as a contributing mechansim in terms of crack growth retardation according to overload cycling.

These phenomena are discussed in greater detail in section 5.5. Nevertheless here it is important to highlight that crack tip blunting is not fully captured by the implimentation of analytical models developed as part of this programme. Therefore since blunting of the crack tip is thought to provide some crack growth retardation during overload cycling, this further complicates comparisons between empirically derived data and those gathered analytically in terms of "degree of retardation" or experimentally derived incubation time.

5.3.6 Influence of Microstructure

Microstructural influences on dwell crack growth rates is explored in much detail in section 5.2; nevertheless here it is worth discussing any influences microstructural variations might have on the retardation effect itself.

Clearly, incubation time (and therefore "degree of retardation") is a function of the creep properties of the alloy. If a particular alloy (or microstructure) possesses poor creep resistance, crack tip stresses may creep back more quickly to those normally associated with dwell loading (after having preferentially unloaded immediately following the partial

unloading of nominal stresses from the overload segment) when compared with otherwise similarly stressed microstructures with superior creep properties.

This is indeed confirmed by the data in this programme. Udimet 720Li test pieces CC013, CC014 and CC015 are all confirmed as comprising much finer grain sized microstructures (Figure 4-37, Figure 4-38 and Figure 4-39; reported in detail in section 5.2), and materials with finer grained microstructures possess poorer creep resistance when compared with coarser grained microstructures (reported in section 2.4.2 and discussed throughout section 5.2). Crack growth rates in all three test pieces do indeed show a degree of retardation (in terms of crack growth rates) during the application of overload cycles when compared with otherwise similar dwell crack growth rates (Figure A-7). Nevertheless the extent to which crack growth rates are slowed down is less pronounced when compared with otherwise similarly tested Udimet 720Li from batches of material known to comprise coarser grained microstructures (test piece CC003 for example, (Figure A-17); showing a repeat, in terms of testing conditions, of those applied to test piece CC013; and showing a greater degree of retardation). Experimentally derived values for the incubation time were around 826 seconds for test piece CC003 and around 290 seconds for CC013 (Table 29); a reduction of around 60 – 65% despite similar testing conditions.

(It is important to highlight here that, given the discussion in 5.2.3; grain size also has a significant impact on the environmentally assisted dwell (only) crack growth resistance of the alloy. Therefore, these factors may compete with those discussed above to influence the extent to which dwell crack growth is reduced during overload cycling. It is difficult to

suggest with the data available, which factor (if either) dominates the effect; nevertheless the general observations are made that both creep resistance and dwell crack growth resistance (both influenced by microstructure) may influence the overload retardation effect.)

Furthermore, the effect of microstructure is also examined when incubation times (whether analytically or experimentally derived) pertaining to Udimet 720Li are compared with those pertaining to RR1000. Analytically derived incubation and crossing times for otherwise similarly modelled conditions are longer for RR1000; known to possess superior properties in creep (and indeed superior dwell crack growth resistance) when compared with Udimet 720Li (Figure 4-80 and Figure 4-81). This trend is also highlighted by Table 29 and Table 30; which shows that for each condition where a comparison can be made; analytically derived incubation times, crossing times and experimentally derived incubation times are all longer for RR1000 when compared with similarly analysed Udimet 720Li.

To clarify; a complete and comprehensive microstructural characterisation has not been carried out on all test pieces tested. Nevertheless careful conclusions can be drawn from the data available and referenced above: namely that finer grained microstructures (associated with poorer creep resistance, and poorer resistance to dwell crack growth) give less pronounced retardation effects when compared with otherwise similarly tested coarser grained microstructures.

5.3.7 Time at Overload

One of the most complete methods by which to summarise the conclusions pertaining to dwell and overload crack growth rates is to test materials with a "dwell time" at the peak overload load. Such waveforms represent in-service conditions even more thoroughly since the time at which stresses and temperatures are at a maximum (i.e. during take-off) is usually itself a dwell time.

Analytical models to calculate t_{inc} and t_x indicate that incubation times are considerably increased when time at overload is increased from 1 second to 120 seconds (Figure 4-82). There doesn't appear to be a clear trend across the relatively limited number of conditions analysed between variables such as overload factor, test temperature and background load and the extent to which t_{inc} and t_x increases; nevertheless incubation and relaxation times increase between 5 and 20 times when compared with similar 1 second only overload periods for the conditions analysed.

This increase could be explained by the fact that further, deeper and more profound creep strain accumulates at the crack tip during the 120 second hold period at peak load when compared with just a 1 second hold at this load. Crack tip stresses then unload preferentially as "normal" (as with 1 second overload waveforms) upon unloading, but they relax back much more slowly than previously modelled since the extra creep damage has had a work-hardening effect. This adds to the discussion that the accumulation of inelastic creep strain at the crack tip is itself a time-dependent mechanism and that it can be beneficial in terms of crack growth rates.

One might therefore expect empirical data to suggest that 120 seconds dwell (or more) at the overload results in a more profound retardation effect when compared with retardation in similarly tested 1 second overload waveforms. While the sample size in this programme is relatively small, comparisons suggest that this is not the case: the introduction of a 120 second hold period at the overload load has little effect on the degree of retardation (Figure A-20 and Figure A-39).

This is because, while creep and plasticity models suggest further incubation times (which may very well accurately represent empirical activity); they fail to include time-dependent high temperature dwell crack growth *during* the 120 second hold period at peak (overload) load. Based on previously discussed concepts, it is suggested that during this time, fast intergranular crack growth occurs as a result of time-dependent oxygen induced grain boundary embrittlement. This is then followed by a period of little to no crack growth when the crack tip stresses unload preferentially as the nominal load unloads from the overload to the dwell load. Crack tip stresses may very well then relax back to those normally associated with dwell loading over a relatively longer period of time due to the accumulation of inelastic creep strain at the crack tip during the overload segment; which would mean that under otherwise similar conditions the crack might be fully retarded over a longer dwell time. Nevertheless this crack retardation is balanced by fast, time-dependent dwell crack growth at the beginning of the cycle, during the “dwell” at overload.

This rather eloquently (although with great complexity) illustrates the fact that there are many mechanisms of fatigue crack growth which compete and combine to make up whole, total

crack growth rates and mechanisms. Cycle-dependent crack growth relies simply on loading and unloading between maximum and minimum stresses and is dependent in part on temperature, microstructure mean stresses and R ratio. Time-dependent mechanisms such as oxygen induced grain boundary embrittlement and creep are also influencing factors which depend largely upon time at peak load, temperature, atmosphere and microstructure; and even compete with one another when loading waveforms are complex and involve overloading, partial unloading and various dwell times at various load levels. Hence lifing methodologies for these applications are complex and must involve careful analysis of cycle and time-dependent crack growth components and understanding of retardation phenomena.

5.3.8 Implication of Data

Finally, it is important to put these findings in to context in terms of their application to, and impact upon complex lifing methodologies within Rolls-Royce plc. As discussed, current linear superposition lifing methodologies which represent take-off and climb associated crack growth rates as a single dwell cycle have been proven to be unnecessarily conservative. In actual fact, the effect of partial unloading within the dwell waveform causes the retardation of crack growth rates for all conditions and for a variety of fairly well understood reasons. Therefore empirical and analytical understanding generated in this programme has been combined with extensive stress analysis and associated lifing stratagies within Rolls-Royce plc. to include a retadation parameter alongside current linear superposition of cycle and time-dependent crack growth rates. These retardation parameters are alloy and condition specific and have been generated for fine-grained Udimet 720Li and RR1000 both

empirically and analytically using (in part) data gathered in this programme. For some conditions, the lives of compressor disc engine components have been shown to increase by around 10,000 flight hours due to the implimentation of these retardation parameters.

Another implication of these findings is that it might be beneficial, in terms of crack growth rates, to change the flight profile of a typical journey. If the ratio between engine capacity during take-off and engine capacity during climb is high, crack growth rates might be reduced during the climb stage of the flight cycle. This is also true when considering the degree to which climb associated engine capacity is higher than that which is associated with the long crusing period. This is due to the higher effective overload factor (the ratio of stresses pertaining to take-off and those pertaining to climb, for example). In the same way that increasing the overload factor in stress waveforms applied to test pieces causes the reduction or retardation of subsequent time-dependent dwell crack growth rates, increasing the engine capacity during take-off might cause a similar effect in service during the climb stage.

Put more pratically, it means that if aircraft operators take-off and climb more quickly (and hence at greater engine capacity) the total life of the engine might be improved significantly. Cruising represents one of the more efficient parts of the flight cycle, hence if altitude can be reached more quickly, a greater portion of the total flight profile can be assigned to cruise associated engine capacity. This might improve fuel comsumption and even flight duration.

Furthermore these changes might have a beneficial impact upon passanger comfort since during the take off and climb stages passangers are usually required to remain seated. If these stages are performed more quickly, this gives greater freedom and mobility to passengers. Furthermore it enables stewarding staff to bring out refreshments at an earlier stage in the flight.

5.3.9 Summary

To sumarise therefore; empirical high temperature dwell crack growth data obtained for fine-grained Udimet 720Li and RR1000 agree well with those gathered for other alloys. Longer dwell periods at peak load results in increased crack growth rates when compared with baseline loading, and this increase is indeed associated with a mechnism change from transgranular (for baseline) to intergranular (for dwell). The phenomenon is alloy and condition specific, occuring at temperature and in air. Furthermore it is possible to "switch off" this time-dependent mechanism (at least, in part) by introducing an overload and subsequent unload segment in the dwell waveform, which significantly retards crack growth rates. Empirical and analytical data seem to suggest that this retardation is due, in part, to preferential unloading of crack tip stresses while nominal stresses unload from the overload to the dwell load. Further influencing factors might include crack tip blunting due to creep which occurs at high temperatures and under extended periods of relatively high loads. The extent to which retardation occurs depends upon overload factor, background load, test temperature, dwell time and microstructure. Effects of retardation must be included in current linear superposition lifing methdologies in order to optimise engine performance.

The current testing technique has proven to be successful in identifying retardation behaviour, and analytical techniques have been validated in helping to understand the mechanism by which overload crack growth retardation occurs.

5.4 Time-dependent ΔK_{th}

5.4.1 Introduction

Many of the implications of the above discussions rely upon the assumption that time-dependent crack growth occurs only after a critical threshold is applied, in terms of "effective" crack tip ΔK values. It is assumed that while crack tip stresses are relatively low, time-dependent, intergranular crack growth does not occur. The analytical derivation of t_{inc} for example simply refers to the time it takes for crack tip stresses to relax back to those which are normally associated with otherwise similar dwell loading. Time-dependent, fast intergranular crack growth may actually begin to occur at effective ΔK values well below those represented by that particular relative dwell cycling. For these reasons it is important to try to define, for a series of representative in-service conditions, the threshold for which time-dependent crack growth occurs and indeed the mechanism by which it occurs, even at threshold.

5.4.2 Crack Growth Mechanisms

Several conclusions can be drawn from the testing of Udimet 720Li to investigate a threshold in terms of time-dependent crack growth. Firstly, high temperature time-dependent crack growth according to dwell cycling occurs in the intergranular regime, which is confirmed even at near-threshold (Figure A-70 for example). Assuming that this intergranular mechanism of crack growth is due to the oxygen embrittlement of grain boundaries, explored in previous sections, this implies that the maximum stress relating to the ΔK value required to

initiate crack growth is sufficient to assist the ingress of oxygen along grain boundaries. It also implies that despite the irregular crack path it becomes energetically favourable to propagate along grain boundaries even at low ΔK values.

More specifically however, a transition band (in terms of switching between transgranular crack growth pertaining to 1 Hz sinusoidal cyle-dependent fatigue and intergranular crack growth pertaining to high temperature two minute dwell cycling) was observed in test piece CC040 (Figure 4-20). This band of crack growth is predominantly transgranular in terms of mechanism, switching over to intergranular only after a definite period of crack growth has occurred (Figure 4-19 and Figure 4-20).

The further analysis of crack growth mechanisms, made by studying SEM images taken from sectioned test pieces looking along the face of the crack (Figure 4-21, Figure 4-22 and Figure 4-23) reveal that crack growth according to dwell cycling occurs in the intergranular regime, and that crack growth according to fast-cycling (1-1-1-1 baseline) at high values of ΔK occurs in the transgranular.

Interestingly, they also reveal that crack growth pertaining to fast-cycling at lower values of ΔK (~11 MPa√m) occurs according to a mixture of modes where (more specifically) the crack will propagate through large γ grains (transgranularaly) but preferentially along the boundaries of primary γ' and the γ grains; and even between the boundaries between γ grains through regions of relatively fine grain sizes. These phenomena are explored in more detail in section 5.2.1; nevertheless here it is important to highlight that it might be the breaking of

these particular boundaries at lower ΔK values, even under fast-cycle fatigue, which triggers the propagation of time-dependent high temperature dwell cracking along γ grain boundaries when dwell stress cycles are applied.

5.4.3 Effect of Dwell Period

Furthermore, comparisons between the values of the stress intensity factor range required for crack growth (ΔK_{th}) for fatigue or cyclic-only dependent crack growth and those relating to time-dependent crack growth can be made. At the conditions tested, the fast-cycle fatigue threshold was shown to lie below the threshold for time-dependent crack growth (Figure A-21). In Figure A-21 both fatigue and dwell values for ΔK were obtained by applying the load shedding technique. It is important to highlight that (in some cases) the method by which the fatigue threshold was obtained (or rather, estimated) was different to that by which time-dependent thresholds were obtained. Namely; that fatigue threshold values were obtained by applying the decreasing ΔK technique (by "load shedding") and time-dependent threshold values were (in the majority of cases) obtained by applying an increasing ΔK technique. Nevertheless there is some evidence (Figure A-22) to suggest that either technique gives relatively similar results within acceptable scatter, and these observations are discussed in subsequent paragraphs.

The observation that fatigue thresholds lie below time-dependent threshold values may be attributed to several factors. It may be that the extended periods of high temperature stress causes the blunting of the crack tip as reported in detail in section 5.5.3. This may occur at

threshold (or even below threshold, in the cases of "increasing ΔK" tests) and hence would result in the suppression of crack growth until a greater ΔK is applied to overcome this blunting effect. It may also be explained by the fact that crack paths are shown to be intergranular in morphology and hence irregular in terms of their propagation through the material. These multiple changes in direction might require higher ΔK values in order to initiate crack growth.

5.4.4 Influence of Microstructure

Furthermore, investigations have revealed the influence of microstructure (namely, grain size) in terms of time-dependent threshold values for the material. The data suggest that a finer grain size causes both an increase in linear Paris Law crack growth pertaining to high temperature dwell cycling and a decrease in the stress intensity range required for this type of crack growth to initiate, when compared with larger grain sizes (Figure A-23 for crack growth rates and time-dependent threshold values and Figure 4-46 and Figure 4-47 for a comparison of grain size distributions). This can be seen in the analysis of test piece CC045, which was tested according to a dwell period of 1,200 seconds. Given the above discussion, it was expected that testing the material under such conditions might place the threshold ΔK value obtained at larger than those associated with 120 second dwell cycling (CC040, CC041 and CC044: ~12-14 MPa√m) and smaller than those associated with 3,600 second dwell cycling (CC019: ~18.5 MPa√m). Nevertheless the data showed a threshold value significantly lower than even those associated with 120 second dwell loading; a value of around 10.5 MPa√m (Figure A-23). Since test piece CC045 was shown to comprise

significantly smaller grains in terms of size (Figure 4-46 and Figure 4-47); it is therefore thought that the discrepancy in terms of threshold values for time-dependent crack growth may be explained, at least in part, by these differences in microstructure.

A more detailed analysis of the effect of microstructure on high temperature dwell crack propagation behaviour of fine-grained Udimet 720Li is presented in section 5.2. Nevertheless, specifically relating to near threshold behaviour; it might be able to suggest given the data available that coarser grained microstructures require higher stress intensity factor ranges to cause the onset of intergranular failure according to time-dependent dwell crack growth when compared with finer grained microstructures. Similarly to the discussion presented in section 5.2, the reasons for this may be related to the susceptibility of each respective microstructural variation to the accumulation of creep strain around the crack tip. More finely grained microstructures will accumulate larger and more profound amounts of creep strain, which may therefore lead to the breaking of brittle oxides as they form along grain boundaries just ahead of the crack tip; which when compared with coarser grained microstructures (which accumulate smaller amounts of creep strain at the crack tip for the same levels of crack tip stress or stress intensity factors) might require smaller driving forces to occur.

Furthermore, test piece CC011 represents a repeat, in terms of testing conditions, of those applied to test piece CC019; namely a dwell period of 3,600s at 650°C in air. Nevertheless; both the linear crack growth rate and the threshold values for crack growth to initiate are significantly different when the data is compared (Figure A-23). Linear crack growth in test

piece CC011 is unusually slow (for similar values for ΔK) and the threshold value for crack growth to initiate is relatively high (~27.5 MPa√m) when compared with test piece CC019 (~18.5 MPa√m). Although a comprehensive microstructural study has not been carried out as part of this programme, Stevens [95] found test piece CC011 to have an average grain size of 13 μm; significantly larger than those associated with more usual behaviour.

5.4.5 Effect of Testing Procedure

Finally, the effect of testing methodology has also been investigated. Although the sample size is relatively small it appears as though time-dependent threshold values for a 120 second dwell period at 650°C are comparable for both increasing and decreasing ΔK testing methodologies (Figure A-22). Although this appears counter intuitive and requires some further investigation, it adds confidence to the threshold values obtained; suggesting that they are independent of testing methodology.

5.5 Transient Crack Growth Behaviour

5.5.1 Introduction

The majority of baseline, dwell and overload crack growth resistance curves presented in Appendix VI have shown that transient crack growth behaviour is observed as a result of changing the loading waveform. This transient behaviour can be organised in to three distinct categories. Firstly, it is observed as a result of the transition between relatively slow, cycle-dependent crack growth associated with baseline (and in some cases, overload) cycling, and fast, time-dependent dwell crack growth. Here, crack growth rates at the start of a period of dwell cycling immediately following baseline loading are usually relatively fast when compared with more stable crack growth rates in this regime; and "settle down" (shown, for example in Figure A-10). Secondly, it is observed as a result of the inverse transition, namely that between fast, time-dependent intergranular crack growth as a result of dwell (or in some cases, overload) loading and a period of relatively slow cycle-dependent crack growth associated with baseline loading. Crack growth rates at the start of the last period of baseline loading (following overload crack growth or simple dwell loading) usually begin slower than those normally associated with these waveforms; and "settle up" (also shown in Figure A-10).

Finally, a third type of transition is also observed; the transition of crack growth rates pertaining to the application of dwell cycles and those associated with overload cycling. Crack growth rates associated with overload cycling whether partial or full retardation occurs

usually begin relatively fast and stabilise by "settling down" (again, exampled in Figure A-10).

5.5.2 Oxygen Induced Damage Zone

Consider first the settling down of crack growth rates pertaining to overload cycling following a period of dwell cycling. Since the settling down occurs after a period of high rate, intergranular dwell crack growth, it might be that the phenomenon is due (in part) to a damage zone ahead of the crack tip which could be caused by the ingress of oxygen and subsequent degradation (embrittlement) of grain boundary material ahead of a crack tip. A few tests displayed settling down behaviour of baseline crack growth rates after overloading (Figure A-7 and Figure A-38); however this was usually only observed when the conditions were such that retardation was limited, and overload crack growth rates were high and (possibly) driven largely by time-dependent oxygen embrittlement of grain boundaries ahead of the crack tip. Therefore their behaviour could be explained in much the same way as the settling down from dwell conclusions.

The da/dN vs ΔK graphs can be used to estimate the depth of this damage zone by measuring the range (in terms of crack lengths) over which this settling down phenomenon occurs in each case (Table 20 and Table 21). The measurements are far too high to attribute solely (or simply) to oxidation or oxygen embrittlement ahead of the crack tip since maximum oxygen diffusion depths are modelled at orders of magnitudes lower. Nevertheless it is appropriate to suggest that the oxidation models underestimate the selective nature of oxygen penetration.

Oxygen diffusion will occur in a highly selective manner; the path will not be uniform across the quarter-circular crack path front. The diffusion paths will be favoured by certain grain orientations for example, and by grain mismatch orientations. It will also be favoured by certain microstructural characteristics, following a series of smaller grain boundaries for example, or along grains with naturally varying amounts of chromium. It is therefore possible that while average bulk oxygen penetration depths are small, the crack front will comprise regions of much deeper oxygen embrittlement. Cycle-dependent crack growth immediately following a period of dwell crack growth may then display higher crack growth rates than those predicted normally because it is influenced by this damage. It follows that to begin with, oxygen damage is likely to be highly concentrated and uniform along the crack front, and as the crack grows it involves more and more "fresh" material. This model agrees well with fractography generated by SEM which reveals that time-dependent dwell crack growth fronts are not smooth and quarter-circular in shape but rather branch out in non-uniform, random "fingers" (shown clearly by optical images presented in Appendix V and in Figure 5-3). Therefore the gradually decreasing crack growth rates over such distances are explained by the gradually decreasing extent of oxygen damage as the crack grows through to new material. As the crack grows it will gradually incorporate and involve more "fresh" material between ever decreasing oxygen embrittled "finger" widths as it propagates through to completely fresh material.

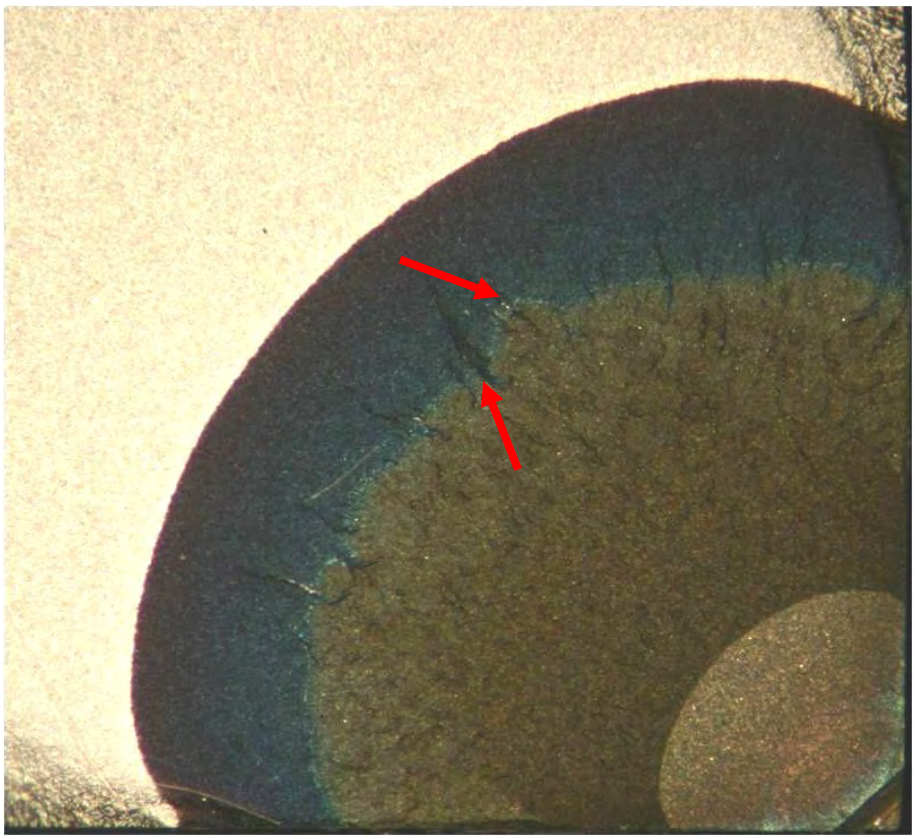


Figure 5-3: Optical micrograph to show non-uniform crack front relating to dwell cycling. Arrows show "fingers" of materials relating to dwell and baseline crack fronts.

To further support these suggestions, it is also highlighted that the depth over which this damage zone occurs increases with increasing test temperature (Table 20 and Table 21). Higher temperatures are associated with higher energies and hence further diffusion of oxygen ahead of the crack tip.

Having hypothesised an oxygen induced damage zone, it is also true to suggest that the settling down behaviour discussed here might also occur as a result of creep induced crack tip blunting, discussed in more detail in section 5.5.3. Such behaviour is also dependent upon testing temperature in much the same way: more profound creep damage (crack tip blunting)

might occur at higher temperatures. It might not be possible to conclusively isolate either factor; nevertheless discussion pertaining to crack tip blunting is presented below:

5.5.3 Crack Tip Blunting

"Settling down" also occurs as the result of the transition from baseline loading to dwell loading in some of the conditions tested (Figure A-10 provides another example, and the conclusions are summarised in Table 20 and Table 21). This behaviour may be explained by the fact that crack tip blunting occurs as a result of time-dependent creep when time at peak load is increased to a dwell time. Perhaps the most significant evidence for this is the "settling down" of crack growth rates pertaining to overload conditions on Udimet 720Li test piece CC001 (Figure A-15). This settling down occurs immediately following a period of baseline loading, hence cycle-dependent transgranular crack growth, with a sharp crack tip front. It is suggested therefore that this settling down occurs due to the blunting of the crack tip rather than the effect of an oxygen induced damage zone. This is further evidence to suggest the effect of crack tip blunting on the retardation of crack growth rates, whether pertaining to overload or dwell only cycling.

Crack tip blunting may also help to explain "settling up" of baseline crack growth rates following overload of dwell cycling. Almost all settling up occurs during baseline cycling, immediately following the application of either dwell or partially retarded overload cycling, hence after a period of time-dependent crack growth. It is suggested therefore that the settling up of baseline crack growth rates occurs due to the fact that crack tip fronts pertaining to

time-dependent dwell (or partially retarded overload) cycling are likely to be relatively blunt and that in order for cycle-dependent cracks to propagate at rates more usually associated with fast cycling, the crack tip must first become sharpened. This sharpening occurs over a distance (in terms of crack length growth) which varies as a function of dwell time (in terms of previously applied dwell cycles), during which time it will do so at a relatively slow rate, gaining speed as the crack front gradually becomes more and more sharp.

As previously discussed, this blunting of the crack tip during dwell cycling is likely caused by the accumulation of inelastic creep strain at the crack tip (due to the combination of high stresses and high temperatures). As previously suggested, this also implies that crack tip blunting may be partially responsible for the overload retardation effect itself. (This might further complicate the comparison of empirical data with those gathered analytically. Nevertheless, as reported in section 5.3 and Figure 4-84, the general trends and conclusions agree well.)

Although it is difficult to accurately measure the depth of the zone over which this crack tip sharpening may occur it is possible to make some suggestions. “Tails” on the crack growth resistance curves show that for otherwise similar conditions an increase in overload factor causes a deeper affected zone (Table 20 and Table 21). This agrees well with previous suggestions that the phenomena might be caused by creep since higher overload factors involve higher maximum stresses which would induce deeper plastic zone sizes and a deeper zone of accumulated creep damage. As previously discussed, it also appears as though longer dwell periods and higher test temperatures also cause a deeper effected zone (also Table 20

Table 21). This further suggests that the effect is due, at least in part; to the accumulation of inelastic creep strain ahead of the crack tip, since creep is both time and temperature dependent.

Nevertheless there is a further complication; namely that for dwell cycling and for overload cycling pertaining to partially retarded crack growth rates, the crack will advance in the intergranular mode as a result of time-dependent oxidation for at least some of the subsequent dwell period. Therefore this potentially beneficial effect of creep in blunting the crack tip is competing with the oxygen embrittlement mechanism. Hence crack growth rates are (in part) slowed down by creep, and increased by oxygen embrittlement.

It is important to note that only "true" (stable, linear) overload crack growth is used to determine the extent to which crack growth retardation has occurred.

5.5.4 Summary

To summarise therefore; time-dependent creep and oxygen induced grain boundary embrittlement have been show to interact and compete with one another in terms of crack growth rates and mechanisms. Both components affect regions of the crack tip ahead of its front over measurable distances. Crack tip blunting due to the accumulation of inelastic creep strain, and oxygen induced grain boundary embrittlement ahead of the crack tip are confirmed, or rather suggested as competing mechanisms in high temperature dwell and overload fatigue crack growth of fine-grained Udimet 720Li and RR1000. Crack tip blunting

is suggested as a factor in the retardation of crack growth rates pertaining to overload cycling when compared with otherwise similar dwell only cycling.

6 Conclusions

1) Dwell crack growth rates in air are significantly faster than those associated with otherwise similarly tested baseline waveforms for fine-grained Udimet 720Li and RR1000.

2) This increase in crack growth rate is associated with a mechanism change from transgranular (baseline) to intergranular (dwell).

3) Dwell crack growth rates in a vacuum are largely unaffected and are comparable to those associated with otherwise similarly tested baseline crack growth rates.

4) Dwell crack growth morphologies observed in a vacuum are confirmed to be predominantly transgranular which suggests that accelerated dwell crack growth rates and associated mechanism changes in air are dominated by oxygen effects.

5) The introduction of a one second overload segment in the stress waveform applied before the subsequent dwell period causes crack growth retardation, when compared with otherwise similarly tested dwell crack growth rates; for all conditions.

6) Full retardation (back down to crack growth rates usually associated with otherwise similarly tested baseline waveforms) is observed for some conditions – normally related to larger overload factors, lower test temperatures and shorter dwell times.

7) Full and “nearly full” crack growth retardations are associated with full or partial transgranular fracture surface morphologies. Partial retardation crack growth retardations are associated with intergranular fracture surface morphologies.

8) This retardation effect is due, in part to the fact that crack tip stresses unload preferentially as the nominal stress is reduced. These crack tip stresses will relax back to those normally associated with otherwise similar dwell loading as a result of creep, over what is termed an “incubation time”.

9) Incubation time increases with increasing overload factor and with decreasing temperature. For the same conditions, incubations times are longer in fine-grained RR1000 than in Udimet 720Li.

10) Incubation time increases with increasing dwell time at maximum (overload) load due to the accumulation of creep strain ahead of the crack tip. Nevertheless total high temperature crack growth rates will, under these conditions, also include time-dependent fast crack growth during the dwell at overload segment.

11) Current lifing methodologies employed by Rolls-Royce plc. which assume a linear superposition of cycle and time-dependent crack growth mechanisms to represent take-off and climb associated stress states as a single hold period have been proven to be unnecessarily concervative.

12) Appropriate linear superposition lifing methodologies which seek to optimise engine performance must also include empirically and analytically derived retardation parameters. These parameters are alloy and condition specific.

13) The current testing approach has proved to be successful in identifying the retardation of crack growth rates resulting from the overload waveform.

14) Transitional crack growth rates are observed as a result of switching between each waveform. In general there are two types. Either crack growth rates begin faster than usually observed for a give waveform and “settle down”, or they begin slower than usually observed for a given waveform and “settle up”.

15) Settling down occurs during overload cycling, after dwell crack growth, suggesting that the phenomenon might be attributed (in part) to oxygen embrittlement ahead of the crack tip. The depth over which the settling down behaviour occurs increases with temperature and dwell load.

16) Settling down also occurs after baseline loading when switching to either dwell or overload loading, suggesting that the phenomenon might also be attributed to crack tip blunting due to the accumulation of inelastic creep strain ahead of the crack and an increased plastic zone size, known to occur when time at peak load is increased to a dwell time. This in turn is attributed to higher bulk stresses at high temperatures and for longer periods of time.

17) Settling up occurs during baseline cycling, immediately after dwell cycling or partially retarded overload cycling. This “undershooting” of crack growth rates is thought to occur due to the fact that crack tip blunting occurs during time-dependent (dwell) crack growth. Sharpening of the crack tip then occurs during the advancement of cycle-dependent crack growth pertaining to baseline loading, a process over which crack growth rates stabilise.

18) Crack tip blunting therefore is also suggested as a contributing factor in the retardation of crack growth rates pertaining to overload cycling when compared with otherwise similar dwell only cycling.

19) The cycle-dependent (fatigue) and time-dependent (dwell) ΔK threshold values for which crack growth begins to occur has also been investigated; suggesting that time-dependent, intergranular crack growth has a threshold value greater than that of cycle-dependent crack growth (for otherwise similar conditions and microstructures).

20) This might also be attributed to crack tip blunting which is shown to occur during time-dependent crack growth.

21) High temperature, time-dependent crack growth according to dwell cycling occurs in the intergranular regime, which is confirmed even at threshold. This may also be a factor in causing an increase in the threshold required to initiate time-dependent crack growth.

22) Variations in crack growth rates have been confirmed pertaining to baseline, dwell and overloading cycles, including near threshold behaviour. Furthermore, variation in terms of the nature of crack growth retardation pertaining to overload cycling for the investigated fine-grained Udimet 720Li and RR1000 is also confirmed.

23) This variation is in turn attributed to variations in grain size and primary γ' size and morphology. Smaller grain sizes relate to higher crack growth rates and smaller values for stress intensity factor range thresholds for time-dependent dwell crack growth in (nominally) fine-grained Udimet 720Li, when compared with otherwise similarly tested microstructures comprising larger grain sizes. Smaller grain sizes also relate to less pronounced overload crack growth retardation (shorter experimentally derived incubation times) when compared with coarser grained microstructures.

7 Further Work

7.1 Continuation of Testing Programme

This project has paved the way for several follow-up theses, the first of which will focus on the continuation of overload and TiDI threshold testing programmes. The primary focus will be to investigate the effect of overload on coarse grained RR1000, also used extensively throughout the fleet of current generations of Rolls-Royce plc jet engines. It is recommended that the testing procedure be repeated to a fairly representative extent (in terms of methodology and data processing) on a series of test pieces machined from coarse grained RR1000 material.

The continuation of the testing programme should also include further investigation to study the effect of microstructure on dwell crack growth and on the extent of crack growth retardation pertaining to overload cycling. Therefore it might be of some benefit to carry out a comprehensive study on the remaining test pieces from Batch Two of Phase Two, the "ultra-fine" and therefore "ultra-fast" microstructure. It might be that while overall crack growth rates are significantly higher (faster) in these test pieces when compared with otherwise similarly tested Udimet 720Li with a coarser microstructure, the extent of retardation pertaining to overload cycling remains fairly constant, indicating that the retardation is mainly controlled by mechanical factors. Although some preliminary data has been gathered and discussed in this programme of research, these tests would likely add much further to the discussion.

Furthermore, the TiDI threshold testing programme should be developed to further explore the effect of microstructure, testing condition and testing methodology. The tests carried out in this programme should form the preliminary background on which to build a test matrix which may or may not further solidify the evidence already put forward in this thesis.

One final note is that while the testing programme presented in this thesis is relatively comprehensive, only a very small number of exact repeat tests have been carried out. It would be of great benefit to determine the extent to which these results are repeatable, especially since they go some way to defining the in-service life of a range of engines currently in operation. As such some repeat tests could be carried out as part of a further programme of research.

7.2 Crack Growth within One Cycle

Further to the extended testing matrices discussed above, several novel methods and analyses might also be carried out. Following the discussions relating to suppressed time-dependent crack growth as a result of partial unloading from an overload segment in the waveform; it follows that overload cycling pertaining to partial retardation should show predictable crack growth patterns with respect to rates in terms of a single applied cycle. During the overloading segments, crack growth should be stunted or suppressed until the incubation time is reached, after which time it should begin to grow observably more quickly.

This behaviour might be picked up on crack growth measuring chart recorders in terms of p.d across the sample. Following methodologies described above, crack growth within one cycle is usually too small to be noticed on chart recording data, hence a continuous line is drawn representing a specific number of cycles per mm of paper. It might be possible with increased resolution, increased sensitivity and increased chart speed to measure such a shape in terms of crack growth rates within one cycle. If so, it would add further confidence to the mechanisms suggested to be contributing factors in terms of the retardation of overload crack growth rates discussed above. Further confidence could then also be added to lifing methodologies which incorporate these theories.

7.3 Interrupted Tests

It would be desirable to run a series of dwell and overload tests at a range of temperatures, dwell loads and overload factors for a range of alloys and rather than grow a crack in each test piece to an a/W of 0.5; interrupt them by pausing the test at controlled points during the stress waveform. These interrupted test pieces could be removed from tensile testing rigs, sectioned, mounted and polished according to similar methodologies reported in previous sections.

Several observations of the crack tip could then be made. Firstly, etching samples might reveal the extent to which oxygen has caused the degradation of grain boundaries ahead of the crack tip. It might be possible to quantify the extent of this damage including analysis to

determine the depth at which damage occurs, using scanning electron microscopy and image analysis.

Furthermore, EBSD could be used to observe the extent to which grains of material adjacent to and ahead of the crack path have strained as a result of the applied loading waveform. It could therefore be used to estimate plastic zone sizes and shapes associated with each waveform. It might even be possible to generate images which show stress relaxation ahead of the crack tip as a function of overload factor; which could then be compared with contour plots generated by finite element analysis. Such comparison would add confidence to stress analysing techniques and associated post processing analyses of output data, adding further confidence to analytically derived values of incubation time and crossing time.

7.4 The Effect of Dwell at Overload

It would also be of some benefit to further explore in empirical and analytical terms the extent to which dwell time at overload affects overall crack growth rates. Lifing methodologies which seek to accurately represent crack growth rates during the take-off and climb stages of engine operation must include cycle and time-dependent crack growth components pertaining to a dwell load at take-off level and another dwell load relating to climb stress states. This second dwell load (relating to “climb”) must also include a retardation parameter to incorporate the effect of partial unloading between the two stress states.

Therefore further analytical analysis is required to understand the effect of dwell at overload on incubation and crossing times for all conditions including various dwell periods at overload load. This must then be combined with known cycle and time-dependent crack growth rates and total crack growth rates for all conditions should be predicted. These predictions could be measured against empirically derived crack growth resistance curves which include hold periods at overload load in the waveform.

7.5 The Effect of Bi-Thermal Loading

Each condition studied in this programme whether empirically or analytically assumes an isothermal temperature across the stress-time history. This methodology isolates the effect of temperature and enables a critical review of the effect of waveform. Nevertheless it clearly fails to fully understand in-service stress states during which temperature changes as a function of time according to the example in Figure 1-2.

Therefore it would be beneficial to carry out similar testing methodologies to those described above but with rapidly changing temperature stress states. These may occur in phase with stress-time variations or indeed out of phase and each effect on crack growth rates and crack tip stress states should be studied. In terms of empirical mechanical testing methodologies this may require different heating equipment since fast heating and cooling rates are difficult to achieve with the equipment used in this programme.

As briefly mentioned in section 2.4.3, Rolls-Royce plc. have analytical methodologies in place which seek to incorporate a bi-thermal condition history. Nevertheless the understanding of any effects on dwell crack propagation or overload crack growth retardation are required. It may be that cooling and heating over a continuous cycle would affect the way in which high temperature environmental degradation occurs ahead of a fatigue crack tip. This may therefore influence dwell crack propagation rates.

7.6 Overload Crack Growth Retardation in Inertia Welds

The full body of work in this programme has focussed on parent material. Nevertheless there is a trend for Ni-discs to be joined by solid state inertia welding throughout the engine, eliminating the need for bolts and thus saving weight. Clearly a comprehensive understanding of fatigue and dwell crack growth behaviour for inertia welded Ni-based superalloys is required. Nevertheless this study should be included to understand the effect of overload cycling on crack growth rates. The study would provide a unique opportunity to explore the effect of microstructure on overload crack growth retardation, since welded microstructures are known to comprise different microstructures when compared with their respective parent alloys.

Similar methodologies to those detailed above could be implemented; where corner notch test pieces are machined from inertia welded materials and a notch cut in to the weld. Detailed crack growth analysis should be completed for a range of conditions (temperatures, dwell

loads, overload factors) and subsequent microstructural characterisation should be carried out to highlight the effect of microstructure on overload retardation.

7.7 Understanding Failures in Modelling Codes

As reported in previous sections, simulations for a range of conditions failed to run. These conditions were especially associated with high stresses and low temperatures and were usually observed when running fine-grained RR1000 (RGT) material data.

The reasons for these failures remain unclear and therefore a full investigation is required. It is likely that the failures are caused by the implementation of inappropriate creep data, especially since the alloy is relatively new. Detailed empirical analysis on the creep behaviour for the alloy is required which might highlight anomalies in the analytical material codes.

Appendices

Appendix I Glossary of Common Terms

Except where defined otherwise, the following abbreviations, acronyms or symbols (presented in the order in which they first appear in the text) can be taken to mean:

γ	The γ-Ni phase
γ’	The γ’-Ni phase
σ	Stress (MPa), the σ phase or standard distribution about the mean
$\bar{x}$	The mean of a set of data
TET	Turbine entry temperature
η	Efficiency
W	Work done
Q	Heat
T	Temperature
fcc	Face-centre cubic
APB	Anti-phase boundary
tcp	Topologically close packed
PM	Powder metallurgy
VIM	Vacuum induction melting
ESR	Electro-slag remelting
VAR	Vacuum arc remelting
HIP	Hot isostatic pressing
HCF	High cycle fatigue

LCF	Low cycle fatigue
NDT	Non-destructive testing
K	Crack growth driving force or stress intensity factor
Y	Geometric shape factor
a	Crack Length
w	Test piece width
B	Test piece thickness
σ_y	Yield stress
da/dN	Crack growth rate with respect to number of cycles (usually mm/cycle)
A, m	Empirically derived material constants pertaining to Paris law crack growth rates
ΔK	Difference between maximum and minimum stress intensity factors
$\Delta\sigma$	Difference between maximum and minimum stresses
N_f	Number of cycles to failure
dcpd	Direct current potential drop
r_y	Idealised plastic zone size radius
SEM	Scanning electron microscopy
SAGBO	Stress assisted (or accelerated) grain boundary oxidation
DE	Dynamic embrittlement
ε	Strain (or creep)
$\acute{\varepsilon}$	Creep strain rate
D’	Time-dependent crack growth rate parameter
τ	Shear stress

EBSD	Electron backscatter diffraction
C_p	Empirically derived crack growth retardation parameter
p.d.	Potential difference
t	Time
t_{dwell}	Dwell time (seconds)
OLF	Overload factor
F	Force (N)
BL	Background load (MPa)
TEMP	Temperature input for model
PF	Pressure fraction
SYY	Stress normal to the crack tip
CEQI	Inelastic creep strain normal to the crack tip
REC	Fine-grained Udimet 720Li as modelled by SC03
RGT	Fine-grained RR1000 as modelled by SC03
t_{inc}	Incubation time (seconds)
t_x	Crossing time (seconds)

Appendix II List of Figures

Figure 1-1: Cut away of a Trent 800 series engine showing: low, intermediate, and high pressure compressor stages; the combustion stage; and the low, intermediate, and high pressure turbine stages, with relative temperatures and pressures [2]. 3

Figure 1-2: Variation of the turbine entry temperature (TET) and associated stress states of various components as a function of time for a typical flight cycle of a civil aircraft [1]. 4

Figure 2-1: Stress contours shown around a dovetail rim feature [7]. 12

Figure 2-2: The unit cell showing the crystal structure of γ' [9]. 19

Figure 2-3: Conventional ingot metallurgy processing route. 22

Figure 2-4: Powder metallurgy processing route. 23

Figure 2-5: Example micrograph showing γ grains and primary γ' precipitates in a typical fine-grained Udimet 720Li microstructure, etched using Kalling's reagent. 27

Figure 2-6: Example micrograph showing γ grains and primary γ' precipitates in a typical fine-grained RR1000 microstructure, etched using Kalling's reagent. Note the finer grain size and primary γ' precipitate sizes, and the subtle differences in morphologies when compared with cast and wrought fine-grained Udimet 720Li. 29

Figure 2-7: Schematic showing the three different regions of fatigue crack growth. Region 1 describes threshold behaviour; region 2, linear Paris law growth; region 3 Fast growth to failure [23]. 35

Figure 2-8: Baseline loading cycles with a hold time of 1 second and an R ratio of 0.1 37

Figure 2-9: Dwell cycles with a hold time of 3,600 seconds and an R ratio of 0.1 38

Figure 2-10: Schematic yield model for idealised restricted crack tip plastic deformation and associated stress states [26].....40

Figure 2-11: Showing plastic zone size for a through-thickness edge crack [23]. 41

Figure 2-12: Fatigue crack growth rate curves showing the influence of wave shape. R=0.1, 700^{o}C [31].....44

Figure 2-13: (a) Schematic cross-section profile displaying crack propagation through the interior of grains for transgranular fracture. 45

Figure 2-14: (a) Schematic cross-section profile displaying crack propagation along grain boundaries for intergranular fracture. 46

Figure 2-15: Schematic diagram to show the dynamic embrittlement mechanism, from [43]. 50

Figure 2-16: Showing Onofrio's work in the influence of loading waveform and environment on fatigue crack growths in a Ni-based superalloy [30]. 55

Figure 2-17: A stress-time graph to show typical metal creep behaviour [52], from [53]. 58

Figure 2-18: Showing Andrade's first analysis of the components of the constant-stress creep curve [21], from [53].....59

Figure 2-19: Showing the effect of stress on constant-stress creep deformation curves for metals [21]. 60

Figure 2-20: Schematic showing various damage zones ahead of a crack tip in the dwell regime, from [60].....65

Figure 2-21: Yield surfaces under bi-axial (plane stress) loading conditions defined by Von Mises and Tresca yielding criteria, from [61] and [62]. 74

Figure 2-22: Multi-yield surfaces suggested by Mroz.....76

Figure 2-23: Showing evolution of multi-yield surfaces as represented by Mroz hardening criteria [63].....77

Figure 2-24: Showing the parameter $d\varepsilon_{eff} / \sigma_{eff}$ (the "hardening parameter") for Levy-Mises equations. 80

Figure 2-25: An example of an overload waveform with an overload factor of 1.15. The waveform would normally go on to hold the "dwell" load for between 120 and 3,600 seconds, before unloading over a period of 1 second and holding at the minimum load for a period of 1 second, thereby defining the "cycle".....84

Figure 2-26: Schematic of plastic zone sizes associated with overload and subsequent dwell load stress states. 86

Figure 2-27: A schematic view of the plastic zones induced by nominal cycling and by the application of an overload cycle, as discussed in the Wheeler model, from [75].....90

Figure 3-1: Photograph showing spot welding equipment including attached optical analysis equipment and light source. 102

Figure 3-2: Image showing; a) the spot welded region within 1 mm of the notch and the edge of the test piece and b) the platinum wire running immediately upwards from the spot welded region rather than running flat against the test piece. 103

Figure 3-3: Schematic diagram of the testing rig.....104

Figure 3-4: Photograph showing complete testing rig including servo-hydraulic tensile testing machine, furnace and associated cooling. 105

Figure 3-5: Showing all waveforms used to test each sample. From left to right: sinusoidal precracking; 1-1-1-1 baseline loading; dwell loading; overload loading and final baseline loading.....112

Figure 3-6: An optical image of part of the fracture surface of a sample tested using this methodology. Section one is the first baseline segment, section two is the dwell segment, section three, the overload segment and section four, the final baseline segment. The rest of the fracture surface represents room temperature 1 Hz sinusoidal cyclic fatigue crack growth. For reference, this particular example is fine-grained RR1000, tested at 625°C, with a dwell time of 1,200 seconds and an overload factor of 1.10. 113

Figure 3-7: An optical image of the fracture surface with measurements for the length of the crack after the first 1-1-1-1 segment taken. 114

Figure 3-8: A graph of crack length against p.d. for RR1000 sample CC046. 115

Figure 3-9: Photograph showing chart recorder continuously measuring the potential difference across the sample as a function of constant current (7.2 amps) and electrical resistance across the sample, which itself is a function of growing crack length. 117

Figure 3-10: Showing the 120 second dwell at overload waveform, with an overload factor of 1.15 and a subsequent dwell time of 1,200 seconds. 127

Figure 3-11: The “unloading” waveform, where the overload was gradually unloaded back down to the dwell load over the whole dwell time (1,200 seconds), rather than over a period of one second as in the previous methodology. 129

Figure 3-12: The “reloading” waveform, where after the initial one second overload, the applied stress is gradually increased back to the maximum overload over the dwell period (1,200 seconds). 130

Figure 3-13: Showing a beach-marking effect on the pre-crack fracture surface of Udimet 720Li sample CC044. For reference, the sample was pre-cracked, tested for a time-dependent temperature threshold, pre-cracked again and then tested for decreasing ΔK

threshold for time-dependent crack growth with a dwell period of 120 seconds and at a temperature of 650°C. The final "band" represents a final region of baseline loading. 133
Figure 3-14: Photograph showing Struers automatic polishing equipment. 142
Figure 3-15: Showing the lacations from which images are taken for a; 50x magnification grid, b; 100x and 200x magnification grid and c; 500x magnification grid. 144
Figure 3-16: Snaked 'grid' of random SEM image locations at 1500x magnification. 144
Figure 3-17: a; SEM image formatted in Microsoft Word prepared for tracing, b; Scanned digital trace of the SEM image in a. 145
Figure 3-18: Traced and Cropped Image 146
Figure 3-19: Inverted image, post gamma prime selection, used for automatic grain size analysis. 147
Figure 3-20: Inverted image, post grain selection, used for primary γ' analysis. 148
Figure 3-21: Showing an example of mesh geometry for modelling work. 151
Figure 3-22: Showing the notch radius (0.25 mm) used to represent a crack. The validity of the representation is reported in Appendix V. 152
Figure 3-23: Referencing the parameter "TEMP". 154
Figure 3-24: Defining BL, TEMP and PF through a range of "conditions". 154
Figure 3-25: Defining a time history by assigning "time" (in seconds) to a condition number. 154
Figure 3-26: Defining the pressure load as PF*(-BL) 155
Figure 3-27: An illustration to show the way in which segmented strain is captured analytically. 156

Figure 3-28: Plotting Pressure Fraction (PF) as a function of time plotted throughout its history, as referenced a total of 97 times. 159

Figure 3-29 : Plotting Temperature (TEMP) as a function of time plotted throughout its history, as referenced at similar moments in time to PF above. 160

Figure 3-30: Plotting Background Load (BL) as a function of time plotted throughout its history, as referenced at similar moments in time to PF above. 161

Figure 3-31: Plotting environmental parameters against time; a: PF, b: BL, c: TEMP. The example shows a typical overload waveform, with an OLF of 1.15 162

Figure 3-32: Showing the nodes from which stress and creep versus time plots were analysed; a: crack tip, b: 1.5r ahead of the crack tip. For reference the contours show inelastic creep strain normal to the crack tip (CEQI) after unloading from the dwell load at the end of the cycle. 164

Figure 4-1: da/dN vs. ΔK curves to show a comparison in terms of baseline and dwell crack growth rates for 600°C and 650°C. Samples are fine-grained RR1000; CC003 and CC005 (600°C) and CC001 and CC002 (650°C), tested in air with a dwell load of 26kN. Note the effect of temperature and dwell period on crack growth rates.....171

Figure 4-2: da/dN vs. ΔK curves for fine-grained Udimet 720Li samples CX013, CX014, CX042 and CX045, which were tested at 600°C, with a dwell load of 26 kN, a dwell time of 3,600s in air (CX013 and CX014) and 120s in a vacuum (CX042 and CX045). Note that dwell crack growth rates in a vacuum are similar to those associated with baseline loading. 173

Figure 4-3: da/dN vs. ΔK curves for fine-grained Udimet 720Li samples tested at 650°C at a range of dwell periods, in air and in a vacuum. 174

Figure 4-4: da/dN vs. ΔK curves for RR1000 samples CC019 and CC039 tested at a temperature of 600°C with an overload factor of 1.15. Note that the ΔK values are calculated using the load range between the peak overload and the minimum load (ΔK_{full}) for the overload fatigue crack growth segment. Full retardation. 176

Figure 4-5: da/dN vs. ΔK curves for RR1000 samples CC021 and CC042 tested at a temperature of 600°C with an overload factor of 1.05. Partial retardation.....177

Figure 4-6: da/dN vs. ΔK curves for fine-grained Udimet 720Li samples CC009, CC015 and CX027, all tested at 650°C and with a dwell period of 3,600s, in air. Note that despite similar testing conditions crack growth rates are shown to be variable. Note also that CX027 data represents intermittent "bursts" of baseline (1-1-1-1) loading in order to encourage the crack to grow under a dwell regime. 180

Figure 4-7: da/dN vs. ΔK graph to show the effect of a 120 second dwell period on the stress intensity factor range threshold for high temperature (650°C) crack growth when compared with 1 Hz sinusoidal loading. Note that both sets of data are gathered using the decreasing ΔK (load shedding) technique. Note also the temperature threshold data gathered on the same test piece (CC044), which was found to be ~510 °C for a ΔK of around 30MPa√m. 182

Figure 4-8: da/dN vs. ΔK graph to show comparisons for all ΔK threshold testing on Udimet 720Li sample test pieces. All tests are carried out at 650°C in laboratory air, with dwell periods of 120 or 3,600 seconds. Note that test pieces CC011 and CC045 (showing

unusual results when compared with the other data presented) are found to comprise notably different microstructures. 183

Figure 4-9: Scanning electron micrograph of fine-grained Udimet 720Li sample CC014, during the first baseline segment (ΔK~18MPa√m). The sample was tested at 600°C, and with a dwell load of 29kN. The fracture surface is predonimantly transgranular, nevertheless it can be seen from a) that crack paths have propagated around primary γ' where it has segregated in large amounts of fine precipitates. b) shows an area which contains fewer primary γ' precipitates and hence the crack appears to have propagated through the γ grains. 193

Figure 4-10: Scanning electron micrograph of fine-grained Udimet 720Li sample CC014 (as above), during the dwell segment (ΔK~22MPa√m). The fracture surface is predonimantly intergranular and shows a) segregation of fine primary γ' precipitates and b) areas of clean, faceted transgranular crack growth in regions denuded of primary γ'. 194

Figure 4-11: Scanning electron micrograph of fine-grained RR1000 sample CC021, during the first baseline segment (ΔK~18MPa√m). The sample was tested at 600°C, and with a dwell load of 26kN. The fracture surface is predonimantly transgranular. 195

Figure 4-12: The same sample (RR1000 CC021) under dwell conditions (ΔK~22MPa√m). The test piece was tested at a dwell load of 26 kN and a dwell time of 1,200 seconds. The crack growth morphology is shown to be predominantly intergranular, with delineation of primary γ' from the γ matrix charecterising the fracture surface along with faceted intergranular grain boundary cracking. 196

Figure 4-13: Fractograph of fine-grained Udimet 720Li test piece CC040 tested at a temperature of 650°C and with a dwell time of 120 seconds. The fracture surfaces shows where the crack path has propagated along the boundary between primary γ' and the γ matrix

in which it has precipitated. The image shows a) primary γ' on the fracture surface and b) gaps in the γ matrix from which primary γ' particles have delineated. 197

Figure 4-14: The same fine-grained RR1000 sample as shown above (CC021), during the overload segment (ΔK~34MPa√m). An overload factor of 1.05 was applied, and the amount of retardation was found to be partial. The crack growth morphology appears to be predominantly intergranular despite slower crack growth rates than those observed during dwell only loading.....198

Figure 4-15: Lower magnification fractograph of RR1000 sample CC046 during overload cycling (ΔK~35MPa√m), tested at 650°C with a dwell period of 1,200 seconds and an overload factor of 1.15; conditions which caused full retardation back down to baseline crack growth rates.....199

Figure 4-16: Fractograph of RR1000 sample CC046 taken of the final baseline zone (ΔK~45MPa√m), showing transgranular crack growth. 200

Figure 4-17: (Previous page) A summary of the fractography data, for fine-grained RR1000 sample CC046 – tested at 650°C, a dwell time of 1,200 seconds and an overload factor of 1.15. Full retardation was observed. 202

Figure 4-18: (Previous page) A summary of the fractography data, for fine-grained RR1000 sample CC045 – tested at 650°C, a dwell time of 1,200 seconds and an overload factor of 1.08. Partial retardation was observed. 204

Figure 4-19: SEM image of fine-grained Udimet 720Li test piece CC040 tested for time-dependent threshold in air at 650°C with a dwell period of 120 seconds. The image shows a transition band which occurred near threshold. 205

Figure 4-20: Higher magnification SEM image of the same transition band shown above. .205

Figure 4-21: Cross section view of fine-grained Udimet 720Li test piece CC044 showing the crack profile (propagating left to right) pertaining to 1 Hz sinusoidal precracking at 650°C in air at a ΔK of ~11 MPa√m. Note the mixture of inter and transgranular crack growth. 206

Figure 4-22: Cross section view of fine-grained Udimet 720Li test piece CC044 showing the crack profile (propagating left to right) pertaining to 120 second dwell cycling at 650°C in air at a ΔK of ~16 MPa√m. Note the intergranular mode of crack growth.....207

Figure 4-23: Cross section view of fine-grained Udimet 720Li test piece CC044 showing the crack profile (propagating left to right) pertaining to 1-1-1-1 baseline cycling at 650°C in air at a ΔK of ~40 MPa√m. Note the transgranular mode of crack growth. 208

Figure 4-24: Optical micrographs taken of CC015 at 50x magnification. 214

Figure 4-25: Optical micrographs of 'teardrop' shaped dark region in CC015, ~350um long at a) 100x magnification, b) 200x magnification and c) 500x magnification.....214

Figure 4-26: Optical micrographs of CC009 at 50x magnification. 214

Figure 4-27: Optical micrographs of CX027 at 50x magnification. 215

Figure 4-28: CC009, 1500x mag, 20KeV. Image shows the presence of relatively coarse grains with large primary γ' decorating the grain boundaries. 216

Figure 4-29: CC009, 1500x mag, 20KeV. Image shows a particularly fine grained region with small, finely dispersed primary γ' throughout. 216

Figure 4-30: CC009, 1500x mag, 20KeV. Image shows adjacent regions of fine and relatively coarse grains at the top right and bottom left of the image respectively. 217

Figure 4-31: Micrograph of fine-grained Udimet 720Li sample CC015 at 1500x magnification, 20Kev. The image shows relatively uniform grain size throughout, as also displayed in Figure 4-32 (below). 218

Figure 4-32: Similar micrograph to that shown above, giving an indication of the uniform nature of microstructural characteristics. 218

Figure 4-33: Micrograph of the same sample (CC015) under similar magnification (1500x). The image shows a region of fine grained material. 219

Figure 4-34: Micrograph of fine-grained Udimet 720Li sample CX027 at 1500x magnification, 20Kev. 220

Figure 4-35: Similar micrograph of CX027 taken at a different location, showing relatively uniform microstructural characteristics. 220

Figure 4-36: A third micrograph of CX027 taken at a different location, showing relatively uniform microstructural characteristics. 221

Figure 4-37: Showing the grain size distribution for fine-grained Udimet 720Li sample CC015. 222

Figure 4-38: Showing the grain size distribution for fine-grained Udimet 720Li sample CC009. 223

Figure 4-39: Showing the grain size distribution for fine-grained Udimet 720Li sample CX027. 223

Figure 4-40: Showing the primary γ' size distribution for fine-grained Udimet 720Li sample CC015. 226

Figure 4-41: Showing the primary γ' size distribution for fine-grained Udimet 720Li sample CC009. 226

Figure 4-42: Showing the primary γ' size distribution for fine-grained Udimet 720Li sample CX027. 227

Figure 4-43: Showing the area fraction of primary γ' found in each sample. 228

Figure 4-44: Optical micrograph of fine-grained Udimet 720Li test piece CC041 as etched by Kalling's reagent a 100X magnification (left) and 1000X magnification (right). 229
Figure 4-45: Optical micrograph of fine-grained Udimet 720Li test piece CC045 as etched by Kalling's reagent a 100X magnification (left) and 1000X magnification (right). 230
Figure 4-46: Showing the grain size distribution for fine-grained Udimet 720Li sample CC041. 231
Figure 4-47: Showing the grain size distribution for fine-grained Udimet 720Li sample CC045. 231
Figure 4-48: Showing four representative micrographs of sectioned test piece CC017, tested with a dwell period of 1,200 seconds, and overload factor of 1.08 and at a temperature of 650°C in laboratory air. Note that despite similar testing conditions, baseline dwell and overload crack growth rates were consistently faster in CC017 when compared with CC045 (below, Figure 4-49). 233
Figure 4-49: Showing four representative micrographs of sectioned test piece CC045, tested with a dwell period of 1,200 seconds, and overload factor of 1.08 and at a temperature of 650°C in laboratory air. Note that despite similar testing conditions, baseline dwell and overload crack growth rates were consistently slower in CC045 when compared with CC017 (above, Figure 4-48).....234
Figure 4-50: Showing four representative micrographs of sectioned test piece CC018, tested with a dwell period of 1,200 seconds, and overload factor of 1.08 and at a temperature of 625°C in laboratory air. Note that despite similar testing conditions, baseline dwell and overload crack growth rates were consistently faster in CC018 when compared with CC047 (below, Figure 4-51). 235

Figure 4-51: Showing four representative micrographs of sectioned test piece CC047, tested with a dwell period of 1,200 seconds, and overload factor of 1.08 and at a temperature of 625°C in laboratory air. Note that despite similar testing conditions, baseline dwell and overload crack growth rates were consistently slower in CC047 when compared with CC018 (above, Figure 4-50).....236

Figure 4-52: Micrograph of test piece CX001, slow cooled (at ~0.1°C/s) etched using Kalling's reagent according to methodologies detailed in Table 15.....237

Figure 4-53: Micrograph of test piece CC048, intermediately cooled (at ~1.4°C/s) etched using Kalling's reagent according to methodologies detailed in Table 15.....238

Figure 4-54: Micrograph of test piece CX005, fast cooled (at ~5°C/s) etched using Kalling's reagent according to methodologies detailed in Table 15. 238

Figure 4-55: Micrograph of test piece CX001, slow cooled (at ~0.1°C/s) electro-chemically etched using 10% Phosphoric according to methodologies detailed in Table 15.....239

Figure 4-56: Micrograph of test piece CC048, intermediately cooled (at ~1.4°C/s) electro-chemically etched using 10% Phosphoric according to methodologies detailed in Table 15. 239

Figure 4-57: Micrograph of test piece CX005, fast cooled (at ~5°C/s) electro-chemically etched using 10% Phosphoric according to methodologies detailed in Table 15.....240

Figure 4-58: Micrograph of test piece CX001, slow cooled (at ~0.1°C/s) etched using a Molybdenum based etchant according to methodologies detailed in Table 15.....240

Figure 4-59: Micrograph of test piece CX001, slow cooled (at ~0.1°C/s) etched using a Molybdenum based etchant according to methodologies detailed in Table 15.....241

Figure 4-60: Micrograph of test piece CC048, intermediately cooled (at ~1.4°C/s) etched using a Molybdenum based etchant according to methodologies detailed in Table 15.....241
Figure 4-61: Micrograph of test piece CC048, intermediately cooled (at ~1.4°C/s) etched using a Molybdenum based etchant according to methodologies detailed in Table 15.....242
Figure 4-62: Micrograph of test piece CX005, fast cooled (at ~5°C/s) etched using a Molybdenum based etchant according to methodologies detailed in Table 15. 242
Figure 4-63: Micrograph of test piece CX005, fast cooled (at ~5°C/s) etched using a Molybdenum based etchant according to methodologies detailed in Table 15. 243
Figure 4-64: Contour plot of stress normal to the crack tip (SYY) at time t = 2, after the 1 second hold at maximum (overload) load. 244
Figure 4-65: Contour plot of stress normal to the crack tip (SYY) at time t = 3, immediately after unloading from the one second hold at maximum (overload) load to the dwell load. Note stresses immediately ahead of the crack tip have unloaded preferentially. 245
Figure 4-66: Contour plot of stress normal to the crack tip (SYY) at time $t = t_{inc}/2$ where t_{inc} is the incubation time (reported in section 4.3.2). Note crack tip stresses have begun to relax back to those normally associated with dwell crack tip stress states. 246
Figure 4-67: Contour plot of stress normal to the crack tip (SYY) at time $t = t_{inc}$ where t_{inc} is the incubation time (reported in section 4.3.2). Note that at this stage, crack tip stresses are considered to be equal to those normally associated with dwell crack tip stresses (discussed below). 246
Figure 4-68: Contour plot of stress normal to the crack tip (SYY) for a dwell-only simulation at time $t = t_{inc}$ where t_{inc} is the incubation time (reported in section 4.3.2). Note crack tip stress states are comparable with those presented in Figure 4-67. 247

Figure 4-69: Showing dwell and overload crack tip stress as a function of time and the calculation of t_{inc}.....249

Figure 4-70: Plotting t_{inc} against overload factor for fine-grained Udimet 720Li at 650°C. Models are run with a Background Load of 531MPa and a crack length of 1.025mm which relates to a ΔK of around 18-19MPa√m. 251

Figure 4-71: Plotting t_{inc} against overload factor for a range of temperatures, for fine-grained Udimet 720Li. Models are run with a Background Load of 531MPa and a crack length of 1.025mm which relates to a ΔK of around 18-19MPa√m. 252

Figure 4-72: Plotting t_{inc} against overload factor for a range of temperatures, for fine-grainedRR1000. Models are run with a Background Load of 531MPa and a crack length of 1.025mm which relates to a ΔK of around 18-19MPa√m. 253

Figure 4-73: A graph of SYY against time for a range of overload factors applied to fine-grained Udimet 720Li (REC) simulations at 650°C with a background load of 531 MPa. ..255

Figure 4-74: Showing inelastic creep strain (CEQI) against time for the node at the crack tip and the node 1.5r ahead of the crack tip for a typical overload cycle. For reference, the material simulated is fine-grained Udimet 720Li (REC).....259

Figure 4-75: Showing the same information as Figure 4-74 (above) with higher axes resolution and the use of a secondary axis for 1.5r data. 260

Figure 4-76: Plotting creep strain rate against time for data gathered from the crack tip and 1.5r ahead of the crack tip, for the creep data represented above in Figure 4-74, showing the calculation of parameter t_x 261

Figure 4-77: Plotting the difference between the creep strain rate at 1.5r ahead of the crack tip and the creep strain rate at the crack tip against time for a typical overload cycle. Note that t_x would actually be three seconds less than is represented by the graph. 262

Figure 4-78: Plotting t_x against overload factor for a range of temperatures, for fine-grained Udimet 720Li. Models are run with a Background Load of 531MPa and a crack length of 1.025mm which relates to a ΔK of around 18-19MPa√m. 265

Figure 4-79: Plotting t_x against overload factor for a range of temperatures, for fine-grained RR1000. Models are run with a Background Load of 531MPa and a crack length of 1.025mm which relates to a ΔK of around 18-19MPa√m. 266

Figure 4-80: Plotting crack tip stress (SYY) against time for a typical overload waveform comparing Udimet 720Li with RR1000. Note that t_{inc} is larger for RR1000 when compared with Udimet 720Li for the same conditions. 268

Figure 4-81: Plotting t_x against overload factor for fine-grained U720Li and RR1000 at 650°C. Models are run with a Background Load of 531MPa and a crack length of 1.025mm which relates to a ΔK of around 18-19MPa√m. 269

Figure 4-82: Plotting t_x after a one second period at maximum (overload) load against t_x after a two minute period at overload; for otherwise similar conditions. 271

Figure 4-83: Plotting incubation time (t_{inc}) against crossing time (t_x) for all conditions analysed.....273

Figure 4-84: Plotting modelled t_{inc} against experimentally derived t_{inc} for all conditions analysed.....277

Figure 5-1: Fracture surface of fine-grained Udimet 720Li sample CX027 during high temperature (650°) baseline loading, in air. The image is taken at a ΔK of 14 MPa√m. The

image shows transgranular failure of γ grains and "intergranular" failure of primary γ' precipitates. 287

Figure 5-2: Standard free energies of formation of oxides [94]. 292

Figure 5-3: Optical micrograph to show non-uniform crack front relating to dwell cycling. Arrows show "fingers" of materials relating to dwell and baseline crack fronts. 327

Figure A-1: A comparison of the compliance function as originally determined by Pickard with that defined by RR1000 procedural documentation. The polynomial line fits shorter crack with longer crack compliance behaviour (analysis originally presented by Simpson [96]).....415

Figure A-2 [97]: Plotting t_x against a range of values for $\Delta t/t_x$ used to generate the calculation as calculated for the following conditions: TEMP = 675°C, OLF = 1.25, BL = 531 MPa, K_{dwell} = 35.8 MPa√m. Note that t_x converged to ~1799 seconds at $\Delta t/t_x$ of ~ 0.06 421

Figure A-3: da/dN vs. ΔK curves for fine-grained Udimet 720Li samples CX015, CX020 and CX047, which were tested at 550°C (CX015 and CX020) and 525°C (CX047), with a dwell load of 26 kN, and a dwell time of 3,600 seconds. 425

Figure A-4: da/dN vs. ΔK curves for fine-grained Udimet 720Li samples CX013, CX014, CX042 and CX045, which were tested at 600°C, with a dwell load of 26 kN, a dwell time of 3,600s in air (CX013 and CX014) and 120s in a vacuum (CX042 and CX045).....426

Figure A-5: da/dN vs. ΔK curves for fine-grained Udimet 720Li samples tested at 650°C at a range of dwell periods, in air and in a vacuum. 427

Figure A-6: da/dN vs. ΔK curves for fine-grained Udimet 720Li samples CC009, CC015 and CX027, all tested at 650°C and with a dwell period of 3,600s, in air. Note that despite similar

testing conditions crack growth rates are shown to be variable. Note also that CX027 data represents intermittent “bursts” of baseline (1-1-1-1) loading in order to encourage the crack to grow under a dwell regime. 428

Figure A-7: da/dN vs. ΔK curves for fine-grained Udimet 720Li samples CC013, CC014, CC015 and CC020, which were tested at 600°C (CC013 and CC014) and 650°C (CC015 and CC020), with a dwell load of 26 kN, and overload factor of 1.05 (CC013 and CC014) and 1.15 (CC015and CC020), and a dwell time of 1,200s (CC013) and 3,600s. Note also that crack growth rates in sample CC014 in particular sit almost exactly 50°C lower than perviously tested microstructures. 429

Figure A-8: da/dN vs. ΔK curves for fine-grained Udimet 720Li samples CC003, CC004, CC007, CC008 and CC010, which were tested at 650°C and under various overload factors and dwell times. Note that two sets of baseline, dwell and overload loading has been used on each sample. A plot for each individual test piece is presented below. 430

Figure A-9: da/dN vs. ΔK curve for fine-grained Udimet 720Li sample CC003, which was tested at 650°C, with a dwell load of 26 kN, a dwell period of 3,600s and an overload factor of 1.15. Note that two sets of baseline, dwell and overload loading has been applied to the test piece. Partial retardation. 431

Figure A-10: da/dN vs. ΔK curve for fine-grained Udimet 720Li sample CC004, which was tested at 650°C, with a dwell load of 26 kN, a dwell period of 1,200s and an overload factor of 1.15. Note that two sets of baseline, dwell and overload loading has been applied to the test piece. Note also that overload testing has not been run long enough to determine degree of retardation, nevertheless Full retardation can be inferred. 432

Figure A-11: da/dN vs. ΔK curve for fine-grained Udimet 720Li sample CC007, which was tested at 650°C, with a dwell load of 26 kN, a dwell period of 1,200s and an overload factor of 1.15. Note that two sets of baseline, dwell and overload loading has been applied to the test piece. Partial retardation has occurred at lower ΔK values and Full retardation at higher ΔK values. 433

Figure A-12: da/dN vs. ΔK curve for fine-grained Udimet 720Li sample CC008, which was tested at 675°C, with a dwell load of 22 kN, a dwell period of 1,200s and an overload factor of 1.10. Note that two sets of baseline, dwell and overload loading has been applied to the test piece. Partial retardation. 434

Figure A-13: da/dN vs. ΔK curve for fine-grained Udimet 720Li sample CC010, which was tested at 650°C, with a dwell load of 26 kN, a dwell period of 1,200s and an overload factor of 1.08. Note that two sets of baseline, dwell and overload loading has been applied to the test piece. Partial retardation. 435

Figure A-14: da/dN vs. ΔK curves for fine-grained Udimet 720Li samples CC001, CC002, CC005, CC006 and CC009, which were tested at 600°C and under various overload factors and dwell times. Note that two sets of baseline, dwell and overload loading has been used on each sample. A plot for each individual test piece is presented below.....436

Figure A-15: da/dN vs. ΔK curve for fine-grained Udimet 720Li sample CC001, which was tested at 600°C, with a dwell load of 32.5 kN, a dwell period of 1,200s and an overload factor of 1.15. Note that two sets of baseline, dwell and overload loading has been applied to the test piece. Full retardation. 437

Figure A-16: da/dN vs. ΔK curve for fine-grained Udimet 720Li sample CC002, which was tested at 600°C, with a dwell load of 32.5 kN, a dwell period of 3,600s and an overload factor of 1.15. Note that two sets of baseline, dwell and overload loading has been applied to the test piece. Full retardation. 438

Figure A-17: da/dN vs. ΔK curve for fine-grained Udimet 720Li sample CC005, which was tested at 600°C, with a dwell load of 32.5 kN, a dwell period of 1,200s and an overload factor of 1.05. Note that two sets of baseline, dwell and overload loading has been applied to the test piece. Partial retardation. 439

Figure A-18: da/dN vs. ΔK curve for fine-grained Udimet 720Li sample CC006, which was tested at 600°C, with a dwell load of 32.5 kN, a dwell period of 3,600s and an overload factor of 1.05. Note that two sets of baseline, dwell and overload loading has been applied to the test piece. Partial retardation. 440

Figure A-19: da/dN vs. ΔK curve for fine-grained Udimet 720Li sample CC009, which was tested at 625°C, with a dwell load of 29 kN, a dwell period of 1,200s and an overload factor of 1.08. Note that two sets of baseline, dwell and overload loading has been applied to the test piece. Partial retardation. 441

Figure A-20: da/dN vs. ΔK graph for Udimet 720Li samples CC029 and CC032 tested at a temperature of 650°C, dwell loads of 26 kN, an overload factor of 1.15 and a dwell periods of 1,200s. Overload segments in both cases were extended to hold periods rather than conventional 1s in previous tests: 120s for CC029 and 600s for CC032. 442

Figure A-21: da/dN vs. ΔK graph to show the effect of a 120 second dwell period on the stress intensity factor range threshold for high temperature (650°C) crack growth when

compared with 1 Hz sinusoidal loading. Note that both sets of data are gathered using the decreasing ΔK (load shedding) technique. Note also the temperature threshold data gathered on the same test piece (CC044), which was found to be ~510 °C for a ΔK of around 30MPa√m.....443

Figure A-22: da/dN vs. ΔK graph to show increasing ΔK threshold testing on Udimet 720Li test pieces CC040 and CC041, and decreasing ΔK threshold testing on test piece CC044; both tested at 650°C and with a dwell period of 120s. Note threshold values obtained were around 13, 12 and 12.5 MPa√m respectively. Note also therefore that time-dependent threshold values are shown to be independent of testing methodology (in terms of increasing vs decreasing ΔK methods). 444

Figure A-23: da/dN vs. ΔK graph to show comparisons for all ΔK threshold testing on Udimet 720Li sample test pieces. All tests are carried out at 650°C in laboratory air, with dwell periods of 120 or 3,600 seconds. Note that test pieces CC011 and CC045 (showing unusual results when compared with the other data presented) are found to comprise notably different microstructures. 445

Figure A-24: da/dN vs. ΔK curves for fine-grained RR1000 samples CC003 and CC005, which were tested at 600°C, with a dwell load of 26 kN, a dwell time of 3,600s in air. Note the effect of introducing a dwell period on crack growth rates when compared with those associated with baseline loading. Note also the “tails” on the final segments of baseline loading crack growth rates. 447

Figure A-25: da/dN vs. ΔK curves for fine-grained RR1000 samples CC001 and CC002, which were tested at 650°C, with a dwell load of 26 kN, a dwell time of 3,600s in air.....448

Figure A-26: da/dN vs. ΔK curves to show a comparison in terms of baseline and dwell crack growth rates for 600°C and 650°C. Samples are fine-grained RR1000; CC003 and CC005 (600°C) and CC001 and CC002 (650°C), tested in air with a dwell load of 26kN. 449

Figure A-27: da/dN vs. ΔK curves to show the effect of dwell testing in a vacuum when compared with otherwise similar testing in air. Test pieces are fine-grained RR1000, tested at a temperature of 650°C and with a dwell load of 26 kN. CC003 is tested in air, with a dwell period of 3,600 seconds. CC030 is tested in a vacuum; with dwell periods of 120 seconds and 3,600 seconds. Note crack growth rates drop down to below baseline under 3,600 second dwell loading in a vacuum. 450

Figure A-28: da/dN vs. ΔK curves for RR1000 samples CC019 and CC039 tested at a temperature of 600°C with an overload factor of 1.15. Note that the ΔK values are calculated using the load range between the peak overload and the minimum load (ΔK_{full}) for the overload fatigue crack growth segment. Full retardation. Note also that the curves show "settling down" behaviour for crack growth rates pertaining to both dwell and overload cycling, and "settling up" behaviour for crack growth rates pertaining to the final segment of baseline loading. 451

Figure A-29: da/dN vs. ΔK curves for RR1000 samples CC021 and CC042 tested at a temperature of 600°C with an overload factor of 1.05. Partial retardation.....452

Figure A-30: da/dN vs. ΔK curves for RR1000 samples CC021 and CC019 tested at a temperature of 600°C with a dwell time of 1,200s and overload factors of 1.05 and 1.15 respectively, to show the effect of overload factor. 453

Figure A-31: da/dN vs. ΔK curves for RR1000 samples CC042 and CC039 tested at a temperature of 600°C with a dwell time of 3,600s and overload factors of 1.05 and 1.15 respectively, to show the effect of overload factor. 454

Figure A-32: da/dN vs. ΔK curves for RR1000 samples CC047 and CC018 tested at a temperature of 625°C with an overload factor of 1.08 and a dwell time of 1,200s. Note that despite similar testing conditions, variation between fatigue crack growth rates has been observed. Nevertheless both samples display nearly full retardation. 455

Figure A-33: da/dN vs. ΔK curves for RR1000 samples CC050 and CC051 tested at a temperature of 650°C with an overload factor of 1.05, and dwell times of 120s and 300s respectively. Note that dwell crack growth data clearly show the effect of increasing the dwell time. Nearly full and partial retardation respectively. 456

Figure A-34: da/dN vs. ΔK curves for RR1000 samples CC049 and CC045 tested at a temperature of 650°C with an overload factor of 1.08 and dwell periods of 600s and 1,200s respectively. Again these graphs highlight (among other things) the effect of increasing the dwell period. Partial retardation.....457

Figure A-35: da/dN vs. ΔK curves for RR1000 samples CC046 and CC048, which were tested at 650°C, with a dwell load of 26 kN, and overload factor of 1.15 and a dwell time of 1,200 and 3,600 seconds respectively. Full retardation. 458

Figure A-36: da/dN vs. ΔK curves for RR1000 samples CC017 and CC045, both tested at a temperature of 650°C with an overload factor of 1.08 and a dwell time of 1,200s. Note that these results also confirm variation between samples in terms of crack growth resistance behaviour. Partial retardation.....459

Figure A-37: da/dN vs. ΔK curves for RR1000 samples CC020 and CC048, both tested at a temperature of 650°C with an overload factor of 1.15 and a dwell time of 3,600s. Note that these results also confirm variation between samples in terms of crack growth resistance behaviour. Nearly full retardation. 460

Figure A-38: da/dN vs. ΔK graph for RR1000 samples CC052, CC053 and CC034 tested at a temperature of 675°C and at dwell periods of 120s, 600s and 1,200s and overload factors of 1.05, 1.08 and 1.10 respectively. Nearly full and partial retardation respectively. 461

Figure A-39: da/dN vs. ΔK graph for RR1000 samples CC029 and CC035 tested at a temperature of 650°C, an overload factor of 1.15 and at dwell periods of 120s and 3,600s respectively. The overload segment in test piece CC029 was extended to a 120s hold time rather than conventional 1s previous tests. The second "band" of overload cycling applied to test piece CC035 (dark green, filled circles above) also included a 120s hold time at the overload load. 462

Figure A-40: da/dN vs. ΔK graph for RR1000 samples CC056 and CC057 tested at a temperature of 650°C, an overload factor of 1.065 and a dwell period of 1,200s. Samples were tested under the "Unloading" and "Reloading" regime respectively (Figure 3-11 and Figure 3-12). 463

Figure A-41: da/dN vs. ΔK graph for RR1000 samples CX001, CC048 and CX005 tested at a temperature of 650°C, and a dwell period of 3,600s. Samples were slow-cooled, intermediately cooled and fast-cooled respectively. 464

Figure A-42: Showing fractographs of fine-grained Udimet 720Li test piece CX015; tested at 550°C in laboratory air, with a dwell load of 26 kN and a dwell time of 3,600 seconds. Each

image shows the crack propagating from bottom left to top right. The band labelled A is the precrack region, which was undertaken at temperature and in air; bands B, D and F are baseline (1-1-1-1) regions and bands C, E and G are dwell regions. Note the marked difference in terms of crack growth mechanism when regions of baseline are compared with those relating to dwell cycling. Higher magnification images are taken at points relating to the following crack growth driving forces (ΔK): B: ~19 MPa√m; C: ~21.5 MPa√m; E: ~30 MPa√m; G: ~39.5 MPa√m.....469

Figure A-43: Showing fractographs of fine-grained Udimet 720Li test piece CX020; tested at 550°C in laboratory air, with a dwell load of 26 kN and a dwell time of 3,600 seconds. Each image shows the crack propagating from bottom right to top left. The band labelled A is the precrack region, which was undertaken at temperature and in air; bands B, D, F and H are baseline (1-1-1-1) regions and bands C, E and G are dwell regions. Note the marked difference in terms of crack growth mechanism when regions of baseline are compared with those relating to dwell cycling. Note also the final region of dwell cycling (G) which involves higher values of ΔK includes evidence of secondary cracking (out of plane) and uneven crack propagation. Higher magnification images are taken at points relating to the following crack growth driving forces (ΔK): B: ~19 MPa√m; C: ~21.5 MPa√m; E: ~30 MPa√m; G: ~39.5 MPa√m 473

Figure A-44: Showing fractographs of fine-grained Udimet 720Li test piece CX013; tested at 600°C in laboratory air, with a dwell load of 26 kN and a dwell time of 3,600 seconds. Each image shows the crack propagating from top left to bottom right. The band labelled A is the precrack region, which was undertaken at temperature and in air; bands B, D, and F are baseline (1-1-1-1) regions and bands C, E and G are dwell regions. Note the marked

difference in terms of crack growth mechanism when regions of baseline are compared with those relating to dwell cycling. Note also the final region of dwell cycling (G) which involves higher values of ΔK includes evidence of secondary cracking (out of plane) and uneven crack propagation. Higher magnification images are taken at points relating to the following crack growth driving forces (ΔK): B: ~17.5 MPa√m; C: ~22.5 MPa√m; E: ~30 MPa√m; G: ~39.5 MPa√m 477

Figure A-45: Showing fractographs of fine-grained Udimet 720Li test piece CX014; tested at 600°C in laboratory air, with a dwell load of 26 kN and a dwell time of 3,600 seconds. Each image shows the crack propagating from bottom right to top left. The band labelled A is the precrack region, which was undertaken at temperature and in air; bands B, D, F and H are baseline (1-1-1-1) regions and bands C, E and G are dwell regions. Note the marked difference in terms of crack growth mechanism when regions of baseline are compared with those relating to dwell cycling. Higher magnification images are taken at points relating to the following crack growth driving forces (ΔK): B: ~17.5 MPa√m; C: ~19 MPa√m; E: ~27.5 MPa√m; G: ~35 MPa√m.....481

Figure A-46: Showing fractographs of fine-grained Udimet 720Li test piece CC009; tested at 650°C in laboratory air, with a dwell load of 26 kN and a dwell time of 3,600 seconds. Each image shows the crack propagating from bottom left to top right. The band labelled A is the baseline (1-1-1-1) region, and band B is the dwell region. Note the marked difference in terms of crack growth mechanism when regions of baseline are compared with those relating to dwell cycling. Note also delineation of primary γ' precipitates away from the γ matrix during high temperature fast cycling (1-1-1-1), as discussed in section 5.2.1. Higher

magnification images are taken at points relating to the following crack growth driving forces (ΔK): A: ~15 MPa√m; B: ~25 MPa√m 484
Figure A-47: Showing fractographs of fine-grained Udimet 720Li test piece CC019; tested at 650°C in laboratory air, with a dwell load of 27 kN and a dwell time of 3,600 seconds. Each image shows the crack propagating from bottom right to top left. The band labelled A is the baseline (1-1-1-1) region, and band B is the dwell region. Note the marked difference in terms of crack growth mechanism when regions of baseline are compared with those relating to dwell cycling. Note also delineation of primary γ' precipitates away from the γ matrix during high temperature fast cycling (1-1-1-1), as discussed in section 5.2.1. Higher magnification images are taken at points relating to the following crack growth driving forces (ΔK): A: ~15 MPa√m; B: ~25 MPa√m 486
Figure A-48: Showing fractographs of fine-grained Udimet 720Li test piece CX023; tested at 650°C in laboratory air, with a dwell load of 29 kN and a dwell time of 3,600 seconds. Each image shows the crack propagating from bottom left to top right. The band labelled A is the precrack region, which was undertaken at temperature and in air; bands B, D and F are baseline (1-1-1-1) regions and bands C and E are dwell regions. Note the marked difference in terms of crack growth mechanism when regions of baseline are compared with those relating to dwell cycling. Higher magnification images are taken at points relating to the following crack growth driving forces (ΔK): Transition from B to C: ~19 MPa√m; C: ~23 MPa√m; E: ~34 MPa√m 489
Figure A-49: Showing fractographs of fine-grained Udimet 720Li test piece CX027; tested at 650°C in laboratory air, with a dwell load of 23 kN and a dwell time of 3,600 seconds. Each image shows the crack propagating from top left to bottom right. The band labelled A is the

precrack region, which was undertaken at temperature and in air; bands B and D are baseline (1-1-1-1) regions and bands C and E are dwell regions. Note that in between B and C (labelled on the lower magnification overview image) dwell cycles were applied; and the crack failed to grow. Consequently fast cycles (1-1-1-1) were applied to bring the crack growth driving force up and dwell cycles were then applied again. For the second time the crack failed to grow, and the process was repeated until a ΔK of around 25 MPa√m was applied (C). Note the delineation of primary γ' precipitates away from the γ matrix during high temperature fast cycling (1-1-1-1), as discussed in section 5.2.1. Note also that at higher crack growth driving forces the crack growth mechanisms are even more intergranular even under baseline loading (D). Higher magnification images are taken at points relating to the following crack growth driving forces (ΔK): B: ~15 MPa√m; C: ~27.5 MPa√m; D: ~31 MPa√m; E: ~35 MPa√m.....493

Figure A-50: Showing fractographs of fine-grained Udimet 720Li test piece CX030; tested at 650°C in laboratory air, with a maximum load of 26 kN and a dwell time of 3,600 seconds. Note that in this test; the waveform applied comprised of holding the test piece at minimum load during the 3,600 second dwell period, and only applying the maximum load for a period of 1 second per cycle. Each image shows the crack propagating from bottom left to top right. The band labelled A is the precrack region, which was undertaken at temperature and in air; bands B, D and F are baseline (1-1-1-1) regions and bands C and E are dwell regions (1-1-1-3,600). Note the more subtle differences in terms of crack growth mechanism when regions of baseline are compared with those relating to dwell at minimum load cycling. Higher magnification images are taken at points relating to the following crack growth

driving forces (ΔK): B: ~22 MPa√m; transition from B to C: ~28 MPa√m; E: ~47 MPa√m; F: ~55 MPa√m 496

Figure A-51: Showing fractographs of fine-grained Udimet 720Li test piece CX025; tested at 650°C in laboratory air, with a maximum load of 26 kN and a dwell time of 3,600 seconds. Note that in this test; the waveform applied comprised of holding the test piece at minimum load during the 3,600 second dwell period, and only applying the maximum load for a period of 1 second per cycle. Each image shows the crack propagating from bottom right to top left. The band labelled A is the precrack region, which was undertaken at temperature and in air; bands B, D and F are baseline (1-1-1-1) regions and bands C and E are dwell regions (1-1-1-3,600). Note the more subtle differences in terms of crack growth mechanism when regions of baseline are compared with those relating to dwell at minimum load cycling. Higher magnification images are taken at points relating to the following crack growth driving forces (ΔK): Transition through from B, C and D: ~23.5 MPa√m; transition from C to D: ~24 MPa√m; transition through from C, D and E: ~27 MPa√m; F: ~38 MPa√m.....499

Figure A-52: Showing fractographs of fine-grained Udimet 720Li test piece CX031; tested at 650°C in a vacuum, with a dwell load of 26 kN and a dwell time of 120 seconds. Each image shows the crack propagating from bottom left to top right. The band labelled A is the precrack region, which was undertaken at temperature and also in a vacuum; bands B, D and F are baseline (1-1-1-1) regions and bands C and E are dwell regions. Note that crack growth mechanisms are transgranular even under dwell loading when the test is performed in a vacuum. Higher magnification images are taken at points relating to the following crack growth driving forces (ΔK): C: ~25 MPa√m; transition from C to D: ~28 MPa√m; D: ~30 MPa√m; transition from D to E: ~35 MPa√m; E: ~42 MPa√m 502

Figure A-53: Showing fractographs of fine-grained Udimet 720Li test piece CX034; tested at 650°C in a vacuum, with a dwell load of 26 kN and a dwell time of 3,600 seconds. Each image shows the crack propagating from bottom right to top left. The band labelled A is the precrack region, which was undertaken at temperature and also in a vacuum; bands B, D and F are baseline (1-1-1-1) regions and bands C, E and G are dwell regions. Note that fracture surfaces pertaining to dwell cycling appear rough and intergranular; even under vacuum conditions. Higher magnification images are taken at points relating to the following crack growth driving forces (ΔK): Transition from B through C to D: ~22 MPa√m; transition from D through E to F: ~32 MPa√m; D: ~30 MPa√m; transition from D to E: ~35 MPa√m; E: ~35 MPa√m; G: ~45 MPa√m.....506

Figure A-54: Showing fractographs of fine-grained Udimet 720Li test piece CC013; tested at 600°C in air, with a dwell load of 29 kN, an overload factor of 1.05 and a dwell time of 1,200 seconds. Each image shows the crack propagating from bottom left to top right. Note that this test piece is sourced from Phase Two, Batch Two material and was found to comprise notably smaller grain sizes including regions of ultra fine grain sized clusters. The band labelled A is the precrack region, which was undertaken at temperature and in air; bands B and E represent baseline (1-1-1-1) regions, band C the dwell region and band D the overload region. Note that crack growth mechanisms are mixed under baseline conditions, thought to occur due to the ultra fine grain microstructure of the material. Under higher crack growth driving forces it could be suggested that the mechanism is more intergranular when compared with mechanisms under lower crack growth driving forces (B compared with E). Note also that fracture surfaces pertaining to dwell and overload cycling appear rough and intergranular.

Higher magnification images are taken at points relating to the following crack growth driving forces (ΔK): B: ~20 MPa√m; C: ~27.5 MPa√m; D: ~40 MPa√m; E: ~55 MPa√m .509

Figure A-55: Showing fractographs of fine-grained Udimet 720Li test piece CC014; tested at 600°C in air, with a dwell load of 29 kN, an overload factor of 1.05 and a dwell time of 3,600 seconds. Each image shows the crack propagating from bottom left to top right. Note that this test piece is sourced from Phase Two, Batch Two material and was found to comprise notably smaller grain sizes including regions of ultra fine grain sized clusters. The band labelled A is the precrack region, which was undertaken at temperature and in air; bands B and E represent baseline (1-1-1-1) regions, band C the dwell region and band D the overload region. Note that crack growth mechanisms are mixed under baseline conditions, thought to occur due to the ultra fine grain microstructure of the material. Under higher crack growth driving forces it could be suggested that the mechanism is more intergranular when compared with mechanisms under lower crack growth driving forces (B compared with E). Note also that fracture surfaces pertaining to dwell and overload cycling appear rough and intergranular. Higher magnification images are taken at points relating to the following crack growth driving forces (ΔK): B: ~22.5 MPa√m; C: ~30 MPa√m; D: ~40 MPa√m; E: ~55 MPa√m .512

Figure A-56: Showing fractographs of fine-grained Udimet 720Li test piece CC015; tested at 650°C in air, with a dwell load of 26 kN, an overload factor of 1.15 and a dwell time of 3,600 seconds. Each image shows the crack propagating from bottom left to top right. Note that this test piece is sourced from Phase Two, Batch Two material and was found to comprise notably smaller grain sizes including regions of ultra fine grain sized clusters. The band labelled A is the precrack region, which was undertaken at temperature and in air; band B represents the baseline (1-1-1-1) region, band C the dwell region and band D the overload region. Note that

crack growth mechanisms are mixed under baseline conditions, thought to occur due to the ultra fine grain microstructure of the material. Note also that fracture surfaces pertaining to dwell and overload cycling appear rough and intergranular. Higher magnification images are taken at points relating to the following crack growth driving forces (ΔK): B: ~22.5 MPa√m; C: ~30 MPa√m; D: ~40 MPa√m; E: ~55 MPa√m.....515

Figure A-57: Showing fractographs of fine-grained Udimet 720Li test piece CC003; tested at 650°C in air, with a dwell load of 26 kN, an overload factor of 1.15 and a dwell time of 3,600 seconds. Each image shows the crack propagating from bottom left to top right. Note that two sets of baseline, dwell and overload loading has been applied to the test piece. Bands labelled A, C, F and I are baseline (1-1-1-1) regions, bands labelled B, D and G are dwell regions and bands labelled E and H; the overload regions. Higher magnification images are taken at points relating to the following crack growth driving forces (ΔK): A: ~18 MPa√m; B: ~19.5 MPa√m; transition from C to D: ~26 MPa√m; D: ~28 MPa√m; E: ~30 MPa√m; G: ~39 MPa√m; H: ~45 MPa√m; I: ~52.5 MPa√m.....520

Figure A-58: Showing fractographs of fine-grained Udimet 720Li test piece CC004; tested at 650°C in air, with a dwell load of 26 kN, an overload factor of 1.15 and a dwell time of 1,200 seconds. Each image shows the crack propagating from bottom left to top right. Note that two sets of baseline, dwell and overload loading has been applied to the test piece. Bands labelled A, D and G are baseline (1-1-1-1) regions, bands labelled B and E are dwell regions and bands labelled C and F; the overload regions. Note that crack growth mechanisms are partially intergranular under baseline loading. Higher magnification images are taken at points relating to the following crack growth driving forces (ΔK): A: ~27 MPa√m;

B: ~34 MPa√m; C: ~38 MPa√m; D: ~40 MPa√m; E: ~42.5 MPa√m; F: ~47 MPa√m; G: ~52.5 MPa√m 524

Figure A-59: Showing fractographs of fine-grained Udimet 720Li test piece CC007; tested at 650°C in air, with a dwell load of 26 kN, an overload factor of 1.15 and a dwell time of 1,200 seconds. Each image shows the crack propagating from bottom left to top right. Note that two sets of baseline, dwell and overload loading has been applied to the test piece. Bands labelled A, C, E and H are baseline (1-1-1-1) regions, bands labelled B and F are dwell regions and bands labelled D and G; the overload regions. Note that crack growth mechanisms are partially intergranular under baseline loading. Higher magnification images are taken at points relating to the following crack growth driving forces (ΔK): C: ~25 MPa√m; D: ~31 MPa√m; E: ~39 MPa√m; transition from E to F: ~44 MPa√m; G: ~48 MPa√m; H: ~57 MPa√m 528

Figure A-60: Showing fractographs of fine-grained Udimet 720Li test piece CC008; tested at 675°C in air, with a dwell load of 22 kN, an overload factor of 1.10 and a dwell time of 1,200 seconds. Each image shows the crack propagating from bottom left to top right. Note that two sets of baseline, dwell and overload loading has been applied to the test piece. Bands labelled A, D and G are baseline (1-1-1-1) regions, bands labelled B and E are dwell regions and bands labelled C and F; the overload regions. Note that crack growth mechanisms are partially intergranular under baseline loading. Higher magnification images are taken at points relating to the following crack growth driving forces (ΔK): A: ~16 MPa√m; B: ~19 MPa√m; C: ~22.5 MPa√m; D: ~27.5 MPa√m; E: ~32.5 MPa√m; F: ~39 MPa√m; G: ~45 MPa√m 532

Figure A-61: Showing fractographs of fine-grained Udimet 720Li test piece CC010; tested at 650°C in air, with a dwell load of 26 kN, an overload factor of 1.08 and a dwell time of 1,200 seconds. Each image shows the crack propagating from bottom left to top right. Note that two sets of baseline, dwell and overload loading has been applied to the test piece. Bands labelled A, D and G are baseline (1-1-1-1) regions, bands labelled B and E are dwell regions and bands labelled C and F; the overload regions. Higher magnification images are taken at points relating to the following crack growth driving forces (ΔK): A: ~20 MPa√m; B: ~26 MPa√m; C: ~31 MPa√m; D: ~37 MPa√m; E: ~42 MPa√m; F: ~49 MPa√m; G: ~55 MPa√m 536

Figure A-62: Showing fractographs of fine-grained Udimet 720Li test piece CC001; tested at 600°C in air, with a dwell load of 32.5 kN, an overload factor of 1.15 and a dwell time of 1,200 seconds. Each image shows the crack propagating from bottom left to top right. Note that two sets of baseline, dwell and overload loading has been applied to the test piece. Bands labelled A, C and F are baseline (1-1-1-1) regions, bands labelled B and D are dwell regions and bands labelled E and G; the overload regions. Note that crack growth mechanisms pertaining to overload cycling are predominantly transgranular; note also that full retardation has occurred. Higher magnification images are taken at points relating to the following crack growth driving forces (ΔK): A: ~20 MPa√m; B: ~25 MPa√m; C: ~33.5 MPa√m; D: ~37.5 MPa√m; E: ~43 MPa√m; F: ~50 MPa√m; G: ~60 MPa√m 540

Figure A-63: Showing fractographs of fine-grained Udimet 720Li test piece CC002; tested at 600°C in air, with a dwell load of 32.5 kN, an overload factor of 1.15 and a dwell time of 3,600 seconds. Each image shows the crack propagating from bottom left to top right. Note that two sets of baseline, dwell and overload loading has been applied to the test piece. Bands labelled A, C, F and H are baseline (1-1-1-1) regions, bands labelled B and D are dwell

regions and bands labelled E and G; the overload regions. Note that crack growth mechanisms pertaining to overload cycling are predominantly transgranular; note also that full retardation has occurred. Higher magnification images are taken at points relating to the following crack growth driving forces (ΔK): A: ~19 MPa√m; B: ~22.5 MPa√m; C: ~32 MPa√m; D: ~36.5 MPa√m; E: ~40 MPa√m; F: ~45 MPa√m; G: ~55 MPa√m; H: ~63 MPa√m 545

Figure A-64: Showing fractographs of fine-grained Udimet 720Li test piece CC005; tested at 600°C in air, with a dwell load of 32.5 kN, an overload factor of 1.05 and a dwell time of 1,200 seconds. Each image shows the crack propagating from bottom left to top right. Note that two sets of baseline, dwell and overload loading has been applied to the test piece. Bands labelled A, D and G are baseline (1-1-1-1) regions, bands labelled B and E are dwell regions and bands labelled C and F; the overload regions. Note that crack growth mechanisms pertaining to overload cycling are predominantly intergranular for lower crack growth driving forces (C) (where less retardation is achieved) and more transgranular for higher crack growth driving forces (F) (where more retardation is achieved). Higher magnification images are taken at points relating to the following crack growth driving forces (ΔK): A: ~22.5 MPa√m; B: ~28 MPa√m; C: ~34.5 MPa√m; D: ~40 MPa√m; E: ~47 MPa√m; F: ~56 MPa√m; G: ~65 MPa√m 550

Figure A-65: Showing fractographs of fine-grained Udimet 720Li test piece CC006; tested at 600°C in air, with a dwell load of 32.5 kN, an overload factor of 1.05 and a dwell time of 3,600 seconds. Each image shows the crack propagating from bottom left to top right. Note that two sets of baseline, dwell and overload loading has been applied to the test piece. Bands labelled A, D and G are baseline (1-1-1-1) regions, bands labelled B and E are dwell regions

and bands labelled C and F; the overload regions. Note that crack growth mechanisms pertaining to overload cycling are predominantly intergranular where partial retardation is achieved. Higher magnification images are taken at points relating to the following crack growth driving forces (ΔK): A: ~24 MPa√m; B: ~29.5 MPa√m; C: ~35 MPa√m; D: ~40 MPa√m; E: ~46 MPa√m; F: ~55 MPa√m; G: ~69 MPa√m 554

Figure A-66: Showing fractographs of fine-grained Udimet 720Li test piece CC009; tested at 625°C in air, with a dwell load of 29 kN, an overload factor of 1.08 and a dwell time of 1,200 seconds. Each image shows the crack propagating from bottom left to top right. Note that two sets of baseline, dwell and overload loading has been applied to the test piece. Bands labelled A, D and G are baseline (1-1-1-1) regions, bands labelled B and E are dwell regions and bands labelled C and F; the overload regions. Note that crack growth mechanisms pertaining to overload cycling are predominantly intergranular where partial retardation is achieved. Higher magnification images are taken at points relating to the following crack growth driving forces (ΔK): A: ~22.5 MPa√m; B: ~27 MPa√m; C: ~31 MPa√m; D: ~35 MPa√m; E: ~40 MPa√m; F: ~48 MPa√m; G: ~56 MPa√m 558

Figure A-67: Showing fractographs of fine-grained Udimet 720Li test piece CC029; tested at 650°C in air, with a dwell load of 26 kN, an overload factor of 1.15 and a dwell time of 1,200 seconds. Note that in this case; the overload segment was increased to a dwell time of 120 seconds rather than conventional 1 second hold periods in each other overload test. Each image shows the crack propagating from bottom left to top right. Bands labelled A and D are baseline (1-1-1-1) regions, the band labelled B represents the dwell region and the band labelled C; the overload region. Note also that within the large baseline segment (A), a small period of dwell cycling has been applied (hence the band in the image). Higher magnification

images are taken at points relating to the following crack growth driving forces (ΔK): A: ~24 MPa√m; B: ~29 MPa√m; C: ~31 MPa√m; D: ~42 MPa√m.....561

Figure A-68: Showing fractographs of fine-grained Udimet 720Li test piece CC032; tested at 650°C in air, with a dwell load of 26 kN, an overload factor of 1.15 and a dwell time of 1,200 seconds. Note that in this case; the overload segment was increased to a dwell time of 600 seconds rather than conventional 1 second hold periods in each other overload test. Each image shows the crack propagating from bottom left to top right. Bands labelled A and D are baseline (1-1-1-1) regions, the band labelled B represents the dwell region and the band labelled C; the overload region. Higher magnification images are taken at points relating to the following crack growth driving forces (ΔK): A: ~24 MPa√m; B: ~29 MPa√m; C: ~31 MPa√m; D: ~42 MPa√m; E: ~54.5 MPa√m.....564

Figure A-69: Showing fractographs of fine-grained Udimet 720Li test piece CC040; tested at 650°C in air, with a dwell time of 120 seconds. The test piece was tested to determine the stress intensity factor range threshold (ΔK_{th}) for which time-dependent crack growth would occur. In this case, the test was carried out according to the increasing ΔK method, described in section 0. The band labelled A represents 1 Hz sinusoidal loading (carried out in air and at temperature), the band labelled C represents dwell cycling and a transition period between the two (in terms of mechanism) is labelled B. Each image shows the crack propagating from bottom left to top right. Higher magnification images are taken at points relating to the following crack growth driving forces (ΔK): Transition from A through B to C: ~14 MPa√m; C: ~20 MPa√m.....567

Figure A-70: Showing fractographs of fine-grained Udimet 720Li test piece CC041; tested at 650°C in air, with a dwell time of 120 seconds. The test piece was tested to determine the

stress intensity factor range threshold (ΔK_{th}) for which time-dependent crack growth would occur. In this case, the test was carried out according to the increasing ΔK method, described in section 0. The band labelled A represents 1 Hz sinusoidal loading (carried out in air and at temperature), the band labelled C represents dwell cycling and a transition period between the two (in terms of mechanism) is labelled B. Each image shows the crack propagating from bottom left to top right. Higher magnification images are taken at points relating to the following crack growth driving forces (ΔK): Transition from A through B to C: ~12.5 MPa√m; C: ~20 MPa√m.....569

Figure A-71: Showing fractograph of fine-grained Udimet 720Li test piece CC044; tested at 650°C in air, with a dwell time of 120 seconds. The test piece was tested to determine the stress intensity factor range threshold (ΔK_{th}) for which time-dependent crack growth would occur. In this case, the test was carried out according to the decreasing ΔK method, described in section 0. The image is taken of the dwell region, at a ΔK of ~18.5 MPa√m 570

Figure A-72: Showing fractographs of fine-grained Udimet 720Li test piece CC045; tested at 650°C in air, with a dwell time of 1,200 seconds. The test piece was tested to determine the stress intensity factor range threshold (ΔK_{th}) for which time-dependent crack growth would occur. In this case, the test was carried out according to the increasing ΔK method, described in section 0. Each image shows the crack propagating from bottom left to top right. Higher magnification images are taken at points relating to the following crack growth driving forces (ΔK): Near threshold: ~10.5 MPa√m; dwell cycling: ~13 MPa√m.....572

Figure A-73: Showing fractographs of fine-grained RR1000 test piece CC002; tested at 650°C in air, with a dwell load of 26 kN and a dwell time of 3,600 seconds. Each image shows the crack propagating from left to right. Note that crack growth mechanisms according

to 3,600 seconds dwell in air appear to be predominantly intergranular; and that crack growth mechanisms pertaining to baseline loading are predominantly transgranular. Higher magnification images are taken at points relating to the following crack growth driving forces (ΔK): “low ΔK” 3,6000 second dwell: ~22 MPa√m; “high ΔK” 3,6000 second dwell: ~36 MPa√m; baseline: ~43 MPa√m 575

Figure A-74: Showing fractographs of fine-grained RR1000 test piece CC003; tested at 600°C in air, with a dwell load of 26 kN and a dwell time of 3,600 seconds. Each image shows the crack propagating from top to bottom. Note that crack growth mechanisms according to 3,600 seconds dwell in air appear to be predominantly intergranular; and that crack growth mechanisms pertaining to baseline loading are predominantly transgranular. Higher magnification images are taken at points relating to the following crack growth driving forces (ΔK): “low ΔK” 3,6000 second dwell: ~21 MPa√m; “high ΔK” 3,6000 second dwell: ~37 MPa√m; baseline: ~44 MPa√m 578

Figure A-75: Showing fractographs of fine-grained RR1000 test piece CC030; tested at 650°C in a vacuum, with a dwell load of 26 kN, and dwell times of 120 and 3,600 seconds. (The band of 120 second crack growth is indistinguishable on the lower magnification image from baseline regions.) Each image shows the crack propagating from left to right. Note that crack growth mechanisms according to 120 seconds dwell in a vacuum appear to be predominantly transgranular; yet crack growth mechanisms according to 3,600 seconds dwell appear intergranular. Higher magnification images are taken at points relating to the following crack growth driving forces (ΔK): 120 second dwell: ~22 MPa√m; baseline: ~26 MPa√m; 3,600 second dwell: ~28 MPa√m 582

Figure A-76: Showing fractographs of fine-grained RR1000 test piece CC019; tested at 600°C in air, with a dwell load of 26 kN, an overload factor of 1.15 and a dwell time of 1,200 seconds. Each image shows the crack propagating from top right to bottom left. Bands labelled A and D are baseline (1-1-1-1) regions, the band labelled B represents the dwell region and the band labelled C; the overload region. Full retardation is judged to have occurred. Higher magnification images are taken at points relating to the following crack growth driving forces (ΔK): A: ~18 MPa√m; B: ~25 MPa√m; C: ~39 MPa√m; D: ~45 MPa√m 585

Figure A-77: Showing fractographs of fine-grained RR1000 test piece CC021; tested at 600°C in air, with a dwell load of 26 kN, an overload factor of 1.05 and a dwell time of 1,200 seconds. Each image shows the crack propagating from bottom left to top right. Bands labelled A and D are baseline (1-1-1-1) regions, the band labelled B represents the dwell region and the band labelled C; the overload region. Partial retardation is judged to have occurred. Higher magnification images are taken at points relating to the following crack growth driving forces (ΔK): A: ~18 MPa√m; B: ~22.5 MPa√m; C: ~26 MPa√m; D: ~30 MPa√m 588

Figure A-78: Showing fractographs of fine-grained RR1000 test piece CC042; tested at 600°C in air, with a dwell load of 26 kN, an overload factor of 1.05 and a dwell time of 3,600 seconds. Each image shows the crack propagating from bottom left to top right. Bands labelled A and D are baseline (1-1-1-1) regions, the band labelled B represents the dwell region and the band labelled C; the overload region. Partial retardation is judged to have occurred. Higher magnification images are taken at points relating to the following crack growth driving forces (ΔK): A: ~19.5 MPa√m; B: ~25 MPa√m; C: ~34 MPa√m.....590

Figure A-79: Showing fractographs of fine-grained RR1000 test piece CC047; tested at 625°C in air, with a dwell load of 26 kN, an overload factor of 1.08 and a dwell time of 1,200 seconds. Each image shows the crack propagating from bottom right to top left. Bands labelled A and D are baseline (1-1-1-1) regions, the band labelled B represents the dwell region and the band labelled C; the overload region. Nearly full retardation is judged to have occurred. Higher magnification images are taken at points relating to the following crack growth driving forces (ΔK): A: ~17 MPa√m; B: ~24 MPa√m; C: ~35 MPa√m; D: ~44 MPa√m 593

Figure A-80: Showing fractographs of fine-grained RR1000 test piece CC018; tested at 625°C in air, with a dwell load of 26 kN, an overload factor of 1.08 and a dwell time of 1,200 seconds. Each image shows the crack propagating from bottom left to top right. Bands labelled A and D are baseline (1-1-1-1) regions, the band labelled B represents the dwell region and the band labelled C; the overload region. Nearly full retardation is judged to have occurred. Higher magnification images are taken at points relating to the following crack growth driving forces (ΔK): A: ~19 MPa√m; B: ~29 MPa√m; C: ~45 MPa√m; D: ~47.5 MPa√m 596

Figure A-81: Showing fractographs of fine-grained RR1000 test piece CC045; tested at 650°C in air, with a dwell load of 26 kN, an overload factor of 1.08 and a dwell time of 1,200 seconds. Each image shows the crack propagating from bottom right to top left. Bands labelled A and D are baseline (1-1-1-1) regions, the band labelled B represents the dwell region and the band labelled C; the overload region. Partial retardation is judged to have occurred. Higher magnification images are taken at points relating to the following crack

growth driving forces (ΔK): A: ~17.5 MPa√m; B: ~24.5 MPa√m; C: ~32 MPa√m; D: ~42.5 MPa√m 599

Figure A-82: Showing fractographs of fine-grained RR1000 test piece CC046; tested at 650°C in air, with a dwell load of 26 kN, an overload factor of 1.15 and a dwell time of 1,200 seconds. Each image shows the crack propagating from bottom right to top left. Bands labelled A and D are baseline (1-1-1-1) regions, the band labelled B represents the dwell region and the band labelled C; the overload region. Full retardation is judged to have occurred. Higher magnification images are taken at points relating to the following crack growth driving forces (ΔK): A: ~17.5 MPa√m; B: ~24 MPa√m; C: ~33.5 MPa√m; D: ~42 MPa√m 602

Figure A-83: Showing fractographs of fine-grained RR1000 test piece CC048; tested at 650°C in air, with a dwell load of 26 kN, an overload factor of 1.15 and a dwell time of 3,600 seconds. Each image shows the crack propagating from bottom right to top left. Bands labelled A and D are baseline (1-1-1-1) regions, the band labelled B represents the dwell region and the band labelled C; the overload region. Full retardation is judged to have occurred. Higher magnification images are taken at points relating to the following crack growth driving forces (ΔK): A: ~17.5 MPa√m; B: ~24.5 MPa√m; C: ~34 MPa√m; D: ~42 MPa√m 605

Figure A-84: Showing fractographs of fine-grained RR1000 test piece CC017; tested at 650°C in air, with a dwell load of 26 kN, an overload factor of 1.08 and a dwell time of 1,200 seconds. Each image shows the crack propagating from top right to bottom left. The band labelled A represents baseline loading (1-1-1-1), the band labelled B represents the dwell region and the band labelled C; the overload region. Partial retardation is judged to have

occurred. Higher magnification images are taken at points relating to the following crack growth driving forces (ΔK): A: ~19 MPa√m; B: ~25.5 MPa√m; C: ~37 MPa√m.....607

Figure A-85: Showing fractographs of fine-grained RR1000 test piece CC020; tested at 650°C in air, with a dwell load of 26 kN, an overload factor of 1.15 and a dwell time of 3,600 seconds. Each image shows the crack propagating from bottom left to top right. Nearly full retardation is judged to have occurred. Higher magnification images are taken at points relating to the following crack growth driving forces (ΔK): A: ~17.5 MPa√m; B: ~23 MPa√m; C: ~32.5 MPa√m; D: ~45 MPa√m.....609

Figure A-86: Showing fractographs of fine-grained RR1000 test piece CC034; tested at 675°C in air, with a dwell load of 23.5 kN, an overload factor of 1.10 and a dwell time of 1,200 seconds. Each image shows the crack propagating from bottom left to top right. Bands labelled A and D are baseline (1-1-1-1) regions, the band labelled B represents the dwell region and the band labelled C; the overload region. Partial retardation is judged to have occurred. Higher magnification images are taken at points relating to the following crack growth driving forces (ΔK): A: ~17.5 MPa√m; B: ~22.5 MPa√m; C: ~32 MPa√m; D: ~47 MPa√m 612

Figure A-87: Showing fractographs of fine-grained RR1000 test piece CC035; tested at 650°C in air, with a dwell load of 26 kN, an overload factor of 1.15 and a dwell time of 3,600 seconds. Each image shows the crack propagating from bottom left to top right. Note that two segments of overload cycling have been applied; note also that in the second overload segment (labelled F) the time at overload has been increased to a 120 second hold period. Bands labelled A, D and G are baseline (1-1-1-1) regions, bands labelled B and E represent dwell regions and bands labelled C and F; the overload regions (with F being “dwell at

overload). Higher magnification images are taken at points relating to the following crack growth driving forces (ΔK): A: ~18 MPa√m; B: ~22.5 MPa√m; C: ~27 MPa√m; E: ~36 MPa√m; F: ~45 MPa√m 616

Figure A-88: Showing fractographs of fine-grained RR1000 test piece CC056; tested at 650°C in air, with a dwell load of 28.08 kN, an overload factor of 1.065 and a dwell time of 1,200 seconds. Each image shows the crack propagating from bottom left to top right. Note that during the "overload" segment (band C) unloading stress waveforms were applied (Figure 3-11). Bands labelled A and D are baseline (1-1-1-1) regions, the band labelled B represents the dwell region and the band labelled C; the overload (unload) region. Higher magnification images are taken at points relating to the following crack growth driving forces (ΔK): A: ~20 MPa√m; B: ~29 MPa√m; C: ~43.5 MPa√m; D: ~54.5 MPa√m 619

Figure A-89: Showing fractographs of fine-grained RR1000 test piece CC057; tested at 650°C in air, with a dwell load of 28.08 kN, an overload factor of 1.065 and a dwell time of 1,200 seconds. Each image shows the crack propagating from bottom left to top right. Note that during the "overload" segment (band C) reloading stress waveforms were applied (Figure 3-12). Bands labelled A and D are baseline (1-1-1-1) regions, the band labelled B represents the dwell region and the band labelled C; the overload (reload) region. Higher magnification images are taken at points relating to the following crack growth driving forces (ΔK): A: ~20 MPa√m; B: ~27.5 MPa√m; C: ~45 MPa√m; D: ~54.5 MPa√m.....622

Figure A-90: Showing fractographs of fine-grained RR1000 test piece CX001; tested at 650°C in air, with a dwell load of 12 kN (on a test piece 5 x 5 mm in gauge cross section), and a dwell time of 3,600 seconds. Note that this test piece has been purposefully cooled relatively slowly from the maximum heat treatment temperature (~0.1°C/s) and the

morphology of the γ' phase has been significantly affected (reported in section 4.2.2.4 and discussed in section 5.2.4). Each image shows the crack propagating from top right to bottom left. Bands labelled A and C are baseline (1-1-1-1) regions, and the band labelled B represents the dwell region. Note also that at a ΔK of around 22.5 MPa√m, dwell cycles were first applied but the crack did not propagate (beyond a small amount) – hence the band on the lower magnification image during the baseline segment. Higher magnification images are taken at points relating to the following crack growth driving forces (ΔK): A: ~13 MPa√m; B: ~29 MPa√m; C: ~41 MPa√m.....626

Figure A-91: Showing fractographs of fine-grained RR1000 test piece CX005; tested at 650°C in air, with a dwell load of 12 kN (on a test piece 5 x 5 mm in gauge cross section), and a dwell time of 3,600 seconds. Note that this test piece has been purposefully cooled relatively quickly from the maximum heat treatment temperature (~5°C/s) and the morphology of the γ' phase has been significantly affected (reported in section 4.2.2.4 and discussed in section 5.2.4). Each image shows the crack propagating from bottom right to top left. The band labelled A represents the baseline (1-1-1-1) region, and the band labelled B represents the dwell region. Higher magnification images are taken at points relating to the following crack growth driving forces (ΔK): A: ~13 MPa√m; B: ~22 MPa√m.....628

Appendix III List of Tables

Table 1: Roles of various alloying additions in various Ni-based superalloys [10]. 21

Table 2: Nominal chemical compositions for a range of conventional turbine disc alloys, weight %. 25

Table 3: Nominal chemical composition limits (weight percent, balance Nickel) of Udimet 720Li. 96

Table 4: Nominal chemical composition limits (weight percent, balance Nickel) of RR1000 [79]. 96

Table 5: Detailing testing methodology for baseline, dwell and overload tests. Approximate p.d values, crack lengths (a) and ΔK calculations are presented; more accurate and calibrated calculations are completed after each test. 109

Table 6: Detailing "load shedding" pre-cracking methodology including idealised (circular) estimations for associated plane stress plastic zone size radii (r). 110

Table 7: The parameter *n* for each alloy at each temperature; taken from Rolls-Royce in house material database COMMIT; used to determine experimentally derived values for incubation time. 124

Table 8: Overview of the Udimet 720Li Phase 1 test programme. 136

Table 9: Overview of the Udimet 720Li Phase 2 test programme. 137

Table 10: Overview of the Udimet 720Li ΔK_{th} test programme. 137

Table 11: Overview of the RR1000 Phase 1 test programme. 138

Table 12: Overview of the RR1000 Phase 2 test programme. 139

Table 13: Overview of the RR1000 cooling rate tests. 139

Table 14: Detailing polishing methodology for Ni-based superalloy samples. 142

Table 15: Etchant compositions and methods. 143

Table 16: Assigning TEMP, BL and PF to a "condition number". 158

Table 17: Assigning each moment in time to a condition number. 158

Table 18: Summary of the retardation effect observed for fine-grained Udimet 720Li overload tests. Note that "Green", "Amber" and "Blue" denote "full retardation", "nearly full retardation" and "partial retardation" respectively. Note that in most cases, two bands of overload cycling have been applied to each test piece; hence coloured identifications are presented in order of results for low ΔKs and high ΔKs respectively (low/high) 185

Table 19: Summary of the retardation effect observed for fine-grained RR1000 overload tests. Note that "Green", "Amber" and "Blue" denote "full retardation", "nearly full retardation" and "partial retardation" respectively. 187

Table 20: Tabulating the direction of "tails" on crack growth resistance curves as a result of switching the loading waveform, specifically for fine-grained Udimet 720Li test pieces. Shaded areas represent anomalous behaviour. 189

Table 21: Tabulating the direction of "tails" on crack growth resistance curves as a result of switching the loading waveform, specifically for fine-grained RR1000 test pieces. Shaded areas represent anomalous behaviour. Where possible, an estimate for the distance over which stabilisation of crack growth rates occurs is also included. 190

Table 22: Summary of fractographic analysis for the fine-grained Udimet 720Li baseline and dwell testing programme. 209

Table 23: Summary of fractographic analysis for the fine-grained Udimet 720Li baseline, dwell and overload testing programme. 210

Table 24: Summary of fractographic analysis for the fine-grained Udimet 720Li time-dependent threshold testing programme. 210

Table 25: Summary of fractographic analysis for the fine-grained RR1000 baseline and dwell testing programme. 211

Table 26: Summary of fractographic analysis for the fine-grained RR1000 baseline, dwell and overload testing programme. 211

Table 27: Summarising the average grain sizes pertaining to fine-grained Udimet 720Li samples CC015, CC009 and CX027. 222

Table 28: Summary of the average (mean), variance and standard deviation of primary γ' values obtained. 225

Table 29: Summary and comparison of modelled t_{inc}, modelled t_x and experimentally derived t_{inc} values calculated for fine-grained Udimet 720Li (REC) 275

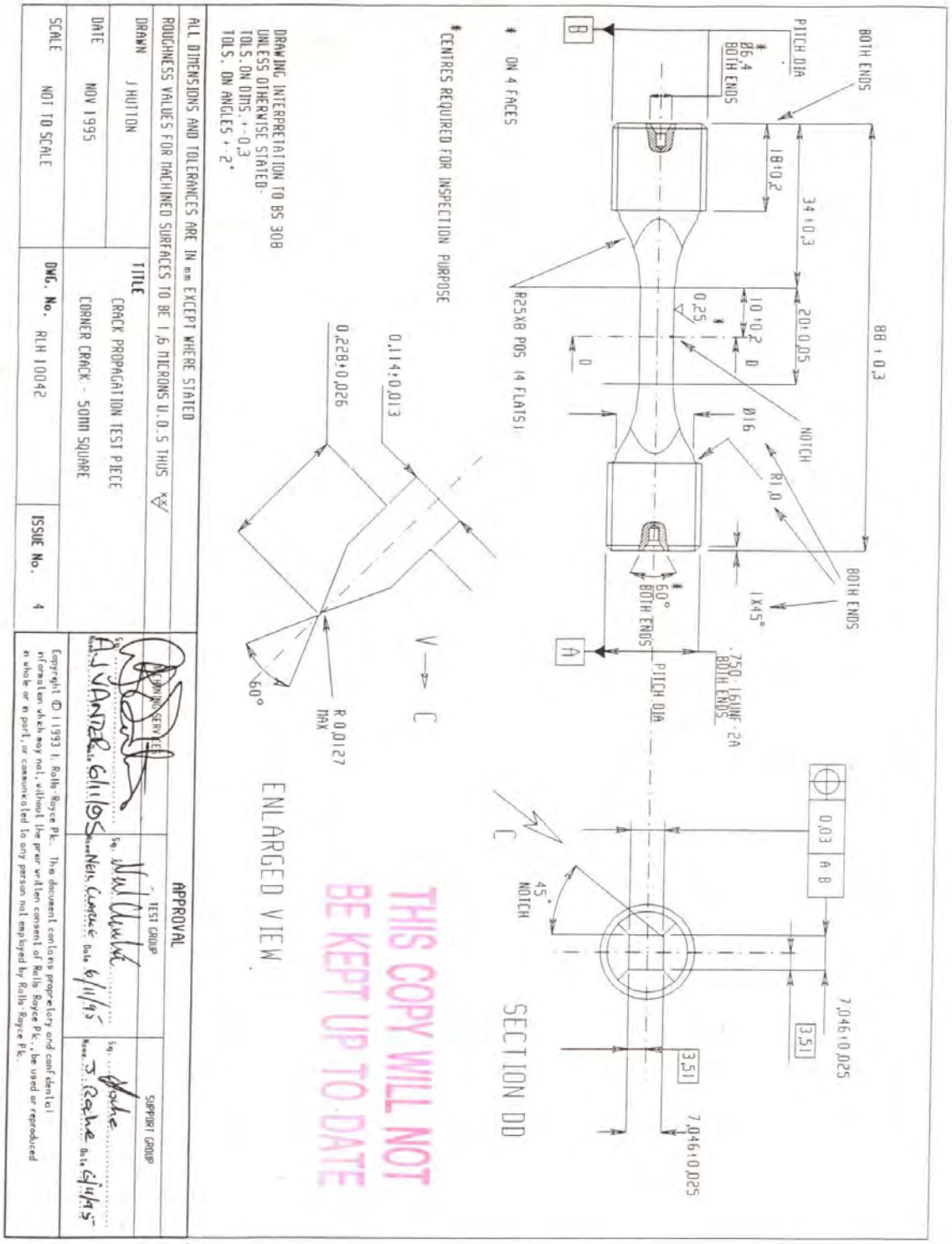
Table 30: Summary and comparison of modelled t_{inc}, modelled t_x and experimentally derived t_{inc} values calculated for fine-grained RR1000 (RGT) 276

Table 31: Values of K as evaluated for each of the three finite element models [83]. 419

Table 32 [97]: Results of t_x for cases with different $\Delta t/t_x$: showing convergence with $\Delta t/t_x \leq 0.06$ 422

Appendix IV Test Piece Drawings

Presented overleaf is a technical drawing to show the geometry of test pieces used in this programme of work.


BOTH ENDS
PITCH DIA
Ø6.4
BOTH ENDS
18±0.2
34±0.3
88±0.3
20±0.05
10±0.2
0.25
R25XB POS (4 FLATS)
ON 4 FACES
CENTRES REQUIRED FOR INSPECTION PURPOSE
NOTCH
Ø16
R1.0
1X45°
60°
BOTH ENDS
.750-16UNF-2A
BOTH ENDS
PITCH DIA
0.03 A B
7.046±0.025
3.51
45°
NOTCH
SECTION DD
0.114±0.013
0.228±0.026
60°
R 0.0127
MAX
ENLARGED VIEW
ALL DIMENSIONS AND TOLERANCES ARE IN mm EXCEPT WHERE STATED
ROUGHNESS VALUES FOR MACHINED SURFACES TO BE 1.6 MICRONS U.O.S THUS
DRAWING INTERPRETATION TO BS 308
UNLESS OTHERWISE STATED:
TOLS. ON DIMS. +-0.3
TOLS. ON ANGLES +-2°
DRAWN J HUTTON
DATE NOV 1995
SCALE NOT TO SCALE
TITLE
CRACK PROPAGATION TEST PIECE
CORNER CRACK - 50MM SQUARE
DWG. No. RLH 10042
ISSUE No. 4
APPROVAL
DRAWING SERVICES
TEST GROUP
SUPPORT GROUP
Sig.
Name A.J. VANDEL
Date 6/11/95
Sig.
Name N.H. CLARKE
Date 6/11/95
Sig.
Name J. ROWE
Date 6/11/95
THIS COPY WILL NOT
BE KEPT UP TO DATE
Copyright © 1993 Rolls-Royce Plc. The document contains proprietary and confidential information which may not, without the prior written consent of Rolls Royce Plc., be used or reproduced in whole or in part, or communicated to any person not employed by Rolls Royce Plc.

Appendix V Validity of Assumptions

Crack Length Calculations

As discussed in section 3.2.4, the continuous calculation of crack length as it propagates through a test piece relies upon two fundamental assumptions: that the relationship between the potential difference across the sample and crack length is linear, and that the crack is quarter circular in shape. Below are a series of plots which show potential difference (in μV) against crack length (in mm) for each individual test (where three or more points could be plotted). They give an indication of the degree to which the relationship is linear; and linearity to an appropriate degree is confirmed in each case.

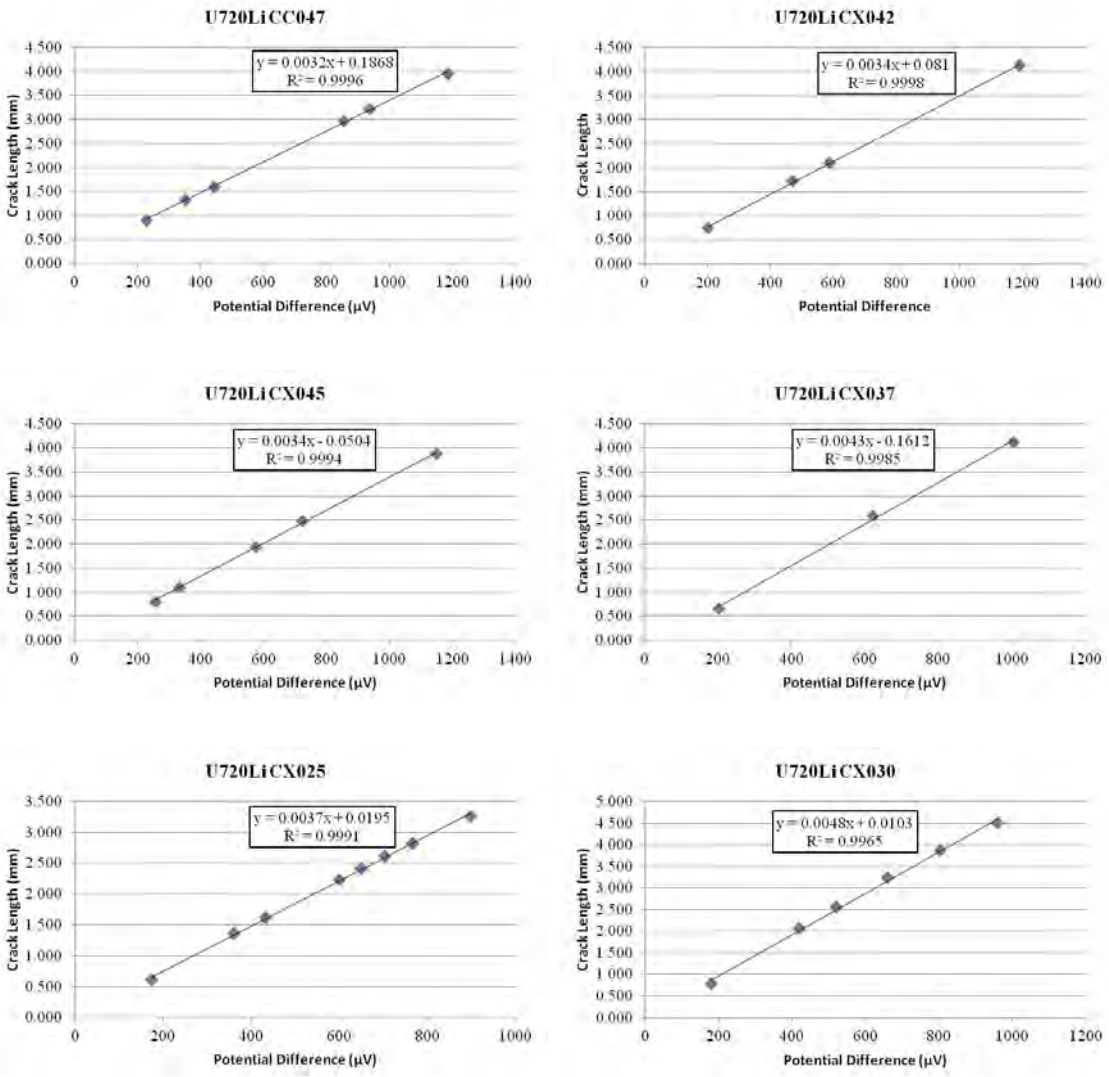
Subsequently, a series of optical images are presented to give an indication of the extent to which crack morphologies are quarter circular in shape. A precise mechanism by which this may be characterised has not been employed; rather, general observations are made, concluding that crack fronts are indeed modelled well as quarter circular in shape for the majority of cases.

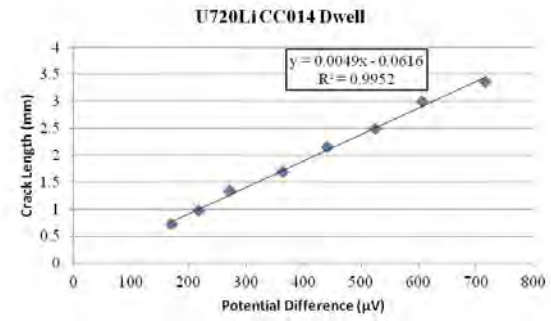
It is important to highlight that, as discussed in several sections above, crack fronts pertaining to dwell crack growth can display a degree of irregularity, including propagation through the test section in "fingers". This is thought to occur due to the selective nature of oxide attack ahead of a crack tip under dwell loading in fatigue. Several of these crack fronts therefore require careful analysis in terms of crack length measurement. Usually, this is carried out by faithfully measuring the irregular shape, assuming a quarter circle and plotting the graph of

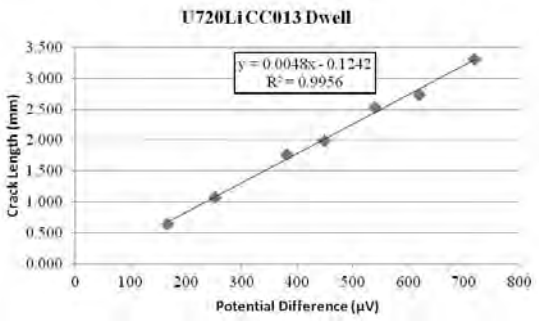
crack length versus p.d. Where the graph was shown to be linear, the value was taken as measured.

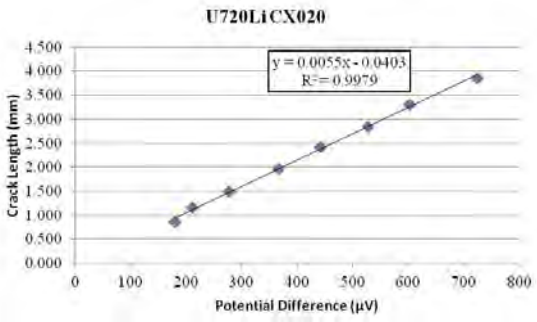
It is also important to highlight that these cases were rare, and that crack fronts were found to be quarter circular in shape for the vast majority of cases.

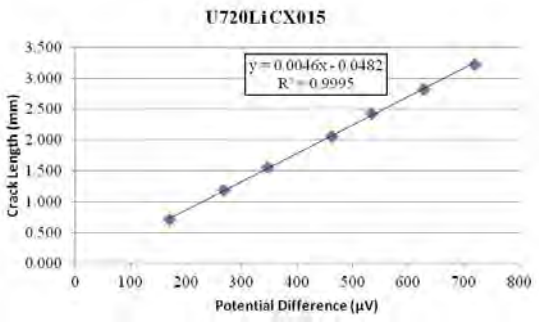
Udimet 720Li Dwell Tests

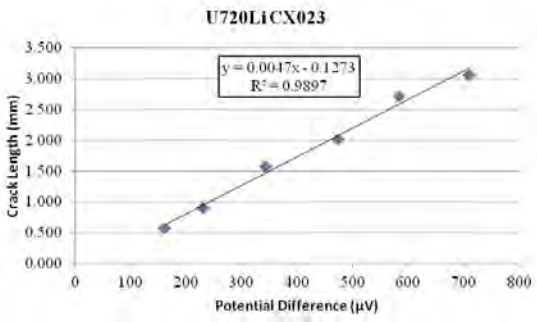


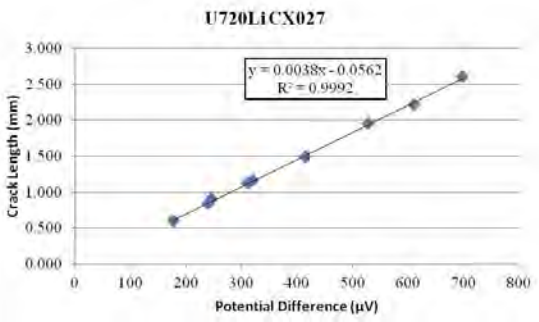

U720LiCC014 Dwell
y = 0.0049x - 0.0616
R² = 0.9952
Crack Length (mm)
Potential Difference (µV)

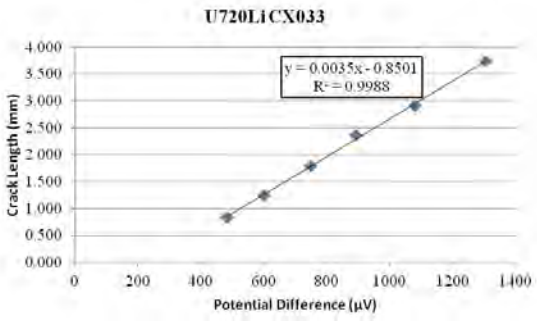

U720LiCC013 Dwell
y = 0.0048x - 0.1242
R² = 0.9956
Crack Length (mm)
Potential Difference (µV)

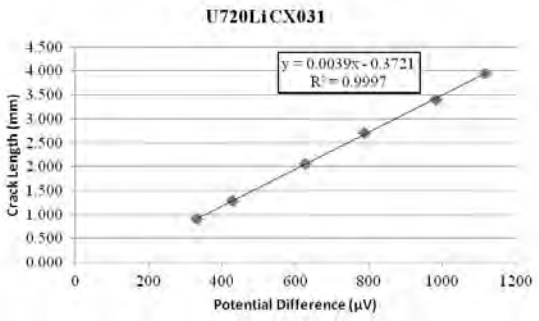

U720LiCX020
y = 0.0055x - 0.0403
R² = 0.9979
Crack Length (mm)
Potential Difference (µV)

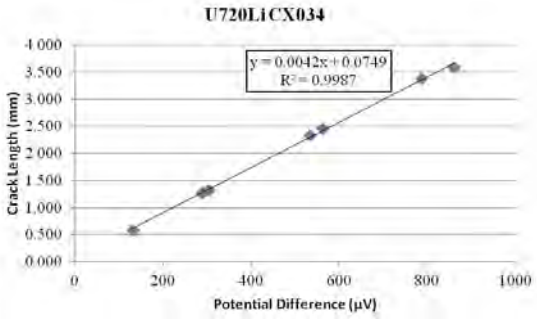

U720LiCX015
y = 0.0046x - 0.0482
R² = 0.9995
Crack Length (mm)
Potential Difference (µV)


U720LiCX023
y = 0.0047x - 0.1273
R² = 0.9897
Crack Length (mm)
Potential Difference (µV)

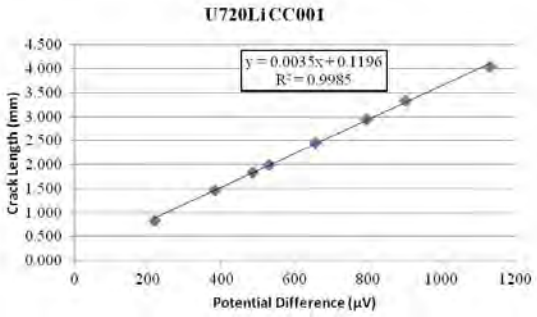

U720LiCX027
y = 0.0038x - 0.0562
R² = 0.9992
Crack Length (mm)
Potential Difference (µV)

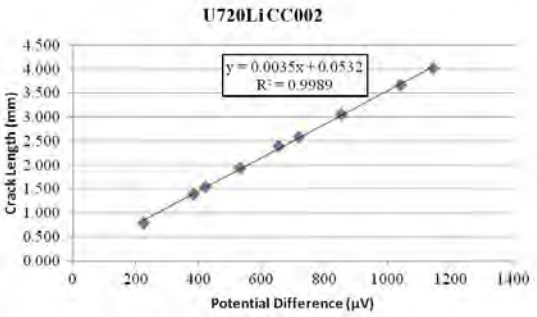

U720LiCX033
y = 0.0035x - 0.8501
R² = 0.9988
Crack Length (mm)
Potential Difference (µV)

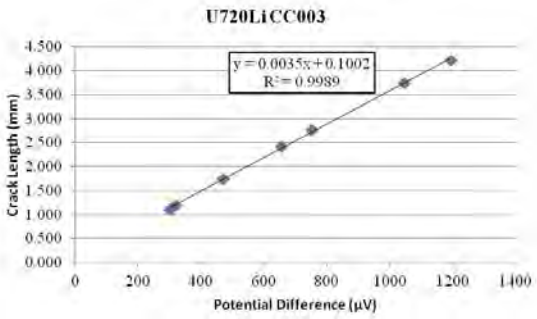

U720LiCX031
y = 0.0039x - 0.3721
R² = 0.9997
Crack Length (mm)
Potential Difference (µV)

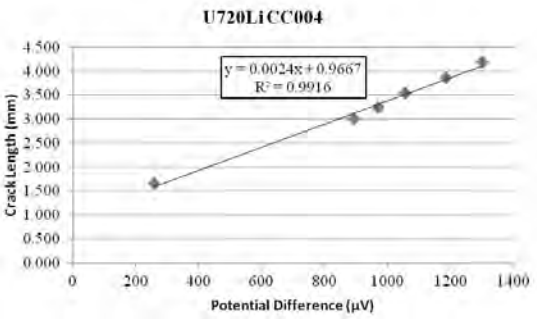


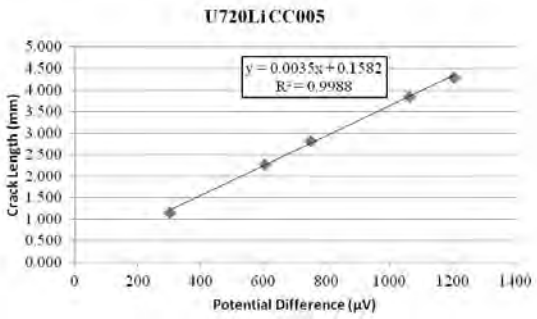
Udimet 720Li Overload Tests

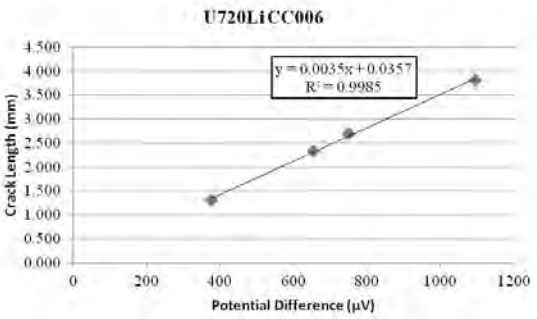


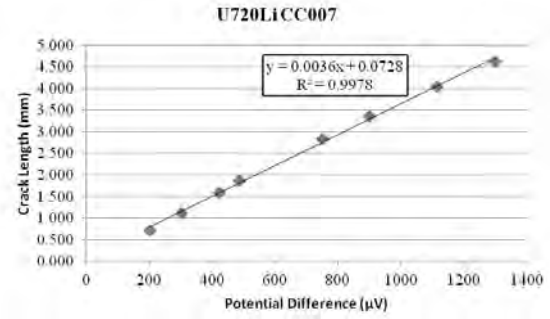


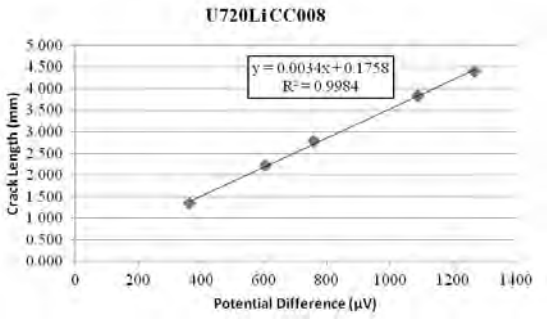


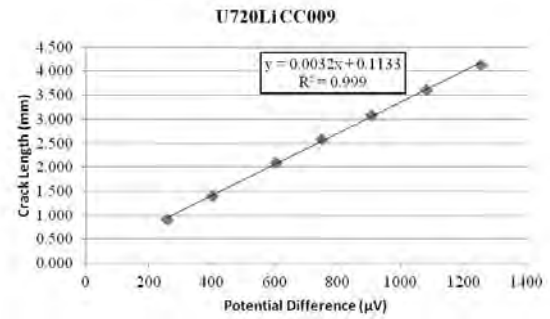


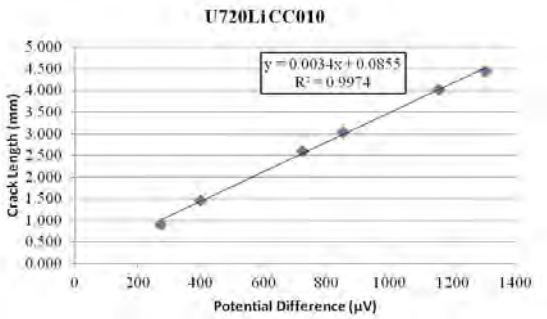


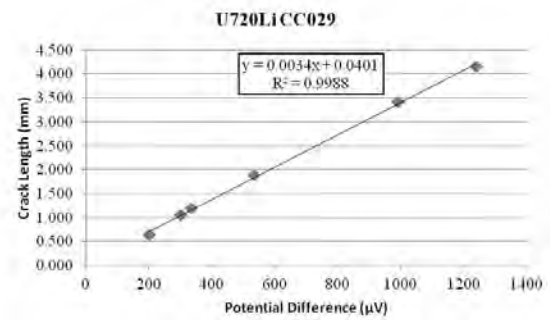


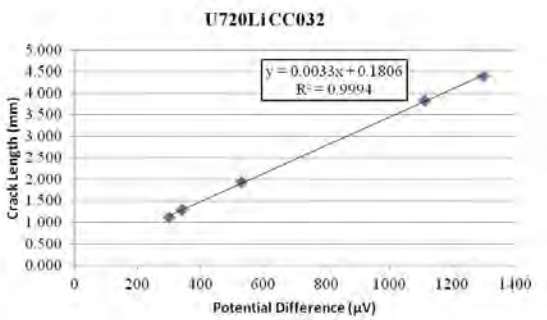

U720LiCC007
y = 0.0036x + 0.0728
R² = 0.9978
Crack Length (mm)
Potential Difference (μV)

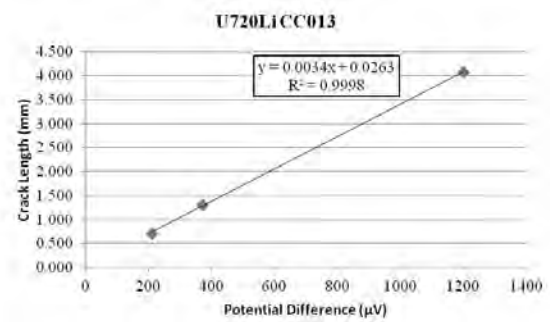

U720LiCC008
y = 0.0034x + 0.1758
R² = 0.9984
Crack Length (mm)
Potential Difference (μV)

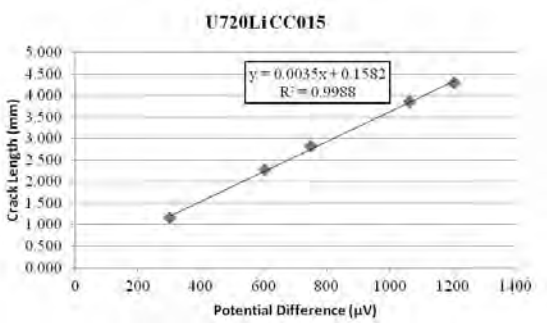

U720LiCC009
y = 0.0032x + 0.1133
R² = 0.999
Crack Length (mm)
Potential Difference (μV)

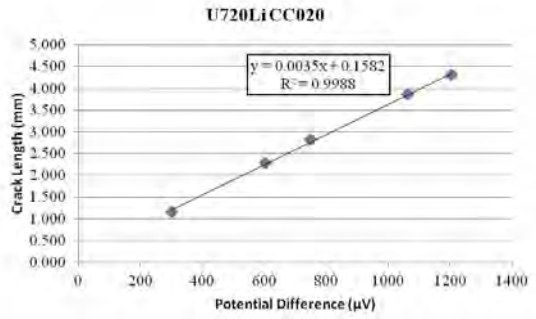

U720LiCC010
y = 0.0034x + 0.0855
R² = 0.9974
Crack Length (mm)
Potential Difference (μV)

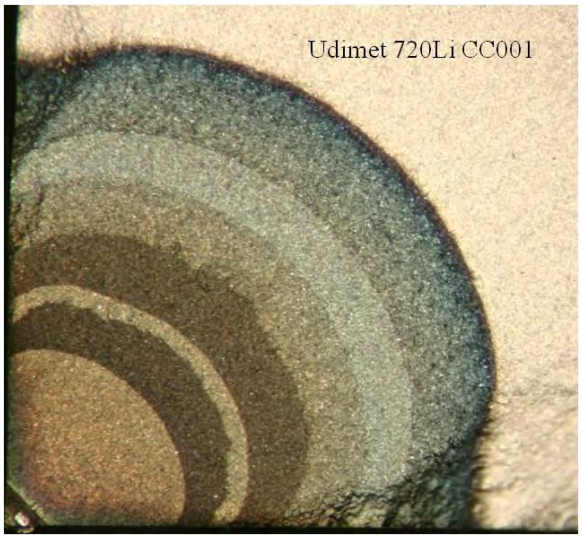

U720LiCC029
y = 0.0034x + 0.0401
R² = 0.9988
Crack Length (mm)
Potential Difference (μV)

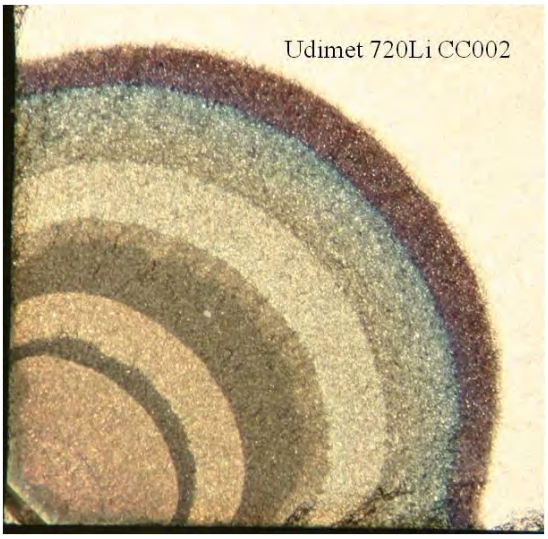

U720LiCC032
y = 0.0033x + 0.1806
R² = 0.9994
Crack Length (mm)
Potential Difference (μV)

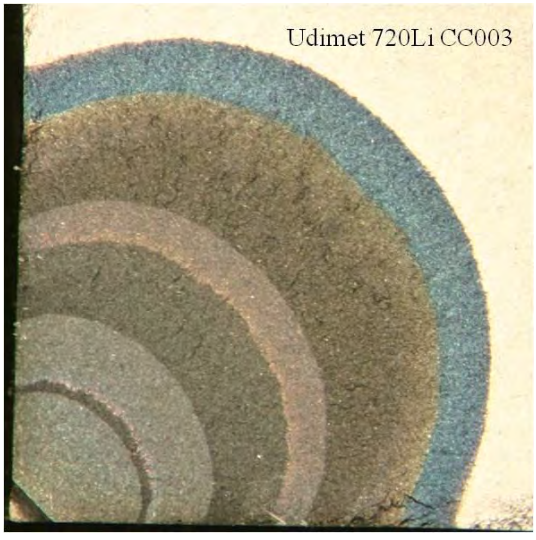

U720LiCC013
y = 0.0034x + 0.0263
R² = 0.9998
Crack Length (mm)
Potential Difference (μV)

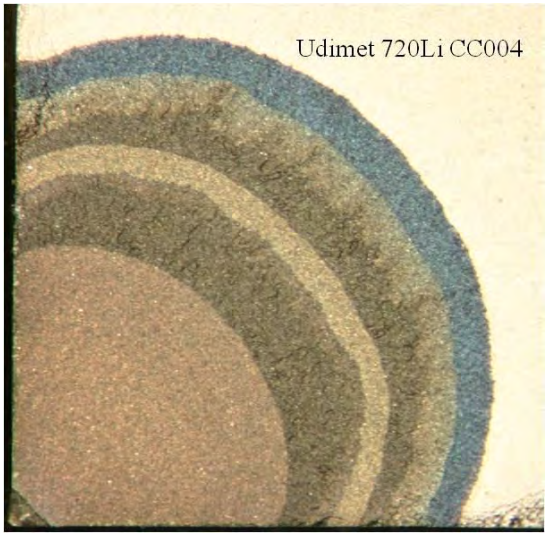

U720LiCC015
y = 0.0035x + 0.1582
R² = 0.9988
Crack Length (mm)
Potential Difference (μV)

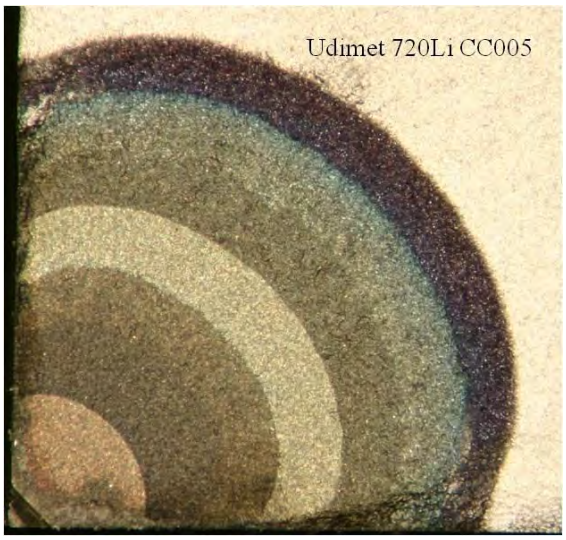

U720Li CC020
y = 0.0035x + 0.1582
R² = 0.9988
Crack Length (mm)
Potential Difference (µV)
5.000
4.500
4.000
3.500
3.000
2.500
2.000
1.500
1.000
0.500
0.000
0
200
400
600
800
1000
1200
1400


Udimet 720Li CC001

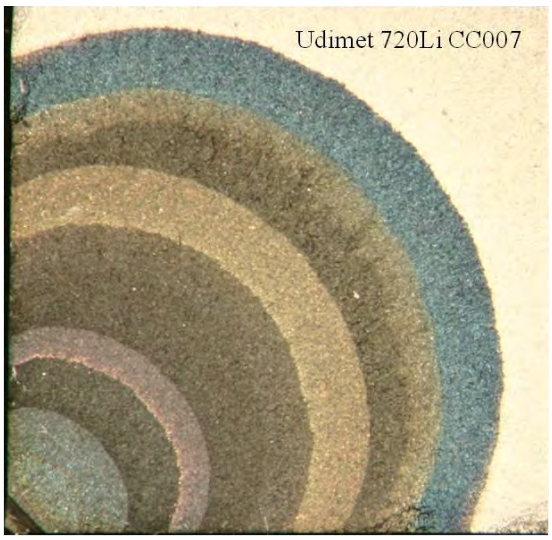

Udimet 720Li CC002

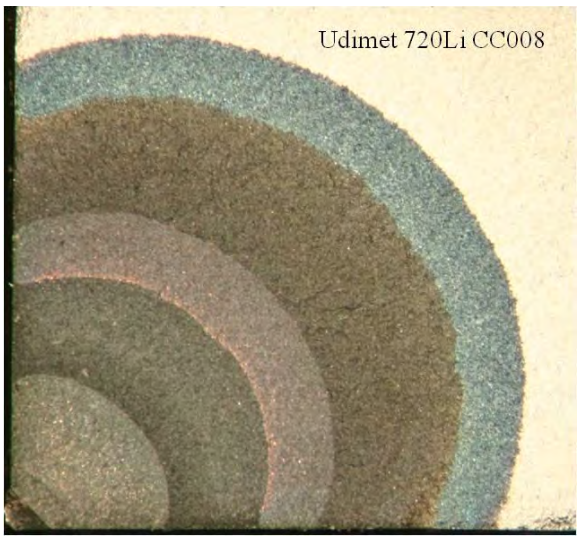

Udimet 720Li CC003

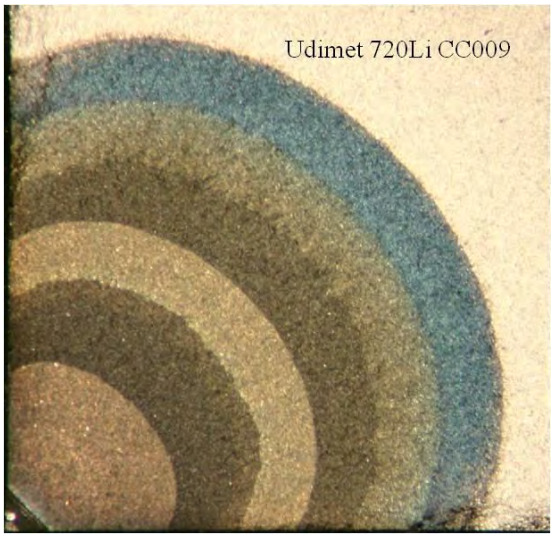

Udimet 720Li CC004

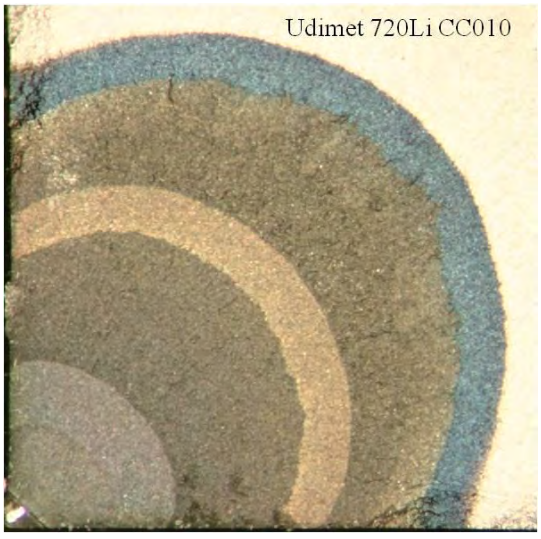

Udimet 720Li CC005


Udimet 720Li CC006

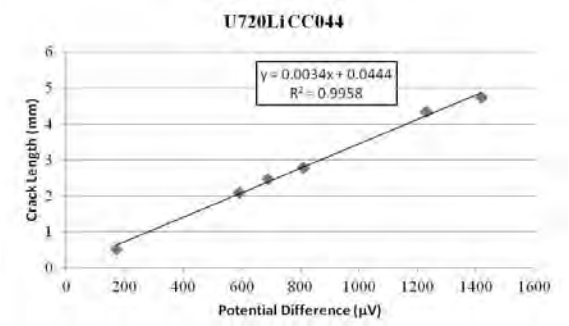

Udimet 720Li CC007

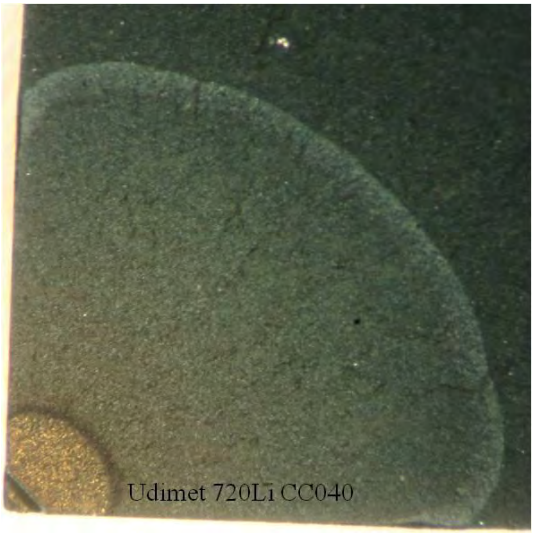

Udimet 720Li CC008

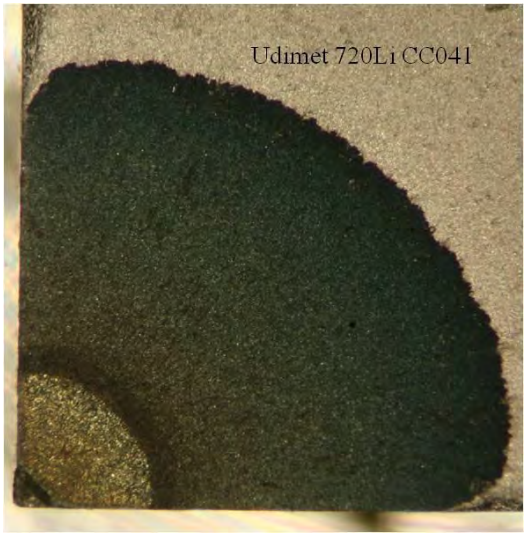

Udimet 720Li CC009

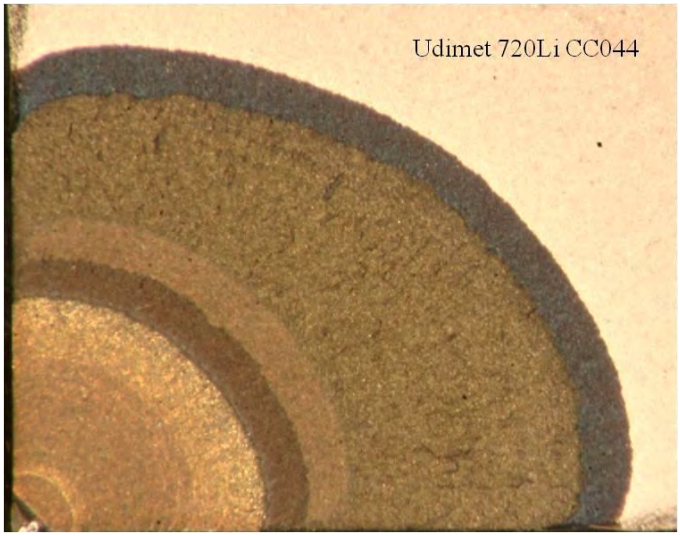

Udimet 720Li CC010

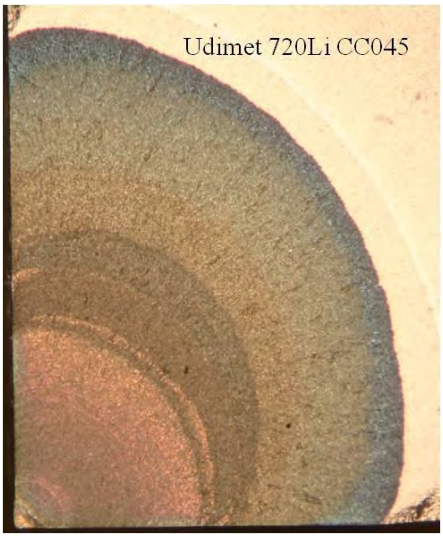
Udimet 720Li Time Dependent Threshold Tests



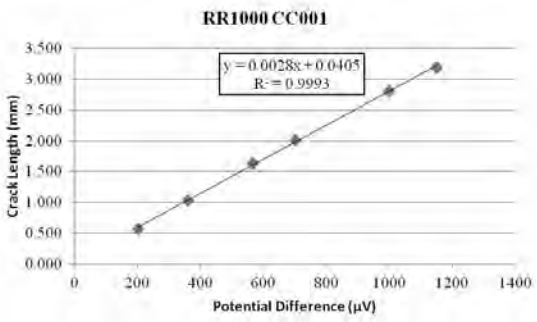


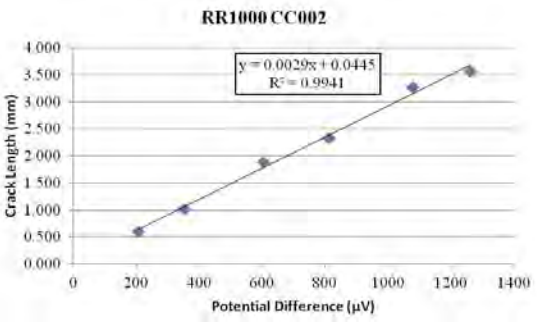


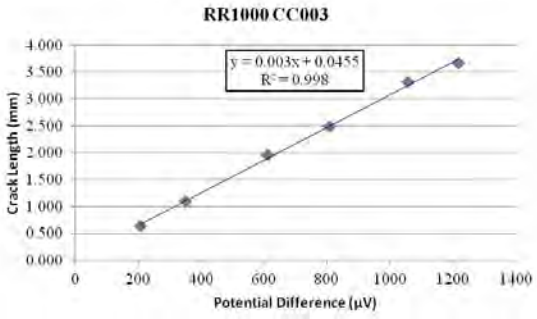


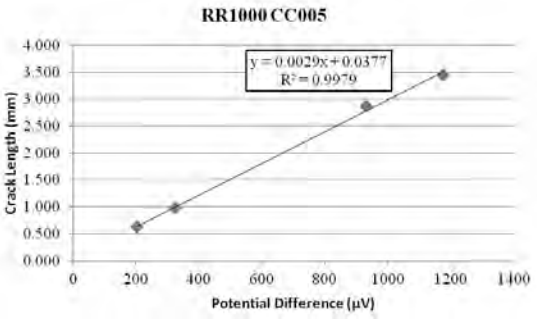


RR1000 Dwell Tests

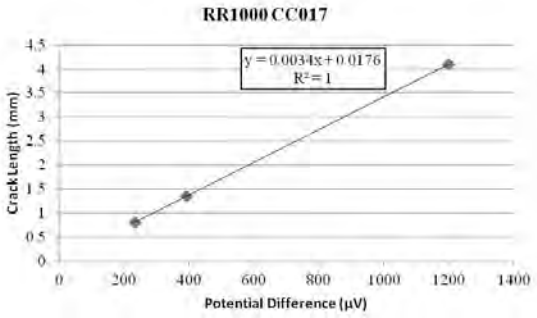


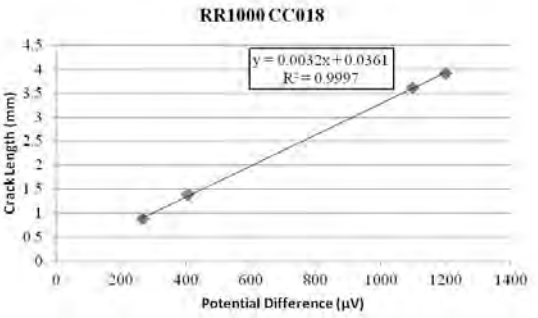


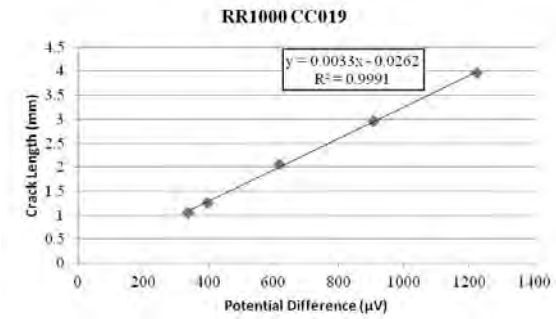


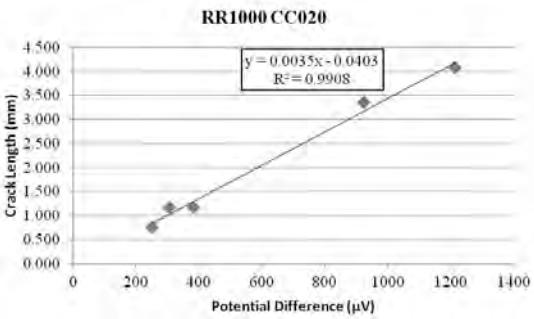


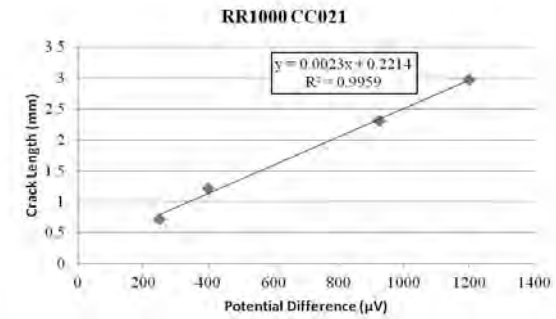
RR1000 Overload Tests

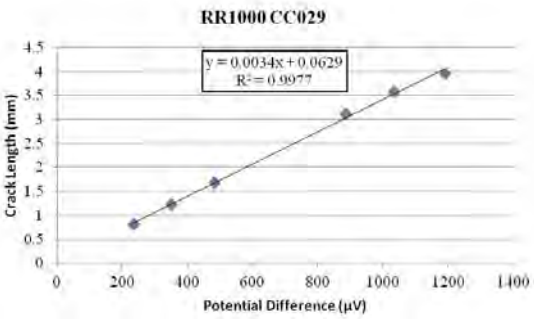


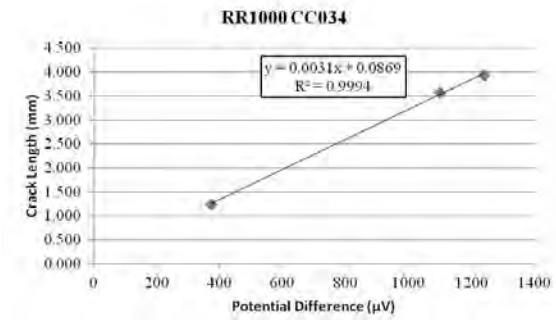


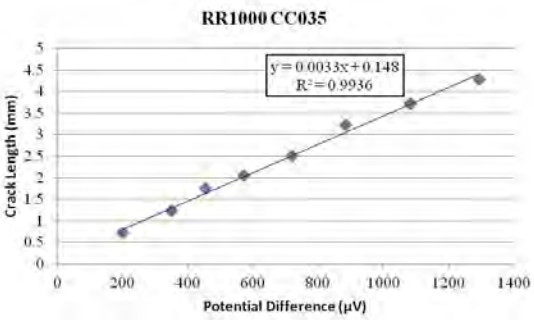

RR1000 CC019
y = 0.0035x - 0.0262
R² = 0.9991
Crack Length (mm)
Potential Difference (μV)

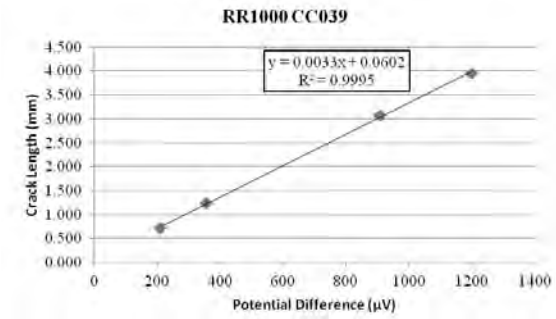

RR1000 CC020
y = 0.0035x - 0.0403
R² = 0.9908
Crack Length (mm)
Potential Difference (μV)

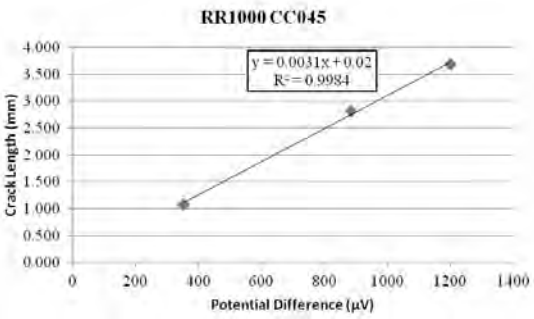

RR1000 CC021
y = 0.0023x + 0.2214
R² = 0.9959
Crack Length (mm)
Potential Difference (μV)

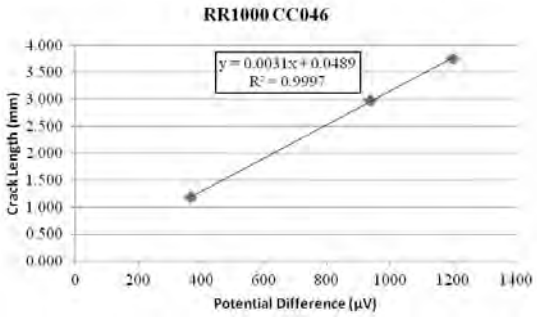

RR1000 CC029
y = 0.0034x + 0.0629
R² = 0.9977
Crack Length (mm)
Potential Difference (μV)

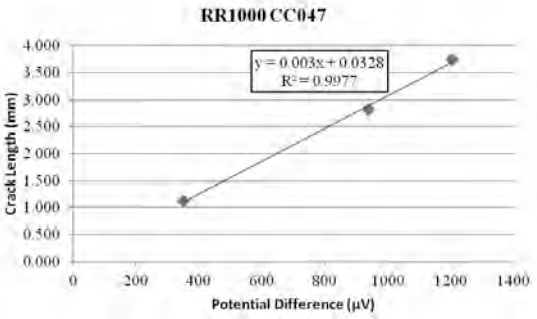

RR1000 CC034
y = 0.0031x + 0.0869
R² = 0.9994
Crack Length (mm)
Potential Difference (μV)

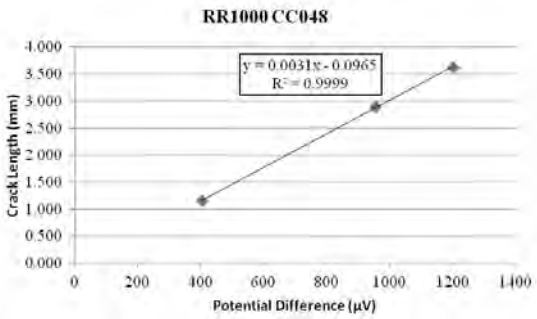

RR1000 CC035
y = 0.0033x + 0.148
R² = 0.9936
Crack Length (mm)
Potential Difference (μV)

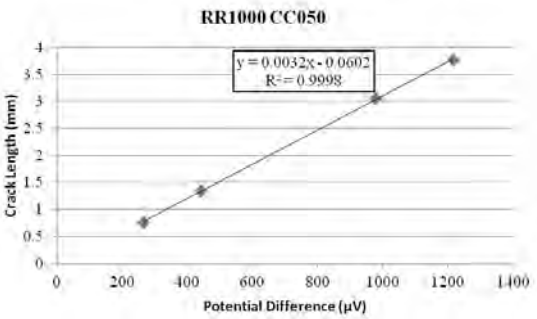

RR1000 CC039
y = 0.0033x + 0.0602
R² = 0.9995
Crack Length (mm)
Potential Difference (μV)

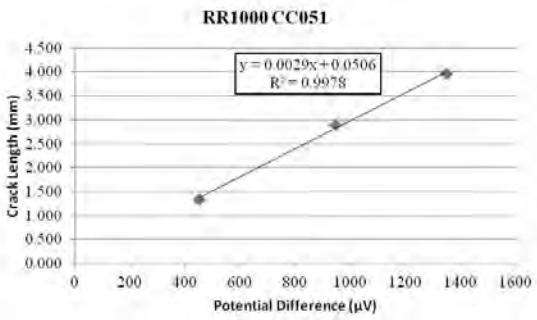

RR1000 CC045
y = 0.0031x + 0.02
R² = 0.9984
Crack Length (mm)
Potential Difference (μV)

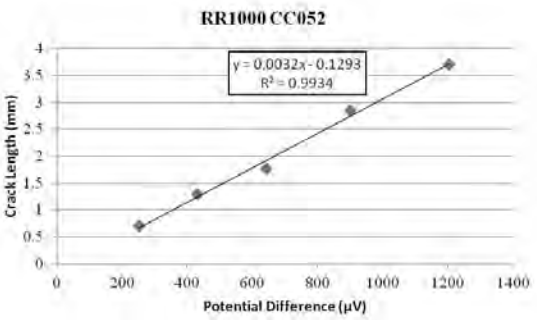

RR1000 CC046
y = 0.0031x + 0.0489
R² = 0.9997
Crack Length (mm)
Potential Difference (μV)

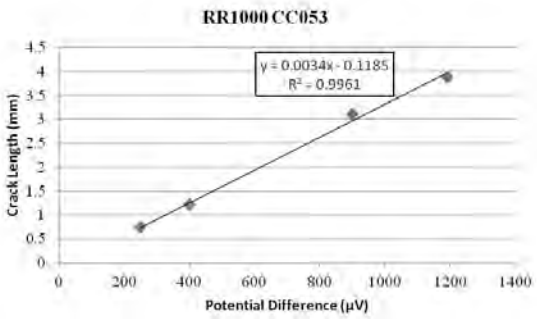

RR1000 CC047
y = 0.003x + 0.0328
R² = 0.9977
Crack Length (mm)
Potential Difference (μV)

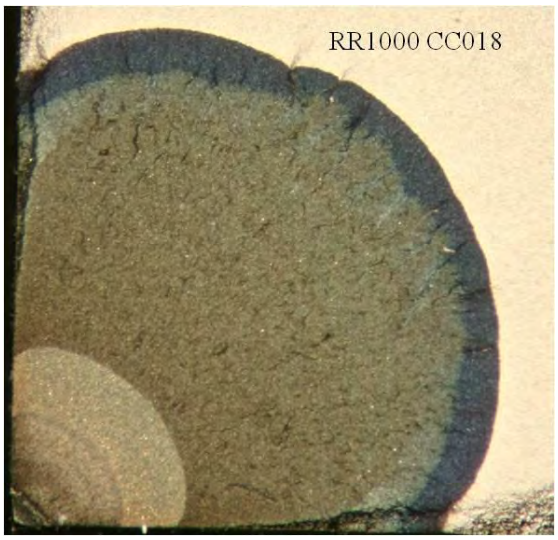

RR1000 CC048
y = 0.0031x - 0.0965
R² = 0.9999
Crack Length (mm)
Potential Difference (μV)

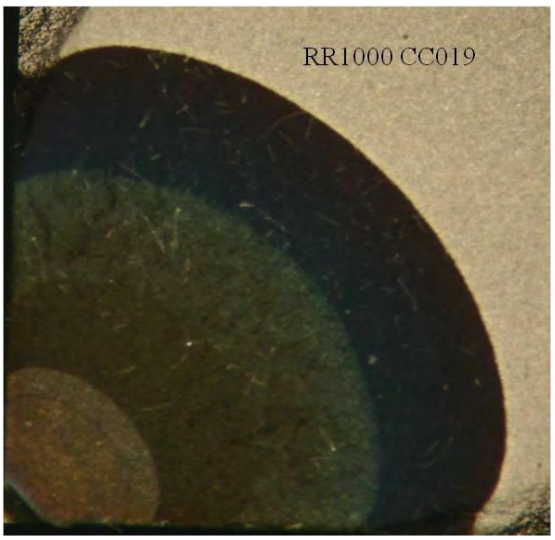

RR1000 CC050
y = 0.0032x - 0.0602
R² = 0.9998
Crack Length (mm)
Potential Difference (μV)

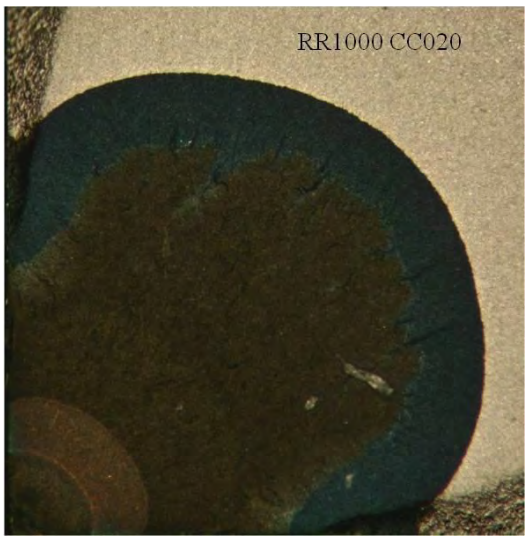

RR1000 CC051
y = 0.0029x + 0.0506
R² = 0.9978
Crack Length (mm)
Potential Difference (μV)


RR1000 CC052
y = 0.0032x - 0.1293
R² = 0.9934
Crack Length (mm)
Potential Difference (μV)

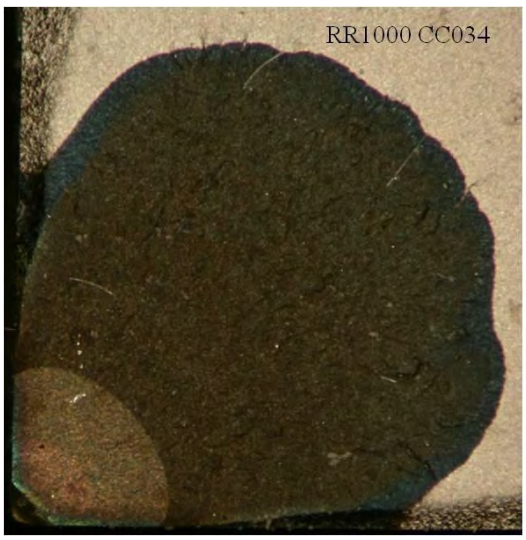

RR1000 CC053
y = 0.0034x - 0.1185
R² = 0.9961
Crack Length (mm)
Potential Difference (μV)


RR1000 CC018

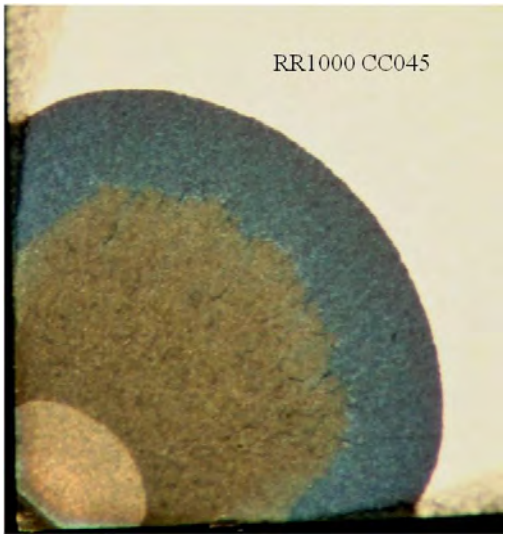

RR1000 CC019


RR1000 CC020

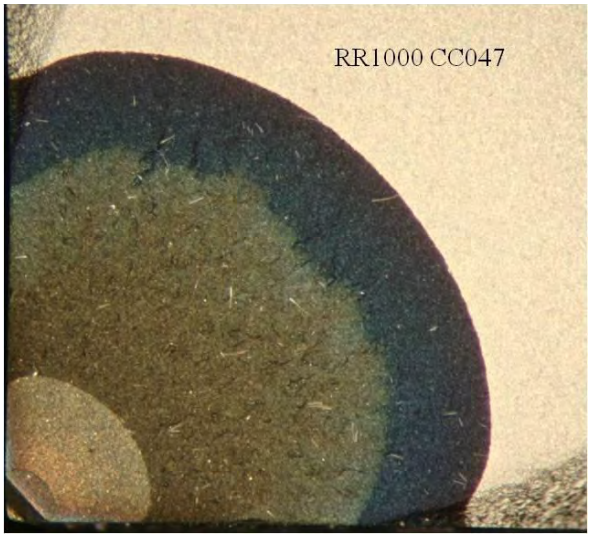

RR1000 CC021

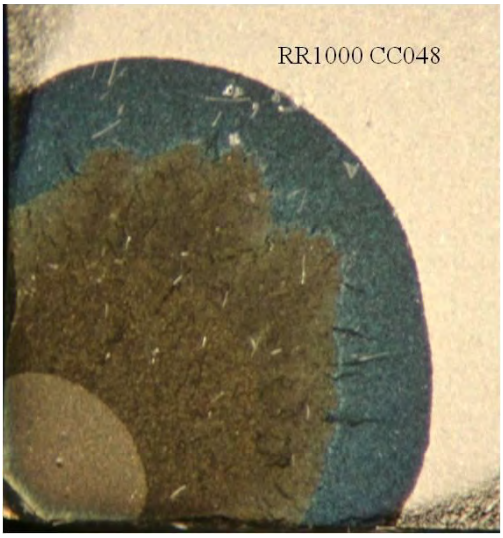

RR1000 CC034


RR1000 CC042


RR1000 CC045

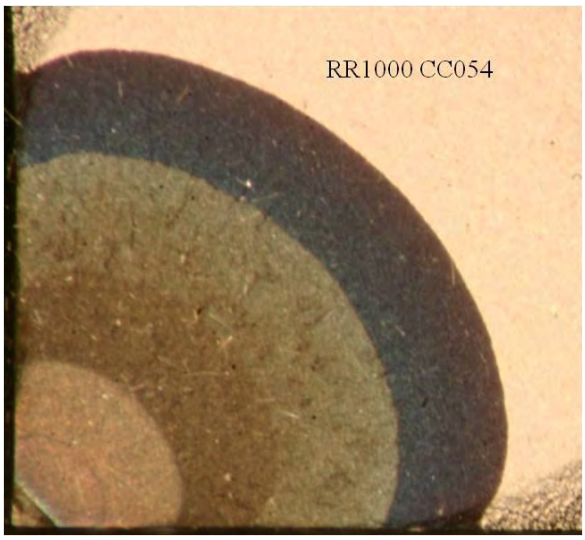

RR1000 CC046


RR1000 CC047

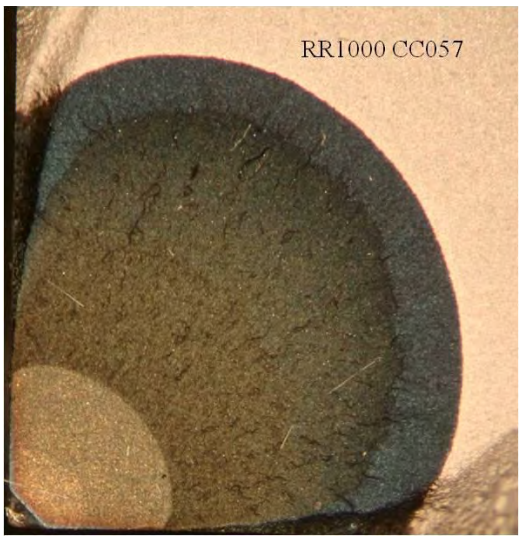

RR1000 CC048

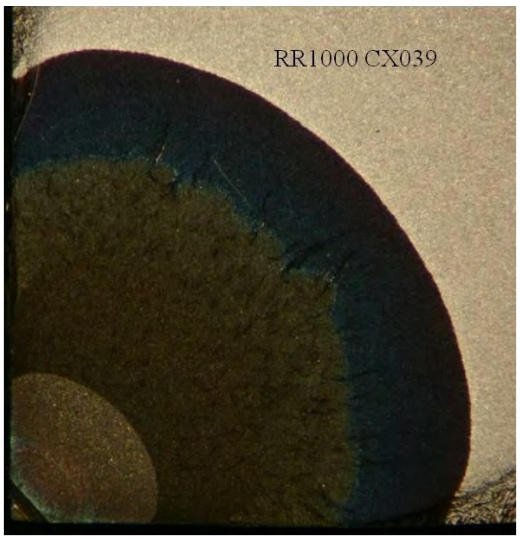

RR1000 CC049


RR1000 CC050









Geometric Shape Factor

As discussed in section 3.2.4, stress intensity factor (ΔK) calculations include a geometric shape factor term (Y) which is a function of the normalised crack length (a/w). Pickard [80] originally developed an expression which he reported to give accurate representations of values for K to within +/- 4% of finite element results, up to an a/w of 0.75. Rolls-Royce plc.

have developed their own methodologies (based upon Pickard's original work) upon which analysis in terms of ΔK calculations in this programme has been based.

Pickard compares the expressions developed within Rolls-Royce plc. with his own and notes that there is a divergence in the data (a/w versus compliance function) between the two methodologies. The comparison is presented in Figure A-1.

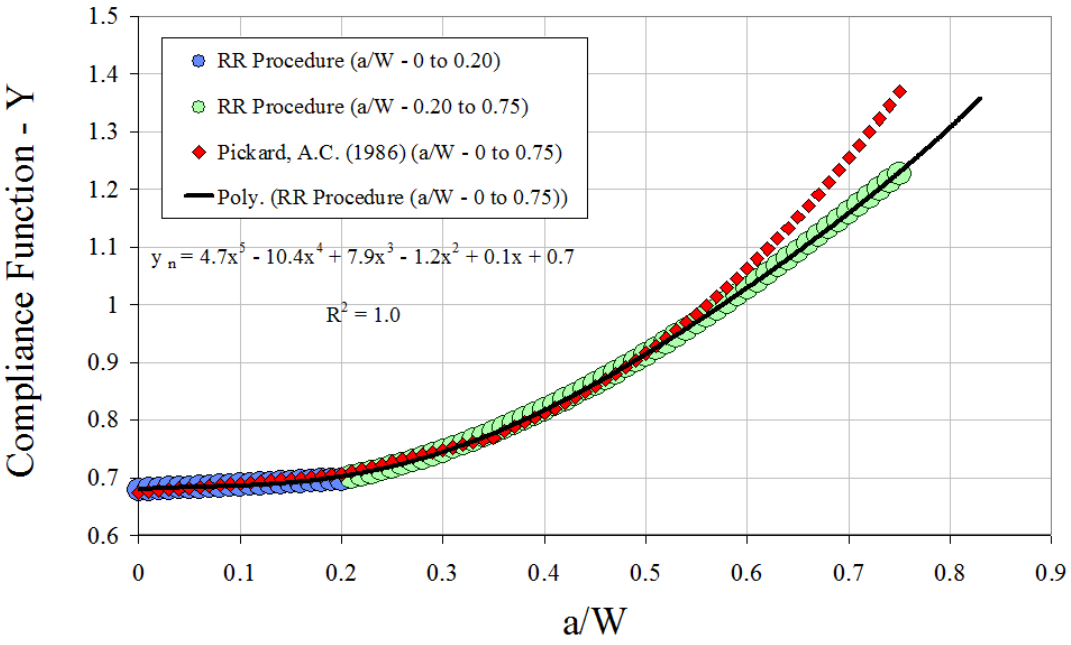


Figure A-1: A comparison of the compliance function as originally determined by Pickard with that defined by RR1000 procedural documentation. The polynomial line fits shorter crack with longer crack compliance behaviour (analysis originally presented by Simpson [96]).

Although it is unclear as to why the discrepancy exists, it is important to highlight that the divergence is kept to below 5% up until an a/W of 0.6 is reached. This gives reason to believe that data gathered in this programme using Rolls-Royce procedures are likely to be accurate and representative.

Model Geometry and Resolution

There are several aspects of the ways in which finite element analysis is implemented and undertaken which require discussion and (where possible) validification. It is important to highlight that the data generated in this programme seeks to improve understanding of the ways in which crack tip stress states and creep strain accumulation at the crack tip can affect crack growth rates. A full interpretation of these sets of data is incorporated in to lifing strategies and methodologies within Rolls-Royce plc; nevertheless this particular interpretation goes beyond the scope of this thesis. Thus, a complete and comprehensive analysis of the validity of each aspect of the running of finite element models is also considered outside the scope of this report.

As discussed in section 3.4.3, the full analysis can be found in Rolls-Royce in-house technical report DNS 160974 authored by Steve Williams and Dr. Lik-Beng Lim [83]. Nevertheless, for completeness, a limited collection of analyses is reproduced (with permission) below, and several discussion points are made, in order to create confidence in the data presented as part of this project.

Mesh Size

As discussed in section 2.5.1, results which are generated using finite element analysis are sensitive to the size of the mesh used to represent the real life component or test piece. Analysis pertaining to the validity of the mesh size would begin by using an extremely large mesh (for which any given output result might be erroneous). One particular output result

such as the maximum von Mises stress is the plotted against the size of the mesh for which the result was generated. The mesh size is then reduced, and another result gathered and plotted. The process is repeated until a solution for the selected result converges is reached (i.e. any further reduction in the mesh size will have a smaller and smaller effect upon the result generated).

This analysis is performed automatically by SC03 during the creation of any particular mesh; and hence a full mesh size convergence analysis is not required as part of this thesis.

Hardening Rule

As discussed in section 2.5.2, there are several methods by which hardening rules may be utilised in finite element codes in order to capture stress and strain variations with time. A Mrotz multi-layer hardening criterion is used in this programme since it most appropriately captures the relevant behaviour.

Crack Tip Geometry

It is important to highlight that the analysis and discussion presented below is reproduced (with permission) from [83] and is not the author's own work. As discussed above, it is included for completeness for it details important analyses pertaining to the development and implementation of finite element models used in this programme of work.

Representing a crack by a small notch radius is discussed in section 3.4.3. Analysis within Rolls-Royce plc pertaining to the models used in this programme involves plotting the elastic stress against the distance from the notch root for a range of notch root radii (25 μm, 5 μm and 0 μm). The data can be manipulated such that elastic stress is plotted against $1/\sqrt{x}$ (where x is the distance from the notch root) which enables a comparison between the three finite element results and those of the classical K solution: $\sigma_{cal} = K/\sqrt{(2\pi x)}$

As discussed in section 3.4.3, a mathematical singularity is introduced at x tends towards zero. Nevertheless, it could be expected that within a suitable range of x, the notched finite element results should be linear with a gradient of $C = K/\sqrt{(2\pi)}$. It therefore follows that once the gradient C is known for the linear notched stress field, K could be evaluated for the sharp notch; and that it should approach the true value for a crack tip.

Graphs for three notch root radii are plotted in the above referenced report; the linear portion for which are plotted with straight lines. (It should be noted that the straight line portion of each graph ranged from $1/\sqrt{x} = 63$ mm$^{-0.5}$ to 253 mm$^{-0.5}$ which correspond to x = 0.25 mm to 0.015 mm respectively.)

An actual K is obtained by assuming an edge through crack with a nominal stress of 531 MPa and a crack length of 1.025 mm, reflecting the conditions used in the finite element models, and the value for C and each corresponding calculation for K is made using the graphs discussed above. Furthermore, using the 0.2% proof stress of fine grained Udimet 720Li

(~1055 MPa), a value for the size of the plastic zone associated with the K used in the above discussed calculations can be estimated. The results are plotted in Table 31.

Table 31: Values of K as evaluated for each of the three finite element models [83].

Finite Element Model	Gradient "C"	Evaluated K (MPa√m)	Actual K (MPa√m)	Plastic Zone (mm)
Notch r = 25 µm	17.12	42.9	35.8	0.1833
Notch r = 5 µm	15.3	38.4		
Notch r = 0 µm	14.22	35.6		

These results demonstrate that the optimised K from all three finite element models matched reasonably well with the theoretical solution, and that the use of a 25 µm notch produces a slightly larger K value that the theoretical (hence will produce conservative results in terms of crack tip stress and strain states).

The analysis also shows that the use of a small but finite root radius has a relatively small effect on the value of the surrounding elastic stress field within and close to the predicted plastic zone. Predictions of K based on evaluating the gradient C for the linear portion of the finite element stress fields over the region of the plastic zone yield similar values for all three assumed notch root radii.

Based on the logic described above and the results of the analysis of elastic stresses, the use of a 25 µm notch to represent a sharp crack, and characterising the resulting stress field by the use of a stress intensity factor is considered to be a reasonable approach.

Plane Stress Vs Plane Strain

Lim [83] also provides data to discuss the effect of plane strain and plane stress conditions when running each simulation. Most significantly, the curve of crack tip stress against time for the dwell-only cycle sits higher on the y-axis (crack tip stress) for plane strain conditions when compared with plane stress conditions (for otherwise similar conditions). This means that crack tip stresses according to overload cycling have further to relax in order to define the incubation time under plane strain conditions; which in turn results in the calculation of higher incubation times when compared with otherwise similarly run simulations under plane stress conditions. For some conditions the incubation time under plane strain conditions can be around twice that of the incubation time for the respective plane stress run simulation.

Therefore, under plane stress conditions, more conservative values for the incubation time are generated; hence these conditions provide a more appropriate way to gather such data.

Time Step Resolution

As discussed in section 3.4.1, the accuracy of the determined value for t_x is sensitive to the size of the time steps (Δt) used to run the model. The output resolution for the dwell loading ramp is set at 91 equal divisions. Hence if a bad prediction is made for t_x and Δt is set too high, t_x will be calculated by performing differentiation on the output data across very large time steps. This is known to produce erroneous numerical solutions.

Lim [97] plots t_x against $\Delta t/t_x$ for a range of Δt on a model whose other conditions remained constant (TEMP = 675°C, OLF = 1.25, BL = 531 MPa, K_{dwell} = 35.8 MPa√m) and shows that as Δt reduces, t_x approaches a converged value. This convergence is shown to occur as $\Delta t/t_x$ tends towards 0.06; thereby suggesting a criterion for the calculation of t_x. The analysis is reproduced with permission in Figure A-2.

Table 32 [97] lists the t_x results for 8 cases with t_x ranging from 25 seconds to 10637 seconds. For each case, a pair of t_x results were produced with different Δt values, keeping $\Delta t/t_x \leq 0.06$. The results show that all cases achieved converged values for t_x with $\Delta t/t_x \leq 0.06$; thereby supporting the above proposed criterion.

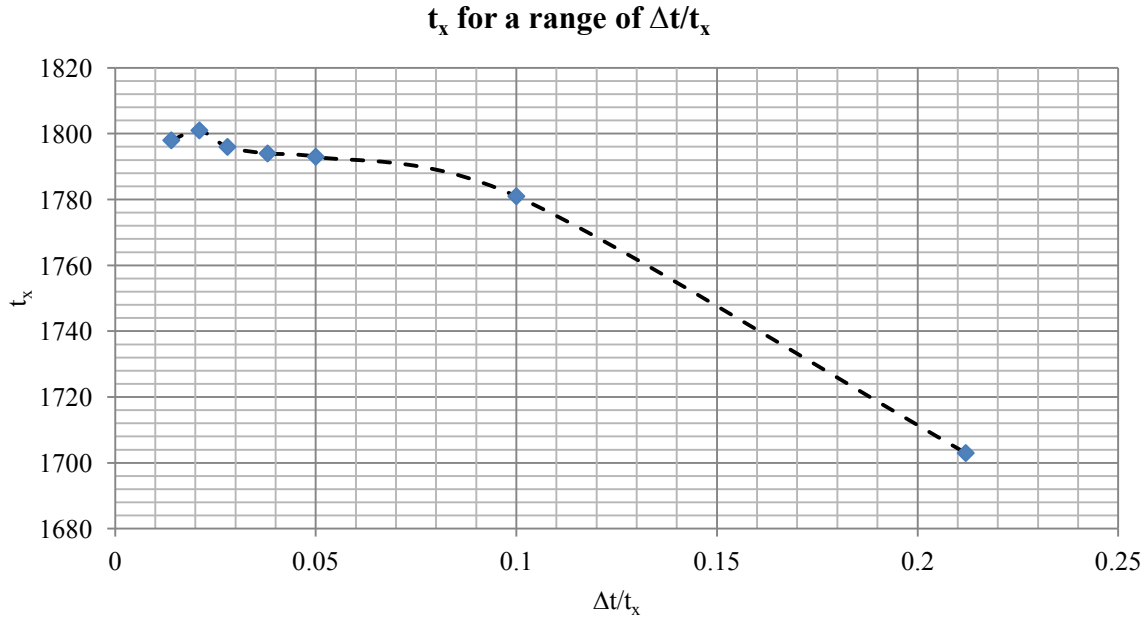


Figure A-2 [97]: Plotting t_x against a range of values for $\Delta t/t_x$ used to generate the calculation as calculated for the following conditions: TEMP = 675°C, OLF = 1.25, BL = 531 MPa, K_{dwell} = 35.8 MPa√m. Note that t_x converged to ~1799 seconds at $\Delta t/t_x$ of ~ 0.06

Table 32 [97]: Results of t_x for cases with different $\Delta t/t_x$: showing convergence with $\Delta t/t_x \leq 0.06$

Model	Temp (°C)	BL (MPa)	Overload Factor	A (mm)	K_{dwell} (MPa√m)	Δt (s)	t_x (s)	$\Delta t/t_x$
1	675	531	1.250	1.025	35.8	25.0	1799	0.01
						90.0	1794	0.05
2	675	531	1.100	1.025	35.8	1.6	25	0.06
						0.4	25	0.02
3	675	310	1.150	2.14	35.8	8.4	441	0.02
						25.3	441	0.06
4	675	530	1.115	1.425	44.4	1.1	35	0.03
						2.2	35	0.06
5	650	531	1.150	1.025	35.8	9.0	486	0.02
						27.0	486	0.06
6	650	310	1.250	2.14	35.8	204.4	10637	0.02
						613.0	10626	0.06
7	650	310	1.150	2.14	35.8	22.6	1181	0.02
						68.0	1180	0.06
8	650	690	1.150	0.525	31.8	4.5	162	0.03
						9.0	163	0.06

1.5r Ahead of the Crack Tip

Section 4.3.3 reports a methodology for the calculation of a new defined termed t_x which compares creep strain rate data obtained from the crack tip with those obtained at a nominal distance ahead of the crack tip over typical fictitious overload stress waveforms. The distance ahead of the crack tip from which this data is obtained is reported to be 1.5 of the notch root radius. The reason for which this distance is chosen is because it describes nominal creep data along the crack plane as uninfluenced by the crack itself.

This analysis is also presented in the above referenced technical report [83] which plots inelastic creep strain (CEQI) against distance from crack tip for a range over dwell and

overload cycles. The graphs show that creep strain converges (plateaus) at a distance of around 1.5 of the notch root radius ahead of the notch root (or crack tip). Hence data from this location is used to represent nominal crack plane creep data and compared with those obtained from the crack tip itself.

Appendix VI Crack Growth Resistance Curves

Udimet 720Li

Presented below are a series of crack growth resistance curves generated by the implementation of methodologies described in section 3.2 on fine-grain Udimet 720Li test pieces.

Udimet 720Li Baseline and Dwell Tests

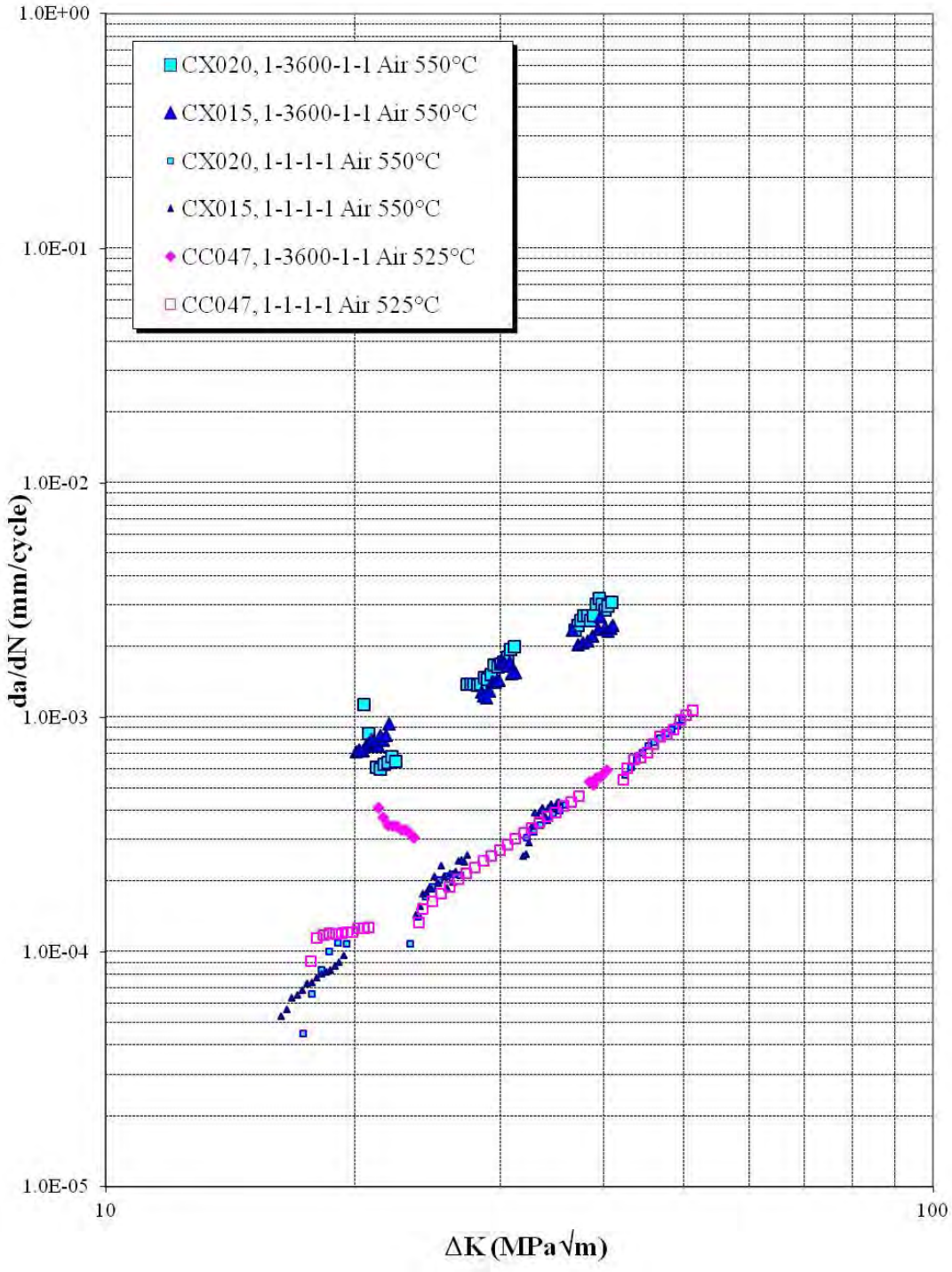


Figure A-3: da/dN vs. ΔK curves for fine-grained Udimet 720Li samples CX015, CX020 and CX047, which were tested at 550°C (CX015 and CX020) and 525°C (CX047), with a dwell load of 26 kN, and a dwell time of 3,600 seconds.

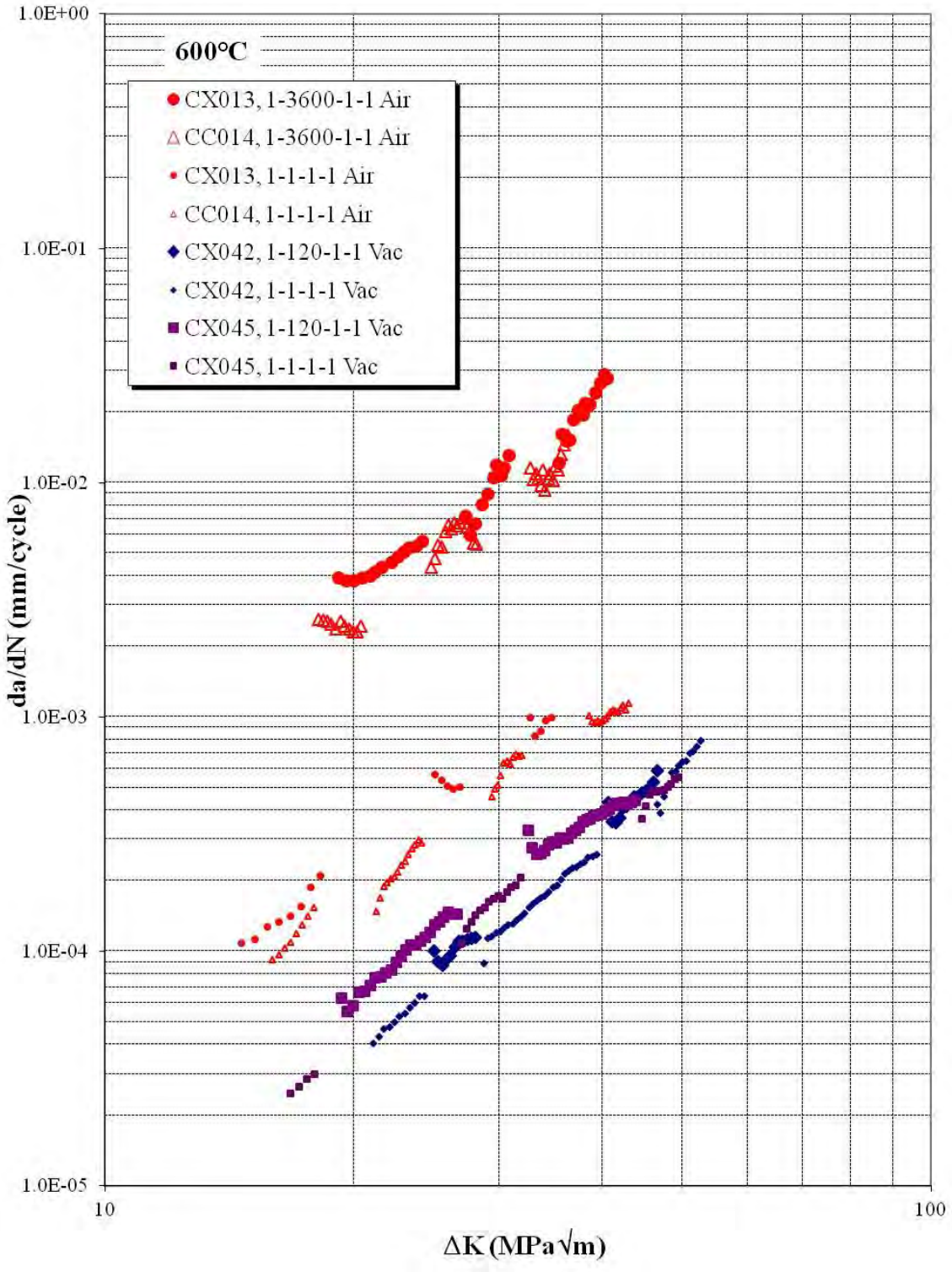


Figure A-4: da/dN vs. ΔK curves for fine-grained Udimet 720Li samples CX013, CX014, CX042 and CX045, which were tested at 600°C, with a dwell load of 26 kN, a dwell time of 3,600s in air (CX013 and CX014) and 120s in a vacuum (CX042 and CX045).

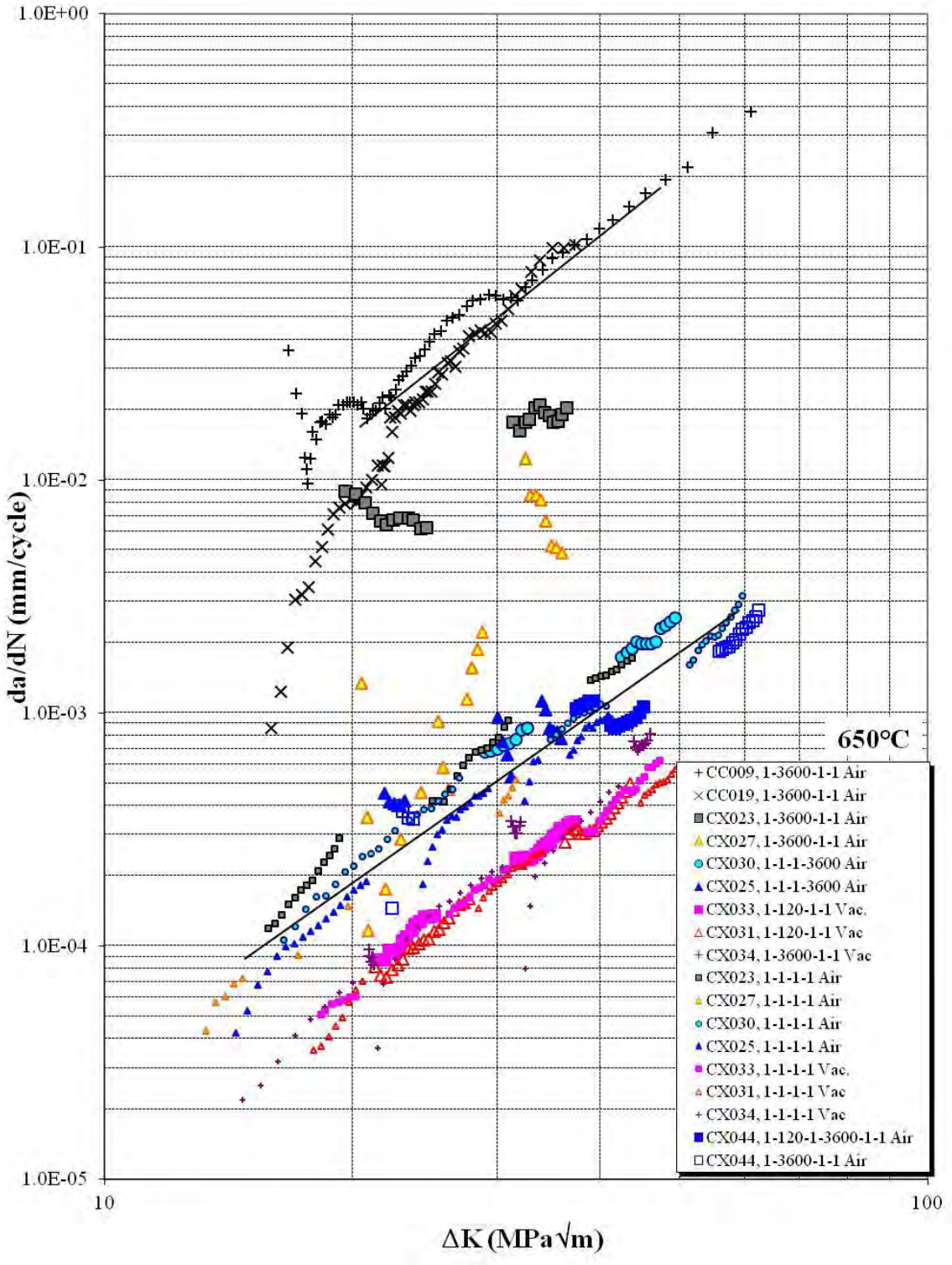


Figure A-5: da/dN vs. ΔK curves for fine-grained Udimet 720Li samples tested at 650°C at a range of dwell periods, in air and in a vacuum.

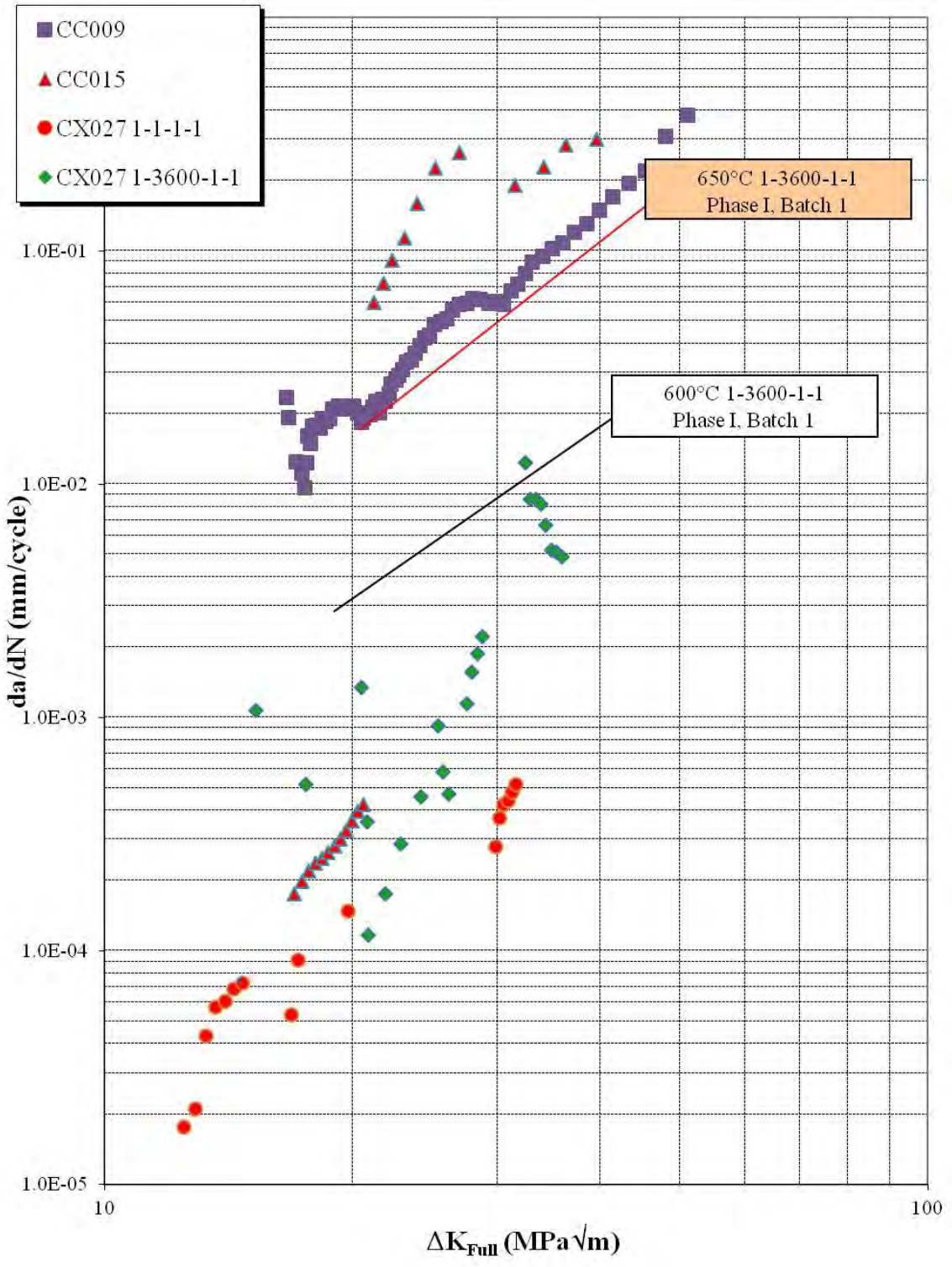


Figure A-6: da/dN vs. ΔK curves for fine-grained Udimet 720Li samples CC009, CC015 and CX027, all tested at 650°C and with a dwell period of 3,600s, in air. Note that despite similar testing conditions crack growth rates are shown to be variable. Note also that CX027 data represents intermittent "bursts" of baseline (1-1-1-1) loading in order to encourage the crack to grow under a dwell regime.

Udimet 720Li Baseline, Dwell and Overload Tests

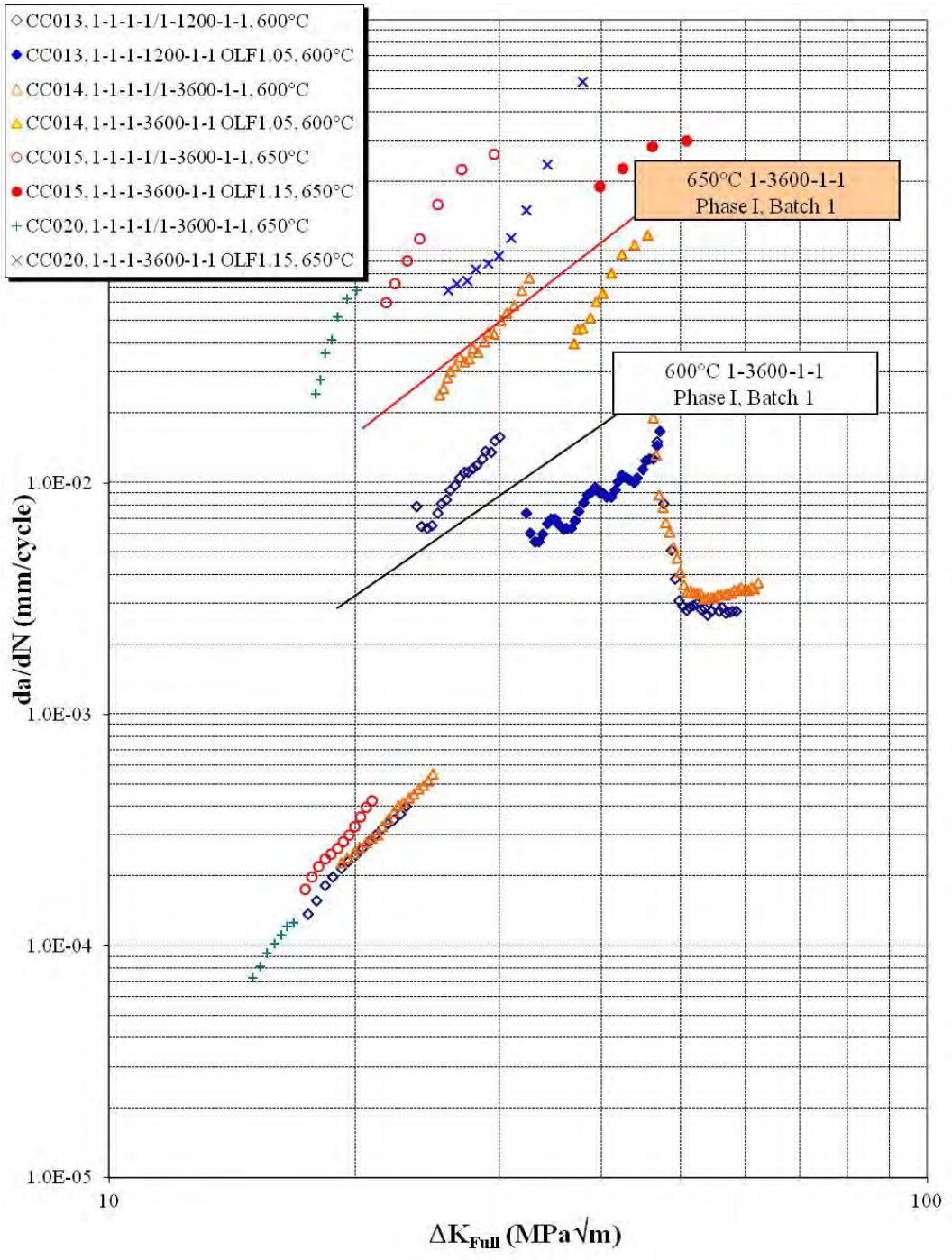


Figure A-7: da/dN vs. ΔK curves for fine-grained Udimet 720Li samples CC013, CC014, CC015 and CC020, which were tested at 600°C (CC013 and CC014) and 650°C (CC015 and CC020), with a dwell load of 26 kN, and overload factor of 1.05 (CC013 and CC014) and 1.15 (CC015and CC020), and a dwell time of 1,200s (CC013) and 3,600s. Note also that crack growth rates in sample CC014 in particular sit almost exactly 50°C lower than perviously tested microstructures.

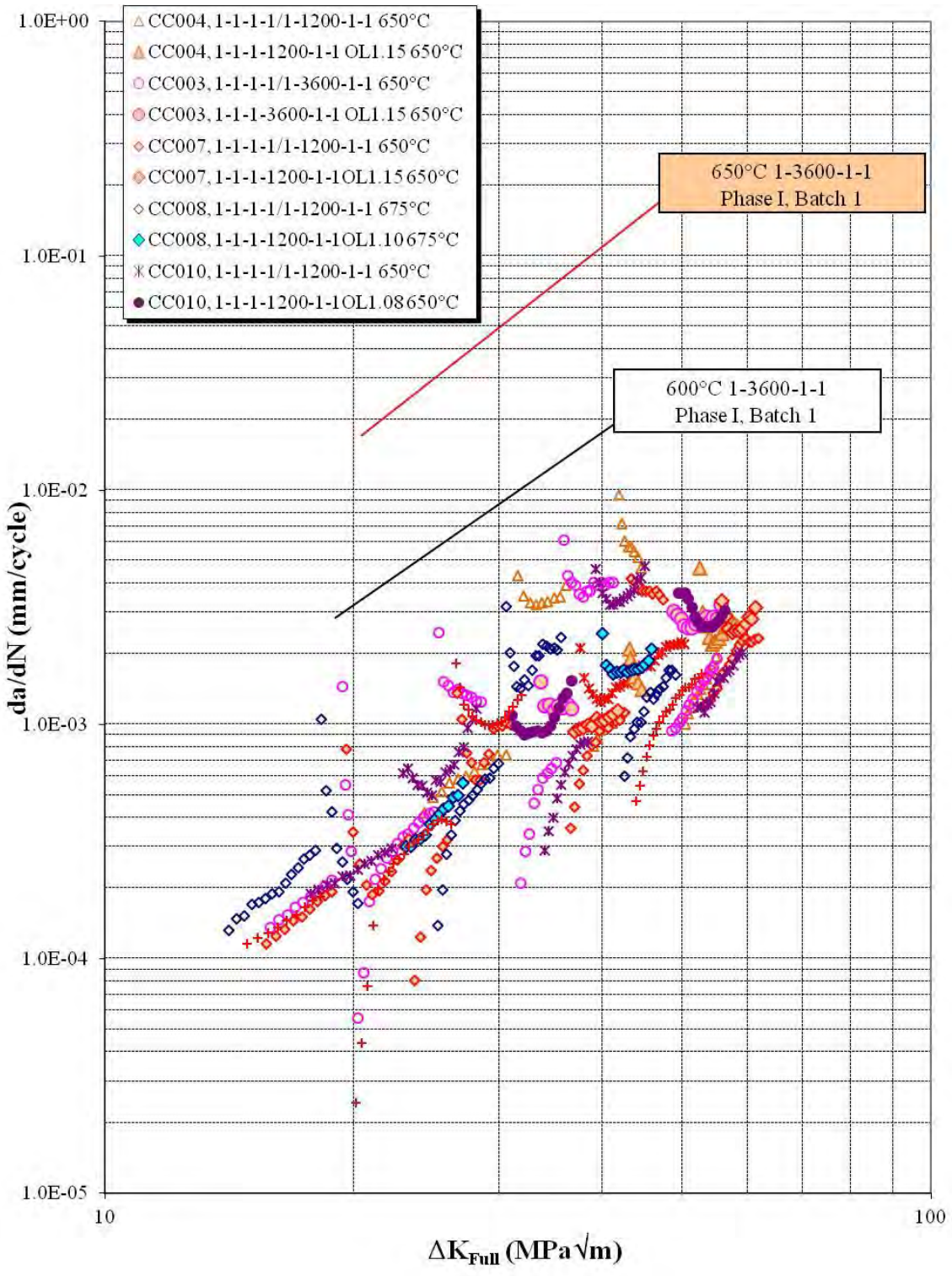


Figure A-8: da/dN vs. ΔK curves for fine-grained Udimet 720Li samples CC003, CC004, CC007, CC008 and CC010, which were tested at 650°C and under various overload factors and dwell times. Note that two sets of baseline, dwell and overload loading has been used on each sample. A plot for each individual test piece is presented below.

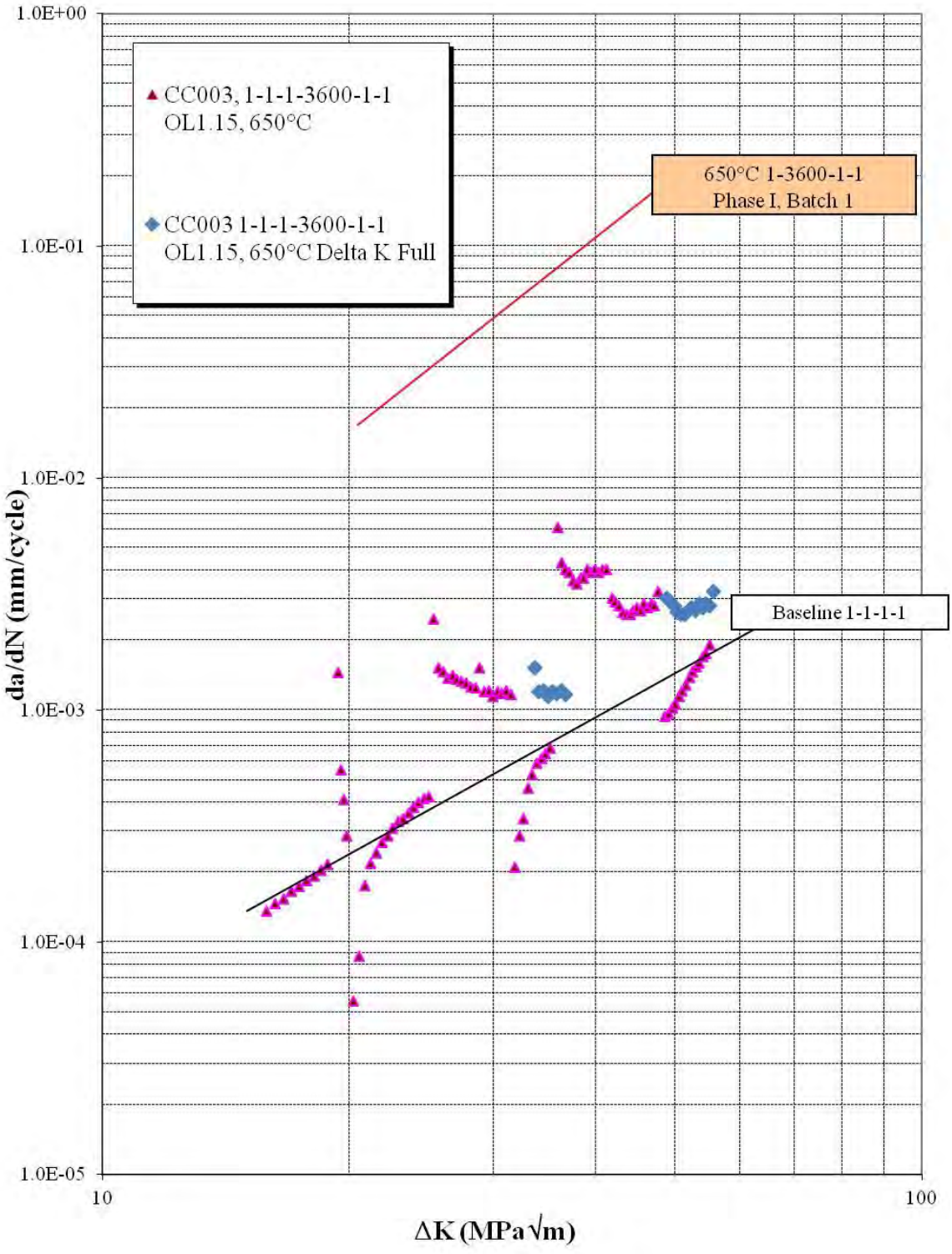


Figure A-9: da/dN vs. ΔK curve for fine-grained Udimet 720Li sample CC003, which was tested at 650°C, with a dwell load of 26 kN, a dwell period of 3,600s and an overload factor of 1.15. Note that two sets of baseline, dwell and overload loading has been applied to the test piece. Partial retardation.

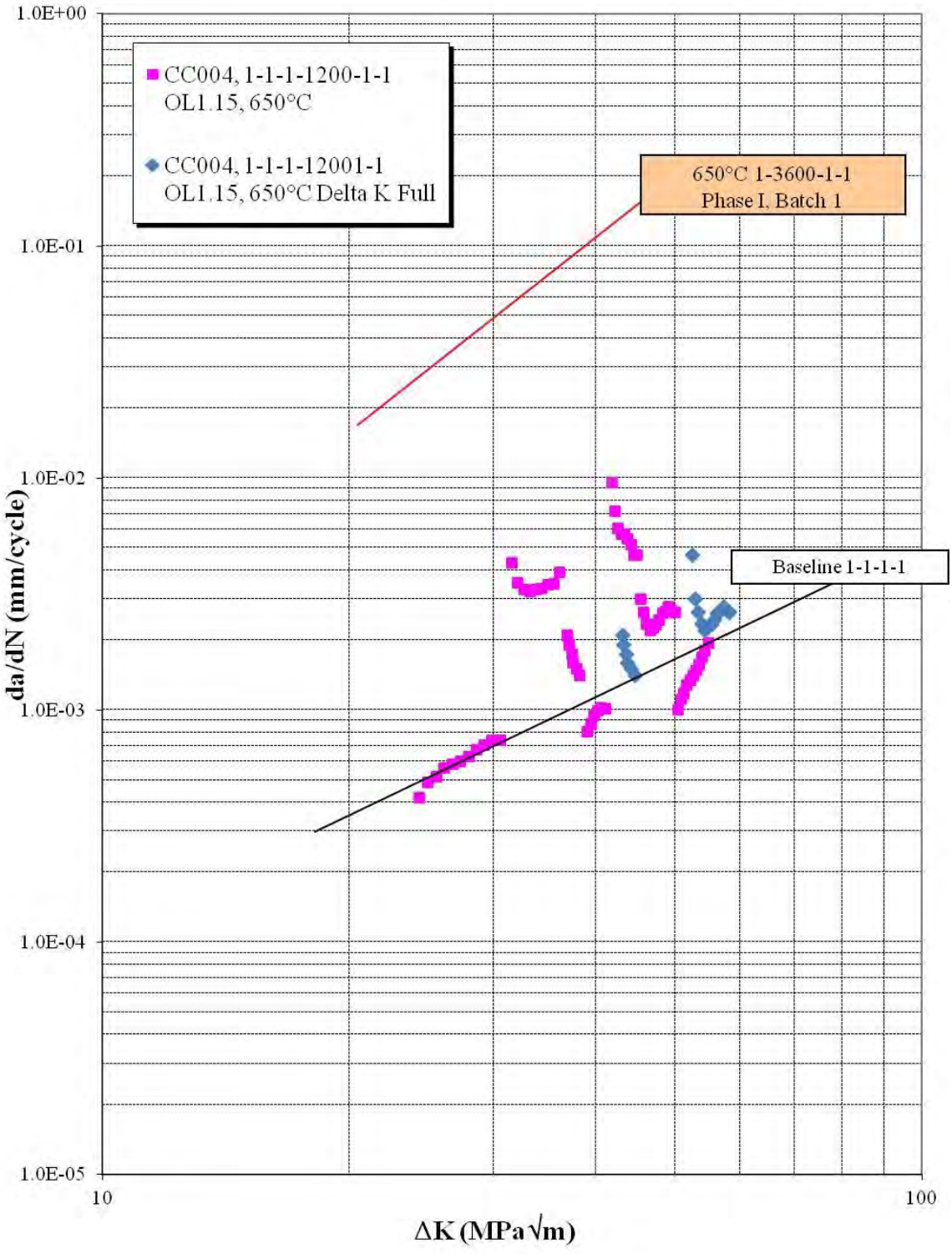


Figure A-10: da/dN vs. ΔK curve for fine-grained Udimet 720Li sample CC004, which was tested at 650°C, with a dwell load of 26 kN, a dwell period of 1,200s and an overload factor of 1.15. Note that two sets of baseline, dwell and overload loading has been applied to the test piece. Note also that overload testing has not been run long enough to determine degree of retardation, nevertheless Full retardation can be inferred.

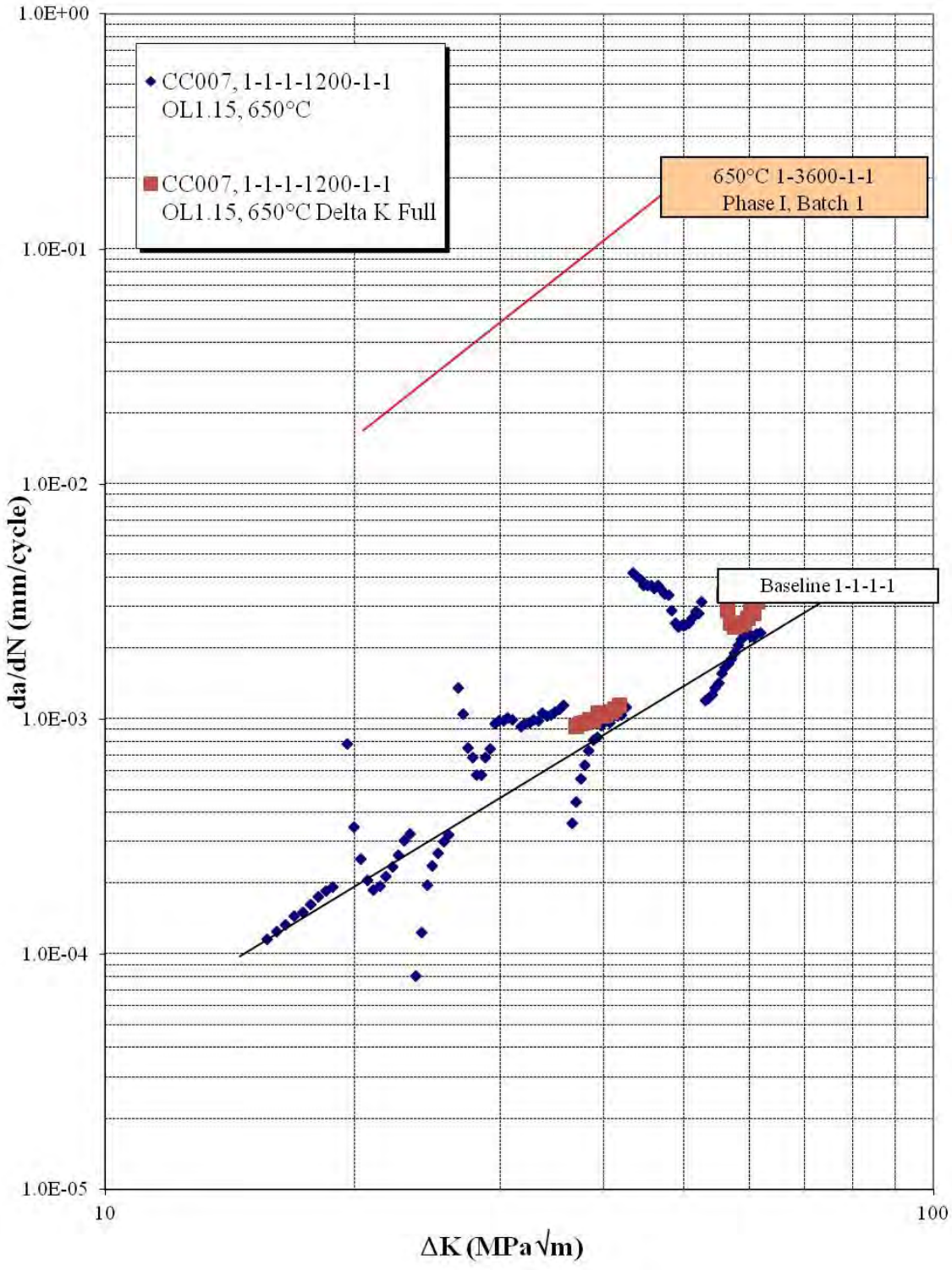


Figure A-11: da/dN vs. ΔK curve for fine-grained Udimet 720Li sample CC007, which was tested at 650°C, with a dwell load of 26 kN, a dwell period of 1,200s and an overload factor of 1.15. Note that two sets of baseline, dwell and overload loading has been applied to the test piece. Partial retardation has occurred at lower ΔK values and Full retardation at higher ΔK values.

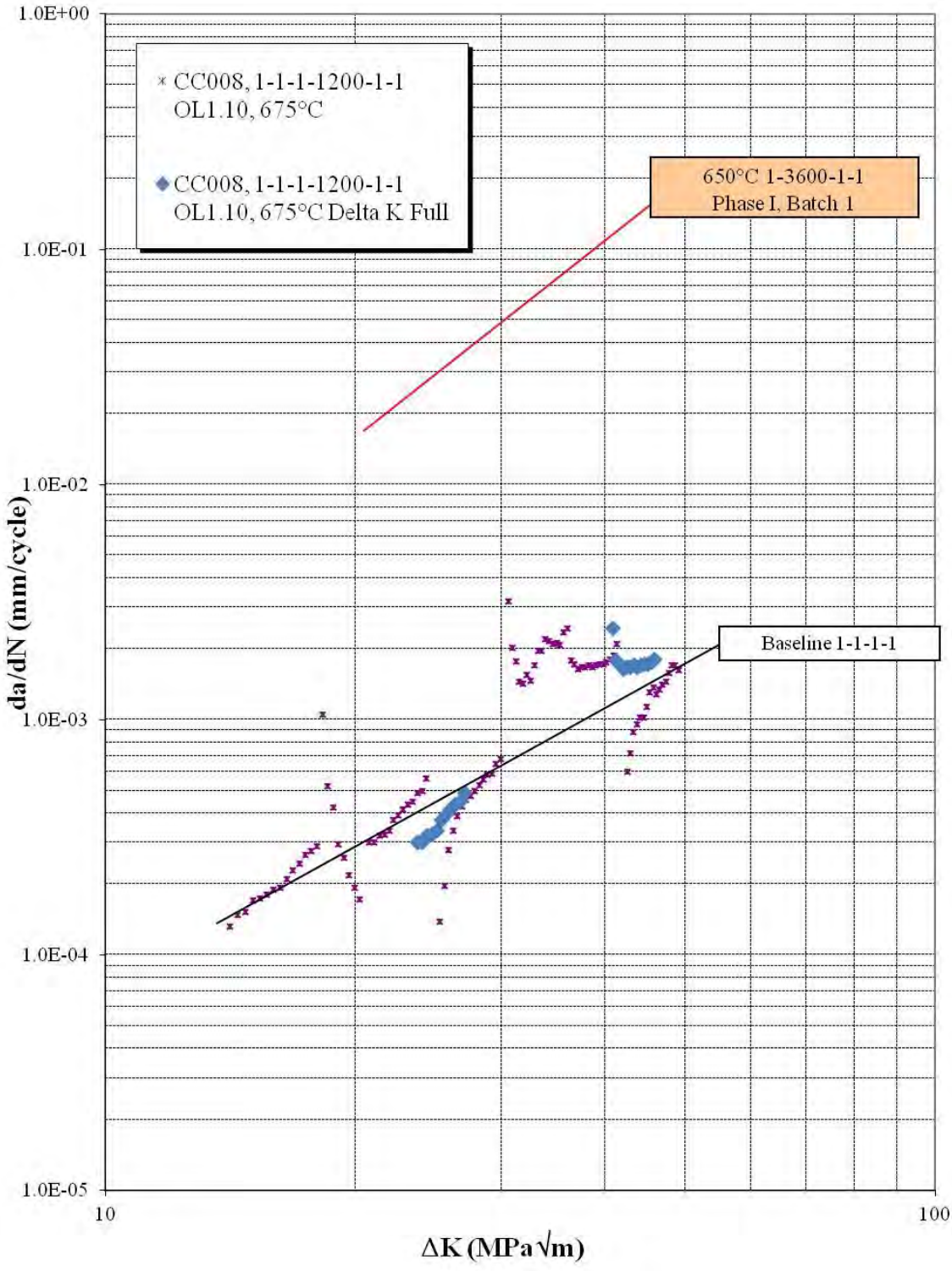


Figure A-12: da/dN vs. ΔK curve for fine-grained Udimet 720Li sample CC008, which was tested at 675°C, with a dwell load of 22 kN, a dwell period of 1,200s and an overload factor of 1.10. Note that two sets of baseline, dwell and overload loading has been applied to the test piece. Partial retardation.

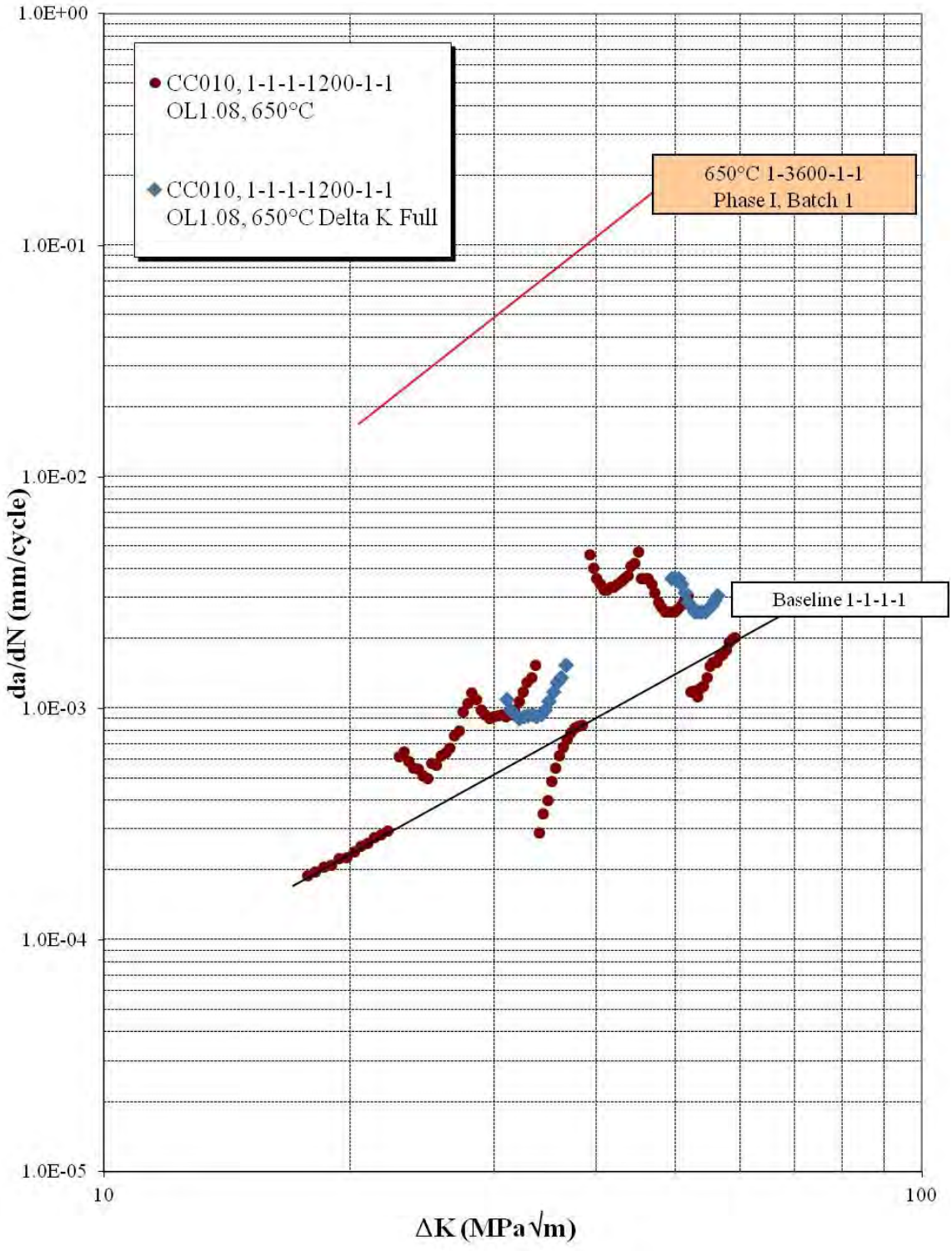


Figure A-13: da/dN vs. ΔK curve for fine-grained Udimet 720Li sample CC010, which was tested at 650°C, with a dwell load of 26 kN, a dwell period of 1,200s and an overload factor of 1.08. Note that two sets of baseline, dwell and overload loading has been applied to the test piece. Partial retardation.

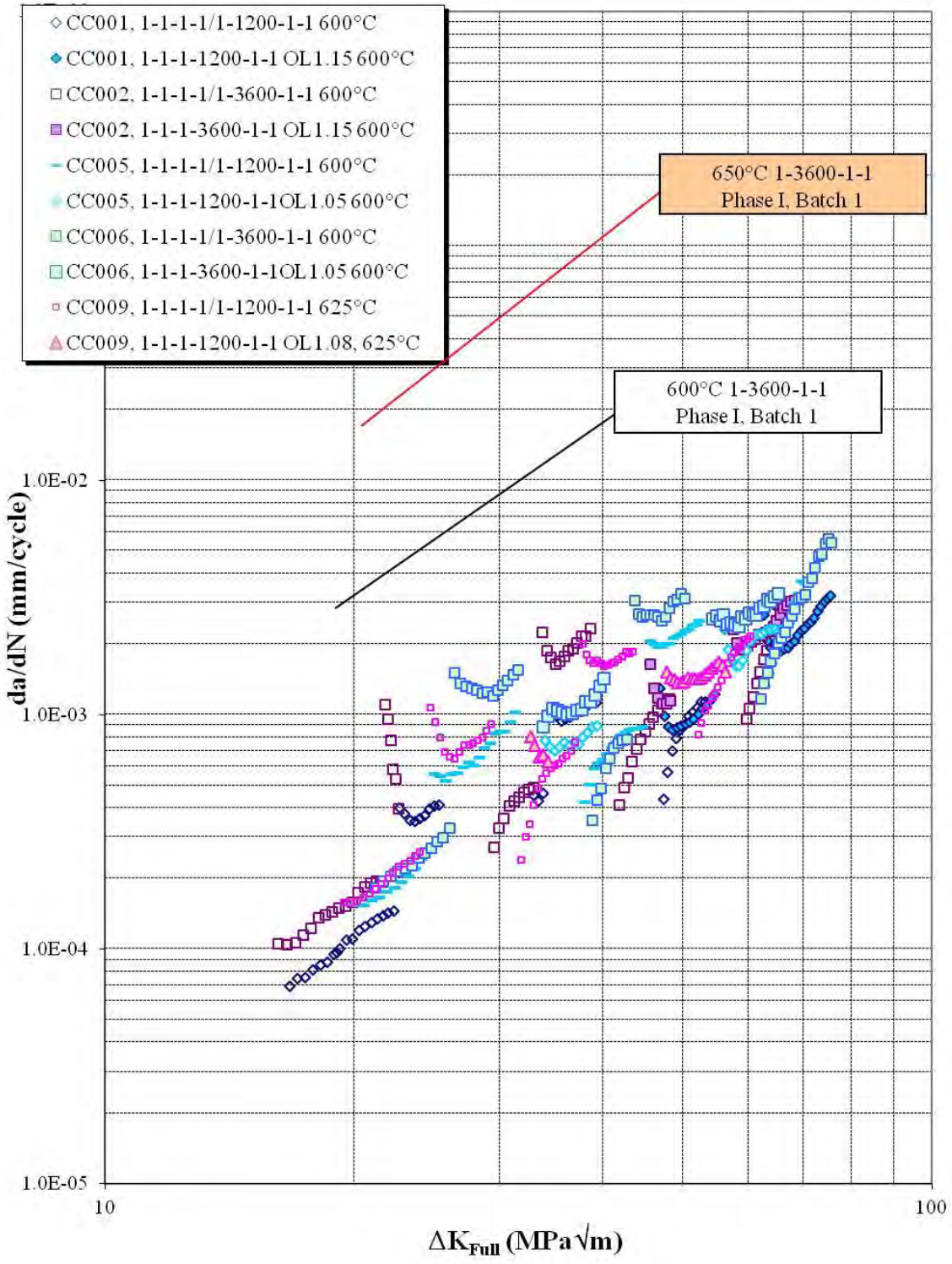


Figure A-14: da/dN vs. ΔK curves for fine-grained Udimet 720Li samples CC001, CC002, CC005, CC006 and CC009, which were tested at 600°C and under various overload factors and dwell times. Note that two sets of baseline, dwell and overload loading has been used on each sample. A plot for each individual test piece is presented below.

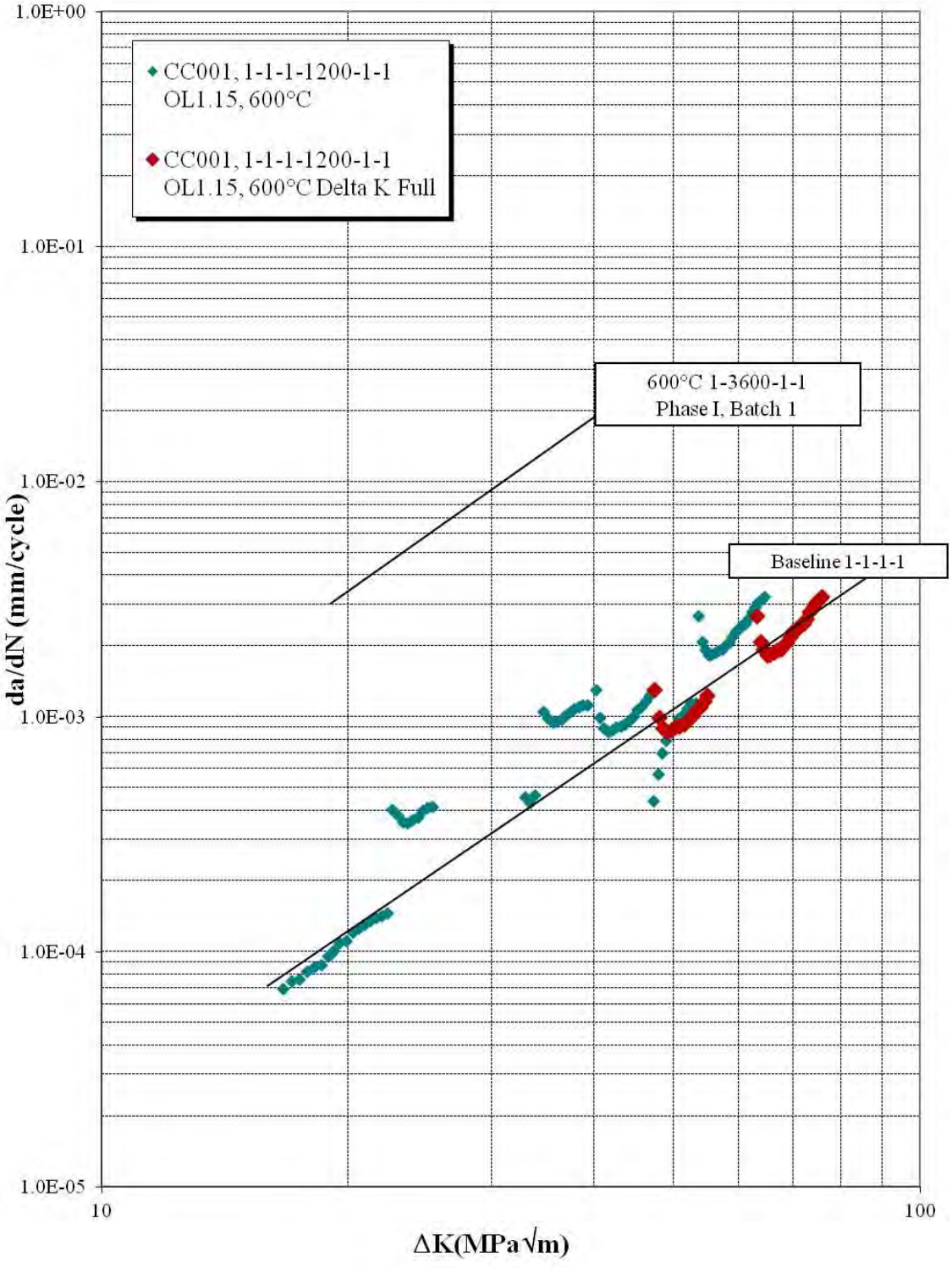


Figure A-15: da/dN vs. ΔK curve for fine-grained Udimet 720Li sample CC001, which was tested at 600°C, with a dwell load of 32.5 kN, a dwell period of 1,200s and an overload factor of 1.15. Note that two sets of baseline, dwell and overload loading has been applied to the test piece. Full retardation.

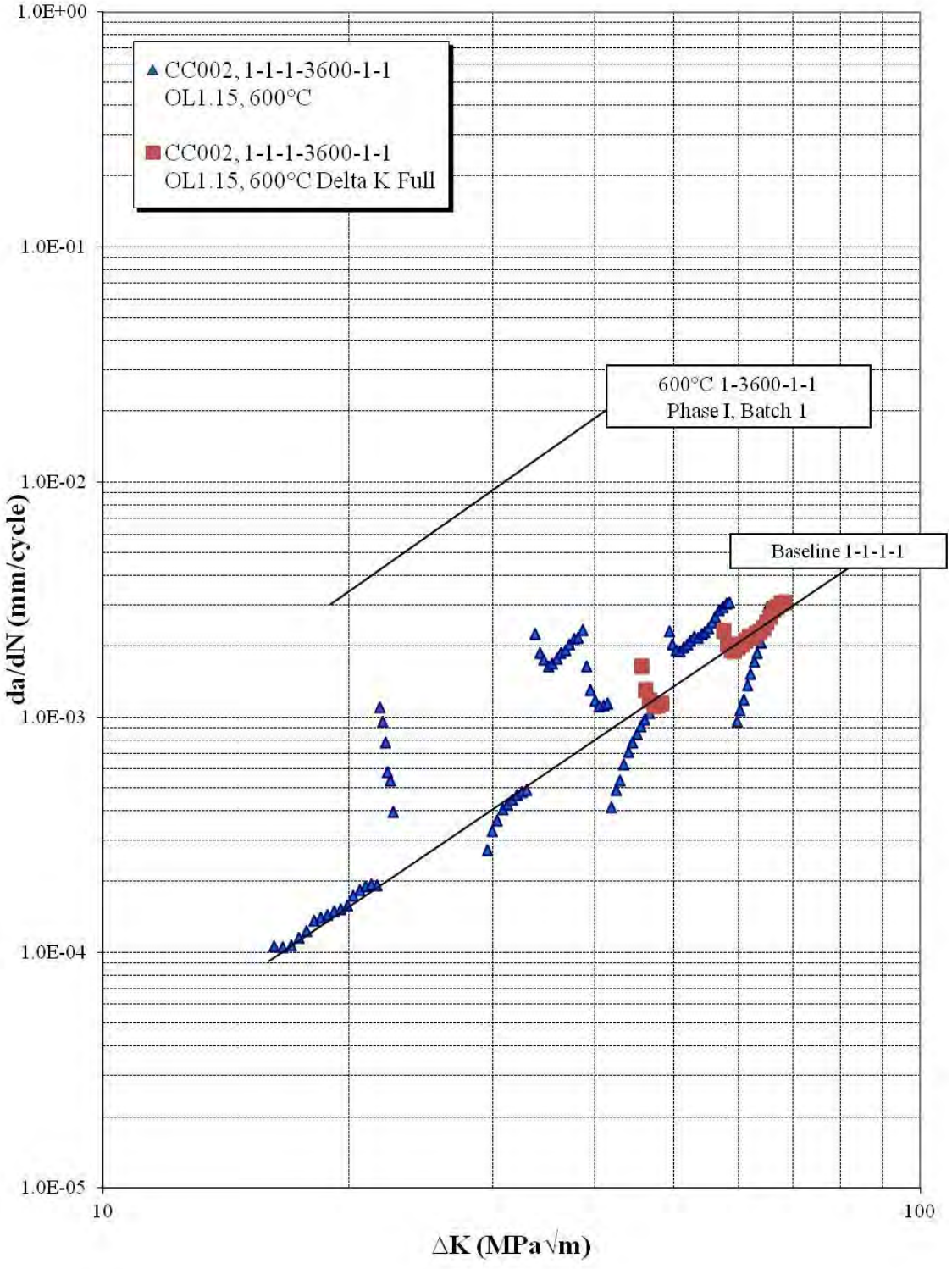


Figure A-16: da/dN vs. ΔK curve for fine-grained Udimet 720Li sample CC002, which was tested at 600°C, with a dwell load of 32.5 kN, a dwell period of 3,600s and an overload factor of 1.15. Note that two sets of baseline, dwell and overload loading has been applied to the test piece. Full retardation.

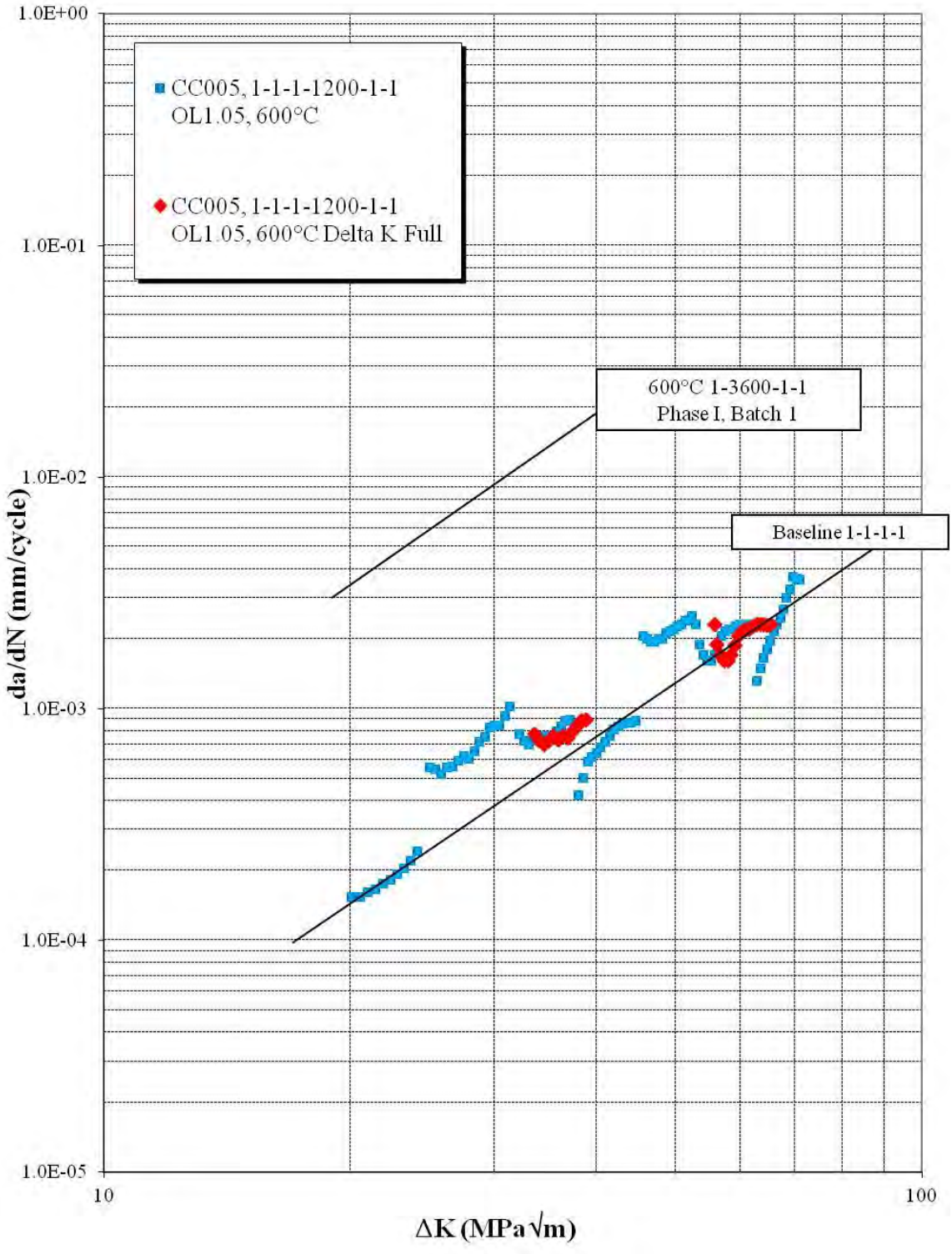


Figure A-17: da/dN vs. ΔK curve for fine-grained Udimet 720Li sample CC005, which was tested at 600°C, with a dwell load of 32.5 kN, a dwell period of 1,200s and an overload factor of 1.05. Note that two sets of baseline, dwell and overload loading has been applied to the test piece. Partial retardation.

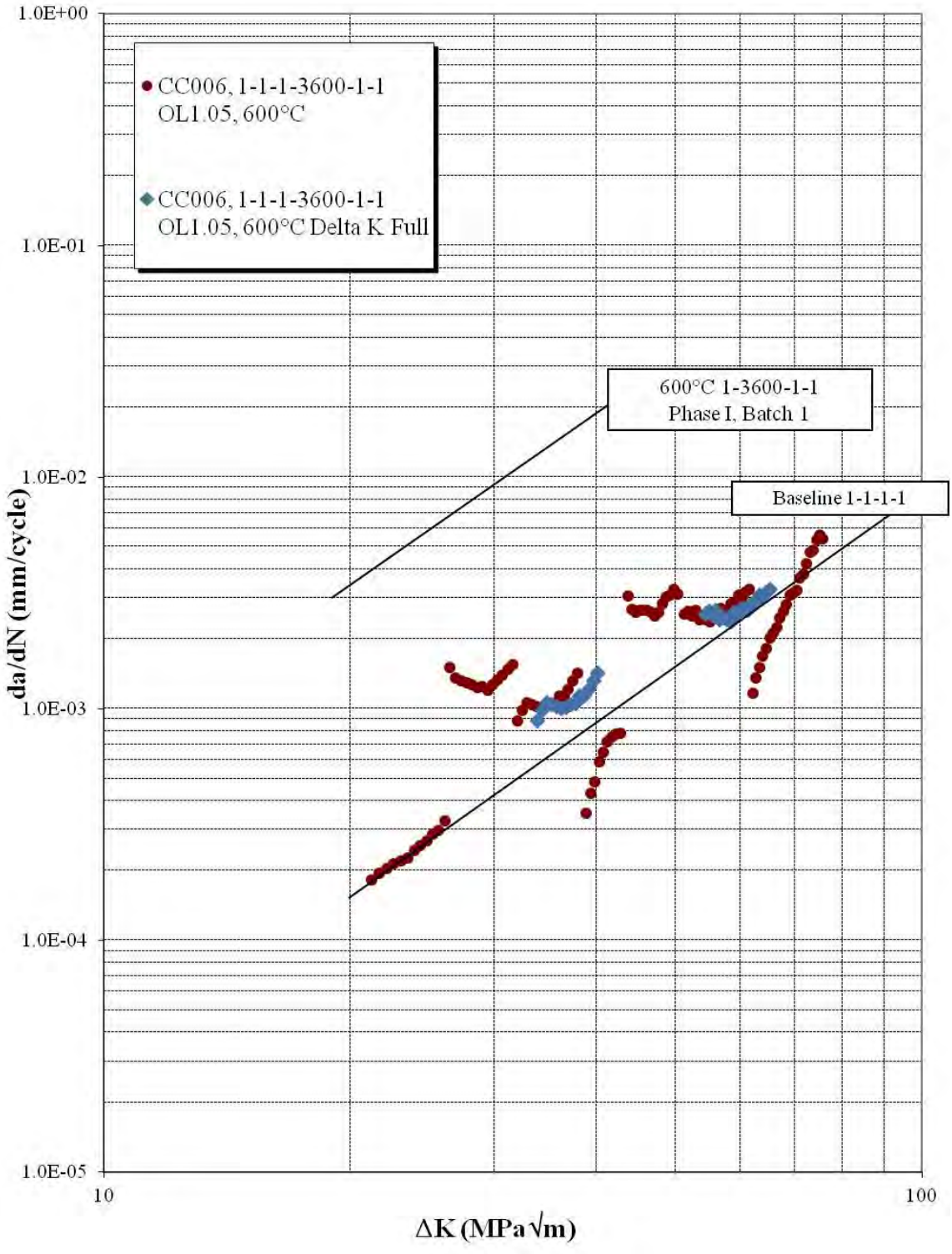


Figure A-18: da/dN vs. ΔK curve for fine-grained Udimet 720Li sample CC006, which was tested at 600°C, with a dwell load of 32.5 kN, a dwell period of 3,600s and an overload factor of 1.05. Note that two sets of baseline, dwell and overload loading has been applied to the test piece. Partial retardation.

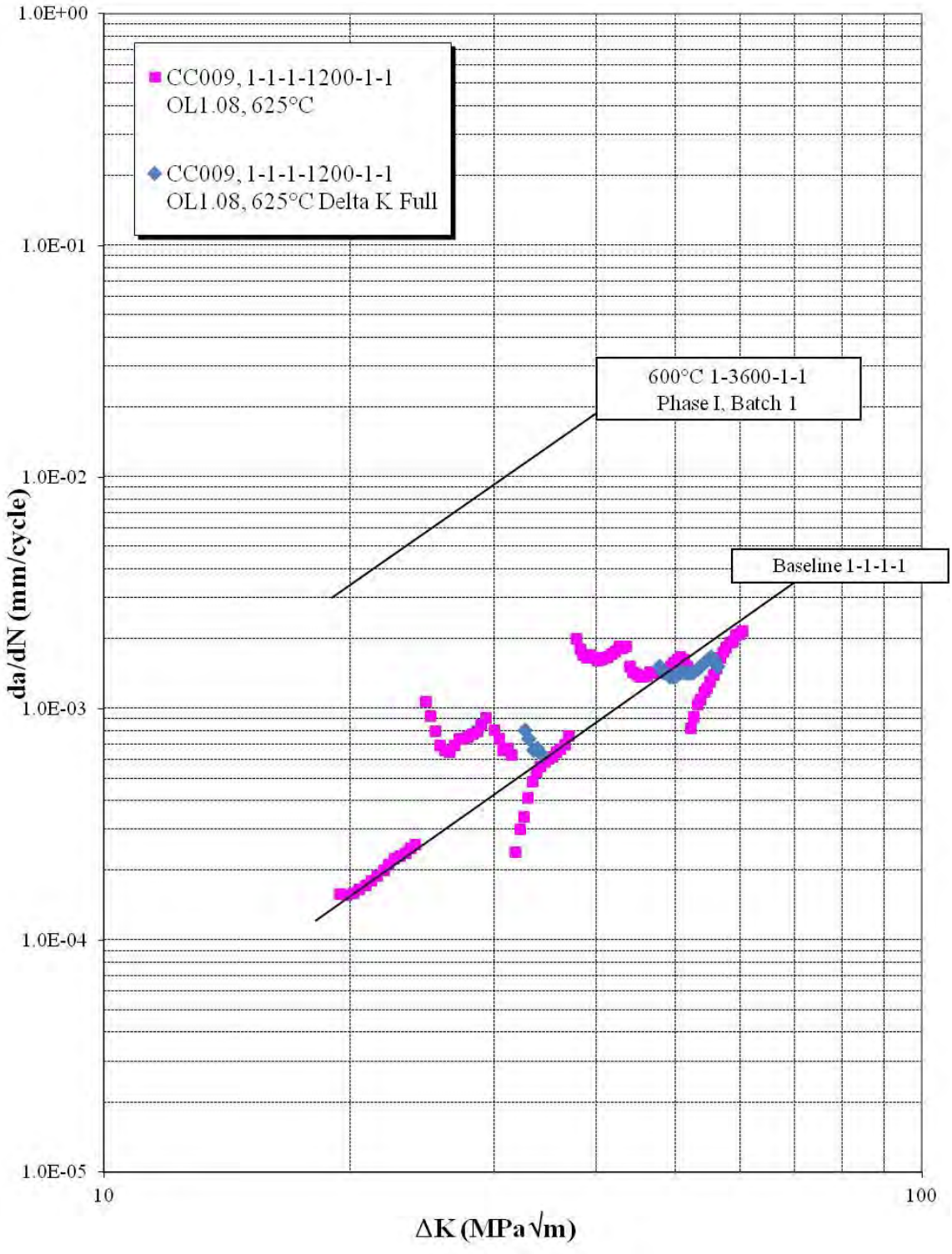


Figure A-19: da/dN vs. ΔK curve for fine-grained Udimet 720Li sample CC009, which was tested at 625°C, with a dwell load of 29 kN, a dwell period of 1,200s and an overload factor of 1.08. Note that two sets of baseline, dwell and overload loading has been applied to the test piece. Partial retardation.

Udimet 720Li Dwell at Overload Tests

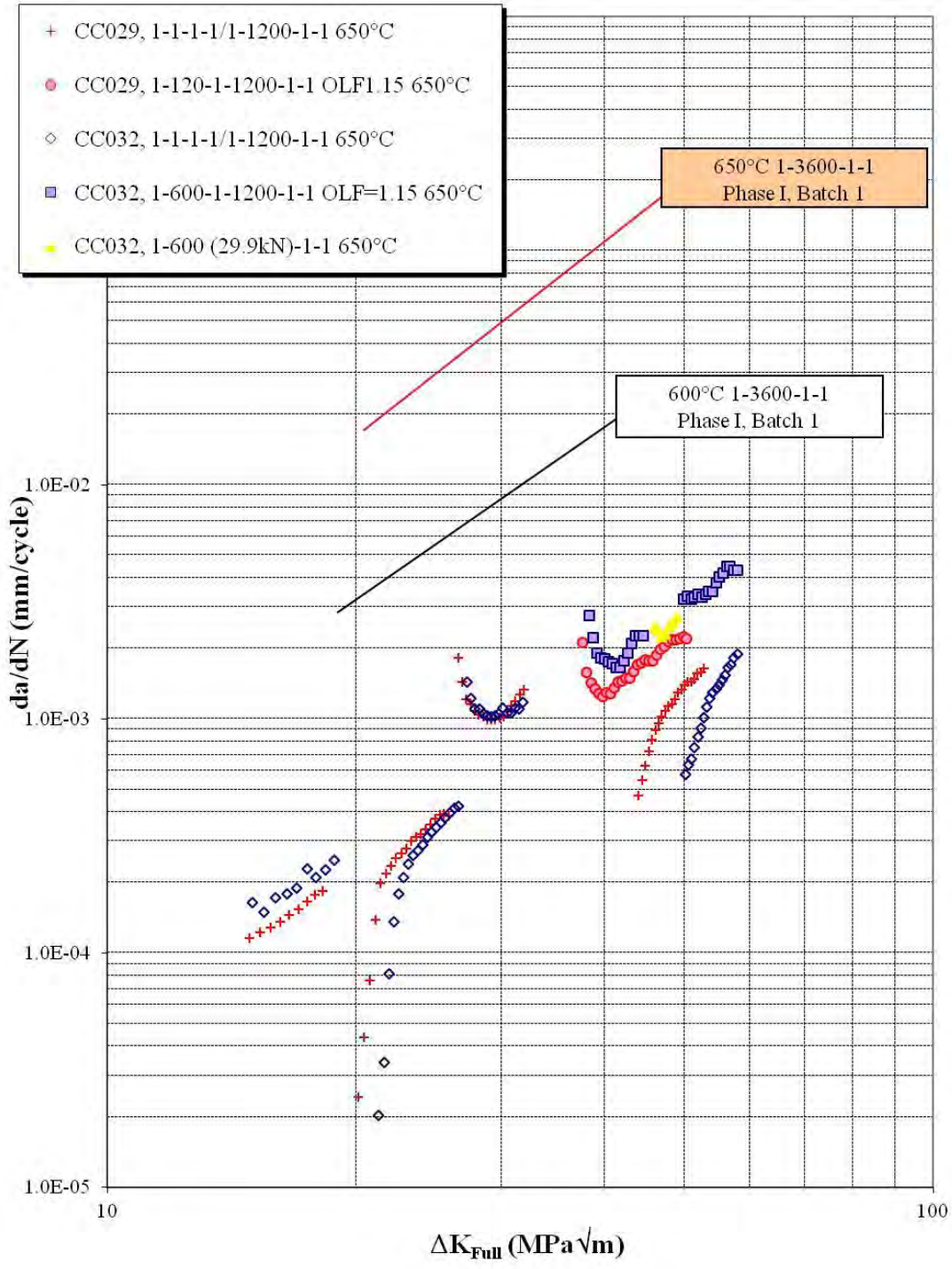


Figure A-20: da/dN vs. ΔK graph for Udimet 720Li samples CC029 and CC032 tested at a temperature of 650°C, dwell loads of 26 kN, an overload factor of 1.15 and a dwell periods of 1,200s. Overload segments in both cases were extended to hold periods rather than conventional 1s in previous tests: 120s for CC029 and 600s for CC032.

Traces labelled “Phase I” in Figure A-7 to Figure A-20 to represent modelled results from previously test samples with a different microstructure.

Udimet 720Li Time-dependent ΔK_{th} Tests

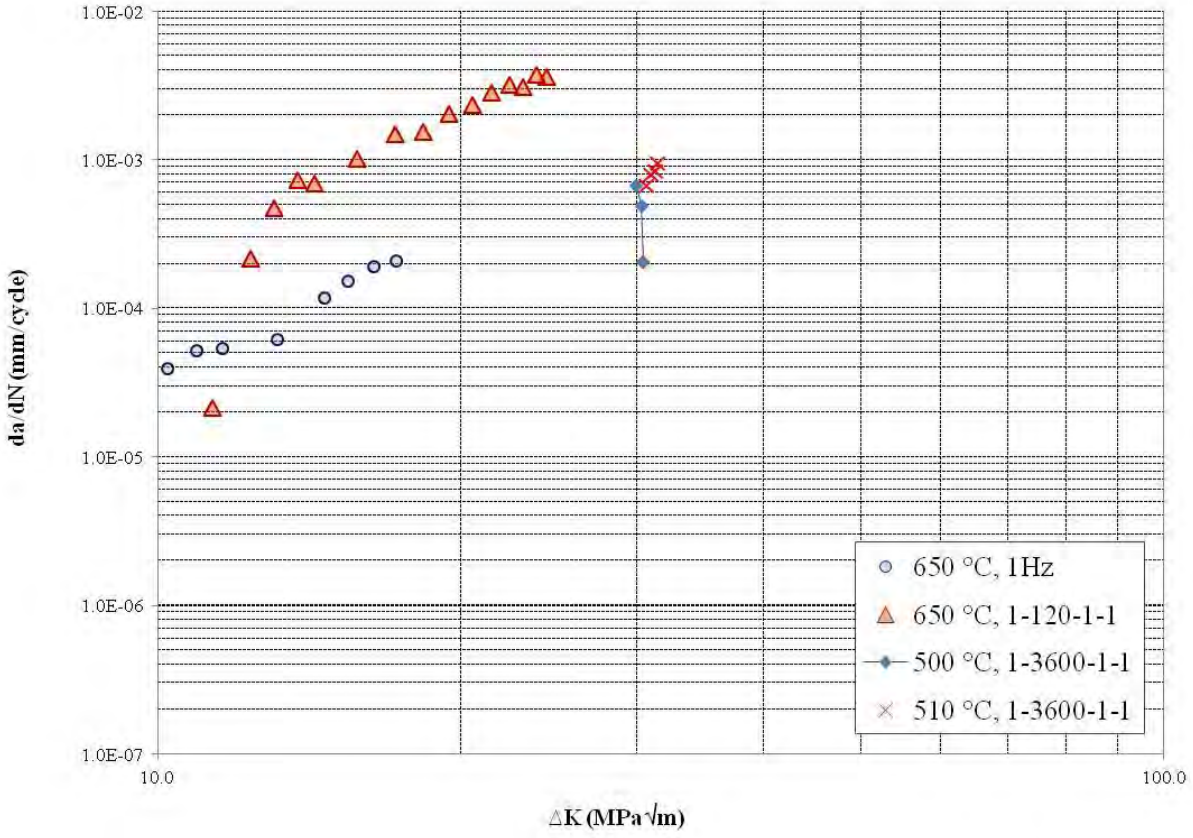


Figure A-21: da/dN vs. ΔK graph to show the effect of a 120 second dwell period on the stress intensity factor range threshold for high temperature (650°C) crack growth when compared with 1 Hz sinusoidal loading. Note that both sets of data are gathered using the decreasing ΔK (load shedding) technique. Note also the temperature threshold data gathered on the same test piece (CC044), which was found to be ~510 °C for a ΔK of around 30MPa√m.

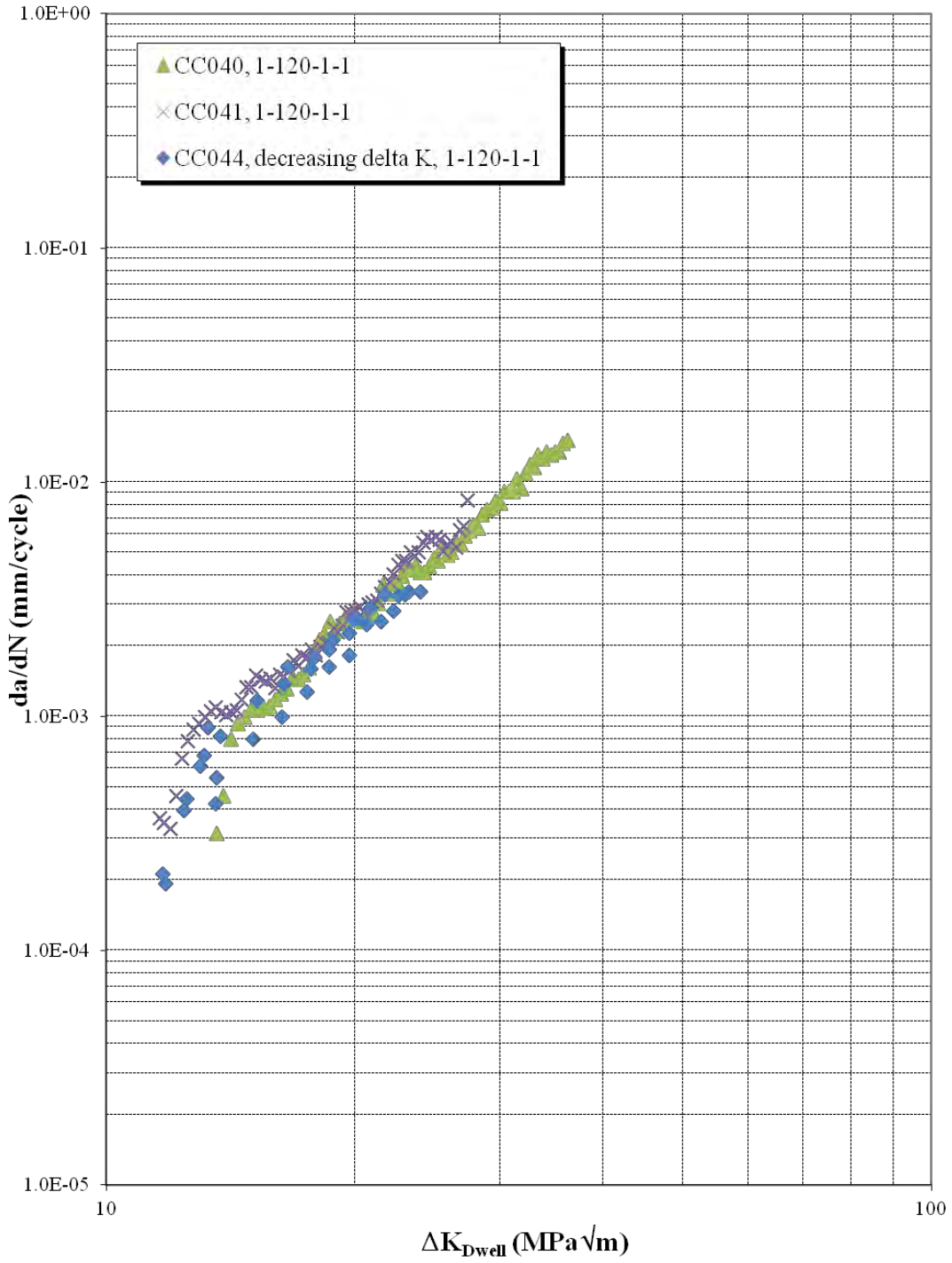


Figure A-22: da/dN vs. ΔK graph to show increasing ΔK threshold testing on Udimet 720Li test pieces CC040 and CC041, and decreasing ΔK threshold testing on test piece CC044; both tested at 650°C and with a dwell period of 120s. Note threshold values obtained were around 13, 12 and 12.5 MPa√m respectively. Note also therefore that time-dependent threshold values are shown to be independent of testing methodology (in terms of increasing vs decreasing ΔK methods).

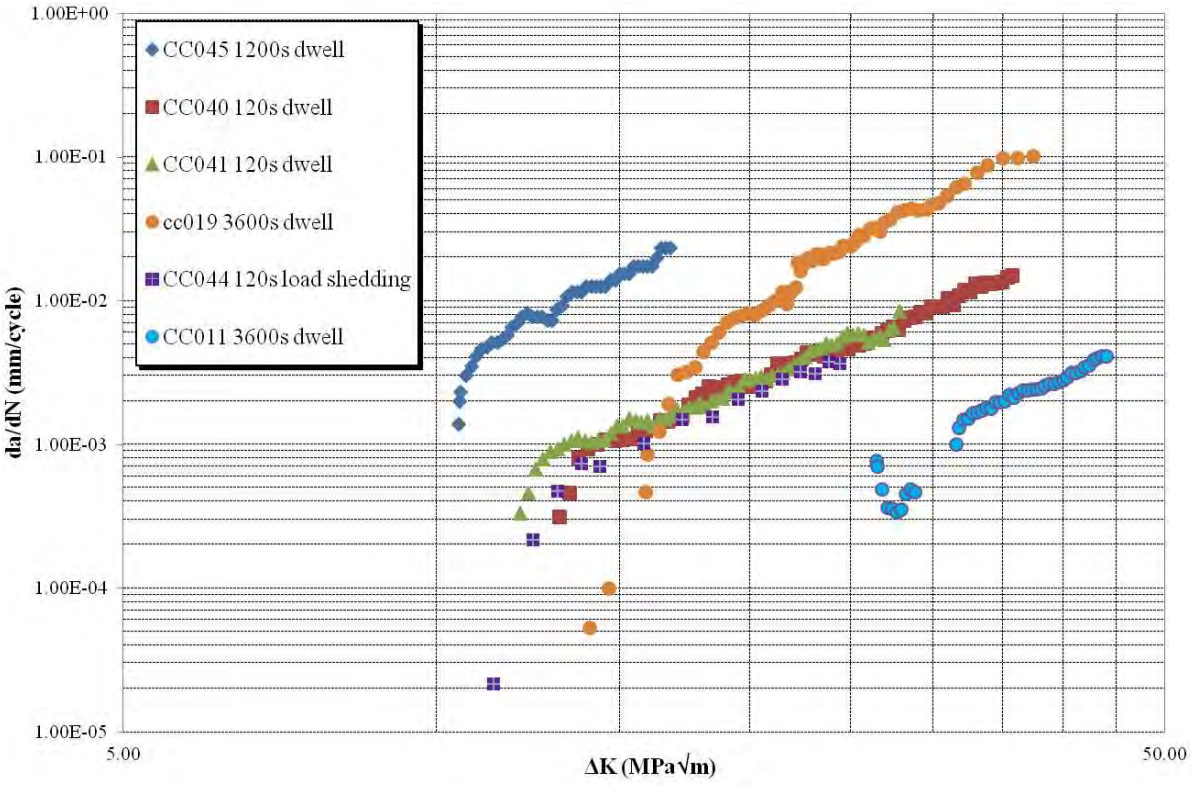


Figure A-23: da/dN vs. ΔK graph to show comparisons for all ΔK threshold testing on Udimet 720Li sample test pieces. All tests are carried out at 650°C in laboratory air, with dwell periods of 120 or 3,600 seconds. Note that test pieces CC011 and CC045 (showing unusual results when compared with the other data presented) are found to comprise notably different microstructures.

RR1000

Presented in subsequent sections are a series of crack growth resistance curves generated by the implementation of previously discussed methodologies on fine-grain RR1000 test-pieces.

RR1000 Baseline and Dwell Tests

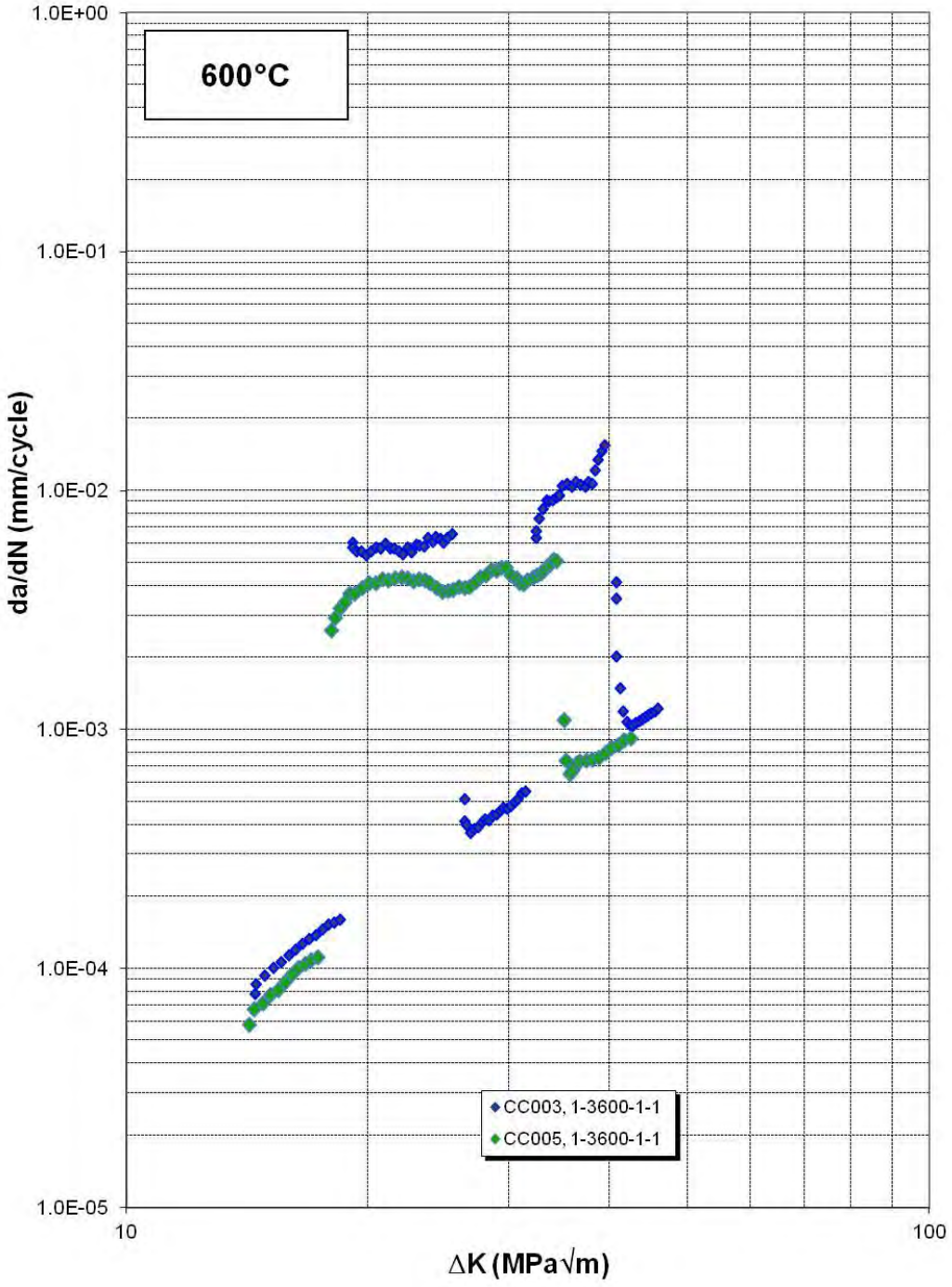


Figure A-24: da/dN vs. ΔK curves for fine-grained RR1000 samples CC003 and CC005, which were tested at 600°C, with a dwell load of 26 kN, a dwell time of 3,600s in air. Note the effect of introducing a dwell period on crack growth rates when compared with those associated with baseline loading. Note also the "tails" on the final segments of baseline loading crack growth rates.

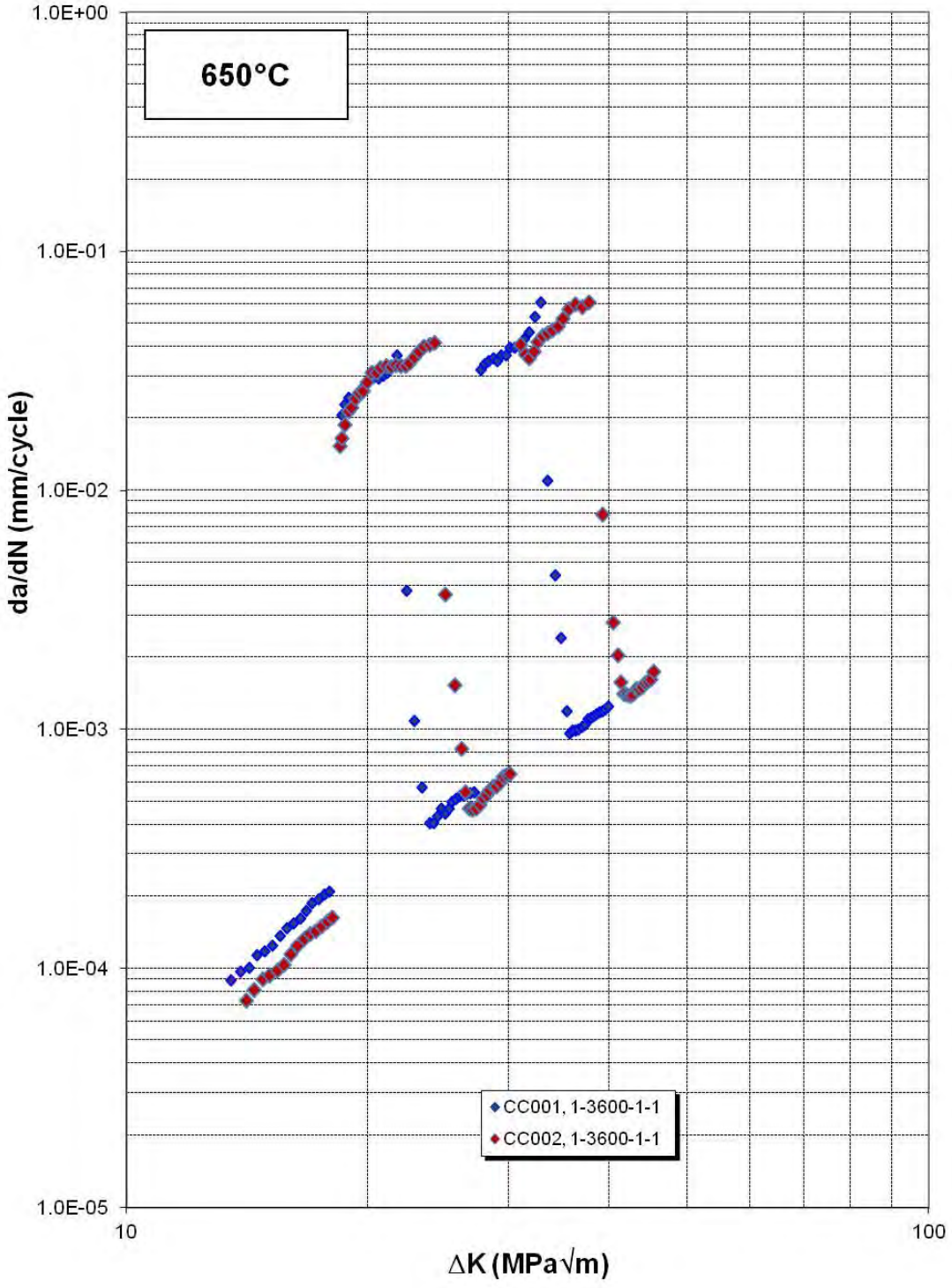


Figure A-25: da/dN vs. ΔK curves for fine-grained RR1000 samples CC001 and CC002, which were tested at 650°C, with a dwell load of 26 kN, a dwell time of 3,600s in air.

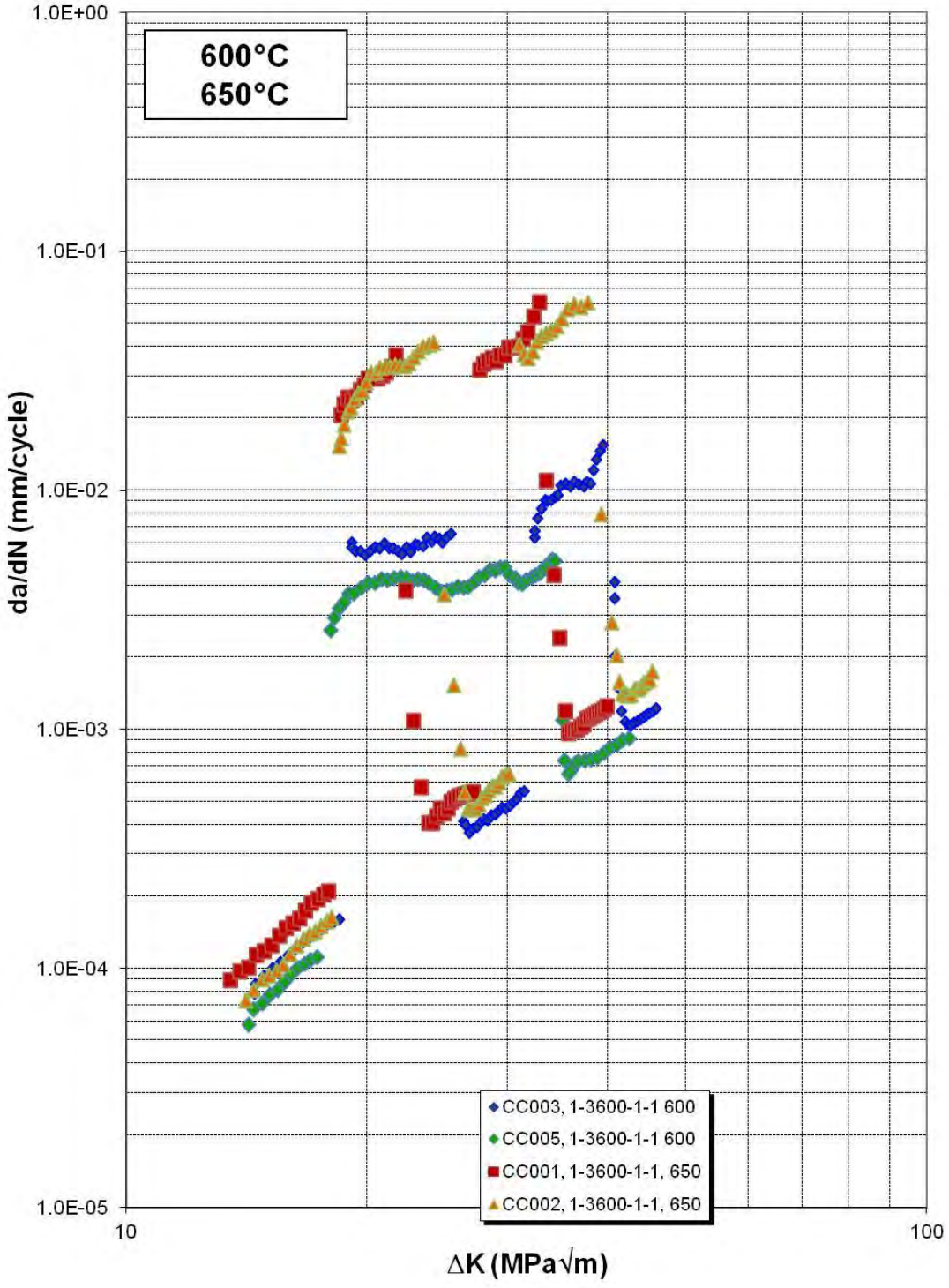


Figure A-26: da/dN vs. ΔK curves to show a comparison in terms of baseline and dwell crack growth rates for 600°C and 650°C. Samples are fine-grained RR1000; CC003 and CC005 (600°C) and CC001 and CC002 (650°C), tested in air with a dwell load of 26kN.

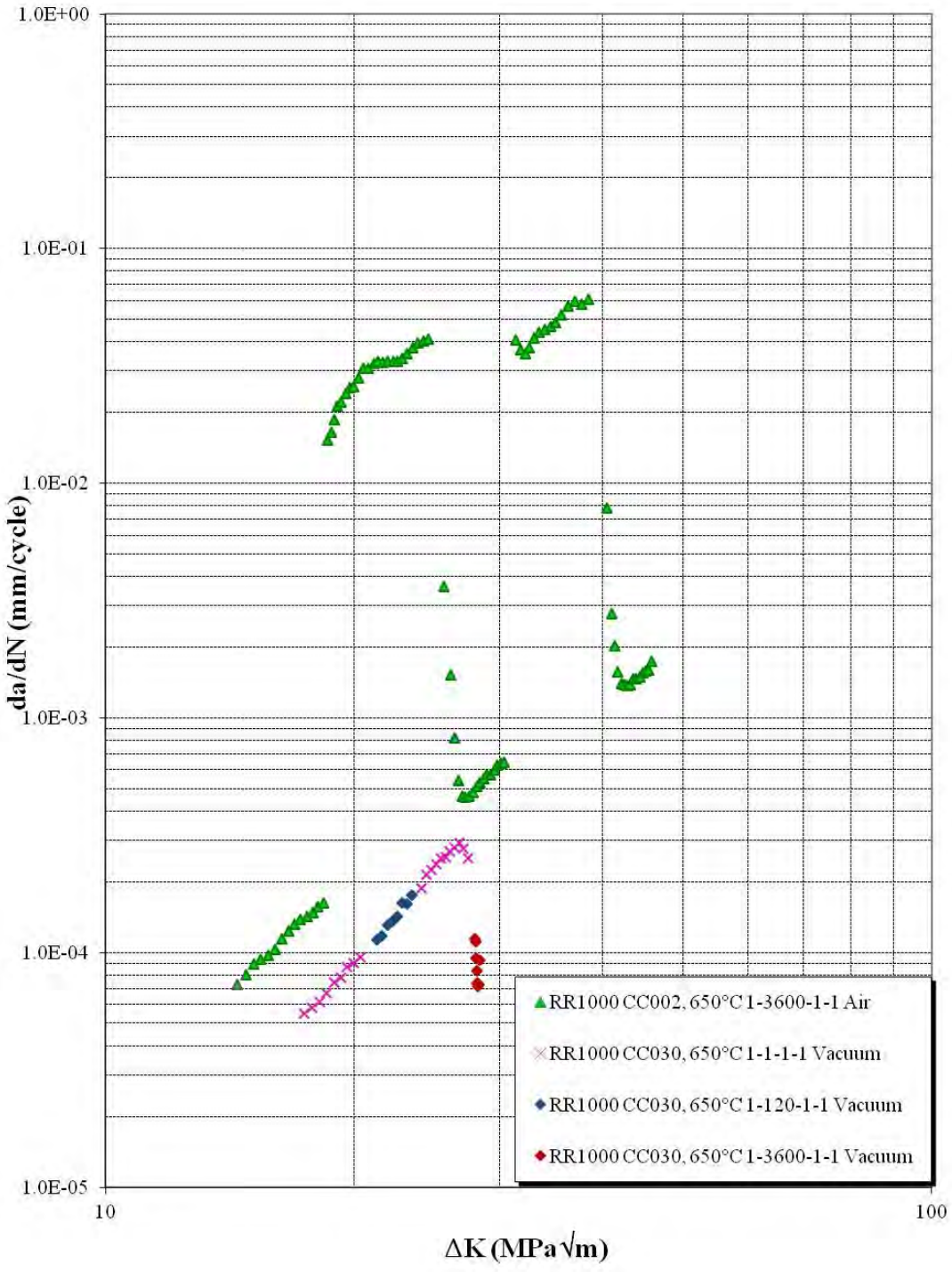


Figure A-27: da/dN vs. ΔK curves to show the effect of dwell testing in a vacuum when compared with otherwise similar testing in air. Test pieces are fine-grained RR1000, tested at a temperature of 650°C and with a dwell load of 26 kN. CC003 is tested in air, with a dwell period of 3,600 seconds. CC030 is tested in a vacuum; with dwell periods of 120 seconds and 3,600 seconds. Note crack growth rates drop down to below baseline under 3,600 second dwell loading in a vacuum.

RR1000 Baseline, Dwell and Overload Tests

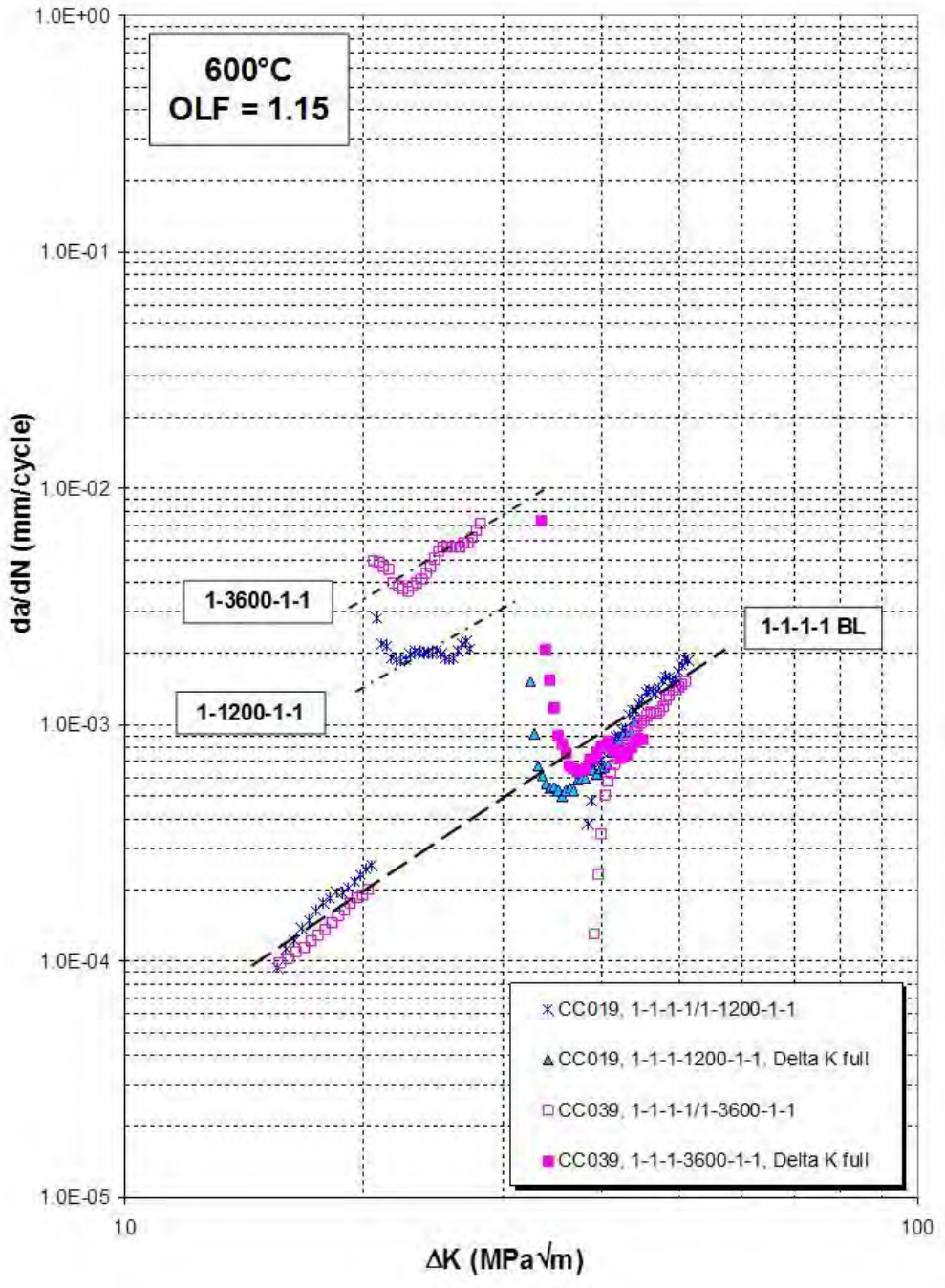


Figure A-28: da/dN vs. ΔK curves for RR1000 samples CC019 and CC039 tested at a temperature of 600°C with an overload factor of 1.15. Note that the ΔK values are calculated using the load range between the peak overload and the minimum load (ΔK_{full}) for the overload fatigue crack growth segment. Full retardation. Note also that the curves show "settling down" behaviour for crack growth rates pertaining to both dwell and overload cycling, and "settling up" behaviour for crack growth rates pertaining to the final segment of baseline loading.

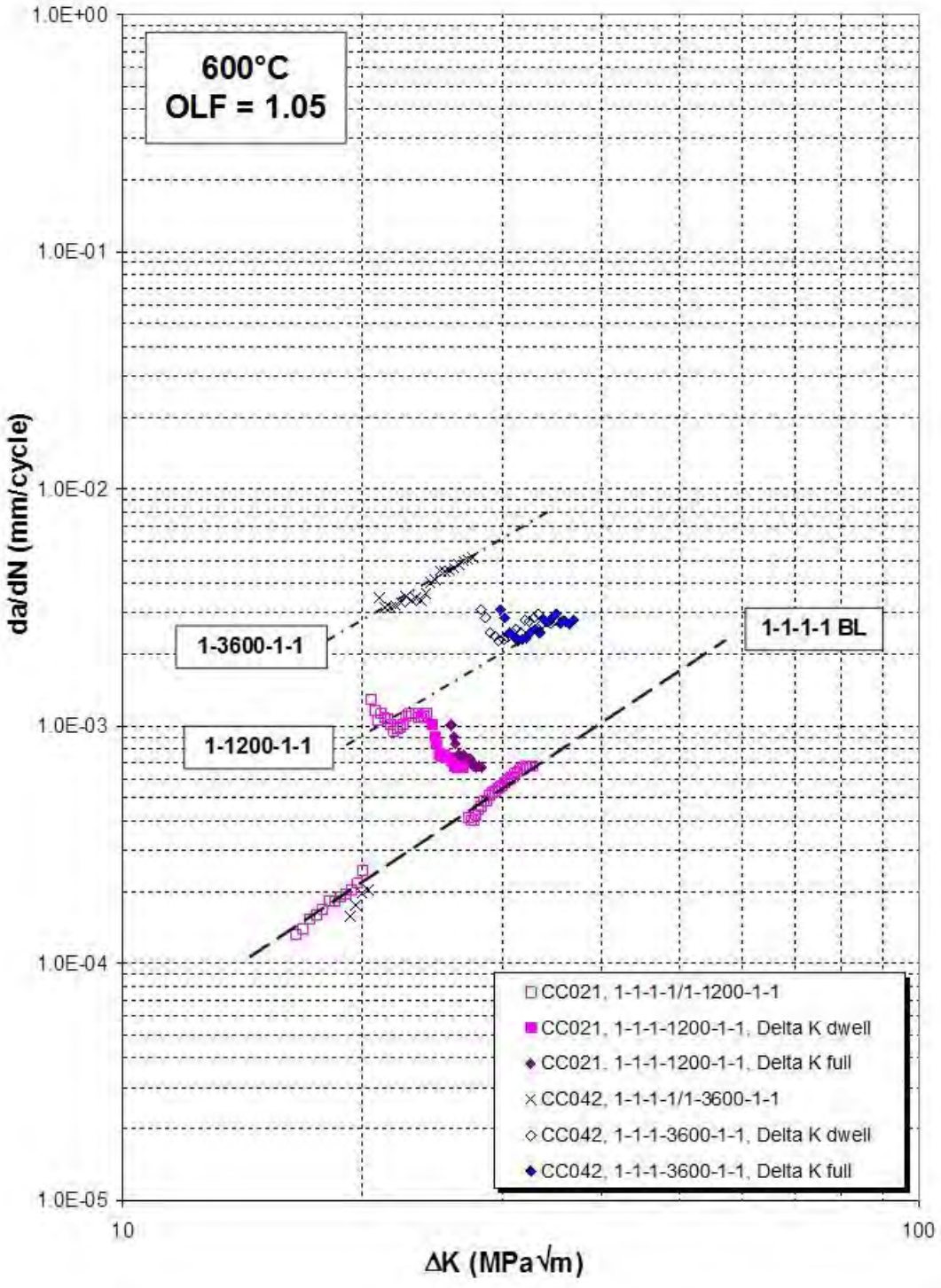


Figure A-29: da/dN vs. ΔK curves for RR1000 samples CC021 and CC042 tested at a temperature of 600°C with an overload factor of 1.05. Partial retardation.

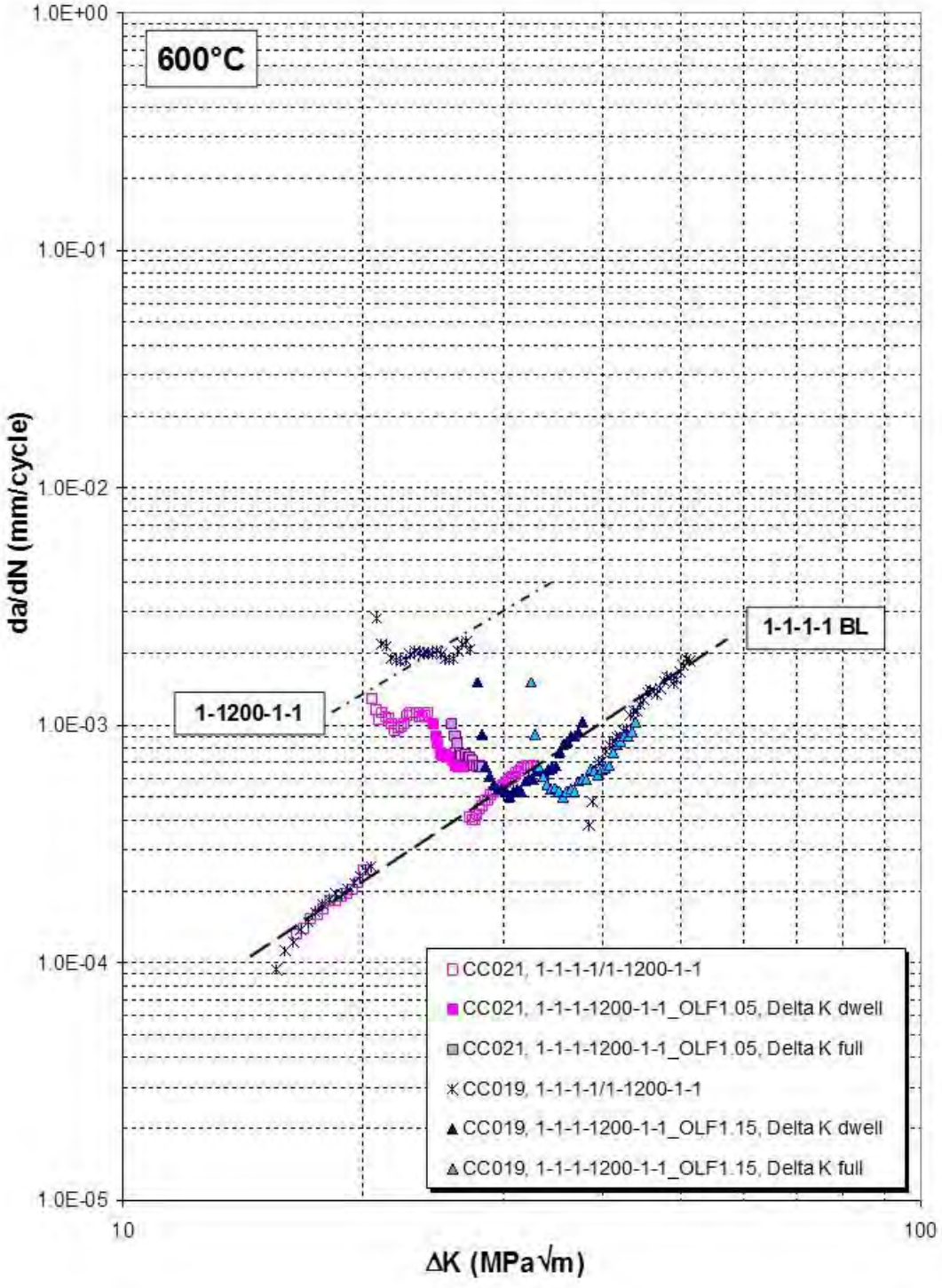


Figure A-30: da/dN vs. ΔK curves for RR1000 samples CC021 and CC019 tested at a temperature of 600°C with a dwell time of 1,200s and overload factors of 1.05 and 1.15 respectively, to show the effect of overload factor.

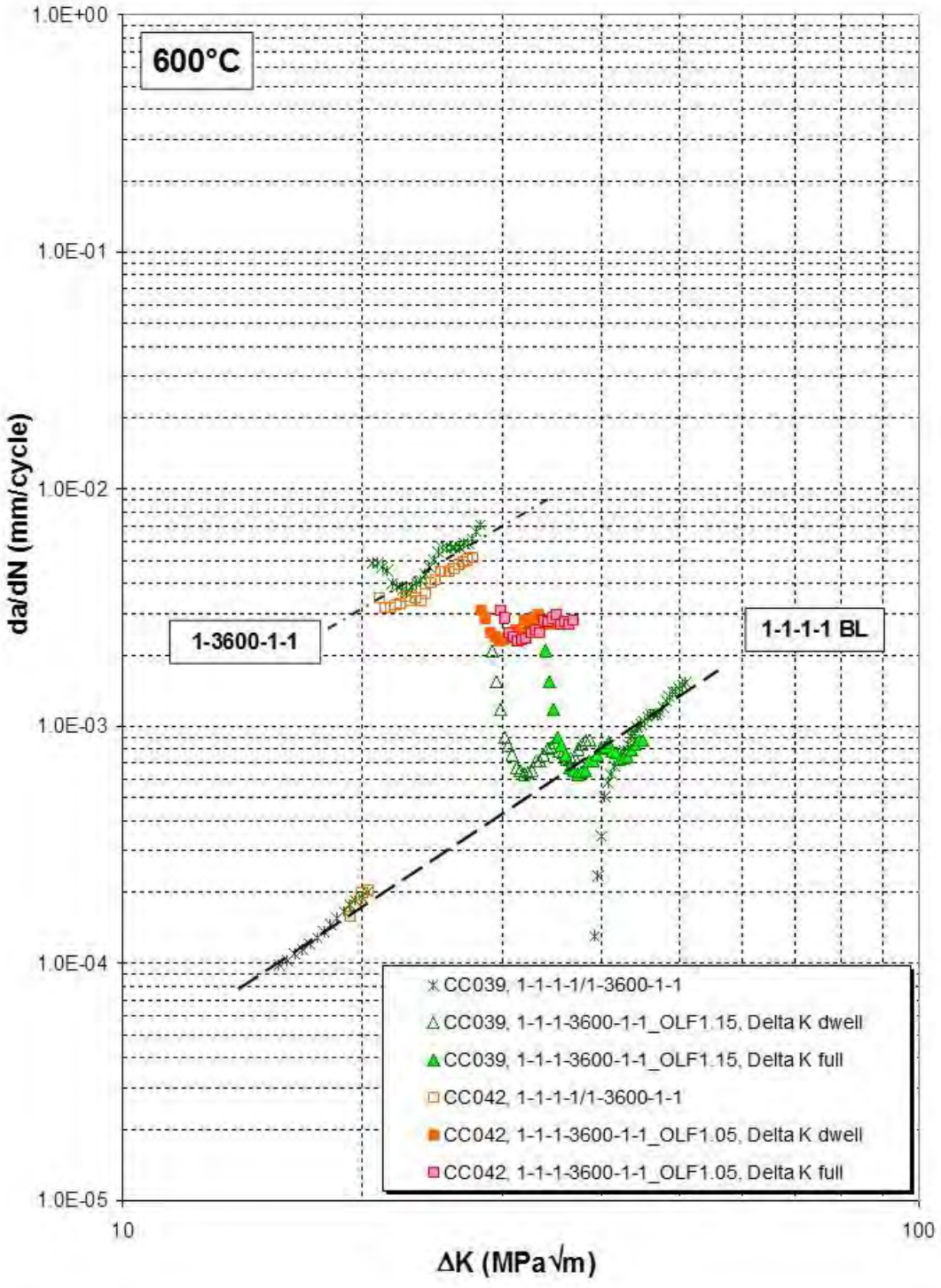


Figure A-31: da/dN vs. ΔK curves for RR1000 samples CC042 and CC039 tested at a temperature of 600°C with a dwell time of 3,600s and overload factors of 1.05 and 1.15 respectively, to show the effect of overload factor.

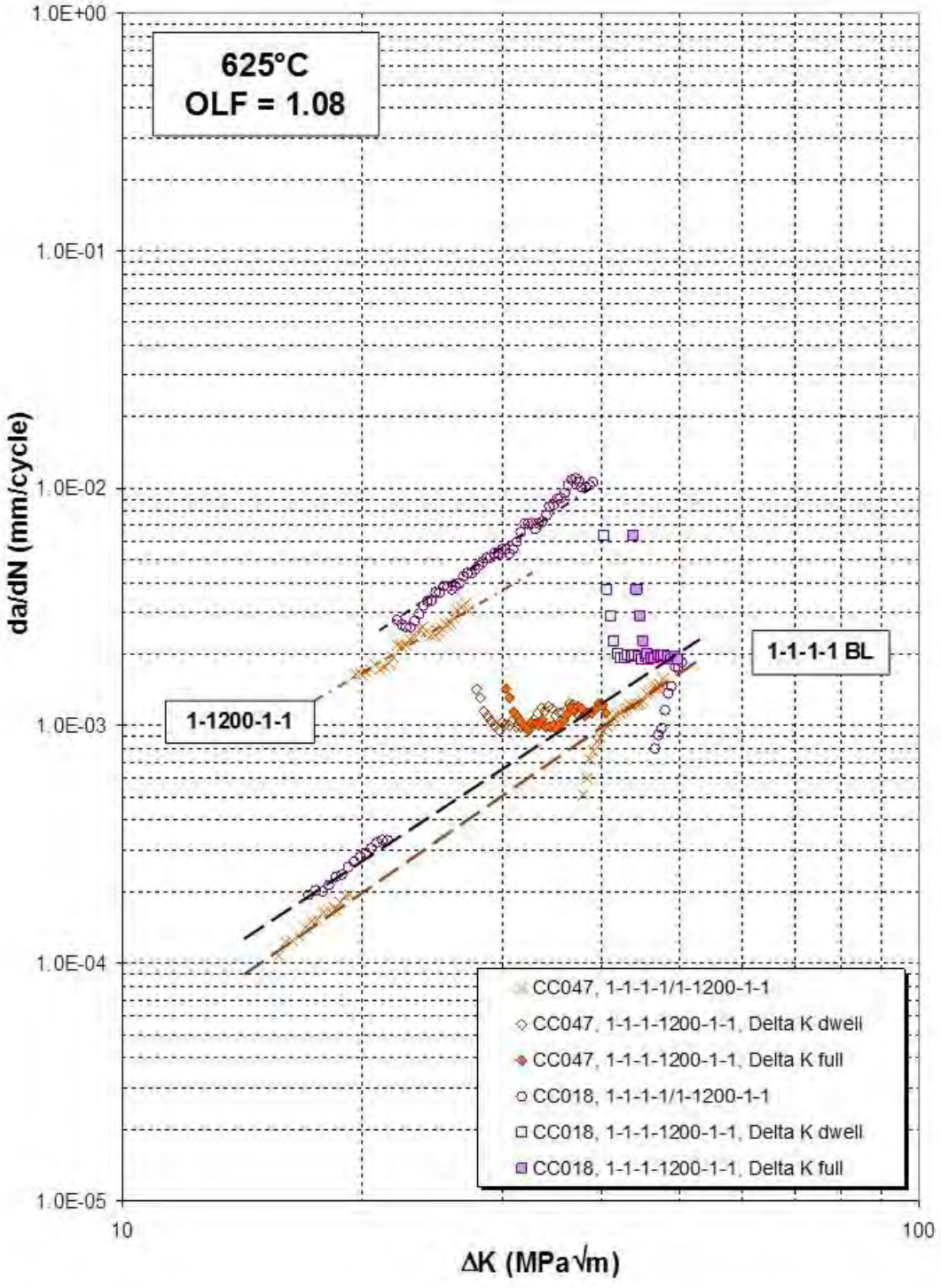


Figure A-32: da/dN vs. ΔK curves for RR1000 samples CC047 and CC018 tested at a temperature of 625°C with an overload factor of 1.08 and a dwell time of 1,200s. Note that despite similar testing conditions, variation between fatigue crack growth rates has been observed. Nevertheless both samples display nearly full retardation.

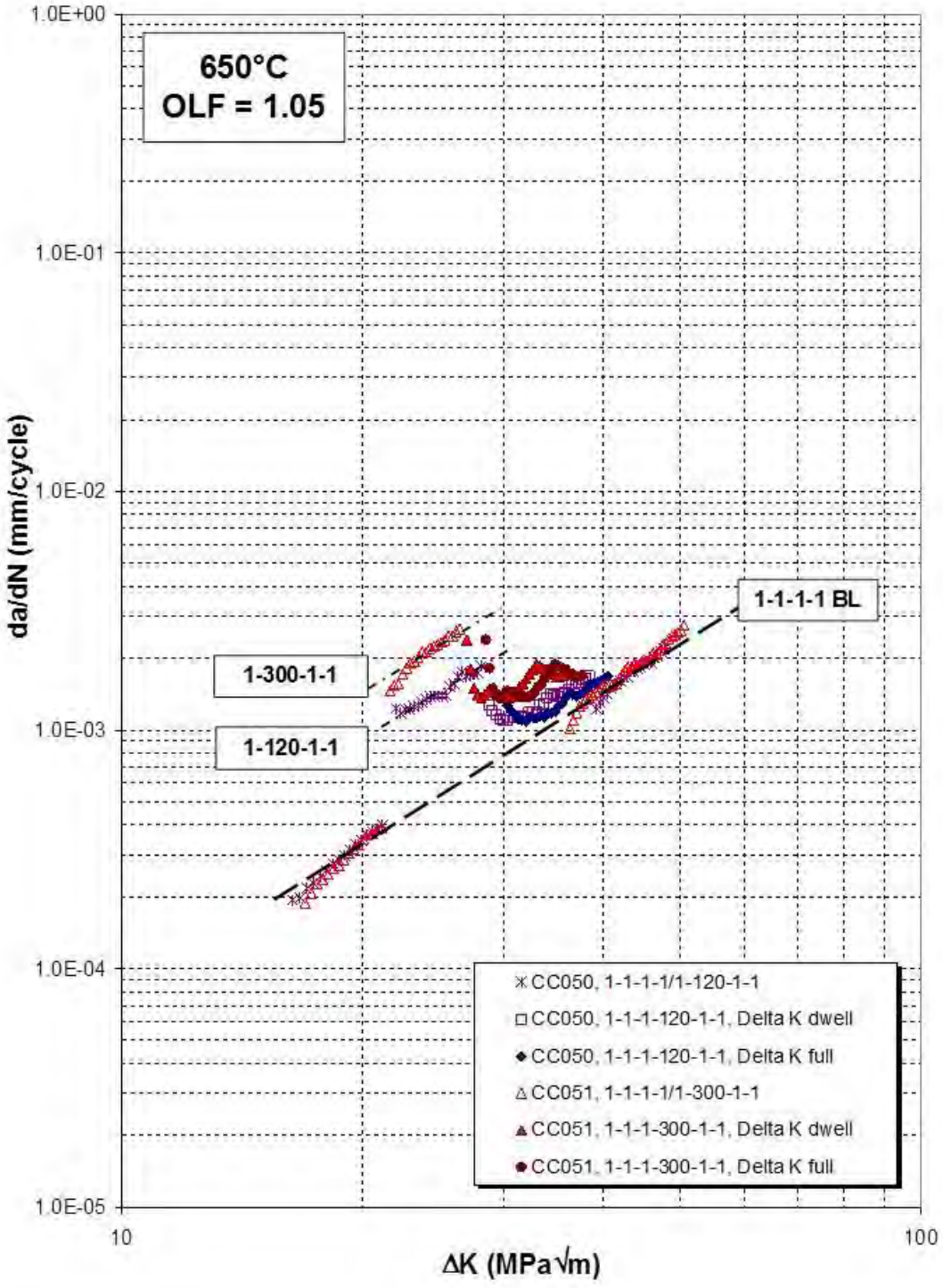


Figure A-33: da/dN vs. ΔK curves for RR1000 samples CC050 and CC051 tested at a temperature of 650°C with an overload factor of 1.05, and dwell times of 120s and 300s respectively. Note that dwell crack growth data clearly show the effect of increasing the dwell time. Nearly full and partial retardation respectively.

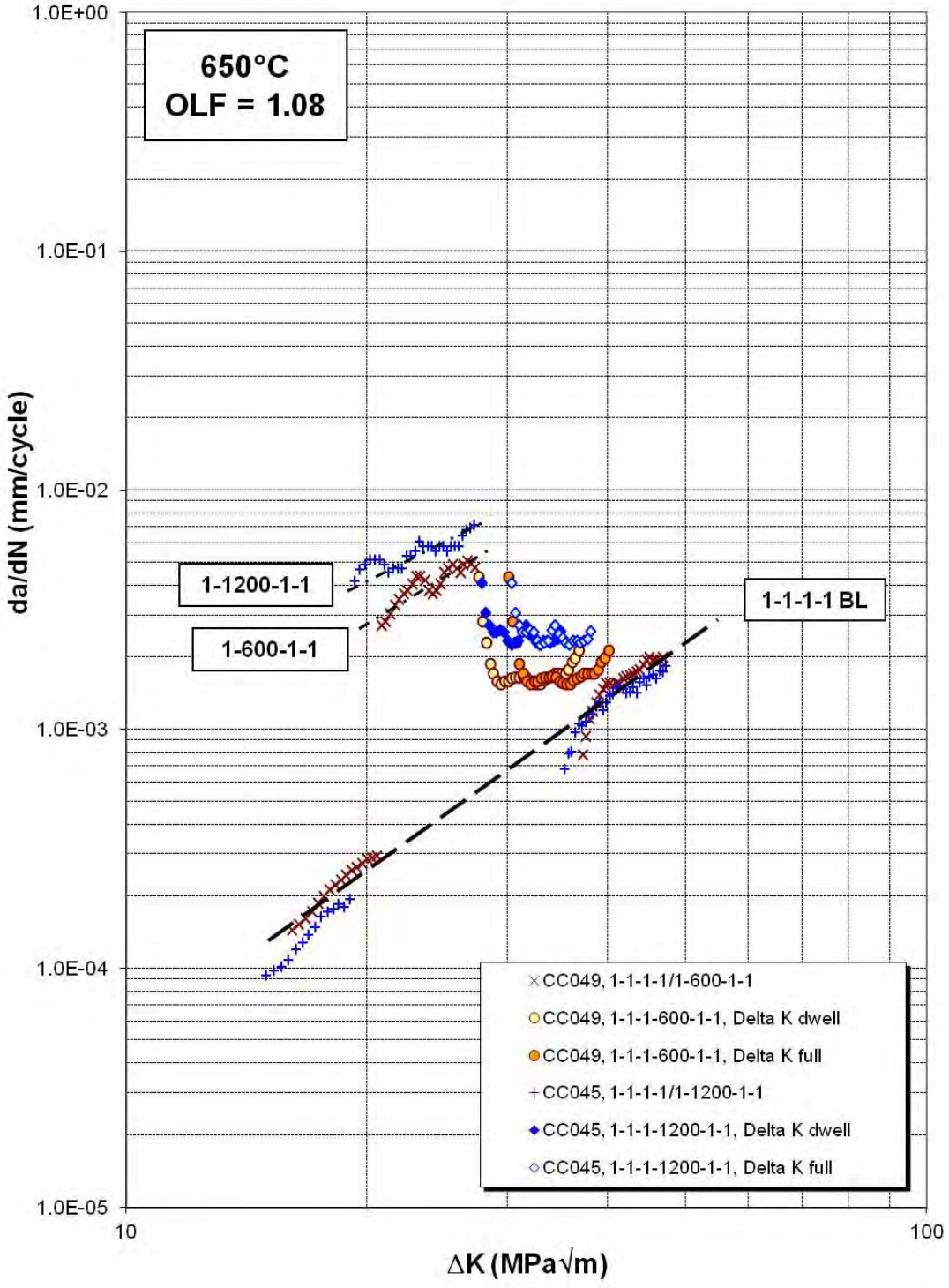


Figure A-34: da/dN vs. ΔK curves for RR1000 samples CC049 and CC045 tested at a temperature of 650°C with an overload factor of 1.08 and dwell periods of 600s and 1,200s respectively. Again these graphs highlight (among other things) the effect of increasing the dwell period. Partial retardation.

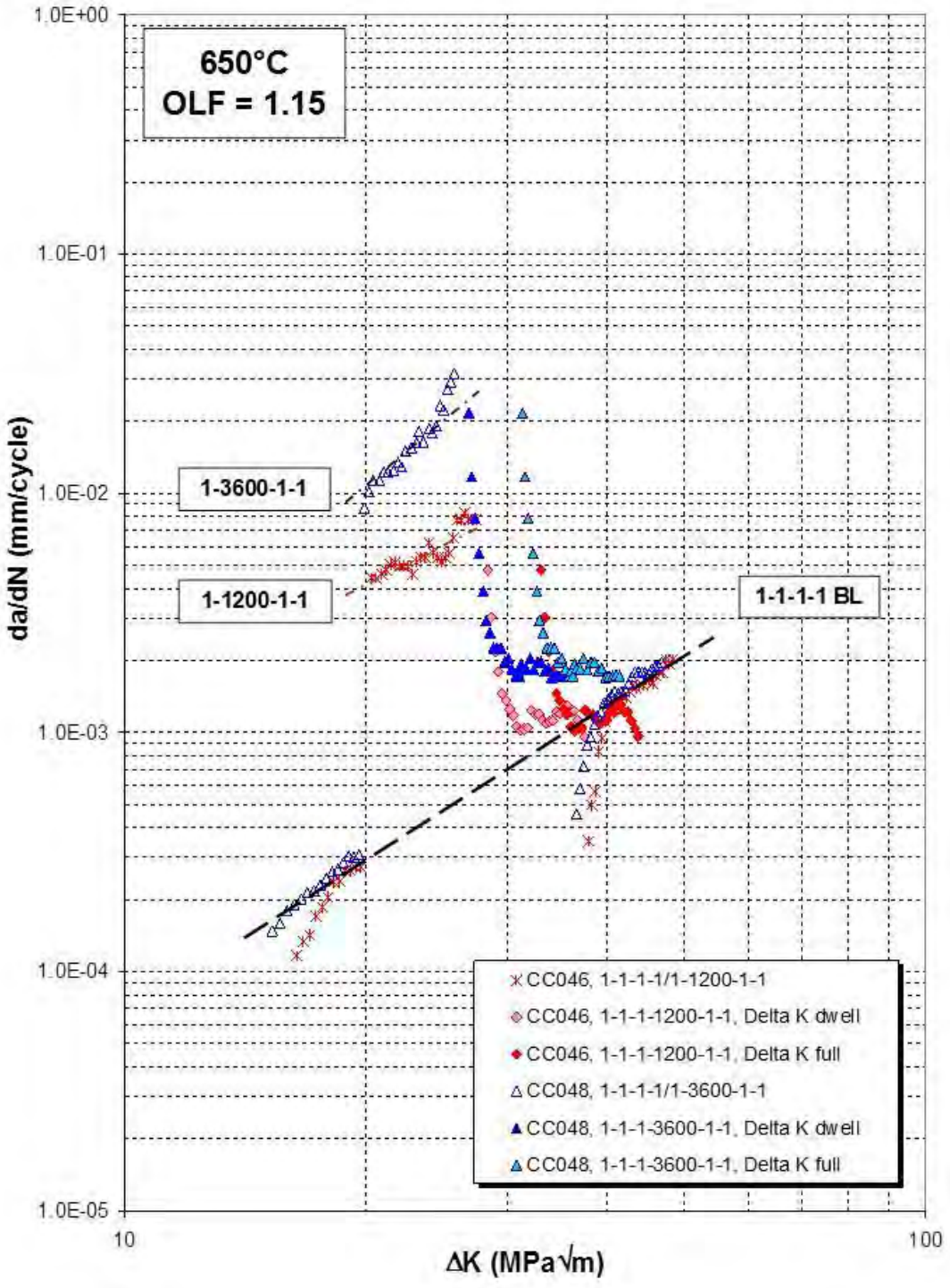


Figure A-35: da/dN vs. ΔK curves for RR1000 samples CC046 and CC048, which were tested at 650°C, with a dwell load of 26 kN, and overload factor of 1.15 and a dwell time of 1,200 and 3,600 seconds respectively. Full retardation.

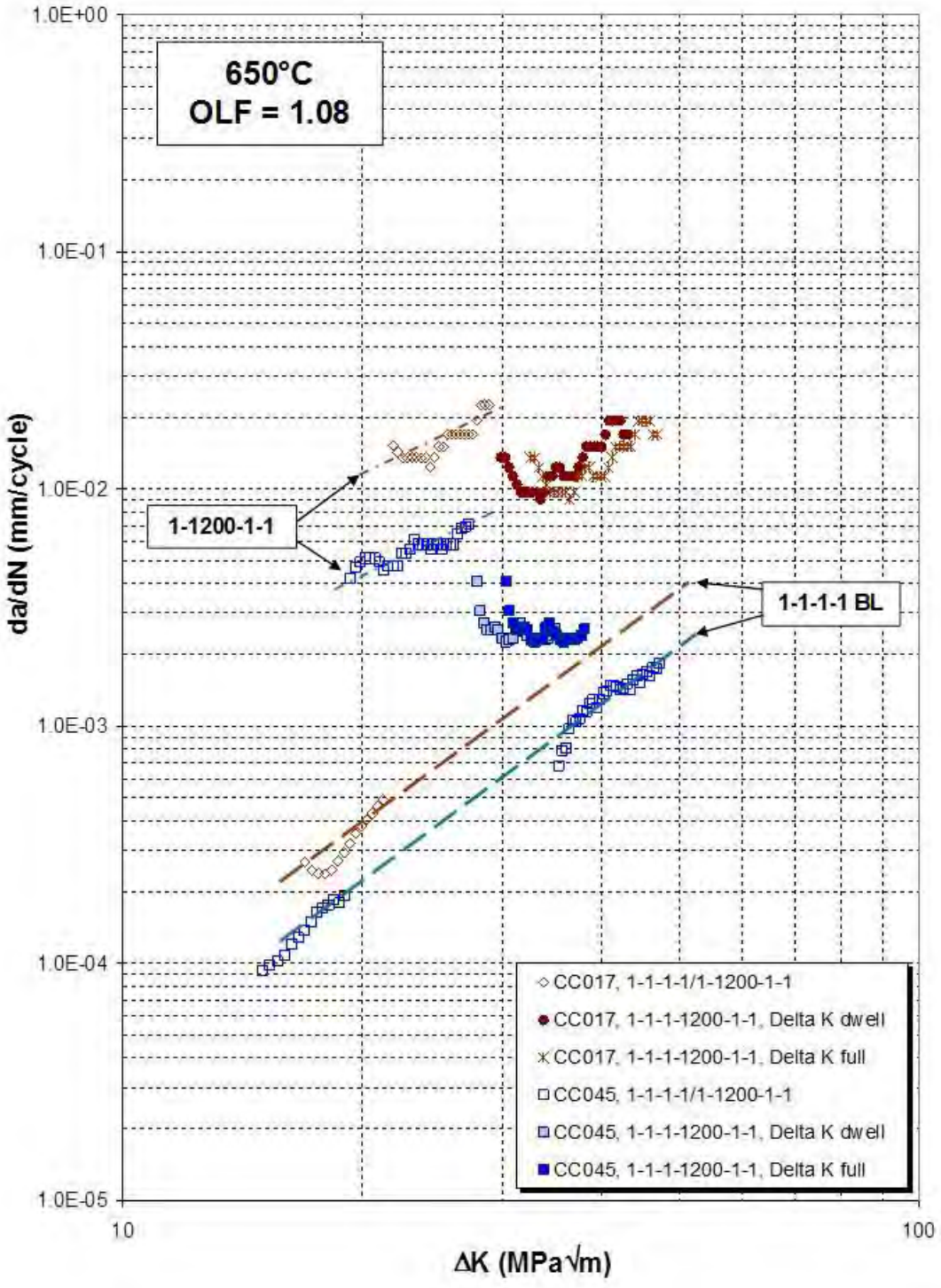


Figure A-36: da/dN vs. ΔK curves for RR1000 samples CC017 and CC045, both tested at a temperature of 650°C with an overload factor of 1.08 and a dwell time of 1,200s. Note that these results also confirm variation between samples in terms of crack growth resistance behaviour. Partial retardation.

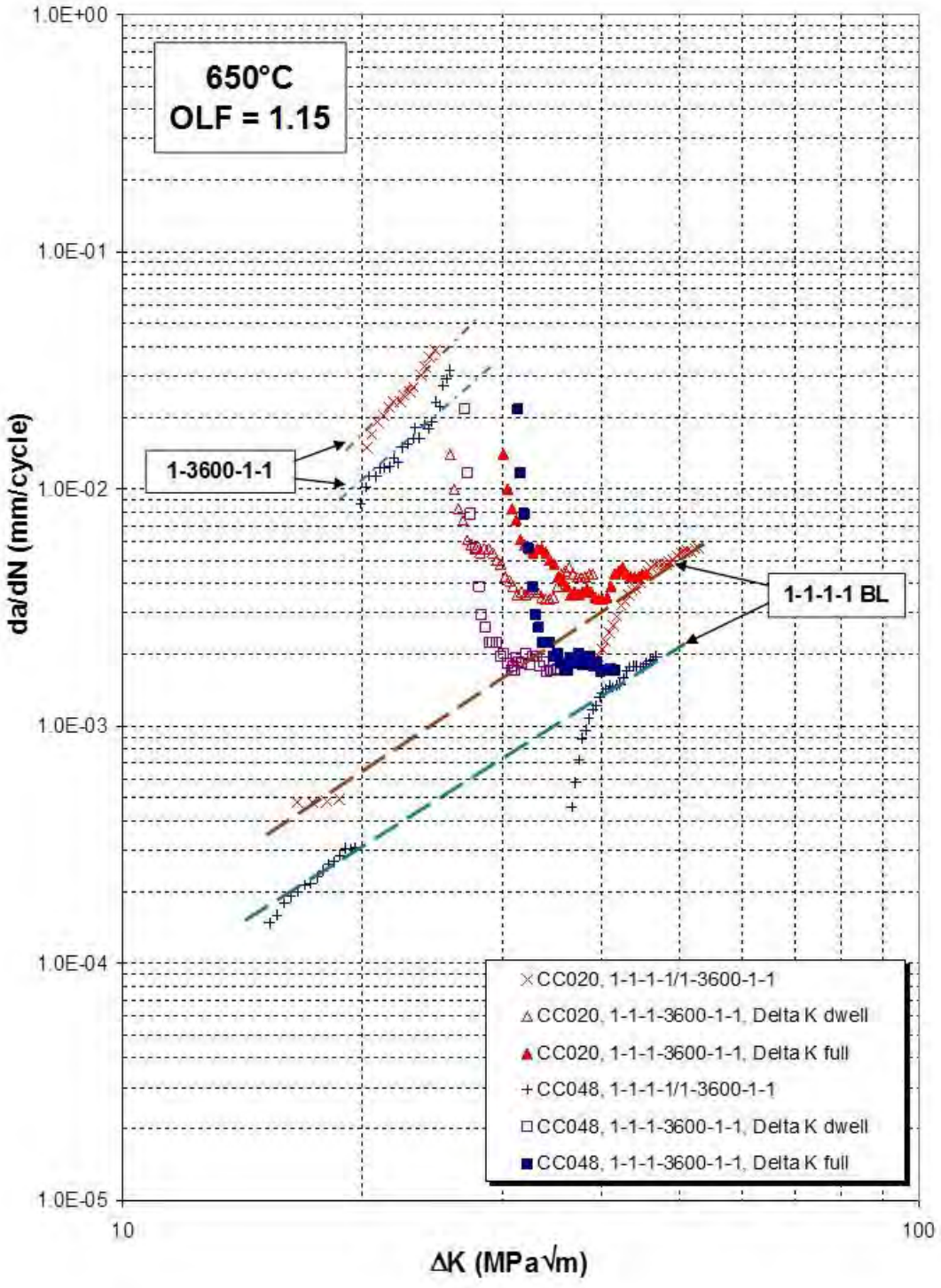


Figure A-37: da/dN vs. ΔK curves for RR1000 samples CC020 and CC048, both tested at a temperature of 650°C with an overload factor of 1.15 and a dwell time of 3,600s. Note that these results also confirm variation between samples in terms of crack growth resistance behaviour. Nearly full retardation.

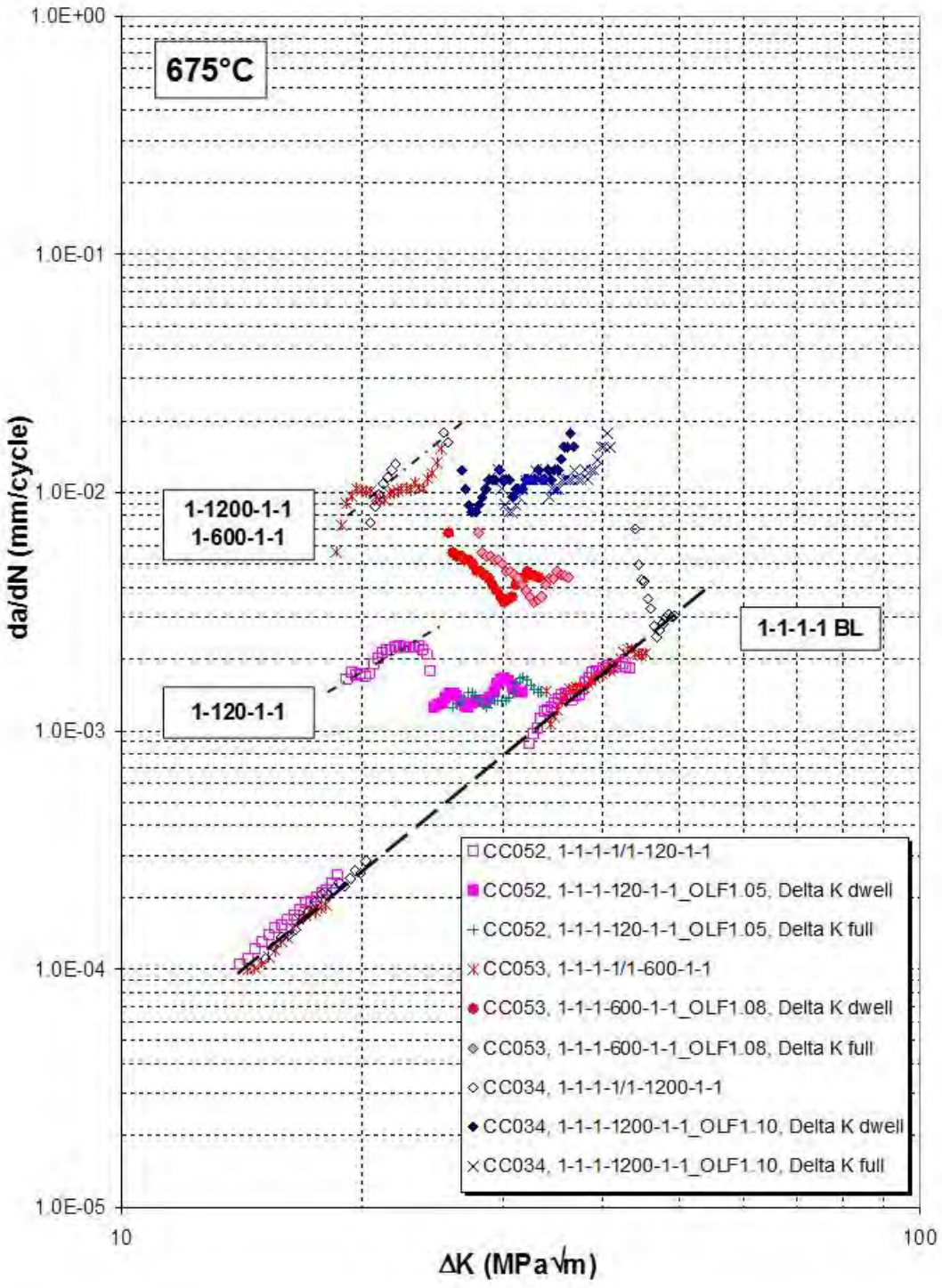


Figure A-38: da/dN vs. ΔK graph for RR1000 samples CC052, CC053 and CC034 tested at a temperature of 675°C and at dwell periods of 120s, 600s and 1,200s and overload factors of 1.05, 1.08 and 1.10 respectively. Nearly full and partial retardation respectively.

RR1000 Dwell at Overload Tests

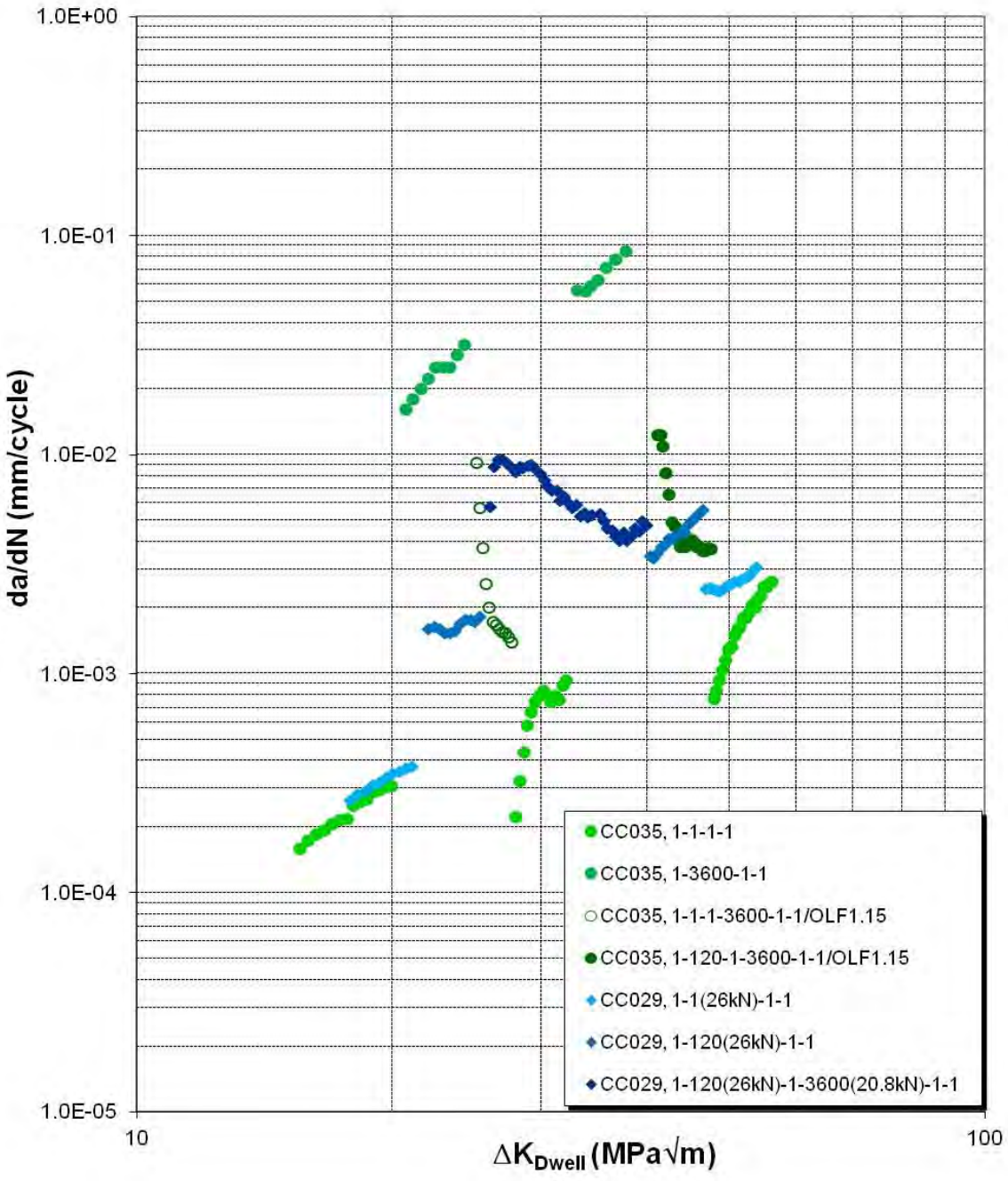


Figure A-39: da/dN vs. ΔK graph for RR1000 samples CC029 and CC035 tested at a temperature of 650°C, an overload factor of 1.15 and at dwell periods of 120s and 3,600s respectively. The overload segment in test piece CC029 was extended to a 120s hold time rather than conventional 1s previous tests. The second "band" of overload cycling applied to test piece CC035 (dark green, filled circles above) also included a 120s hold time at the overload load.

RR1000 Unload and Reload Tests

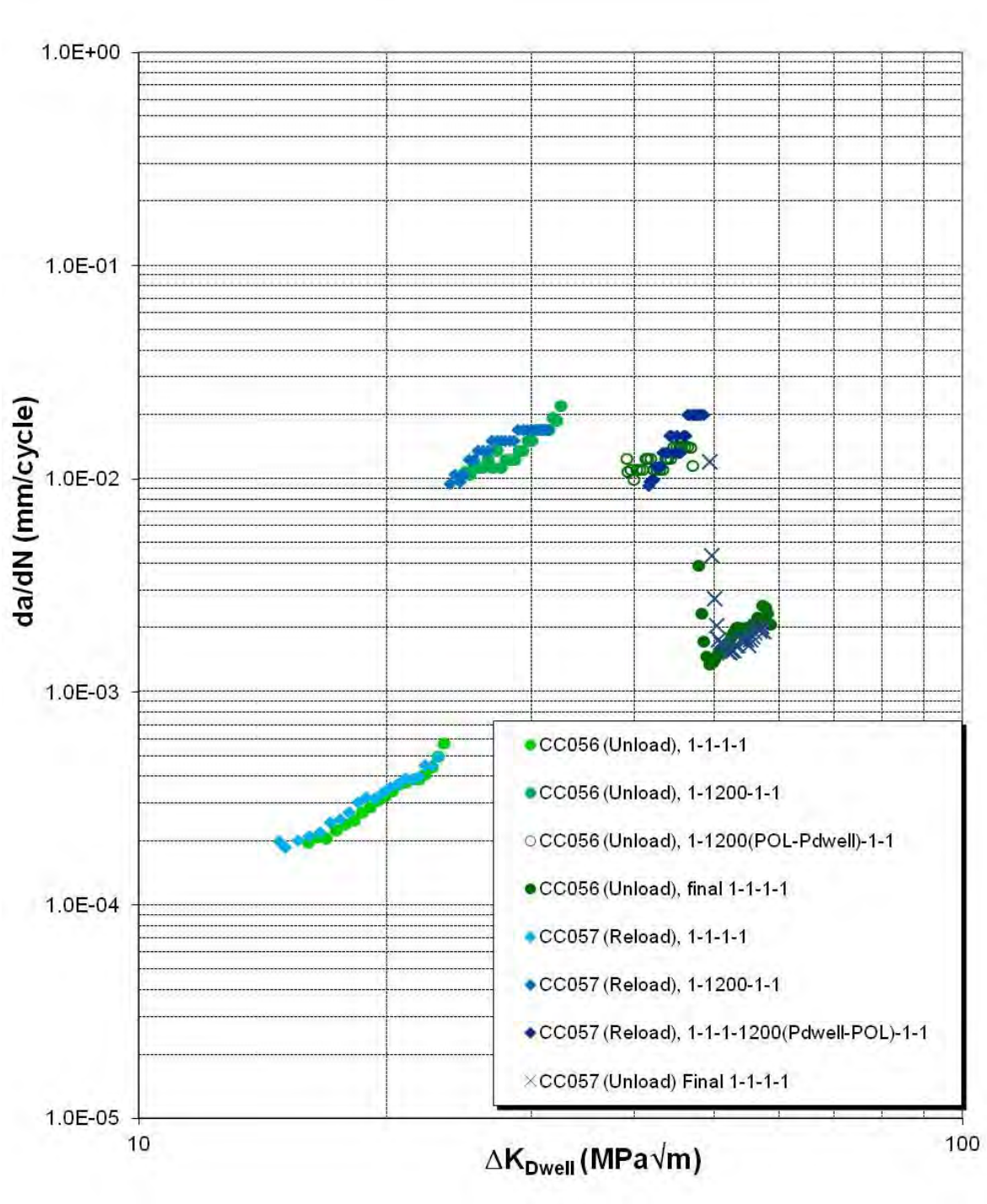


Figure A-40: da/dN vs. ΔK graph for RR1000 samples CC056 and CC057 tested at a temperature of 650°C, an overload factor of 1.065 and a dwell period of 1,200s. Samples were tested under the "Unloading" and "Reloading" regime respectively (Figure 3-11 and Figure 3-12).

RR1000 Cooling Rate Tests

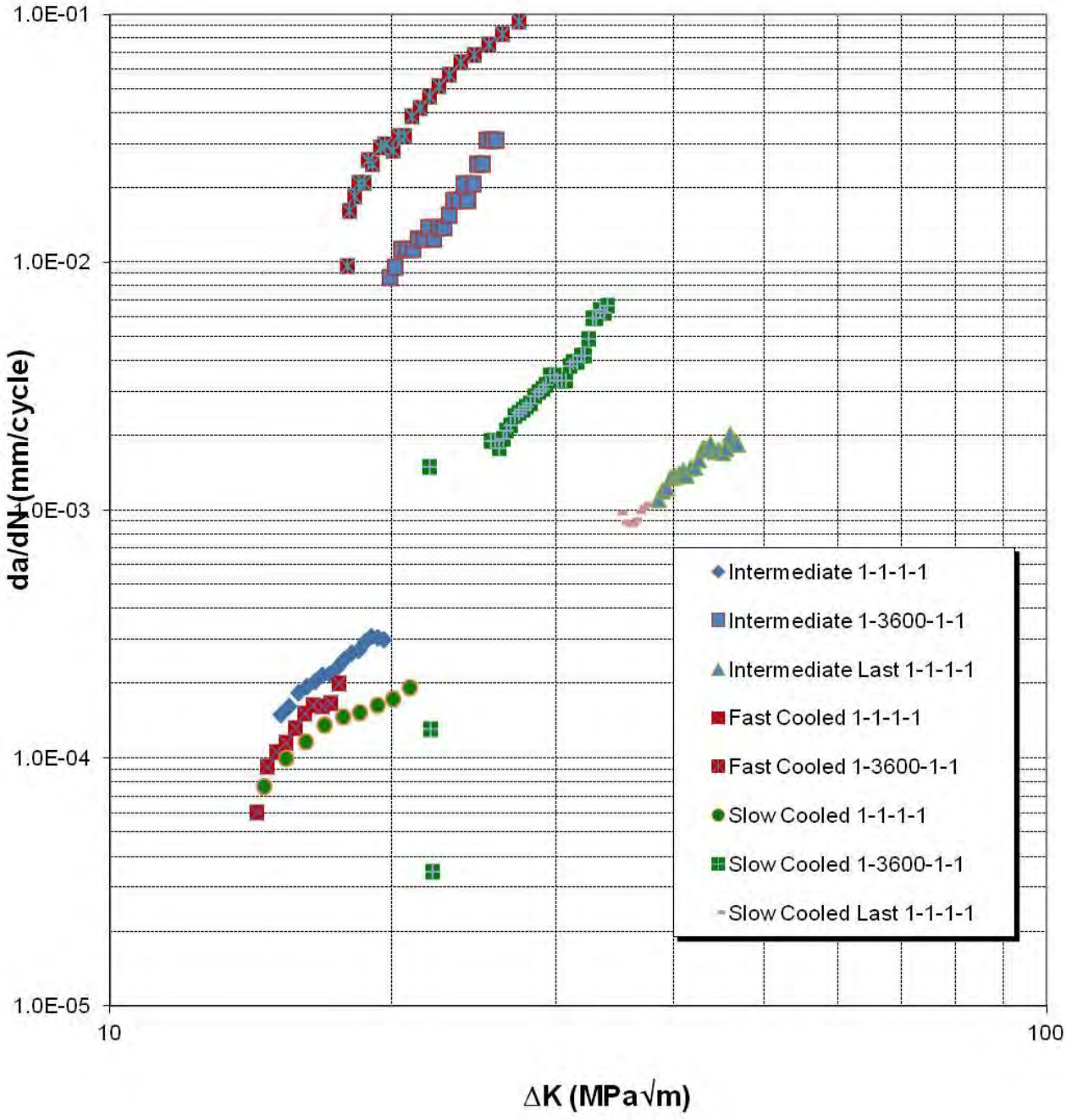


Figure A-41: da/dN vs. ΔK graph for RR1000 samples CX001, CC048 and CX005 tested at a temperature of 650°C, and a dwell period of 3,600s. Samples were slow-cooled, intermediately cooled and fast-cooled respectively.

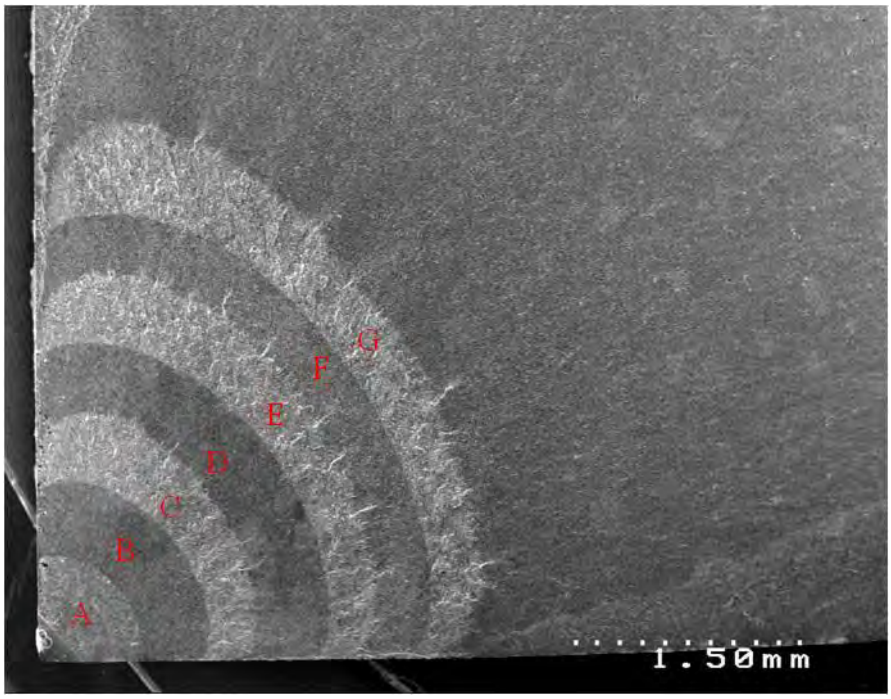
Appendix VII Fractography

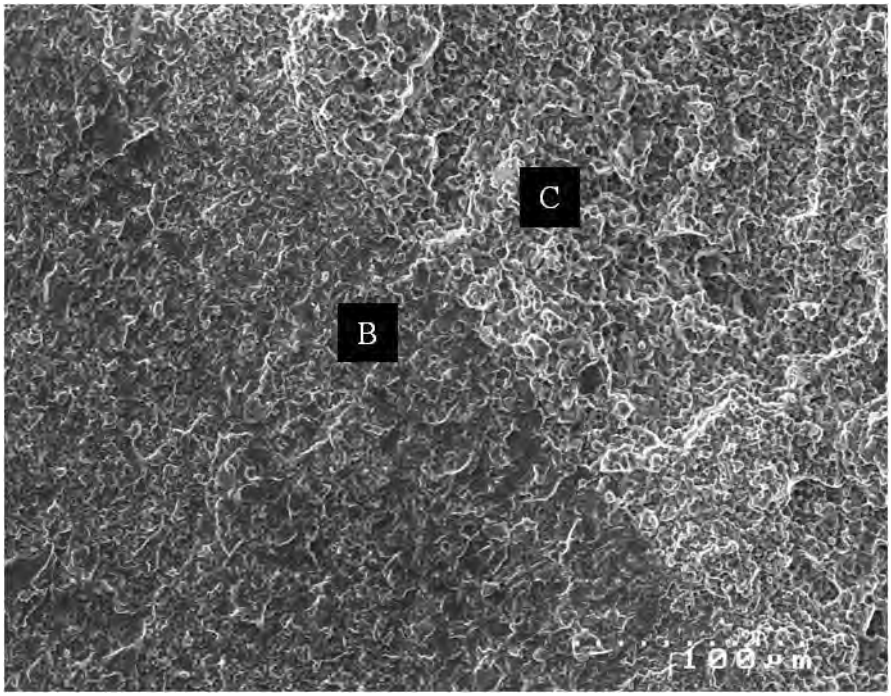
Presented below is a comprehensive selection of fractographs taken according to methodologies described in section 3.3.1, of fractured test pieces tested according to methodologies described in section 3.2, and according to a matrix of testing conditions detailed in Table 8, Table 9, Table 10, Table 11, Table 12 and Table 13. Where possible, fractographs are presented in order of how their results are presented (in terms of crack growth resistance curves) in Appendix VI. Where conditions are repeated, the presentation of fractography is not repeated; rather a representative selection is presented. A summary of the conclusions from studying each fractograph can be found in Table 22, Table 23, Table 24, Table 25 and Table 26.

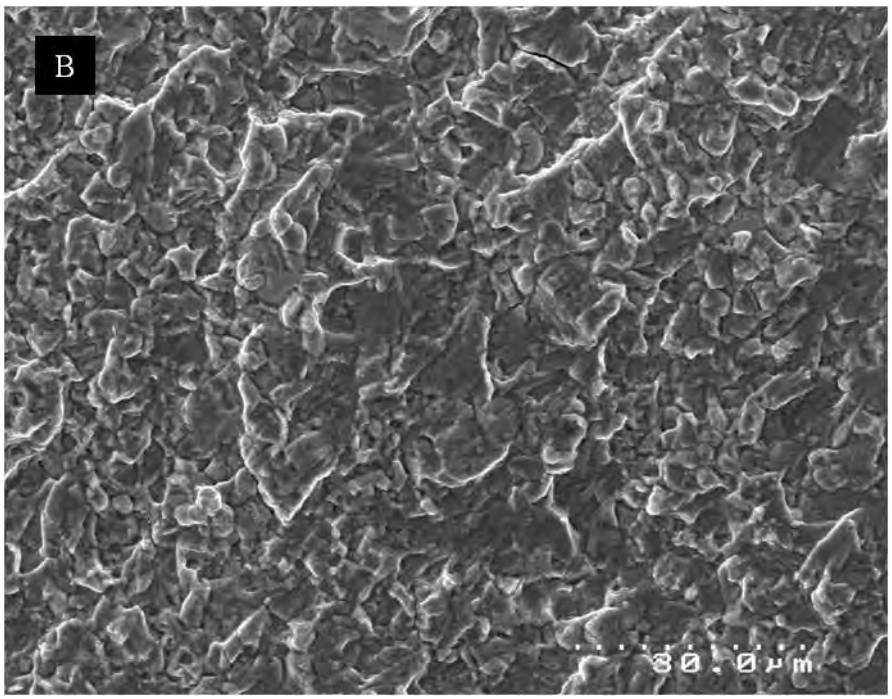
Fractographs are presented in groups of images taken of one test piece, and figure captions describe the testing conditions after each group has been presented.

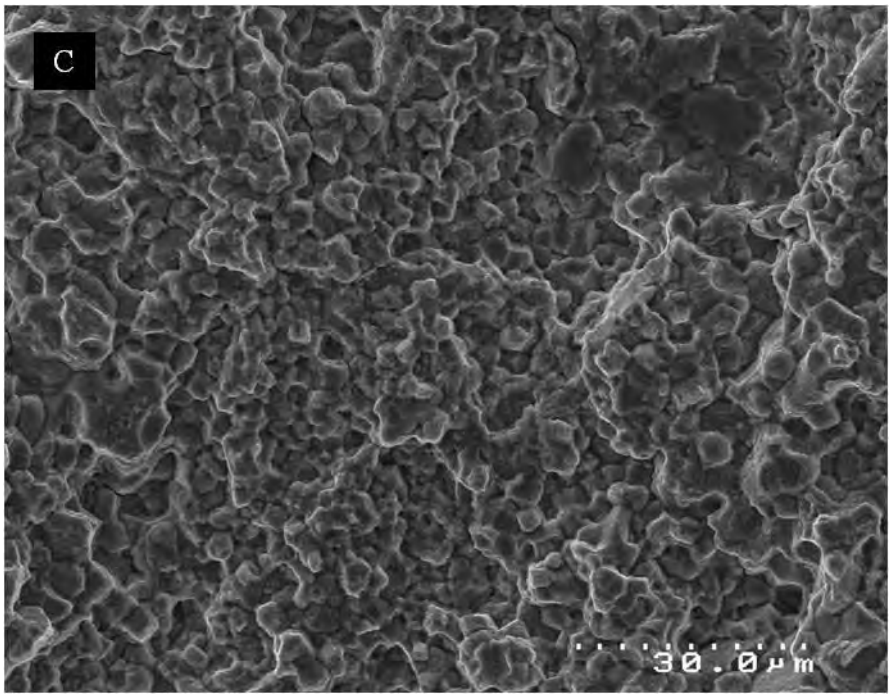
Udimet 720Li

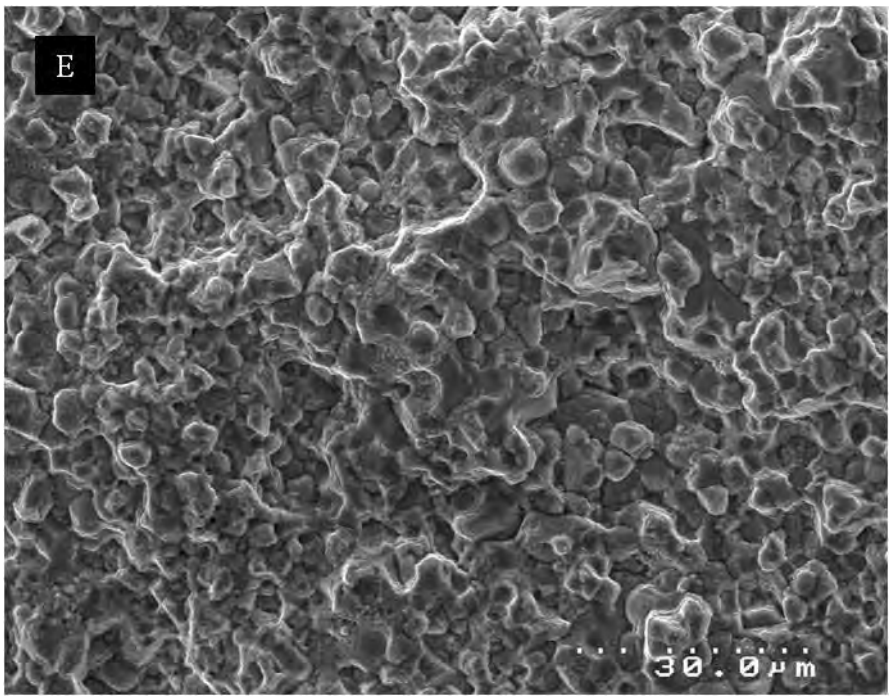
Udimet 720Li Baseline and Dwell Tests

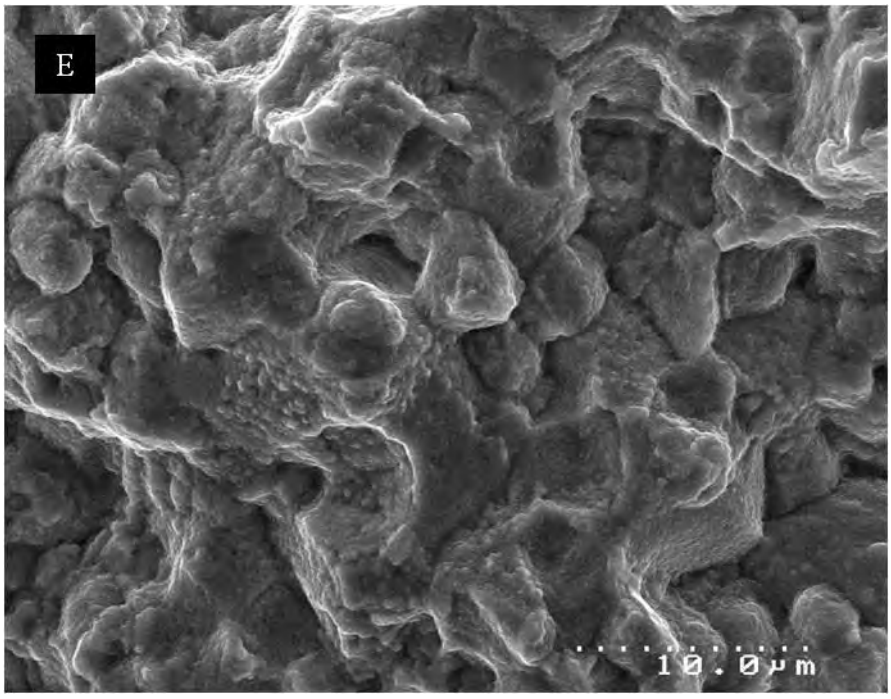





B
30.0µm


C
30.0µm


E
30.0µm


E
10.0µm

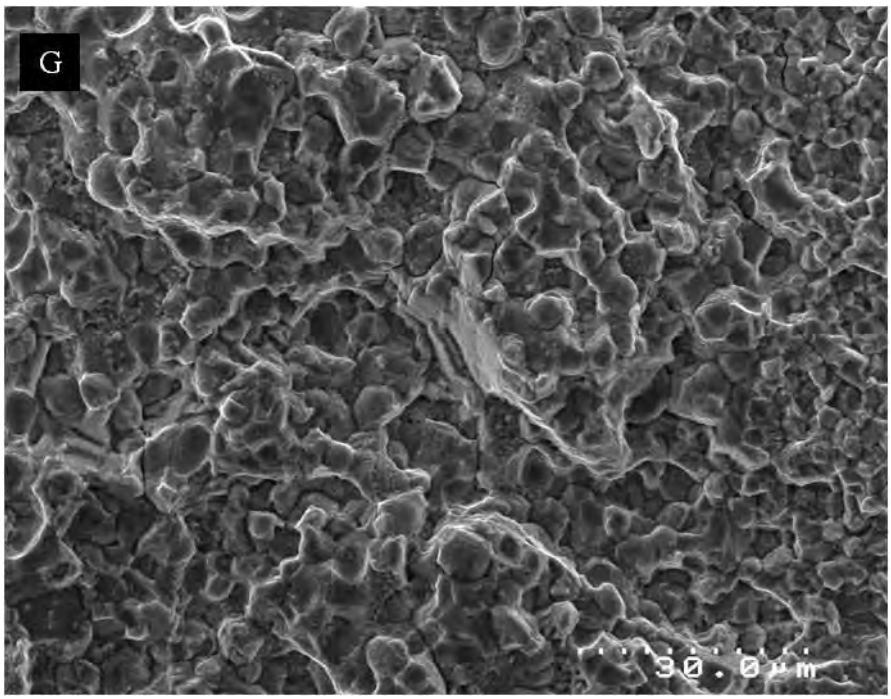
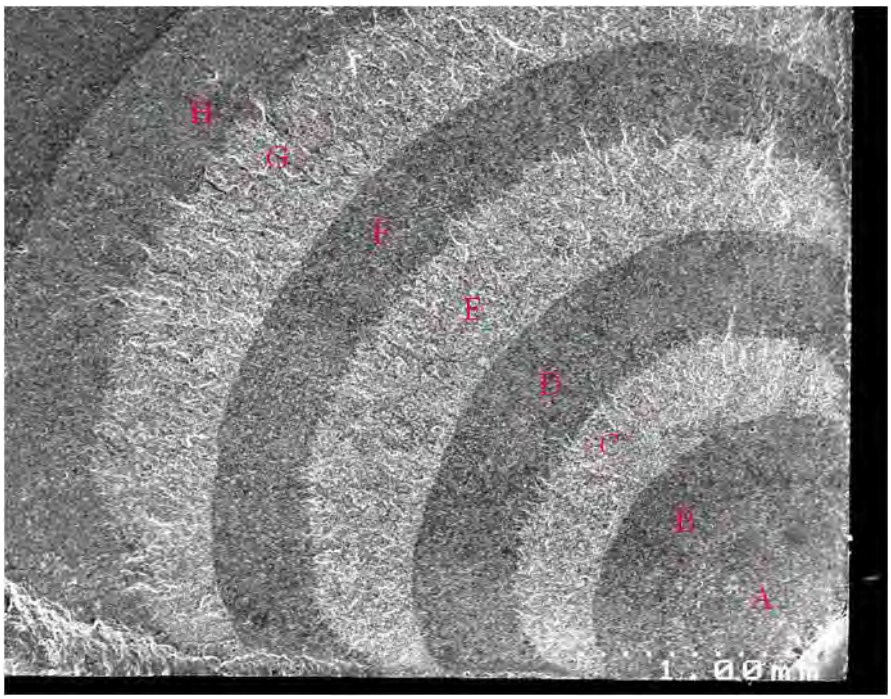
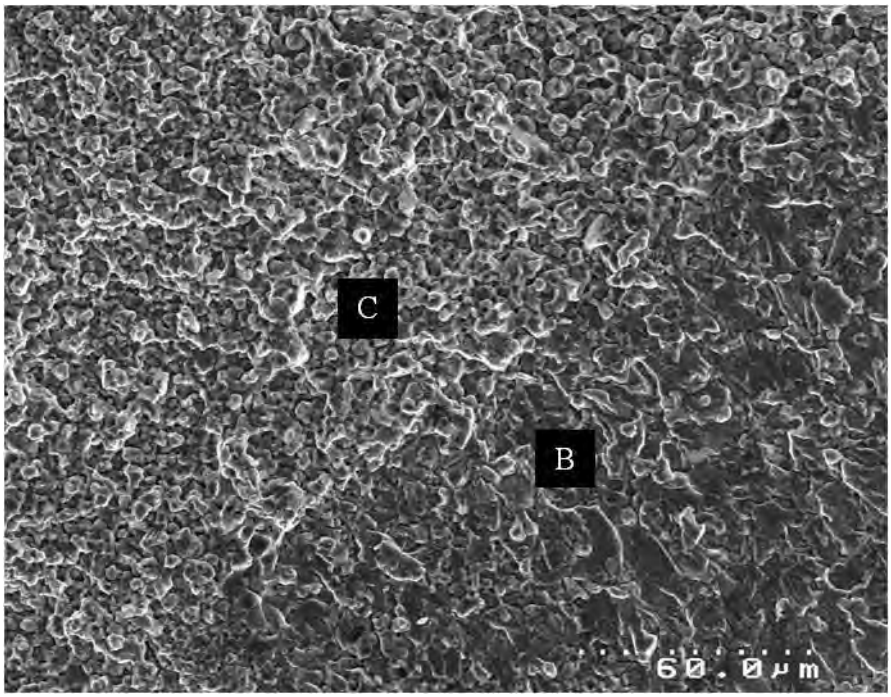
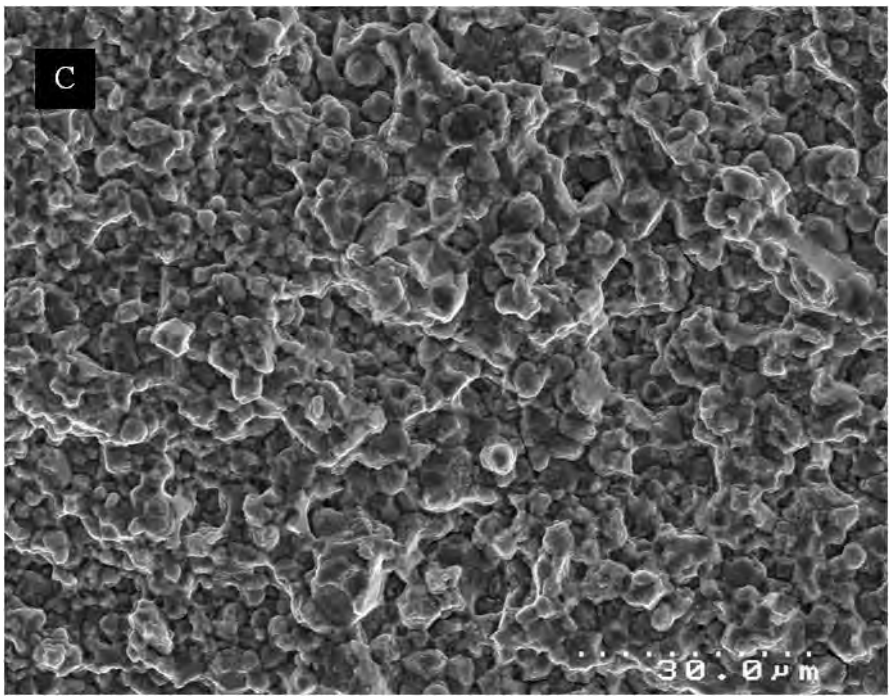
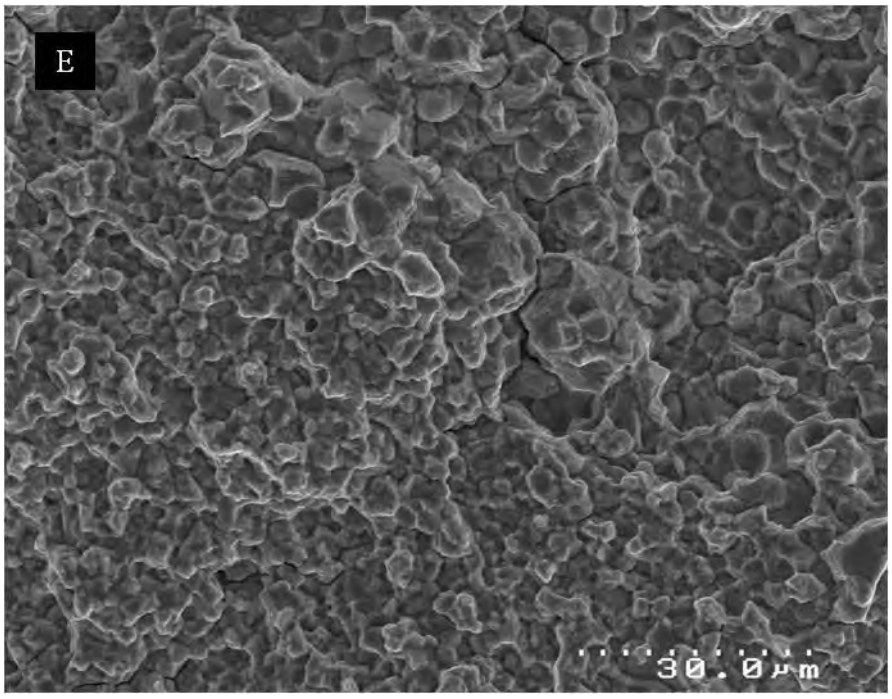


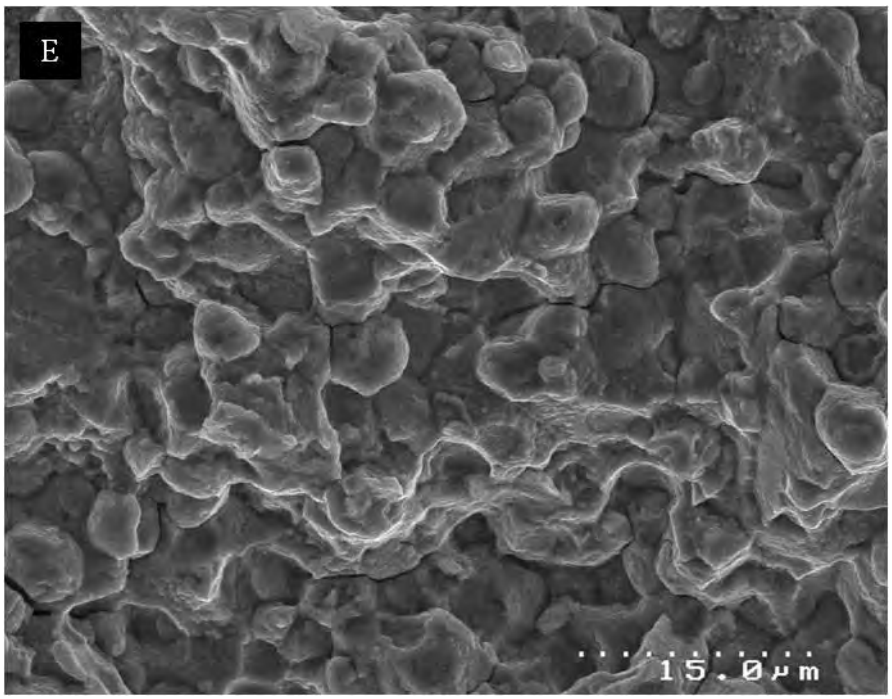
Figure A-42: Showing fractographs of fine-grained Udimet 720Li test piece CX015; tested at 550°C in laboratory air, with a dwell load of 26 kN and a dwell time of 3,600 seconds. Each image shows the crack propagating from bottom left to top right. The band labelled A is the precrack region, which was undertaken at temperature and in air; bands B, D and F are baseline (1-1-1-1) regions and bands C, E and G are dwell regions. Note the marked difference in terms of crack growth mechanism when regions of baseline are compared with those relating to dwell cycling. Higher magnification images are taken at points relating to the following crack growth driving forces (ΔK): B: ~19 MPa√m; C: ~21.5 MPa√m; E: ~30 MPa√m; G: ~39.5 MPa√m

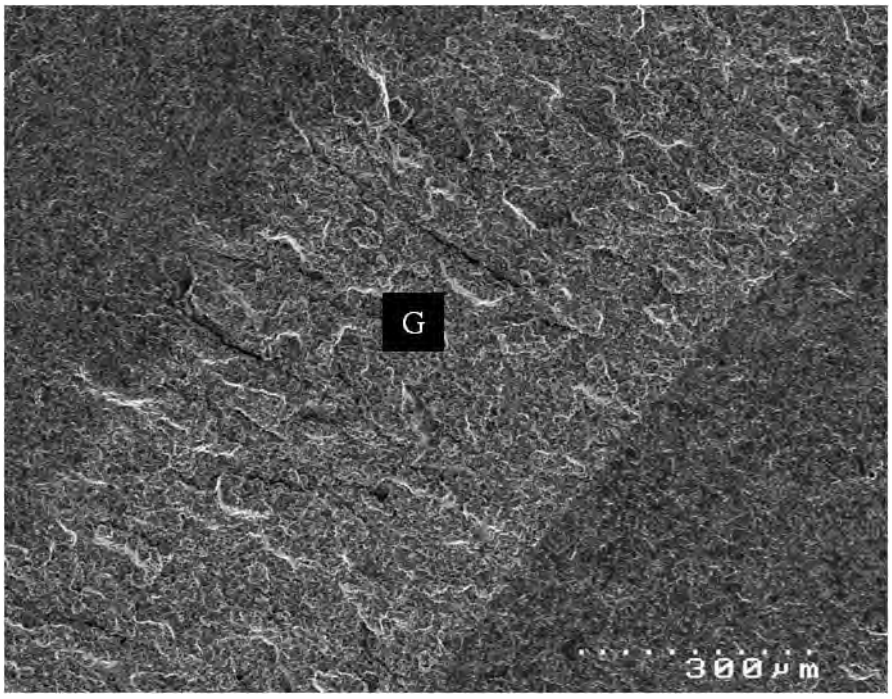

H
G
F
E
D
C
B
A
1.00mm


C
B
60.0µm


C
30.0µm


E
30.0µm


E
15.0µm


G
300µm

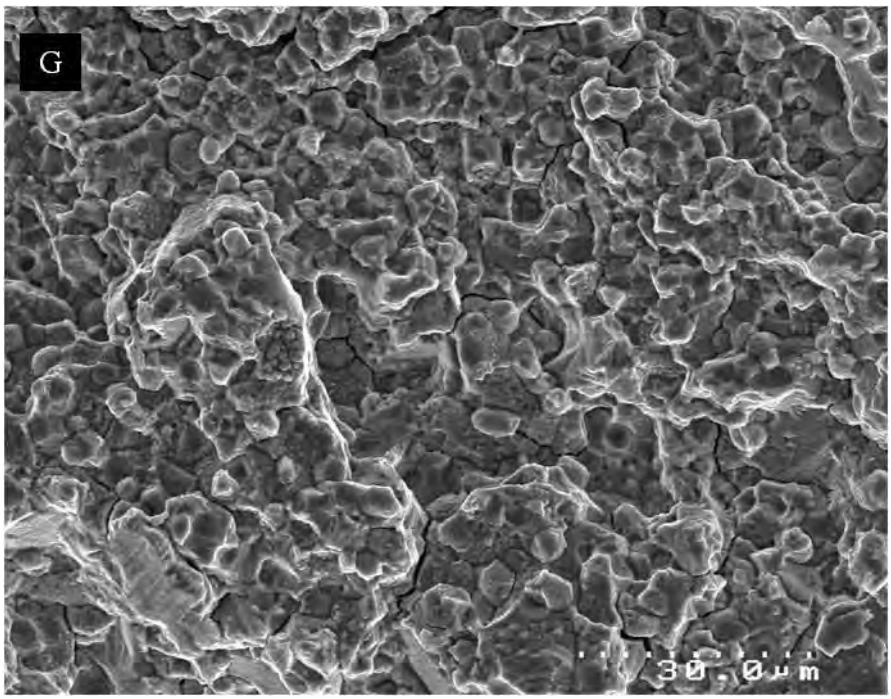
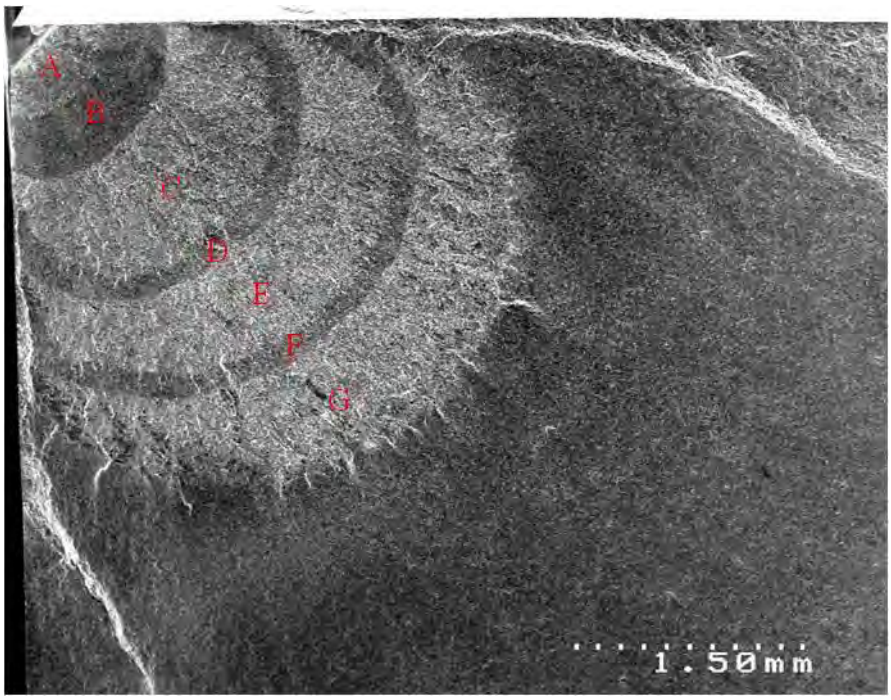
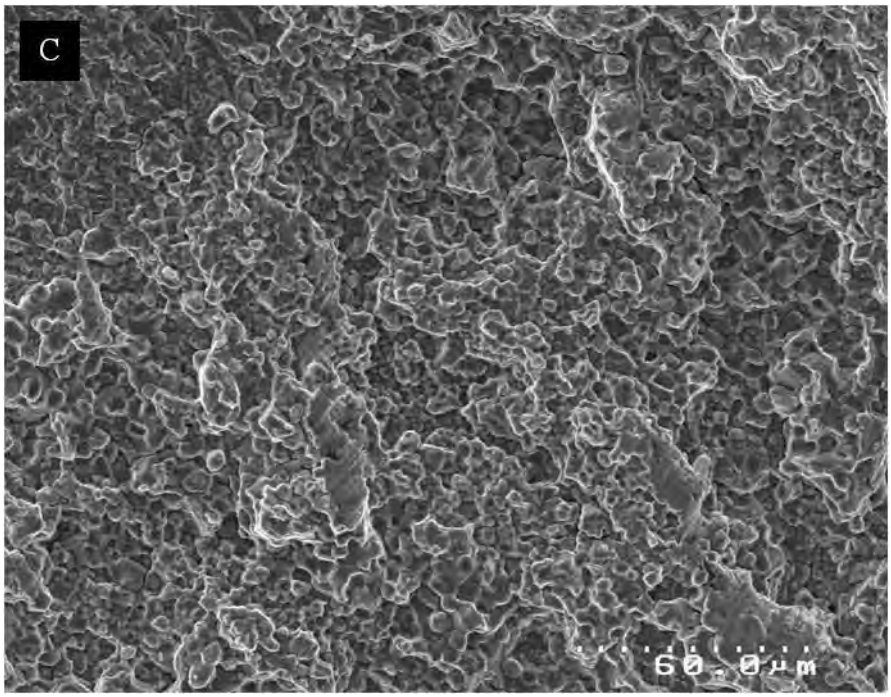
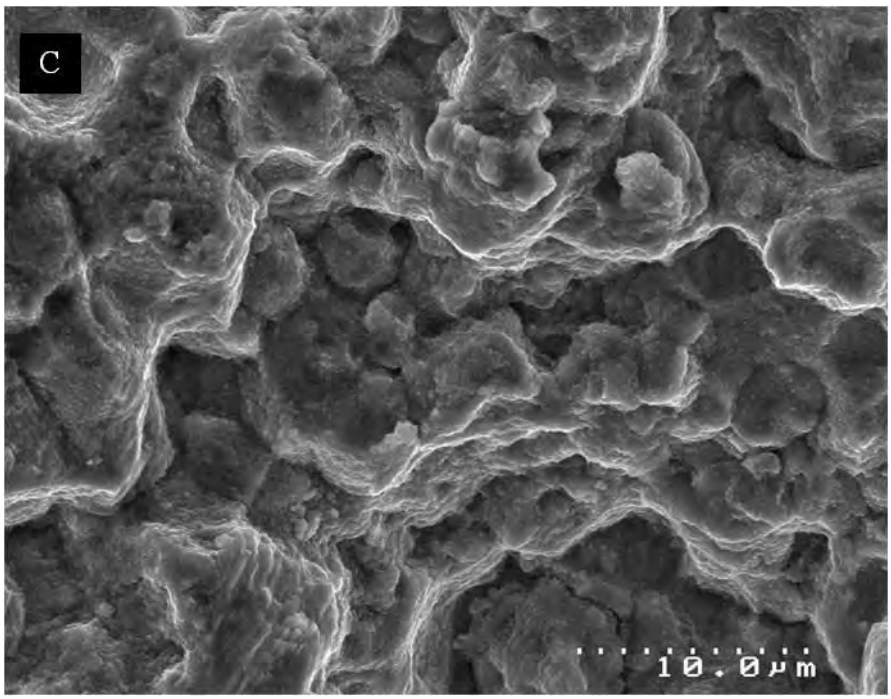
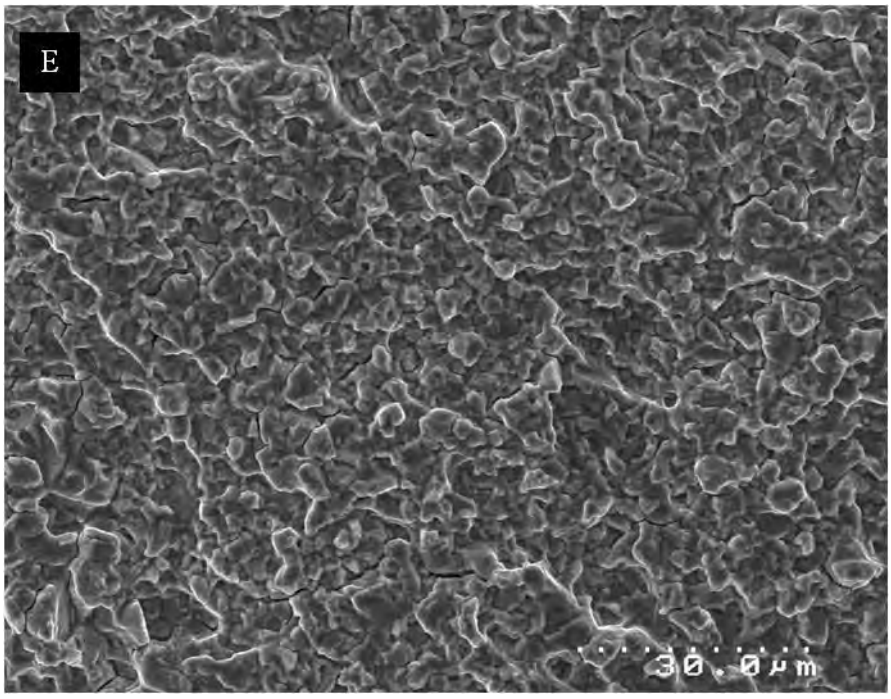


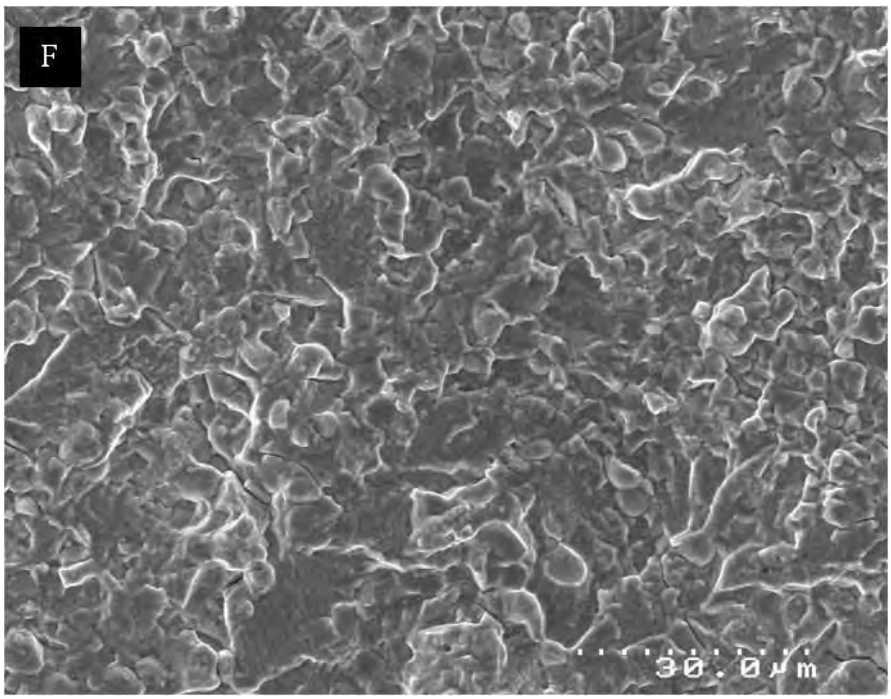
Figure A-43: Showing fractographs of fine-grained Udimet 720Li test piece CX020; tested at 550°C in laboratory air, with a dwell load of 26 kN and a dwell time of 3,600 seconds. Each image shows the crack propagating from bottom right to top left. The band labelled A is the precrack region, which was undertaken at temperature and in air; bands B, D, F and H are baseline (1-1-1-1) regions and bands C, E and G are dwell regions. Note the marked difference in terms of crack growth mechanism when regions of baseline are compared with those relating to dwell cycling. Note also the final region of dwell cycling (G) which involves higher values of ΔK includes evidence of secondary cracking (out of plane) and uneven crack propagation. Higher magnification images are taken at points relating to the following crack growth driving forces (ΔK): B: ~19 MPa√m; C: ~21.5 MPa√m; E: ~30 MPa√m; G: ~39.5 MPa√m

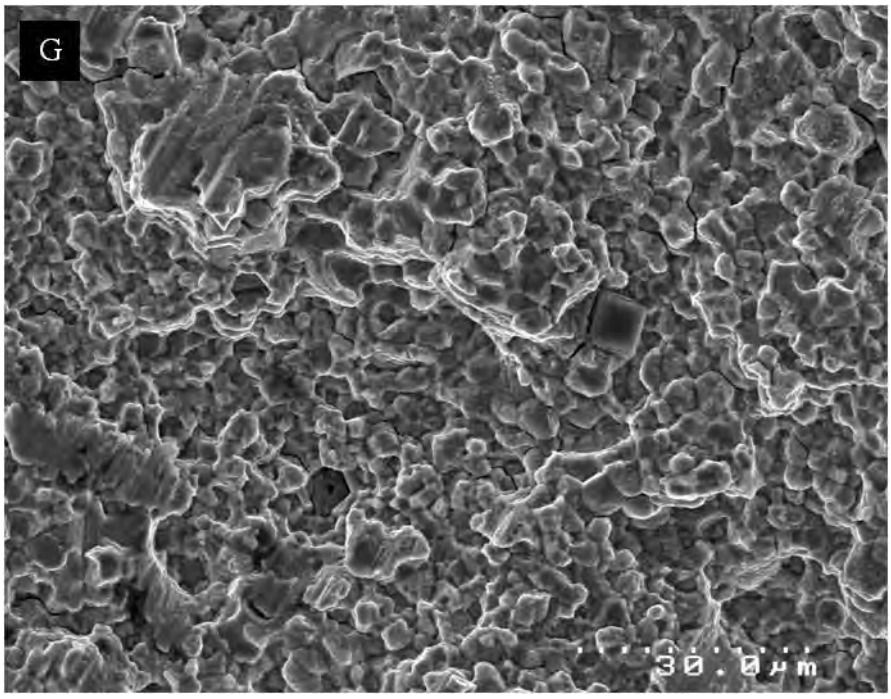

A
B
C
D
E
F
G
1.50mm


C
60.0µm


C
10.0µm


E
30.0µm


F
30.0µm


G
30.0µm

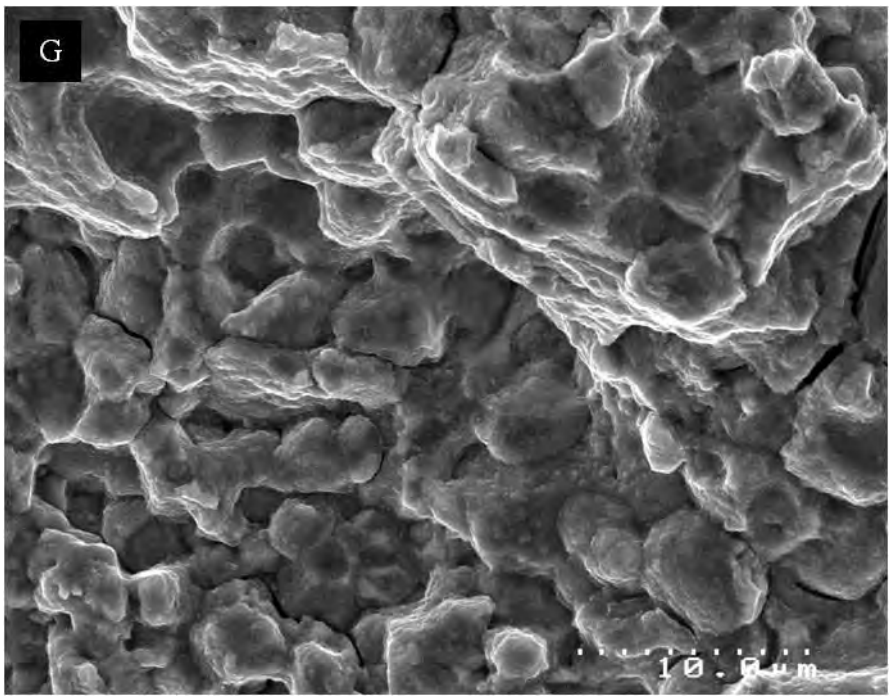
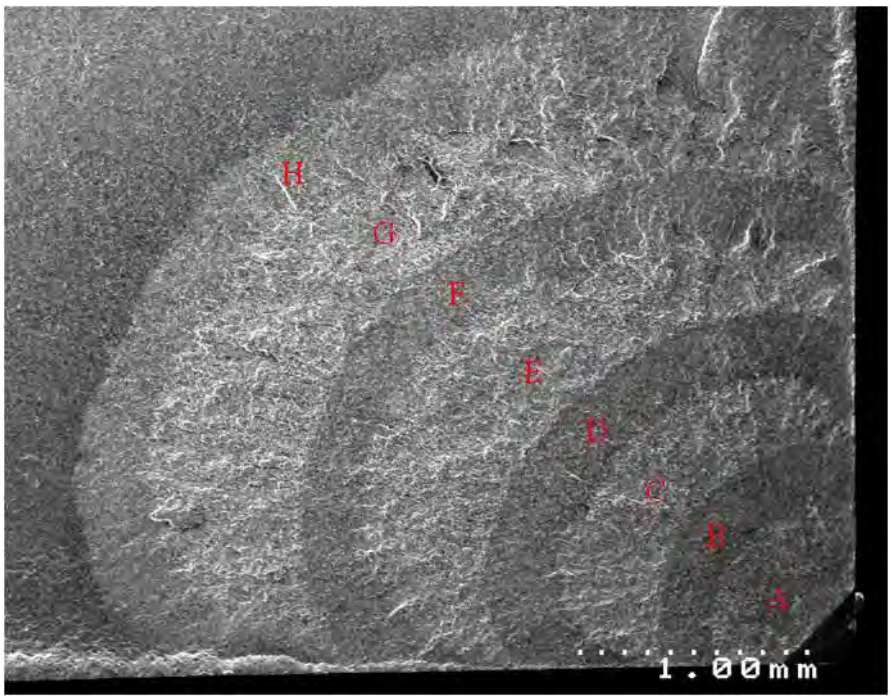
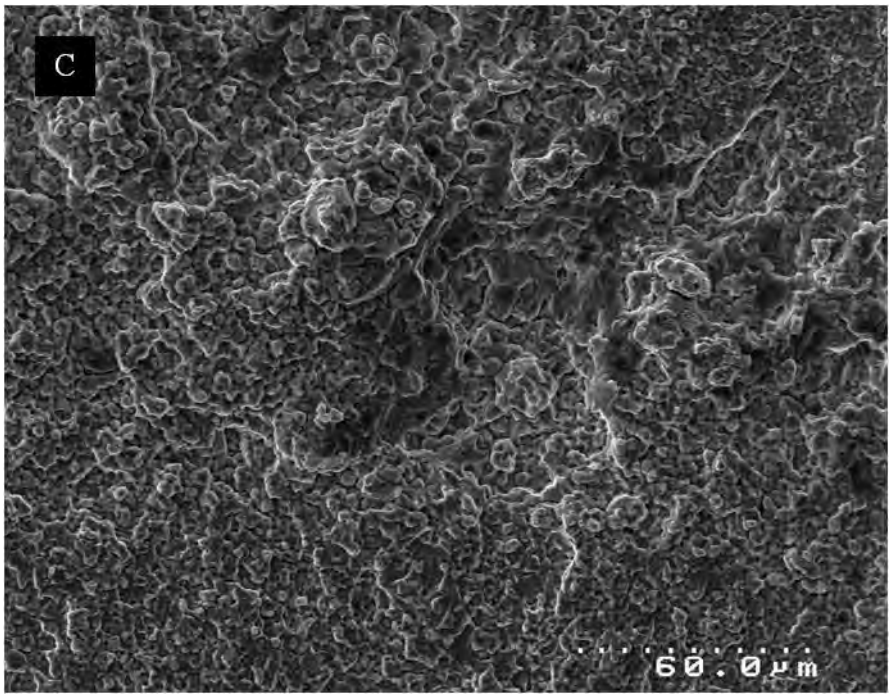
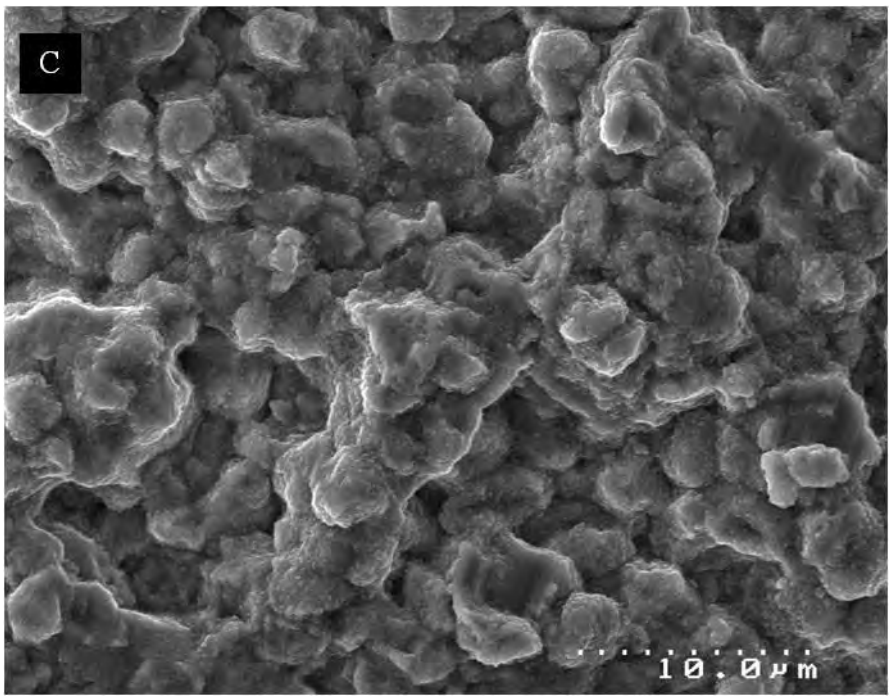
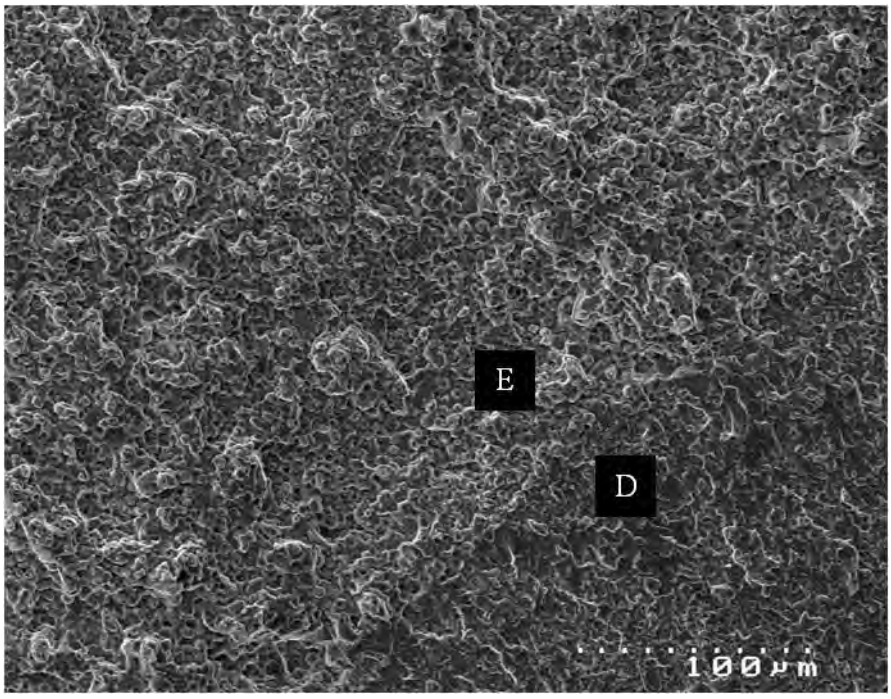


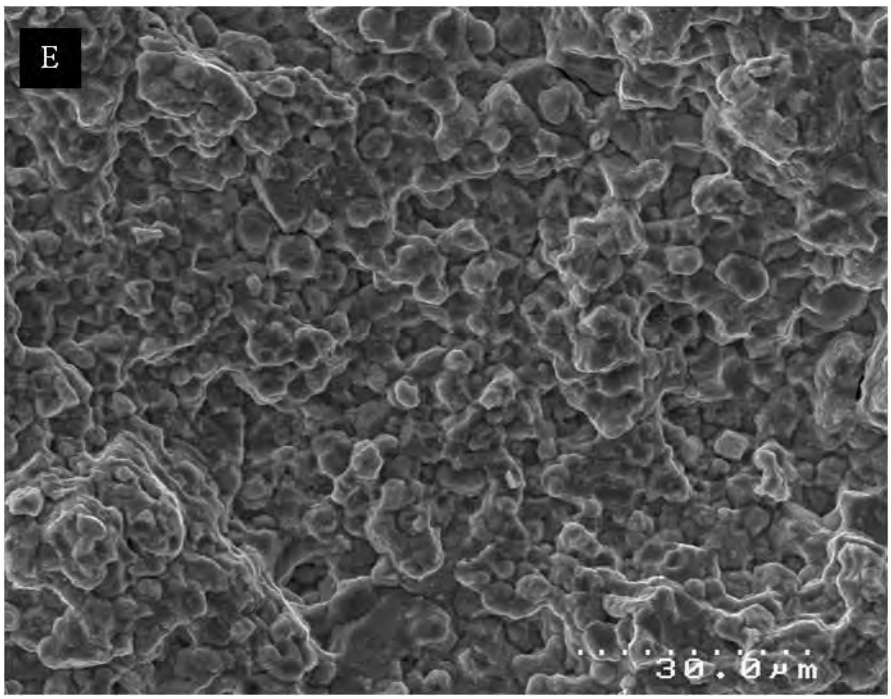
Figure A-44: Showing fractographs of fine-grained Udimet 720Li test piece CX013; tested at 600°C in laboratory air, with a dwell load of 26 kN and a dwell time of 3,600 seconds. Each image shows the crack propagating from top left to bottom right. The band labelled A is the precrack region, which was undertaken at temperature and in air; bands B, D, and F are baseline (1-1-1-1) regions and bands C, E and G are dwell regions. Note the marked difference in terms of crack growth mechanism when regions of baseline are compared with those relating to dwell cycling. Note also the final region of dwell cycling (G) which involves higher values of ΔK includes evidence of secondary cracking (out of plane) and uneven crack propagation. Higher magnification images are taken at points relating to the following crack growth driving forces (ΔK): B: ~17.5 MPa√m; C: ~22.5 MPa√m; E: ~30 MPa√m; G: ~39.5 MPa√m

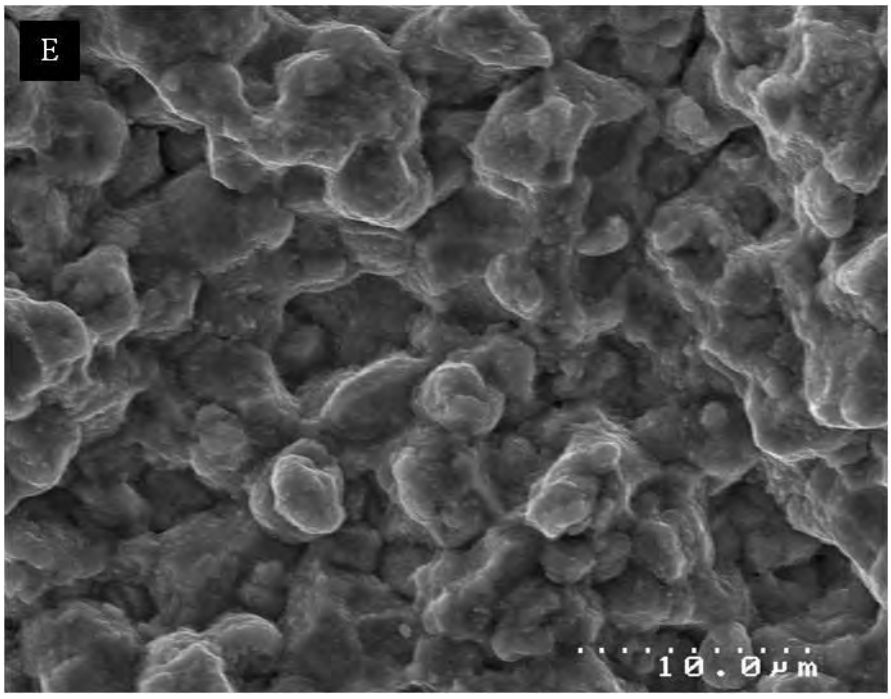

H
G
F
E
D
C
B
A
1.00mm


C
60.0µm


C
10.0µm


E
D
100µm


E
30.0µm


E
10.0µm

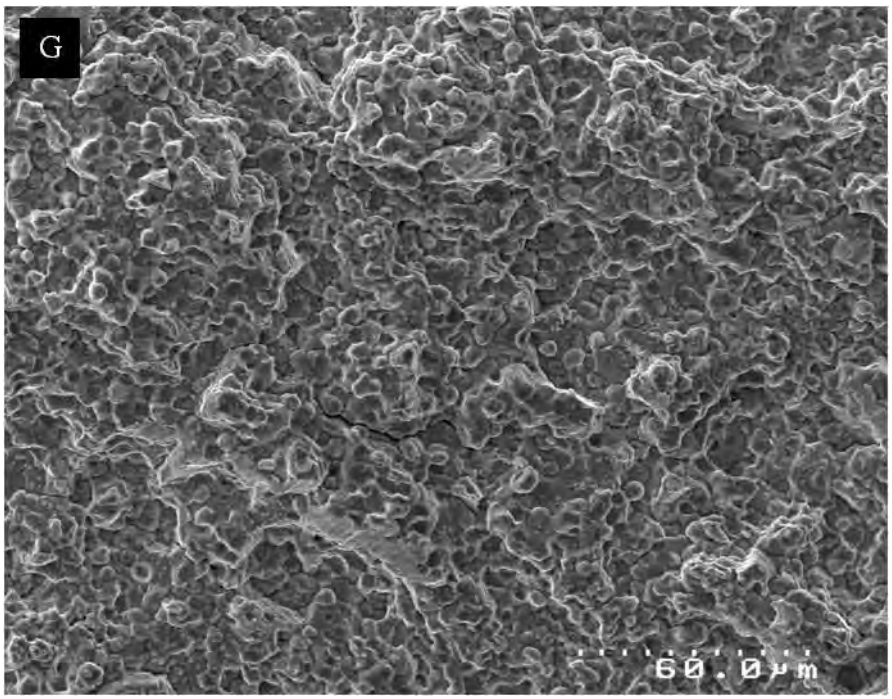
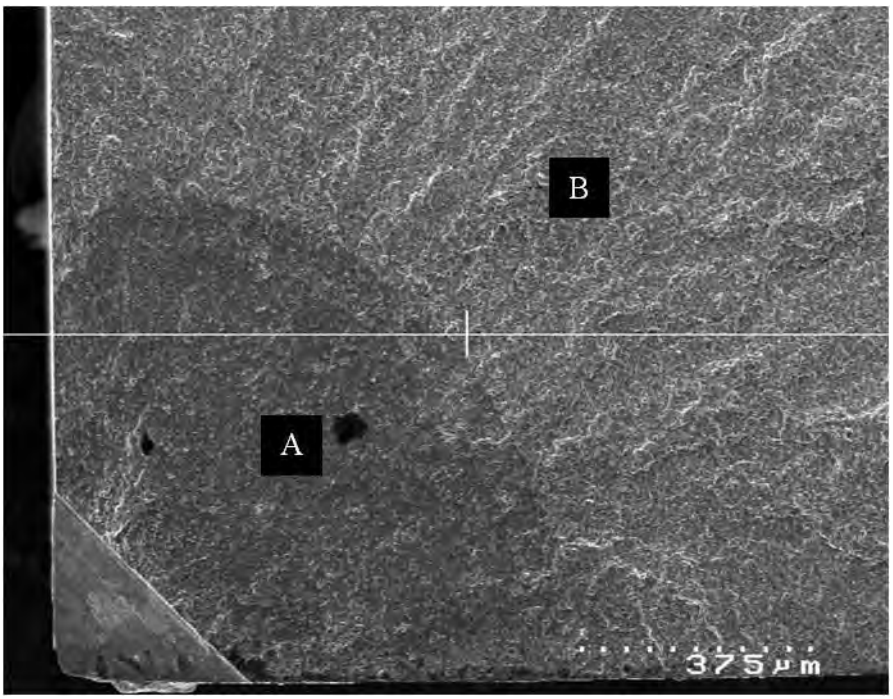
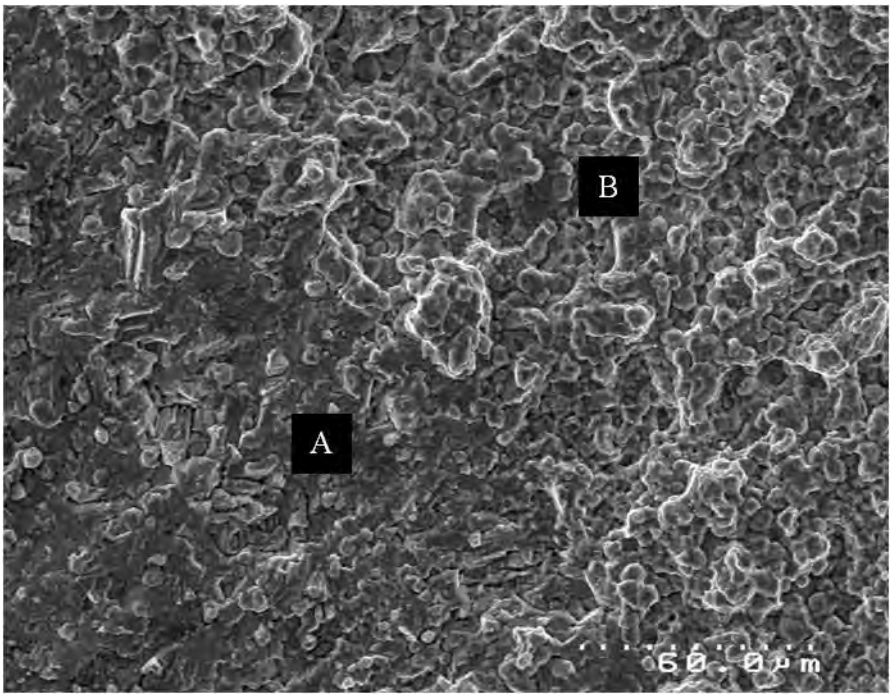
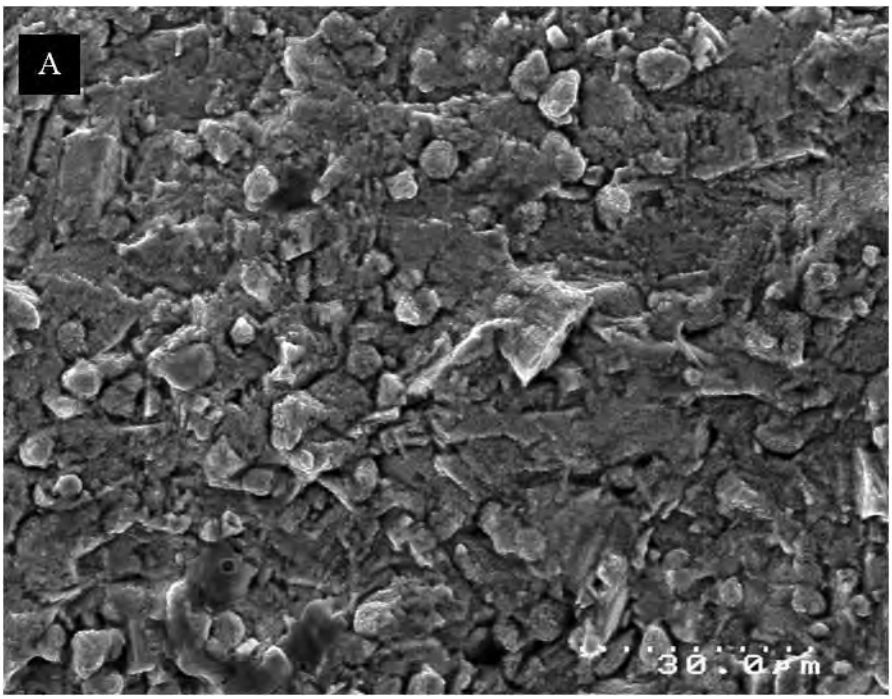
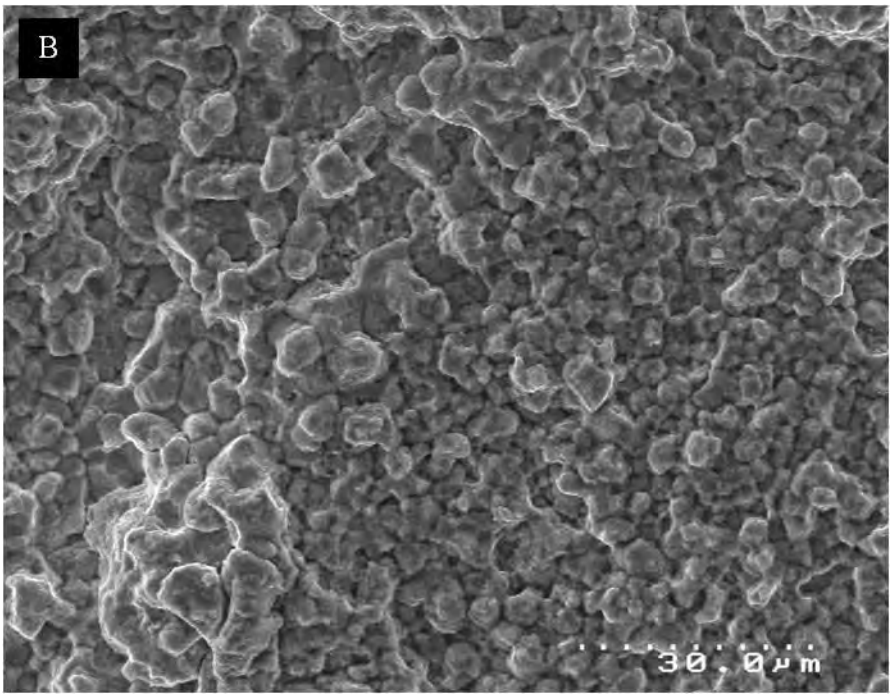


Figure A-45: Showing fractographs of fine-grained Udimet 720Li test piece CX014; tested at 600°C in laboratory air, with a dwell load of 26 kN and a dwell time of 3,600 seconds. Each image shows the crack propagating from bottom right to top left. The band labelled A is the precrack region, which was undertaken at temperature and in air; bands B, D, F and H are baseline (1-1-1-1) regions and bands C, E and G are dwell regions. Note the marked difference in terms of crack growth mechanism when regions of baseline are compared with those relating to dwell cycling. Higher magnification images are taken at points relating to the following crack growth driving forces (ΔK):
B: ~17.5 MPa√m; C: ~19 MPa√m; E: ~27.5 MPa√m; G: ~35 MPa√m


B
A
375µm


B
A
60.0µm


A
30.0µm


B
30.0µm

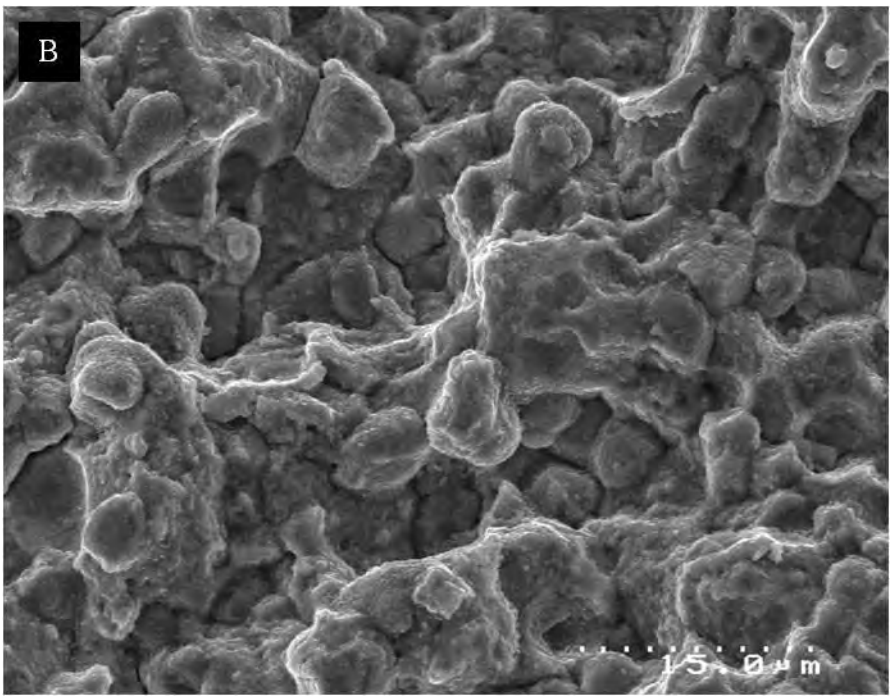
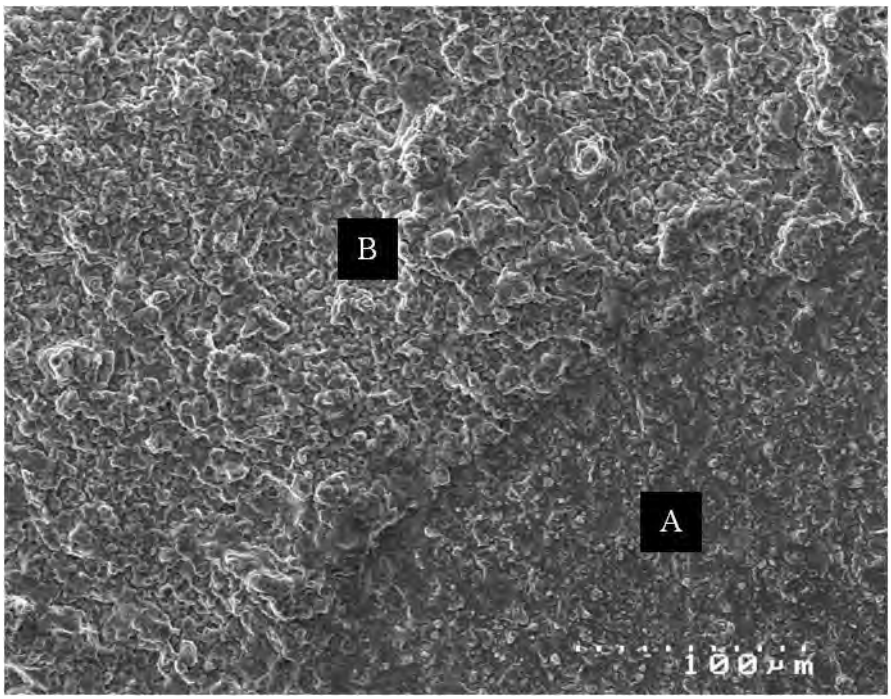
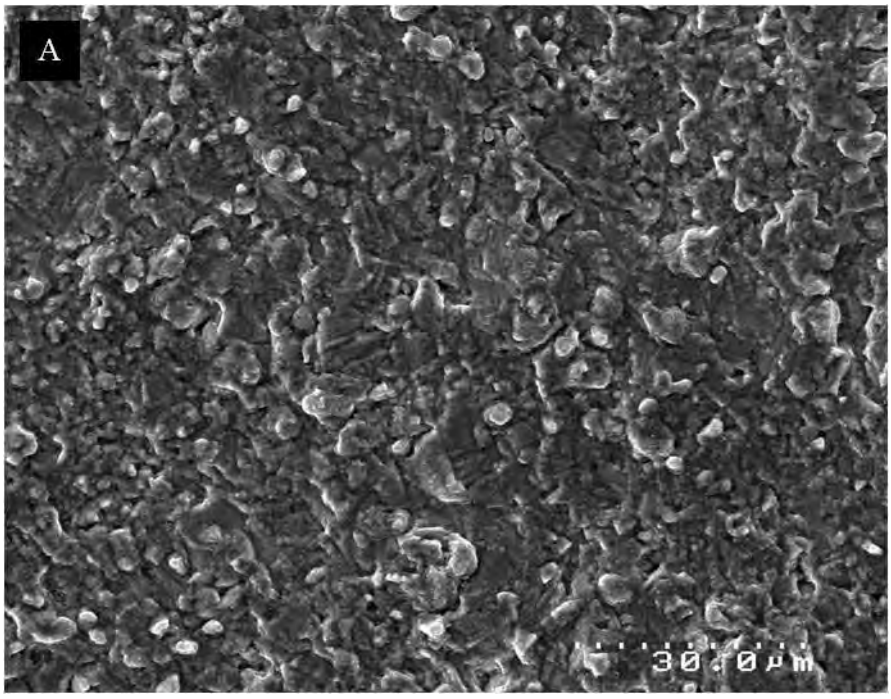


Figure A-46: Showing fractographs of fine-grained Udimet 720Li test piece CC009; tested at 650°C in laboratory air, with a dwell load of 26 kN and a dwell time of 3,600 seconds. Each image shows the crack propagating from bottom left to top right. The band labelled A is the baseline (1-1-1-1) region, and band B is the dwell region. Note the marked difference in terms of crack growth mechanism when regions of baseline are compared with those relating to dwell cycling. Note also delineation of primary γ' precipitates away from the γ matrix during high temperature fast cycling (1-1-1-1), as discussed in section 5.2.1. Higher magnification images are taken at points relating to the following crack growth driving forces (ΔK): A: ~15 MPa√m; B: ~25 MPa√m


B
A
100µm


A
30.0µm

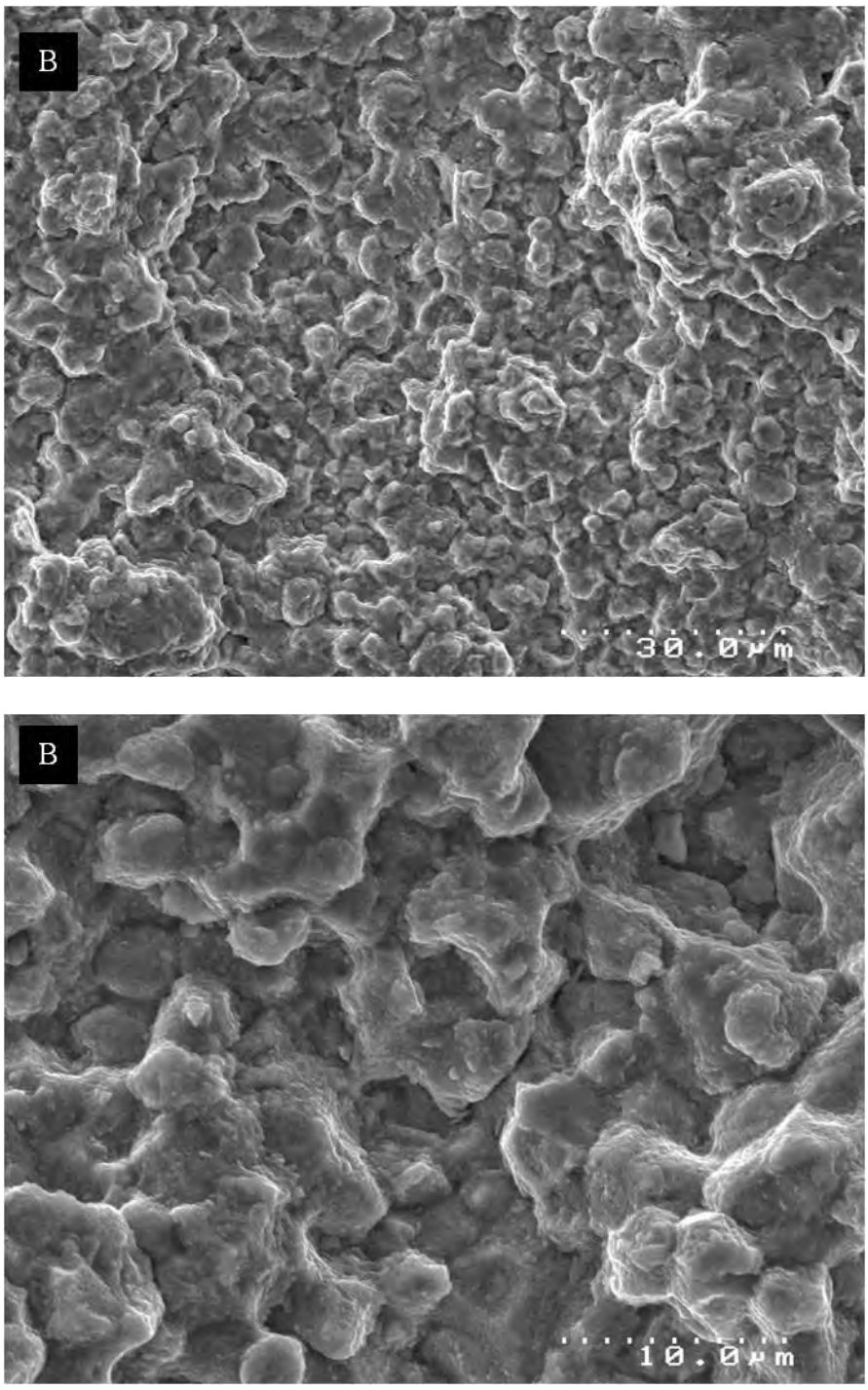
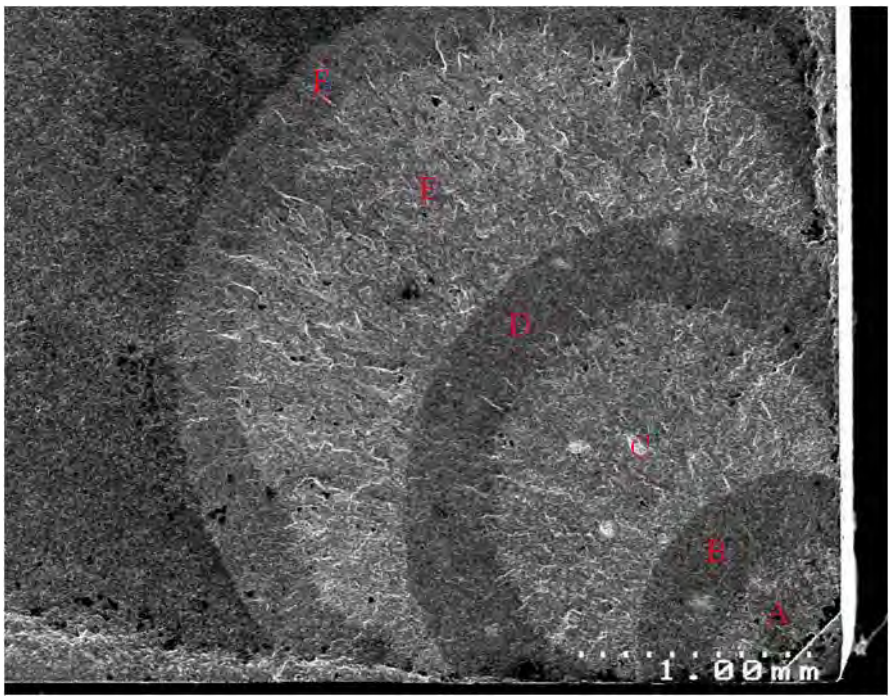
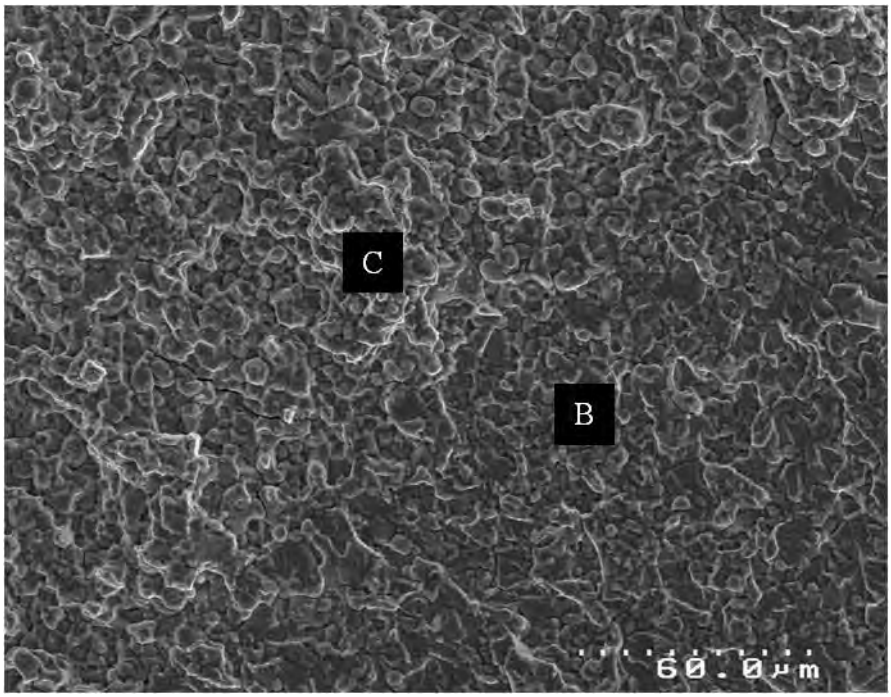
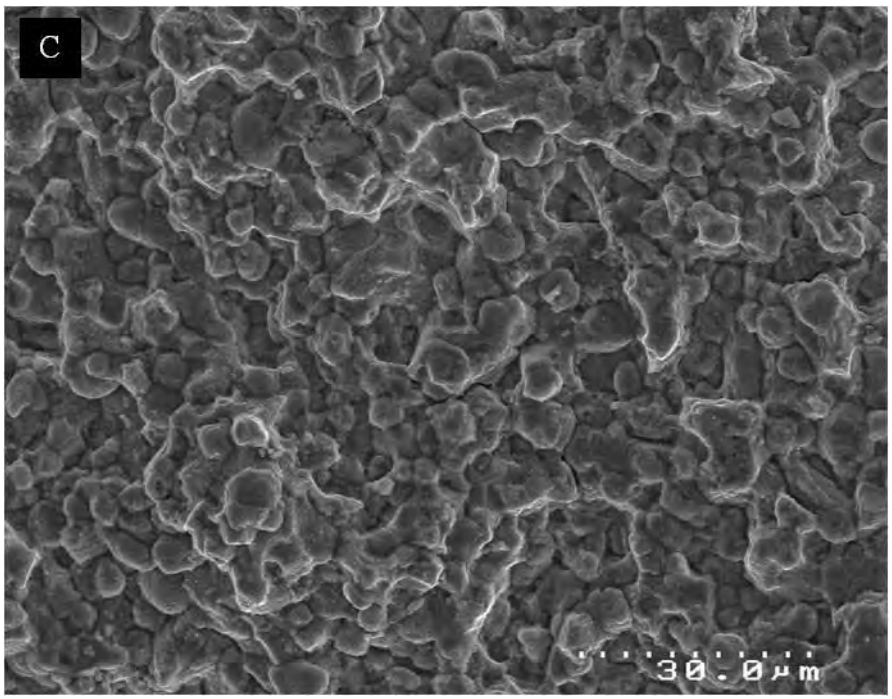
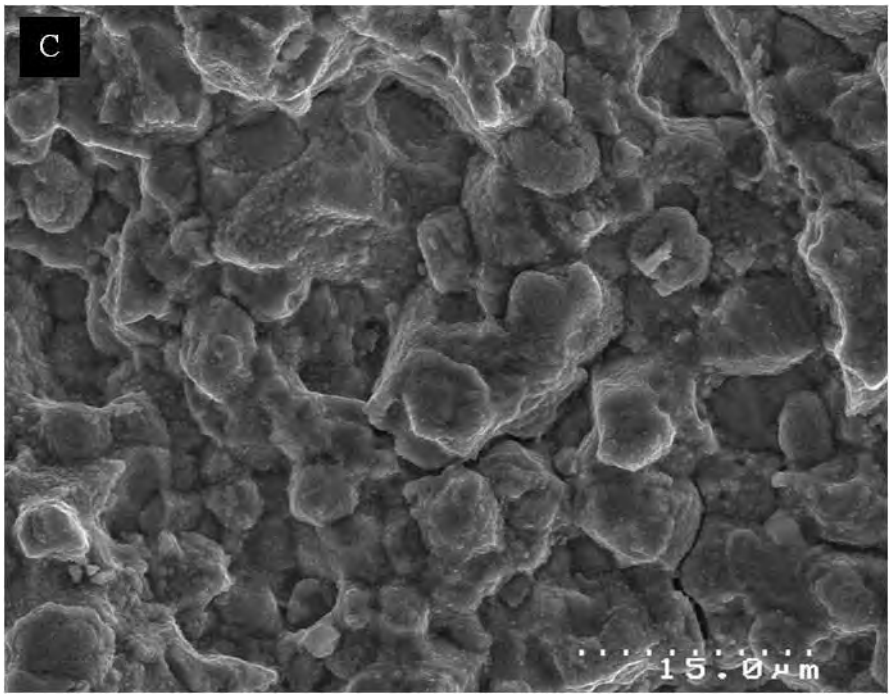


Figure A-47: Showing fractographs of fine-grained Udimet 720Li test piece CC019; tested at 650°C in laboratory air, with a dwell load of 27 kN and a dwell time of 3,600 seconds. Each image shows the crack propagating from bottom right to top left. The band labelled A is the baseline (1-1-1-1) region, and band B is the dwell region. Note the marked difference in terms of crack growth mechanism when regions of baseline are compared with those relating to dwell cycling. Note also delineation of primary γ' precipitates away from the γ matrix during high temperature fast cycling (1-1-1-1), as discussed in section 5.2.1. Higher magnification images are taken at points relating to the following crack growth driving forces (ΔK): A: ~15 MPa√m; B: ~25 MPa√m


F
E
D
C
B
A
1.00mm


C
B
60.0µm


C
30.0µm


C
15.0µm

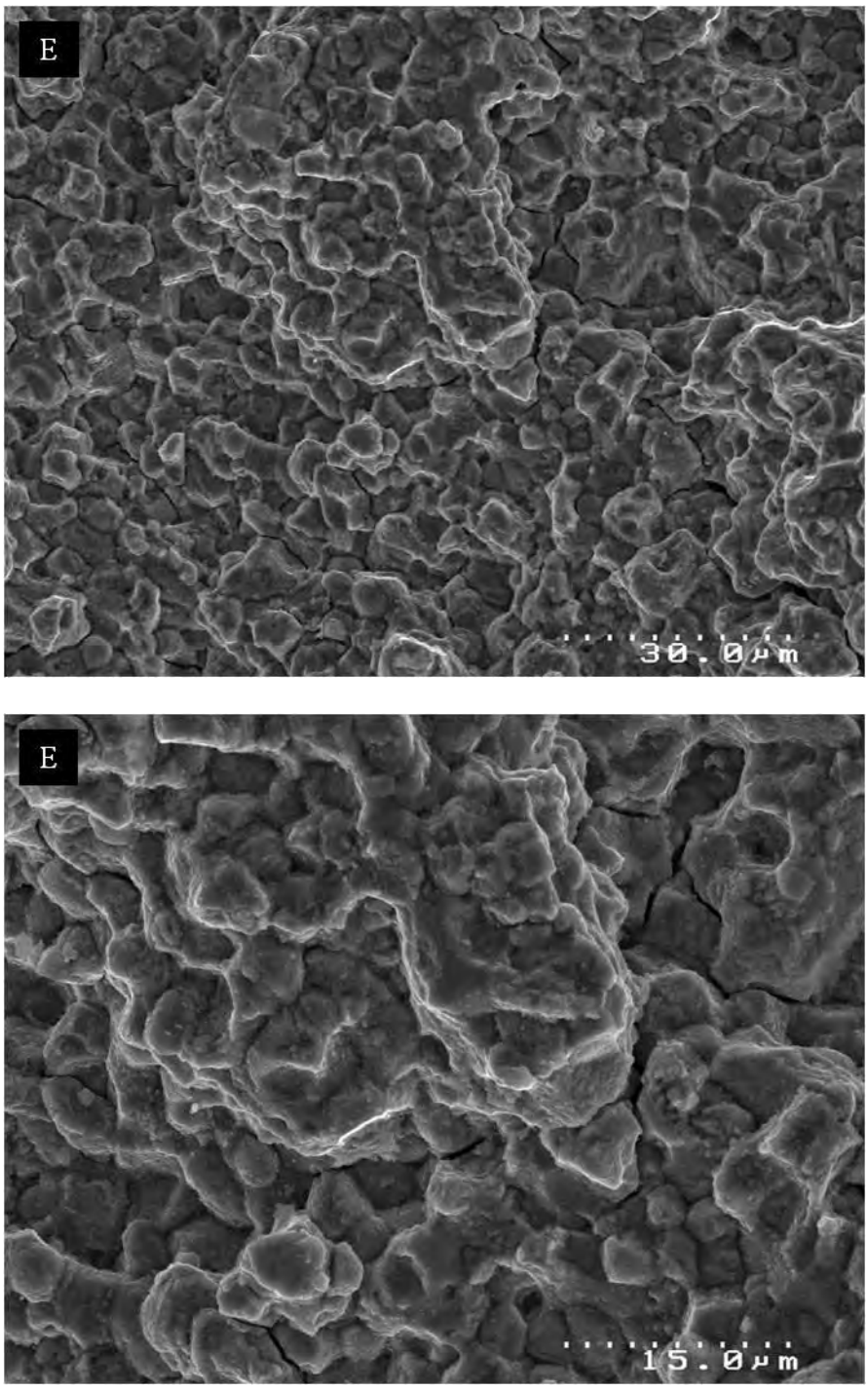
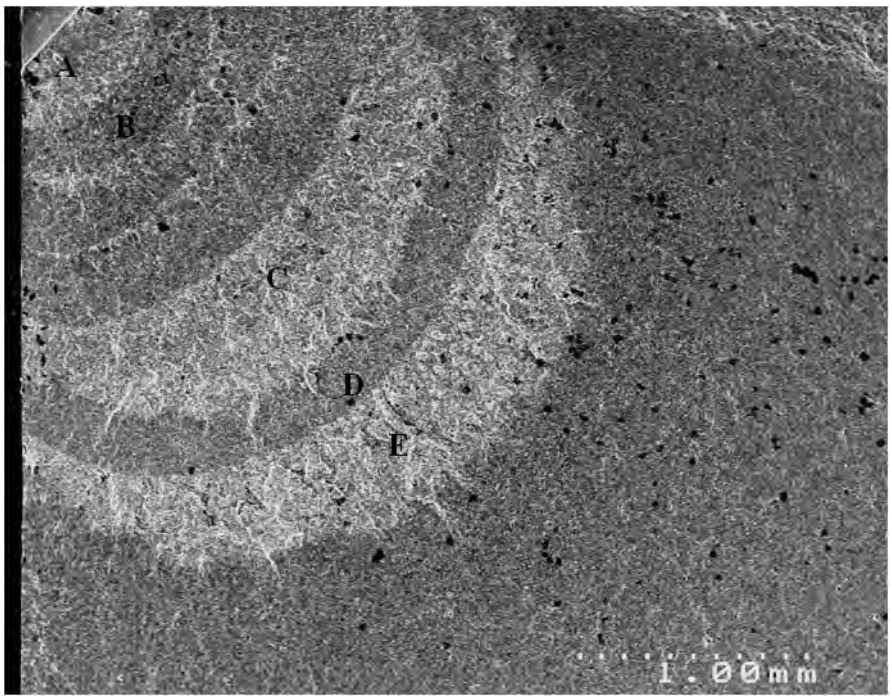
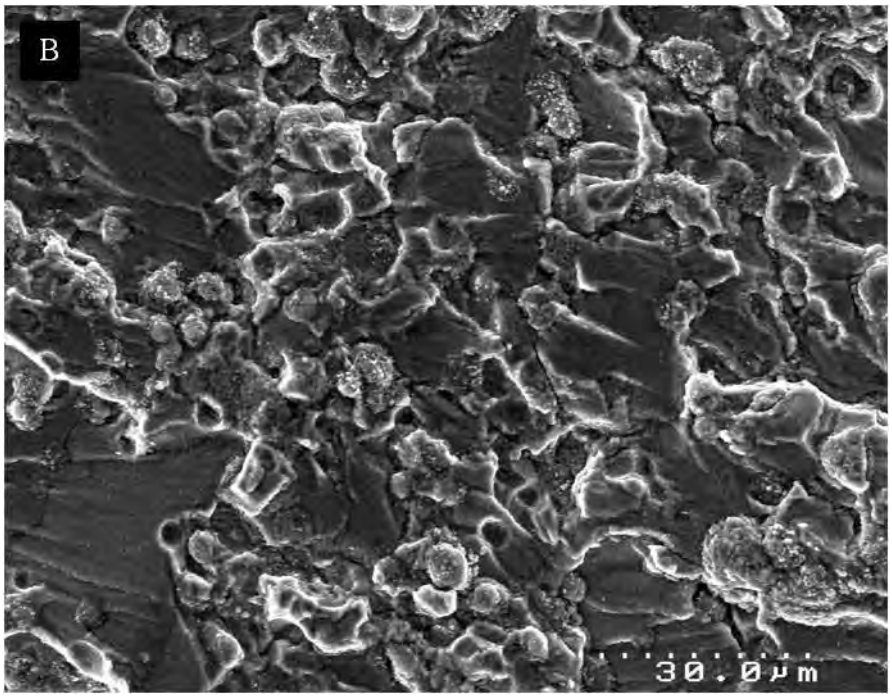
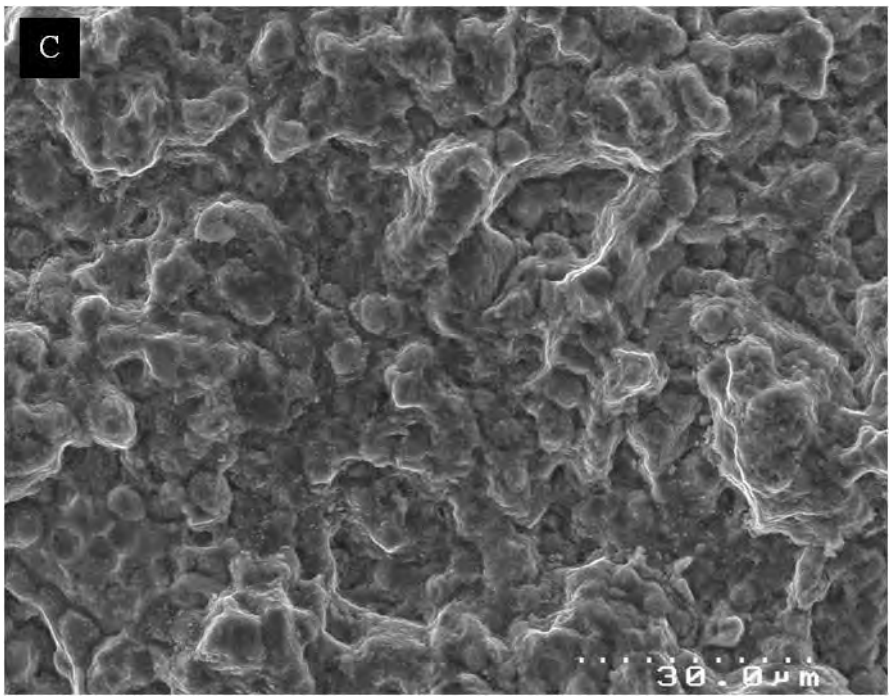
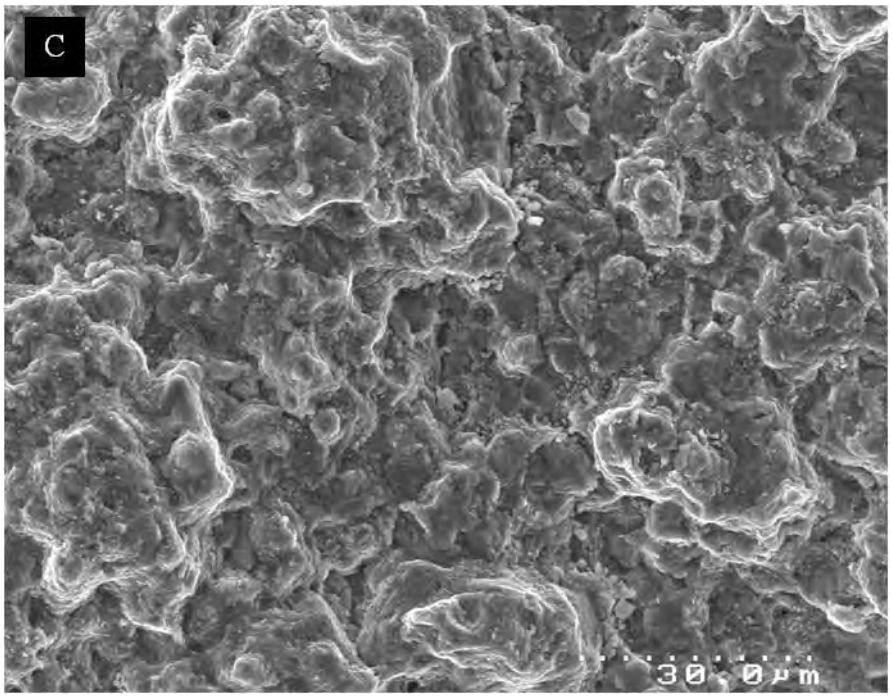


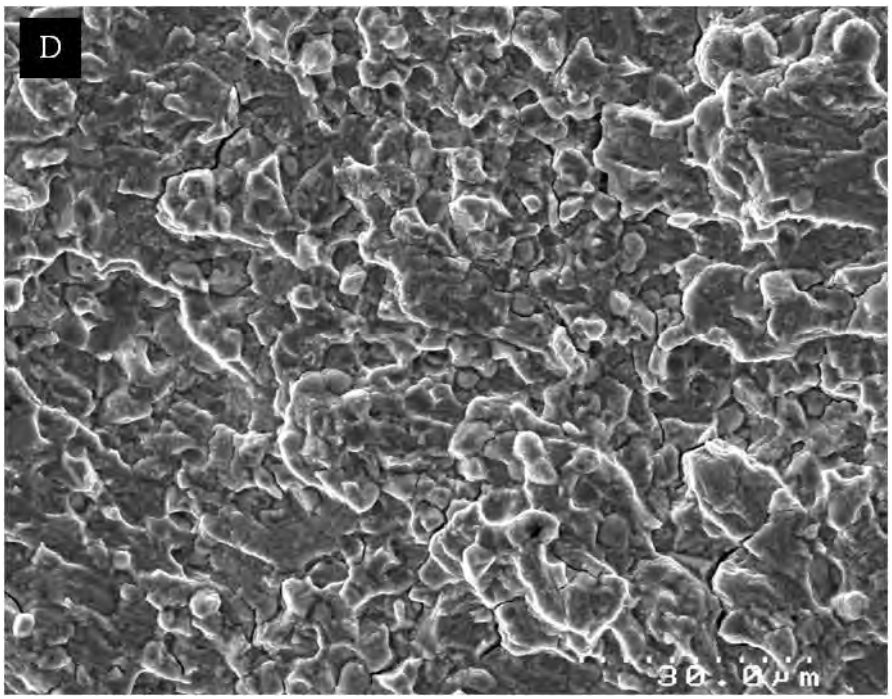
Figure A-48: Showing fractographs of fine-grained Udimet 720Li test piece CX023; tested at 650°C in laboratory air, with a dwell load of 29 kN and a dwell time of 3,600 seconds. Each image shows the crack propagating from bottom left to top right. The band labelled A is the precrack region, which was undertaken at temperature and in air; bands B, D and F are baseline (1-1-1-1) regions and bands C and E are dwell regions. Note the marked difference in terms of crack growth mechanism when regions of baseline are compared with those relating to dwell cycling. Higher magnification images are taken at points relating to the following crack growth driving forces (ΔK): Transition from B to C: ~19 MPa√m; C: ~23 MPa√m; E: ~34 MPa√m

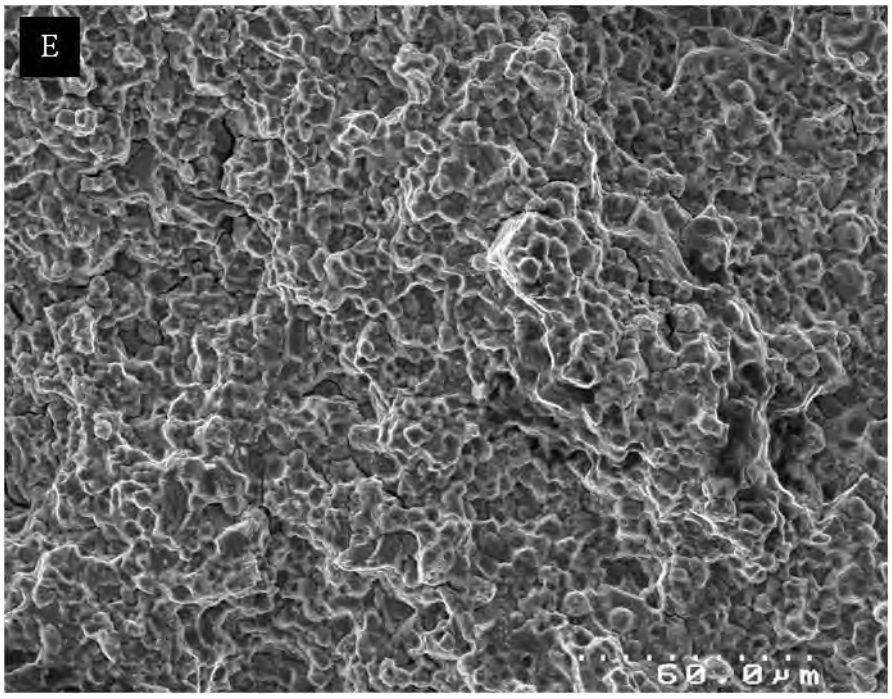

A
B
C
D
E
1.00mm


B
30.0µm


C
30.0µm


C
30.0µm


D
30.0µm


E
60.0µm

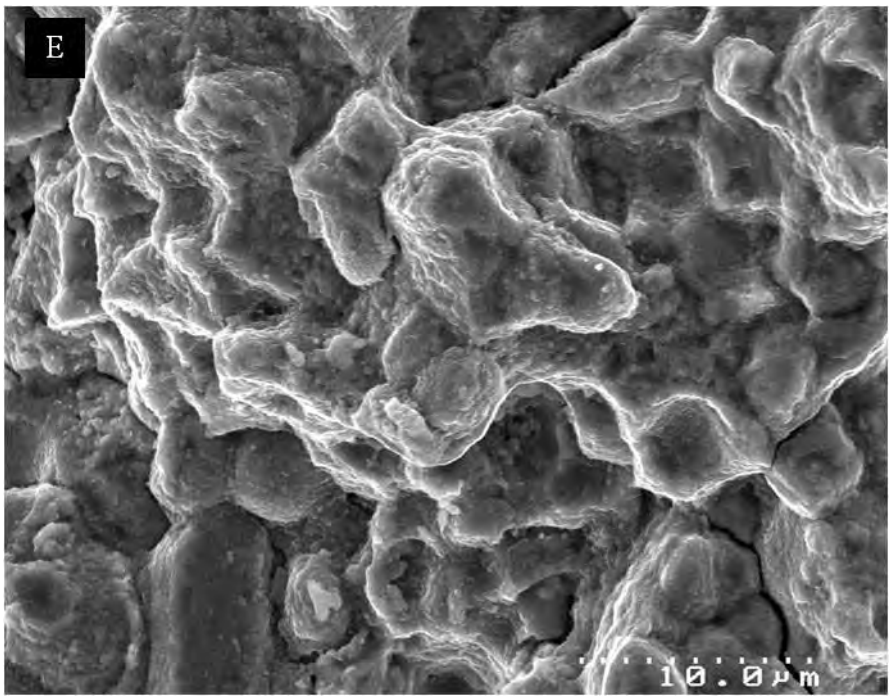
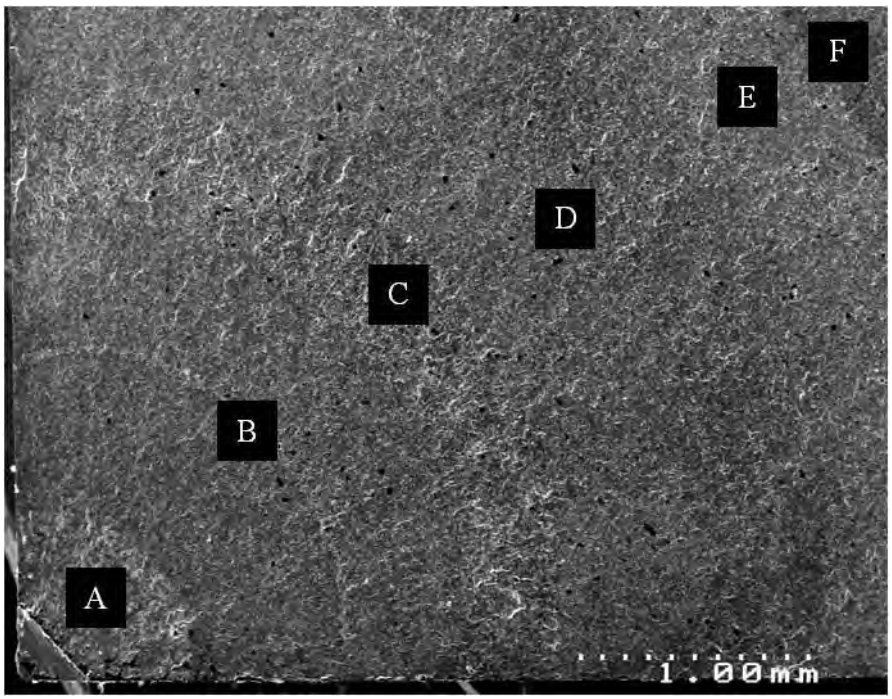
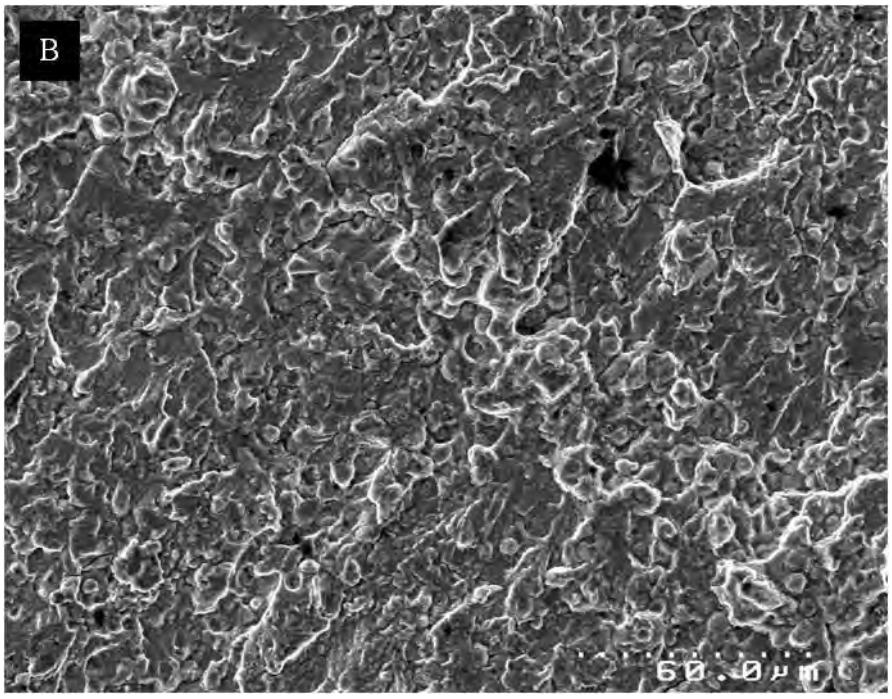
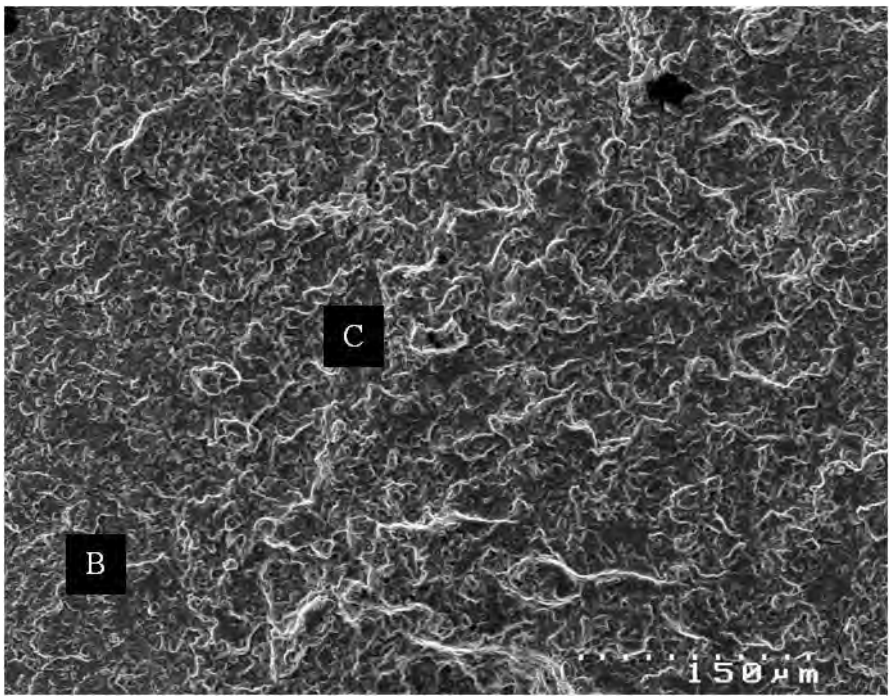
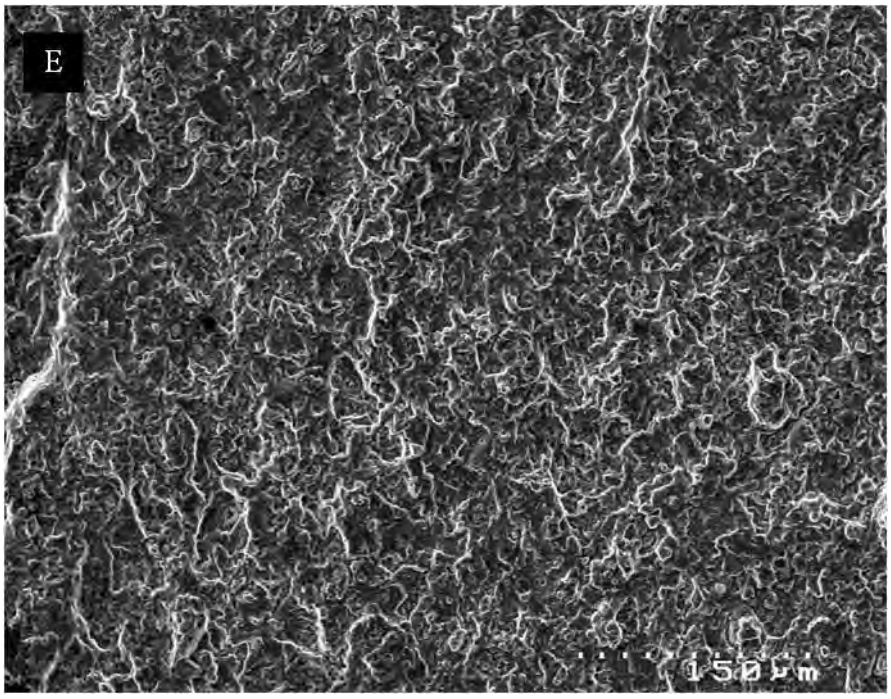


Figure A-49: Showing fractographs of fine-grained Udimet 720Li test piece CX027; tested at 650°C in laboratory air, with a dwell load of 23 kN and a dwell time of 3,600 seconds. Each image shows the crack propagating from top left to bottom right. The band labelled A is the precrack region, which was undertaken at temperature and in air; bands B and D are baseline (1-1-1-1) regions and bands C and E are dwell regions. Note that in between B and C (labelled on the lower magnification overview image) dwell cycles were applied; and the crack failed to grow. Consequently fast cycles (1-1-1-1) were applied to bring the crack growth driving force up and dwell cycles were then applied again. For the second time the crack failed to grow, and the process was repeated until a ΔK of around 25 MPa√m was applied (C). Note the delineation of primary γ' precipitates away from the γ matrix during high temperature fast cycling (1-1-1-1), as discussed in section 5.2.1. Note also that at higher crack growth driving forces the crack growth mechanisms are even more intergranular even under baseline loading (D). Higher magnification images are taken at points relating to the following crack growth driving forces (ΔK): B: ~15 MPa√m; C: ~27.5 MPa√m; D: ~31 MPa√m; E: ~35 MPa√m


F
E
D
C
B
A
1.00mm


B
60.0µm


C
B
150µm


E
150µm

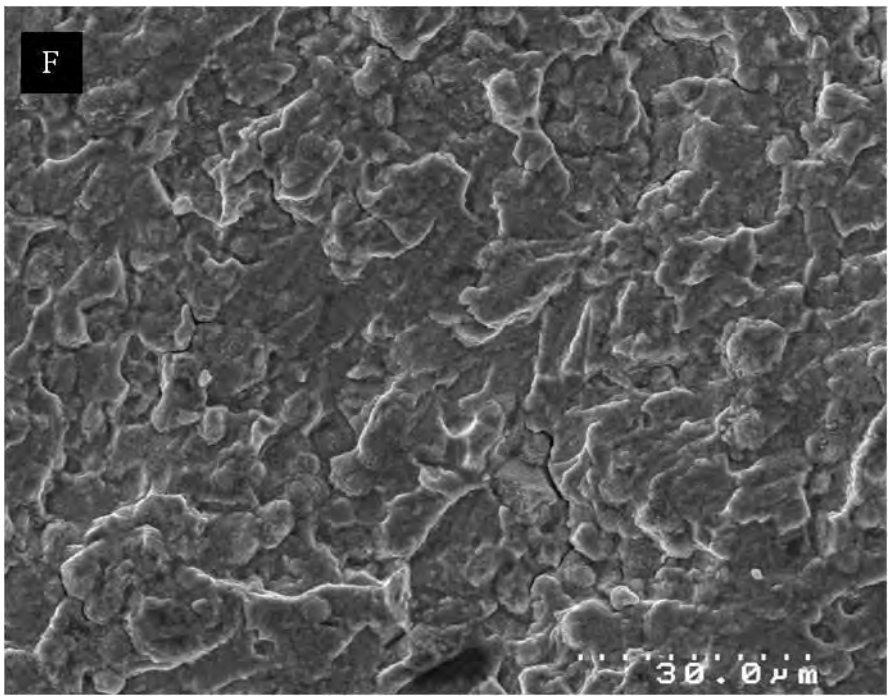
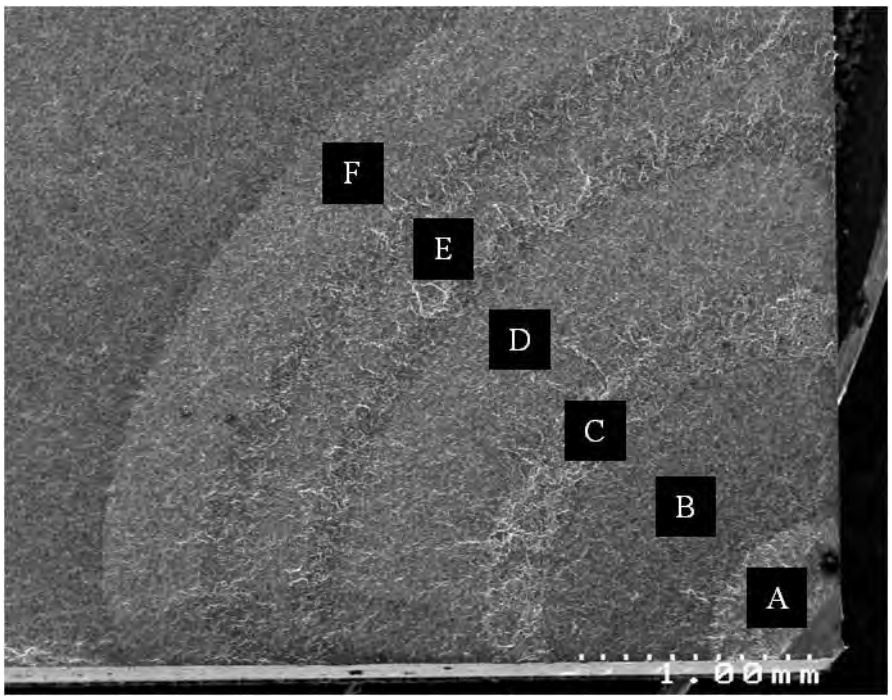
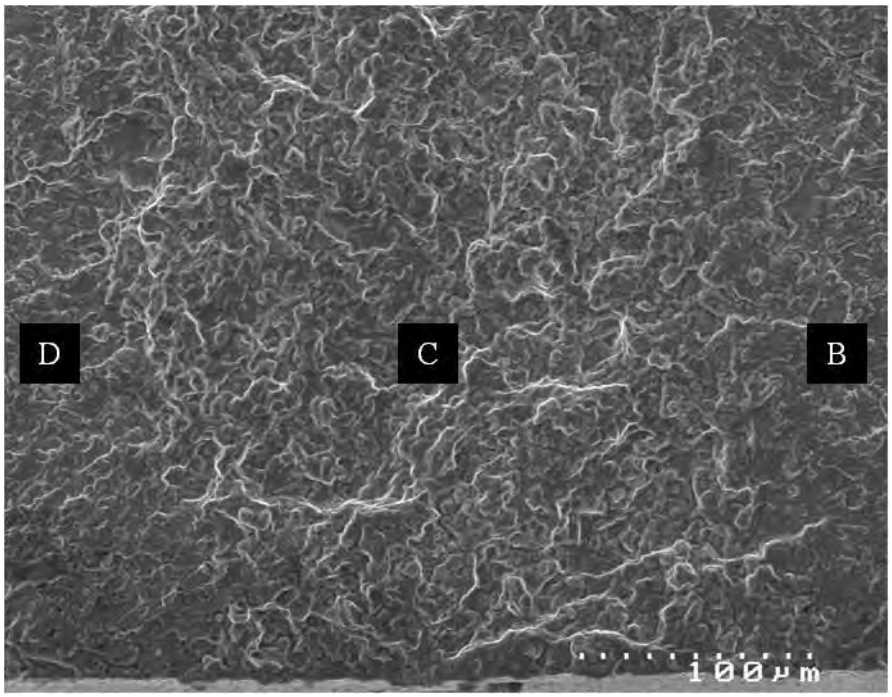
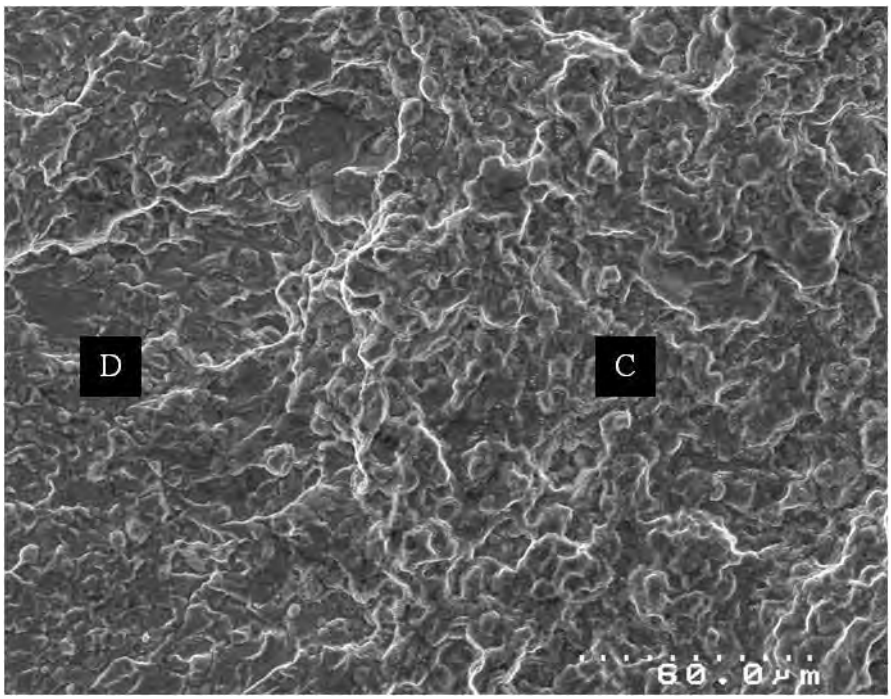
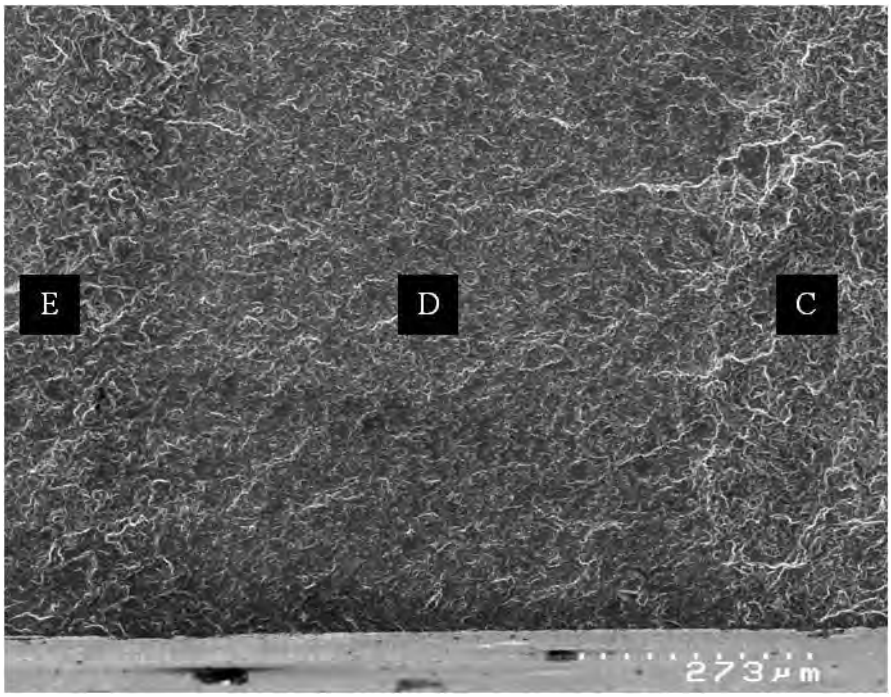


Figure A-50: Showing fractographs of fine-grained Udimet 720Li test piece CX030; tested at 650°C in laboratory air, with a maximum load of 26 kN and a dwell time of 3,600 seconds. Note that in this test; the waveform applied comprised of holding the test piece at minimum load during the 3,600 second dwell period, and only applying the maximum load for a period of 1 second per cycle. Each image shows the crack propagating from bottom left to top right. The band labelled A is the precrack region, which was undertaken at temperature and in air; bands B, D and F are baseline (1-1-1-1) regions and bands C and E are dwell regions (1-1-1-3,600). Note the more subtle differences in terms of crack growth mechanism when regions of baseline are compared with those relating to dwell at minimum load cycling. Higher magnification images are taken at points relating to the following crack growth driving forces (ΔK): B: ~22 MPa√m; transition from B to C: ~28 MPa√m; E: ~47 MPa√m; F: ~55 MPa√m


F
E
D
C
B
A
1.00mm


D
C
B
100μm


D
C
80.0µm


E
D
C
273µm

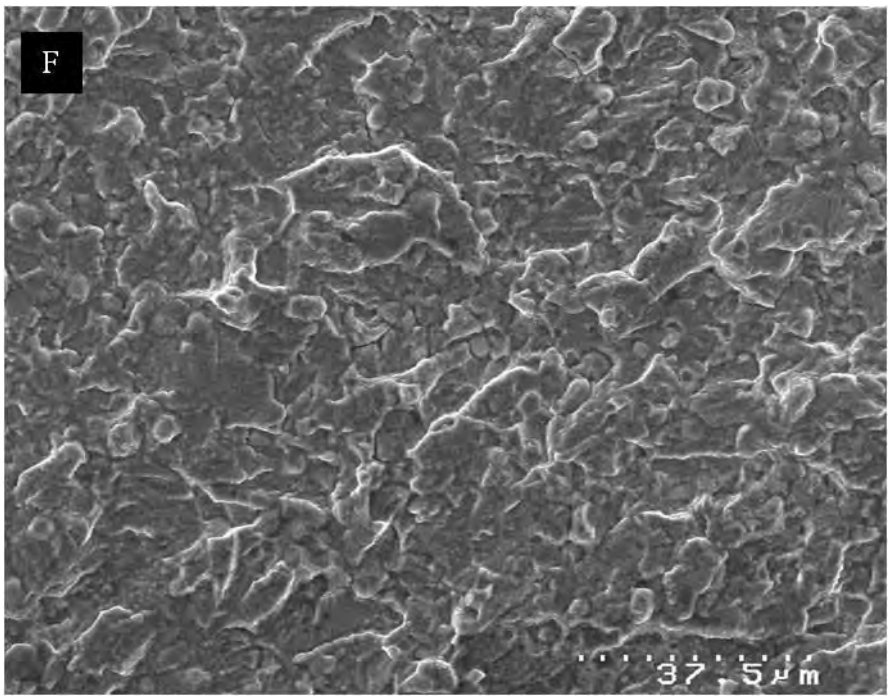
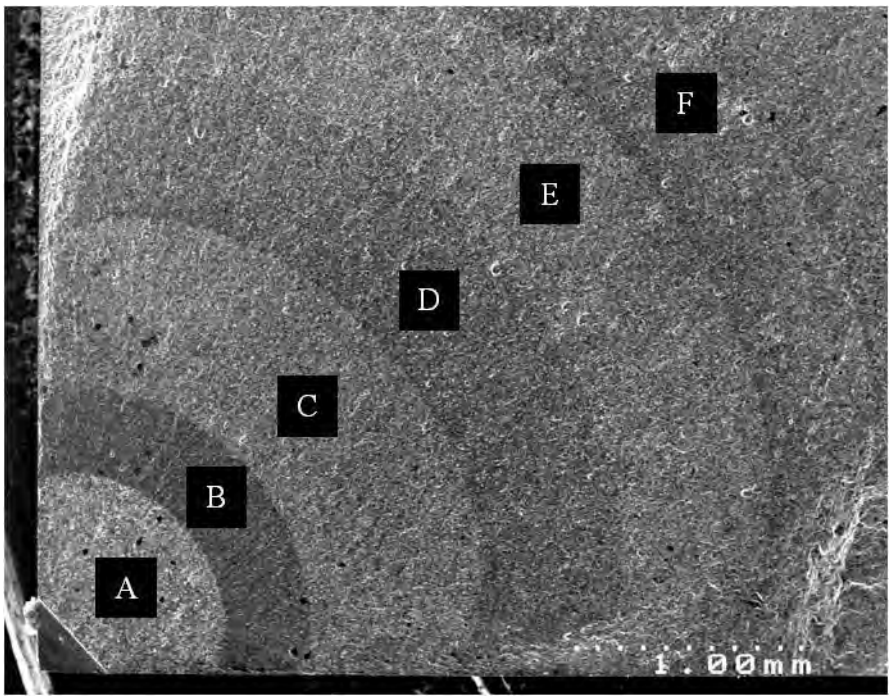
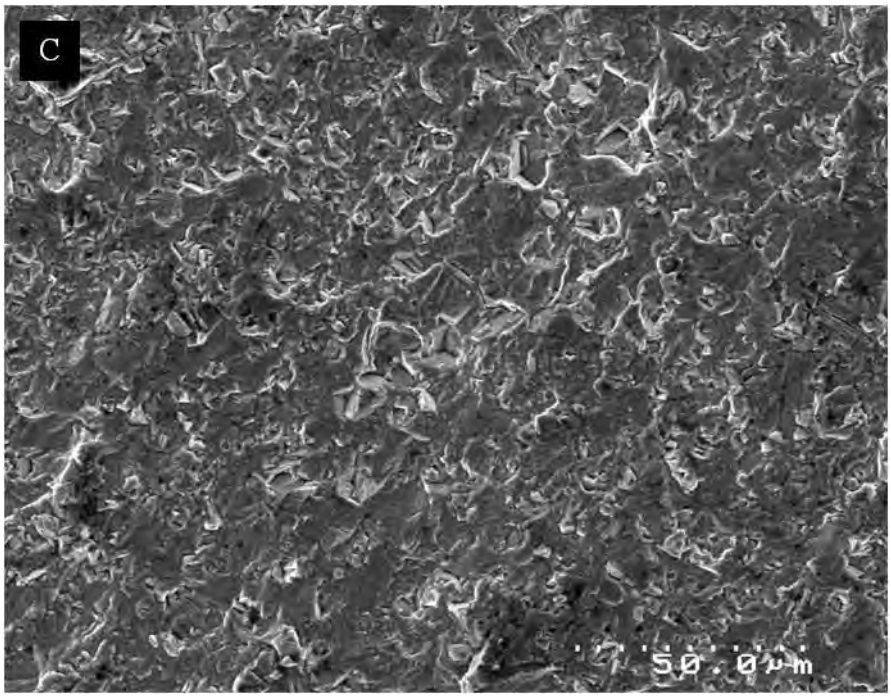
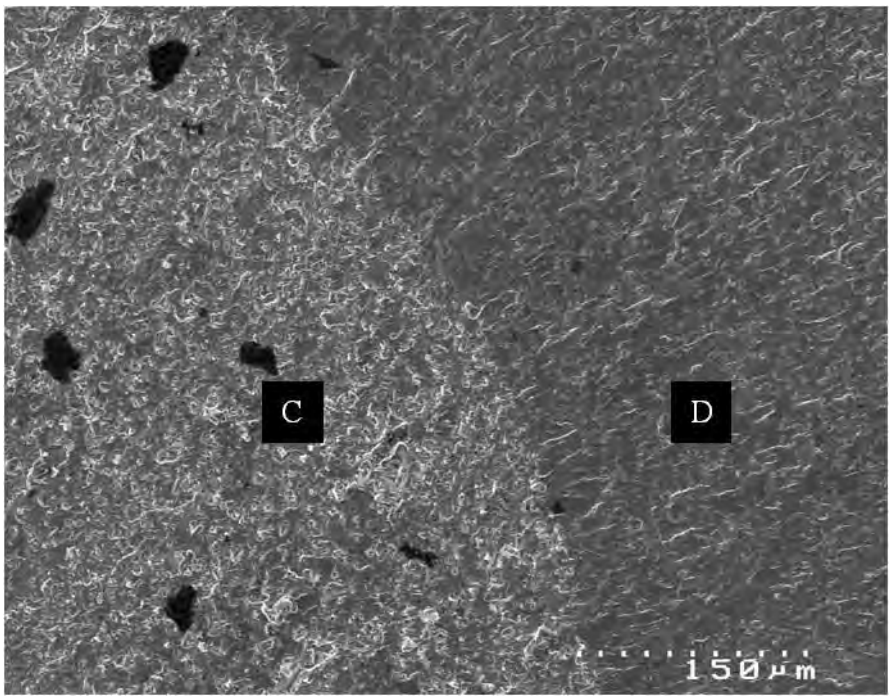
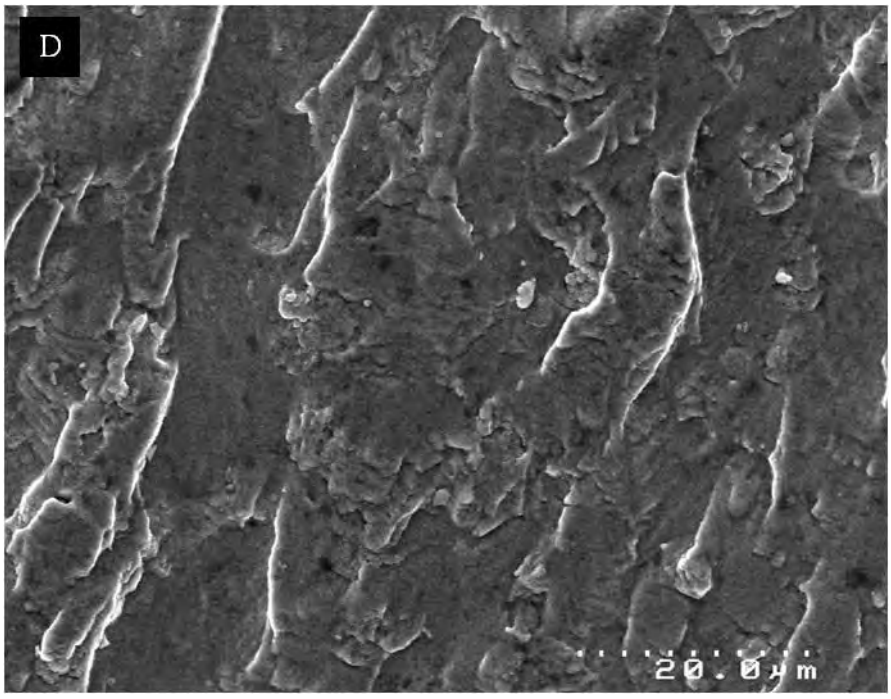


Figure A-51: Showing fractographs of fine-grained Udimet 720Li test piece CX025; tested at 650°C in laboratory air, with a maximum load of 26 kN and a dwell time of 3,600 seconds. Note that in this test; the waveform applied comprised of holding the test piece at minimum load during the 3,600 second dwell period, and only applying the maximum load for a period of 1 second per cycle. Each image shows the crack propagating from bottom right to top left. The band labelled A is the precrack region, which was undertaken at temperature and in air; bands B, D and F are baseline (1-1-1-1) regions and bands C and E are dwell regions (1-1-1-3,600). Note the more subtle differences in terms of crack growth mechanism when regions of baseline are compared with those relating to dwell at minimum load cycling. Higher magnification images are taken at points relating to the following crack growth driving forces (ΔK): Transition through from B, C and D: ~23.5 MPa√m; transition from C to D: ~24 MPa√m; transition through from C, D and E: ~27 MPa√m; F: ~38 MPa√m


F
E
D
C
B
A
1.00mm


C
50.0µm


C
D
150µm


D
20.0µm

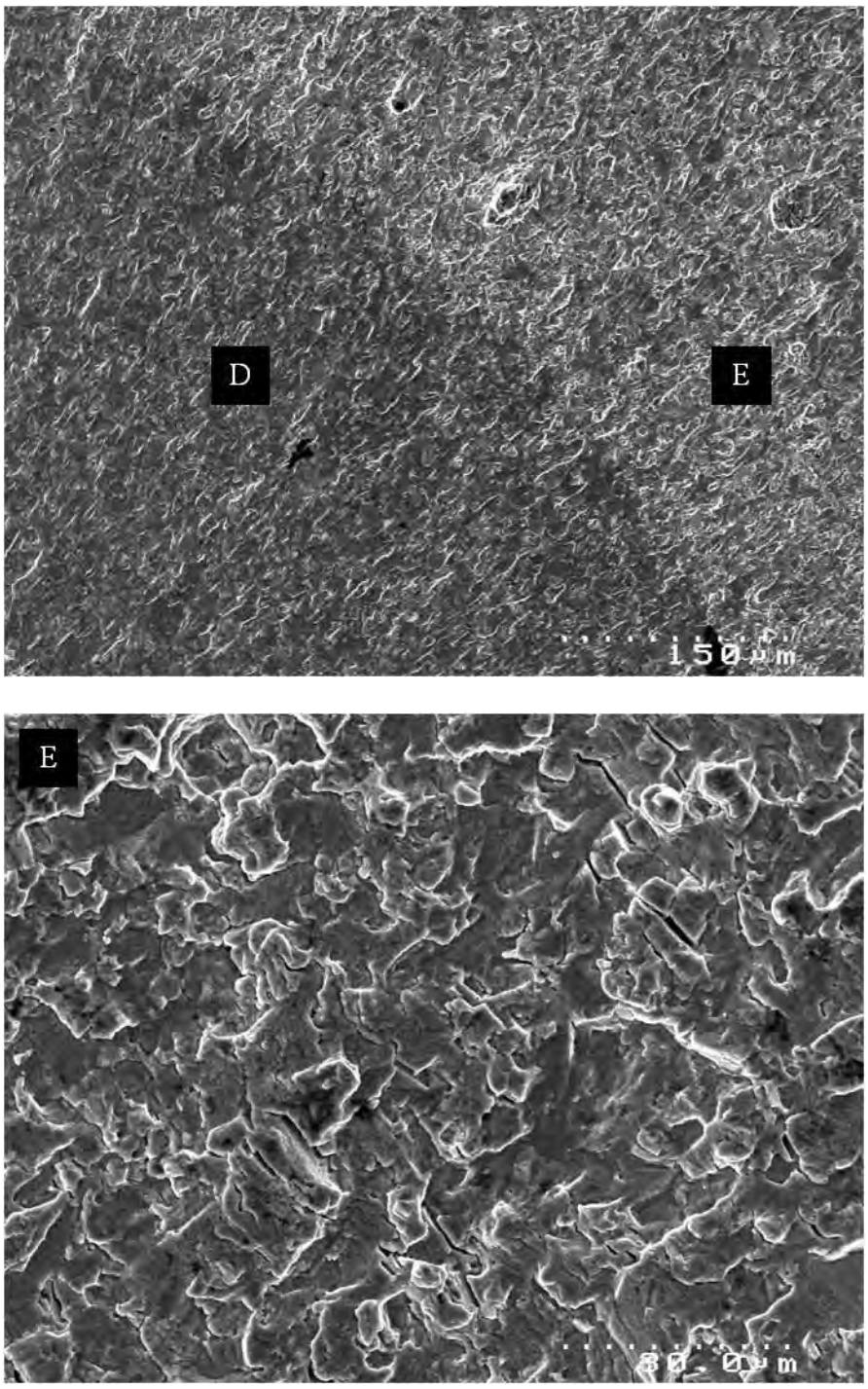
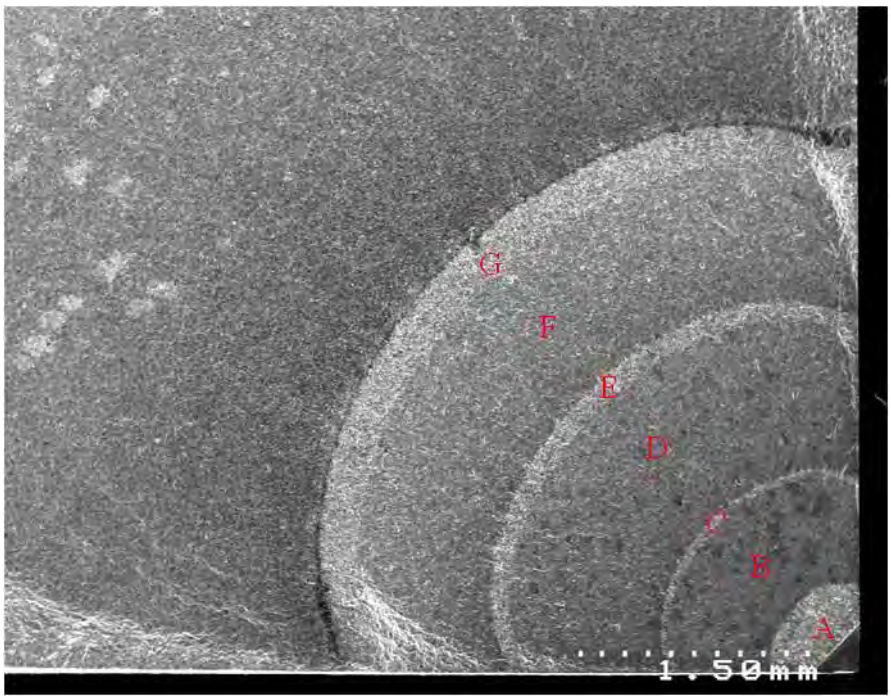
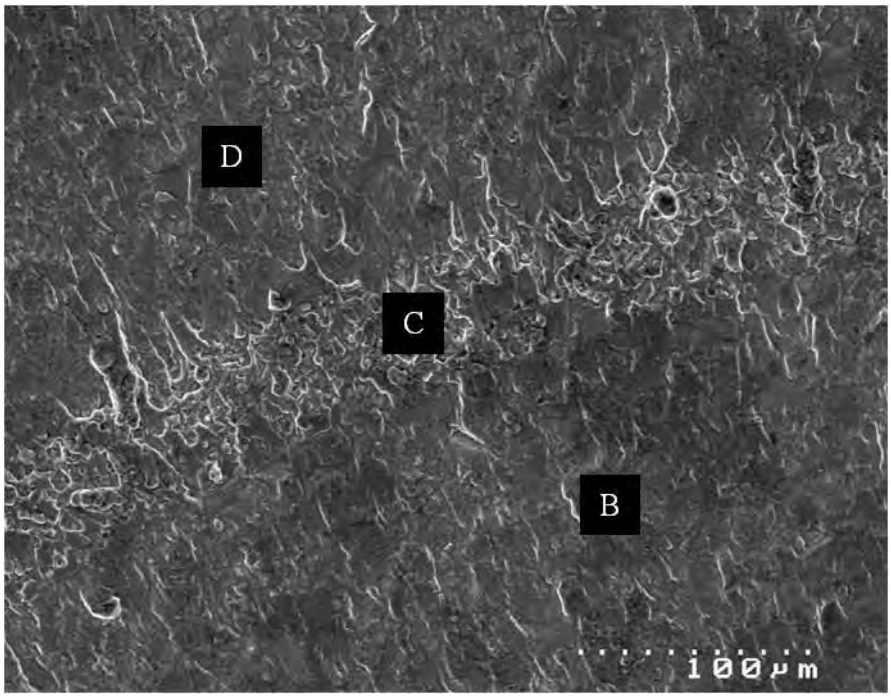
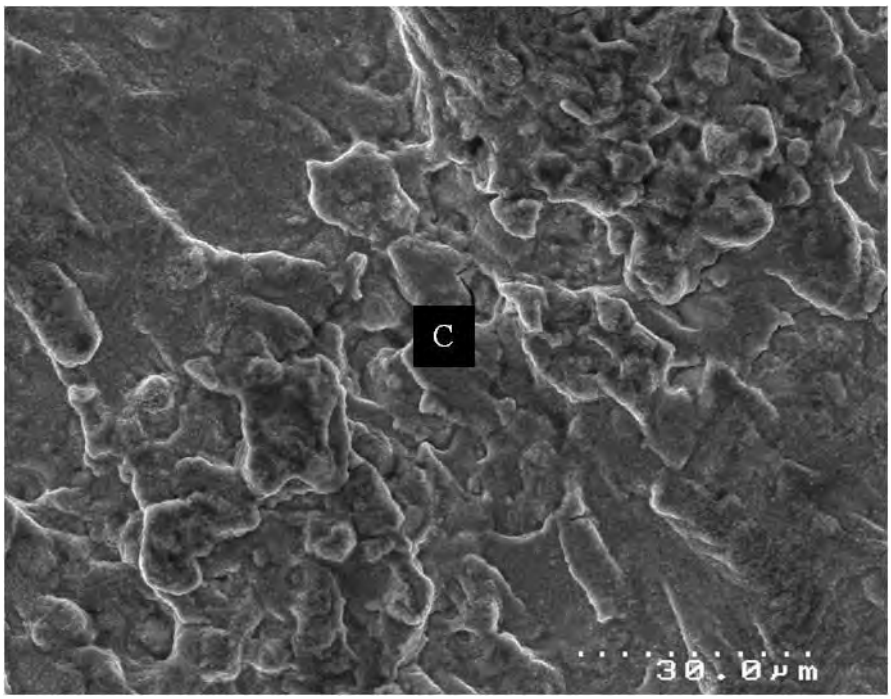
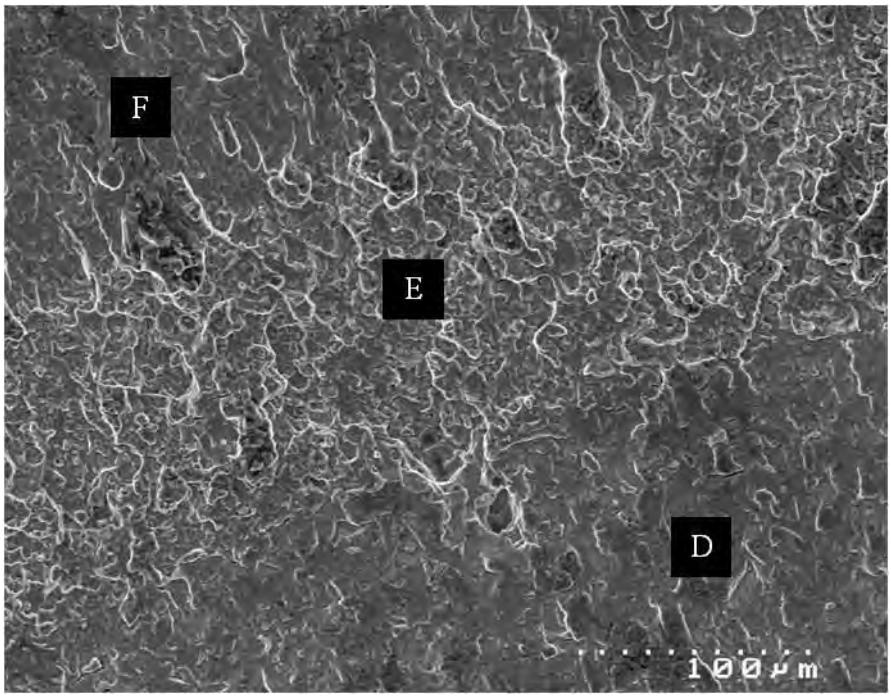


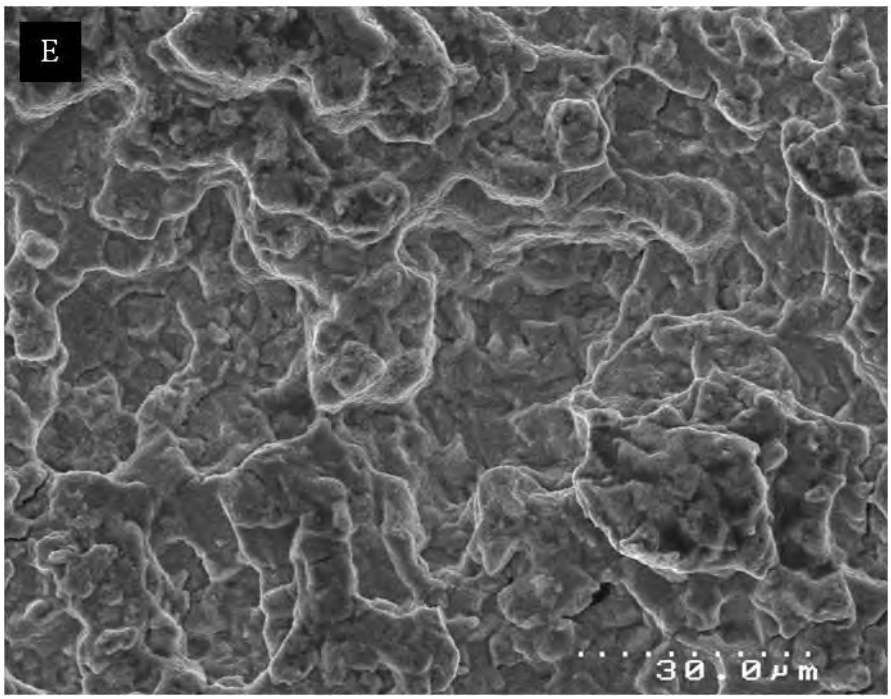
Figure A-52: Showing fractographs of fine-grained Udimet 720Li test piece CX031; tested at 650°C in a vacuum, with a dwell load of 26 kN and a dwell time of 120 seconds. Each image shows the crack propagating from bottom left to top right. The band labelled A is the precrack region, which was undertaken at temperature and also in a vacuum; bands B, D and F are baseline (1-1-1-1) regions and bands C and E are dwell regions. Note that crack growth mechanisms are transgranular even under dwell loading when the test is performed in a vacuum. Higher magnification images are taken at points relating to the following crack growth driving forces (ΔK): C: ~25 MPa√m; transition from C to D: ~28 MPa√m; D: ~30 MPa√m; transition from D to E: ~35 MPa√m; E: ~42 MPa√m


G
F
E
D
C
B
A
1.50mm


D
C
B
100µm


C
30.0µm


F
E
D
100µm


E
30.0µm

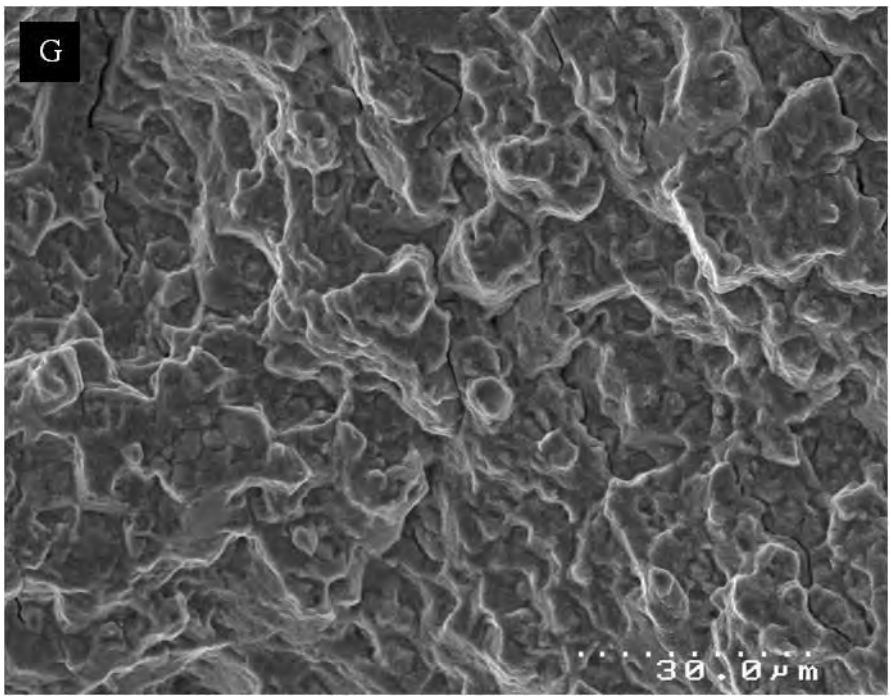
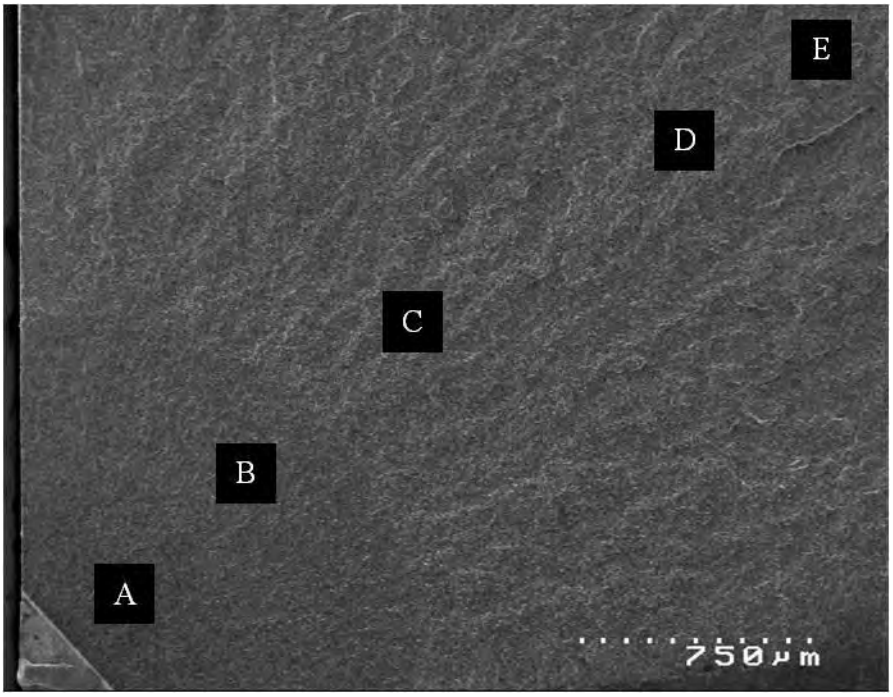
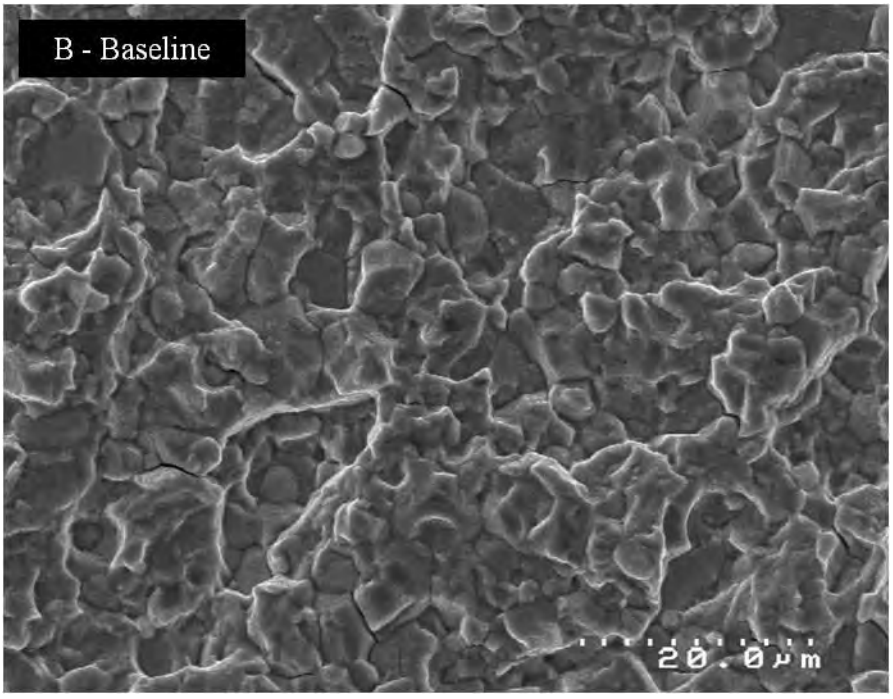
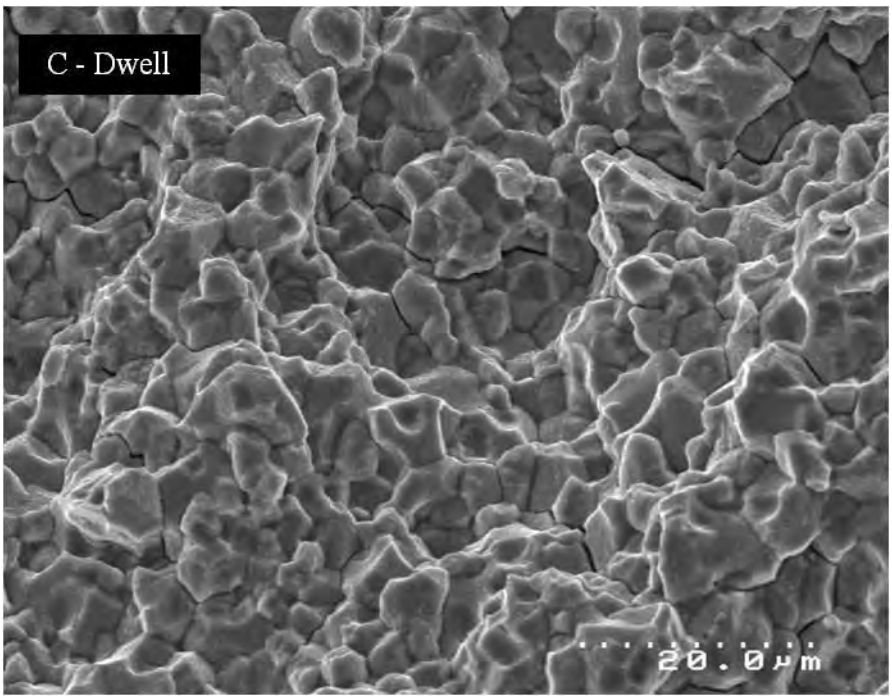


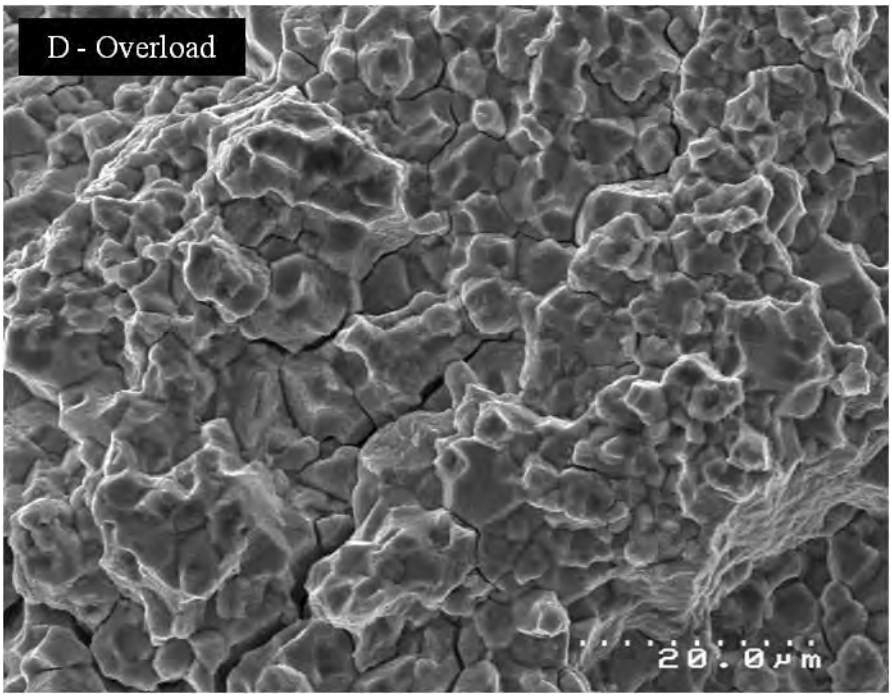
Figure A-53: Showing fractographs of fine-grained Udimet 720Li test piece CX034; tested at 650°C in a vacuum, with a dwell load of 26 kN and a dwell time of 3,600 seconds. Each image shows the crack propagating from bottom right to top left. The band labelled A is the precrack region, which was undertaken at temperature and also in a vacuum; bands B, D and F are baseline (1-1-1-1) regions and bands C, E and G are dwell regions. Note that fracture surfaces pertaining to dwell cycling appear rough and intergranular; even under vacuum conditions. Higher magnification images are taken at points relating to the following crack growth driving forces (ΔK): Transition from B through C to D: ~22 MPa√m; transition from D through E to F: ~32 MPa√m; D: ~30 MPa√m; transition from D to E: ~35 MPa√m; E: ~35 MPa√m; G: ~45 MPa√m

Udimet 720Li Baseline, Dwell and Overload Tests






C - Dwell
20.0µm


D - Overload
20.0µm

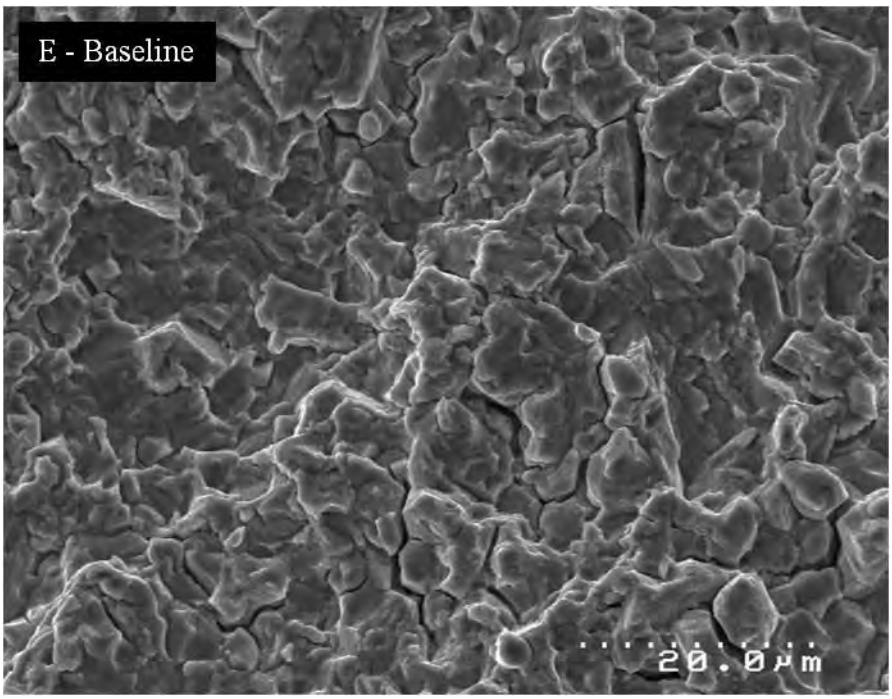
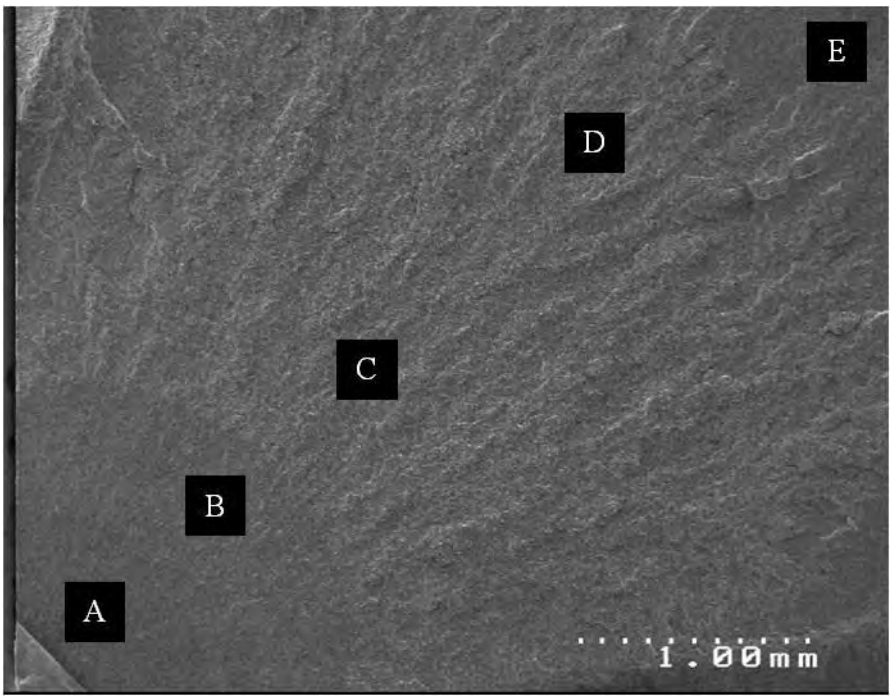
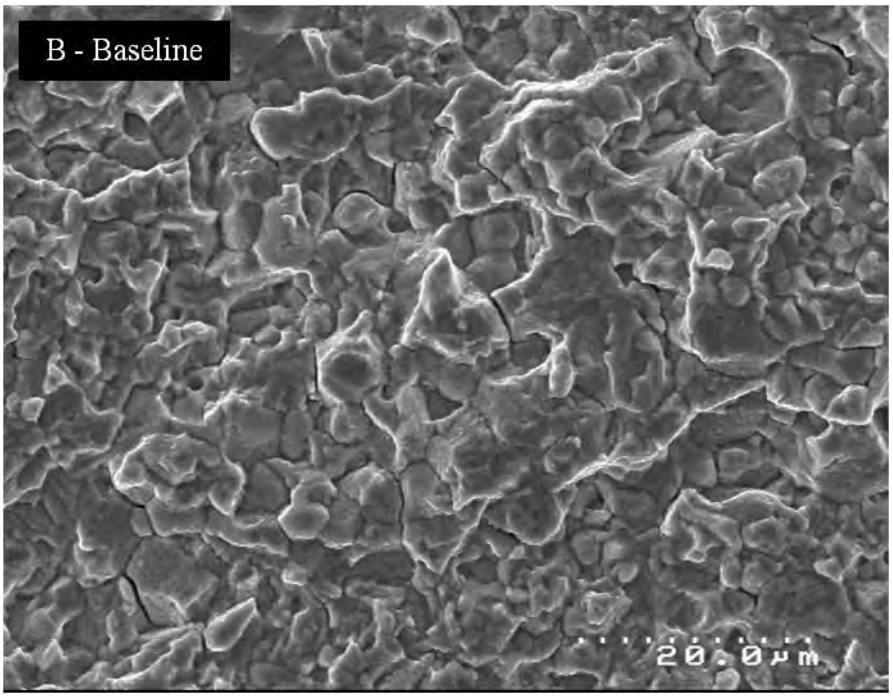
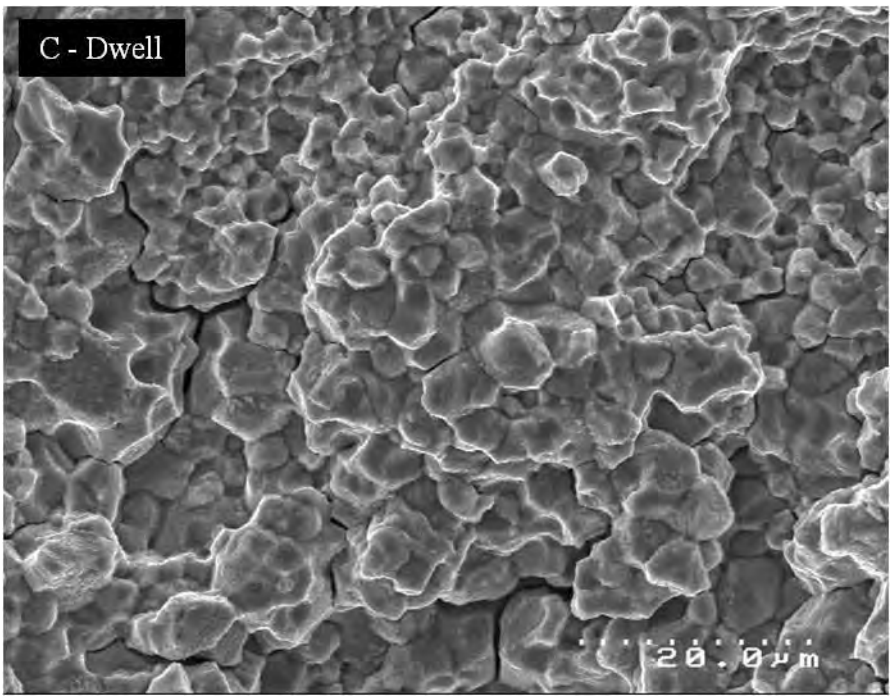
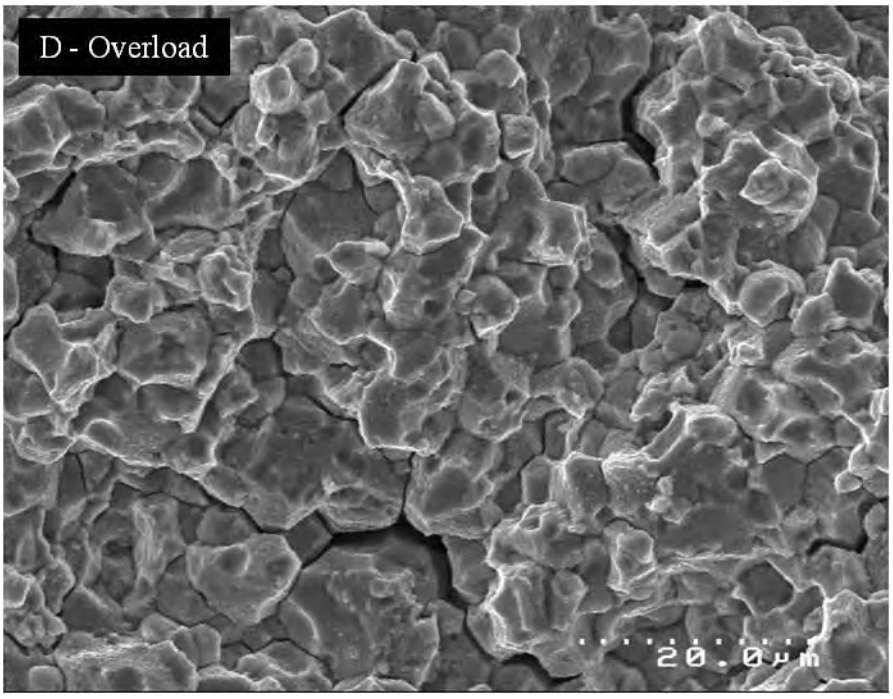


Figure A-54: Showing fractographs of fine-grained Udimet 720Li test piece CC013; tested at 600°C in air, with a dwell load of 29 kN, an overload factor of 1.05 and a dwell time of 1,200 seconds. Each image shows the crack propagating from bottom left to top right. Note that this test piece is sourced from Phase Two, Batch Two material and was found to comprise notably smaller grain sizes including regions of ultra fine grain sized clusters. The band labelled A is the precrack region, which was undertaken at temperature and in air; bands B and E represent baseline (1-1-1-1) regions, band C the dwell region and band D the overload region. Note that crack growth mechanisms are mixed under baseline conditions, thought to occur due to the ultra fine grain microstructure of the material. Under higher crack growth driving forces it could be suggested that the mechanism is more intergranular when compared with mechanisms under lower crack growth driving forces (B compared with E). Note also that fracture surfaces pertaining to dwell and overload cycling appear rough and intergranular. Higher magnification images are taken at points relating to the following crack growth driving forces (ΔK): B: ~20 MPa√m; C: ~27.5 MPa√m; D: ~40 MPa√m; E: ~55 MPa√m


E
D
C
B
A
1.00mm


B - Baseline
20.0µm


C - Dwell
20.0µm


D - Overload
20.0µm

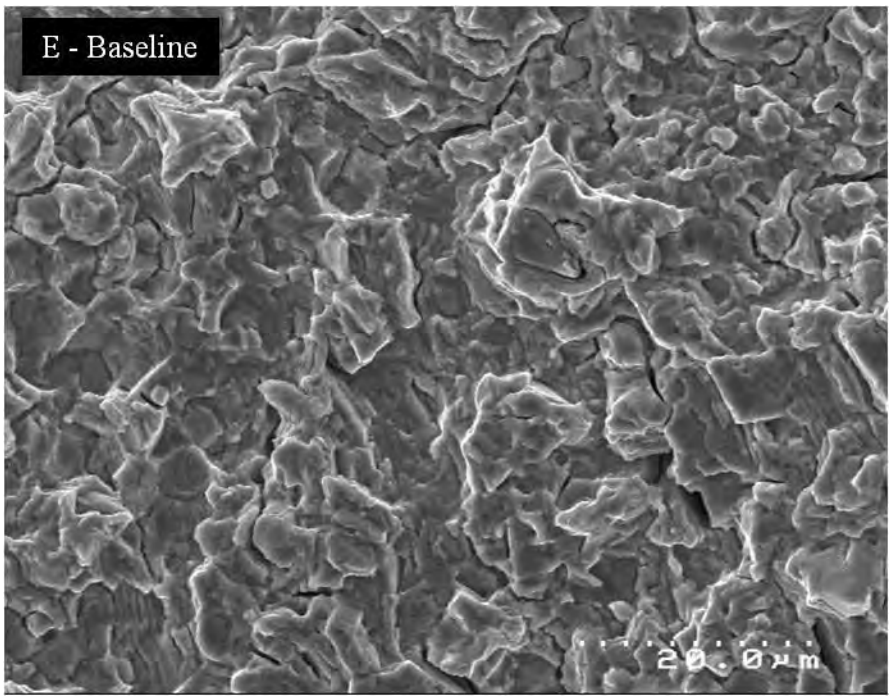
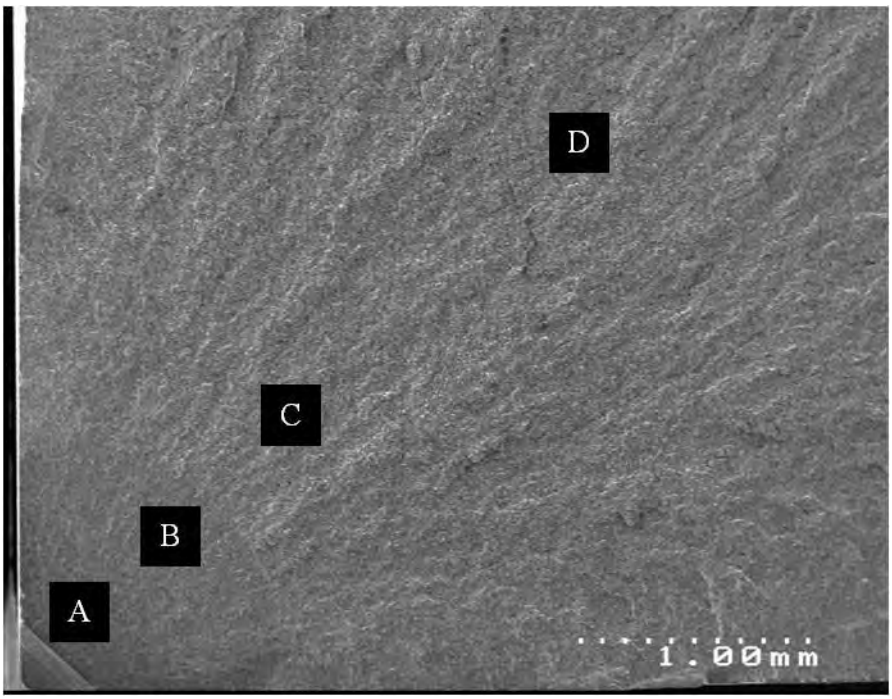
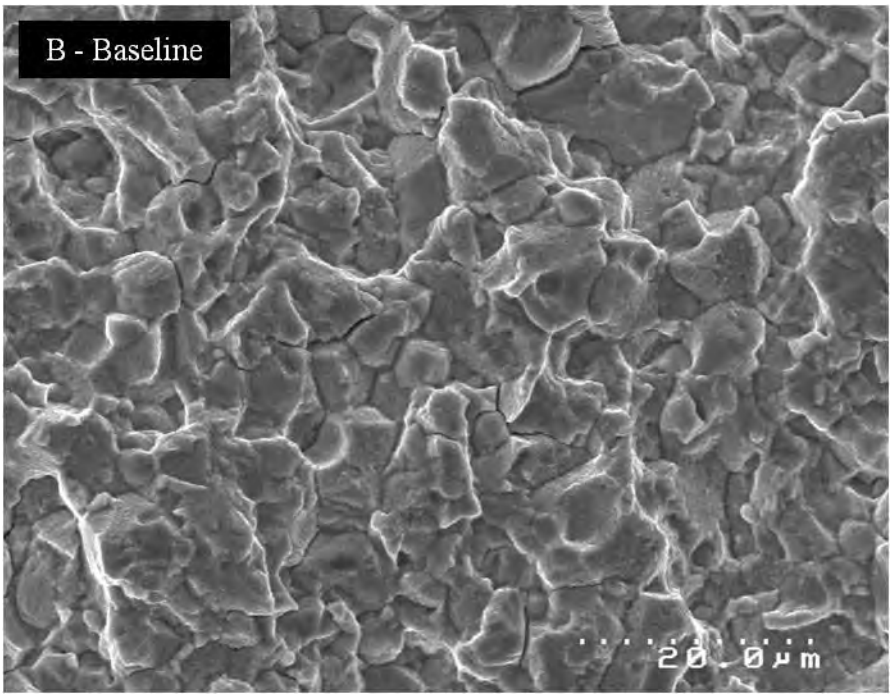
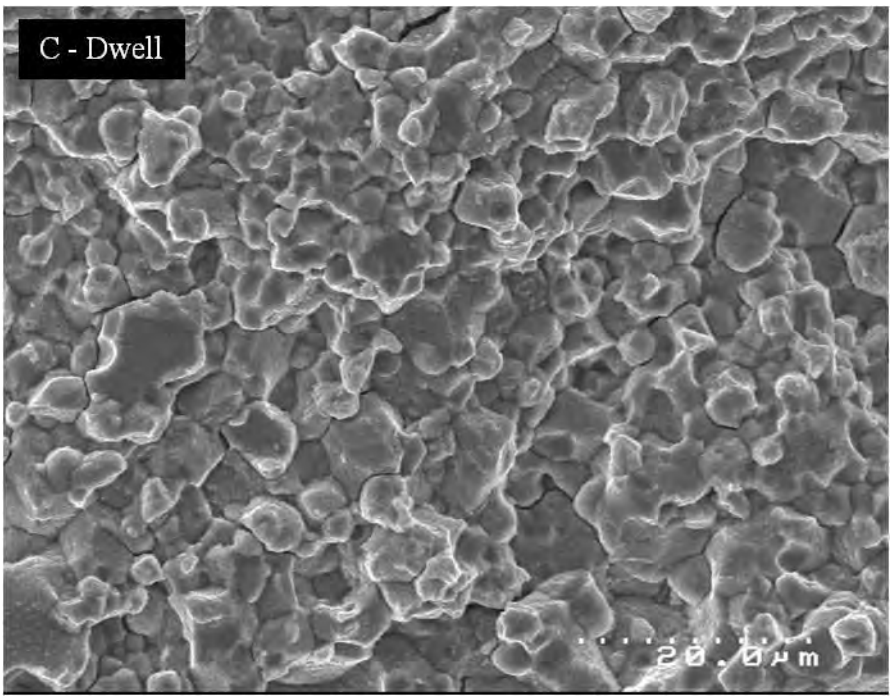


Figure A-55: Showing fractographs of fine-grained Udimet 720Li test piece CC014; tested at 600°C in air, with a dwell load of 29 kN, an overload factor of 1.05 and a dwell time of 3,600 seconds. Each image shows the crack propagating from bottom left to top right. Note that this test piece is sourced from Phase Two, Batch Two material and was found to comprise notably smaller grain sizes including regions of ultra fine grain sized clusters. The band labelled A is the precrack region, which was undertaken at temperature and in air; bands B and E represent baseline (1-1-1-1) regions, band C the dwell region and band D the overload region. Note that crack growth mechanisms are mixed under baseline conditions, thought to occur due to the ultra fine grain microstructure of the material. Under higher crack growth driving forces it could be suggested that the mechanism is more intergranular when compared with mechanisms under lower crack growth driving forces (B compared with E). Note also that fracture surfaces pertaining to dwell and overload cycling appear rough and intergranular. Higher magnification images are taken at points relating to the following crack growth driving forces (ΔK): B: ~22.5 MPa√m; C: ~30 MPa√m; D: ~40 MPa√m; E: ~55 MPa√m


D
C
B
A
1.00mm


B - Baseline
20.0µm


C - Dwell
20.0µm

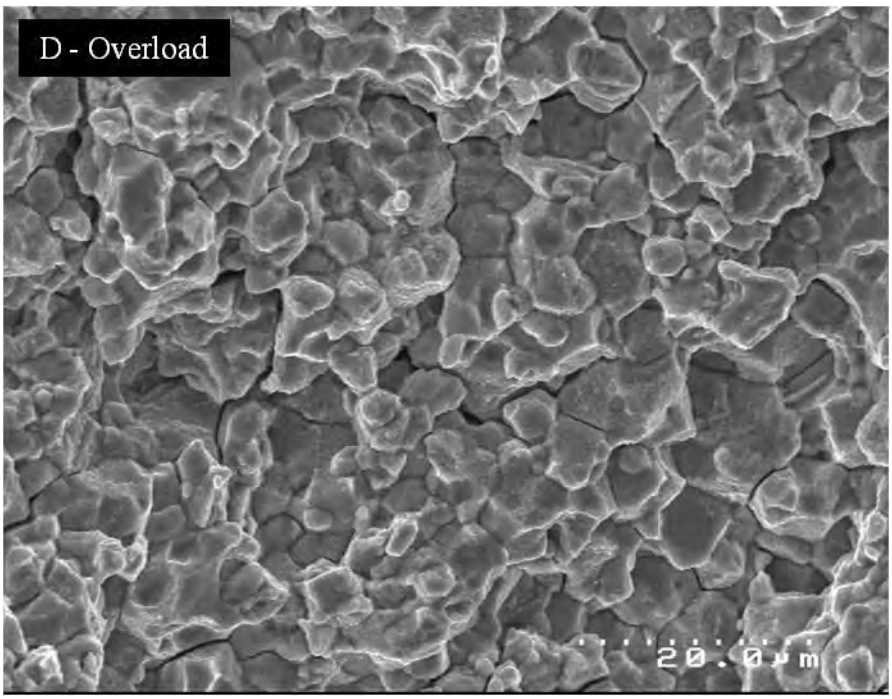
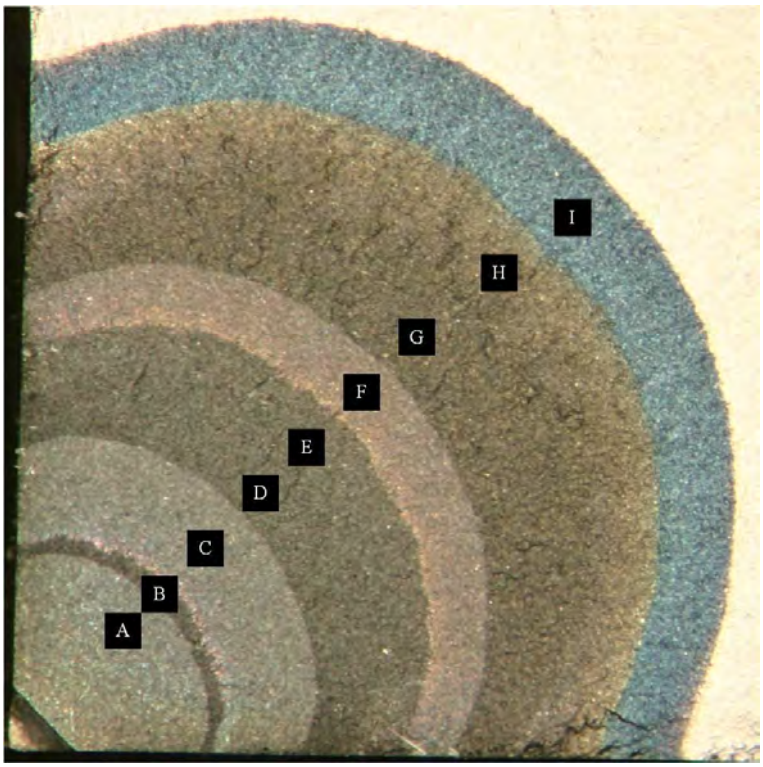
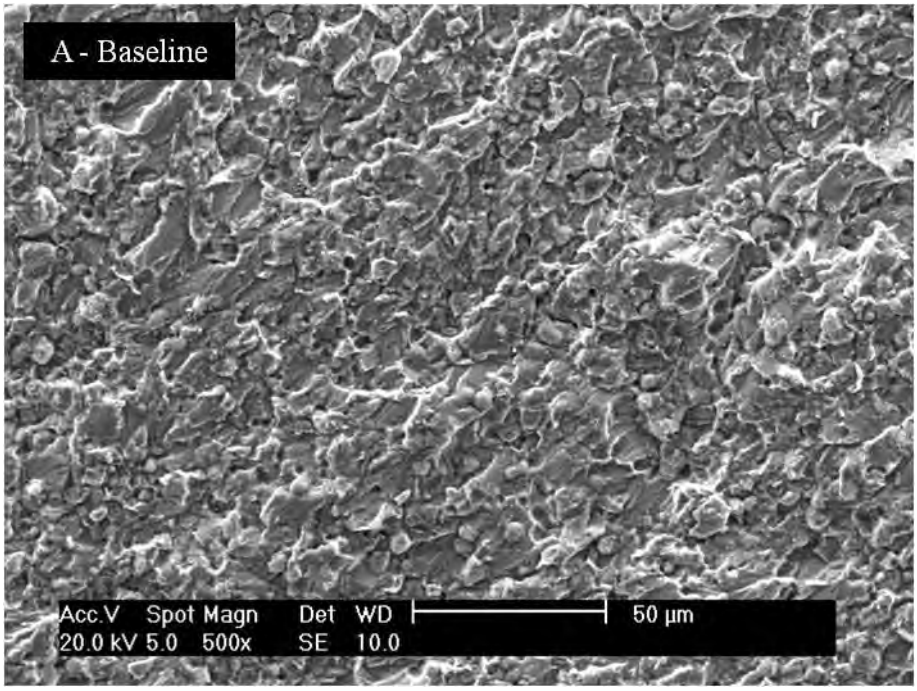
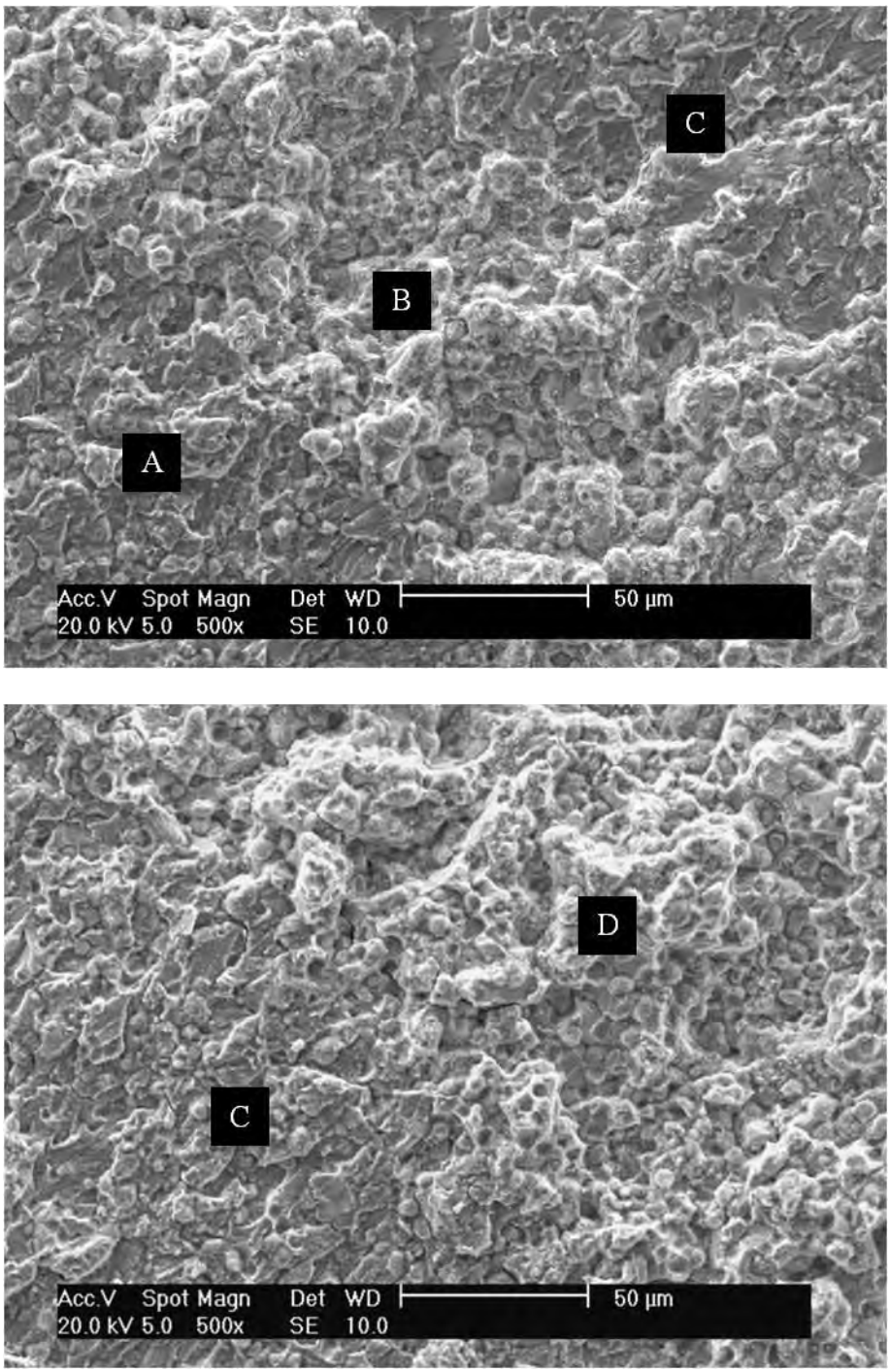
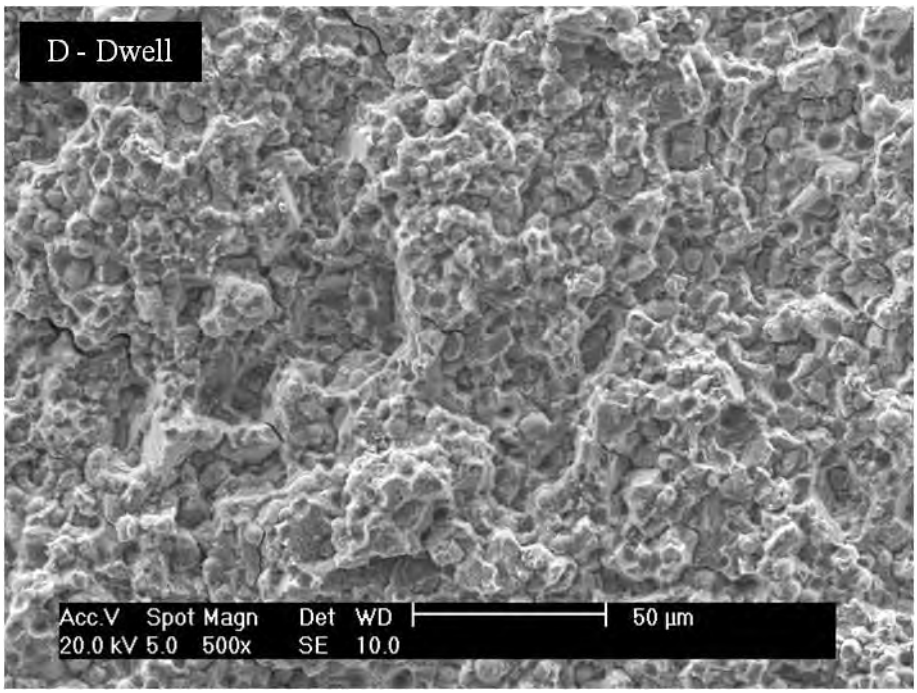


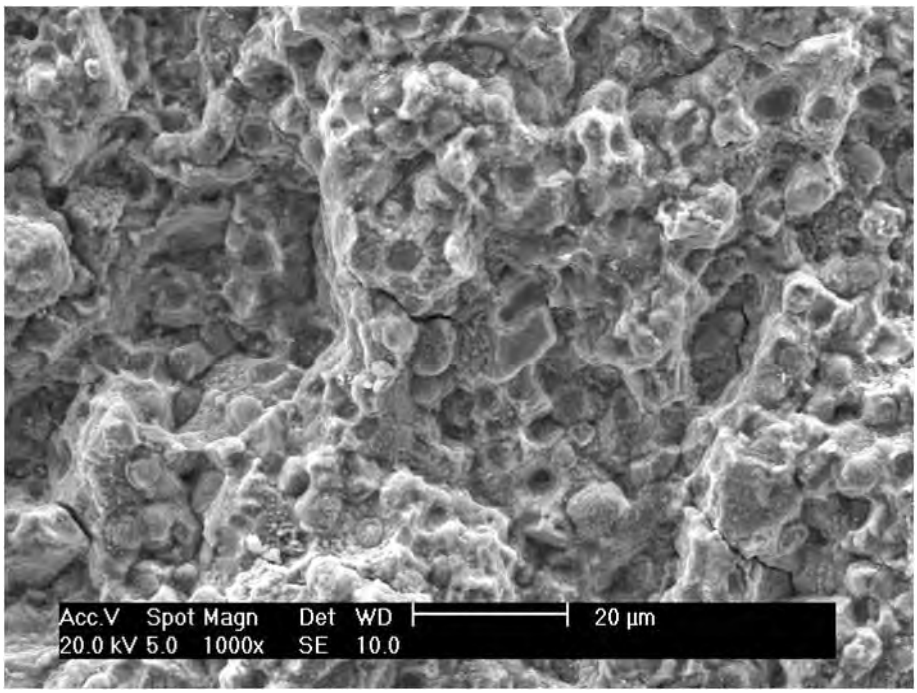
Figure A-56: Showing fractographs of fine-grained Udimet 720Li test piece CC015; tested at 650°C in air, with a dwell load of 26 kN, an overload factor of 1.15 and a dwell time of 3,600 seconds. Each image shows the crack propagating from bottom left to top right. Note that this test piece is sourced from Phase Two, Batch Two material and was found to comprise notably smaller grain sizes including regions of ultra fine grain sized clusters. The band labelled A is the precrack region, which was undertaken at temperature and in air; band B represents the baseline (1-1-1-1) region, band C the dwell region and band D the overload region. Note that crack growth mechanisms are mixed under baseline conditions, thought to occur due to the ultra fine grain microstructure of the material. Note also that fracture surfaces pertaining to dwell and overload cycling appear rough and intergranular. Higher magnification images are taken at points relating to the following crack growth driving forces (ΔK):
B: ~22.5 MPa√m; C: ~30 MPa√m; D: ~40 MPa√m; E: ~55 MPa√m

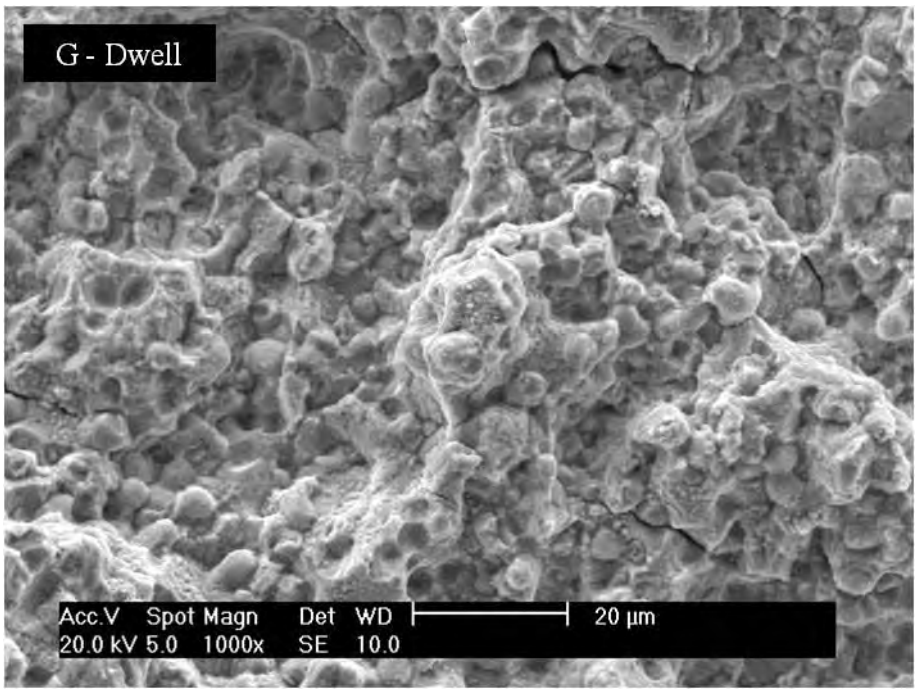

I
H
G
F
E
D
C
B
A

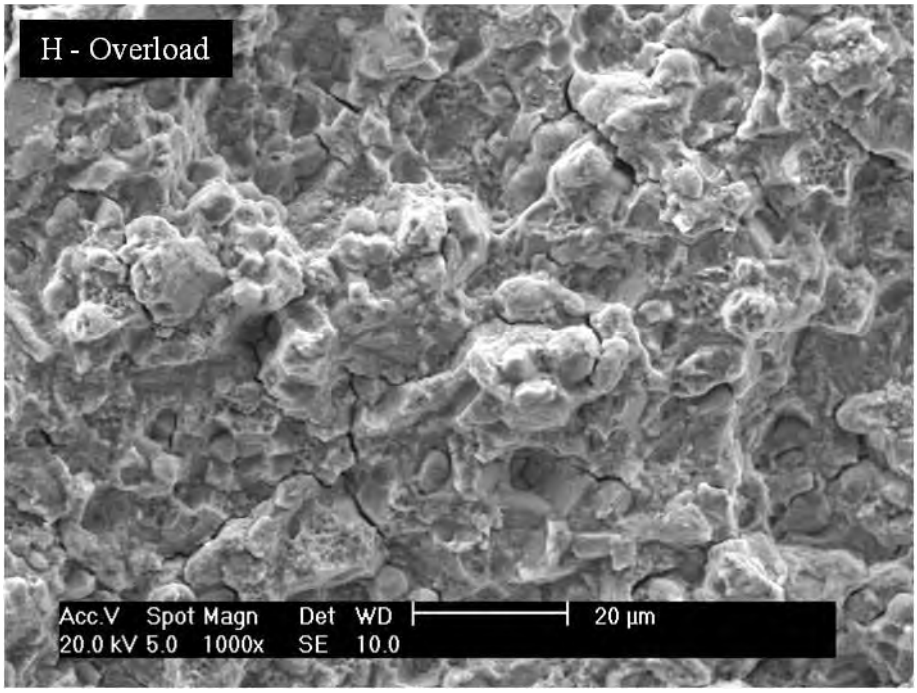

A - Baseline
Acc.V Spot Magn Det WD 50 µm
20.0 kV 5.0 500x SE 10.0


C
B
A
Acc.V Spot Magn Det WD 50 µm
20.0 kV 5.0 500x SE 10.0
D
C
Acc.V Spot Magn Det WD 50 µm
20.0 kV 5.0 500x SE 10.0


D - Dwell
Acc.V Spot Magn Det WD 50 µm
20.0 kV 5.0 500x SE 10.0


Acc.V Spot Magn Det WD 20 µm
20.0 kV 5.0 1000x SE 10.0


G - Dwell
Acc.V Spot Magn Det WD 20 µm
20.0 kV 5.0 1000x SE 10.0


H - Overload
Acc.V Spot Magn Det WD 20 µm
20.0 kV 5.0 1000x SE 10.0

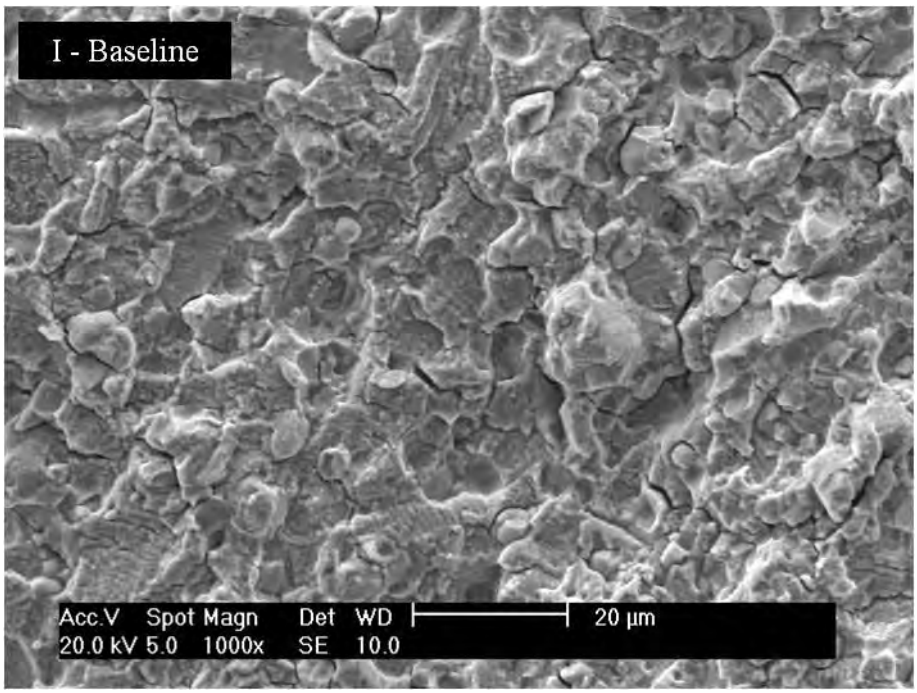
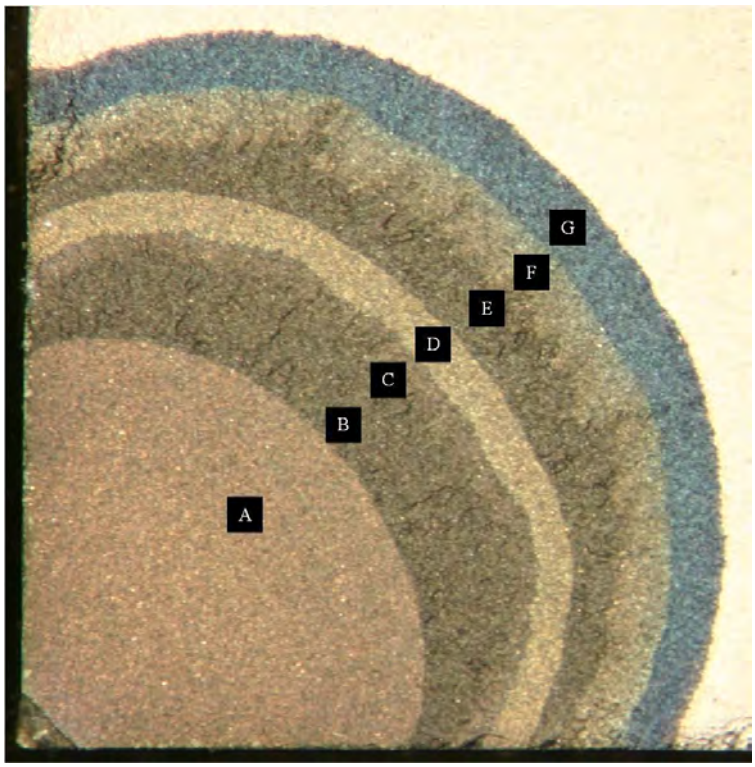
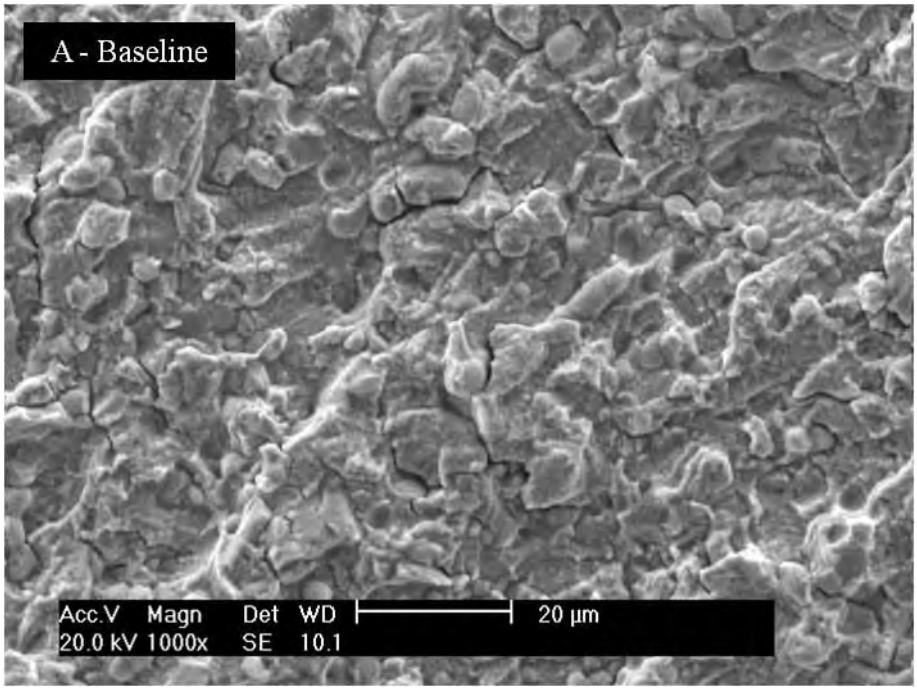
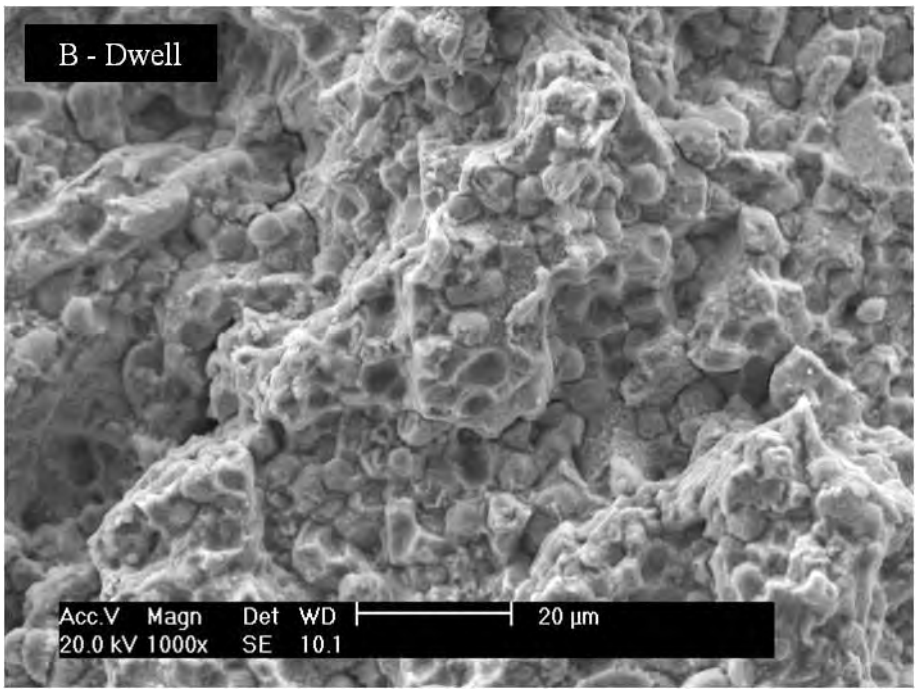
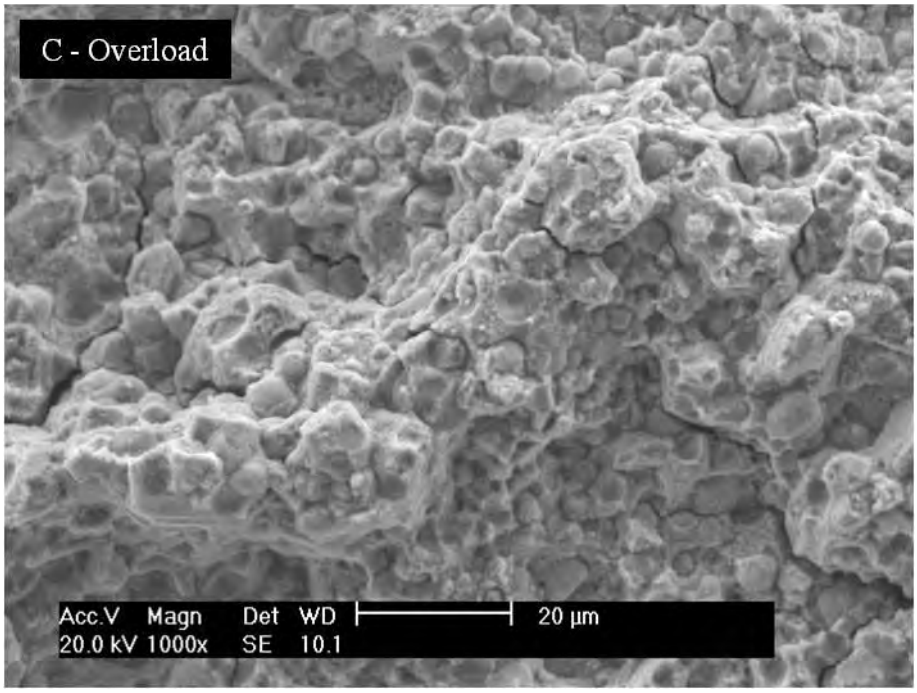


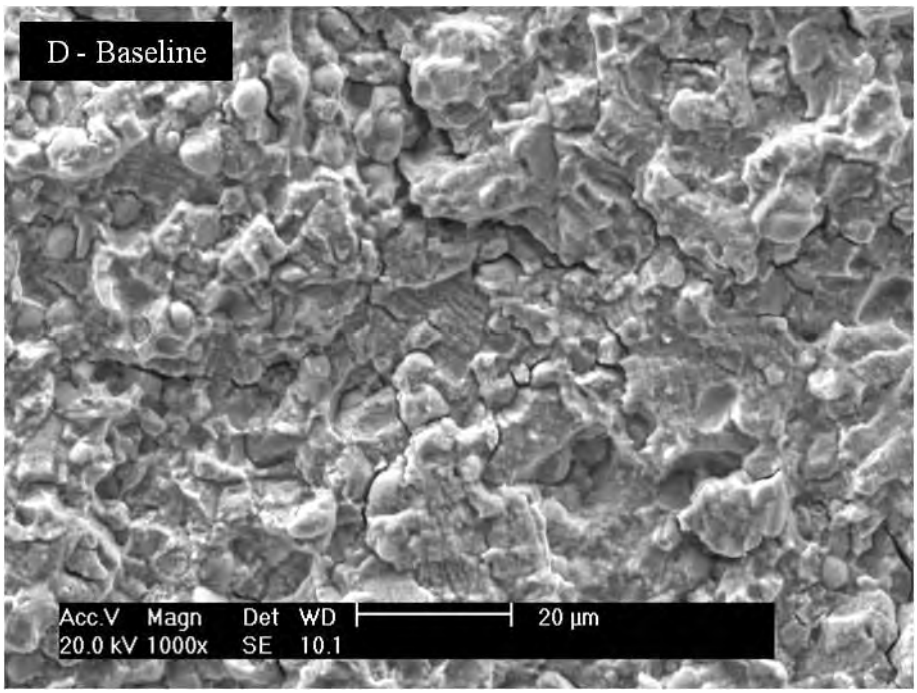
Figure A-57: Showing fractographs of fine-grained Udimet 720Li test piece CC003; tested at 650°C in air, with a dwell load of 26 kN, an overload factor of 1.15 and a dwell time of 3,600 seconds. Each image shows the crack propagating from bottom left to top right. Note that two sets of baseline, dwell and overload loading has been applied to the test piece. Bands labelled A, C, F and I are baseline (1-1-1-1) regions, bands labelled B, D and G are dwell regions and bands labelled E and H; the overload regions. Higher magnification images are taken at points relating to the following crack growth driving forces (ΔK): A: ~18 MPa√m; B: ~19.5 MPa√m; transition from C to D: ~26 MPa√m; D: ~28 MPa√m; E: ~30 MPa√m; G: ~39 MPa√m; H: ~45 MPa√m; I: ~52.5 MPa√m

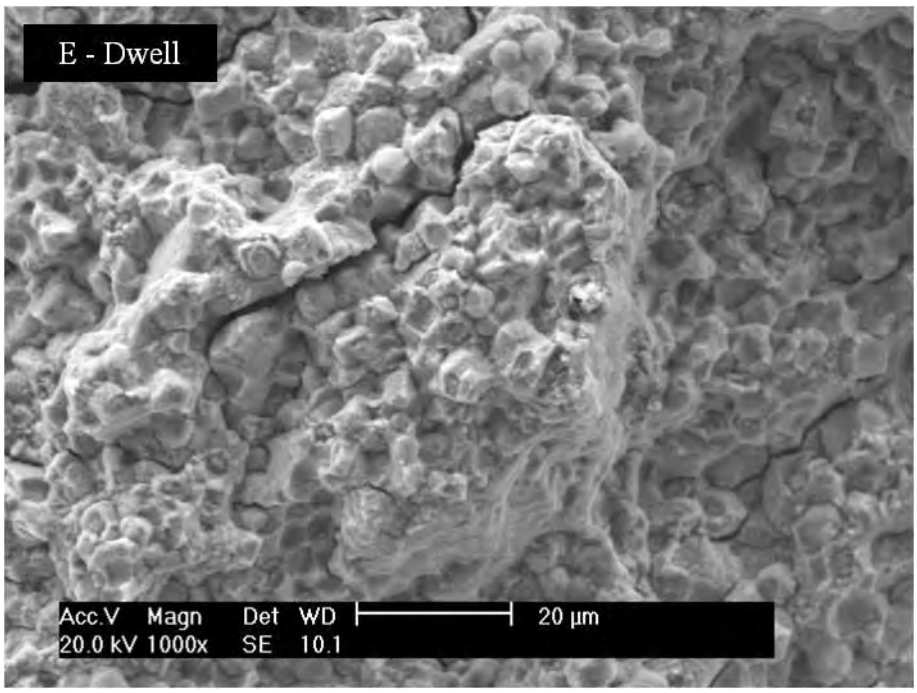

G
F
E
D
C
B
A


A - Baseline
Acc.V Magn Det WD
20.0 kV 1000x SE 10.1
20 µm


B - Dwell
Acc.V Magn Det WD 20 µm
20.0 kV 1000x SE 10.1


C - Overload
Acc.V Magn Det WD 20 µm
20.0 kV 1000x SE 10.1


D - Baseline
Acc.V Magn Det WD 20 µm
20.0 kV 1000x SE 10.1


E - Dwell
Acc.V Magn Det WD 20 µm
20.0 kV 1000x SE 10.1

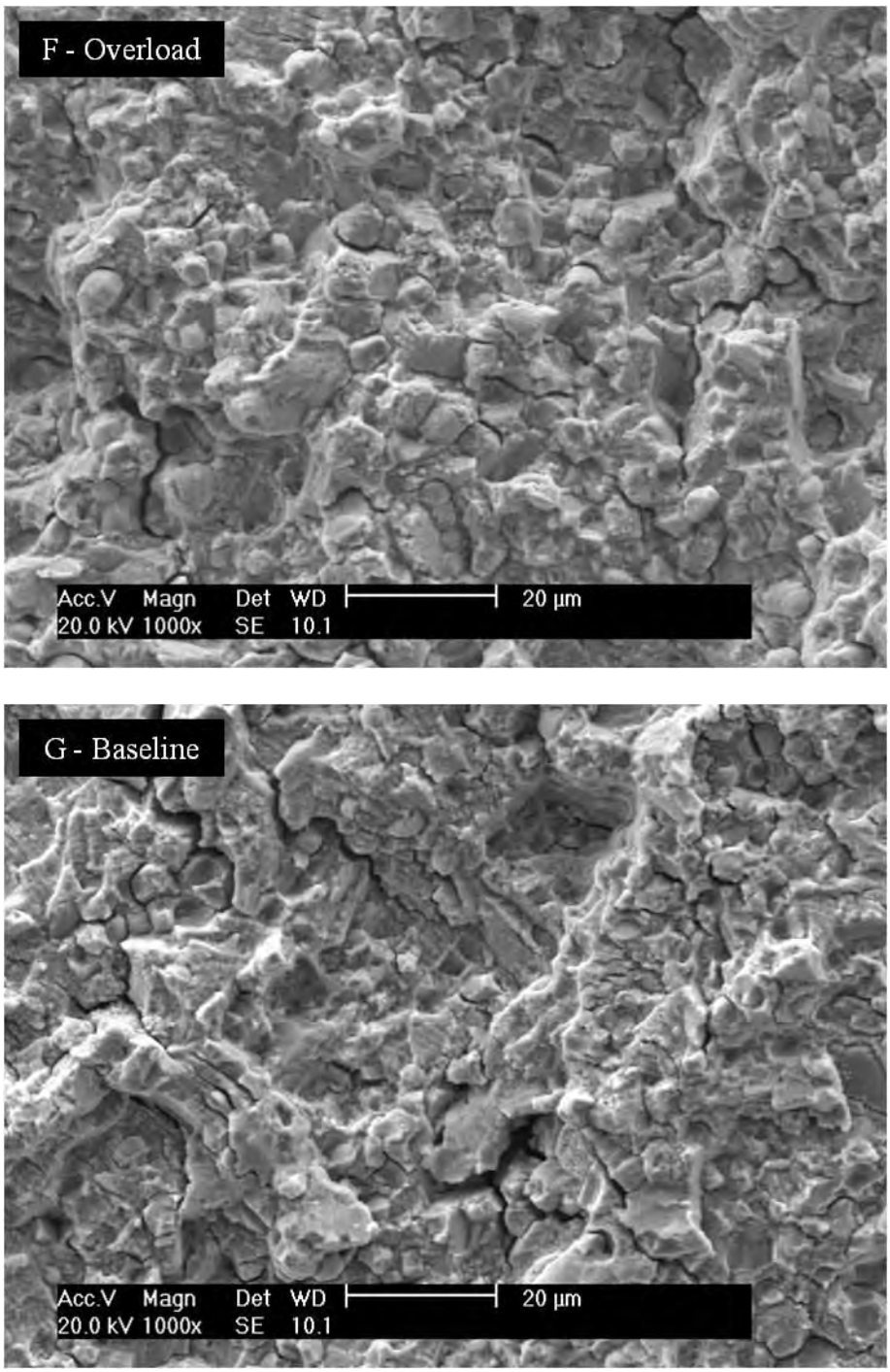
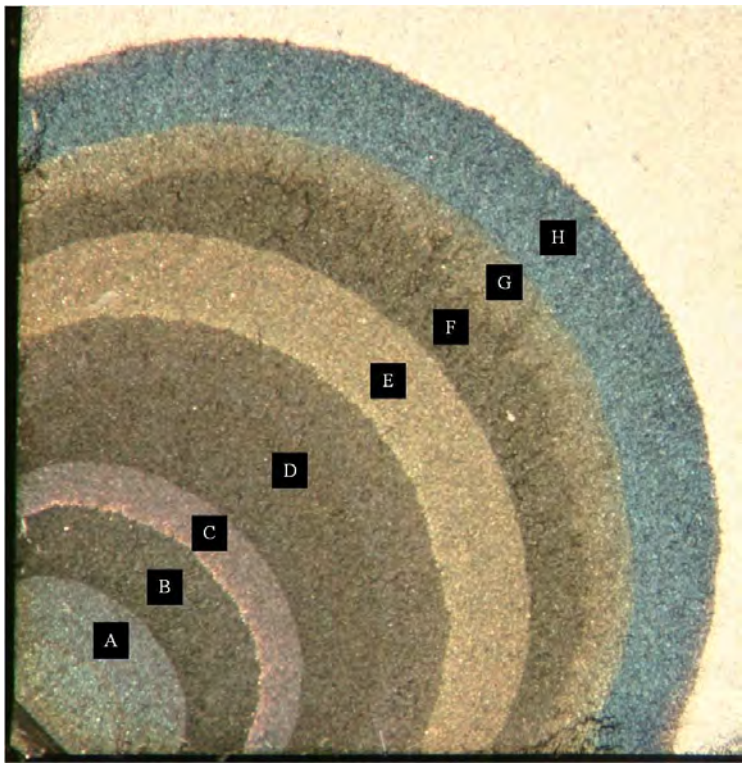
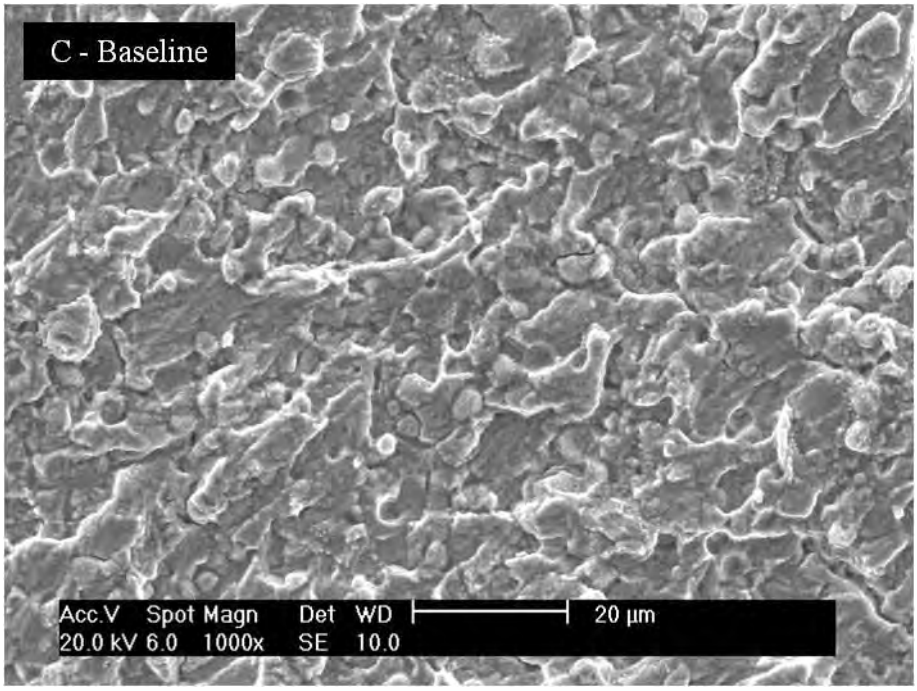
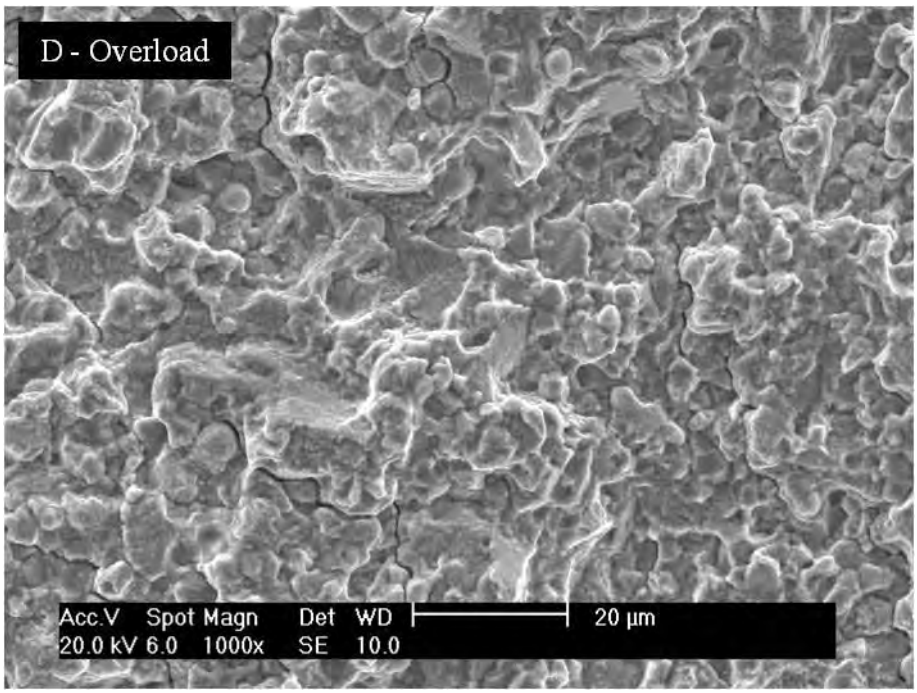
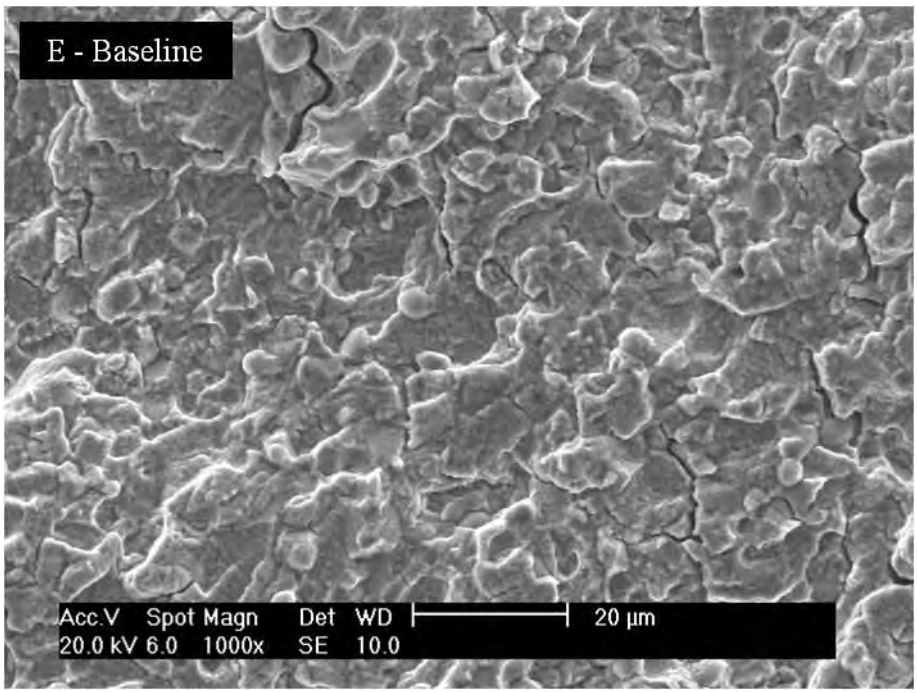


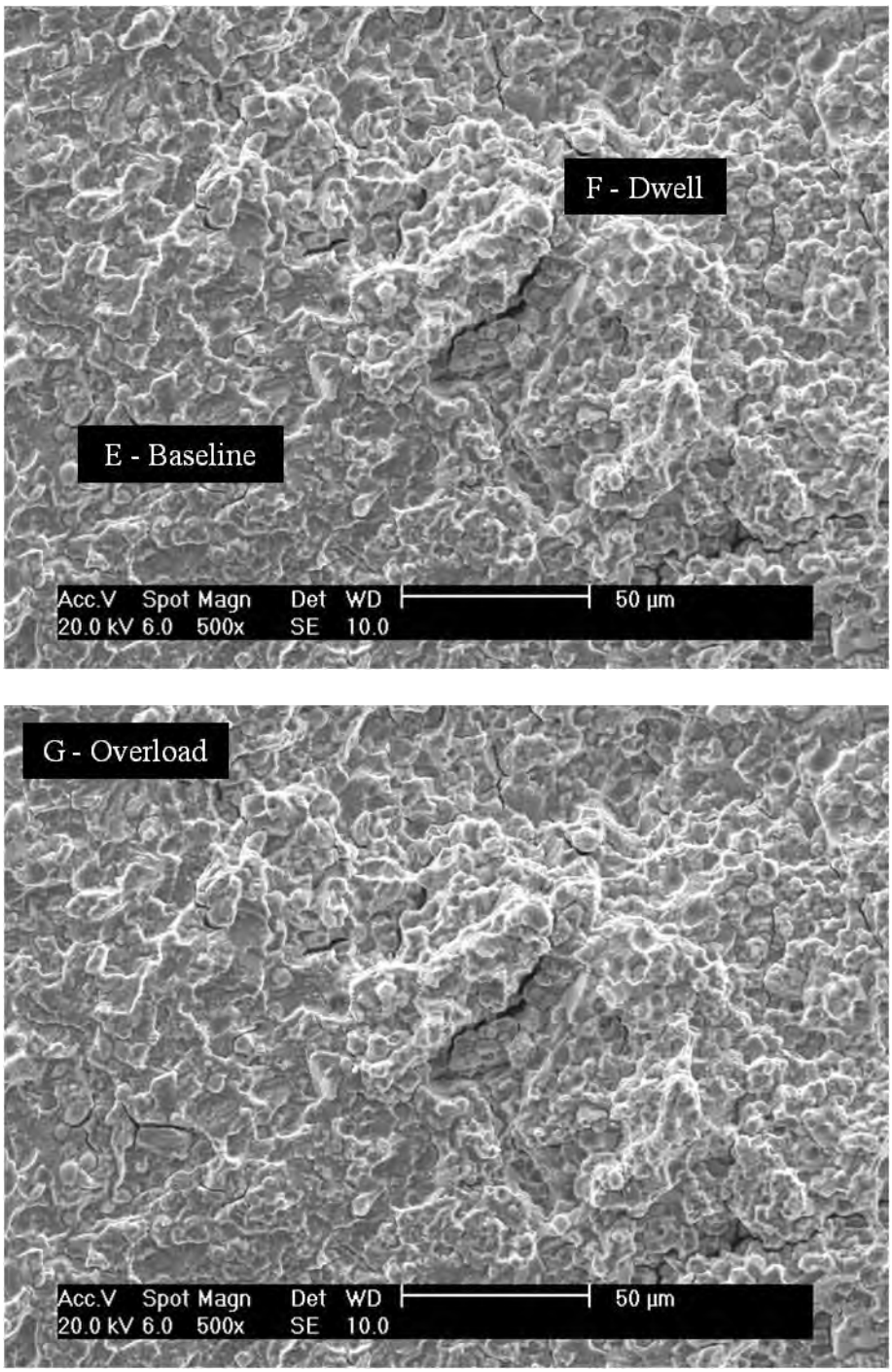
Figure A-58: Showing fractographs of fine-grained Udimet 720Li test piece CC004; tested at 650°C in air, with a dwell load of 26 kN, an overload factor of 1.15 and a dwell time of 1,200 seconds. Each image shows the crack propagating from bottom left to top right. Note that two sets of baseline, dwell and overload loading has been applied to the test piece. Bands labelled A, D and G are baseline (1-1-1-1) regions, bands labelled B and E are dwell regions and bands labelled C and F; the overload regions. Note that crack growth mechanisms are partially intergranular under baseline loading. Higher magnification images are taken at points relating to the following crack growth driving forces (ΔK): A: ~27 MPa√m; B: ~34 MPa√m; C: ~38 MPa√m; D: ~40 MPa√m; E: ~42.5 MPa√m; F: ~47 MPa√m; G: ~52.5 MPa√m


H
G
F
E
D
C
B
A


C - Baseline
Acc.V Spot Magn Det WD 20 µm
20.0 kV 6.0 1000x SE 10.0


D - Overload
Acc.V Spot Magn Det WD 20 µm
20.0 kV 6.0 1000x SE 10.0


E - Baseline
Acc.V Spot Magn Det WD 20 µm
20.0 kV 6.0 1000x SE 10.0


F - Dwell
E - Baseline
Acc.V Spot Magn Det WD 50 µm
20.0 kV 6.0 500x SE 10.0
G - Overload
Acc.V Spot Magn Det WD 50 µm
20.0 kV 6.0 500x SE 10.0

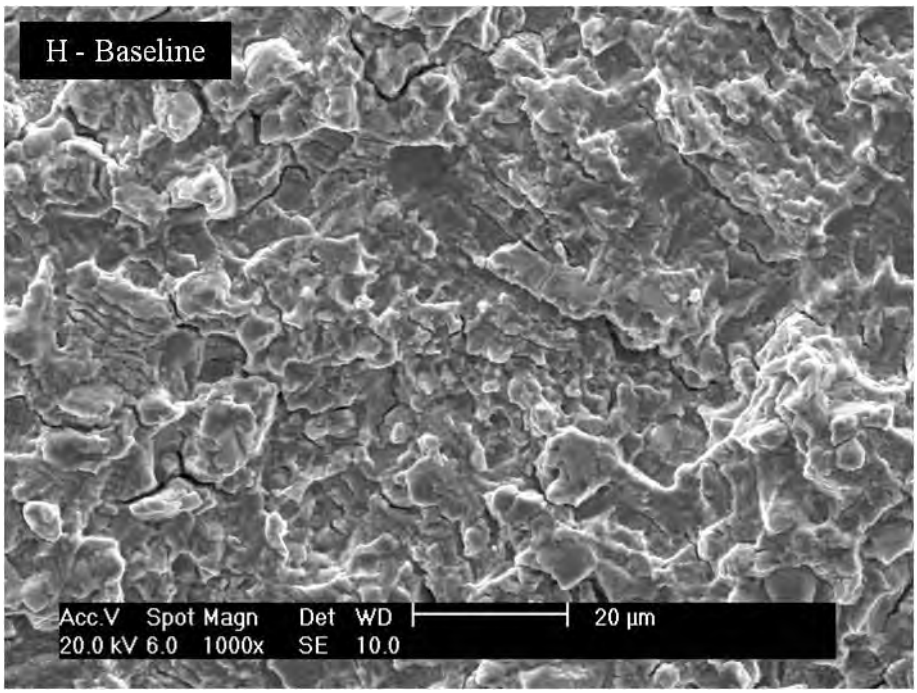
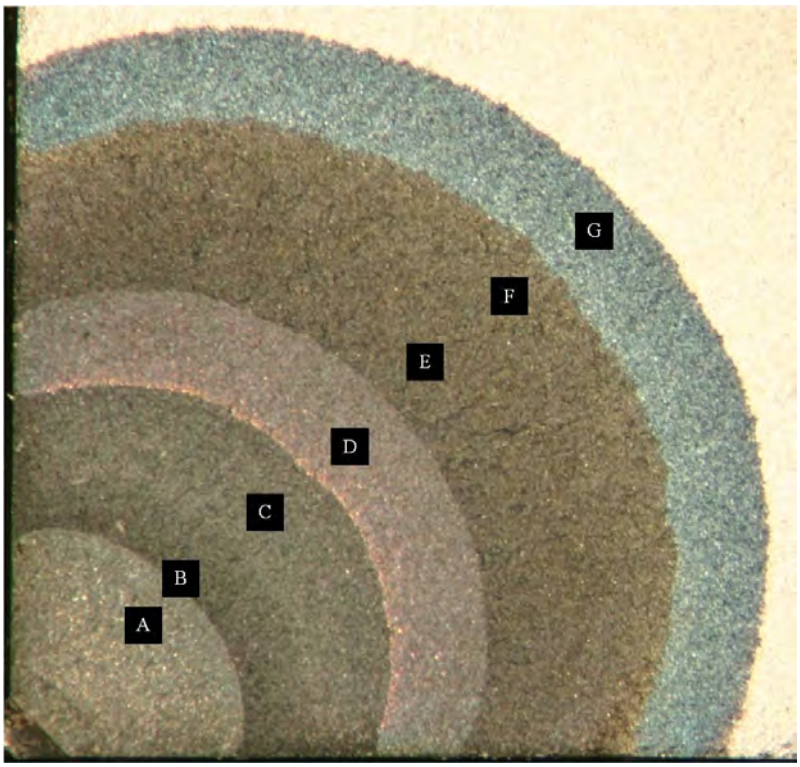
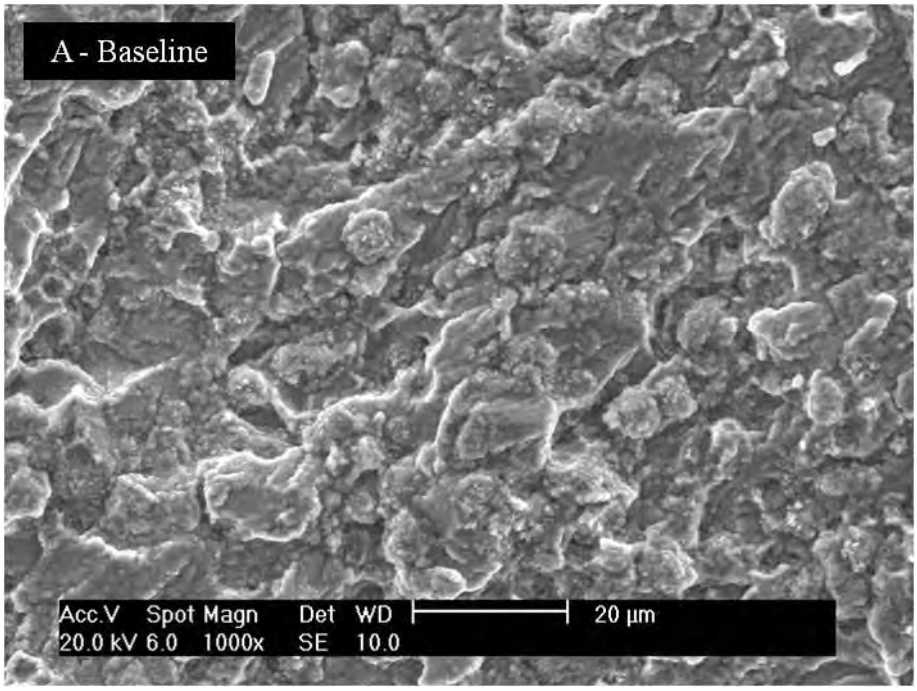
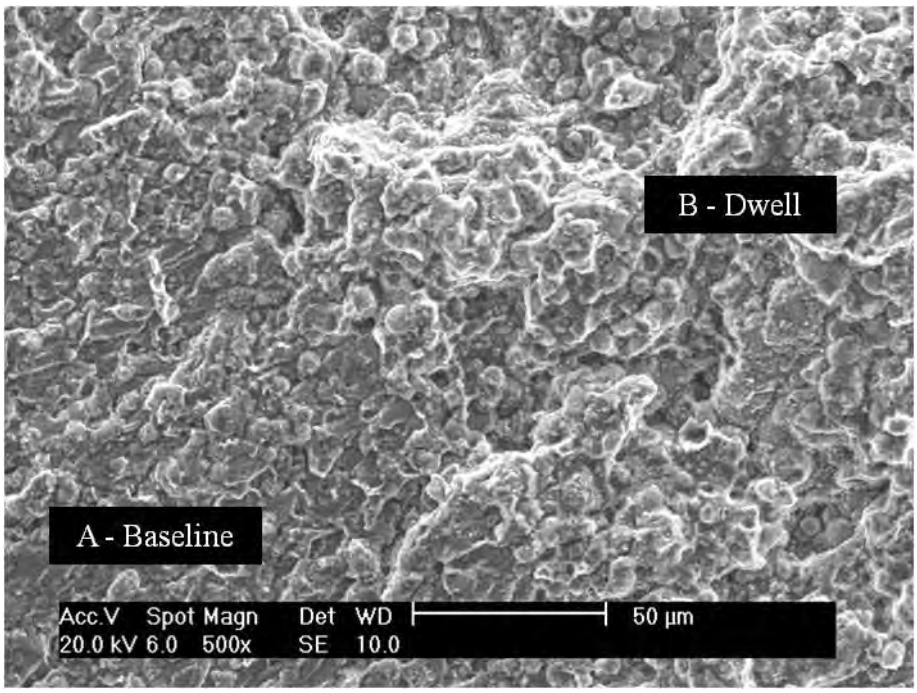
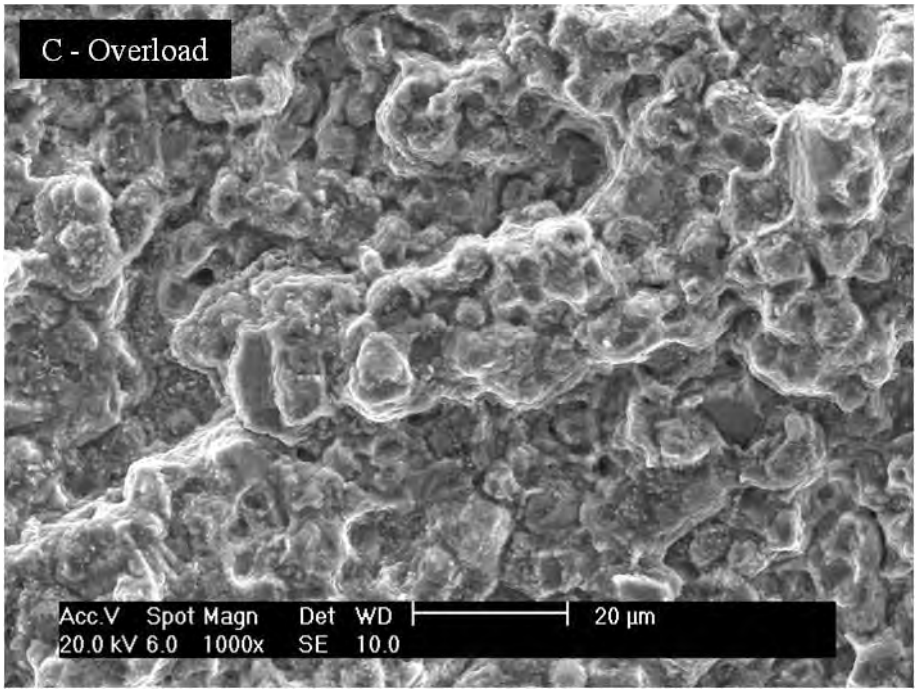


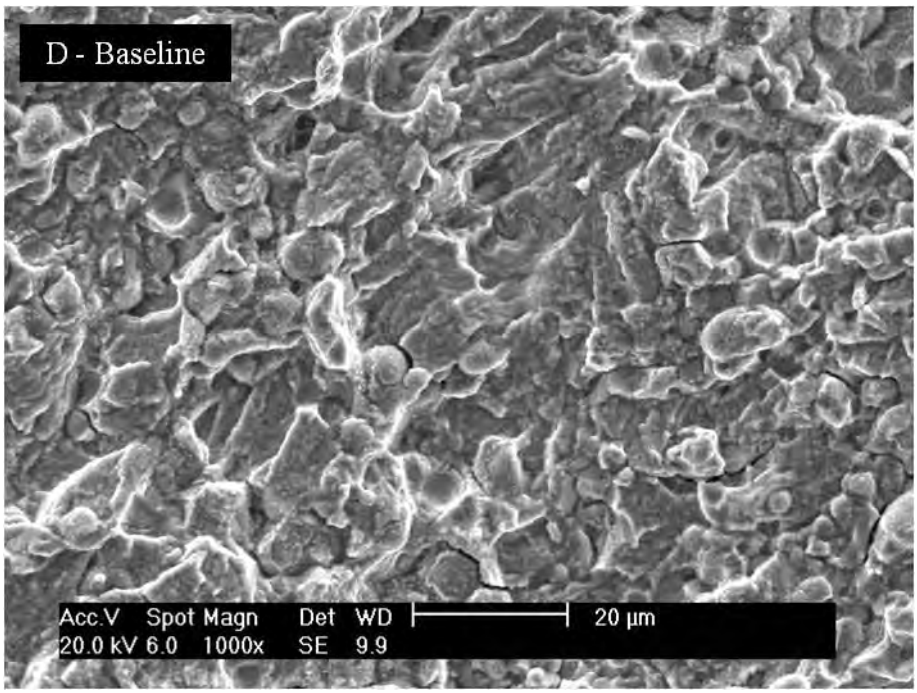
Figure A-59: Showing fractographs of fine-grained Udimet 720Li test piece CC007; tested at 650°C in air, with a dwell load of 26 kN, an overload factor of 1.15 and a dwell time of 1,200 seconds. Each image shows the crack propagating from bottom left to top right. Note that two sets of baseline, dwell and overload loading has been applied to the test piece. Bands labelled A, C, E and H are baseline (1-1-1-1) regions, bands labelled B and F are dwell regions and bands labelled D and G; the overload regions. Note that crack growth mechanisms are partially intergranular under baseline loading. Higher magnification images are taken at points relating to the following crack growth driving forces (ΔK): C: ~25 MPa√m; D: ~31 MPa√m; E: ~39 MPa√m; transition from E to F: ~44 MPa√m; G: ~48 MPa√m; H: ~57 MPa√m

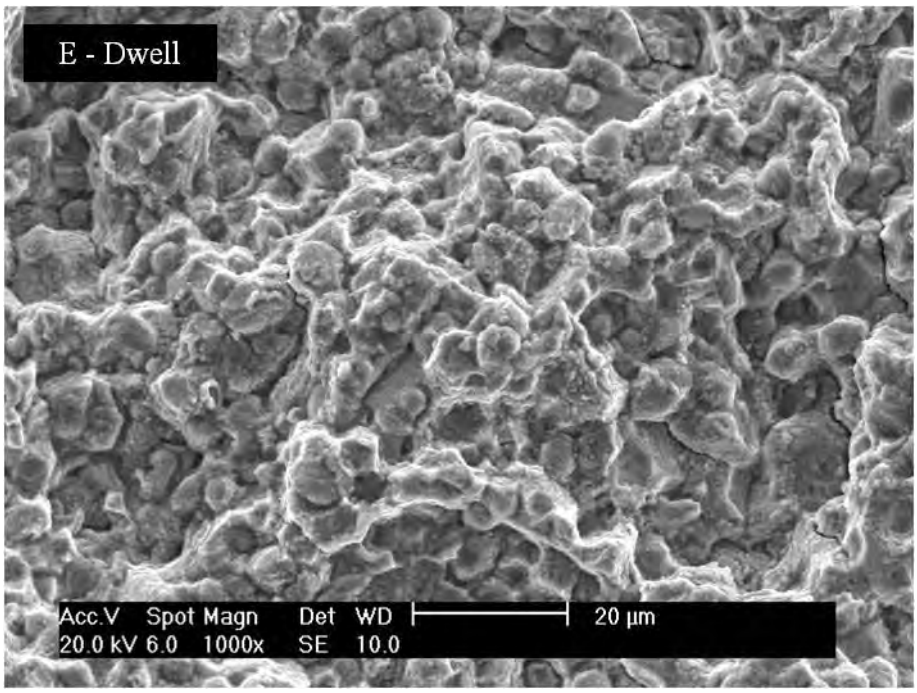

G
F
E
D
C
B
A


A - Baseline
Acc.V Spot Magn Det WD 20 µm
20.0 kV 6.0 1000x SE 10.0


B - Dwell
A - Baseline
Acc.V Spot Magn Det WD 50 µm
20.0 kV 6.0 500x SE 10.0


C - Overload
Acc.V Spot Magn Det WD 20 µm
20.0 kV 6.0 1000x SE 10.0


D - Baseline
Acc.V Spot Magn Det WD 20 µm
20.0 kV 6.0 1000x SE 9.9


E - Dwell
Acc.V Spot Magn Det WD 20 µm
20.0 kV 6.0 1000x SE 10.0

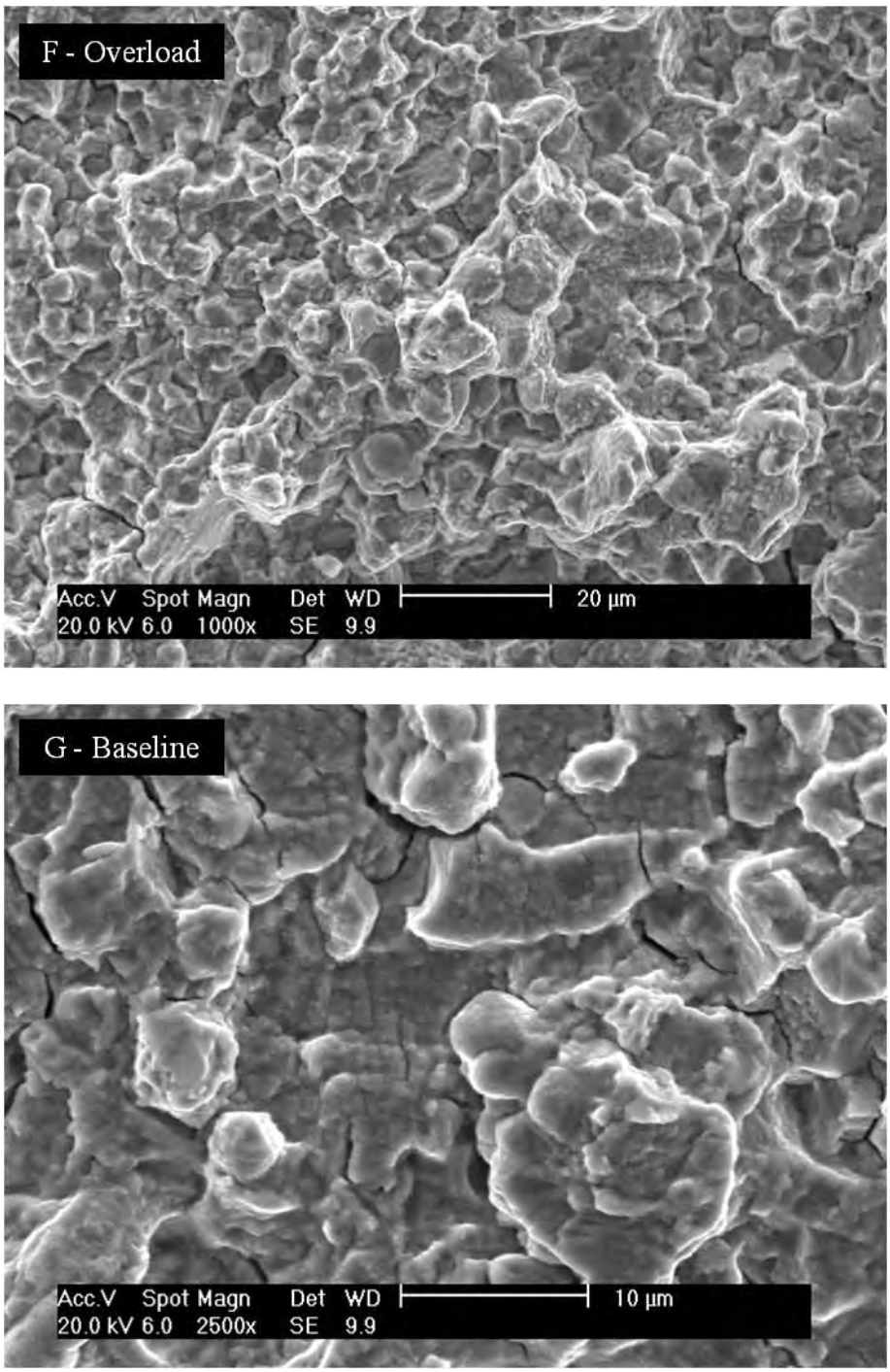
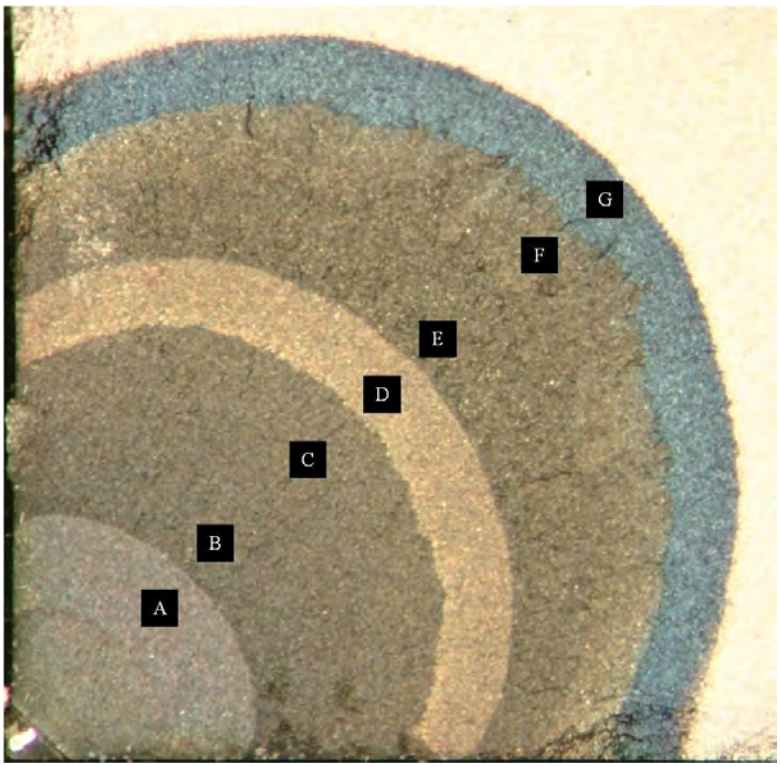
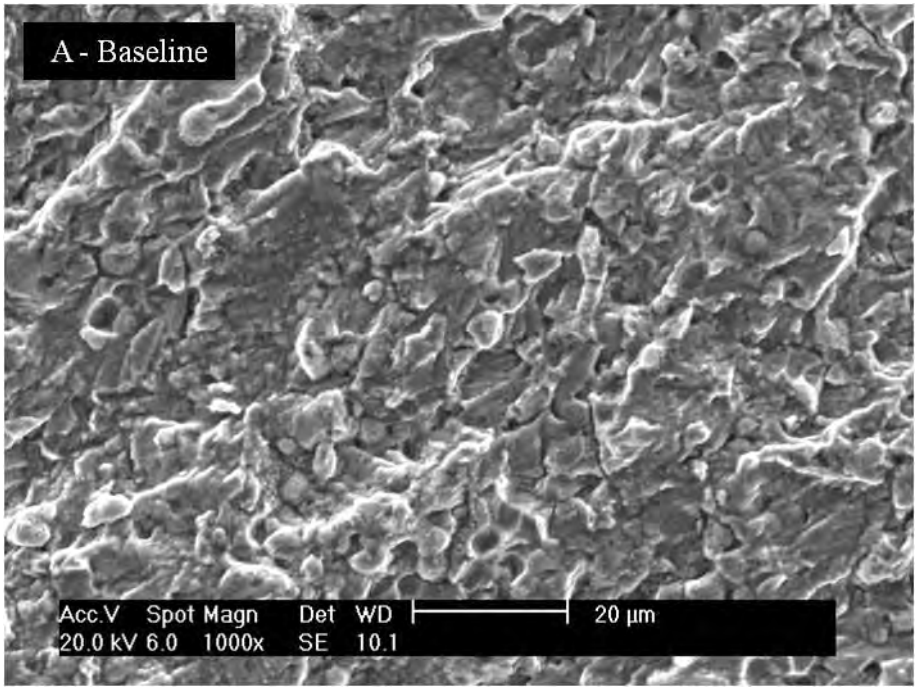
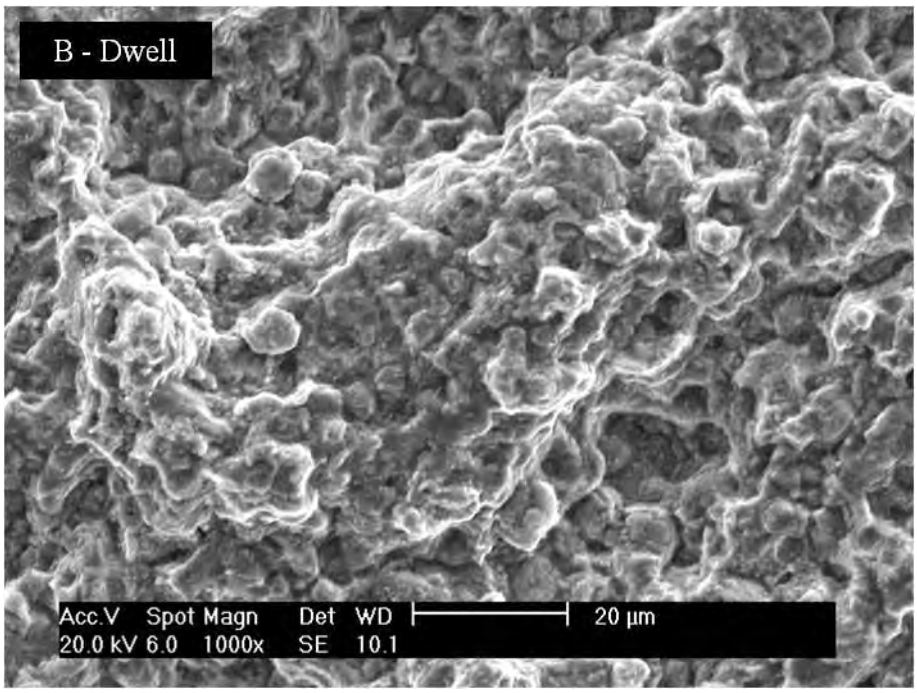
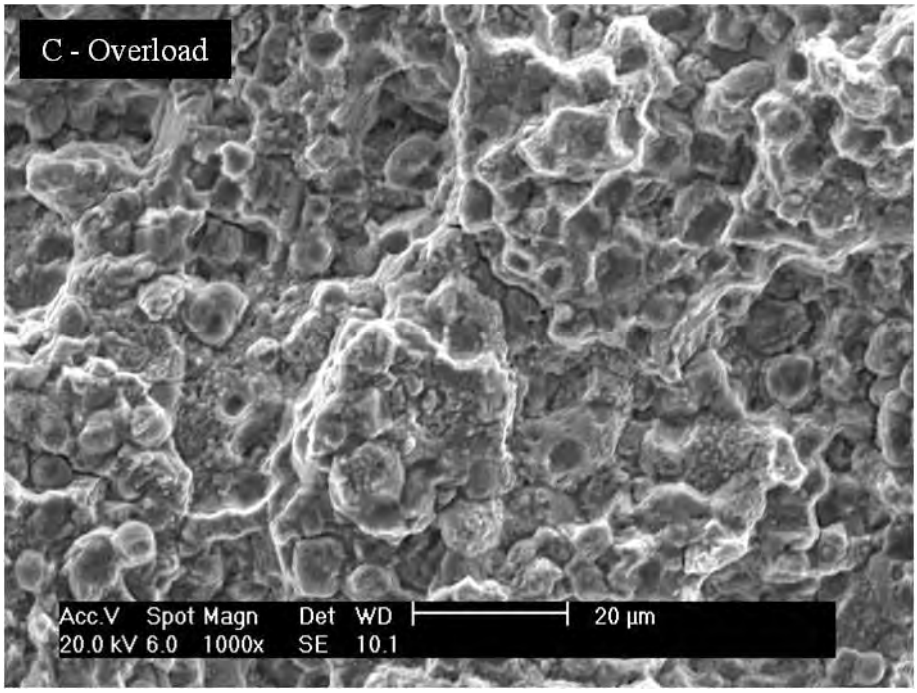


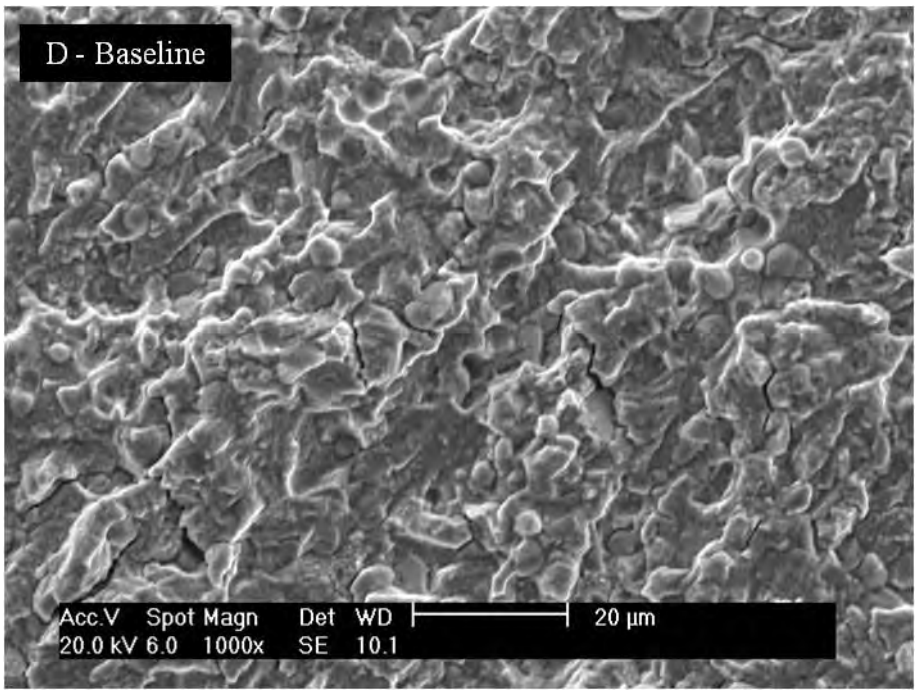
Figure A-60: Showing fractographs of fine-grained Udimet 720Li test piece CC008; tested at 675°C in air, with a dwell load of 22 kN, an overload factor of 1.10 and a dwell time of 1,200 seconds. Each image shows the crack propagating from bottom left to top right. Note that two sets of baseline, dwell and overload loading has been applied to the test piece. Bands labelled A, D and G are baseline (1-1-1-1) regions, bands labelled B and E are dwell regions and bands labelled C and F; the overload regions. Note that crack growth mechanisms are partially intergranular under baseline loading. Higher magnification images are taken at points relating to the following crack growth driving forces (ΔK): A: ~16 MPa√m; B: ~19 MPa√m; C: ~22.5 MPa√m; D: ~27.5 MPa√m; E: ~32.5 MPa√m; F: ~39 MPa√m; G: ~45 MPa√m

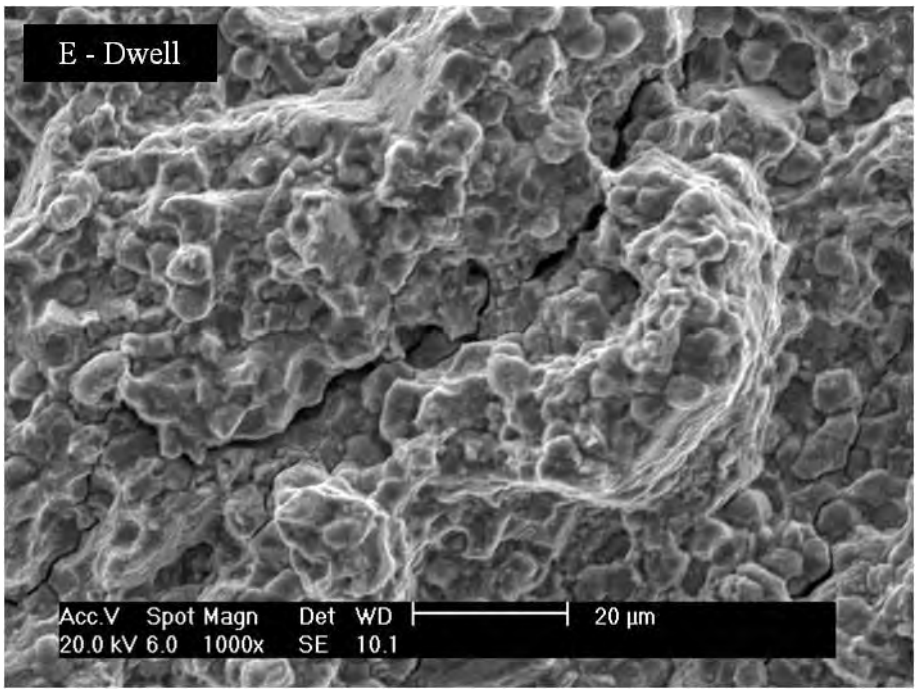

G
F
E
D
C
B
A


A - Baseline
Acc.V Spot Magn Det WD 20 µm
20.0 kV 6.0 1000x SE 10.1


B - Dwell
Acc.V Spot Magn Det WD 20 µm
20.0 kV 6.0 1000x SE 10.1


C - Overload
Acc.V Spot Magn Det WD 20 µm
20.0 kV 6.0 1000x SE 10.1


D - Baseline
Acc.V Spot Magn Det WD 20 µm
20.0 kV 6.0 1000x SE 10.1


E - Dwell
Acc.V Spot Magn Det WD 20 µm
20.0 kV 6.0 1000x SE 10.1

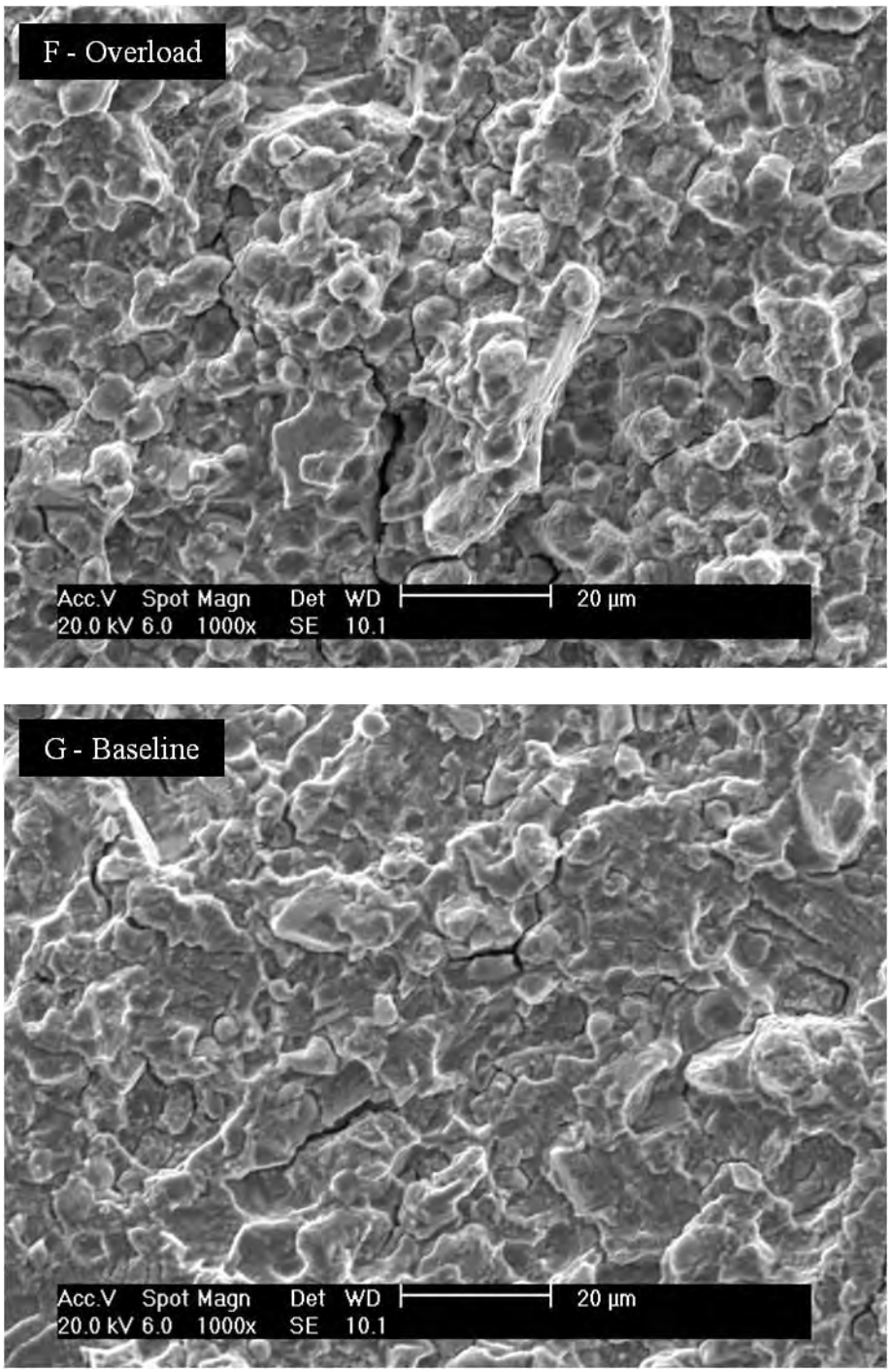
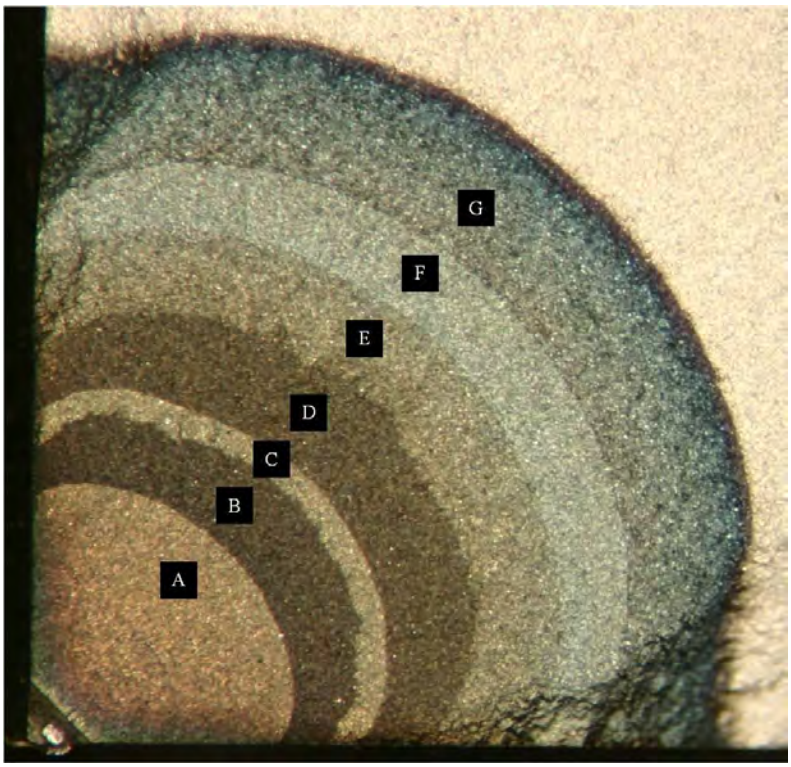
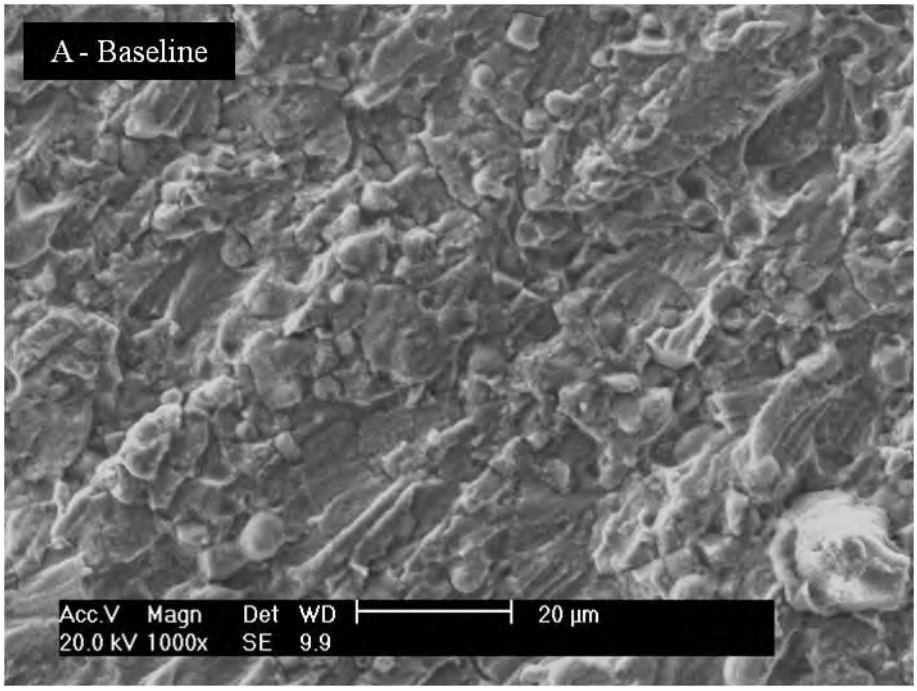
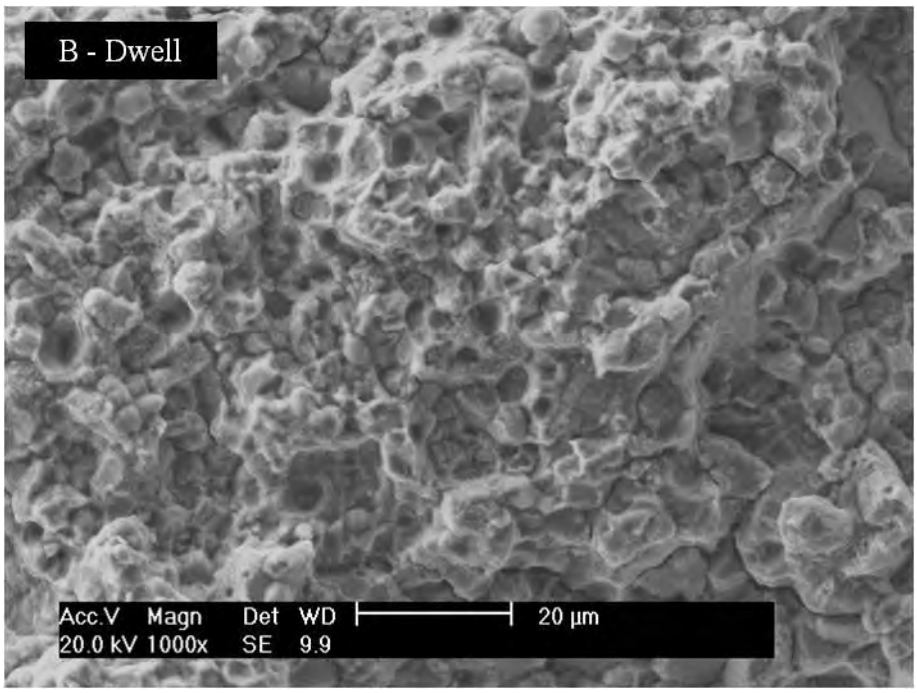
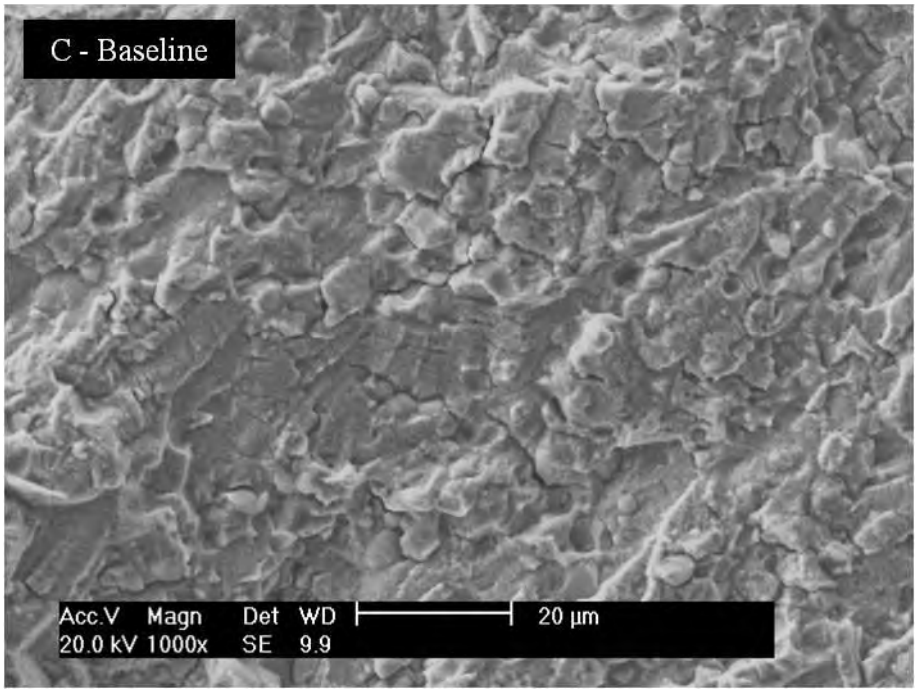


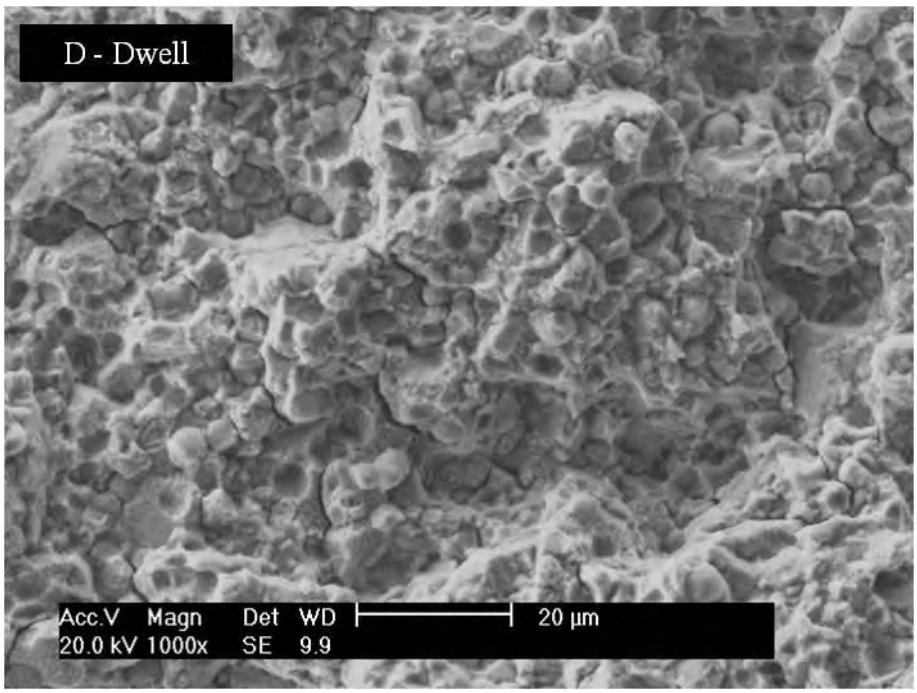
Figure A-61: Showing fractographs of fine-grained Udimet 720Li test piece CC010; tested at 650°C in air, with a dwell load of 26 kN, an overload factor of 1.08 and a dwell time of 1,200 seconds. Each image shows the crack propagating from bottom left to top right. Note that two sets of baseline, dwell and overload loading has been applied to the test piece. Bands labelled A, D and G are baseline (1-1-1-1) regions, bands labelled B and E are dwell regions and bands labelled C and F; the overload regions. Higher magnification images are taken at points relating to the following crack growth driving forces (ΔK): A: ~20 MPa√m; B: ~26 MPa√m; C: ~31 MPa√m; D: ~37 MPa√m; E: ~42 MPa√m; F: ~49 MPa√m; G: ~55 MPa√m

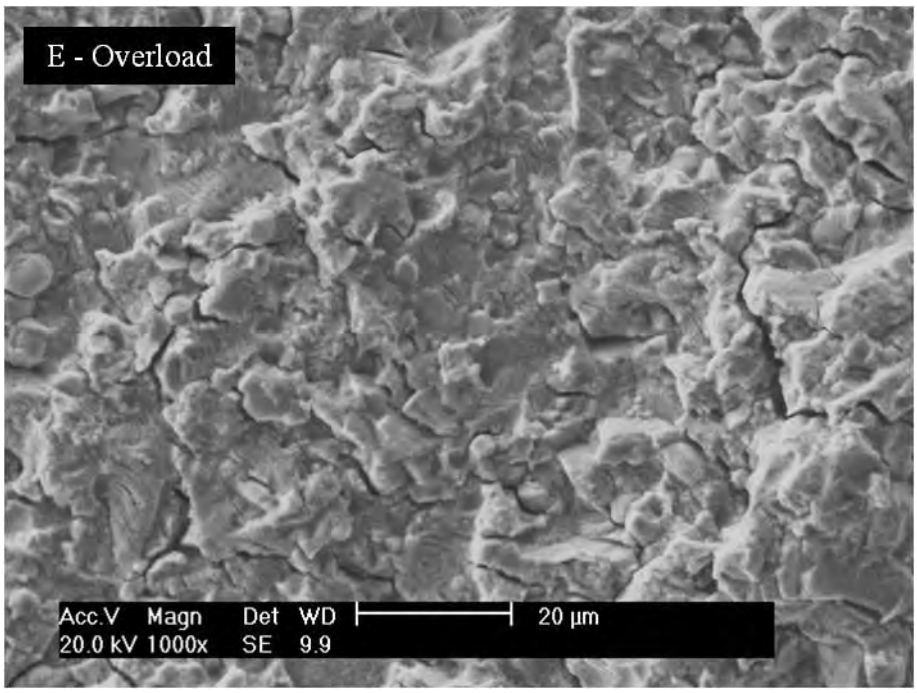

G
F
E
D
C
B
A


A - Baseline
Acc.V Magn Det WD
20.0 kV 1000x SE 9.9
20 µm


B - Dwell
Acc.V Magn Det WD 20 µm
20.0 kV 1000x SE 9.9


C - Baseline
Acc.V Magn Det WD 20 µm
20.0 kV 1000x SE 9.9


D - Dwell
Acc.V Magn Det WD 20 µm
20.0 kV 1000x SE 9.9


E - Overload
Acc.V Magn Det WD 20 µm
20.0 kV 1000x SE 9.9

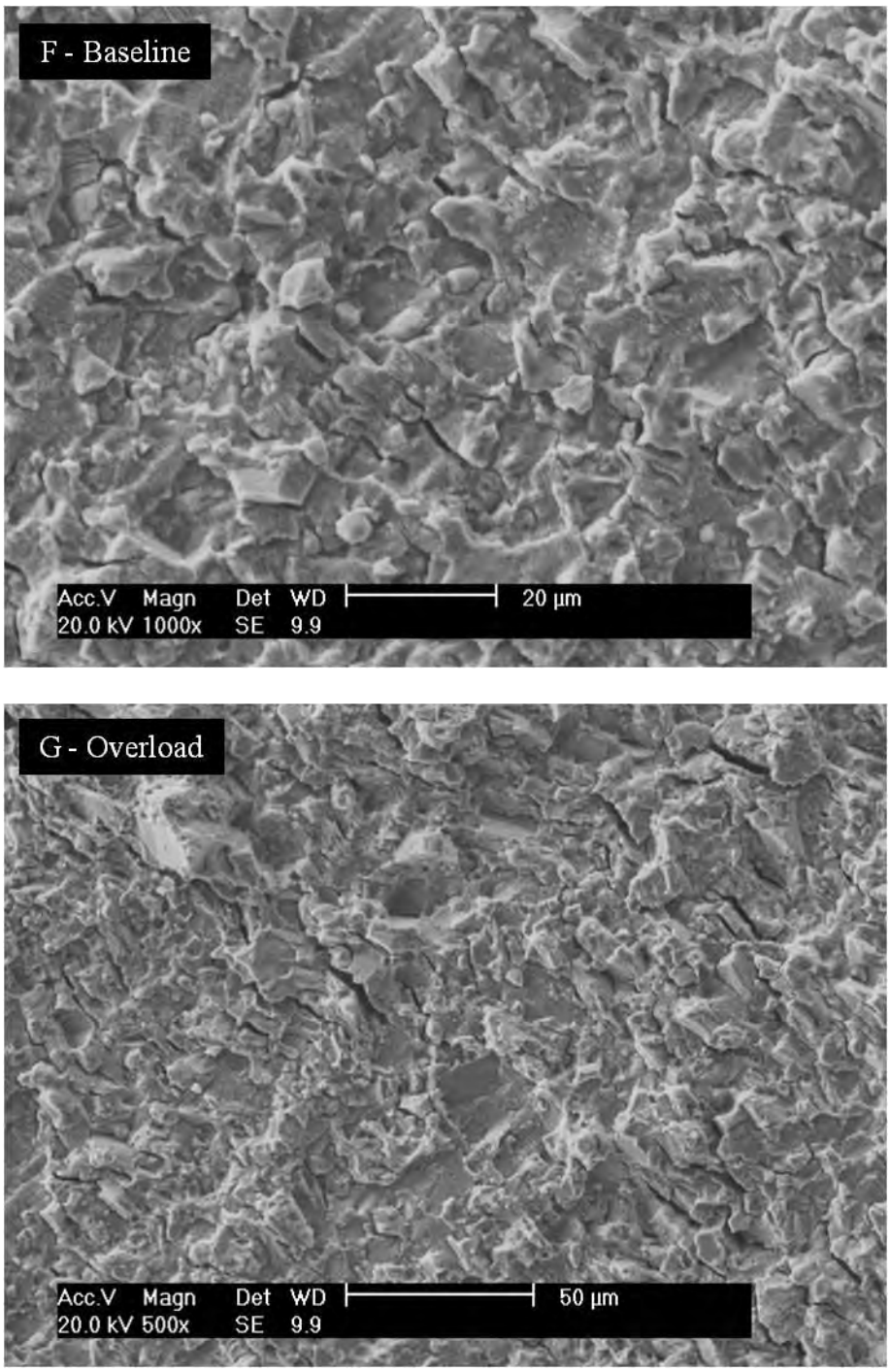
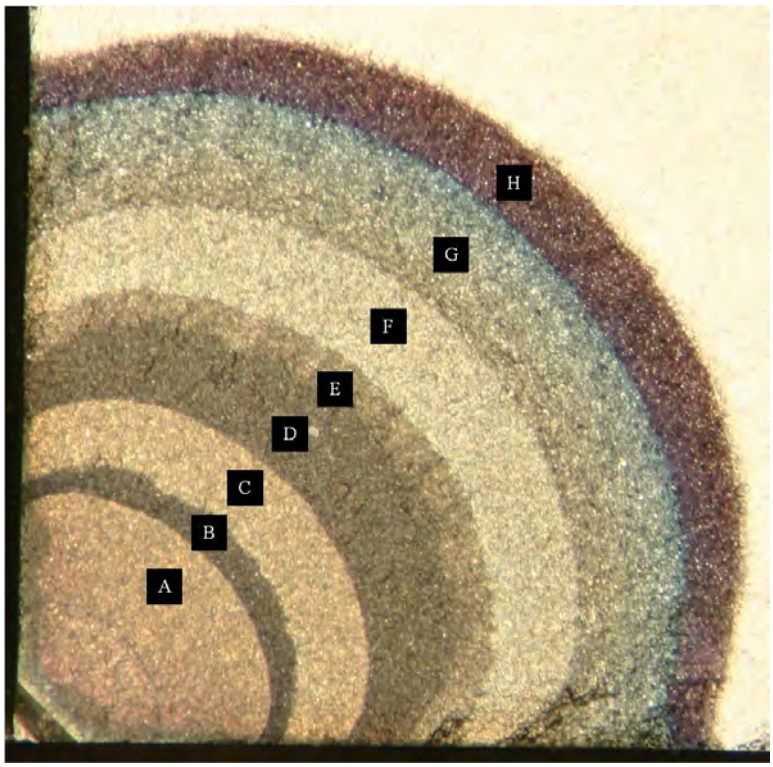
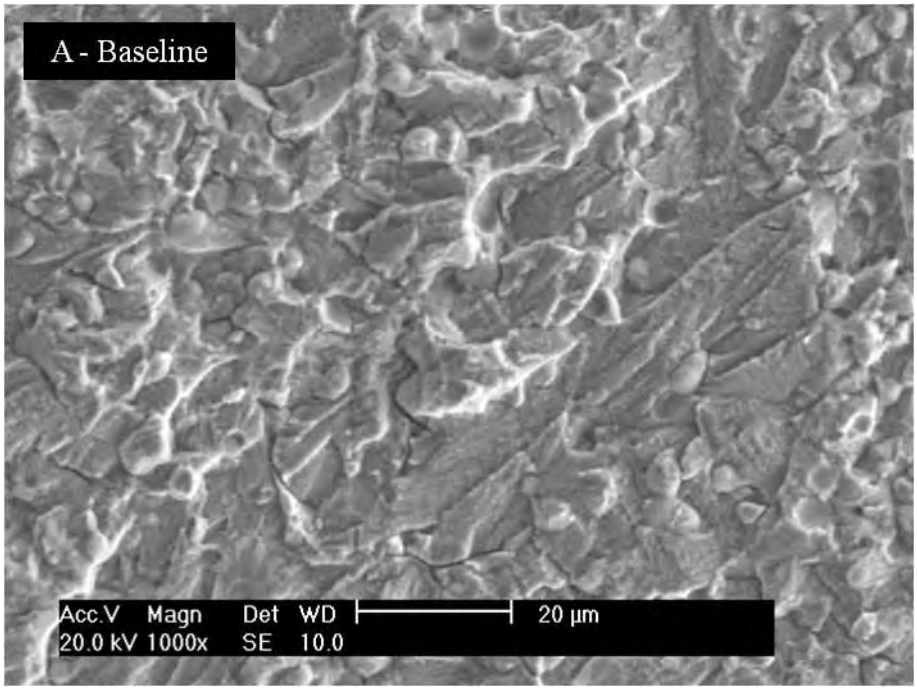
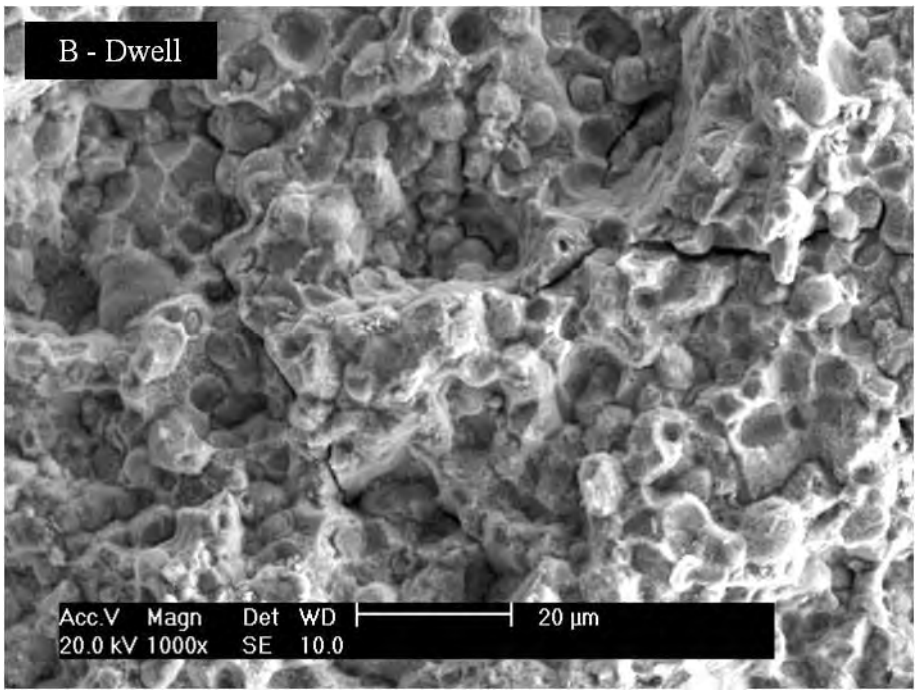
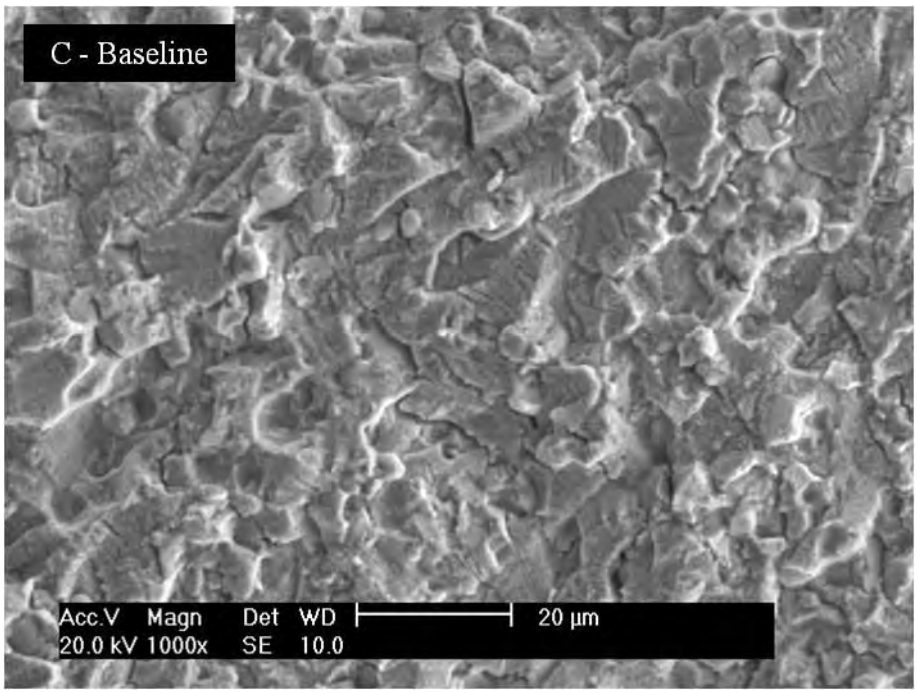


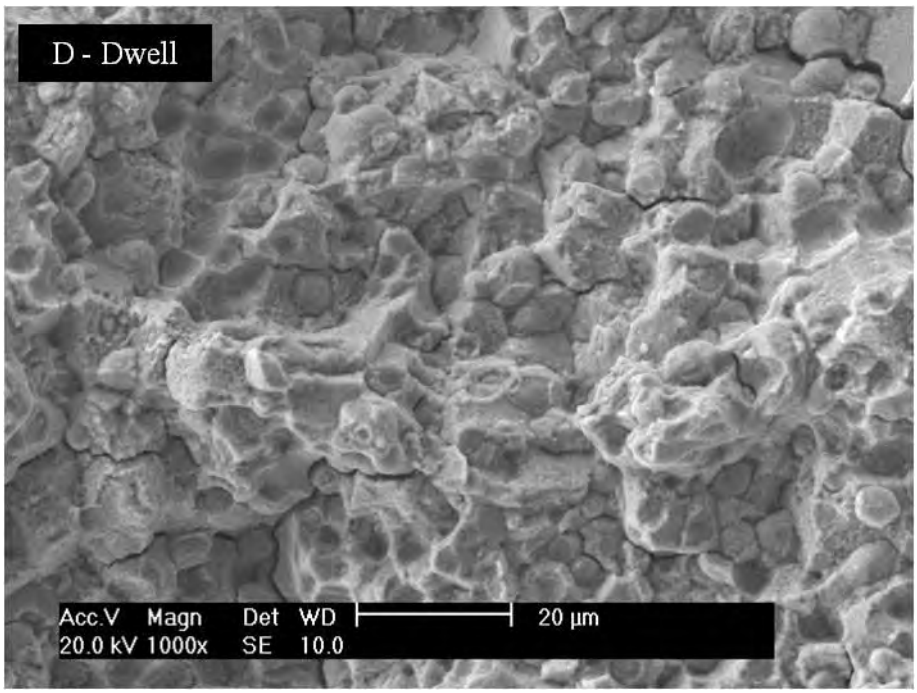
Figure A-62: Showing fractographs of fine-grained Udimet 720Li test piece CC001; tested at 600°C in air, with a dwell load of 32.5 kN, an overload factor of 1.15 and a dwell time of 1,200 seconds. Each image shows the crack propagating from bottom left to top right. Note that two sets of baseline, dwell and overload loading has been applied to the test piece. Bands labelled A, C and F are baseline (1-1-1-1) regions, bands labelled B and D are dwell regions and bands labelled E and G; the overload regions. Note that crack growth mechanisms pertaining to overload cycling are predominantly transgranular; note also that full retardation has occurred. Higher magnification images are taken at points relating to the following crack growth driving forces (ΔK): A: ~20 MPa√m; B: ~25 MPa√m; C: ~33.5 MPa√m; D: ~37.5 MPa√m; E: ~43 MPa√m; F: ~50 MPa√m; G: ~60 MPa√m

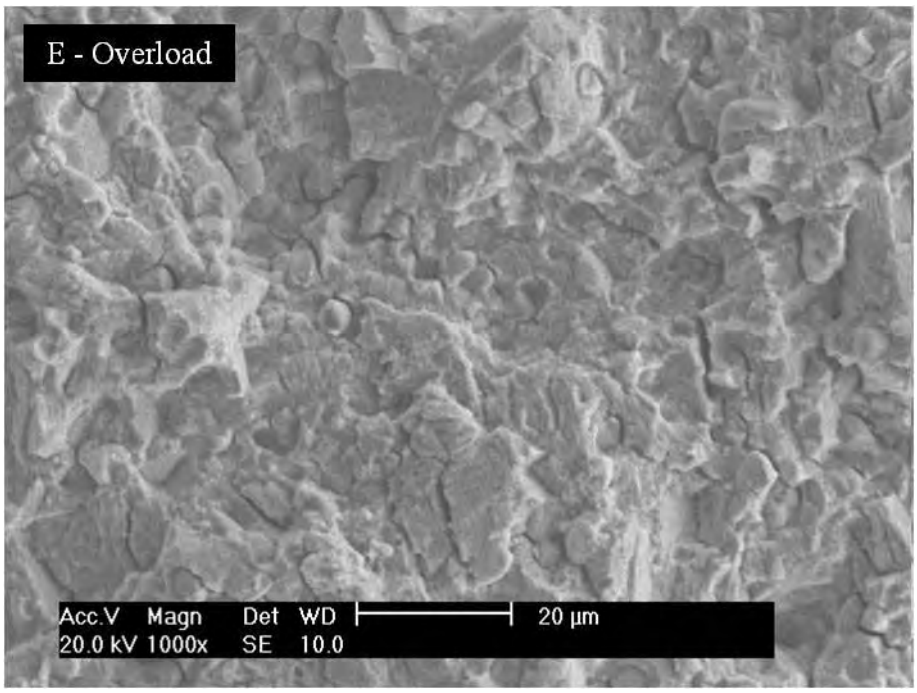

H
G
F
E
D
C
B
A

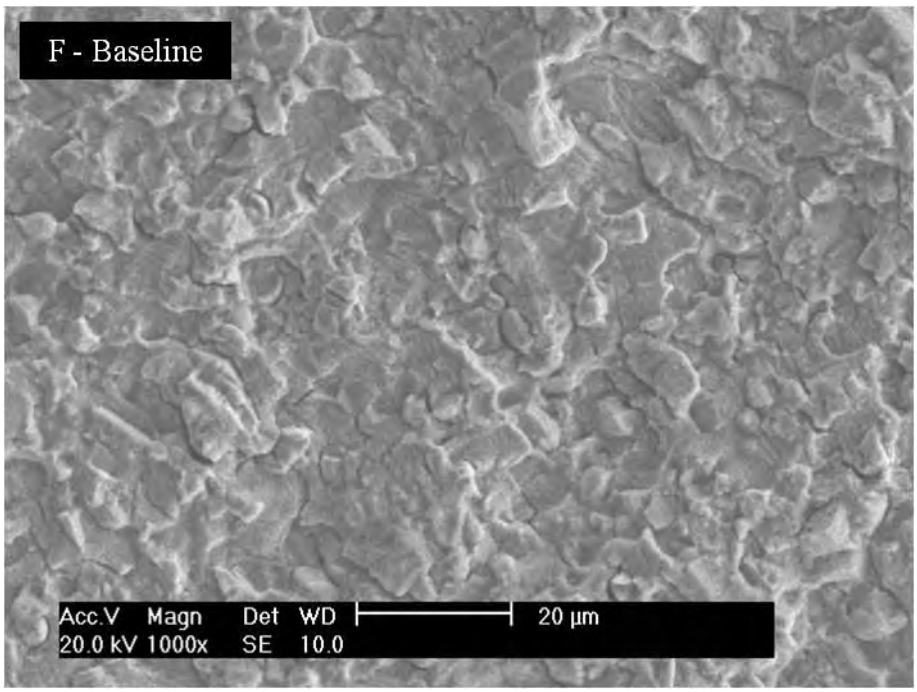

A - Baseline
Acc.V Magn Det WD
20.0 kV 1000x SE 10.0
20 µm

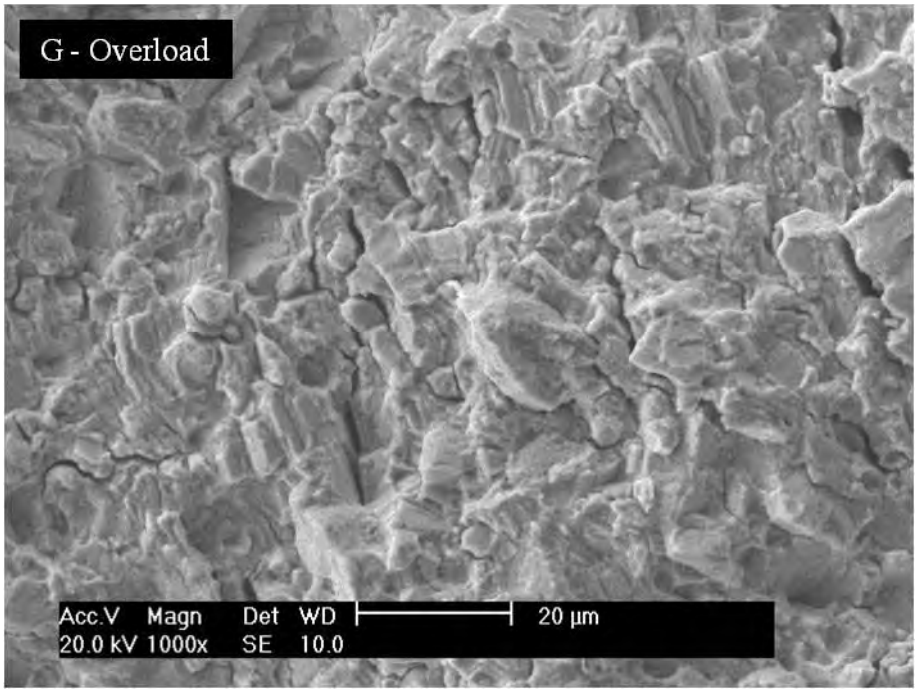

B - Dwell
Acc.V Magn Det WD 20 µm
20.0 kV 1000x SE 10.0


C - Baseline
Acc.V Magn Det WD 20 µm
20.0 kV 1000x SE 10.0


D - Dwell
Acc.V Magn Det WD 20 µm
20.0 kV 1000x SE 10.0


E - Overload
Acc.V Magn Det WD 20 µm
20.0 kV 1000x SE 10.0


F - Baseline
Acc.V Magn Det WD 20 µm
20.0 kV 1000x SE 10.0


G - Overload
Acc.V Magn Det WD 20 µm
20.0 kV 1000x SE 10.0

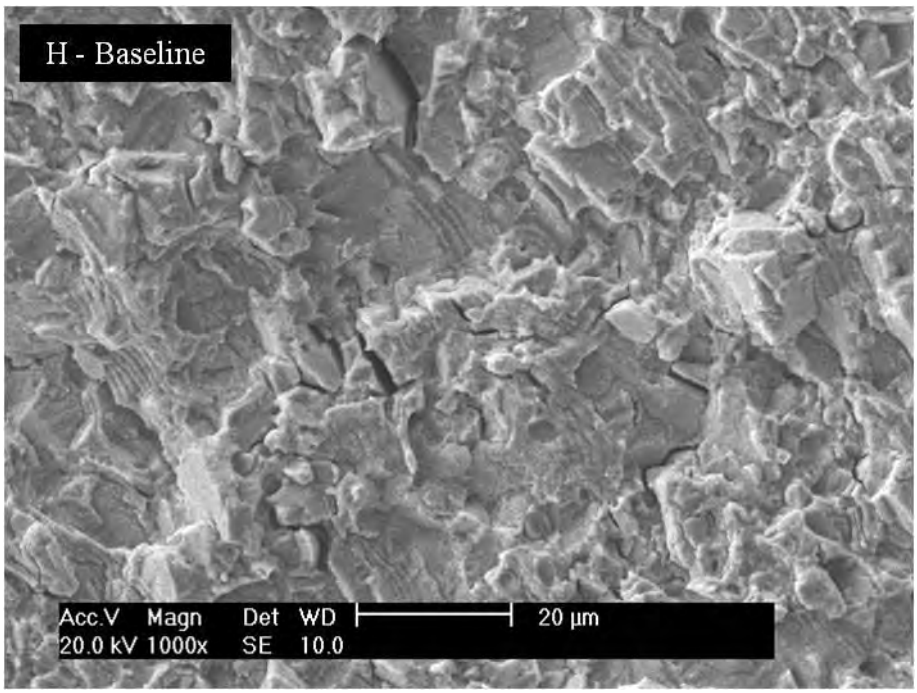
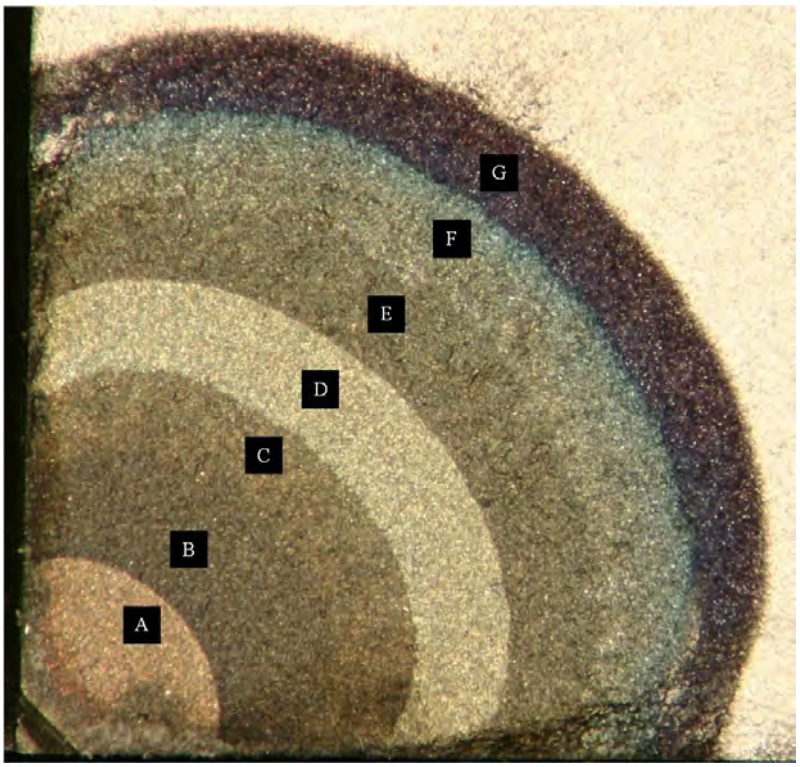
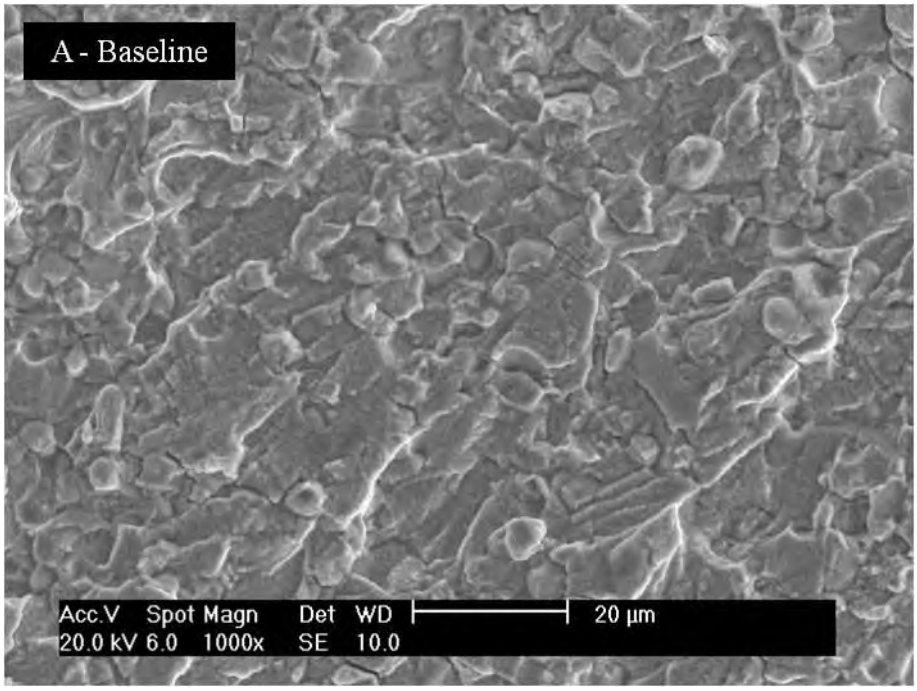
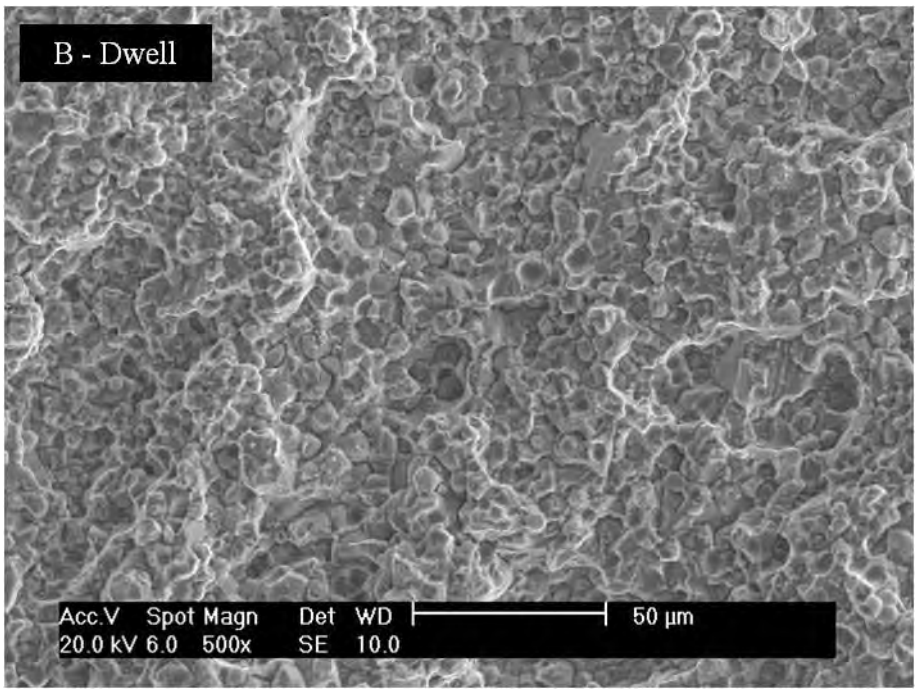
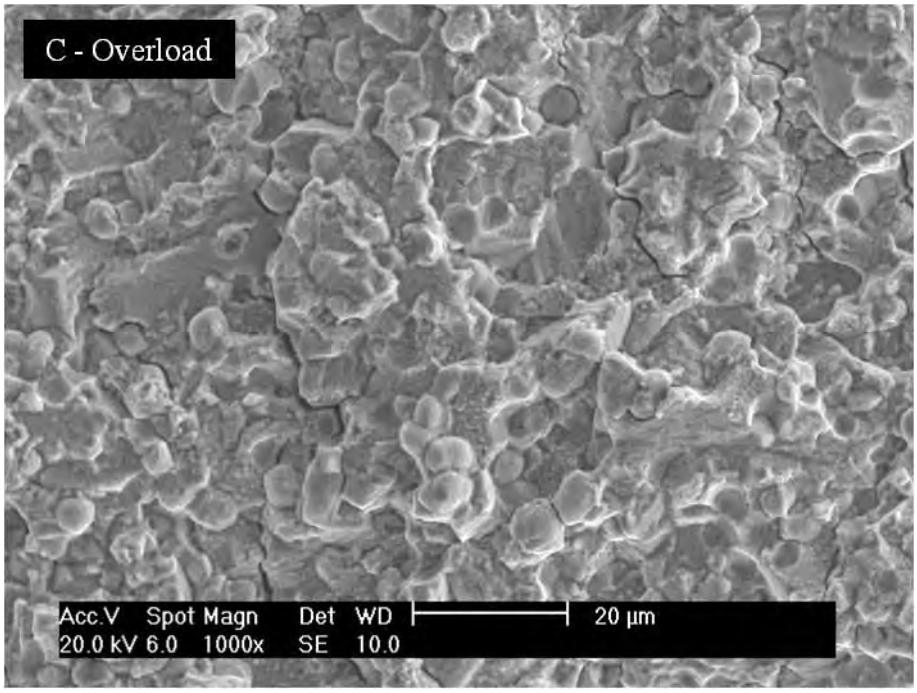


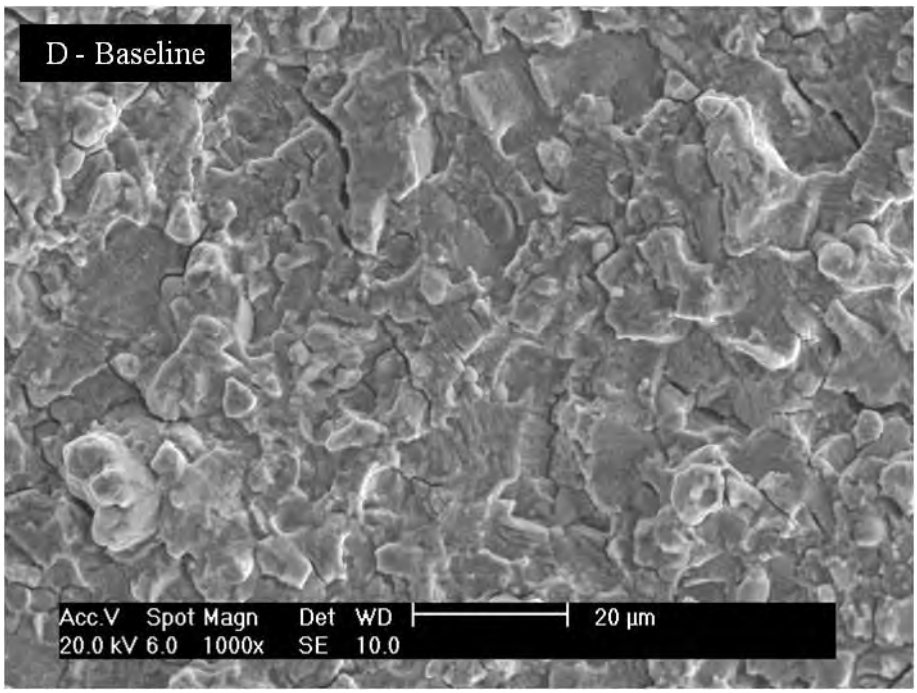
Figure A-63: Showing fractographs of fine-grained Udimet 720Li test piece CC002; tested at 600°C in air, with a dwell load of 32.5 kN, an overload factor of 1.15 and a dwell time of 3,600 seconds. Each image shows the crack propagating from bottom left to top right. Note that two sets of baseline, dwell and overload loading has been applied to the test piece. Bands labelled A, C, F and H are baseline (1-1-1-1) regions, bands labelled B and D are dwell regions and bands labelled E and G; the overload regions. Note that crack growth mechanisms pertaining to overload cycling are predominantly transgranular; note also that full retardation has occurred. Higher magnification images are taken at points relating to the following crack growth driving forces (ΔK): A: ~19 MPa√m; B: ~22.5 MPa√m; C: ~32 MPa√m; D: ~36.5 MPa√m; E: ~40 MPa√m; F: ~45 MPa√m; G: ~55 MPa√m; H: ~63 MPa√m

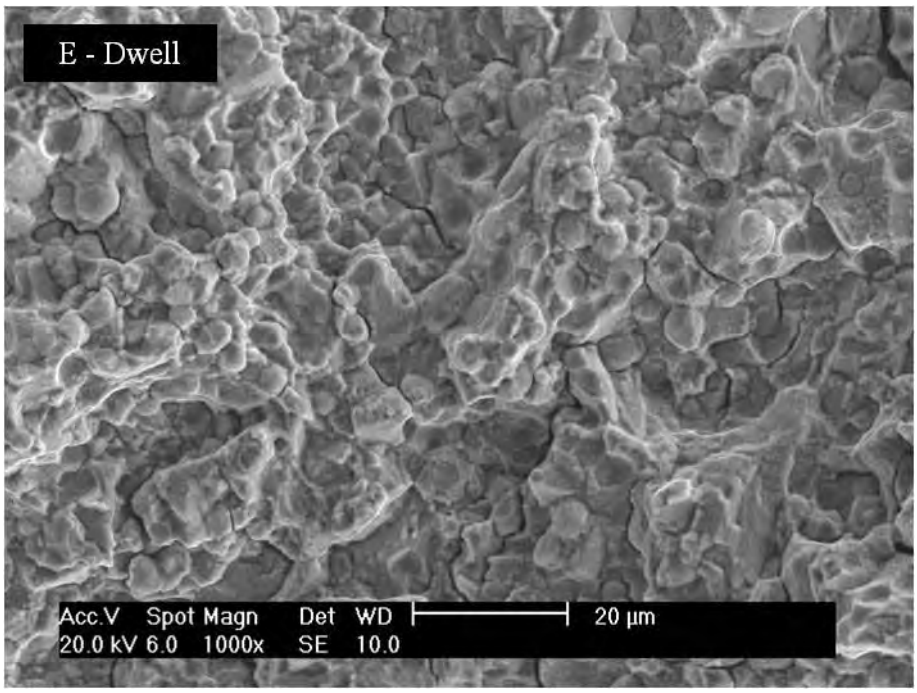

G
F
E
D
C
B
A

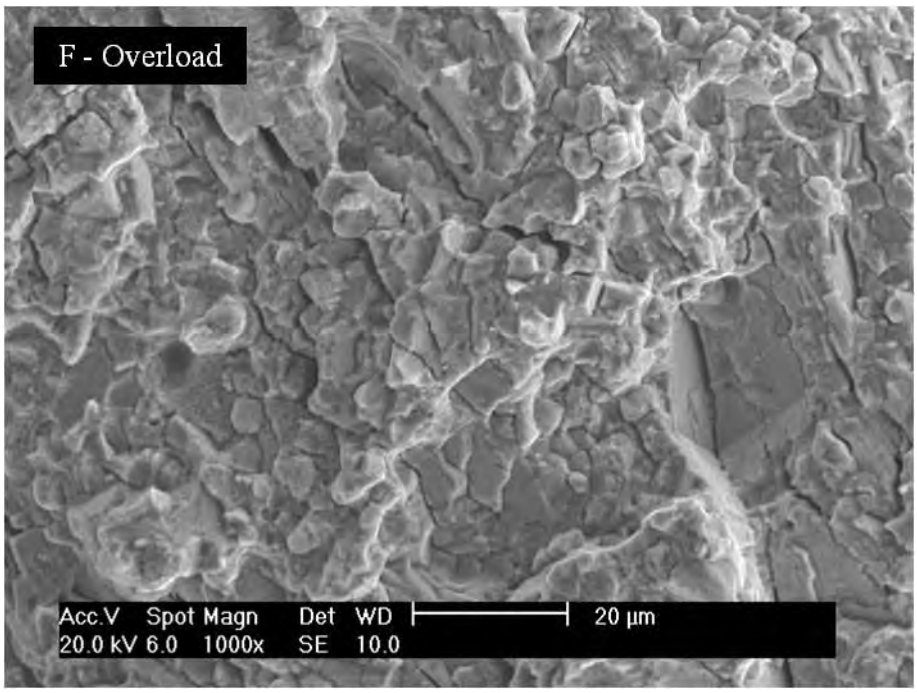

A - Baseline
Acc.V Spot Magn Det WD 20 µm
20.0 kV 6.0 1000x SE 10.0


B - Dwell
Acc.V Spot Magn Det WD 50 µm
20.0 kV 6.0 500x SE 10.0


C - Overload
Acc.V Spot Magn Det WD 20 µm
20.0 kV 6.0 1000x SE 10.0


D - Baseline
Acc.V Spot Magn Det WD 20 µm
20.0 kV 6.0 1000x SE 10.0


E - Dwell
Acc.V Spot Magn Det WD 20 µm
20.0 kV 6.0 1000x SE 10.0


F - Overload
Acc.V Spot Magn Det WD 20 µm
20.0 kV 6.0 1000x SE 10.0

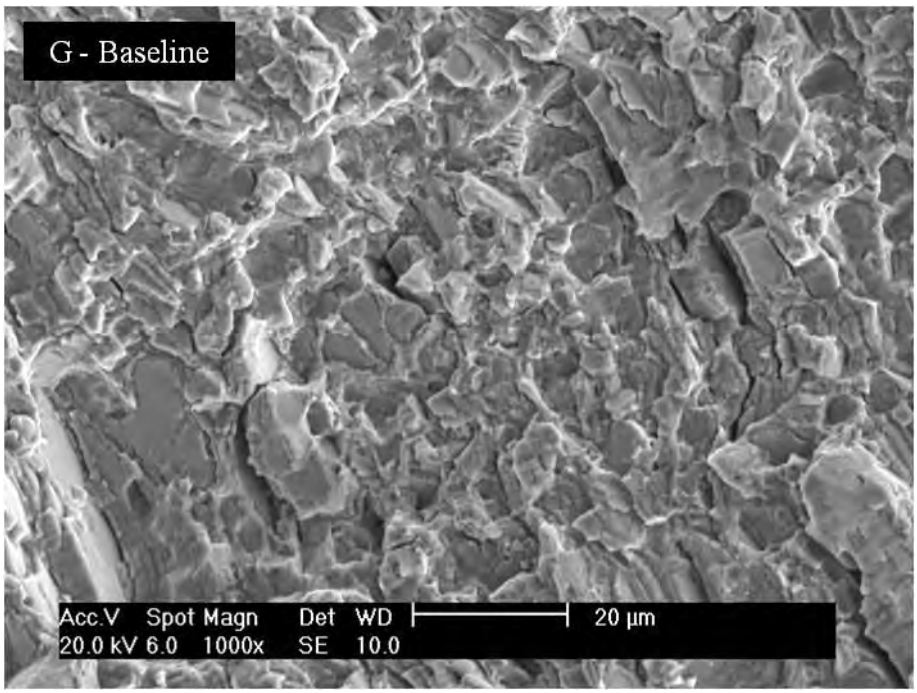
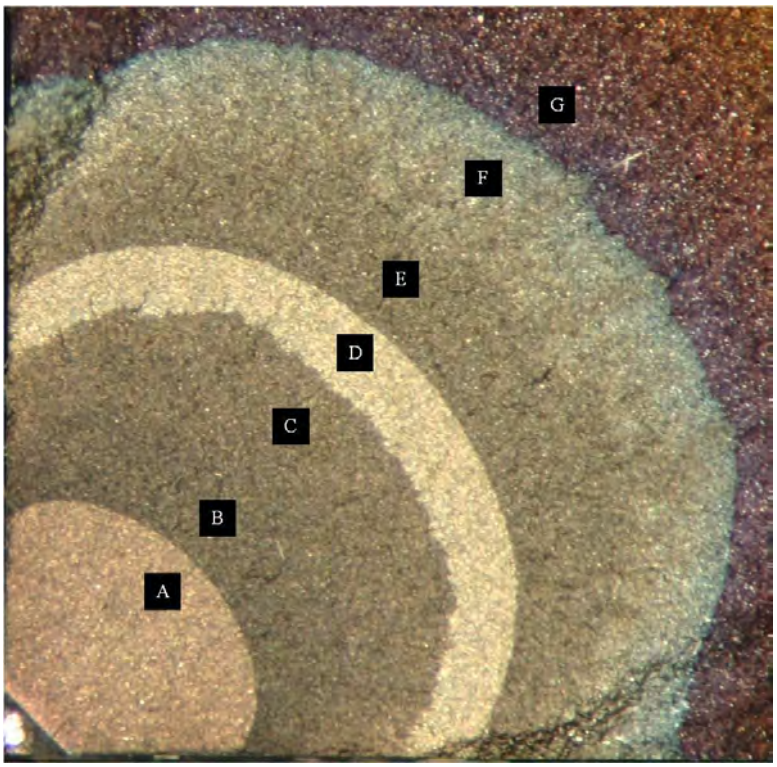
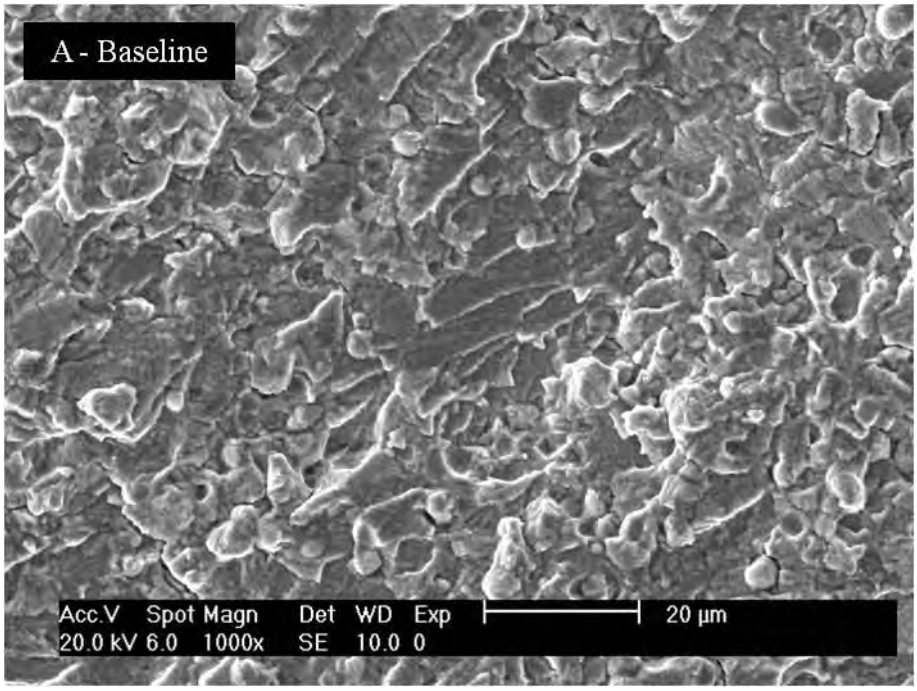
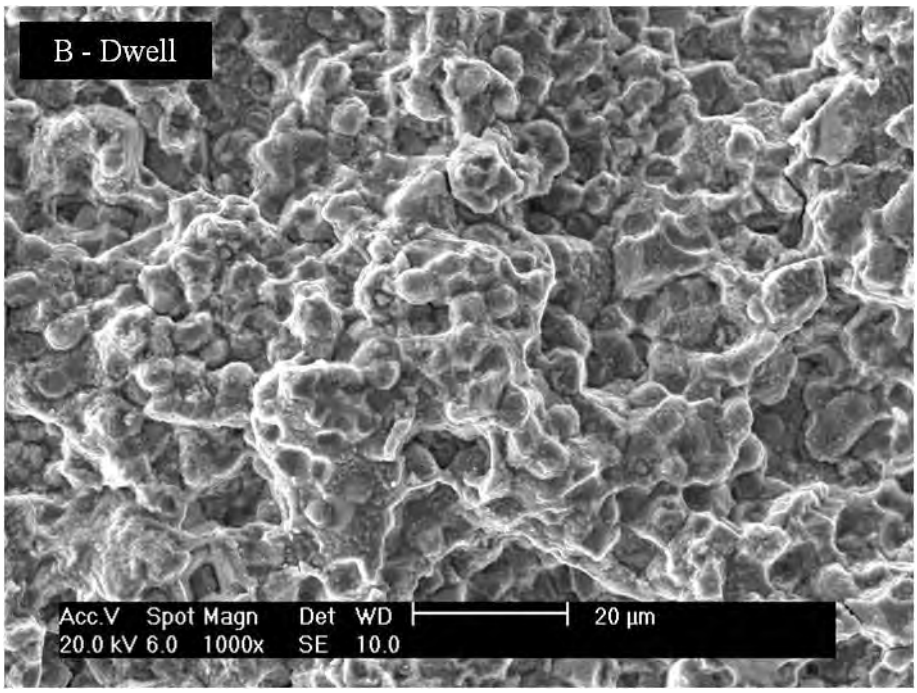
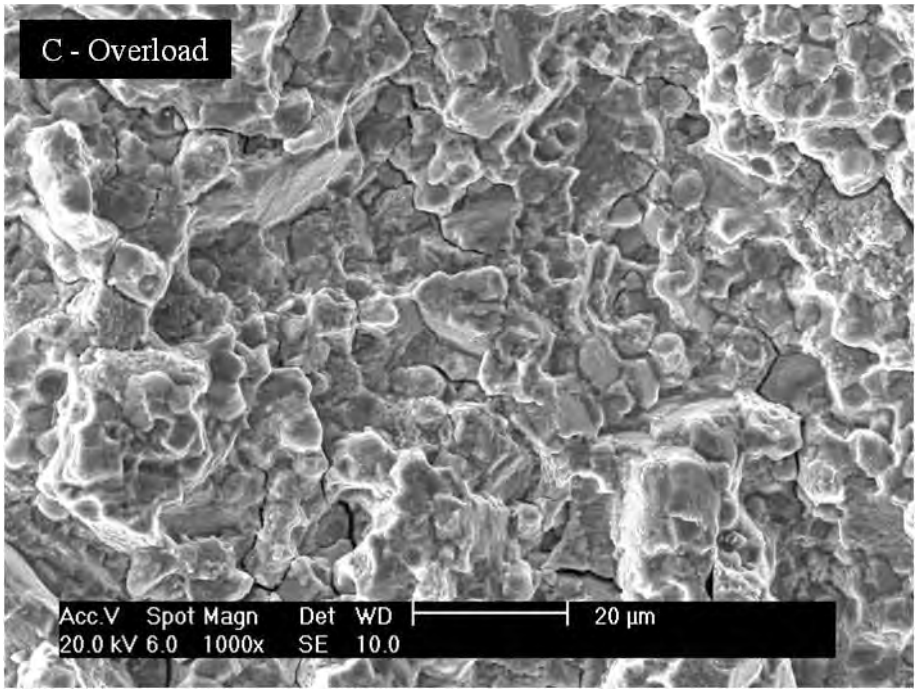


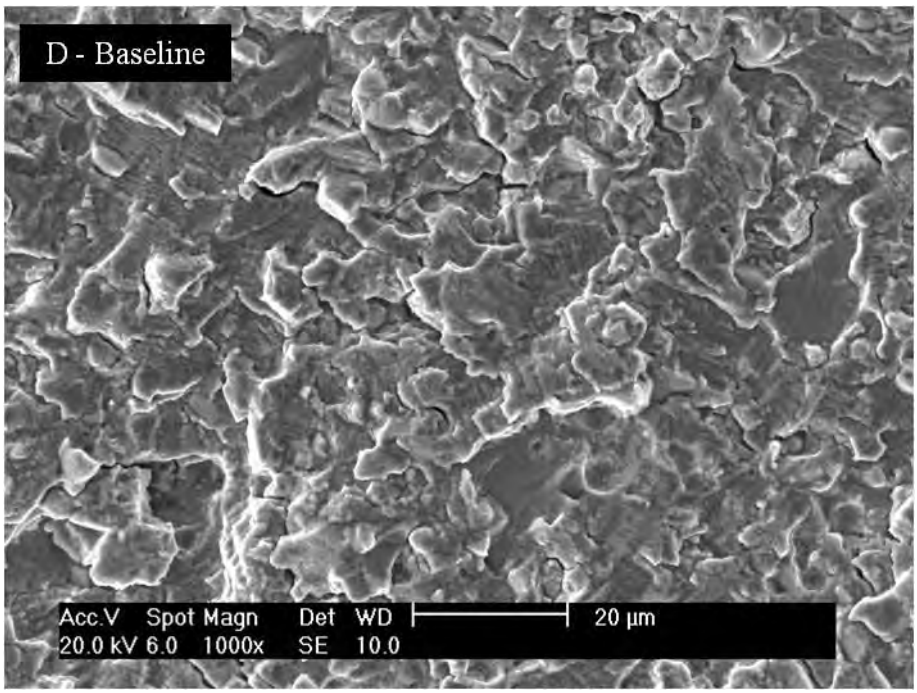
Figure A-64: Showing fractographs of fine-grained Udimet 720Li test piece CC005; tested at 600°C in air, with a dwell load of 32.5 kN, an overload factor of 1.05 and a dwell time of 1,200 seconds. Each image shows the crack propagating from bottom left to top right. Note that two sets of baseline, dwell and overload loading has been applied to the test piece. Bands labelled A, D and G are baseline (1-1-1-1) regions, bands labelled B and E are dwell regions and bands labelled C and F; the overload regions. Note that crack growth mechanisms pertaining to overload cycling are predominantly intergranular for lower crack growth driving forces (C) (where less retardation is achieved) and more transgranular for higher crack growth driving forces (F) (where more retardation is achieved). Higher magnification images are taken at points relating to the following crack growth driving forces (ΔK):
A: ~22.5 MPa√m; B: ~28 MPa√m; C: ~34.5 MPa√m; D: ~40 MPa√m; E: ~47 MPa√m; F: ~56 MPa√m;
G: ~65 MPa√m

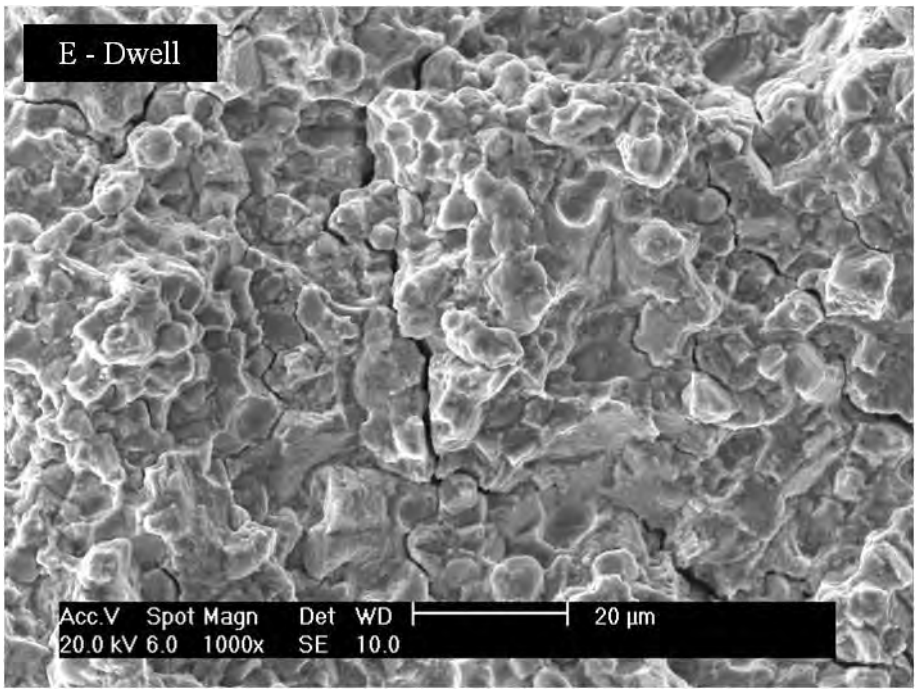

G
F
E
D
C
B
A


A - Baseline
Acc.V Spot Magn Det WD Exp
20.0 kV 6.0 1000x SE 10.0 0
20 µm


B - Dwell
Acc.V Spot Magn Det WD 20 µm
20.0 kV 6.0 1000x SE 10.0


C - Overload
Acc.V Spot Magn Det WD 20 µm
20.0 kV 6.0 1000x SE 10.0


D - Baseline
Acc.V Spot Magn Det WD 20 µm
20.0 kV 6.0 1000x SE 10.0


E - Dwell
Acc.V Spot Magn Det WD 20 µm
20.0 kV 6.0 1000x SE 10.0

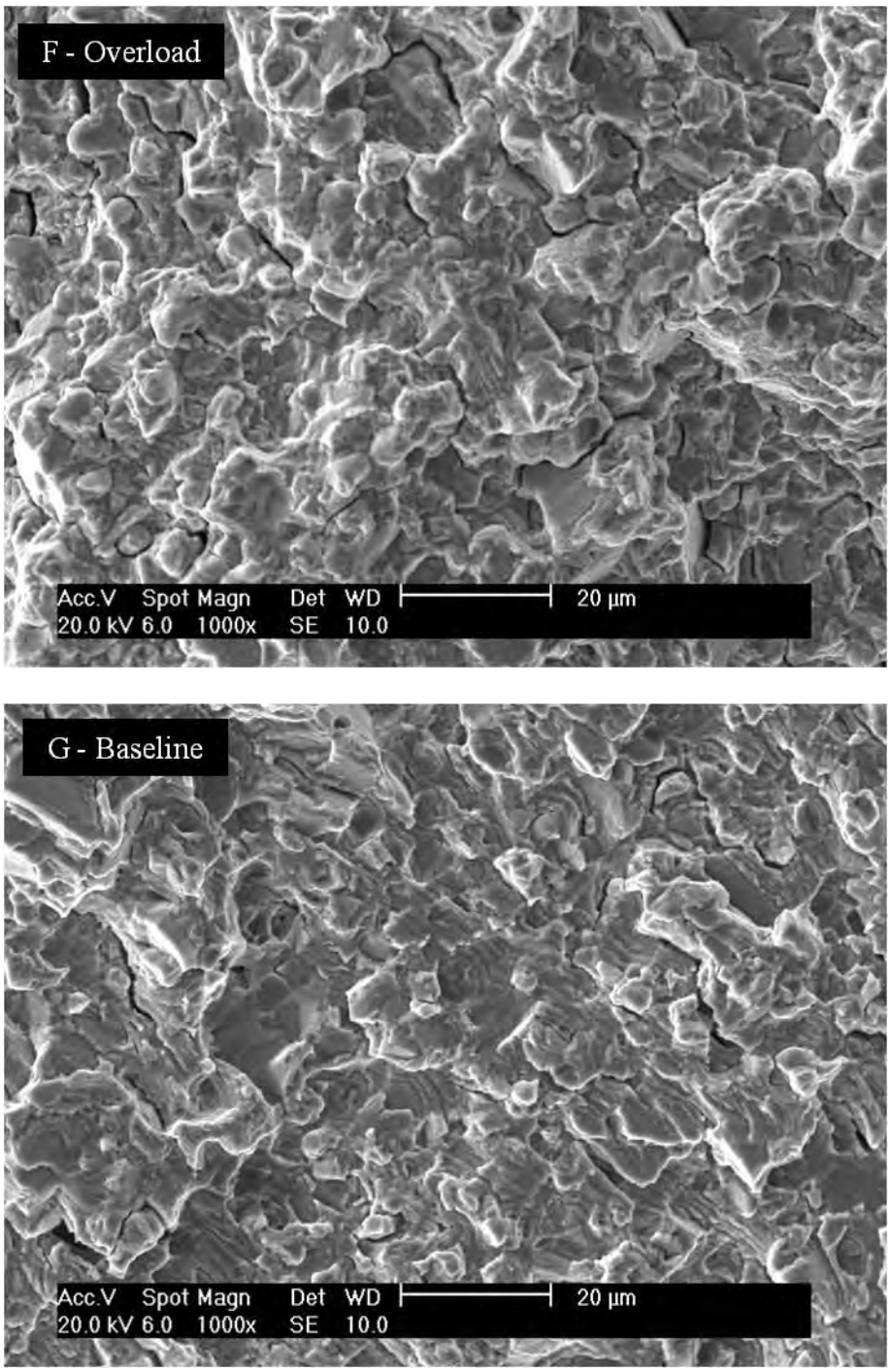
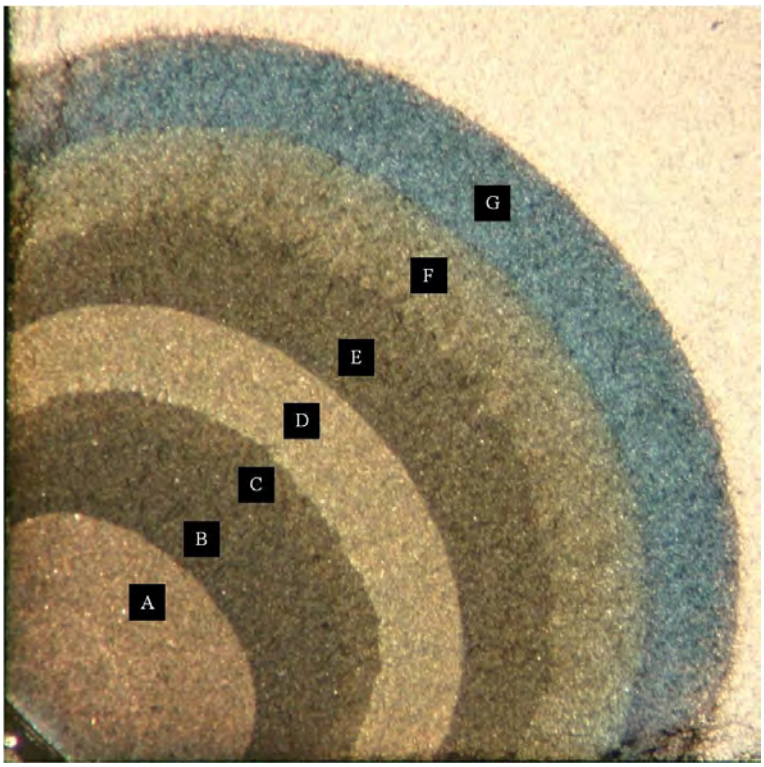
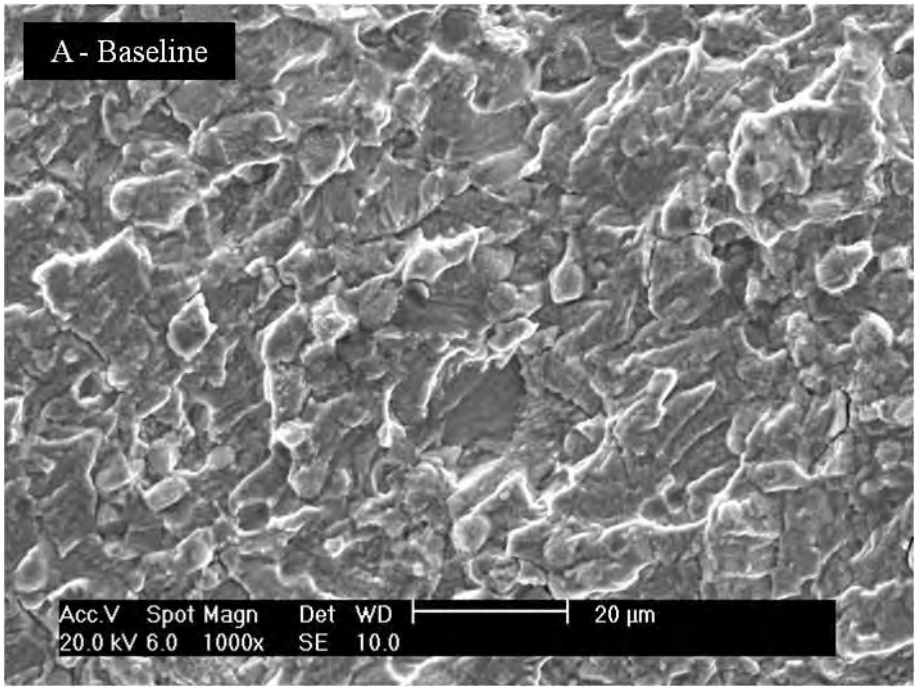
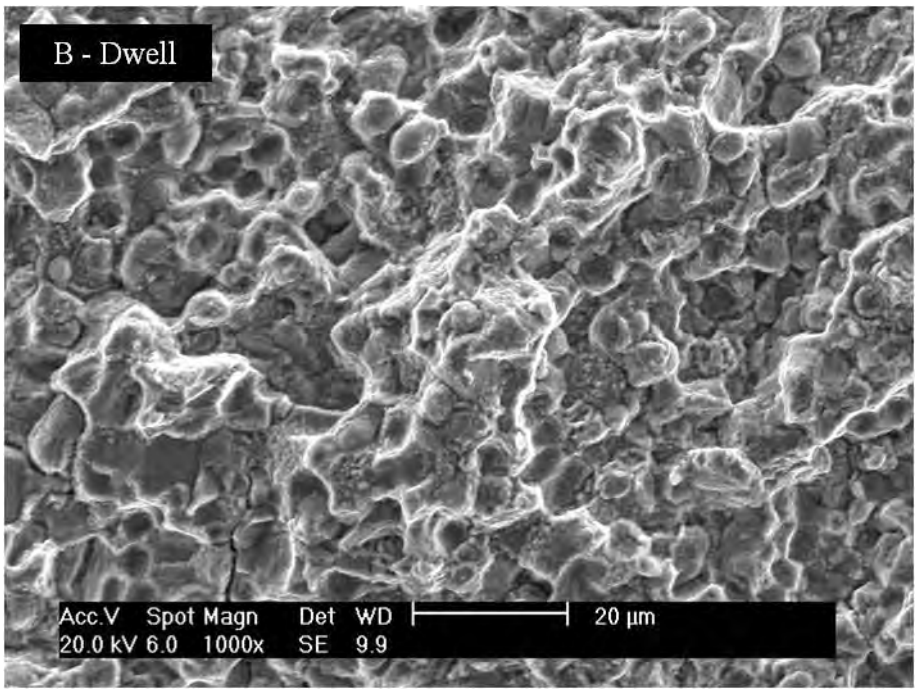
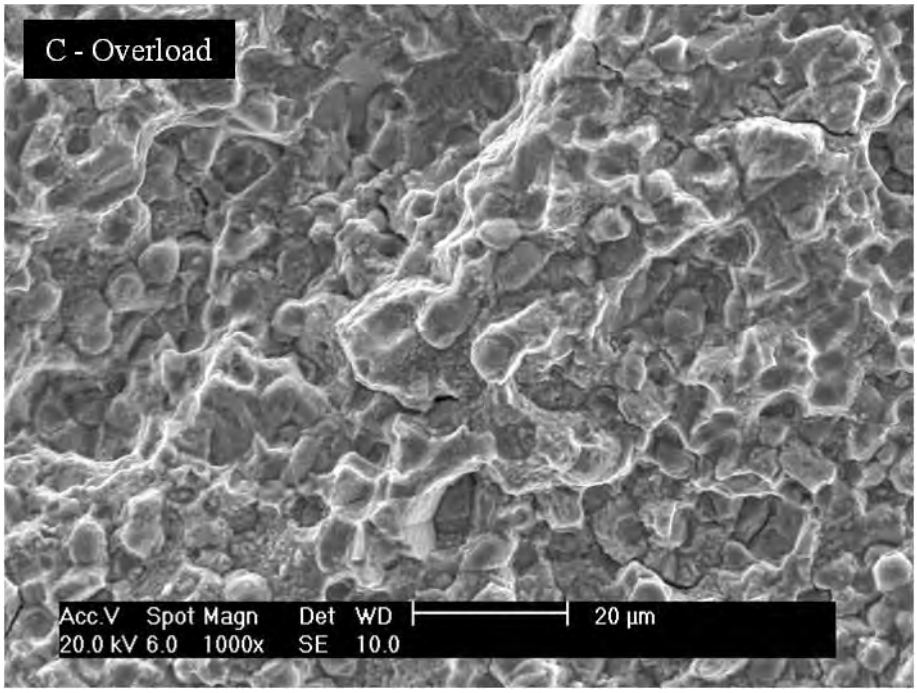


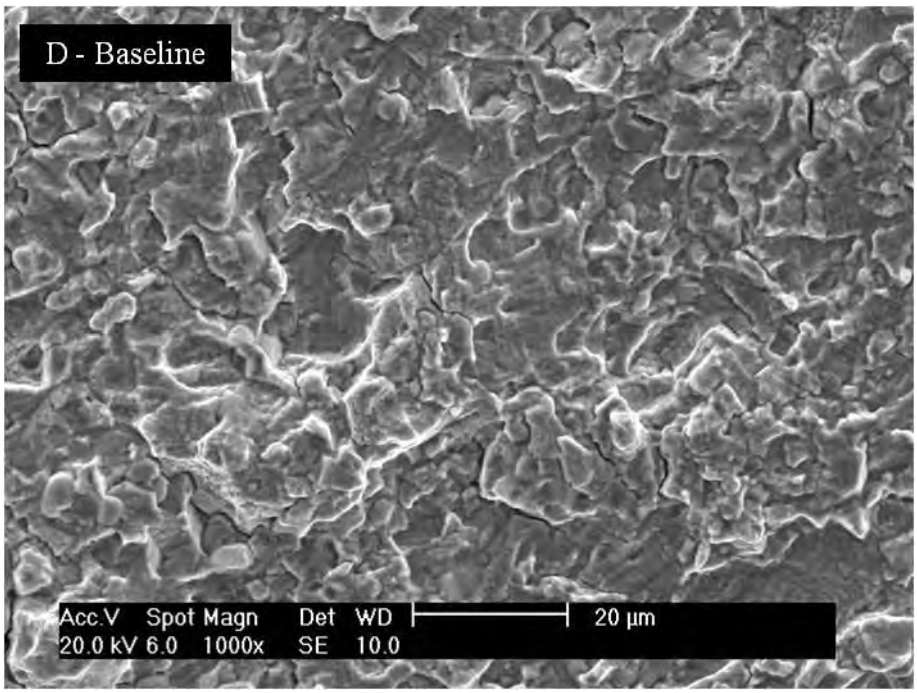
Figure A-65: Showing fractographs of fine-grained Udimet 720Li test piece CC006; tested at 600°C in air, with a dwell load of 32.5 kN, an overload factor of 1.05 and a dwell time of 3,600 seconds. Each image shows the crack propagating from bottom left to top right. Note that two sets of baseline, dwell and overload loading has been applied to the test piece. Bands labelled A, D and G are baseline (1-1-1-1) regions, bands labelled B and E are dwell regions and bands labelled C and F; the overload regions. Note that crack growth mechanisms pertaining to overload cycling are predominantly intergranular where partial retardation is achieved. Higher magnification images are taken at points relating to the following crack growth driving forces (ΔK): A: ~24 MPa√m; B: ~29.5 MPa√m; C: ~35 MPa√m; D: ~40 MPa√m; E: ~46 MPa√m; F: ~55 MPa√m; G: ~69 MPa√m

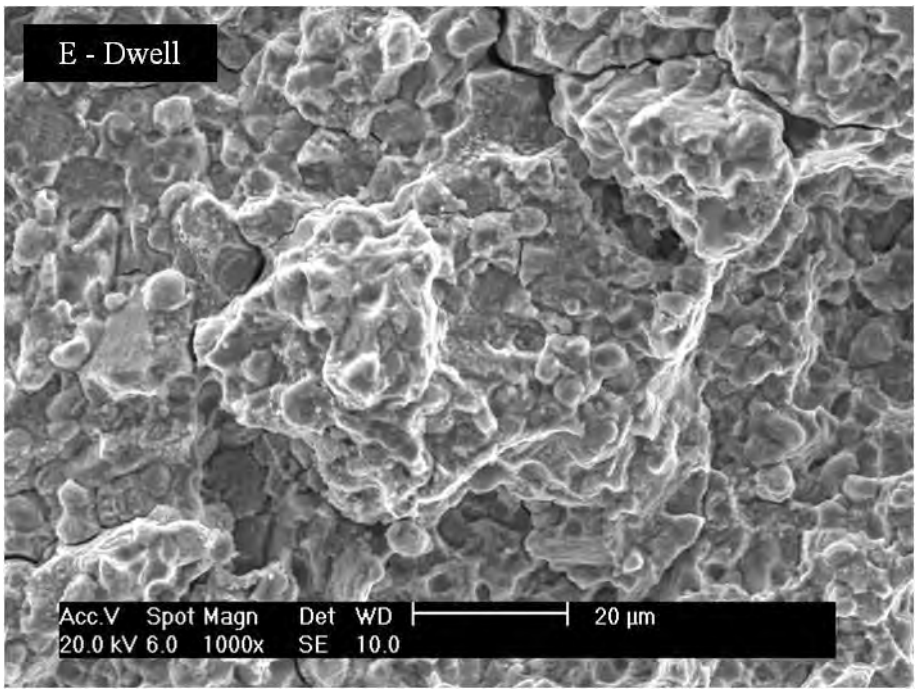

G
F
E
D
C
B
A


A - Baseline
Acc.V Spot Magn Det WD 20 µm
20.0 kV 6.0 1000x SE 10.0


B - Dwell
Acc.V Spot Magn Det WD 20 µm
20.0 kV 6.0 1000x SE 9.9


C - Overload
Acc.V Spot Magn Det WD 20 µm
20.0 kV 6.0 1000x SE 10.0


D - Baseline
Acc.V Spot Magn Det WD 20 µm
20.0 kV 6.0 1000x SE 10.0


E - Dwell
Acc.V Spot Magn Det WD 20 µm
20.0 kV 6.0 1000x SE 10.0

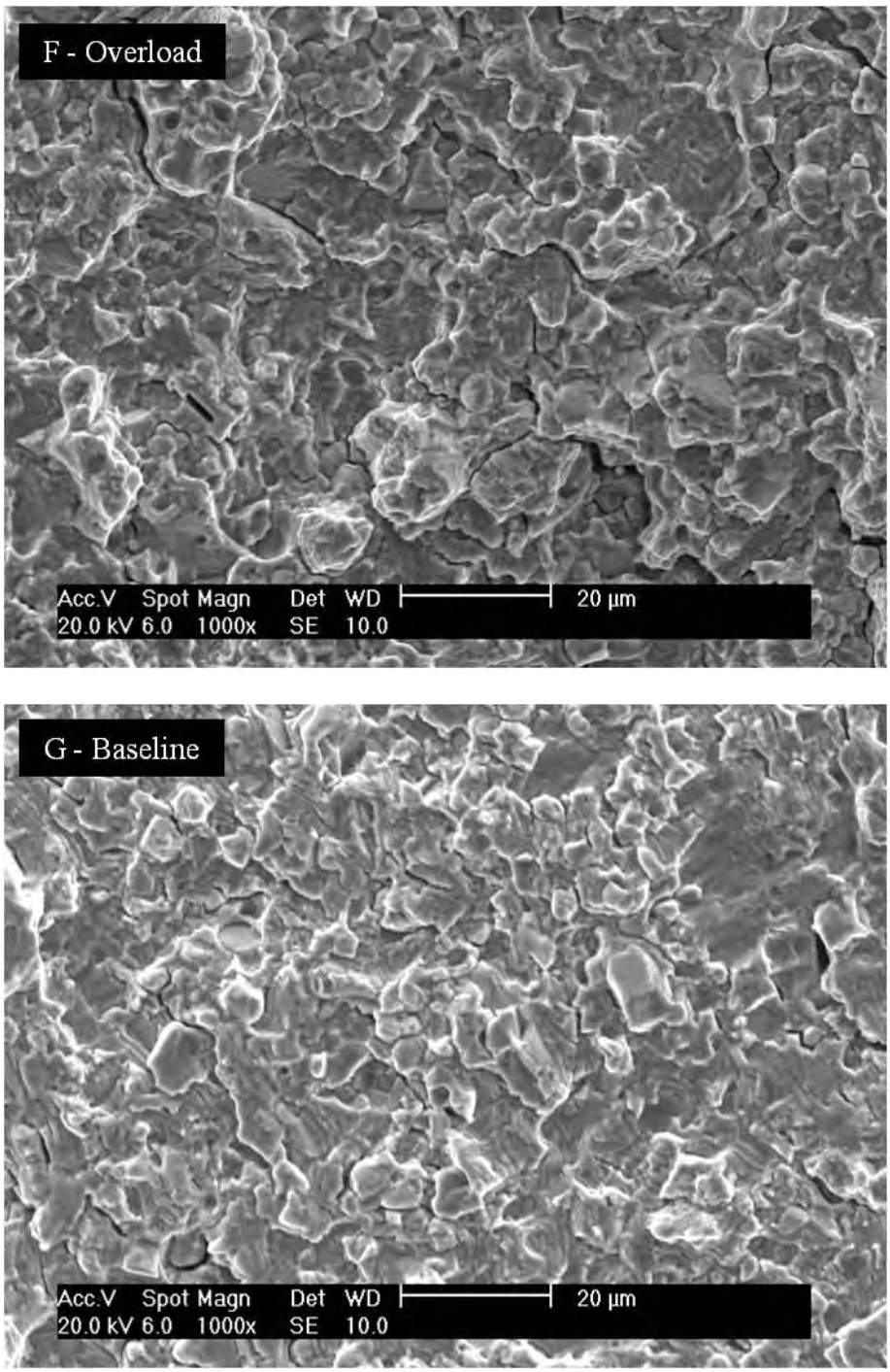
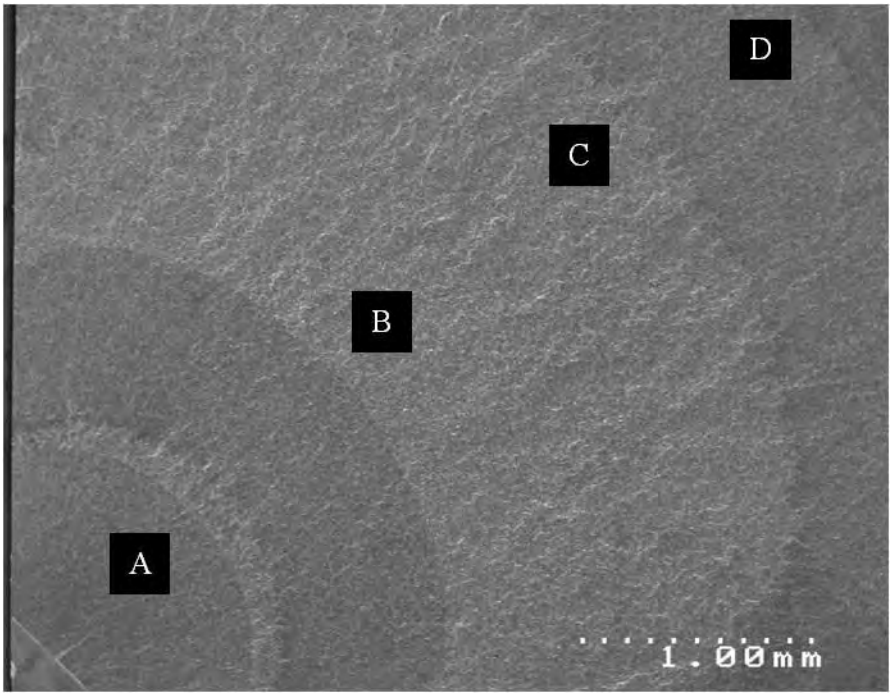
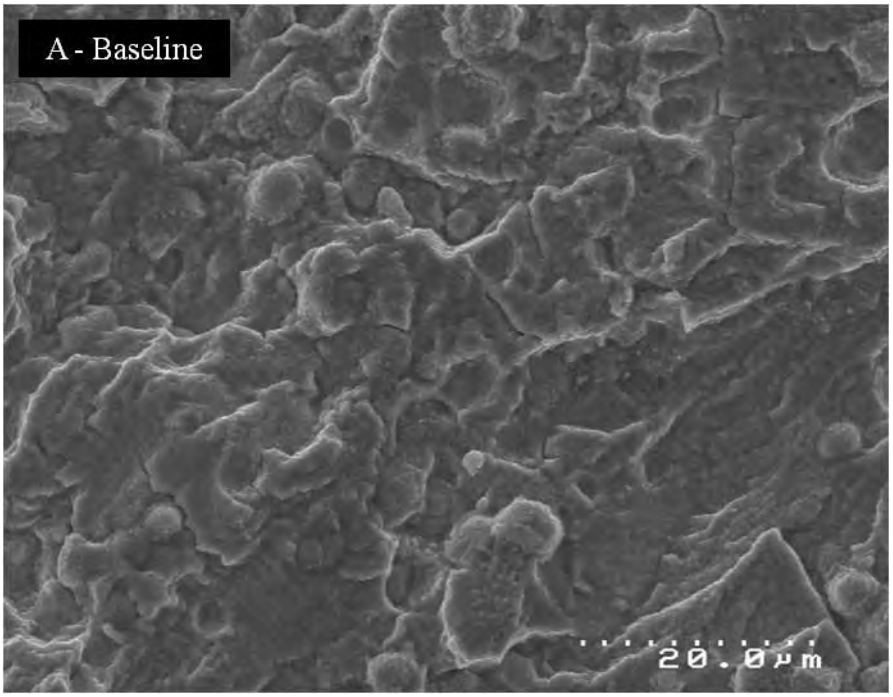
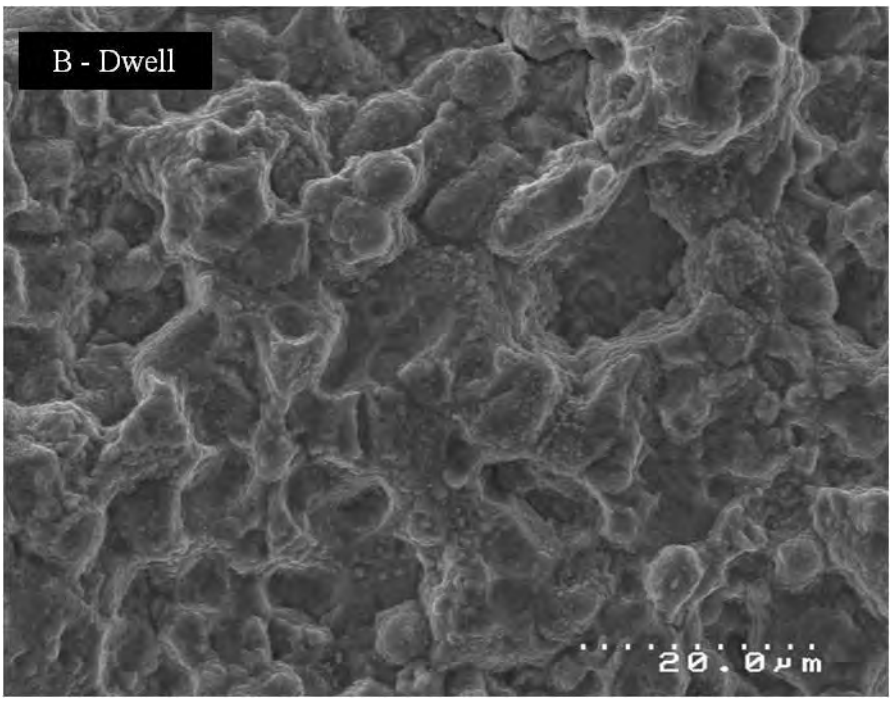


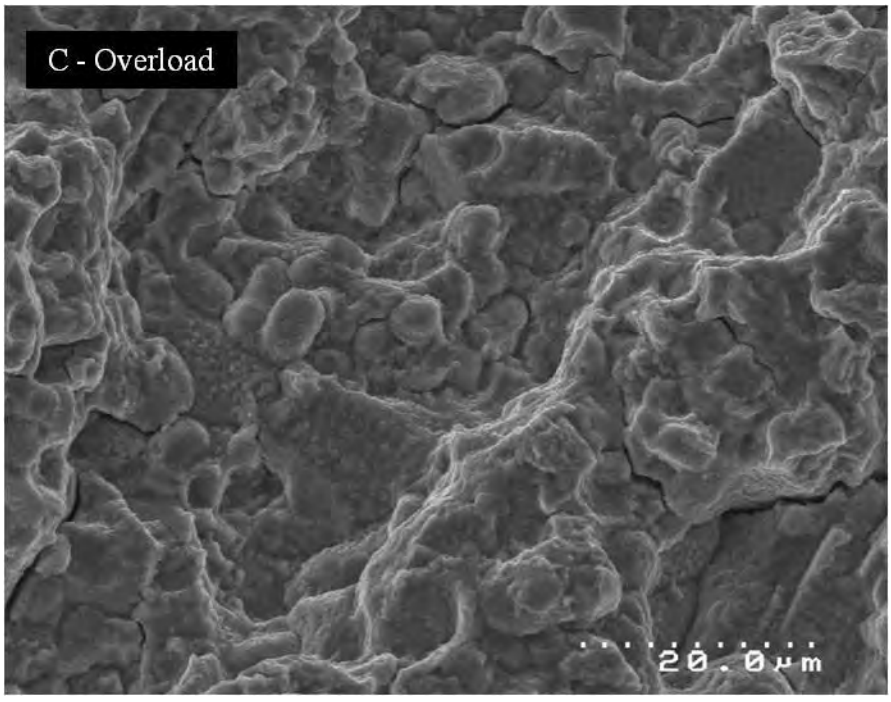
Figure A-66: Showing fractographs of fine-grained Udimet 720Li test piece CC009; tested at 625°C in air, with a dwell load of 29 kN, an overload factor of 1.08 and a dwell time of 1,200 seconds. Each image shows the crack propagating from bottom left to top right. Note that two sets of baseline, dwell and overload loading has been applied to the test piece. Bands labelled A, D and G are baseline (1-1-1-1) regions, bands labelled B and E are dwell regions and bands labelled C and F; the overload regions. Note that crack growth mechanisms pertaining to overload cycling are predominantly intergranular where partial retardation is achieved. Higher magnification images are taken at points relating to the following crack growth driving forces (ΔK): A: ~22.5 MPa√m; B: ~27 MPa√m; C: ~31 MPa√m; D: ~35 MPa√m; E: ~40 MPa√m; F: ~48 MPa√m; G: ~56 MPa√m

Udimet 720Li Dwell at Overload Tests






B - Dwell
20.0µm


C - Overload
20.0µm

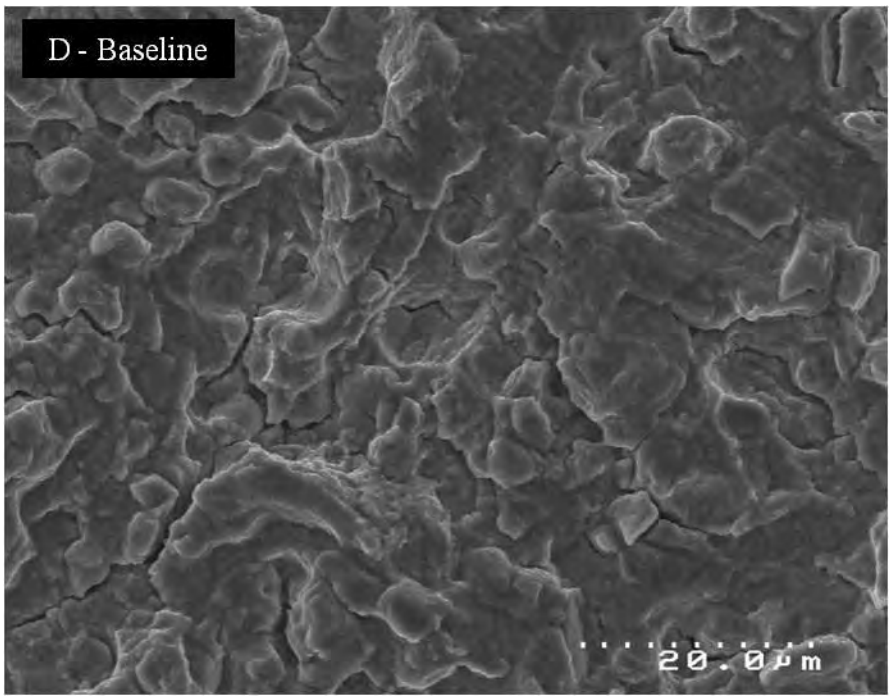
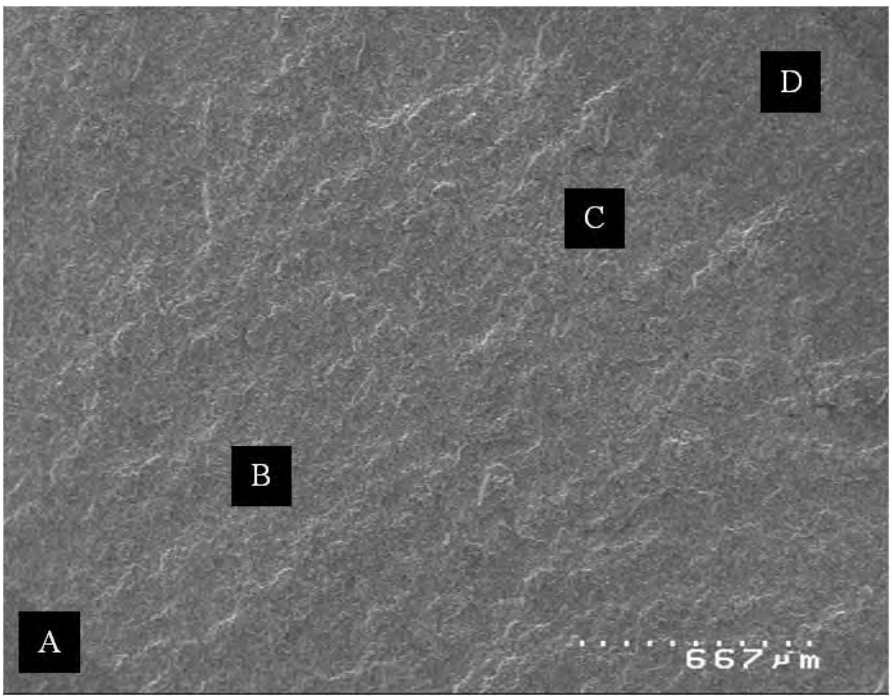
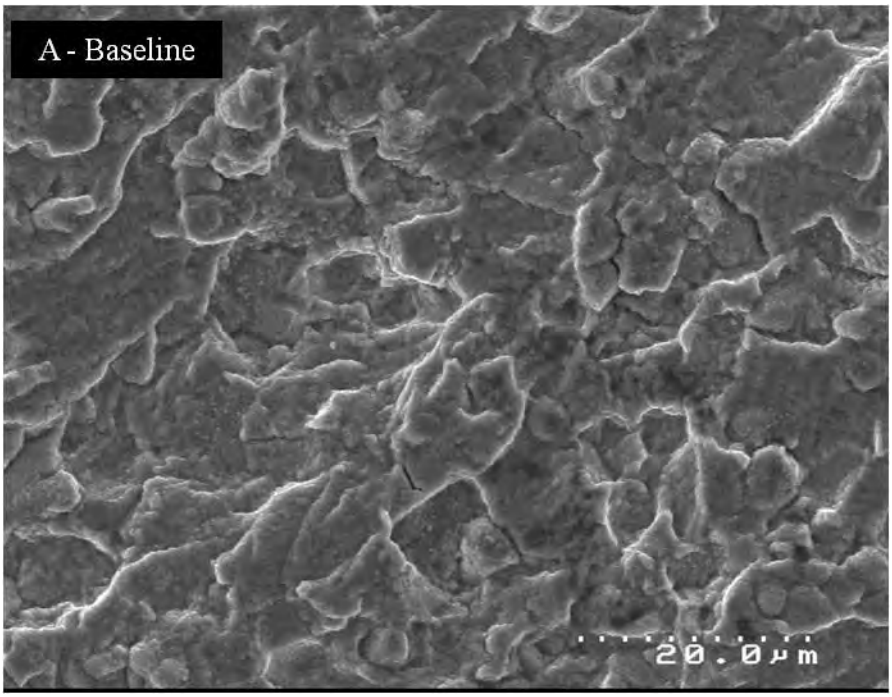
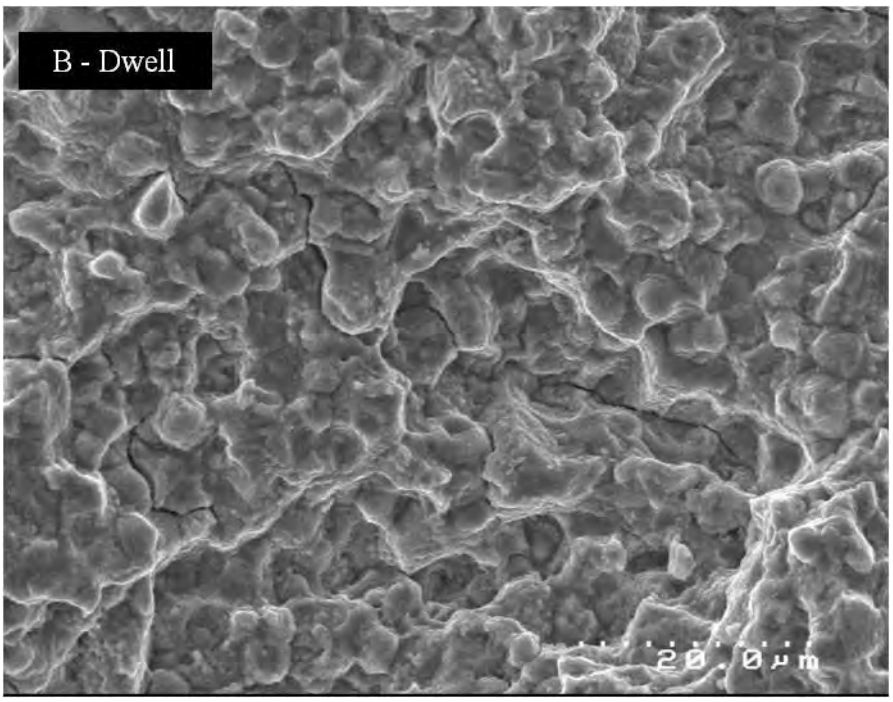
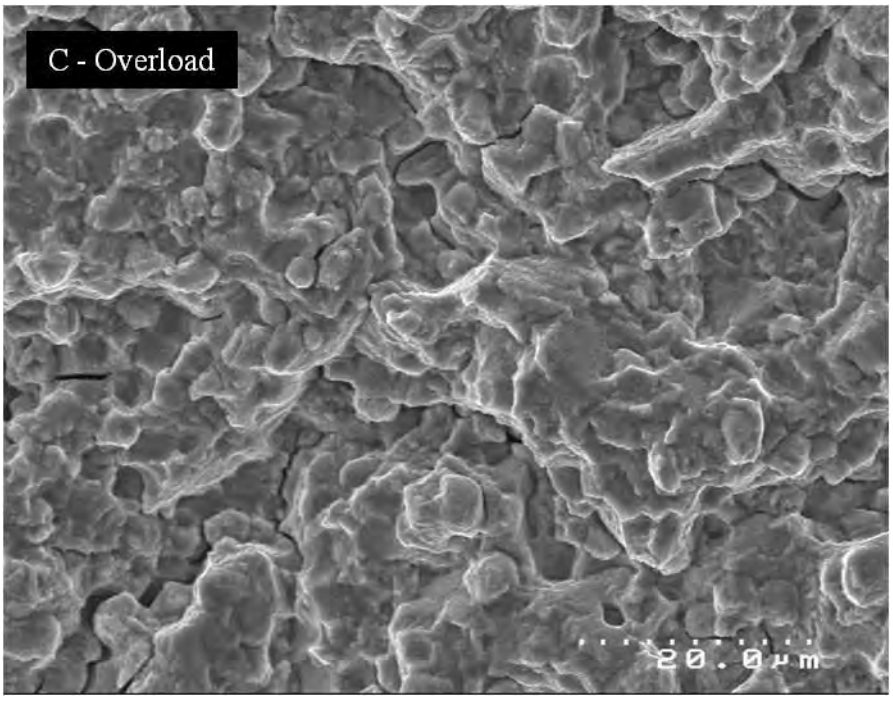


Figure A-67: Showing fractographs of fine-grained Udimet 720Li test piece CC029; tested at 650°C in air, with a dwell load of 26 kN, an overload factor of 1.15 and a dwell time of 1,200 seconds. Note that in this case; the overload segment was increased to a dwell time of 120 seconds rather than conventional 1 second hold periods in each other overload test. Each image shows the crack propagating from bottom left to top right. Bands labelled A and D are baseline (1-1-1-1) regions, the band labelled B represents the dwell region and the band labelled C; the overload region. Note also that within the large baseline segment (A), a small period of dwell cycling has been applied (hence the band in the image). Higher magnification images are taken at points relating to the following crack growth driving forces (ΔK): A: ~24 MPa√m; B: ~29 MPa√m; C: ~31 MPa√m; D: ~42 MPa√m


D
C
B
A
667µm


A - Baseline
20.0µm


B - Dwell
20.0µm


C - Overload
20.0µm

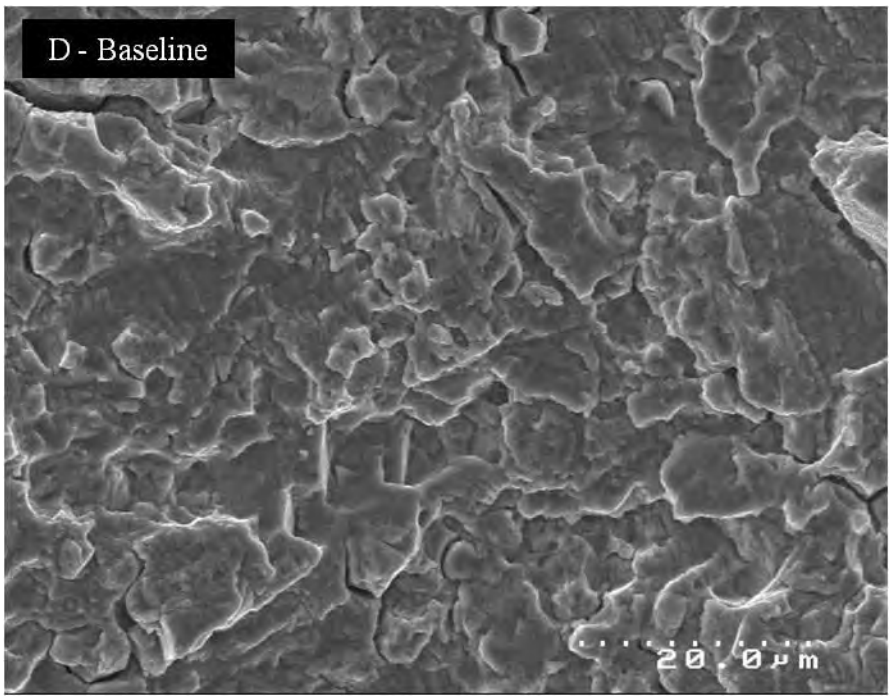
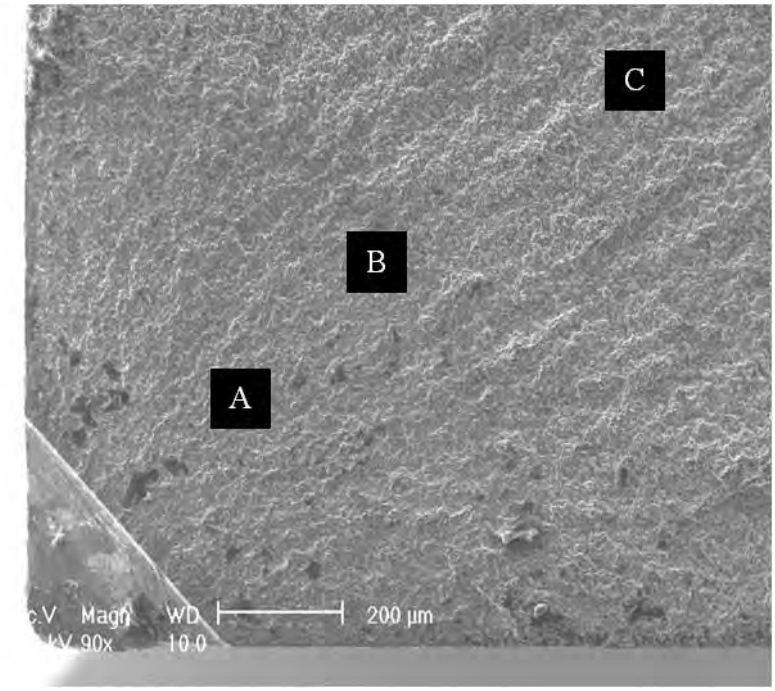
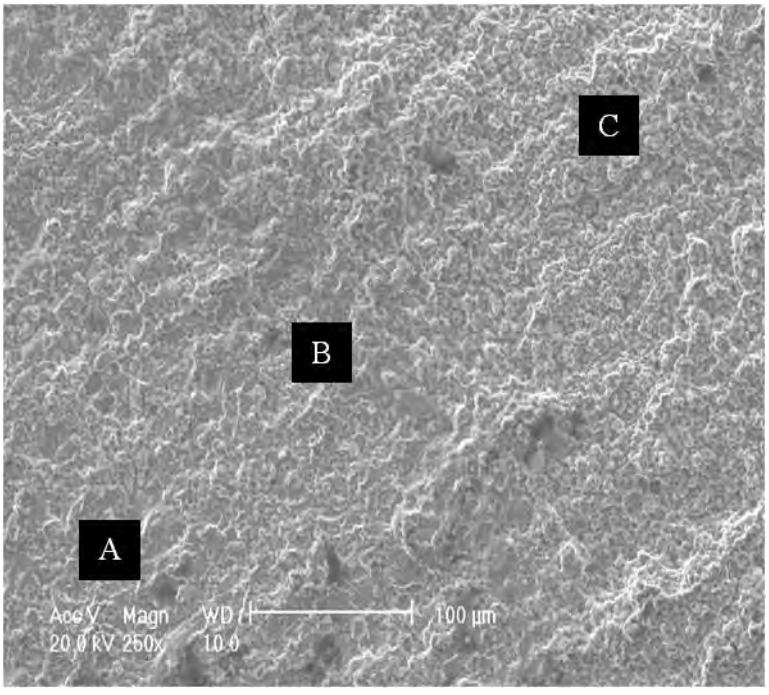
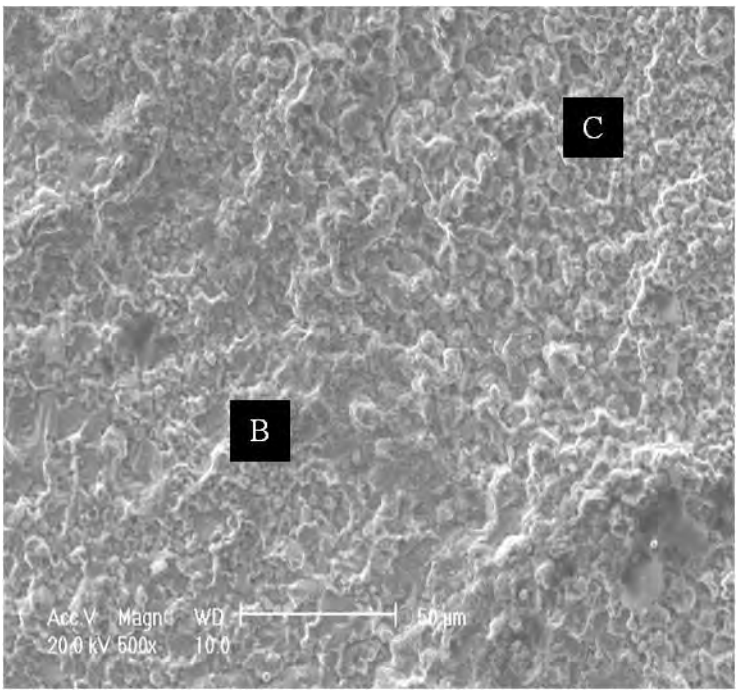


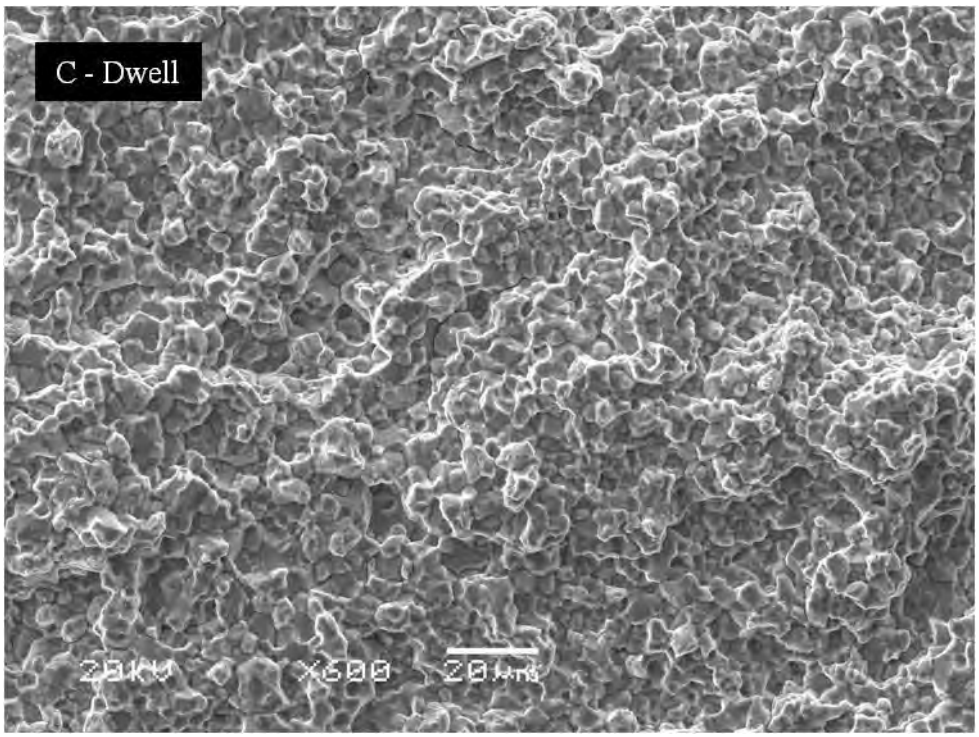
Figure A-68: Showing fractographs of fine-grained Udimet 720Li test piece CC032; tested at 650°C in air, with a dwell load of 26 kN, an overload factor of 1.15 and a dwell time of 1,200 seconds. Note that in this case; the overload segment was increased to a dwell time of 600 seconds rather than conventional 1 second hold periods in each other overload test. Each image shows the crack propagating from bottom left to top right. Bands labelled A and D are baseline (1-1-1-1) regions, the band labelled B represents the dwell region and the band labelled C; the overload region. Higher magnification images are taken at points relating to the following crack growth driving forces (ΔK): A: ~24 MPa√m; B: ~29 MPa√m; C: ~31 MPa√m; D: ~42 MPa√m; E: ~54.5 MPa√m

Udimet 720Li Time-dependent ΔK_{th} Tests






C
B
Acc.V Magn WD
20.0 kV 500x 10.0
50 µm


C - Dwell
20KV X600 20µm

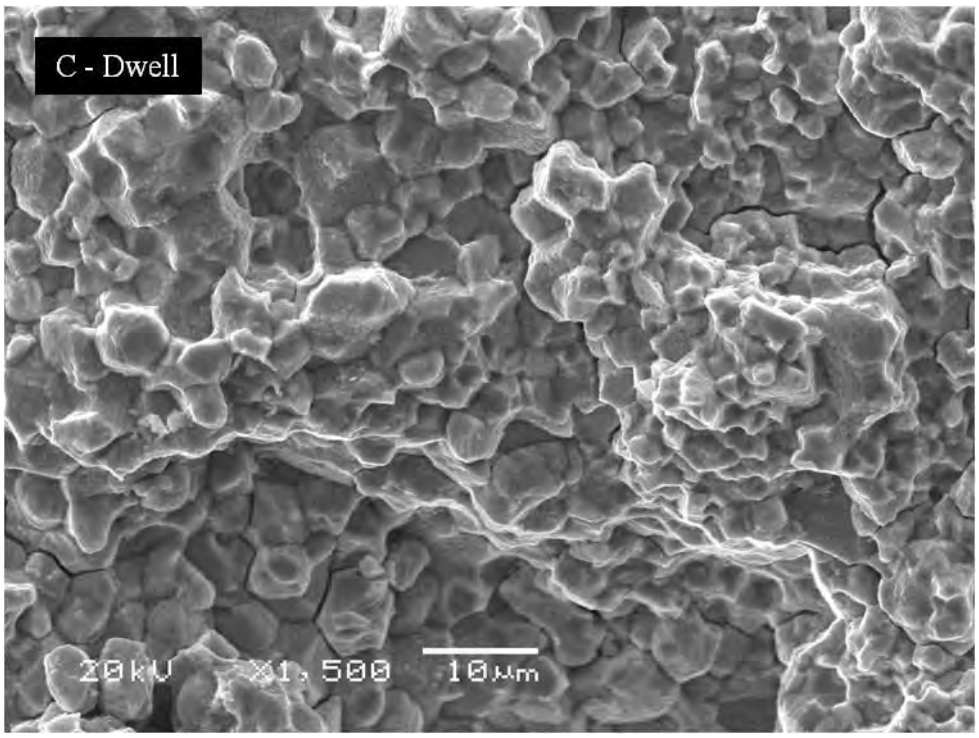
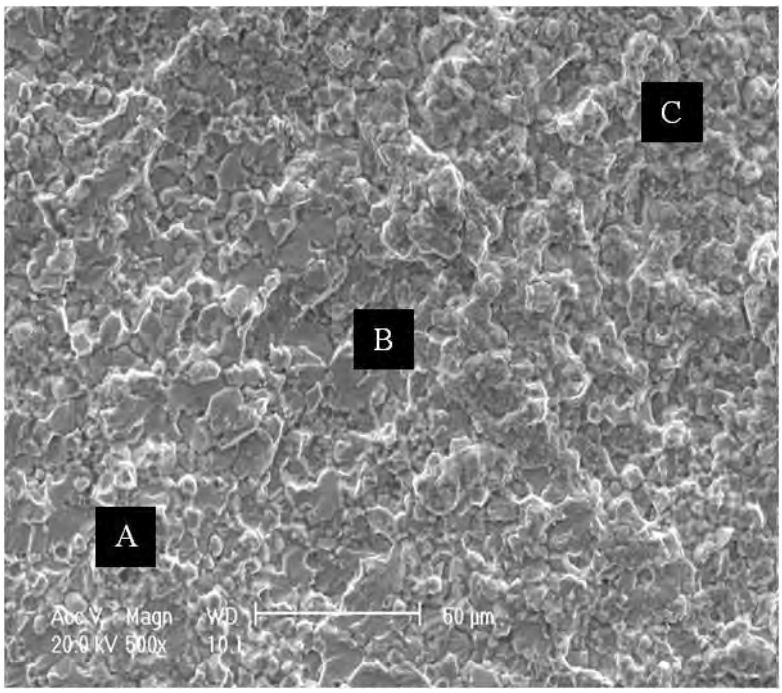
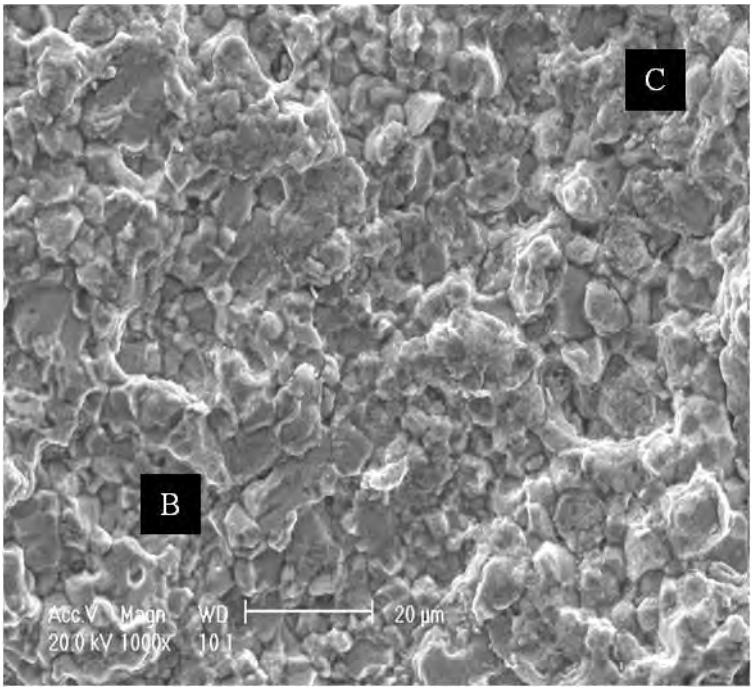


Figure A-69: Showing fractographs of fine-grained Udimet 720Li test piece CC040; tested at 650°C in air, with a dwell time of 120 seconds. The test piece was tested to determine the stress intensity factor range threshold (ΔK_{th}) for which time-dependent crack growth would occur. In this case, the test was carried out according to the increasing ΔK method, described in section 0. The band labelled A represents 1 Hz sinusoidal loading (carried out in air and at temperature), the band labelled C represents dwell cycling and a transition period between the two (in terms of mechanism) is labelled B. Each image shows the crack propagating from bottom left to top right. Higher magnification images are taken at points relating to the following crack growth driving forces (ΔK): Transition from A through B to C: ~14 MPa$\sqrt{m}$; C: ~20 MPa$\sqrt{m}$


C
B
A
Acc.V Magn WD
20.0 kV 500x 10.1
50 µm


C
B
Acc.V Magn WD
20.0 kV 1000x 10.1
20 µm

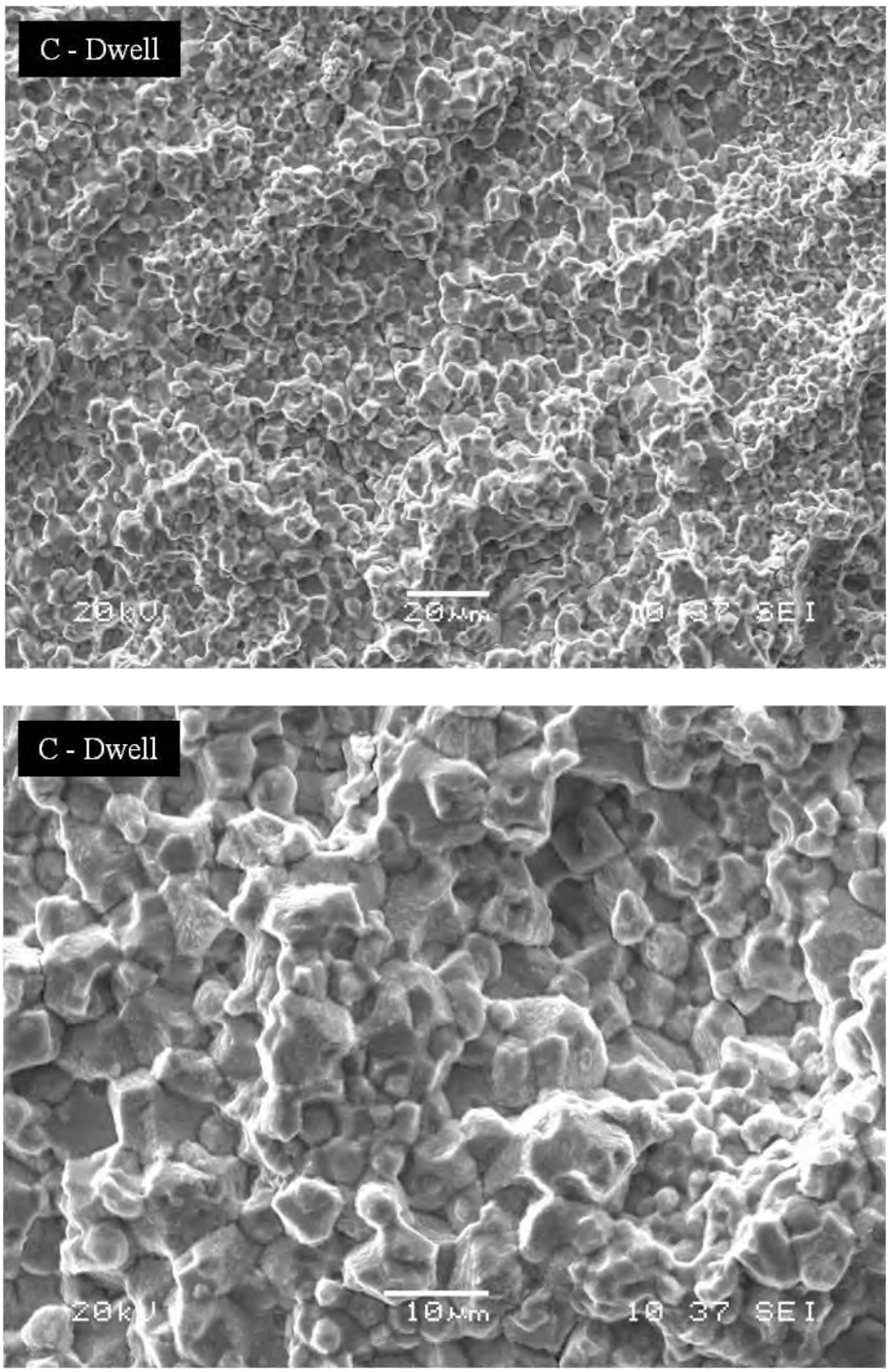


Figure A-70: Showing fractographs of fine-grained Udimet 720Li test piece CC041; tested at 650°C in air, with a dwell time of 120 seconds. The test piece was tested to determine the stress intensity factor range threshold (ΔK_{th}) for which time-dependent crack growth would occur. In this case, the test was carried out according to the increasing ΔK method, described in section 0. The band labelled A represents 1 Hz sinusoidal loading (carried out in air and at temperature), the band labelled C represents dwell cycling and a transition period between the two (in terms of mechanism) is labelled B. Each image shows the crack propagating from bottom left to top right. Higher magnification images are taken at points relating to the following crack growth driving forces (ΔK): Transition from A through B to C: ~12.5 MPa$\sqrt{m}$; C: ~20 MPa$\sqrt{m}$

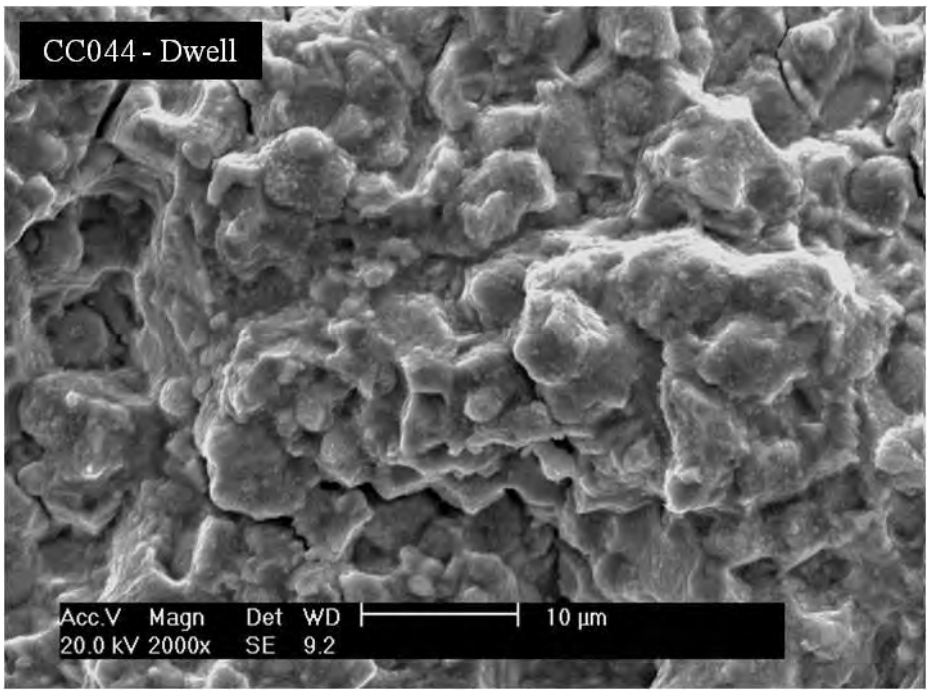
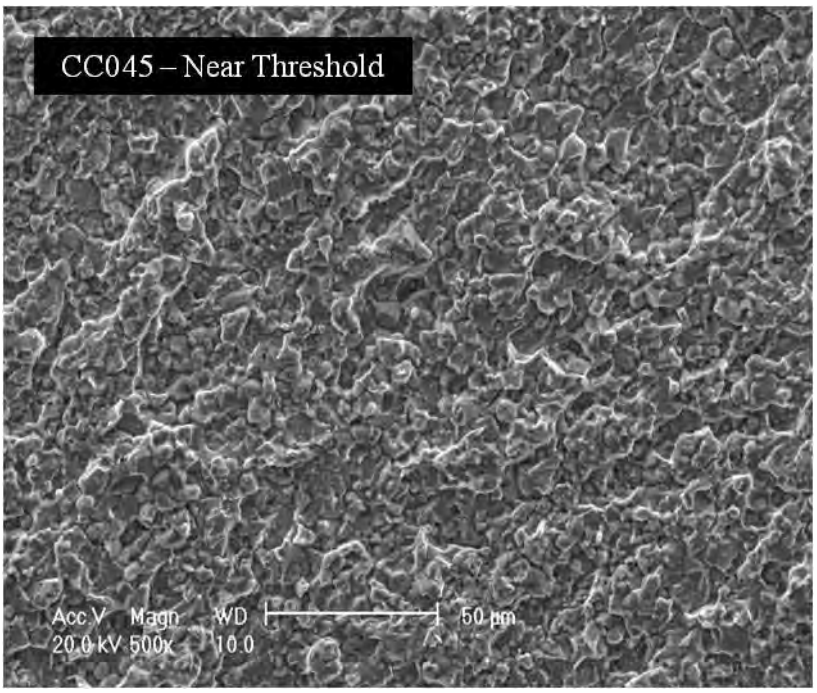
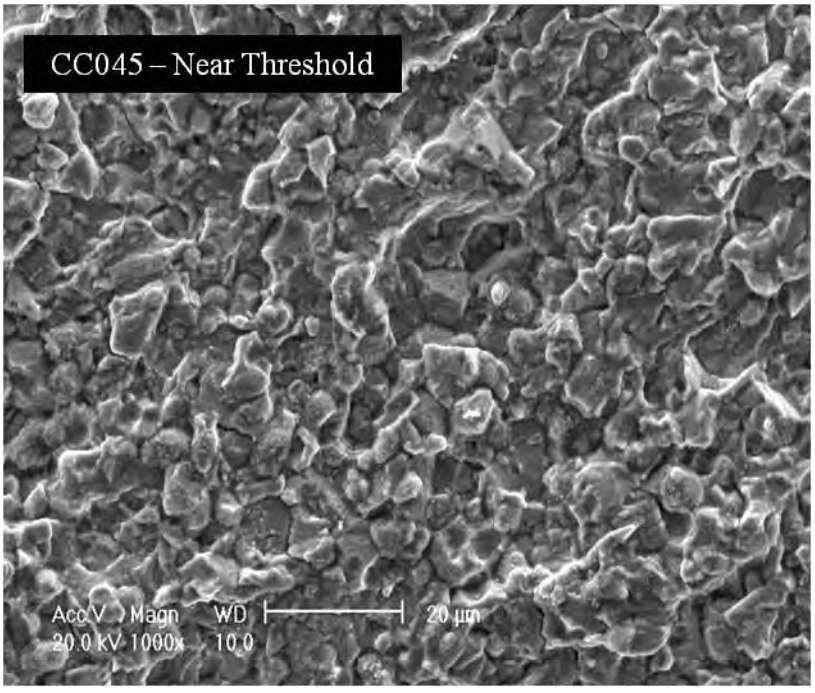


Figure A-71: Showing fractograph of fine-grained Udimet 720Li test piece CC044; tested at 650°C in air, with a dwell time of 120 seconds. The test piece was tested to determine the stress intensity factor range threshold (ΔK_{th}) for which time-dependent crack growth would occur. In this case, the test was carried out according to the decreasing ΔK method, described in section 0. The image is taken of the dwell region, at a ΔK of ~18.5 MPa$\sqrt{m}$


CC045 – Near Threshold
Acc.V Magn WD
20.0 kV 500x 10.0
50 µm


CC045 – Near Threshold
Acc.V Magn WD
20.0 kV 1000x 10.0
20 µm

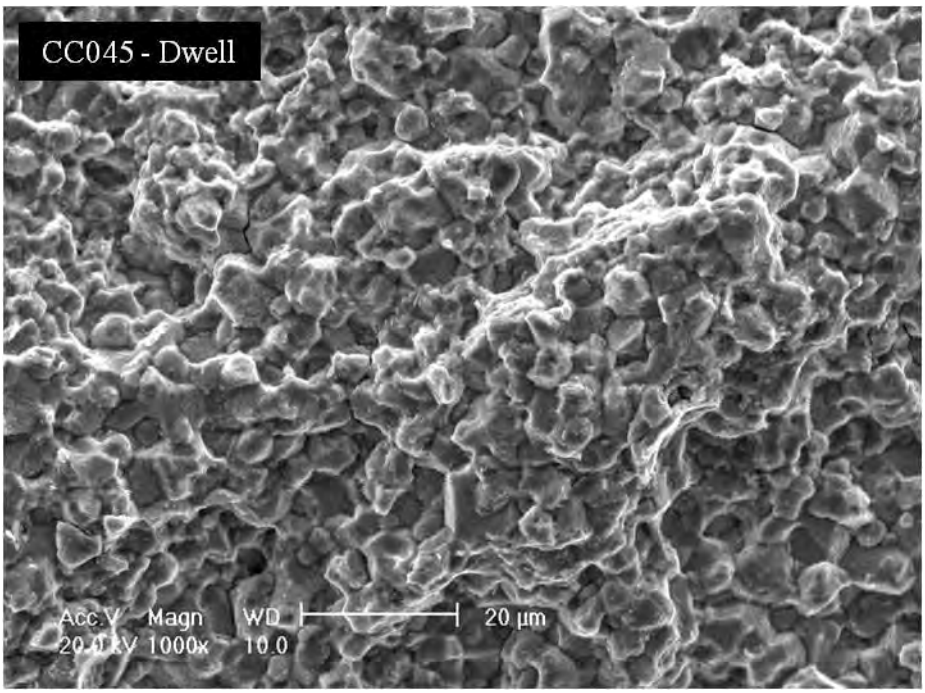
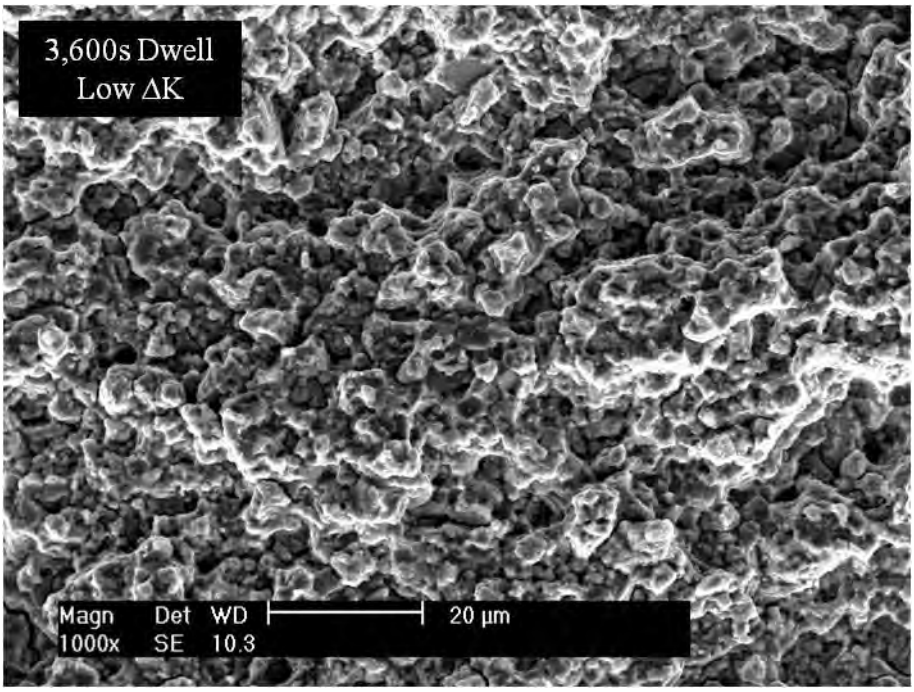
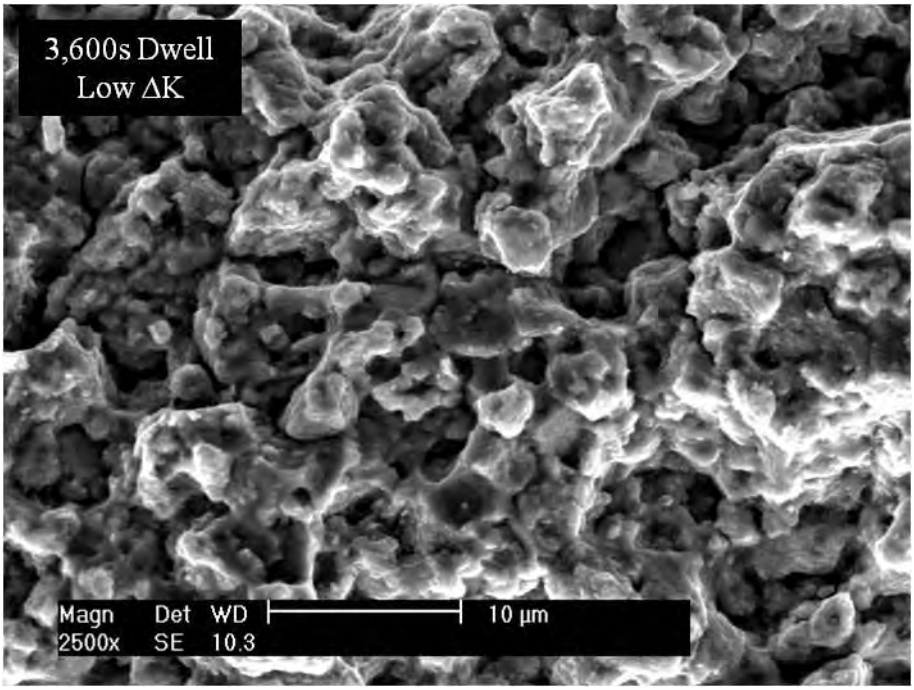


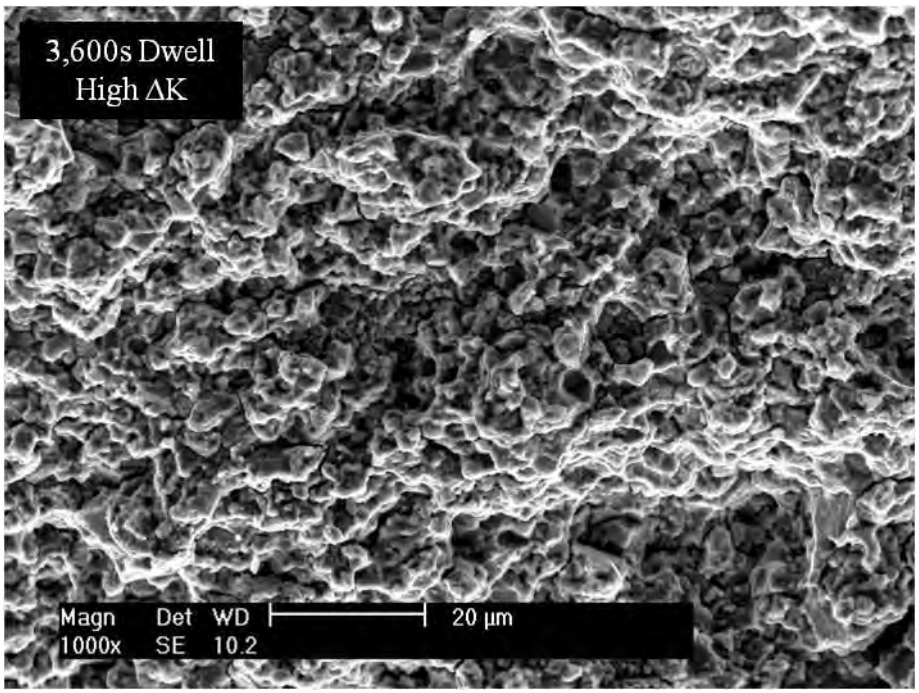
Figure A-72: Showing fractographs of fine-grained Udimet 720Li test piece CC045; tested at 650°C in air, with a dwell time of 1,200 seconds. The test piece was tested to determine the stress intensity factor range threshold (ΔK_{th}) for which time-dependent crack growth would occur. In this case, the test was carried out according to the increasing ΔK method, described in section 0. Each image shows the crack propagating from bottom left to top right. Higher magnification images are taken at points relating to the following crack growth driving forces (ΔK): Near threshold: ~10.5 MPa√m; dwell cycling: ~13 MPa√m

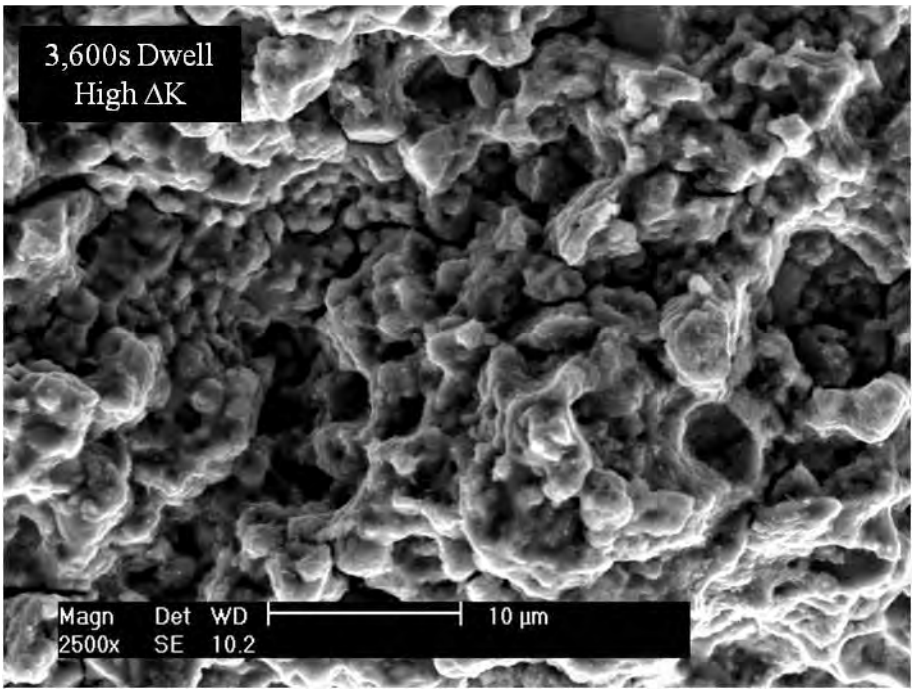
RR1000

RR1000 Baseline and Dwell Tests






3,600s Dwell
High ΔK
Magn Det WD
1000x SE 10.2
20 µm


3,600s Dwell
High ΔK
Magn Det WD
2500x SE 10.2
10 µm

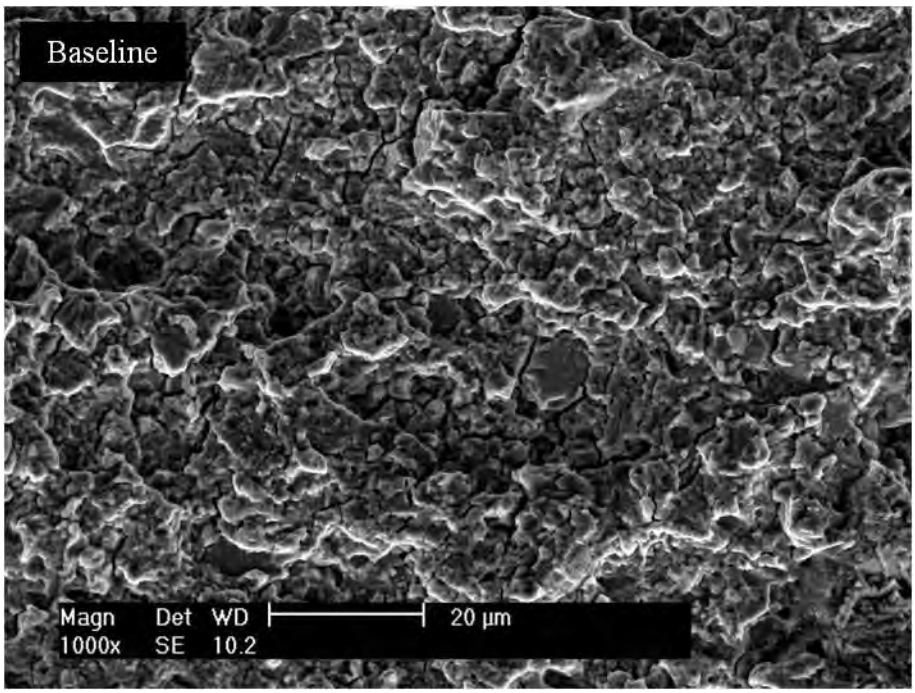
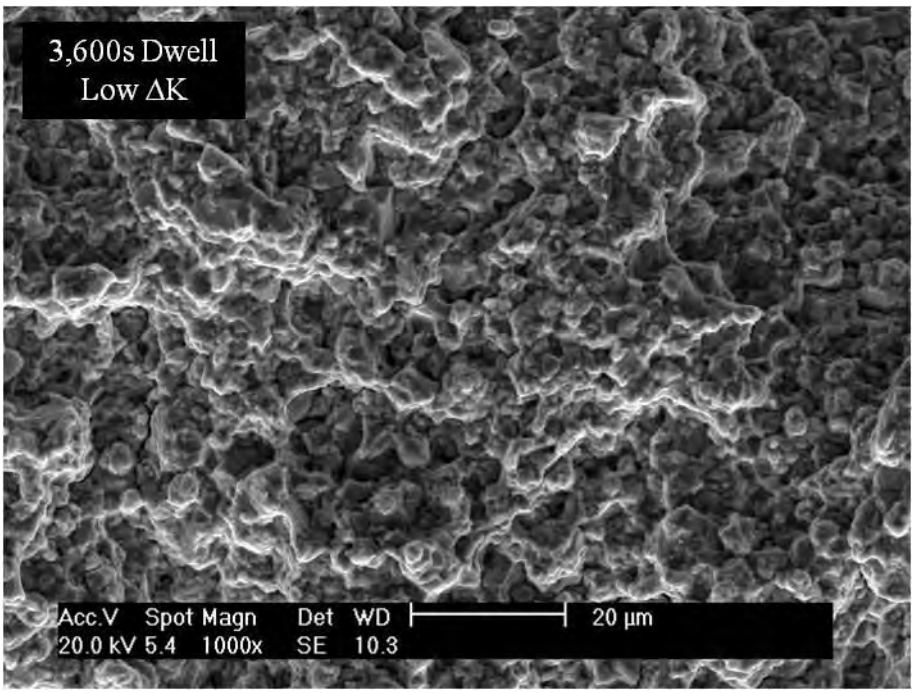
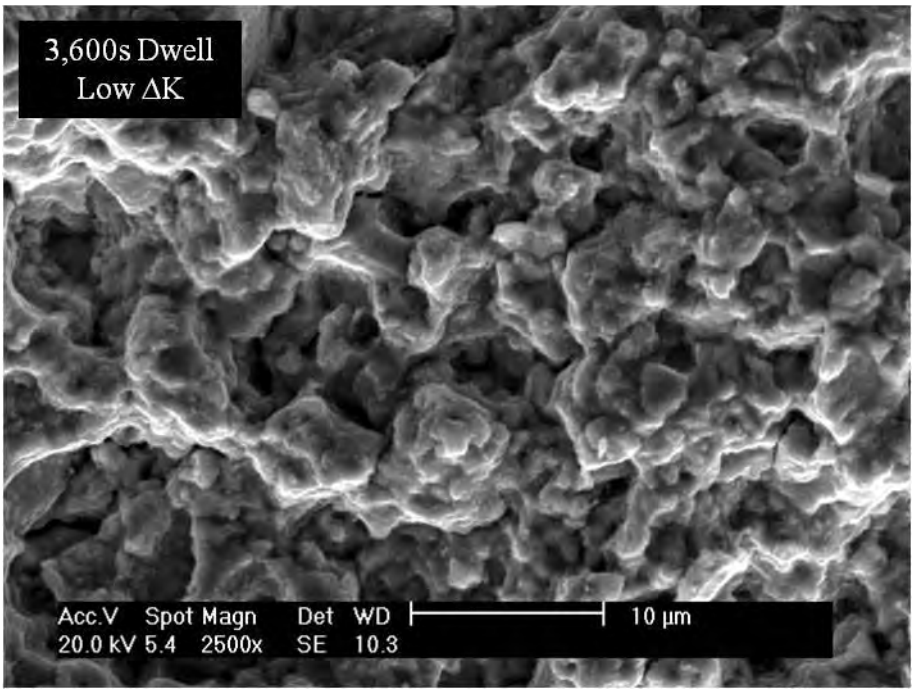
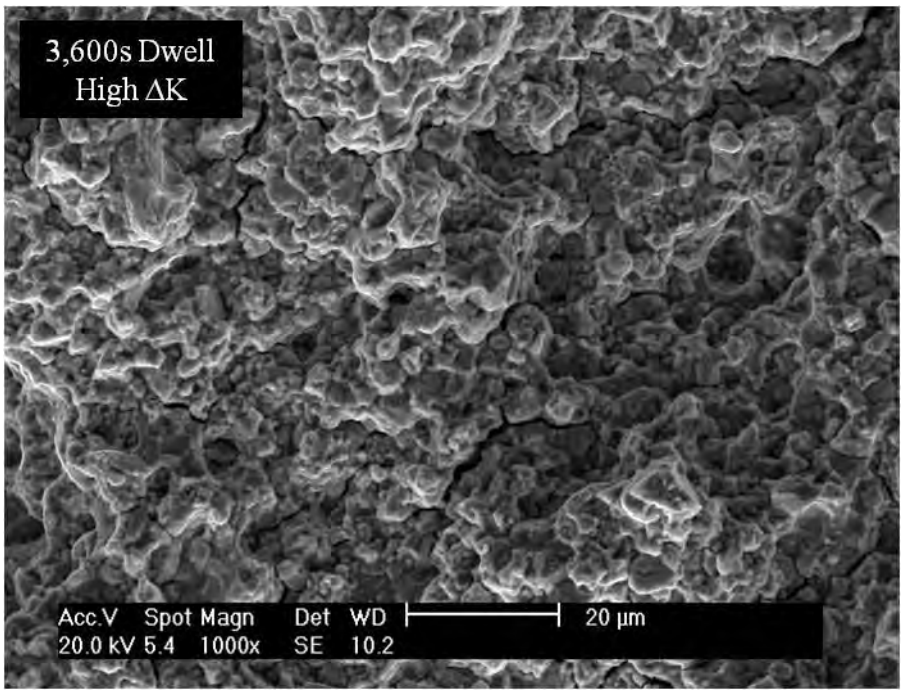
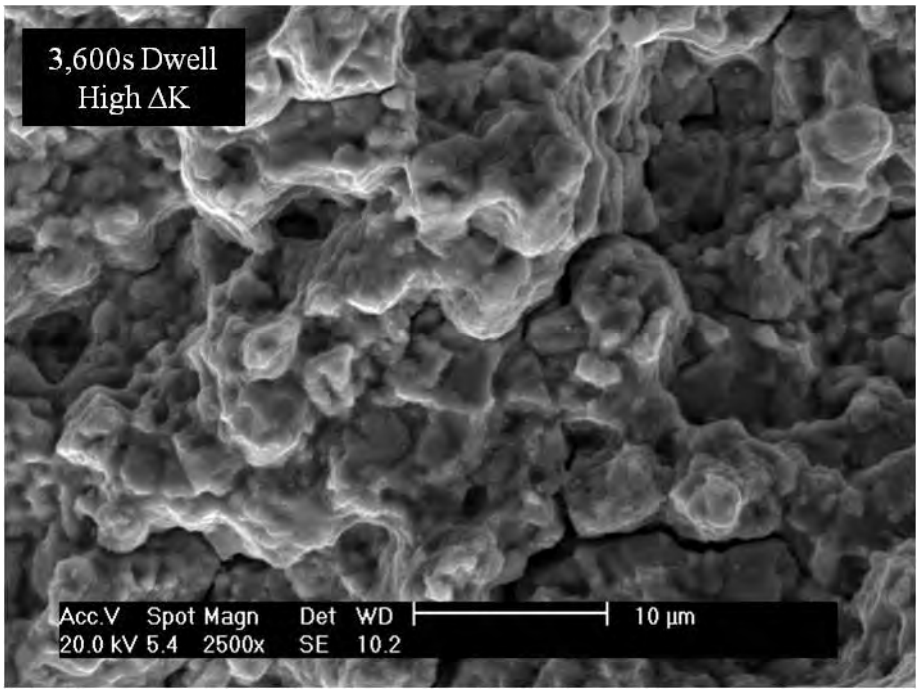


Figure A-73: Showing fractographs of fine-grained RR1000 test piece CC002; tested at 650°C in air, with a dwell load of 26 kN and a dwell time of 3,600 seconds. Each image shows the crack propagating from left to right. Note that crack growth mechanisms according to 3,600 seconds dwell in air appear to be predominantly intergranular; and that crack growth mechanisms pertaining to baseline loading are predominantly transgranular. Higher magnification images are taken at points relating to the following crack growth driving forces (ΔK): "low ΔK" 3,6000 second dwell: ~22 MPa√m; "high ΔK" 3,6000 second dwell: ~36 MPa√m; baseline: ~43 MPa√m


3,600s Dwell
Low ΔK
Acc.V Spot Magn Det WD 20 µm
20.0 kV 5.4 1000x SE 10.3


3,600s Dwell
Low ΔK
Acc.V Spot Magn Det WD 10 µm
20.0 kV 5.4 2500x SE 10.3


3,600s Dwell
High ΔK
Acc.V Spot Magn Det WD 20 µm
20.0 kV 5.4 1000x SE 10.2


3,600s Dwell
High ΔK
Acc.V Spot Magn Det WD 10 µm
20.0 kV 5.4 2500x SE 10.2

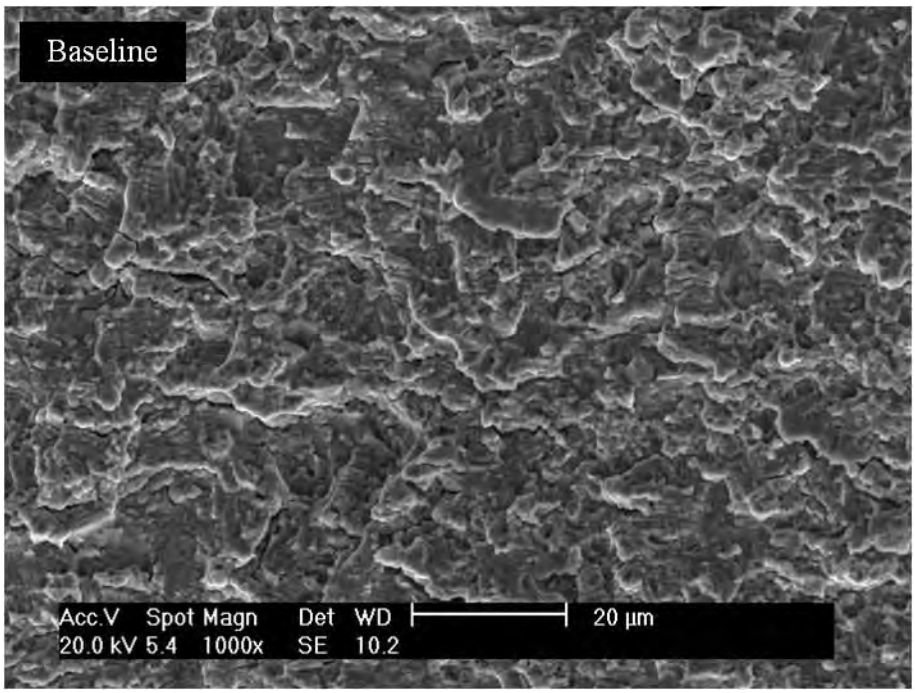
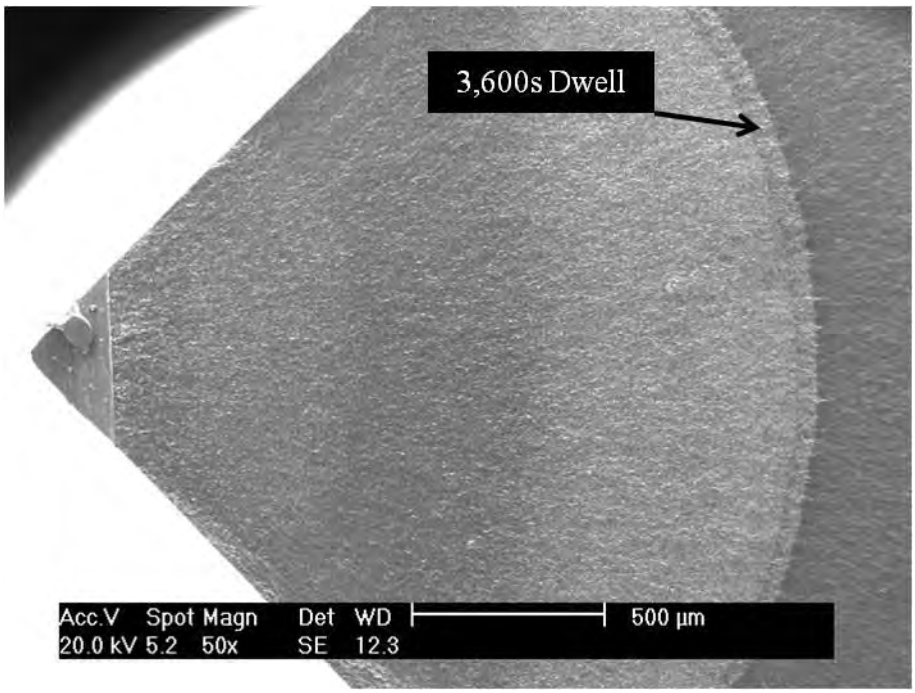
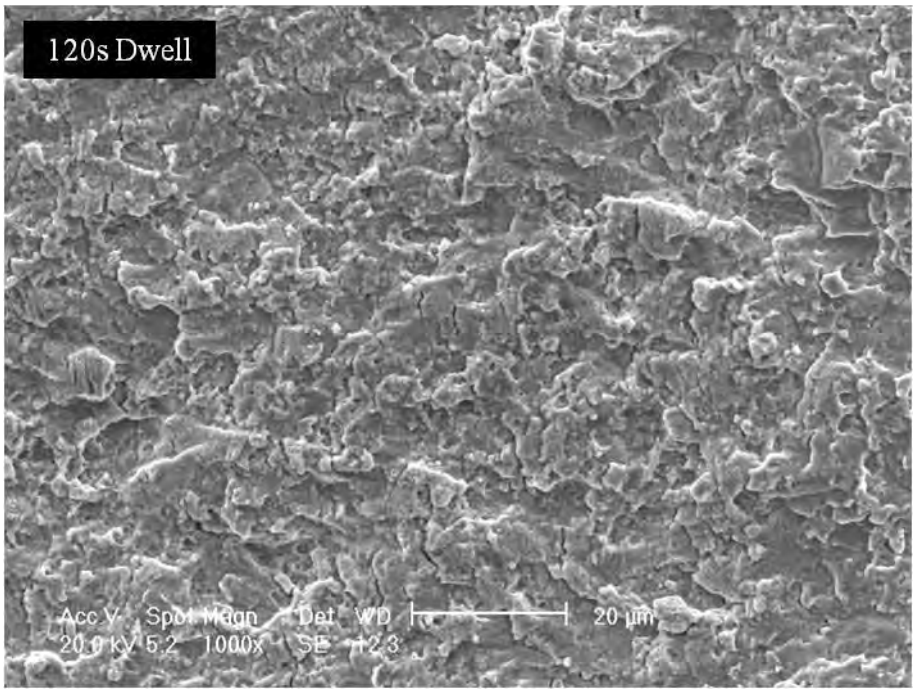
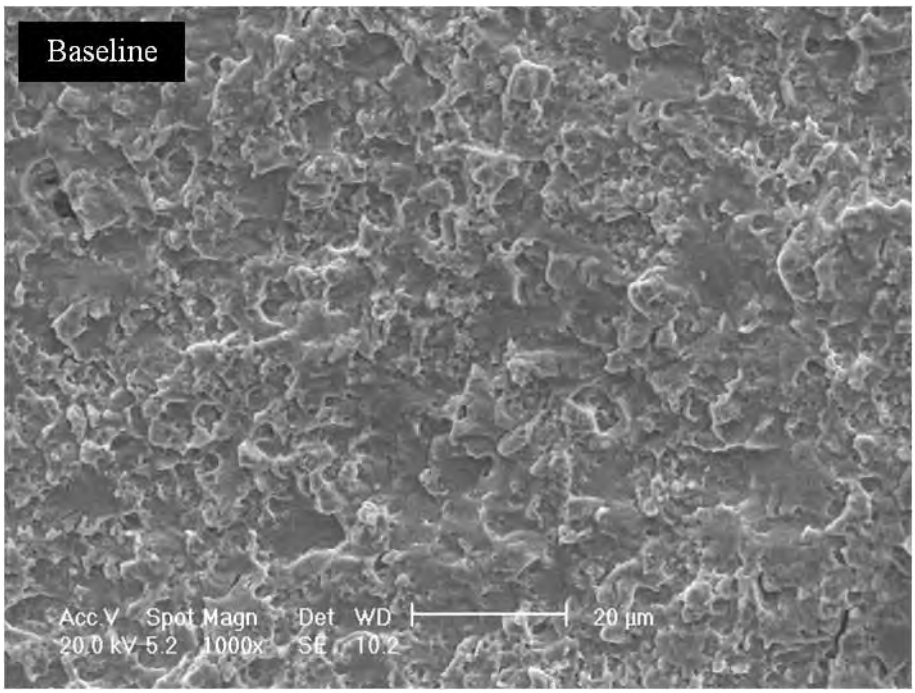
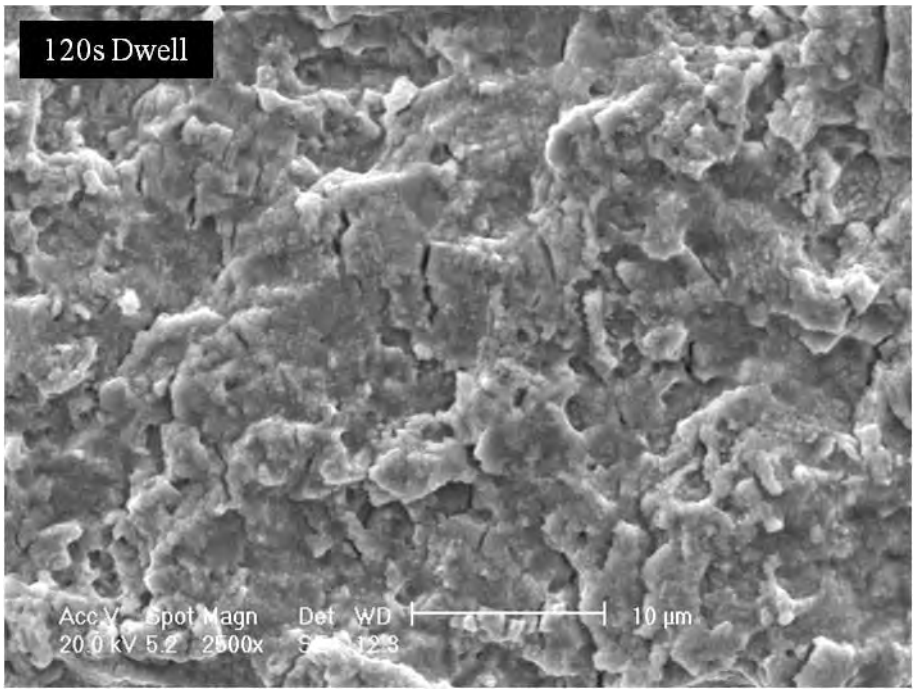


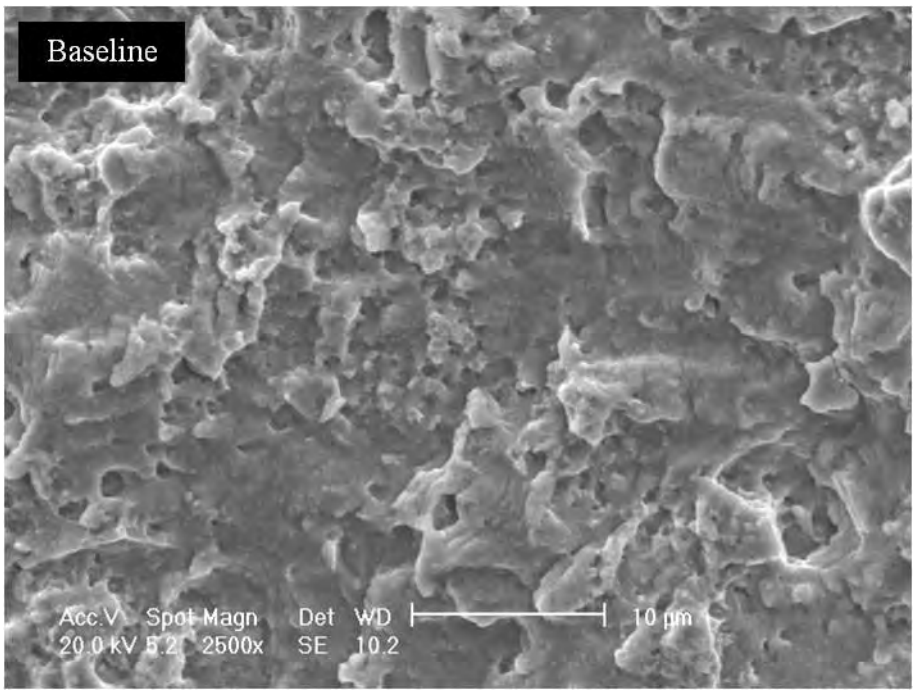
Figure A-74: Showing fractographs of fine-grained RR1000 test piece CC003; tested at 600°C in air, with a dwell load of 26 kN and a dwell time of 3,600 seconds. Each image shows the crack propagating from top to bottom. Note that crack growth mechanisms according to 3,600 seconds dwell in air appear to be predominantly intergranular; and that crack growth mechanisms pertaining to baseline loading are predominantly transgranular. Higher magnification images are taken at points relating to the following crack growth driving forces (ΔK): "low ΔK" 3,6000 second dwell: ~21 MPa√m; "high ΔK" 3,6000 second dwell: ~37 MPa√m; baseline: ~44 MPa√m

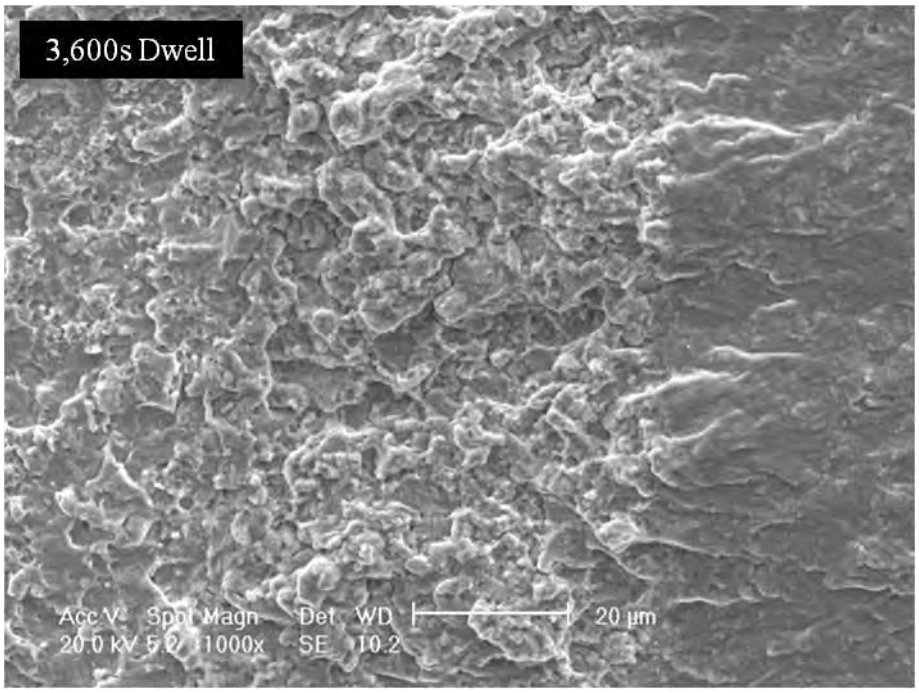

3,600s Dwell
Acc.V Spot Magn Det WD 500 µm
20.0 kV 5.2 50x SE 12.3


120s Dwell
Acc.V Spot Magn Det WD 20 µm
20.0 kV 5.2 1000x SE 12.3


Baseline
Acc.V Spot Magn Det WD 20 µm
20.0 kV 5.2 1000x SE 10.2


120s Dwell
Acc.V Spot Magn Det WD 10 µm
20.0 kV 5.2 2500x


Baseline
Acc.V Spot Magn Det WD 10 µm
20.0 kV 5.2 2500x SE 10.2


3,600s Dwell
Acc.V Spot Magn Det WD 20 µm
20.0 kV 5.2 1000x SE 10.2

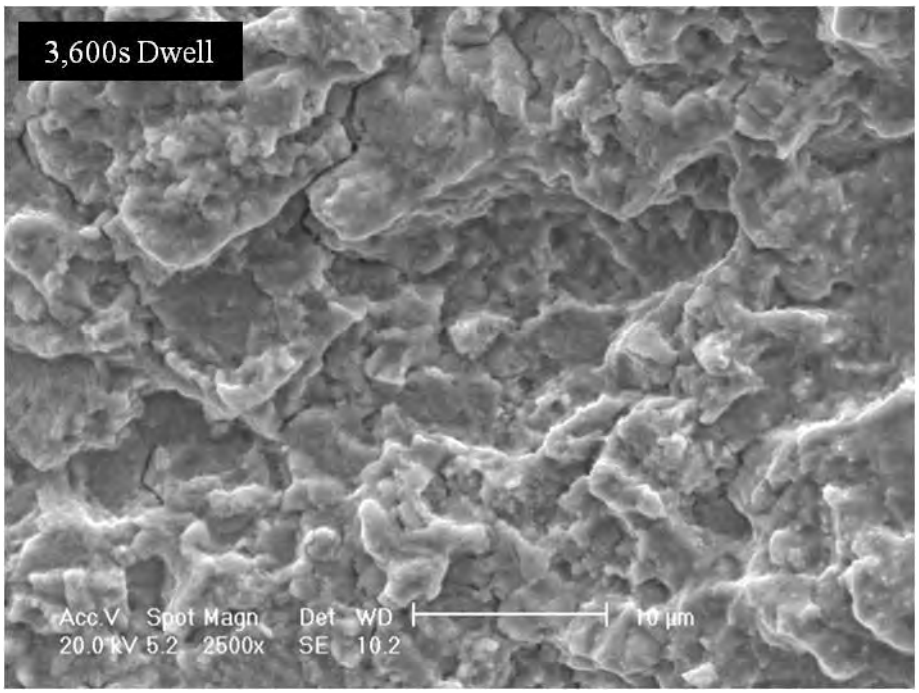
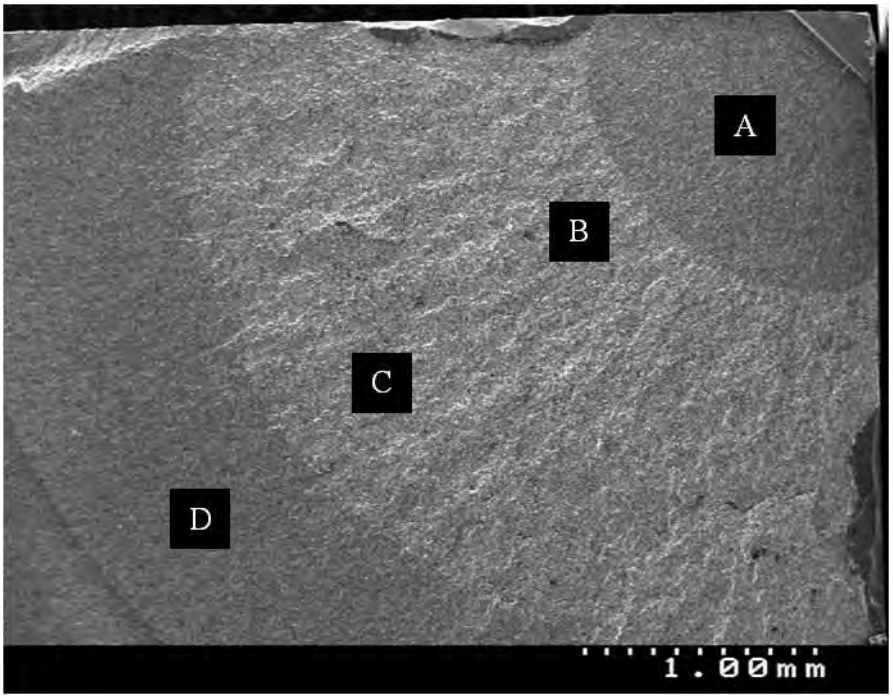
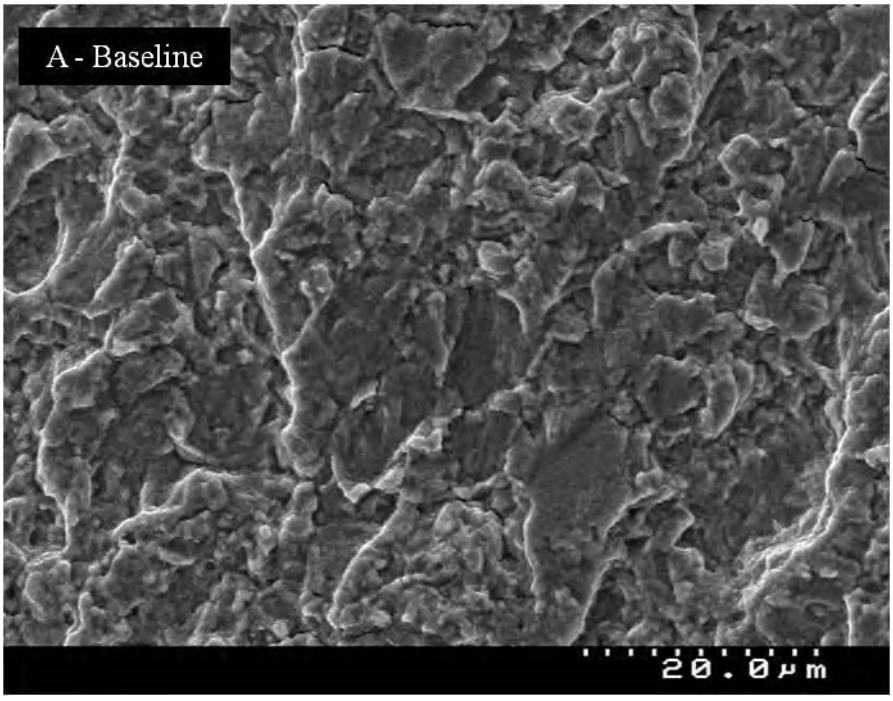
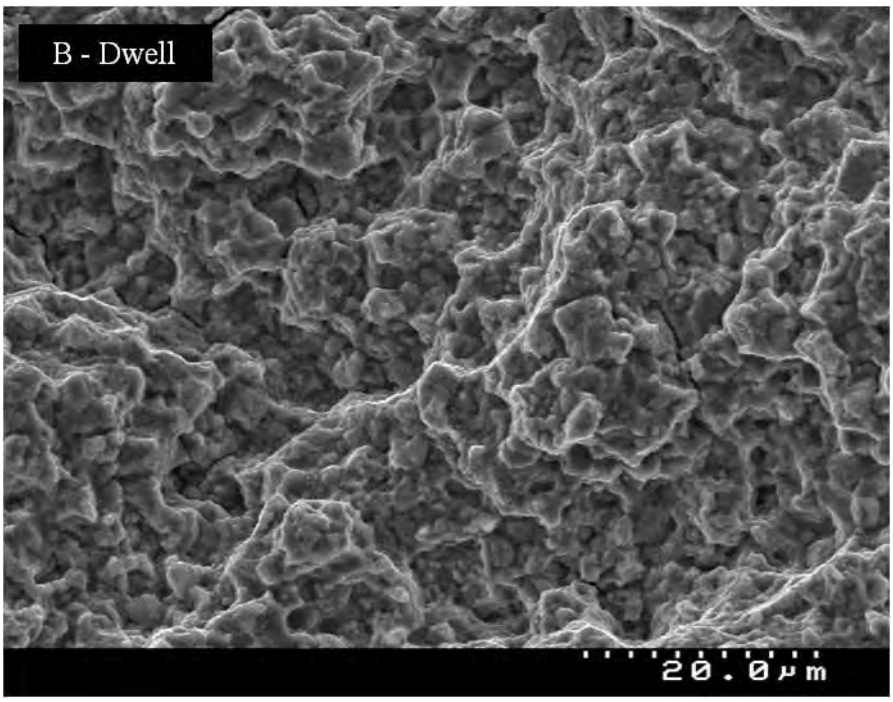


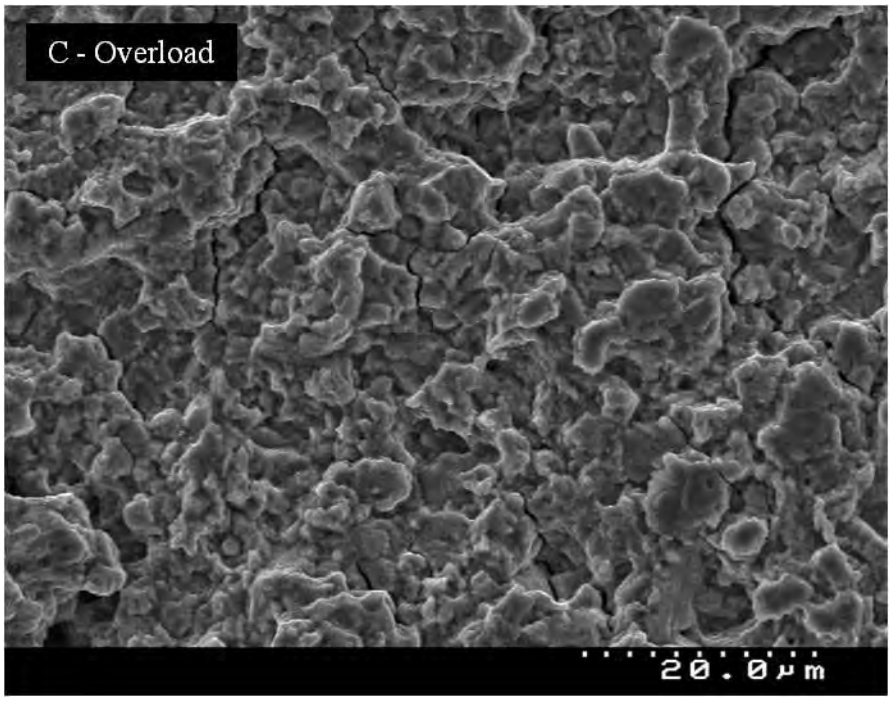
Figure A-75: Showing fractographs of fine-grained RR1000 test piece CC030; tested at 650°C in a vacuum, with a dwell load of 26 kN, and dwell times of 120 and 3,600 seconds. (The band of 120 second crack growth is indistinguishable on the lower magnification image from baseline regions.) Each image shows the crack propagating from left to right. Note that crack growth mechanisms according to 120 seconds dwell in a vacuum appear to be predominantly transgranular; yet crack growth mechanisms according to 3,600 seconds dwell appear intergranular. Higher magnification images are taken at points relating to the following crack growth driving forces (ΔK): 120 second dwell: ~22 MPa√m; baseline: ~26 MPa√m; 3,600 second dwell: ~28 MPa√m

RR1000 Baseline, Dwell and Overload Tests






B - Dwell
20.0µm


C - Overload
20.0µm

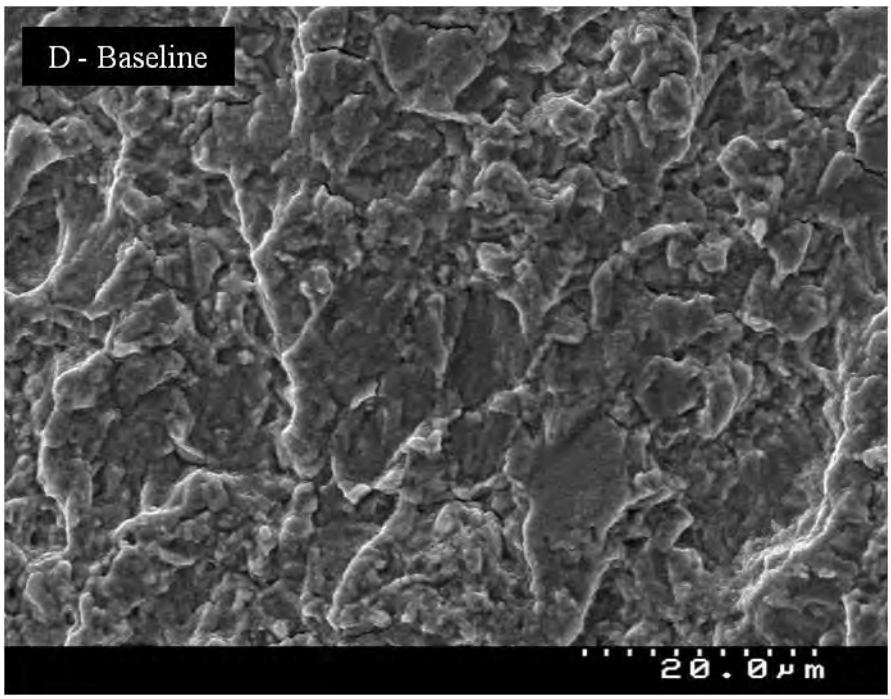
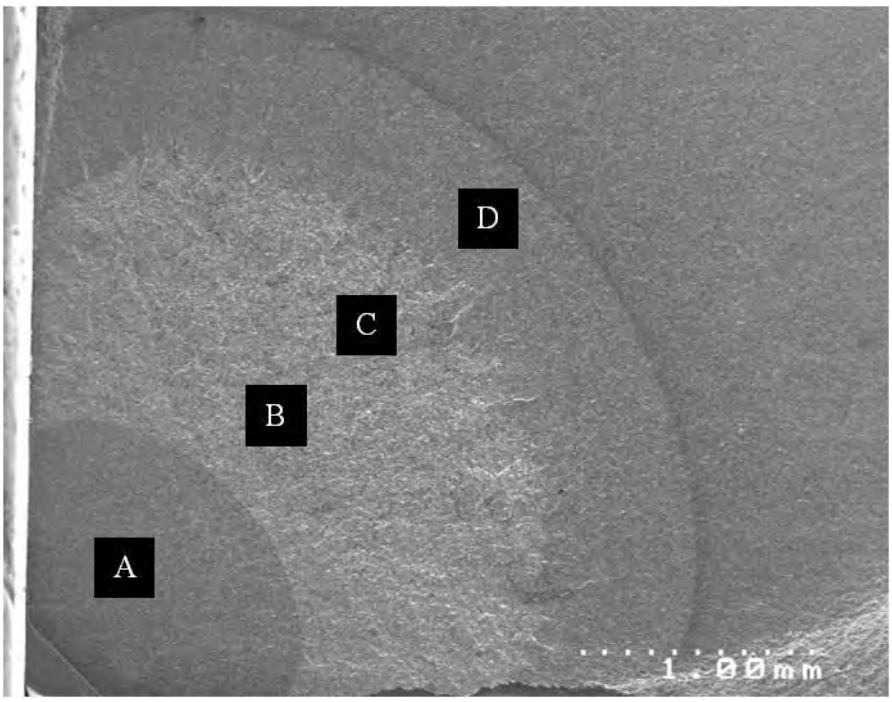
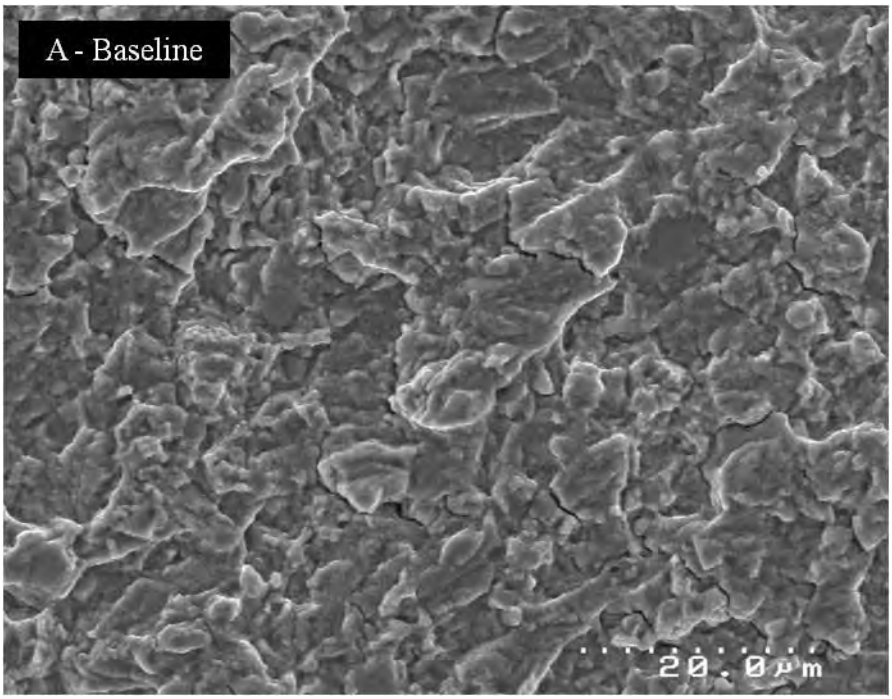
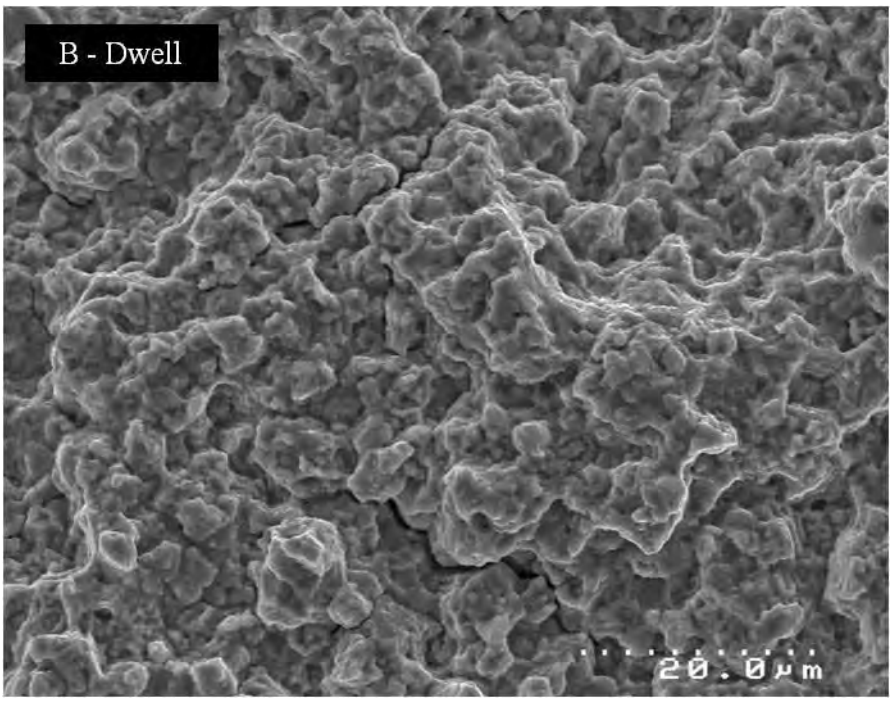
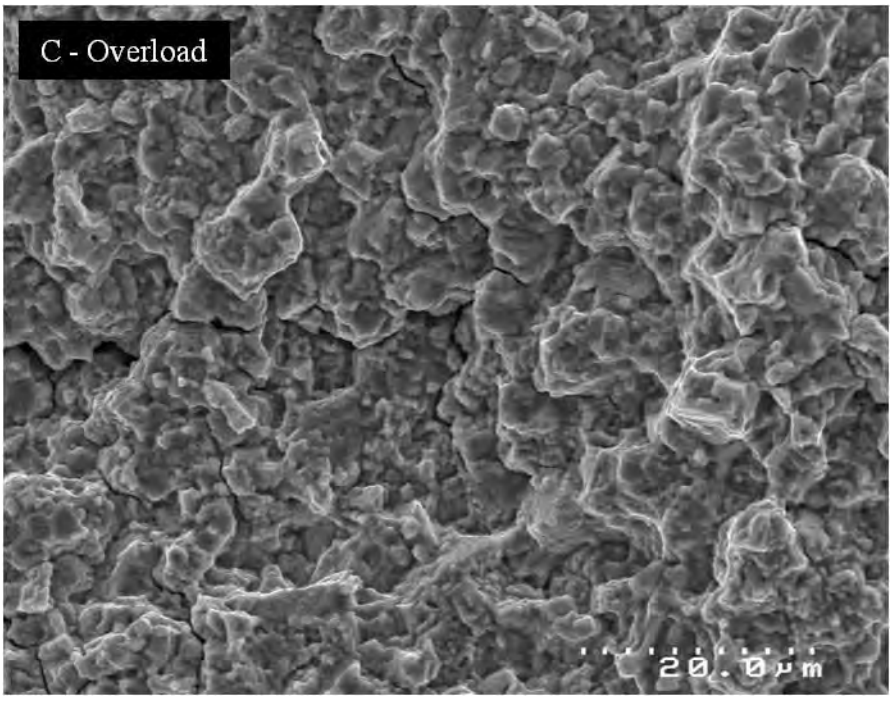


Figure A-76: Showing fractographs of fine-grained RR1000 test piece CC019; tested at 600°C in air, with a dwell load of 26 kN, an overload factor of 1.15 and a dwell time of 1,200 seconds. Each image shows the crack propagating from top right to bottom left. Bands labelled A and D are baseline (1-1-1-1) regions, the band labelled B represents the dwell region and the band labelled C; the overload region. Full retardation is judged to have occurred. Higher magnification images are taken at points relating to the following crack growth driving forces (ΔK): A: ~18 MPa√m; B: ~25 MPa√m; C: ~39 MPa√m; D: ~45 MPa√m


D
C
B
A
1.00mm


A - Baseline
20.0µm


B - Dwell
20.0µm


C - Overload
20.0µm

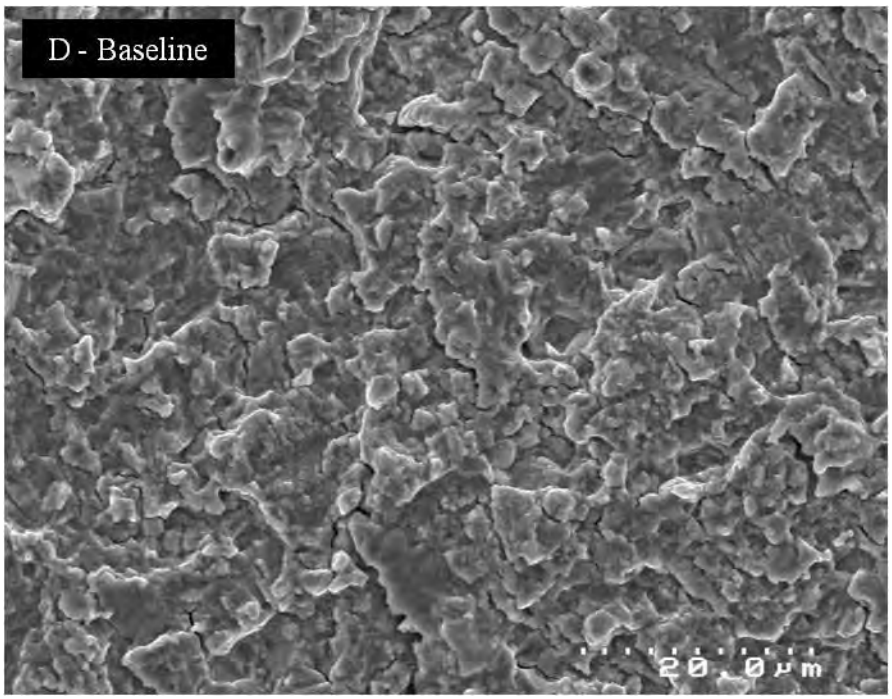
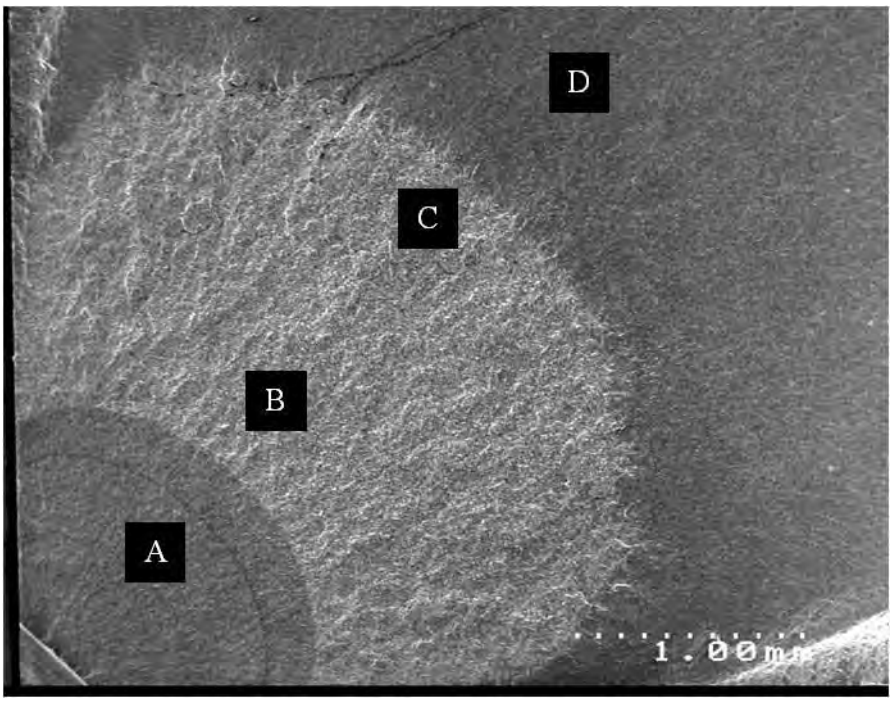
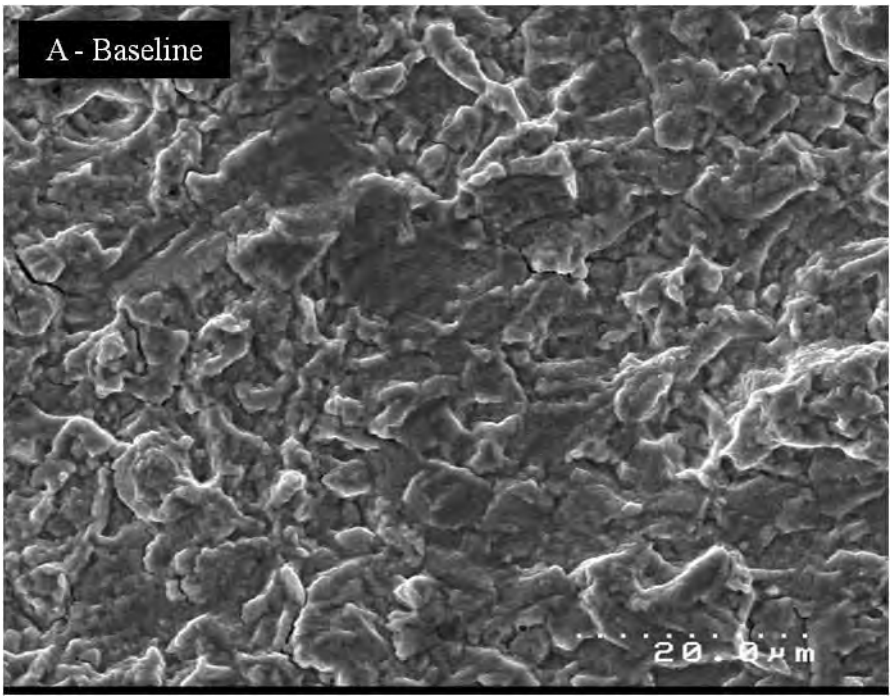


Figure A-77: Showing fractographs of fine-grained RR1000 test piece CC021; tested at 600°C in air, with a dwell load of 26 kN, an overload factor of 1.05 and a dwell time of 1,200 seconds. Each image shows the crack propagating from bottom left to top right. Bands labelled A and D are baseline (1-1-1-1) regions, the band labelled B represents the dwell region and the band labelled C; the overload region. Partial retardation is judged to have occurred. Higher magnification images are taken at points relating to the following crack growth driving forces (ΔK): A: ~18 MPa√m; B: ~22.5 MPa√m; C: ~26 MPa√m; D: ~30 MPa√m


D
C
B
A
1.00mm


A - Baseline
20.0µm

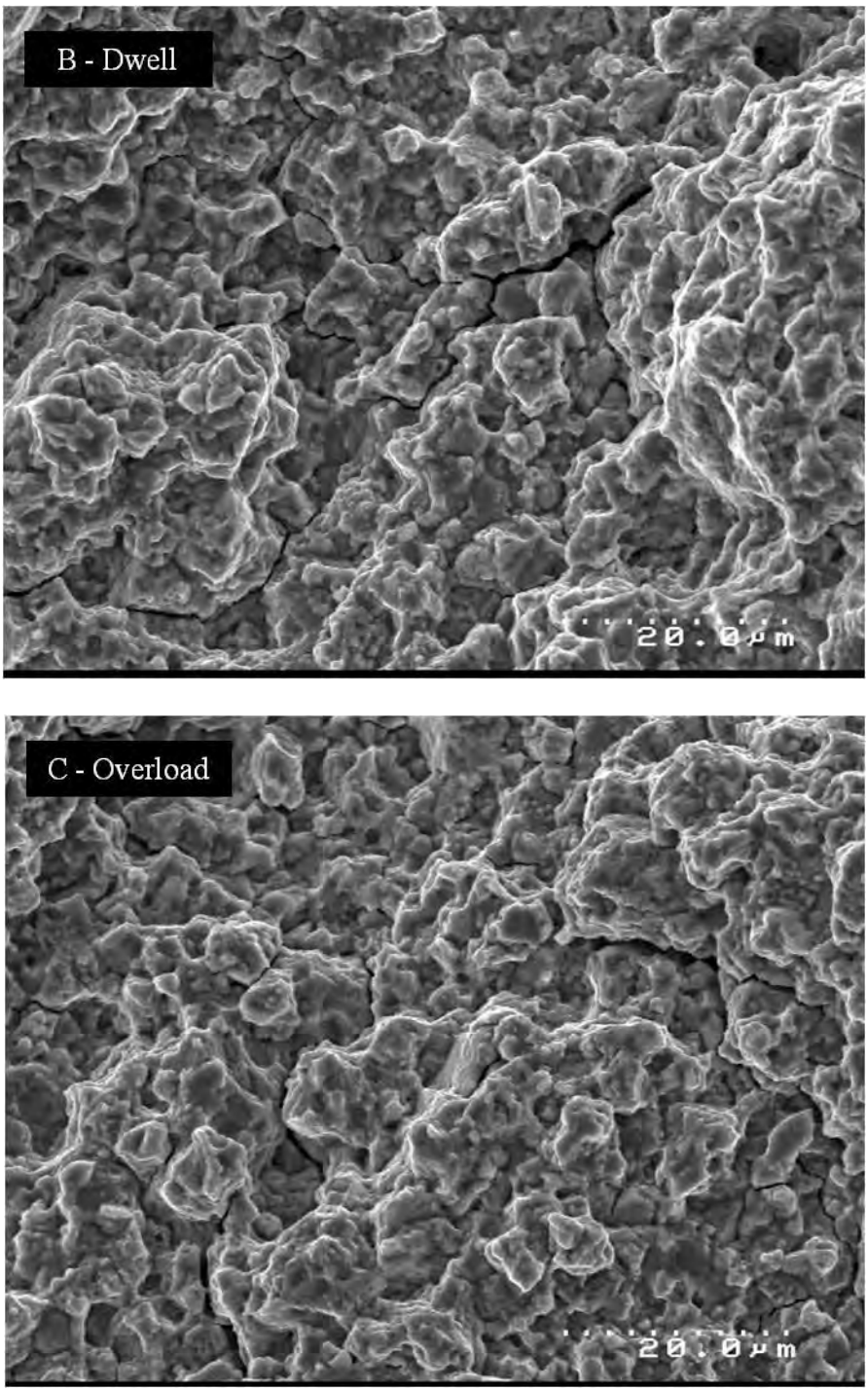
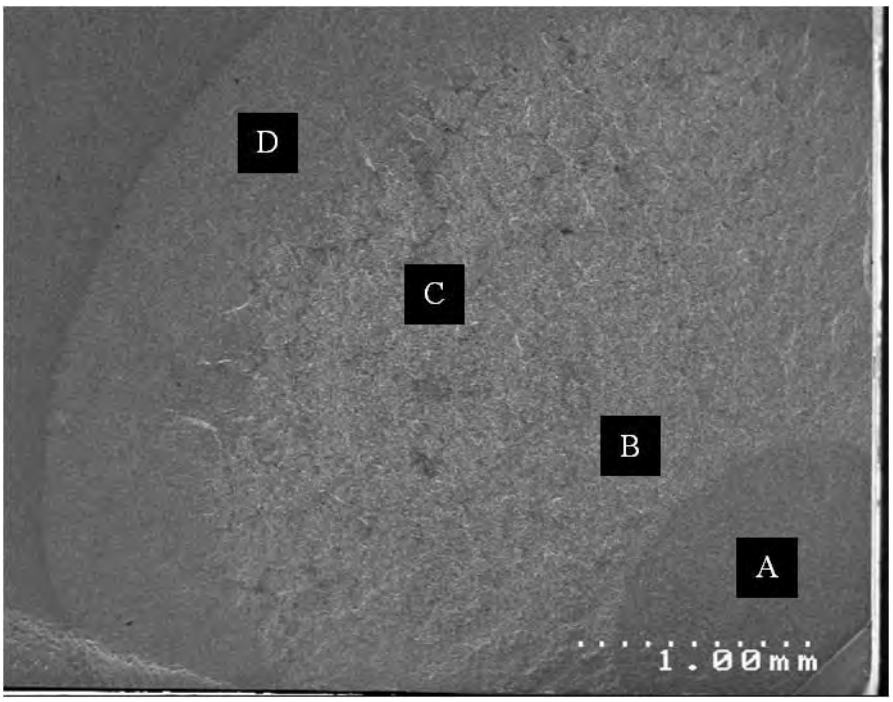
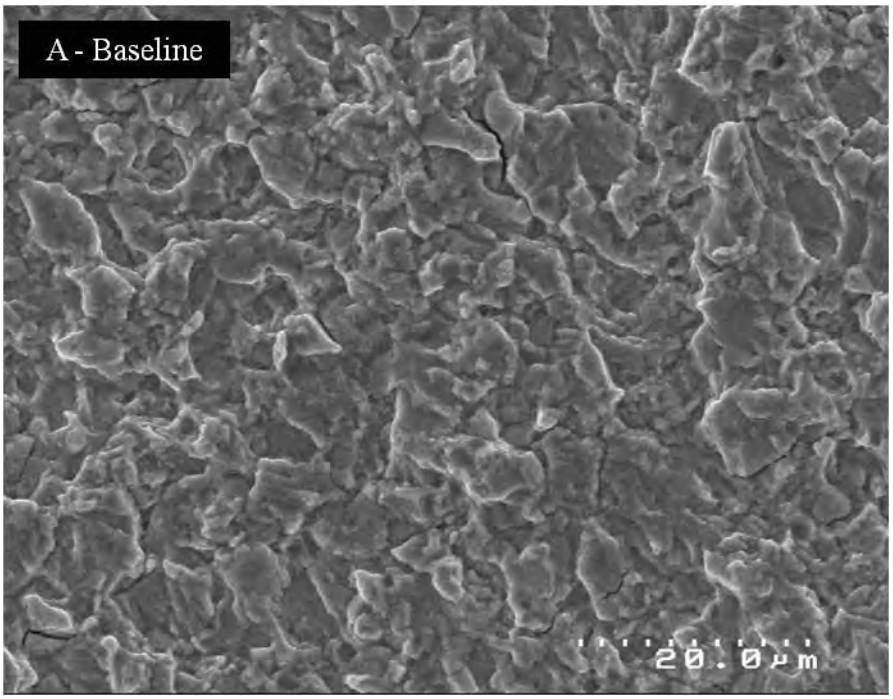
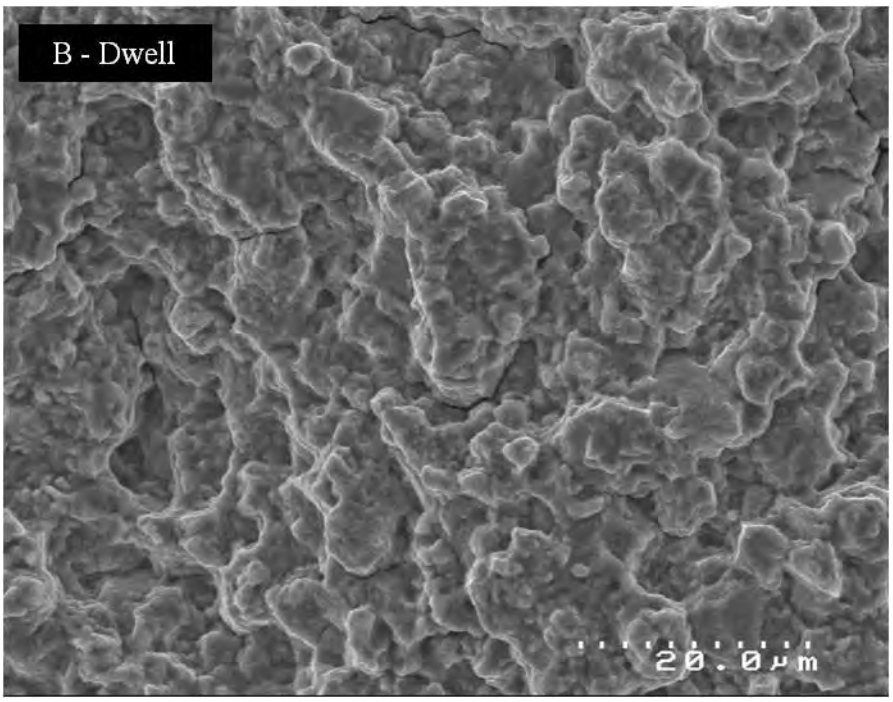
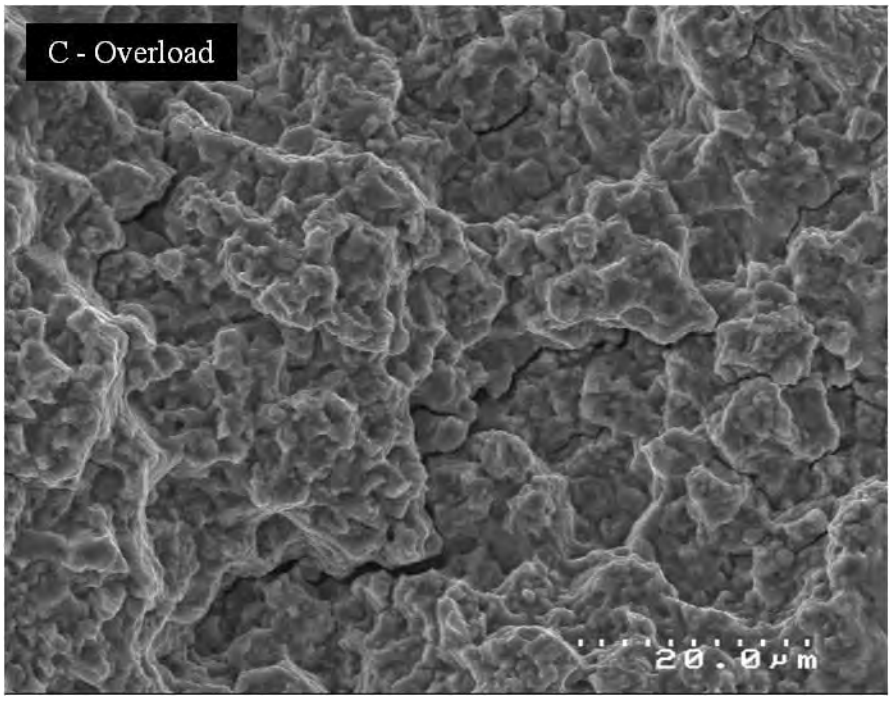


Figure A-78: Showing fractographs of fine-grained RR1000 test piece CC042; tested at 600°C in air, with a dwell load of 26 kN, an overload factor of 1.05 and a dwell time of 3,600 seconds. Each image shows the crack propagating from bottom left to top right. Bands labelled A and D are baseline (1-1-1-1) regions, the band labelled B represents the dwell region and the band labelled C; the overload region. Partial retardation is judged to have occurred. Higher magnification images are taken at points relating to the following crack growth driving forces (ΔK): A: ~19.5 MPa√m; B: ~25 MPa√m; C: ~34 MPa√m


D
C
B
A
1.00mm


A - Baseline
20.0µm


B - Dwell
20.0µm


C - Overload
20.0µm

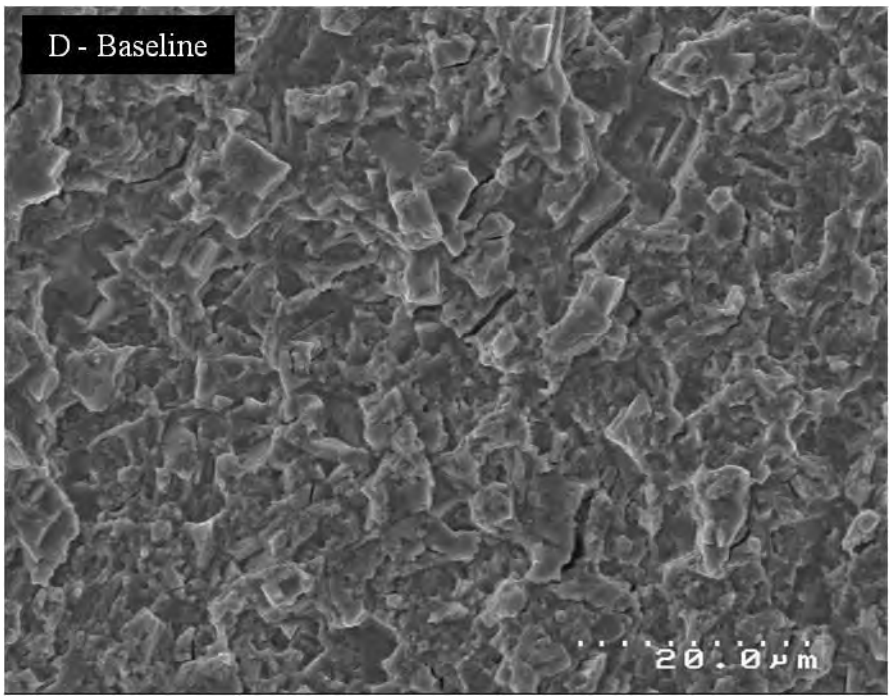
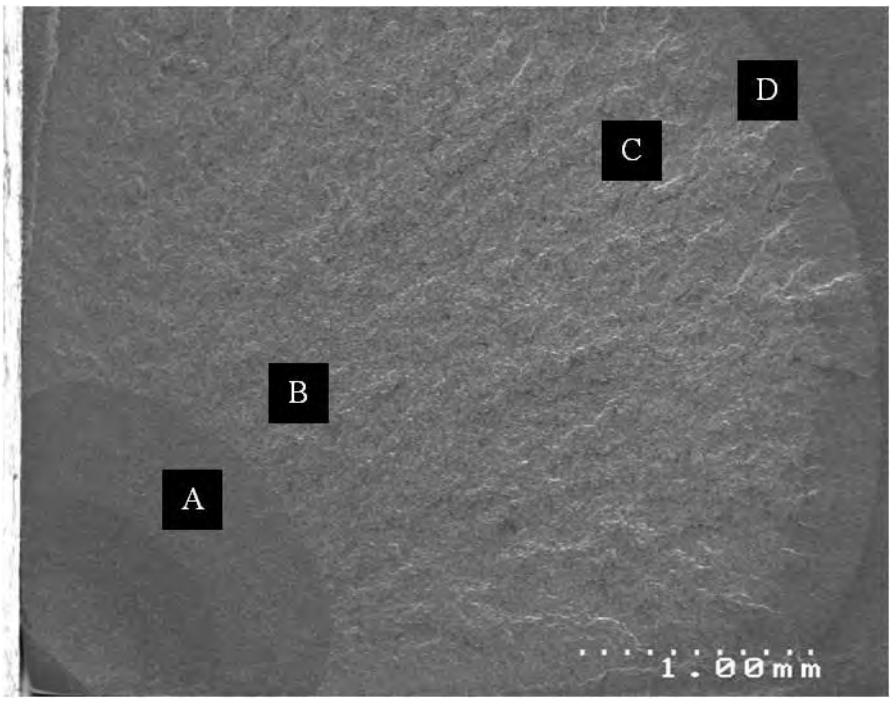
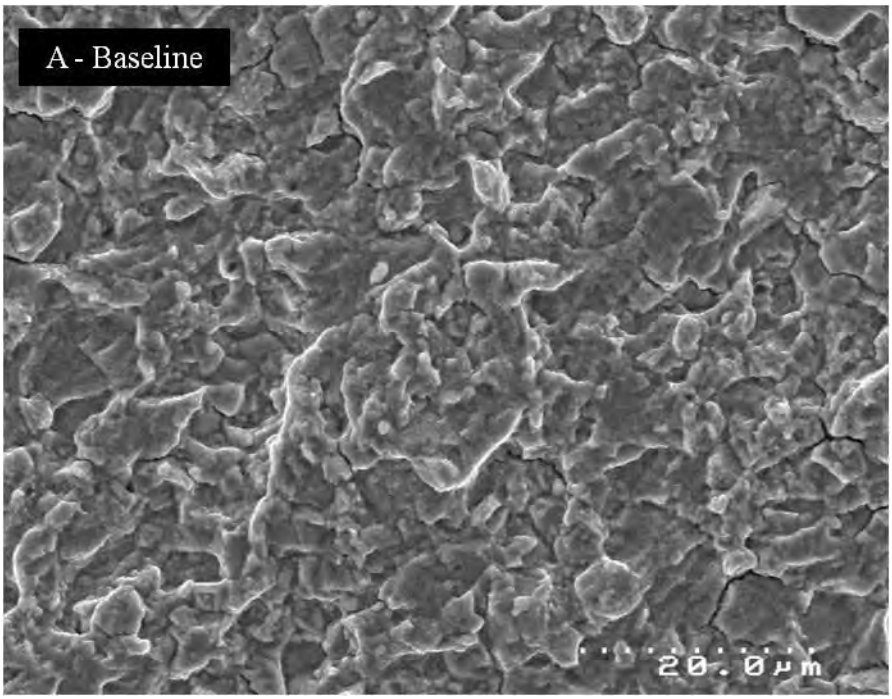
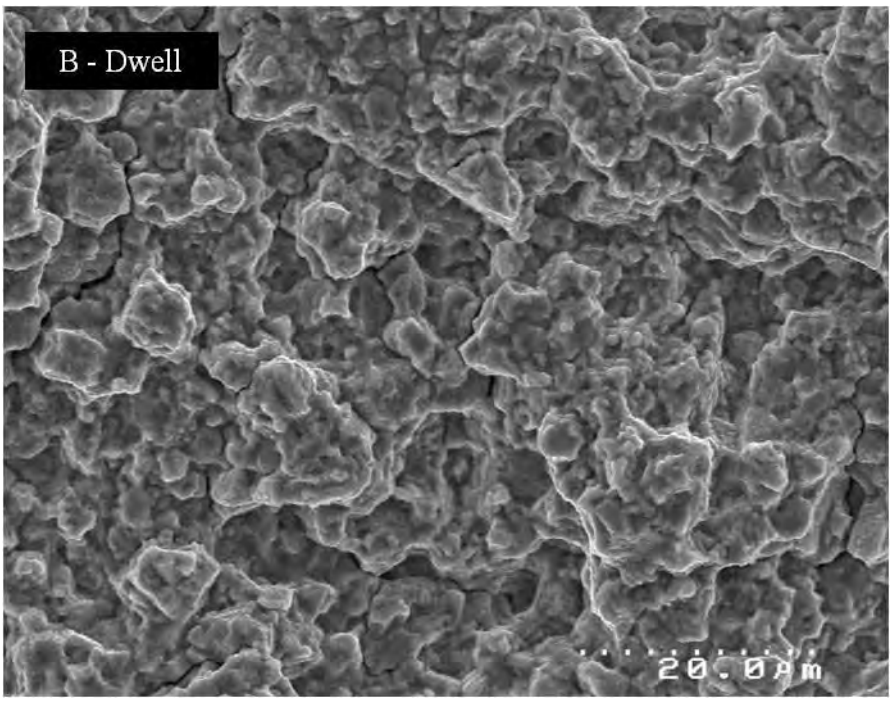
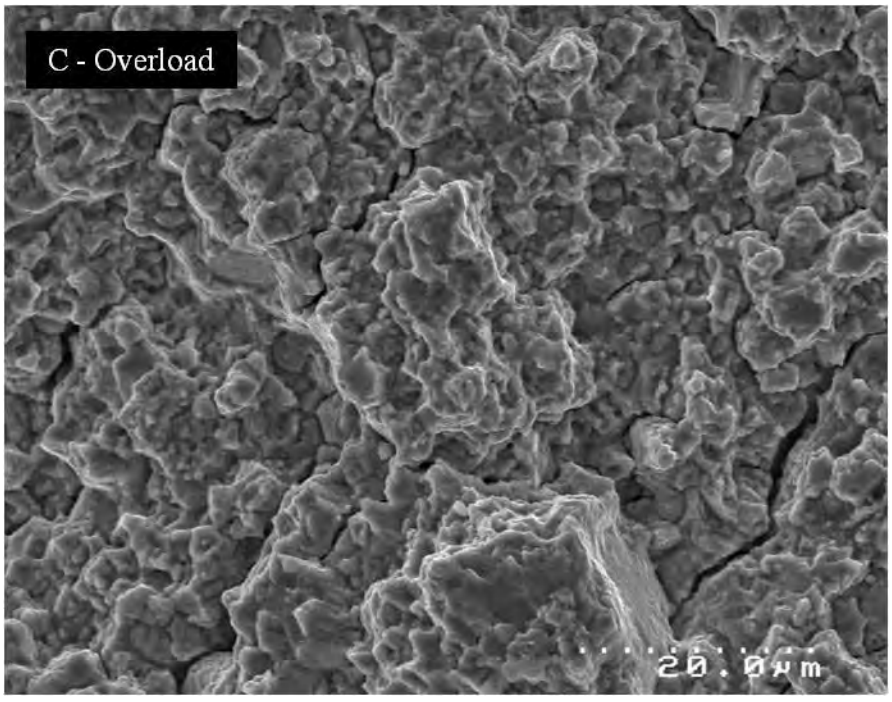


Figure A-79: Showing fractographs of fine-grained RR1000 test piece CC047; tested at 625°C in air, with a dwell load of 26 kN, an overload factor of 1.08 and a dwell time of 1,200 seconds. Each image shows the crack propagating from bottom right to top left. Bands labelled A and D are baseline (1-1-1-1) regions, the band labelled B represents the dwell region and the band labelled C; the overload region. Nearly full retardation is judged to have occurred. Higher magnification images are taken at points relating to the following crack growth driving forces (ΔK): A: ~17 MPa√m; B: ~24 MPa√m; C: ~35 MPa√m; D: ~44 MPa√m


D
C
B
A
1.00mm


A - Baseline
20.0µm


B - Dwell
20.0µm


C - Overload
20.0µm

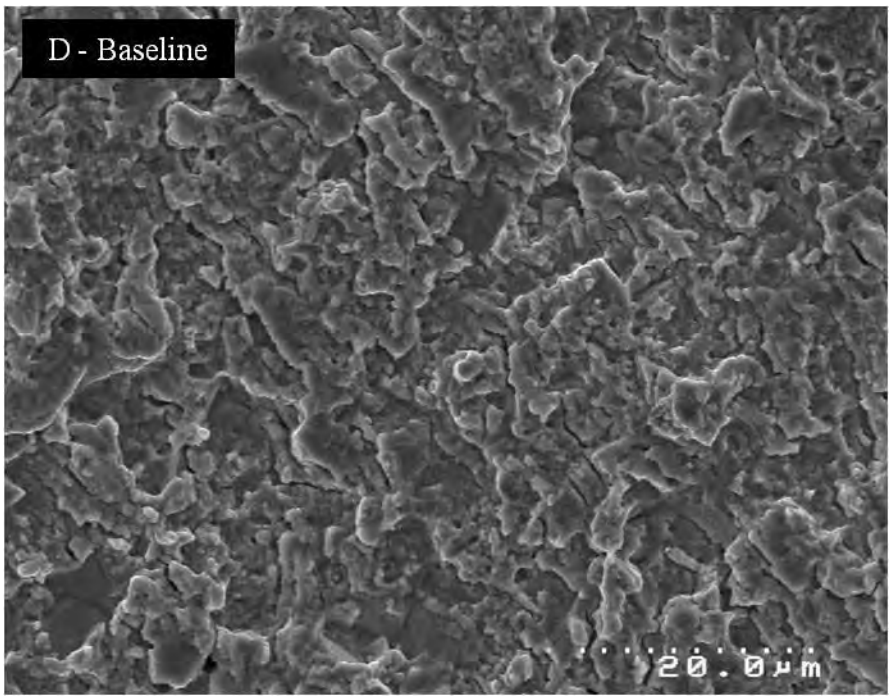
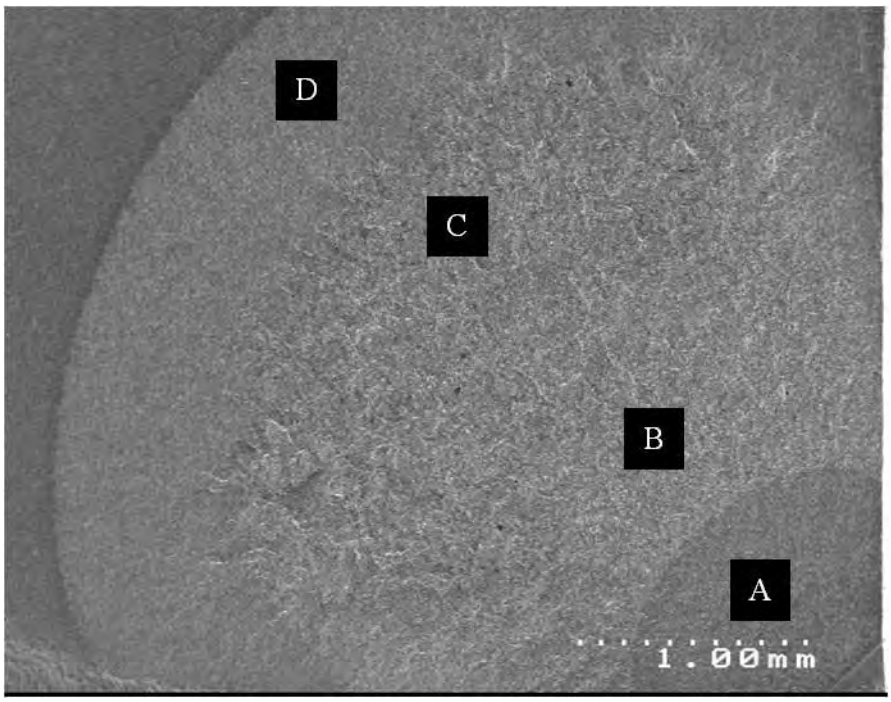
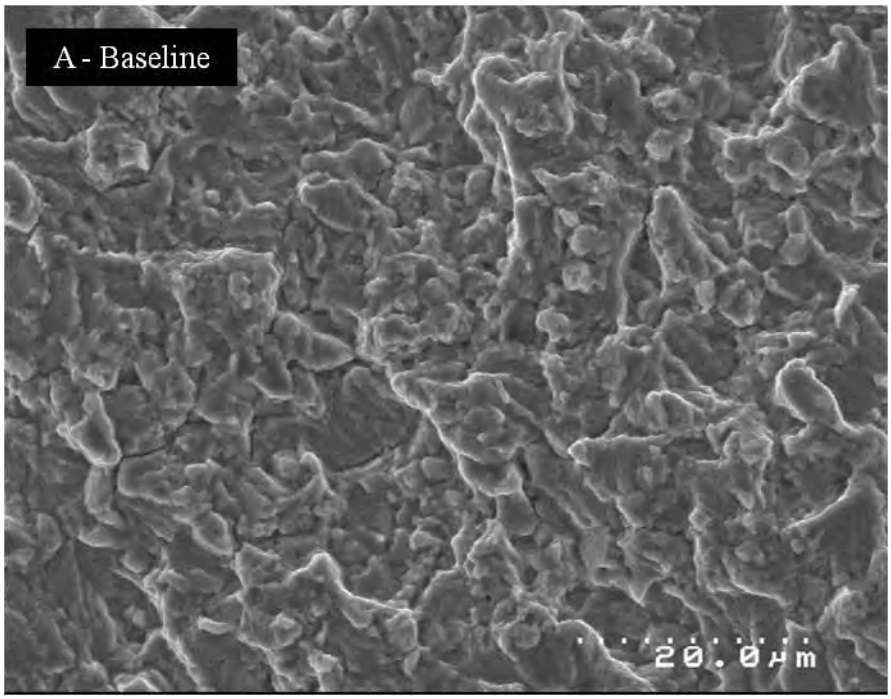
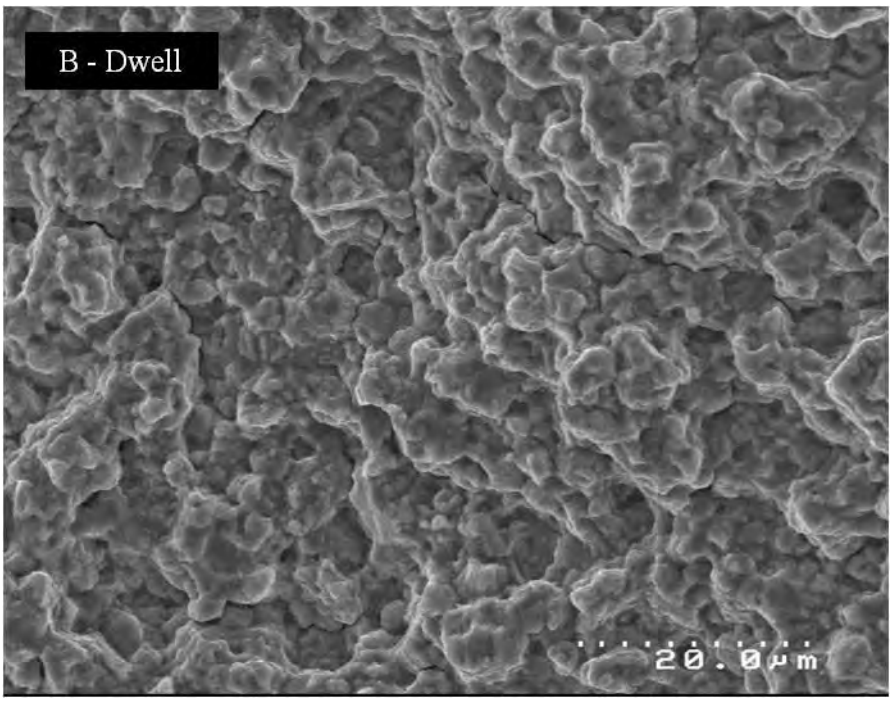
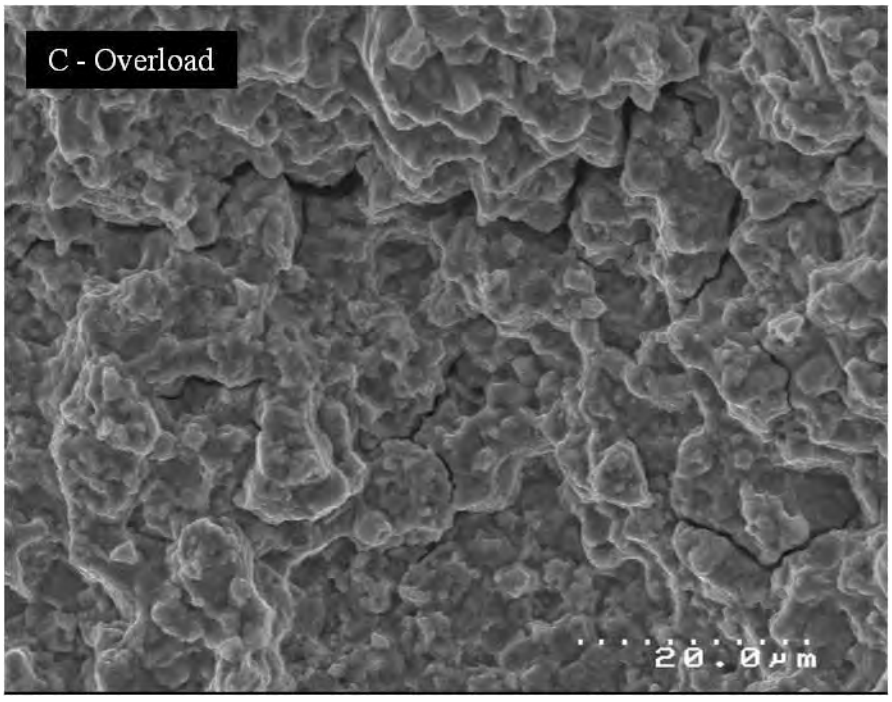


Figure A-80: Showing fractographs of fine-grained RR1000 test piece CC018; tested at 625°C in air, with a dwell load of 26 kN, an overload factor of 1.08 and a dwell time of 1,200 seconds. Each image shows the crack propagating from bottom left to top right. Bands labelled A and D are baseline (1-1-1-1) regions, the band labelled B represents the dwell region and the band labelled C; the overload region. Nearly full retardation is judged to have occurred. Higher magnification images are taken at points relating to the following crack growth driving forces (ΔK): A: ~19 MPa√m; B: ~29 MPa√m; C: ~45 MPa√m; D: ~47.5 MPa√m


D
C
B
A
1.00mm


A - Baseline
20.0µm


B - Dwell
20.0µm


C - Overload
20.0µm

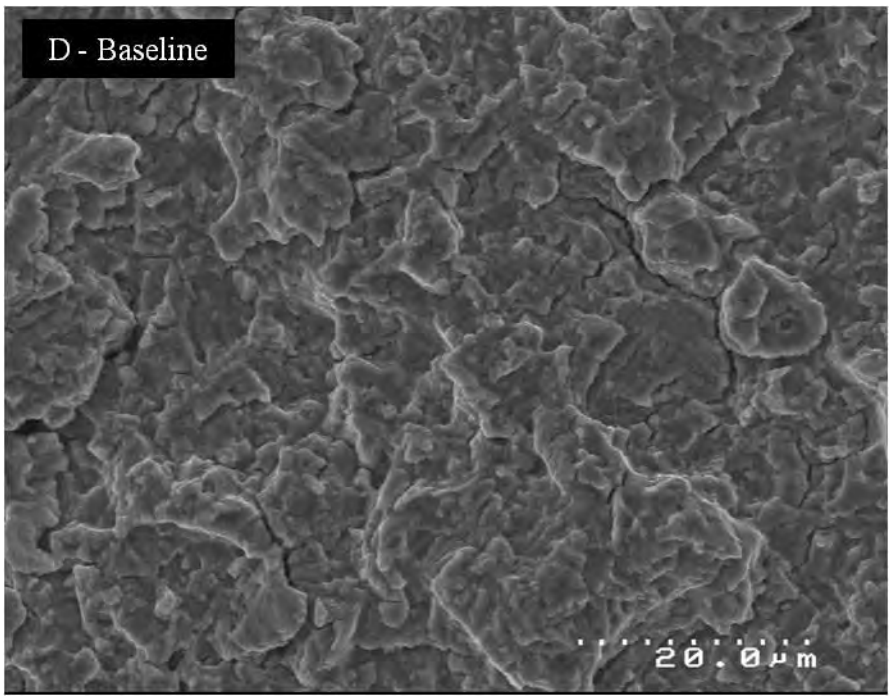
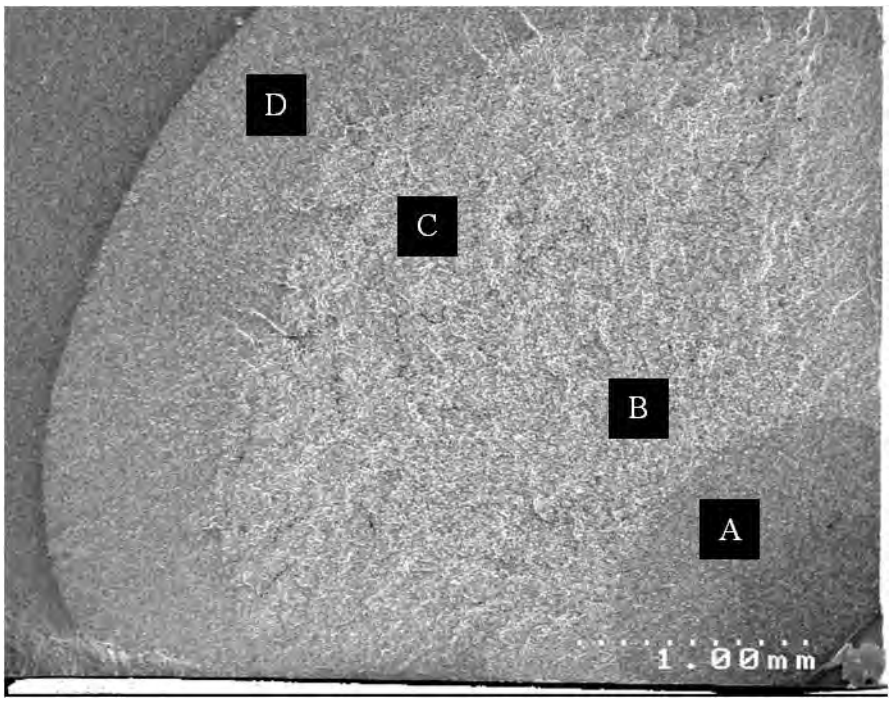
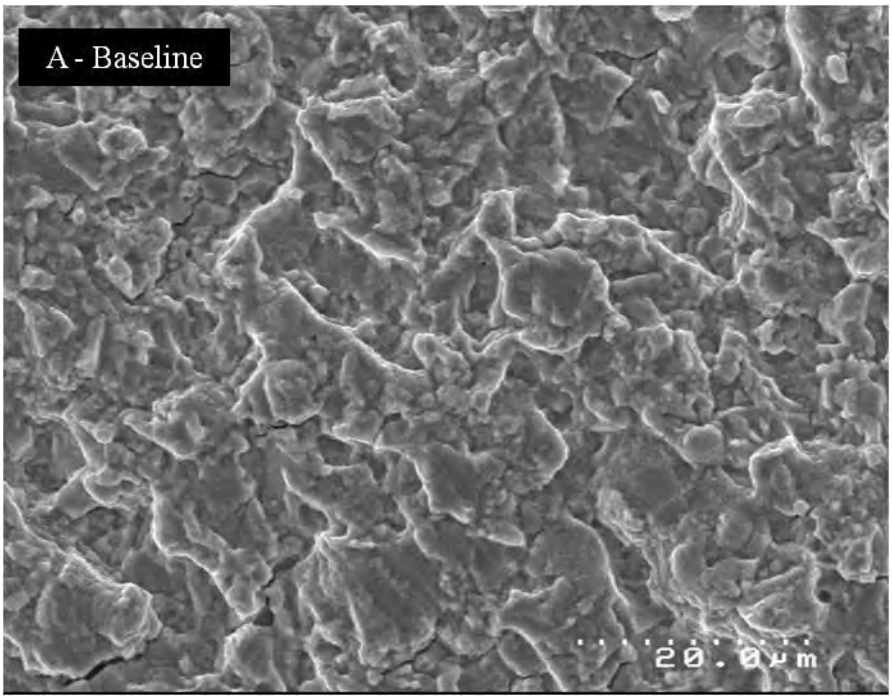
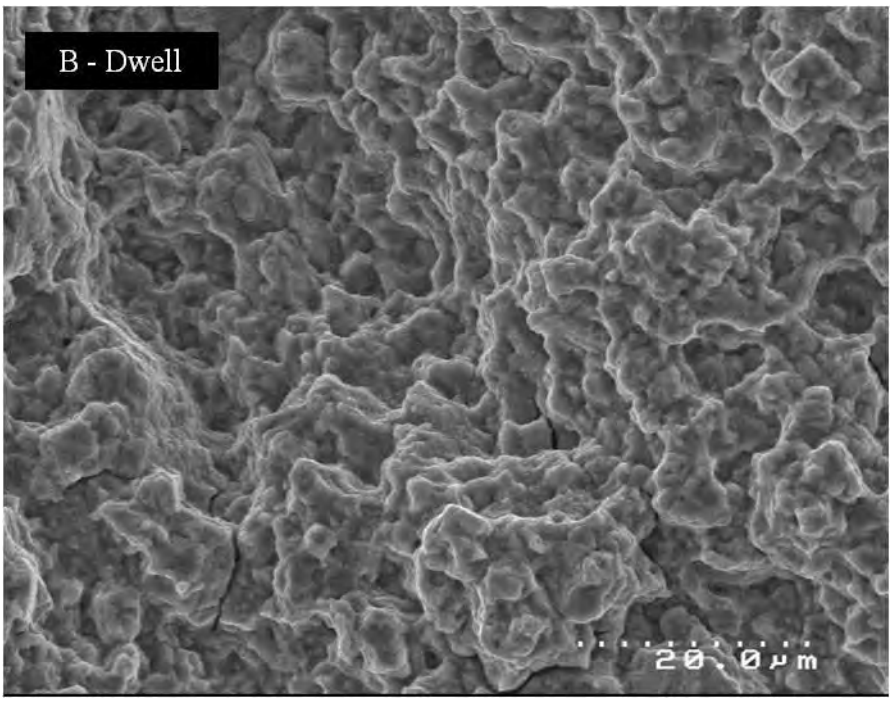
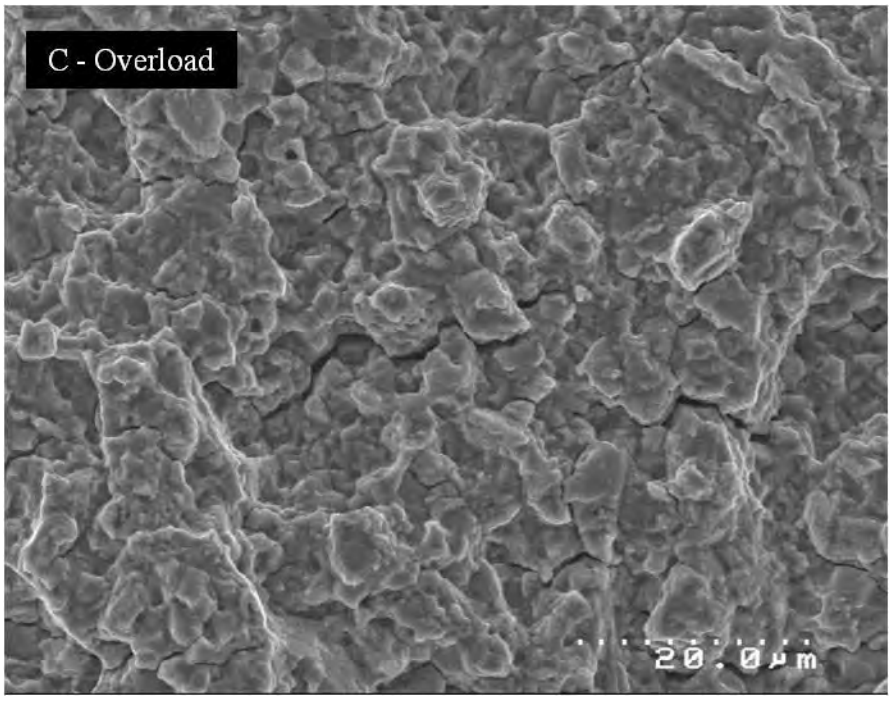


Figure A-81: Showing fractographs of fine-grained RR1000 test piece CC045; tested at 650°C in air, with a dwell load of 26 kN, an overload factor of 1.08 and a dwell time of 1,200 seconds. Each image shows the crack propagating from bottom right to top left. Bands labelled A and D are baseline (1-1-1-1) regions, the band labelled B represents the dwell region and the band labelled C; the overload region. Partial retardation is judged to have occurred. Higher magnification images are taken at points relating to the following crack growth driving forces (ΔK):
A: ~17.5 MPa√m; B: ~24.5 MPa√m; C: ~32 MPa√m; D: ~42.5 MPa√m


D
C
B
A
1.00mm


A - Baseline
20.0µm


B - Dwell
20.0µm


C - Overload
20.0µm

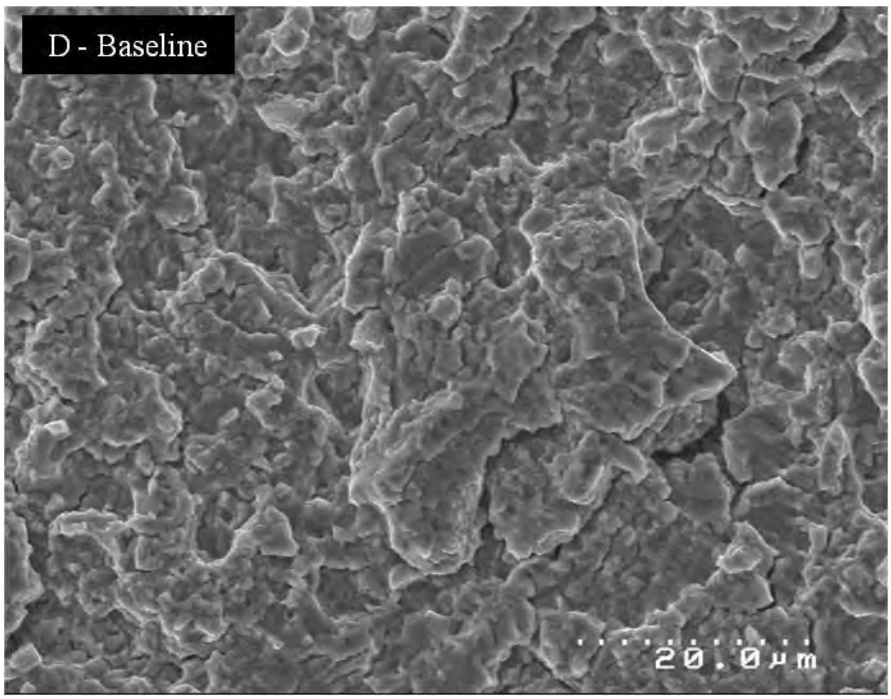
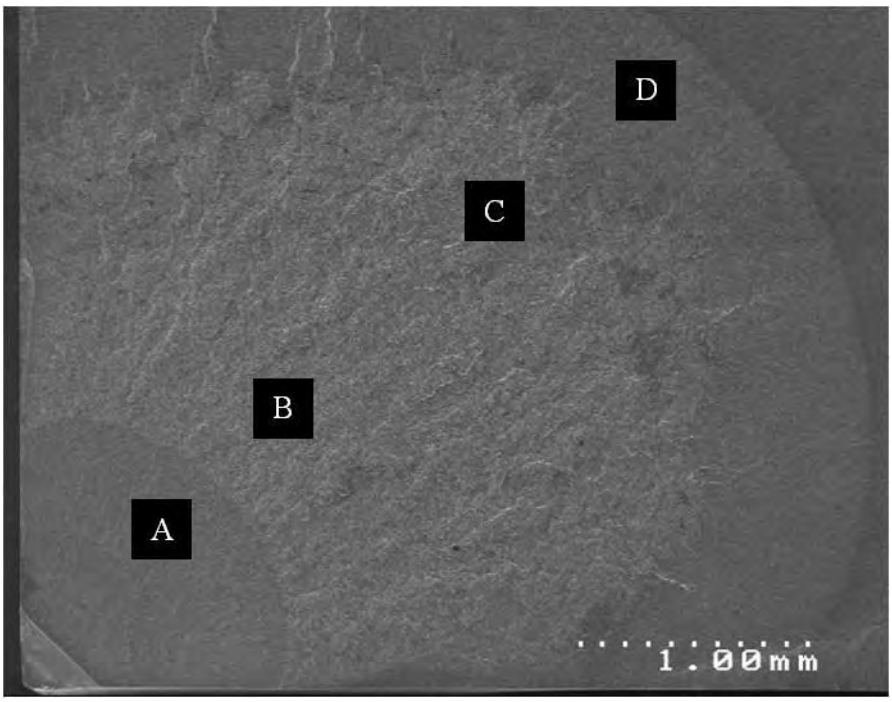
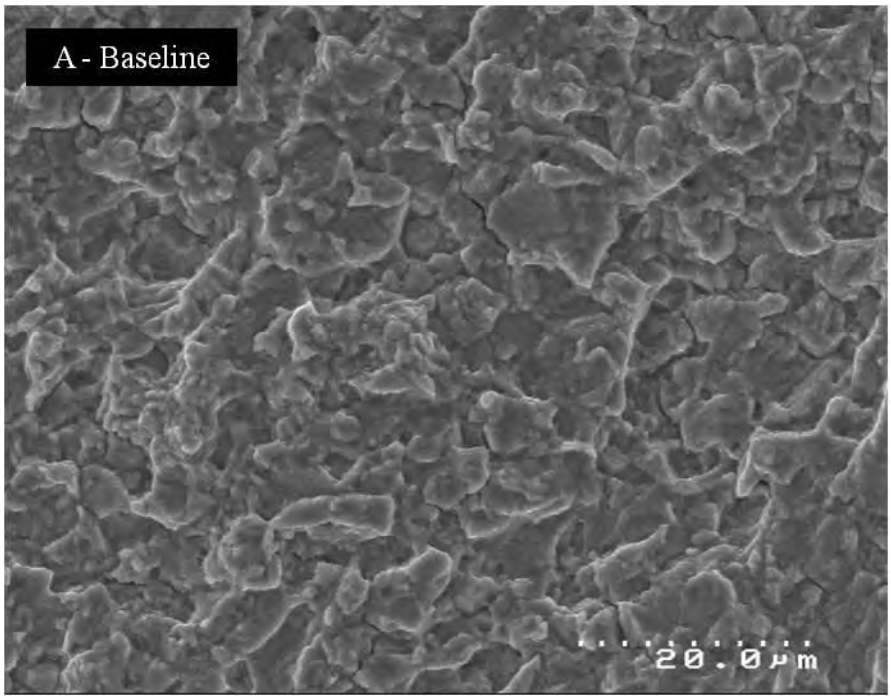
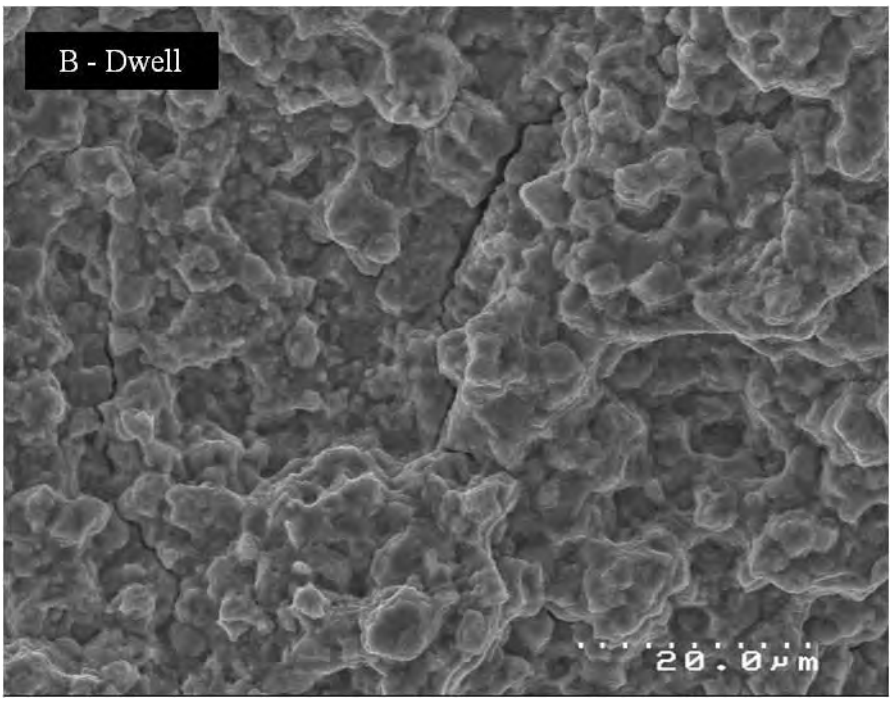
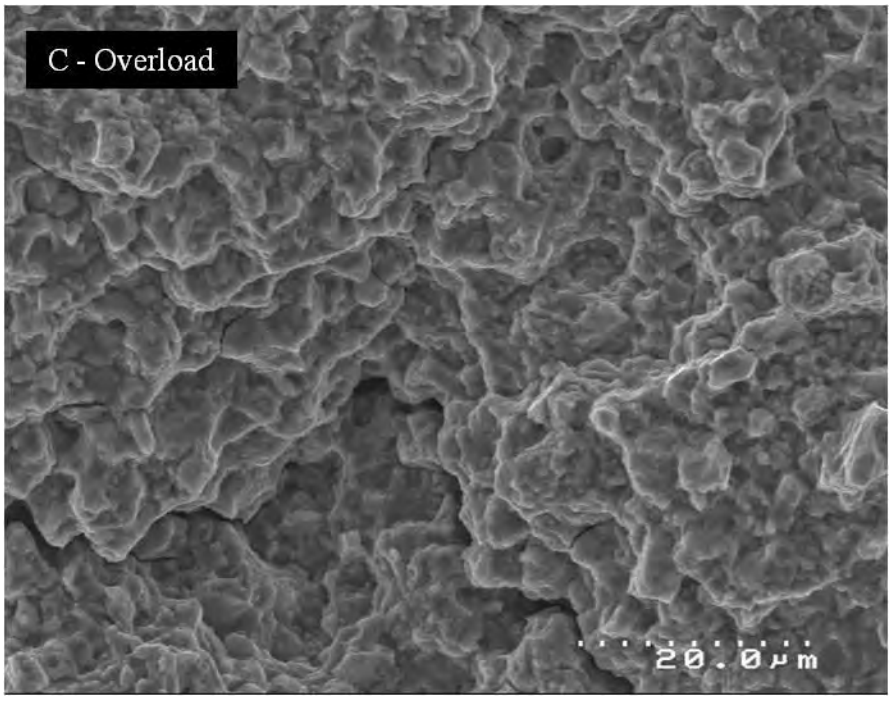


Figure A-82: Showing fractographs of fine-grained RR1000 test piece CC046; tested at 650°C in air, with a dwell load of 26 kN, an overload factor of 1.15 and a dwell time of 1,200 seconds. Each image shows the crack propagating from bottom right to top left. Bands labelled A and D are baseline (1-1-1-1) regions, the band labelled B represents the dwell region and the band labelled C; the overload region. Full retardation is judged to have occurred. Higher magnification images are taken at points relating to the following crack growth driving forces (ΔK):
A: ~17.5 MPa√m; B: ~24 MPa√m; C: ~33.5 MPa√m; D: ~42 MPa√m


D
C
B
A
1.00mm


A - Baseline
20.0µm


B - Dwell
20.0µm


C - Overload
20.0µm

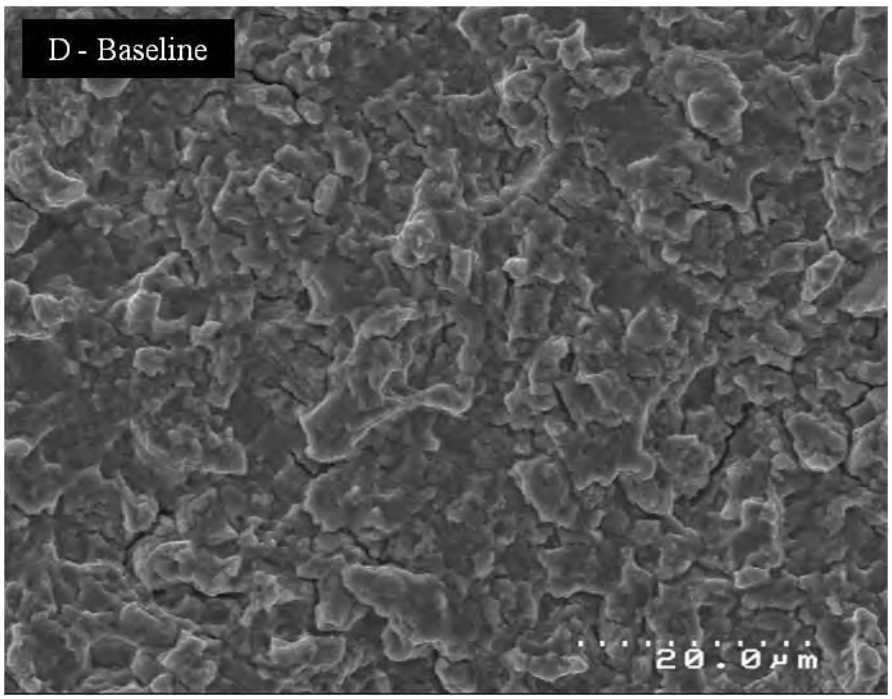
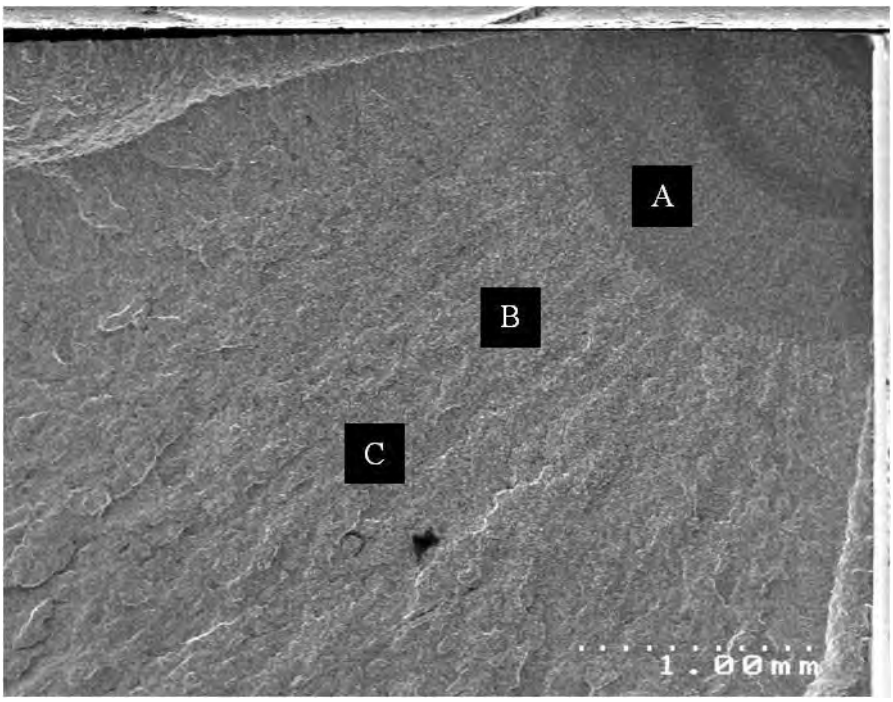
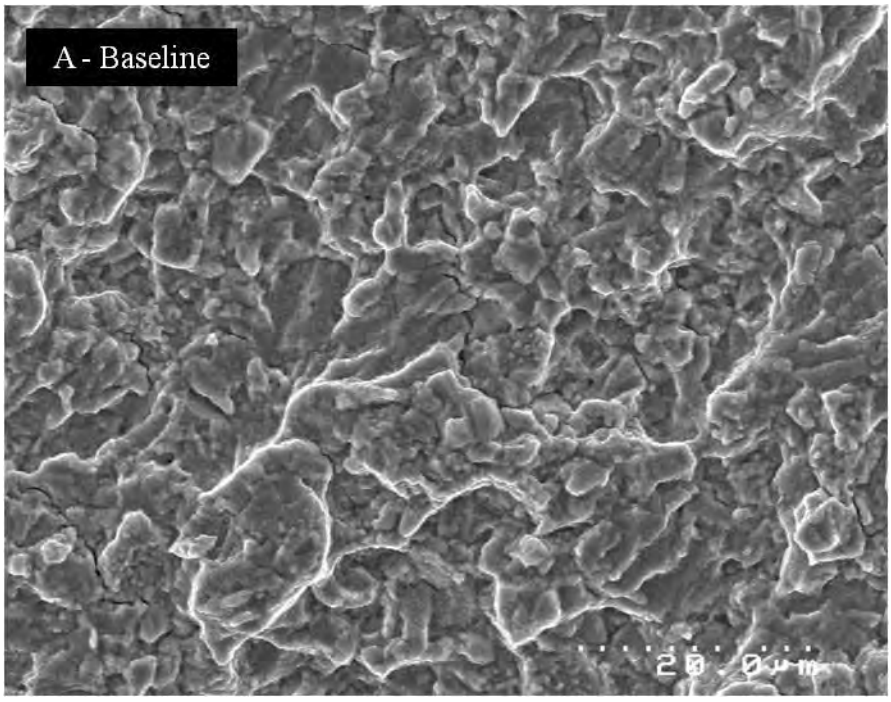


Figure A-83: Showing fractographs of fine-grained RR1000 test piece CC048; tested at 650°C in air, with a dwell load of 26 kN, an overload factor of 1.15 and a dwell time of 3,600 seconds. Each image shows the crack propagating from bottom right to top left. Bands labelled A and D are baseline (1-1-1-1) regions, the band labelled B represents the dwell region and the band labelled C; the overload region. Full retardation is judged to have occurred. Higher magnification images are taken at points relating to the following crack growth driving forces (ΔK):
A: ~17.5 MPa√m; B: ~24.5 MPa√m; C: ~34 MPa√m; D: ~42 MPa√m


A
B
C
1.00mm


A - Baseline
20.0µm

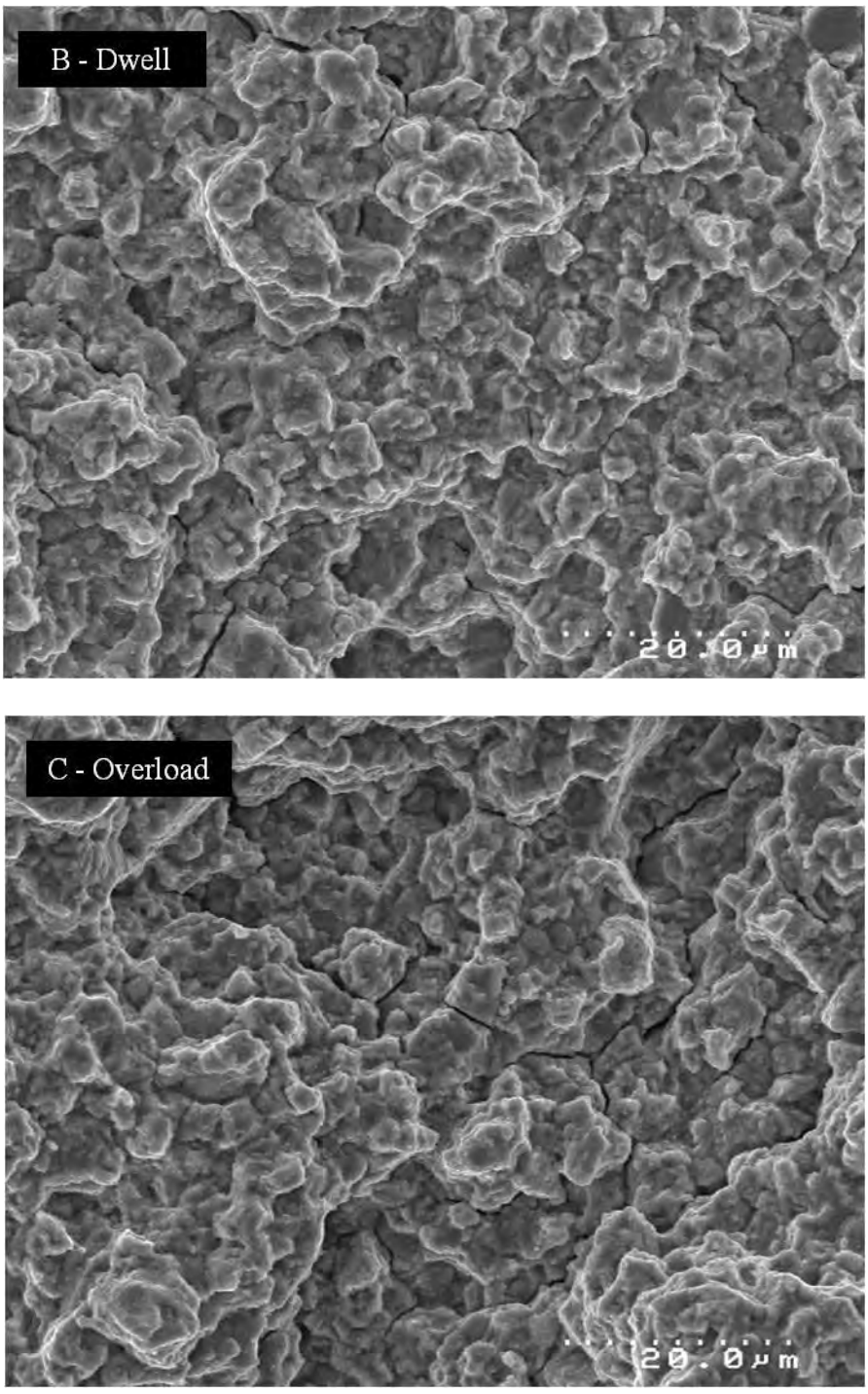
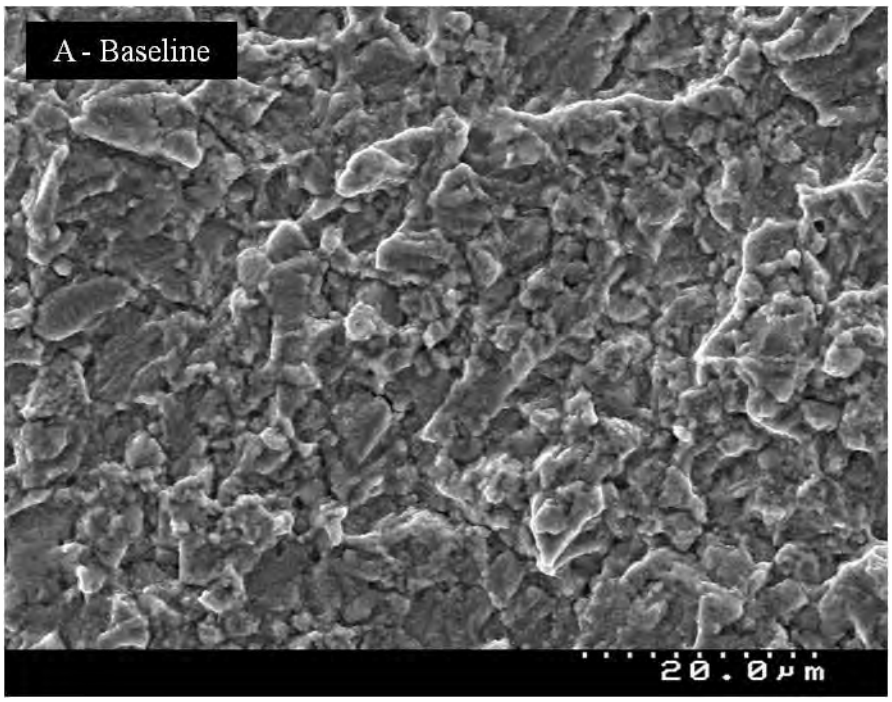
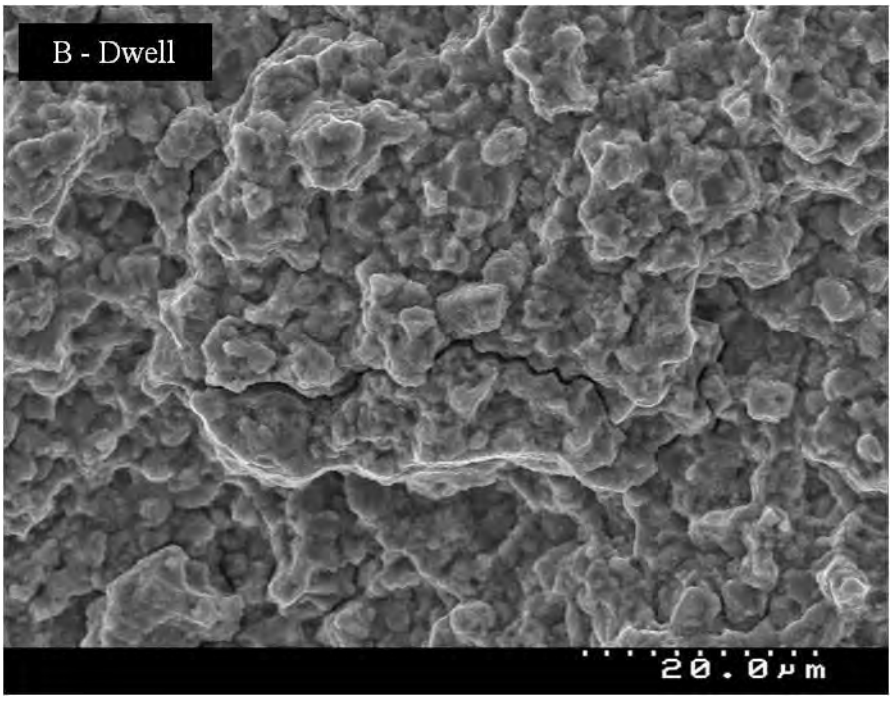


Figure A-84: Showing fractographs of fine-grained RR1000 test piece CC017; tested at 650°C in air, with a dwell load of 26 kN, an overload factor of 1.08 and a dwell time of 1,200 seconds. Each image shows the crack propagating from top right to bottom left. The band labelled A represents baseline loading (1-1-1-1), the band labelled B represents the dwell region and the band labelled C; the overload region. Partial retardation is judged to have occurred. Higher magnification images are taken at points relating to the following crack growth driving forces (ΔK): A: ~19 MPa√m; B: ~25.5 MPa√m; C: ~37 MPa√m


A - Baseline
20.0µm


B - Dwell
20.0µm

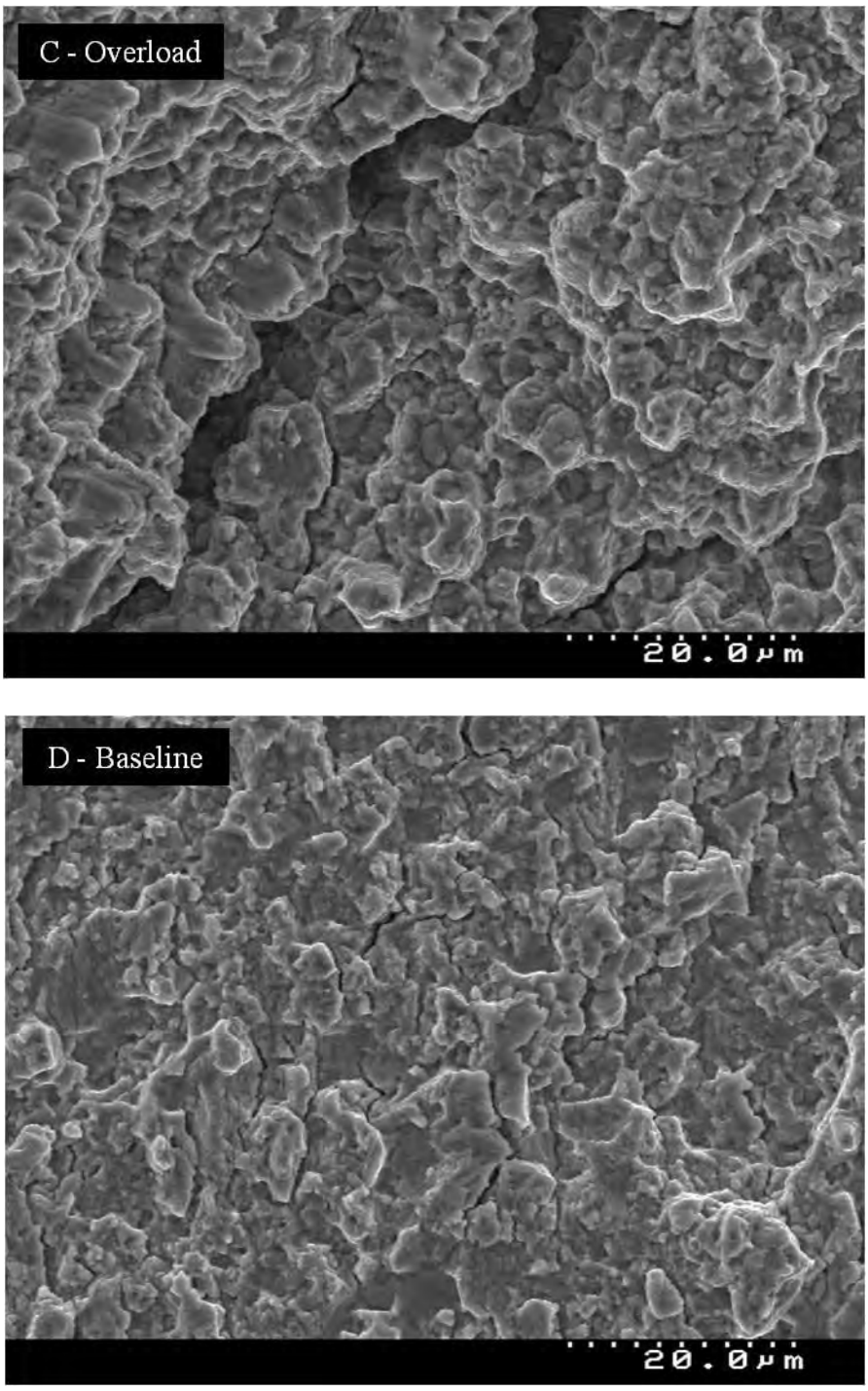
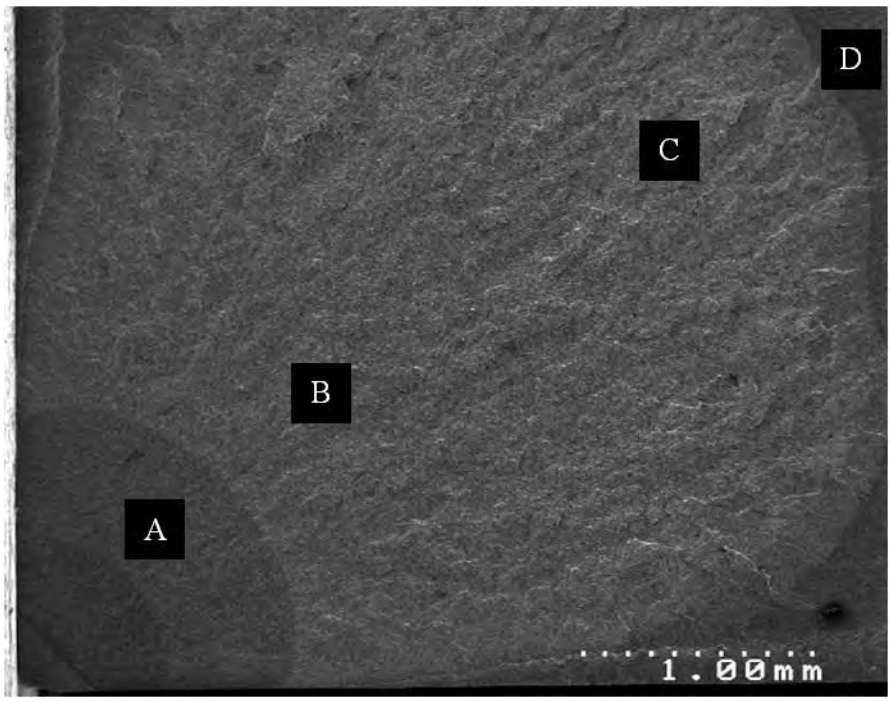
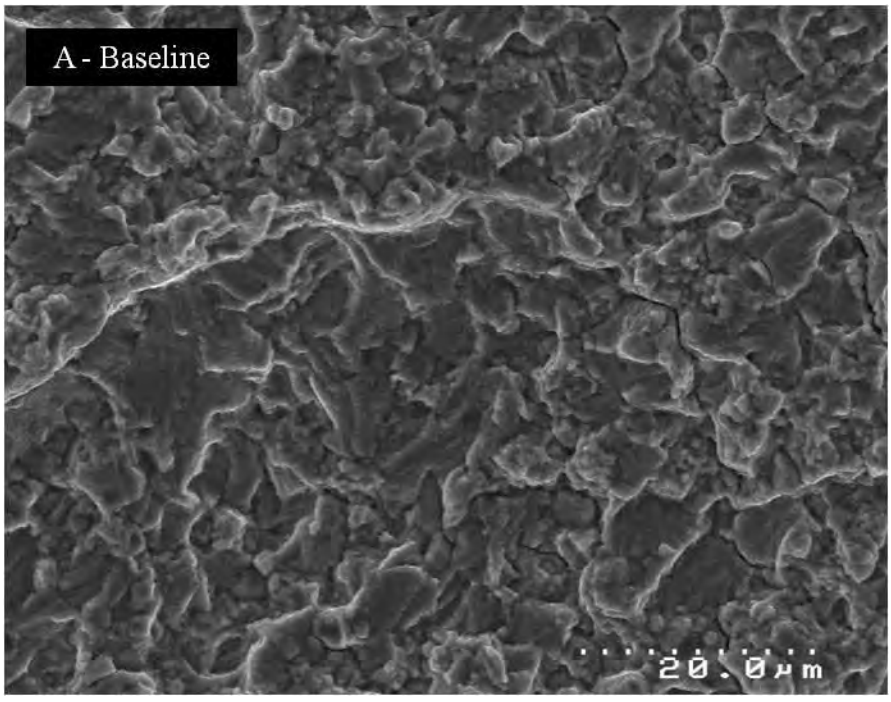
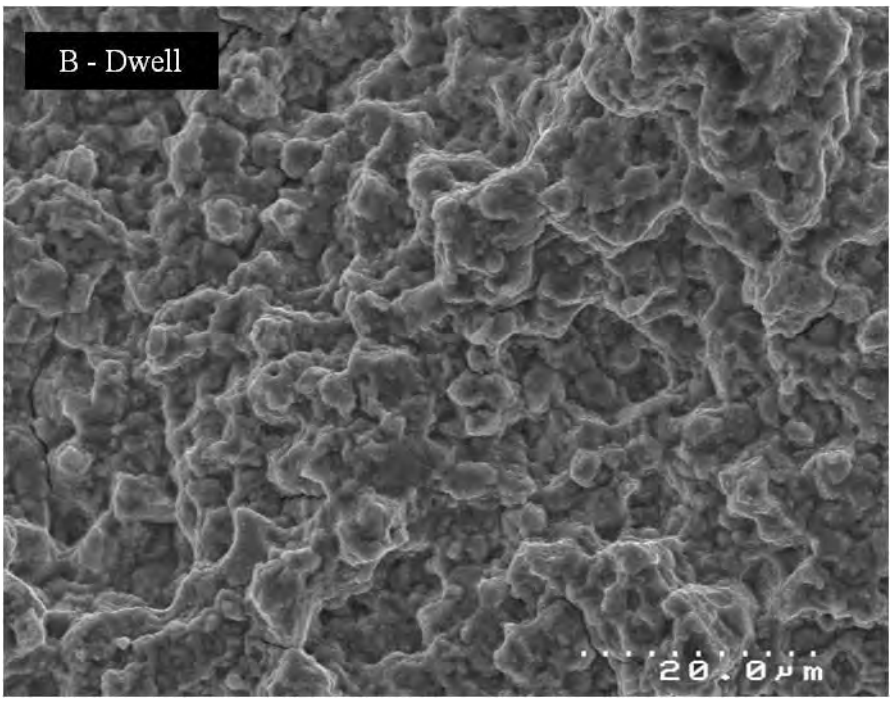
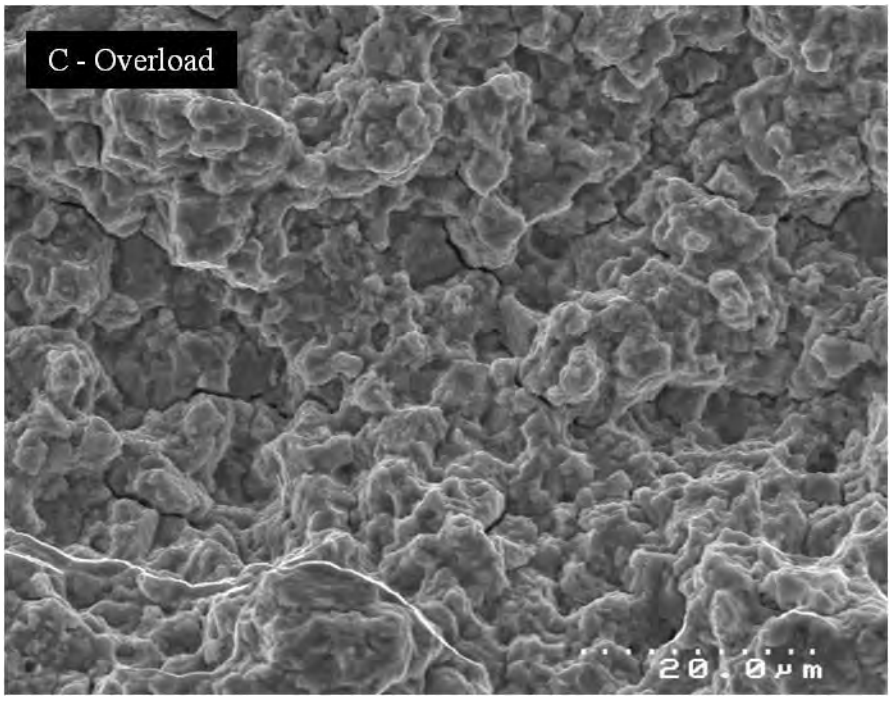


Figure A-85: Showing fractographs of fine-grained RR1000 test piece CC020; tested at 650°C in air, with a dwell load of 26 kN, an overload factor of 1.15 and a dwell time of 3,600 seconds. Each image shows the crack propagating from bottom left to top right. Nearly full retardation is judged to have occurred. Higher magnification images are taken at points relating to the following crack growth driving forces (ΔK): A: ~17.5 MPa√m; B: ~23 MPa√m; C: ~32.5 MPa√m; D: ~45 MPa√m


D
C
B
A
1.00mm


A - Baseline
20.0µm


B - Dwell
20.0µm


C - Overload
20.0µm

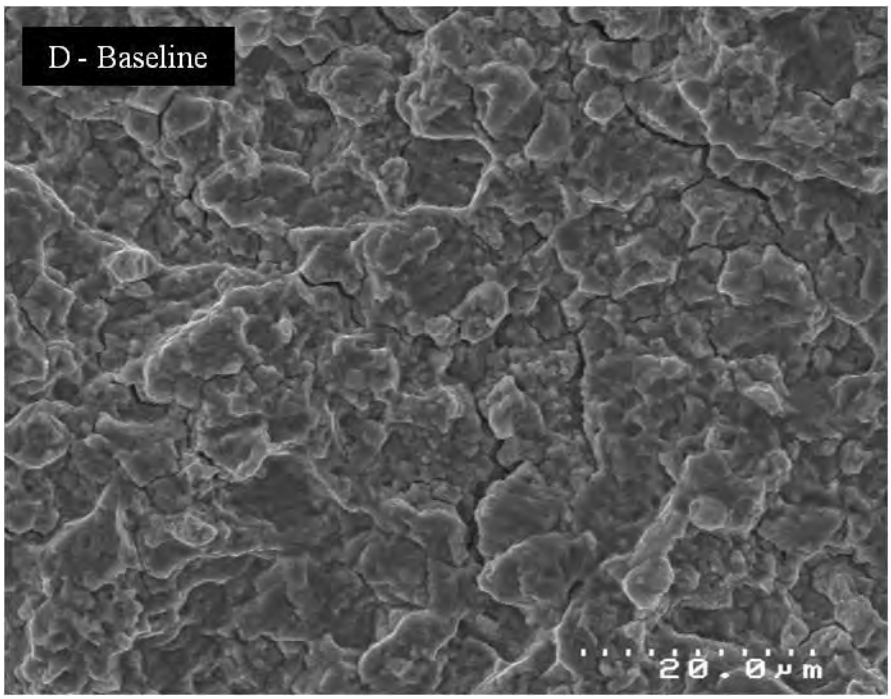
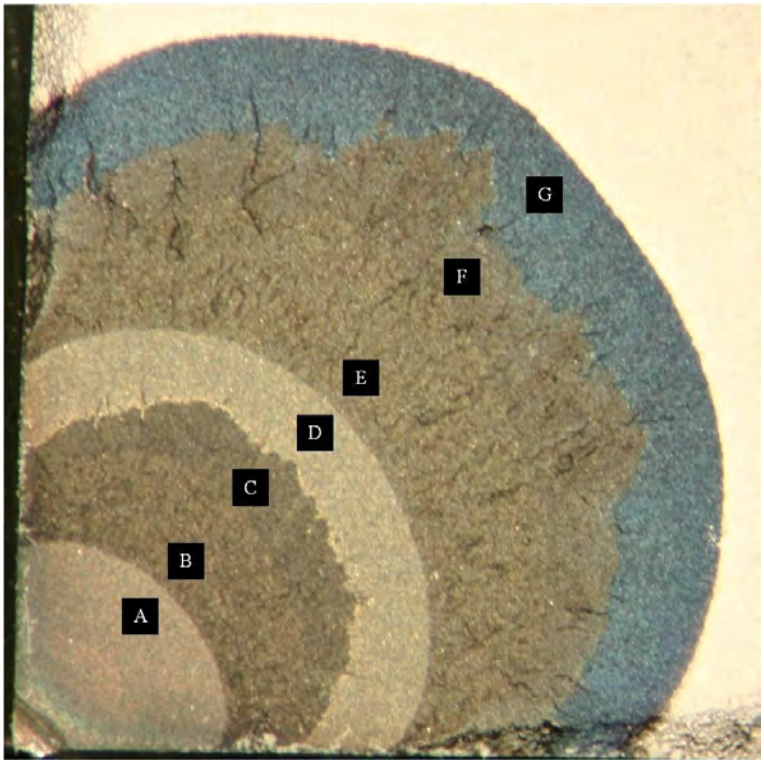
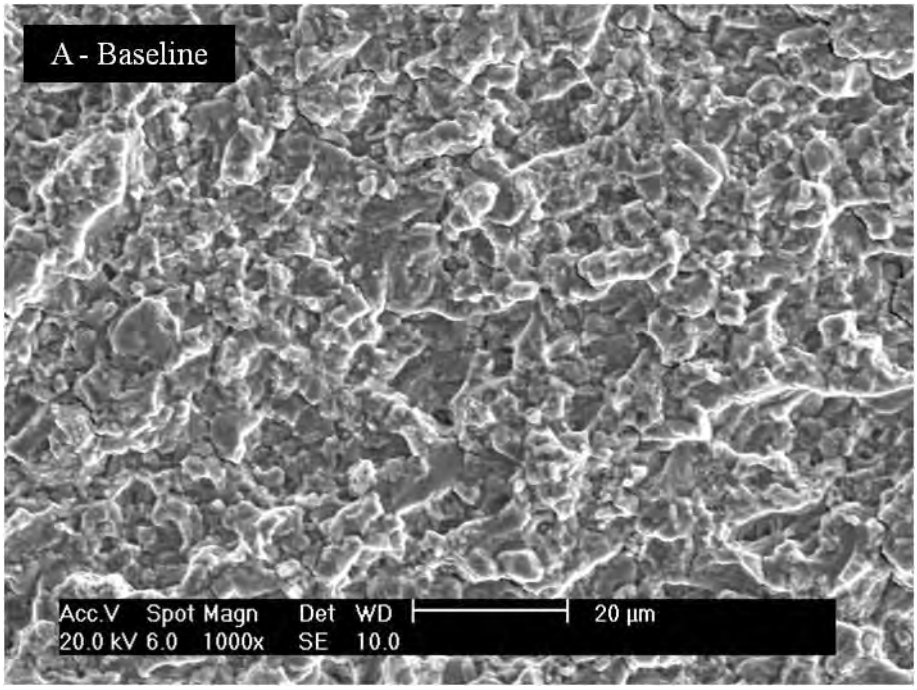
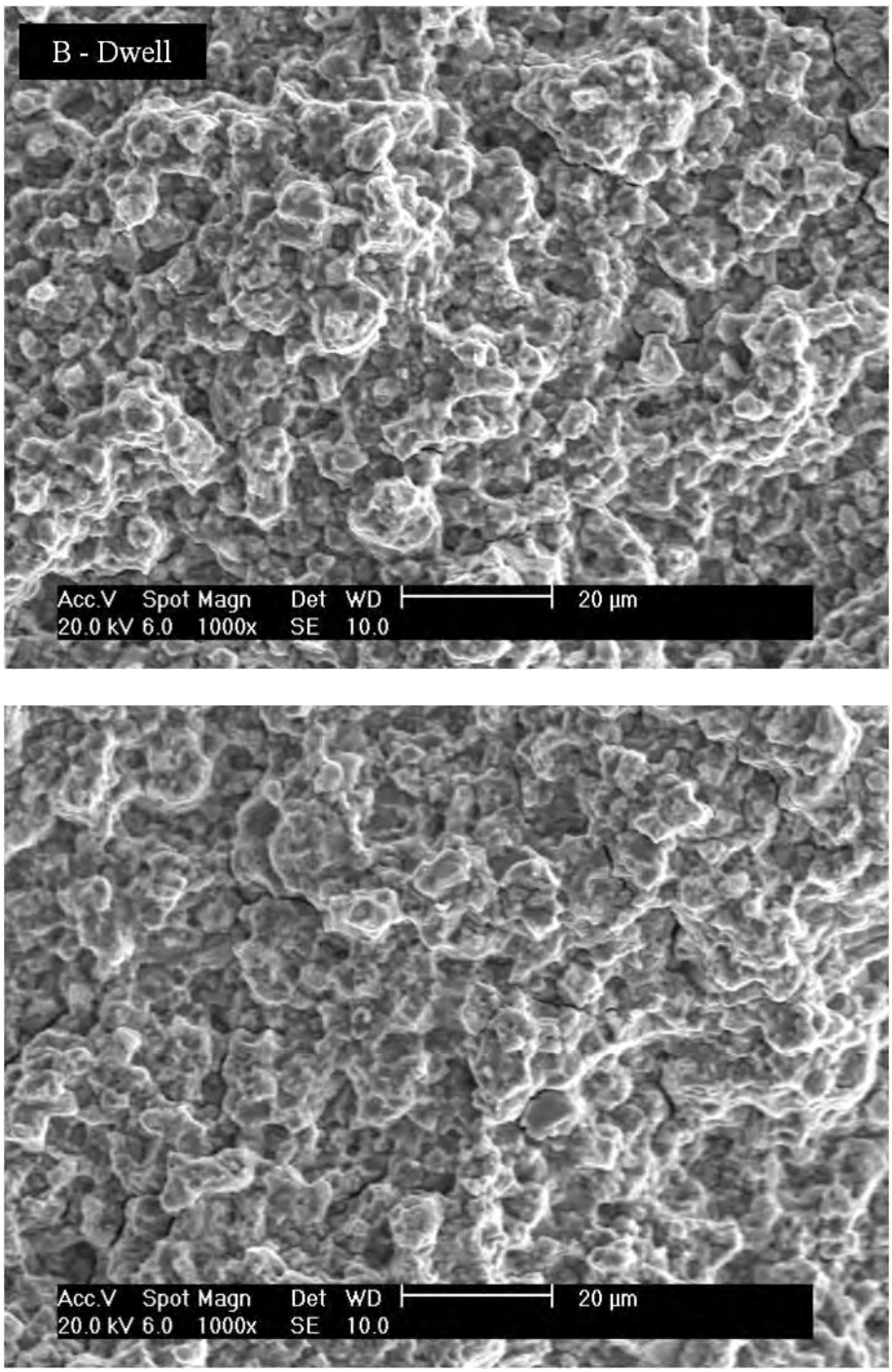


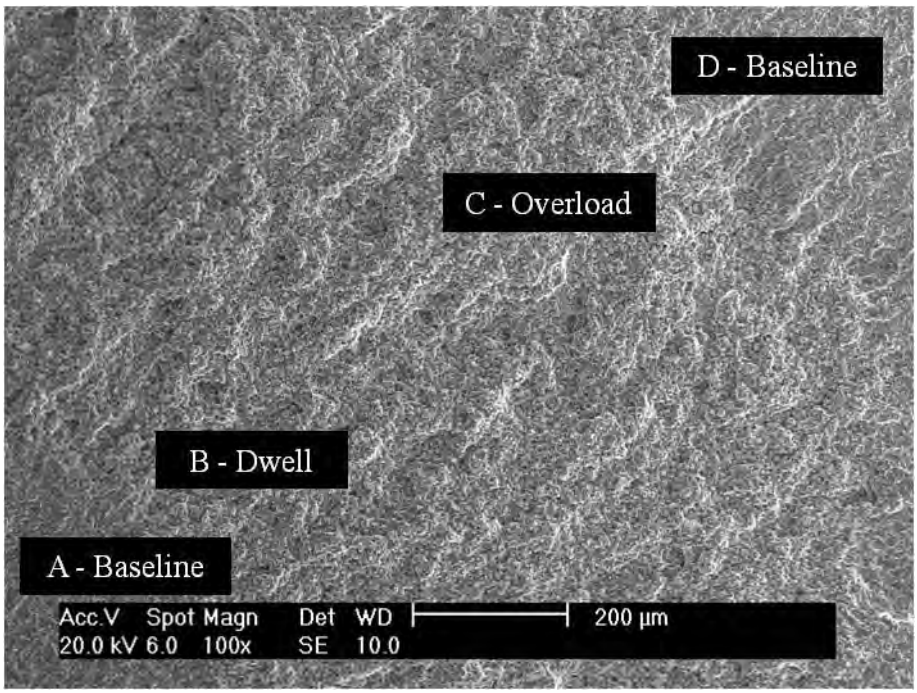
Figure A-86: Showing fractographs of fine-grained RR1000 test piece CC034; tested at 675°C in air, with a dwell load of 23.5 kN, an overload factor of 1.10 and a dwell time of 1,200 seconds. Each image shows the crack propagating from bottom left to top right. Bands labelled A and D are baseline (1-1-1-1) regions, the band labelled B represents the dwell region and the band labelled C; the overload region. Partial retardation is judged to have occurred. Higher magnification images are taken at points relating to the following crack growth driving forces (ΔK):
A: ~17.5 MPa√m; B: ~22.5 MPa√m; C: ~32 MPa√m; D: ~47 MPa√m

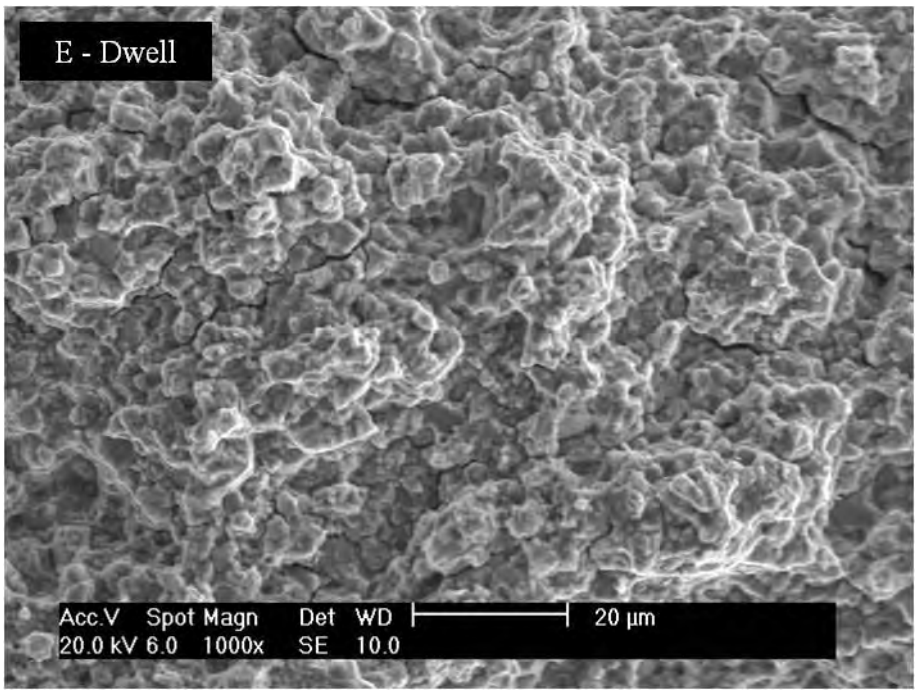
RR1000 Dwell at Overload Tests






B - Dwell
Acc.V Spot Magn Det WD 20 µm
20.0 kV 6.0 1000x SE 10.0
Acc.V Spot Magn Det WD 20 µm
20.0 kV 6.0 1000x SE 10.0


D - Baseline
C - Overload
B - Dwell
A - Baseline
Acc.V Spot Magn Det WD 200 µm
20.0 kV 6.0 100x SE 10.0


E - Dwell
Acc.V Spot Magn Det WD 20 µm
20.0 kV 6.0 1000x SE 10.0

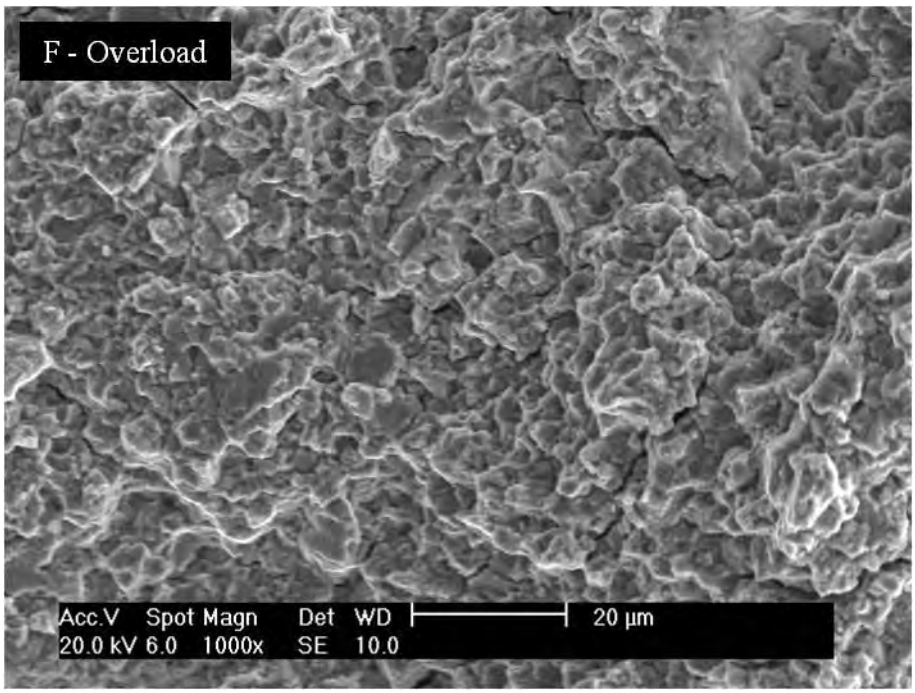
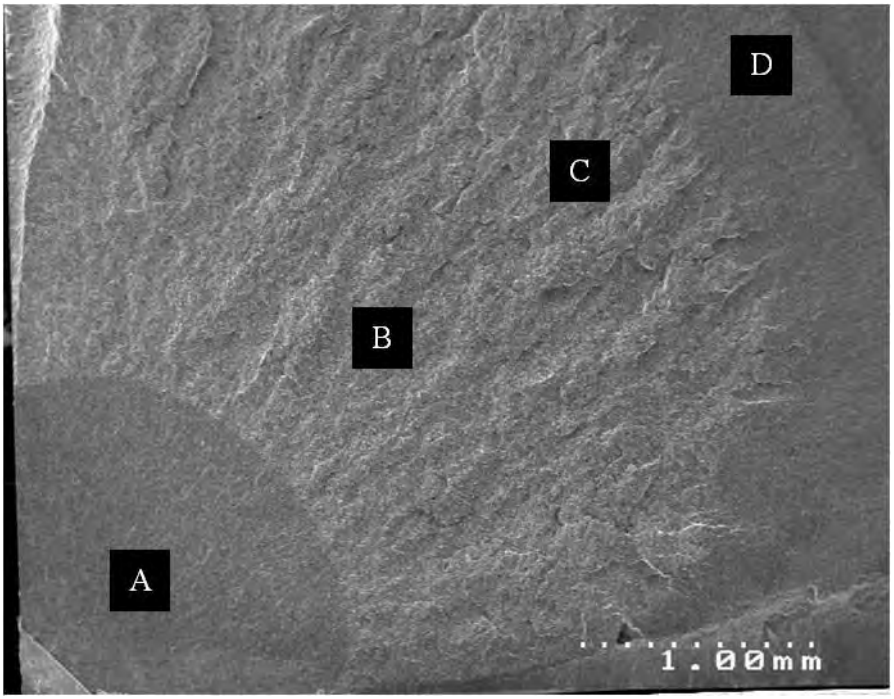
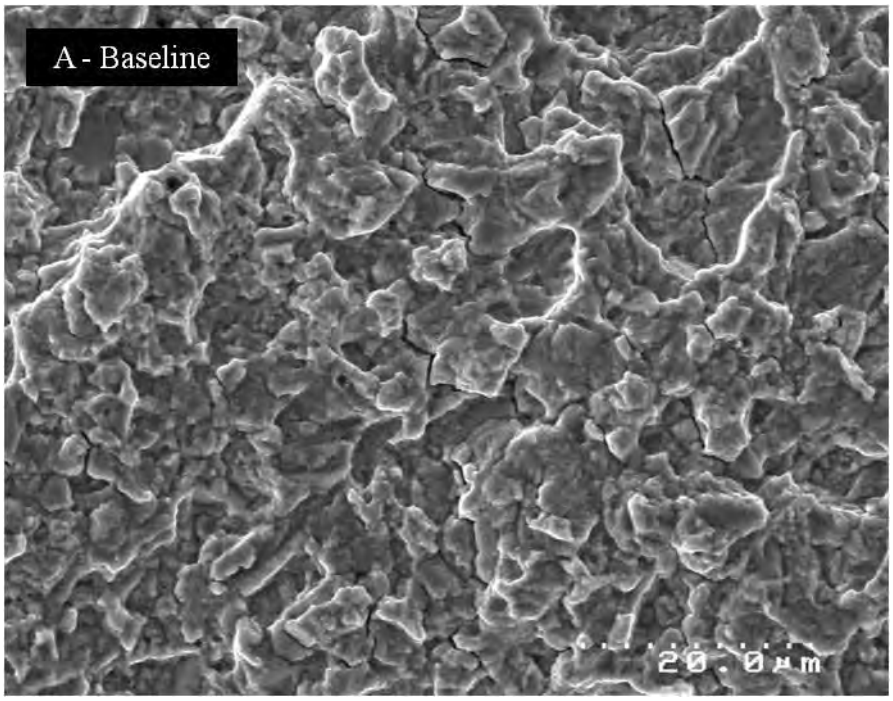
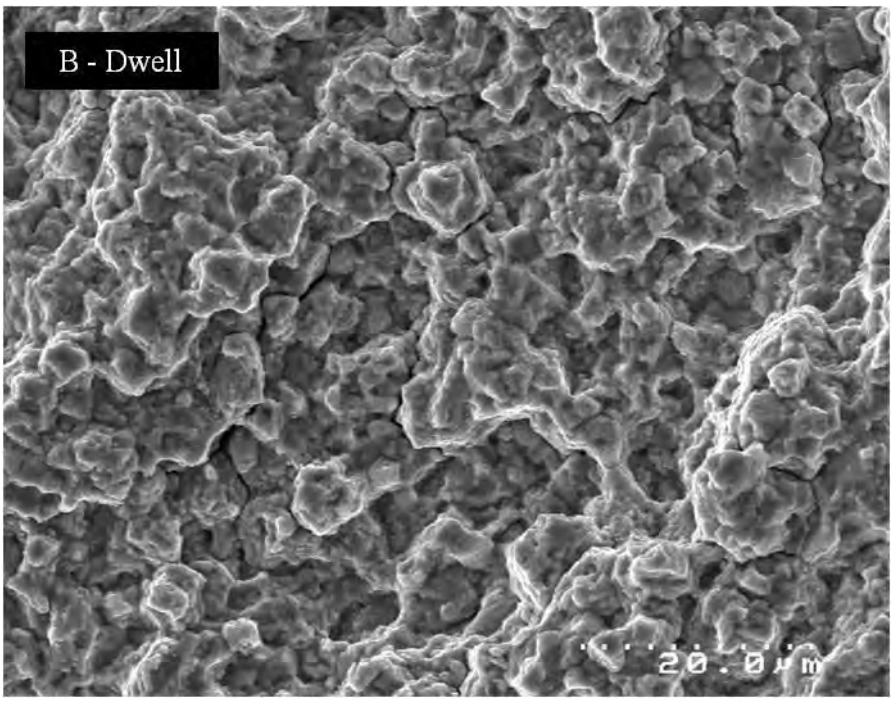


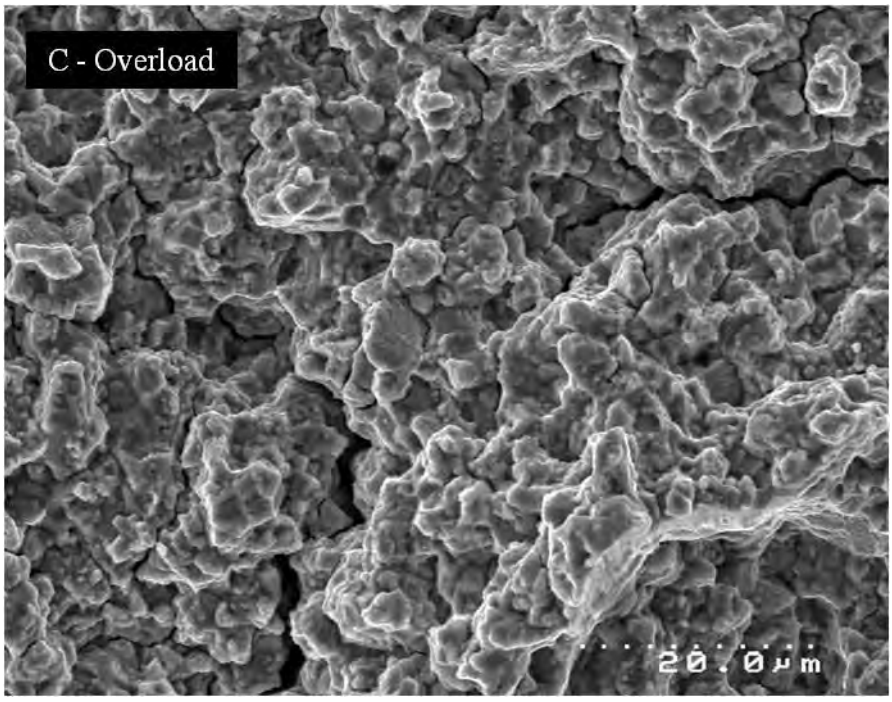
Figure A-87: Showing fractographs of fine-grained RR1000 test piece CC035; tested at 650°C in air, with a dwell load of 26 kN, an overload factor of 1.15 and a dwell time of 3,600 seconds. Each image shows the crack propagating from bottom left to top right. Note that two segments of overload cycling have been applied; note also that in the second overload segment (labelled F) the time at overload has been increased to a 120 second hold period. Bands labelled A, D and G are baseline (1-1-1-1) regions, bands labelled B and E represent dwell regions and bands labelled C and F; the overload regions (with F being "dwell at overload). Higher magnification images are taken at points relating to the following crack growth driving forces (ΔK): A: ~18 MPa√m; B: ~22.5 MPa√m; C: ~27 MPa√m; E: ~36 MPa√m; F: ~45 MPa√m

RR1000 Unload and Reload Tests






B - Dwell
20.0µm


C - Overload
20.0µm

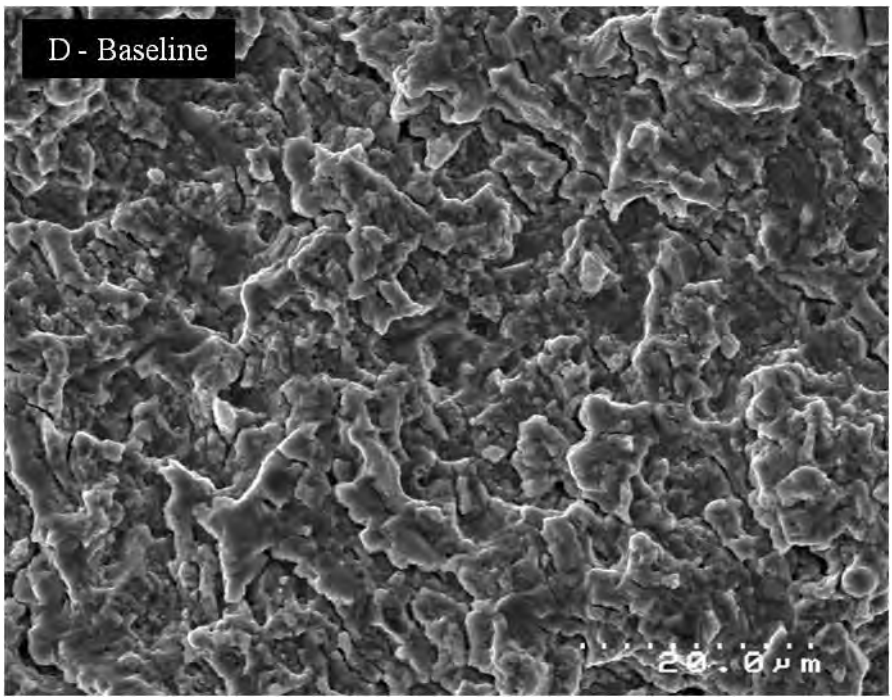
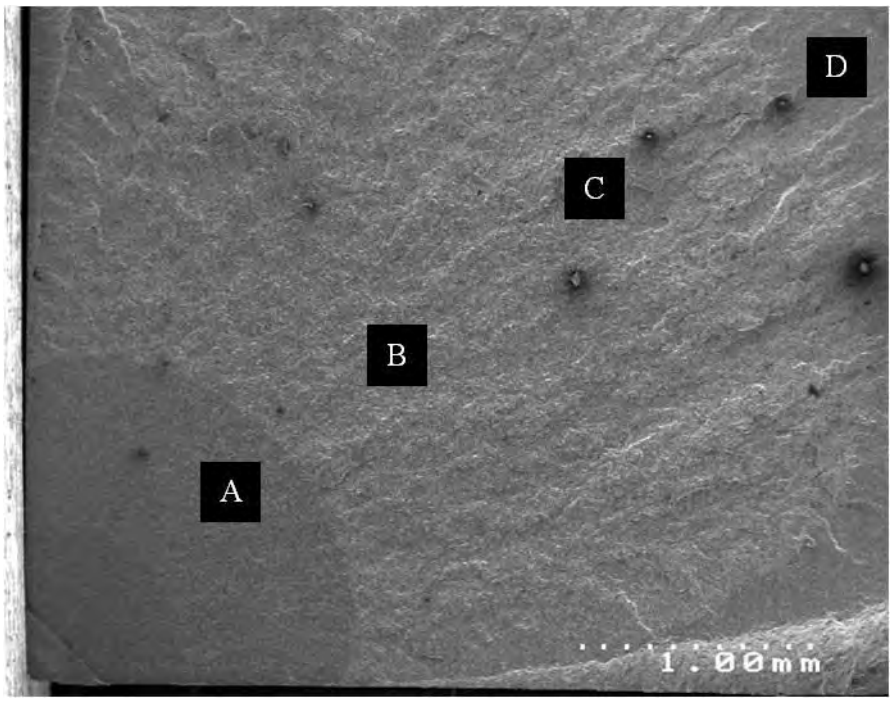
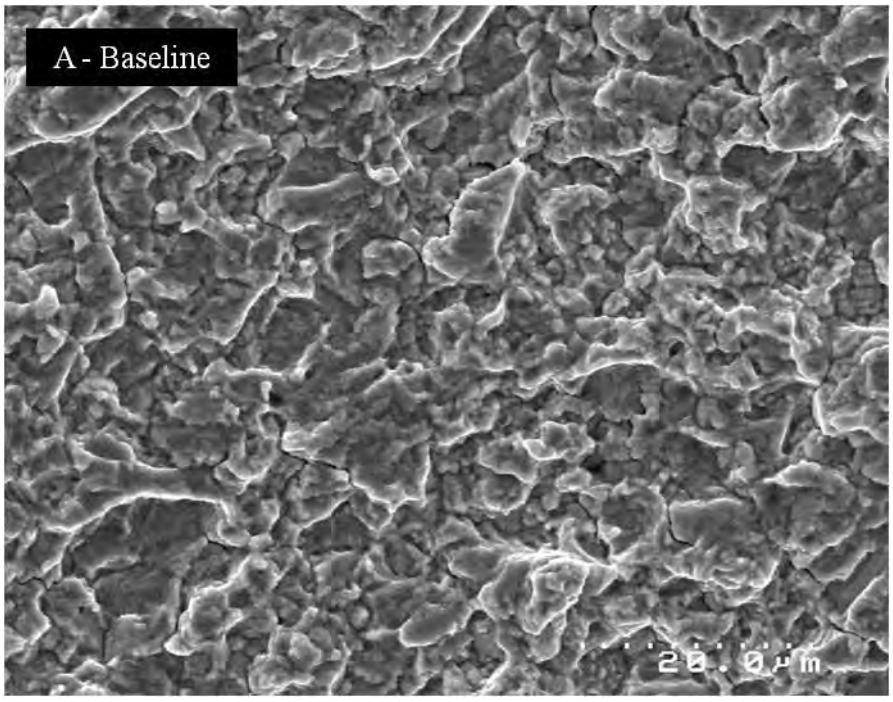
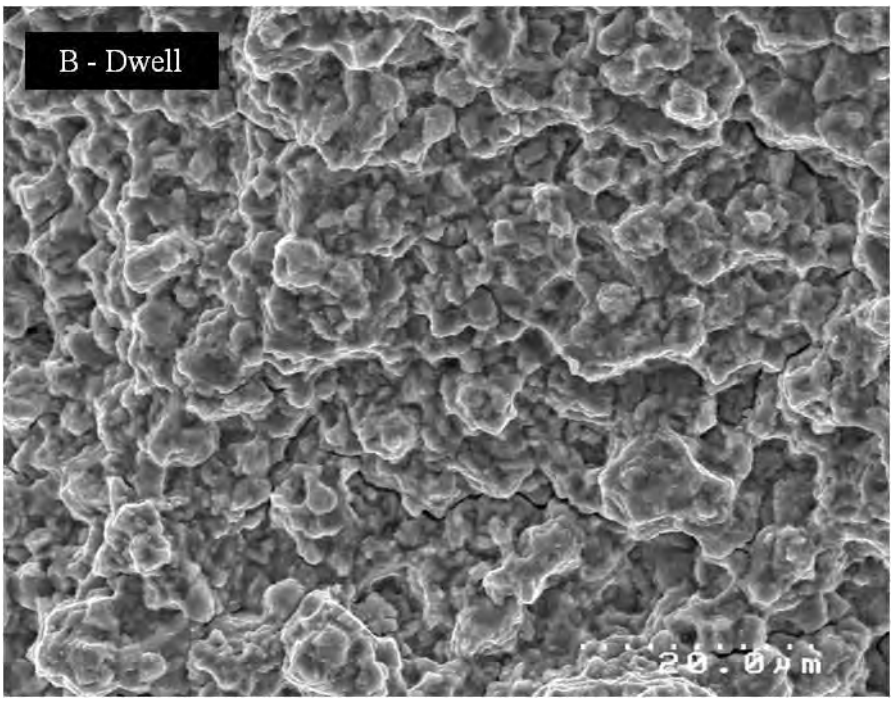
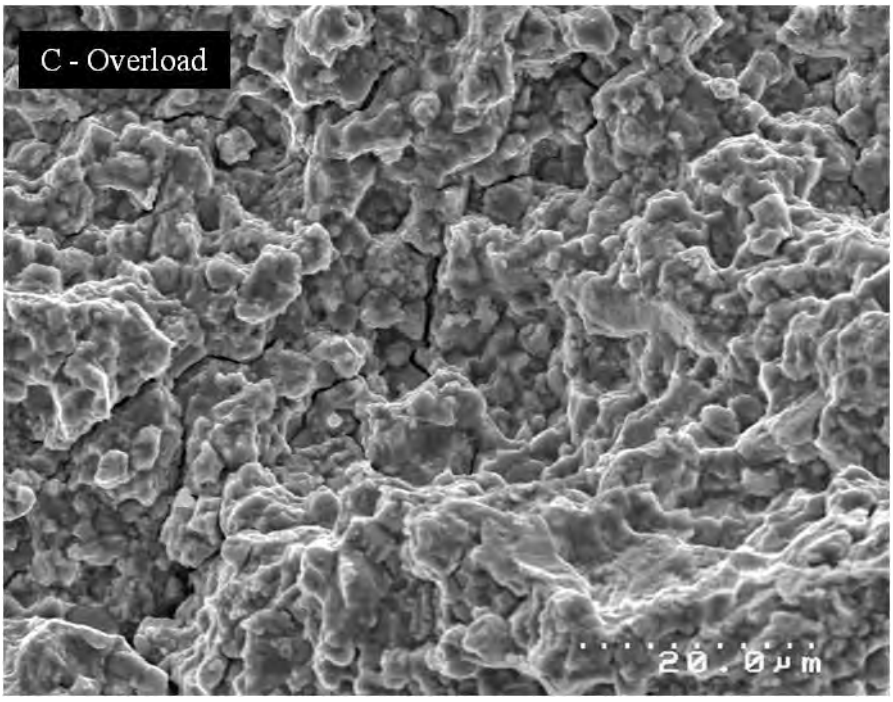


Figure A-88: Showing fractographs of fine-grained RR1000 test piece CC056; tested at 650°C in air, with a dwell load of 28.08 kN, an overload factor of 1.065 and a dwell time of 1,200 seconds. Each image shows the crack propagating from bottom left to top right. Note that during the "overload" segment (band C) unloading stress waveforms were applied (Figure 3-11). Bands labelled A and D are baseline (1-1-1-1) regions, the band labelled B represents the dwell region and the band labelled C; the overload (unload) region. Higher magnification images are taken at points relating to the following crack growth driving forces (ΔK): A: ~20 MPa√m; B: ~29 MPa√m; C: ~43.5 MPa√m; D: ~54.5 MPa√m


D
C
B
A
1.00mm


A - Baseline
20.0µm


B - Dwell
20.0µm


C - Overload
20.0µm

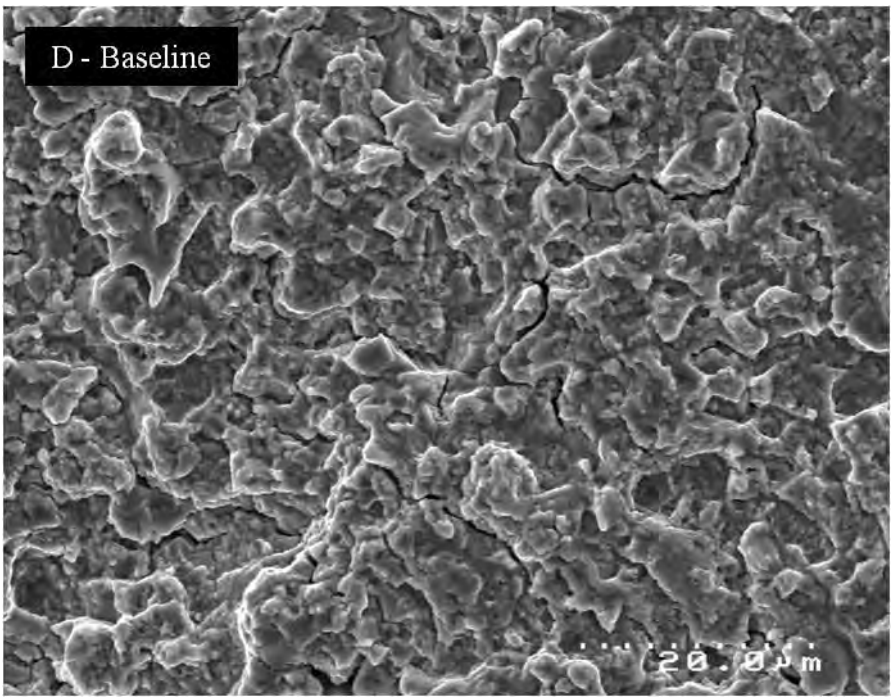
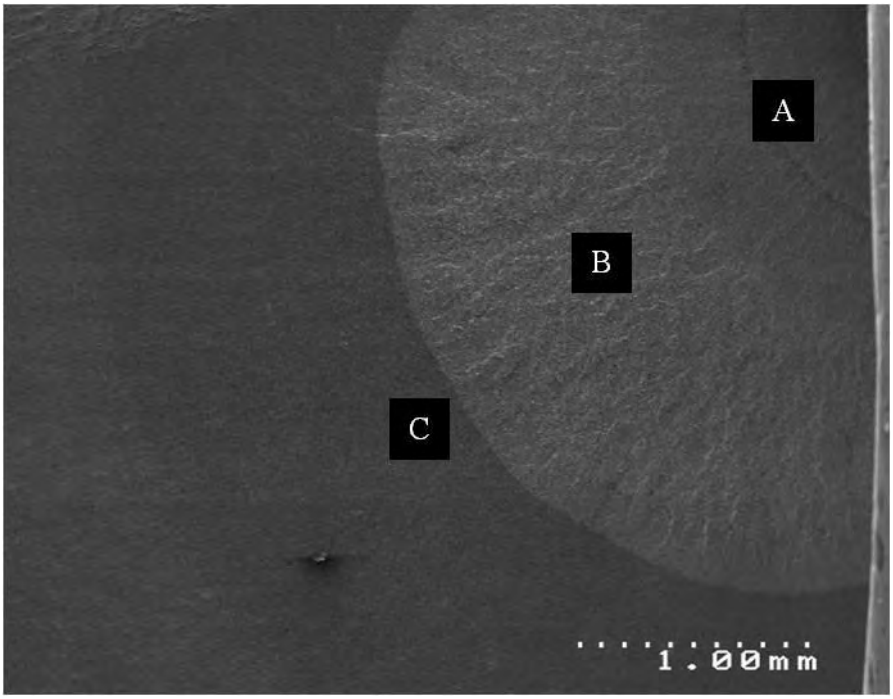
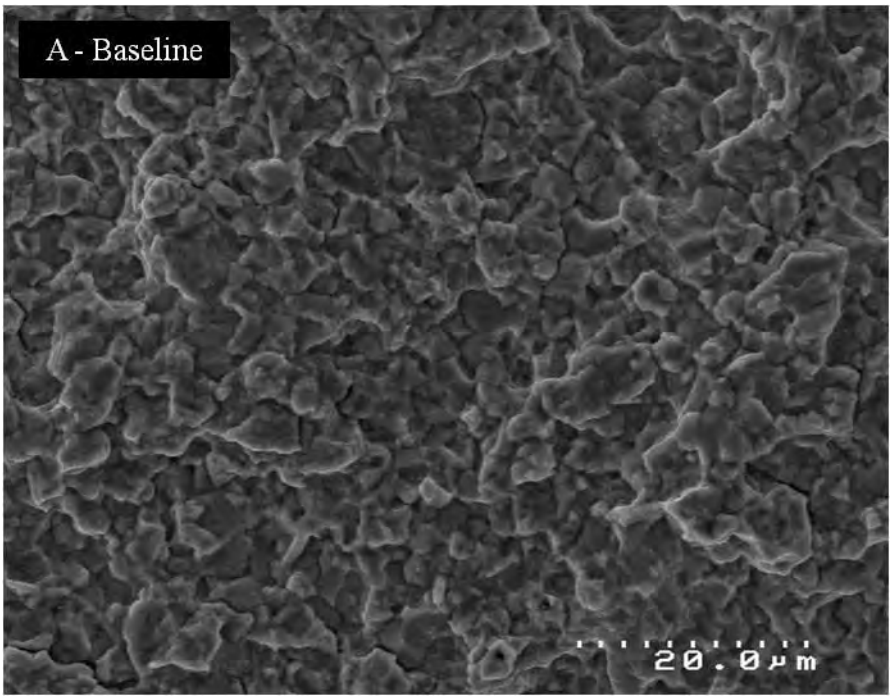
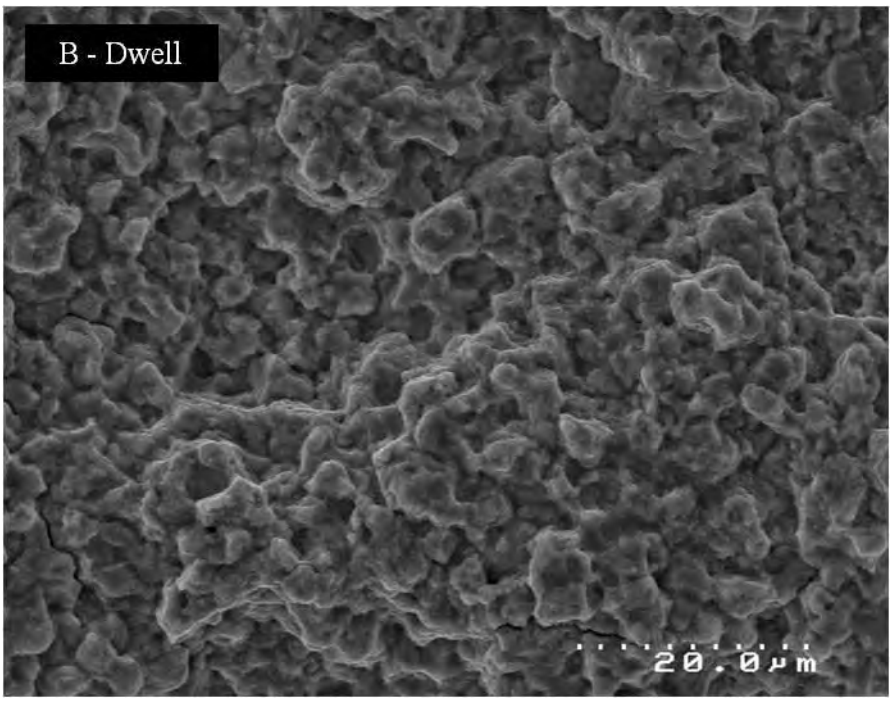


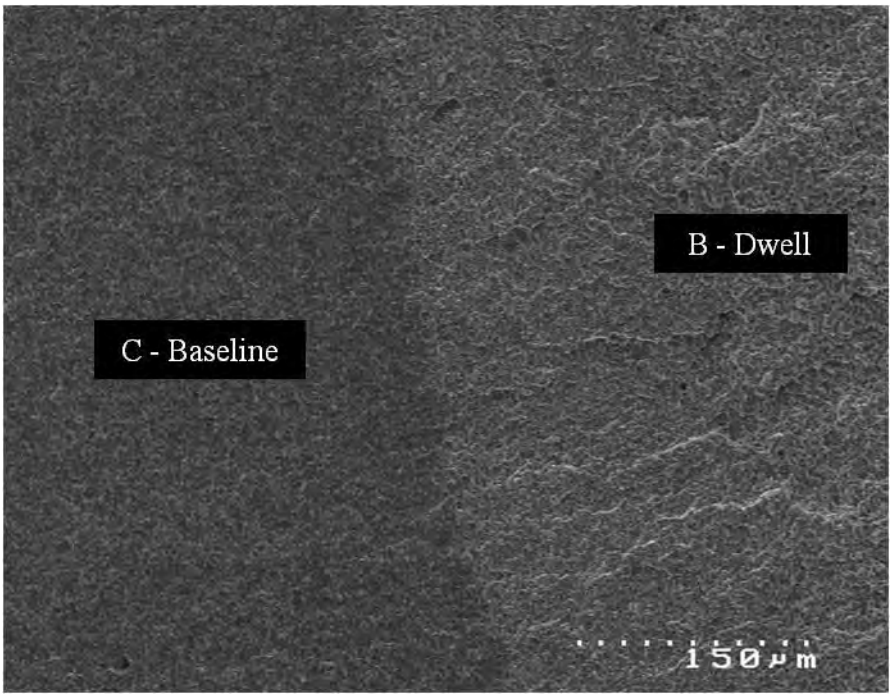
Figure A-89: Showing fractographs of fine-grained RR1000 test piece CC057; tested at 650°C in air, with a dwell load of 28.08 kN, an overload factor of 1.065 and a dwell time of 1,200 seconds. Each image shows the crack propagating from bottom left to top right. Note that during the "overload" segment (band C) reloading stress waveforms were applied (Figure 3-12). Bands labelled A and D are baseline (1-1-1-1) regions, the band labelled B represents the dwell region and the band labelled C; the overload (reload) region. Higher magnification images are taken at points relating to the following crack growth driving forces (ΔK): A: ~20 MPa√m; B: ~27.5 MPa√m; C: ~45 MPa√m; D: ~54.5 MPa√m

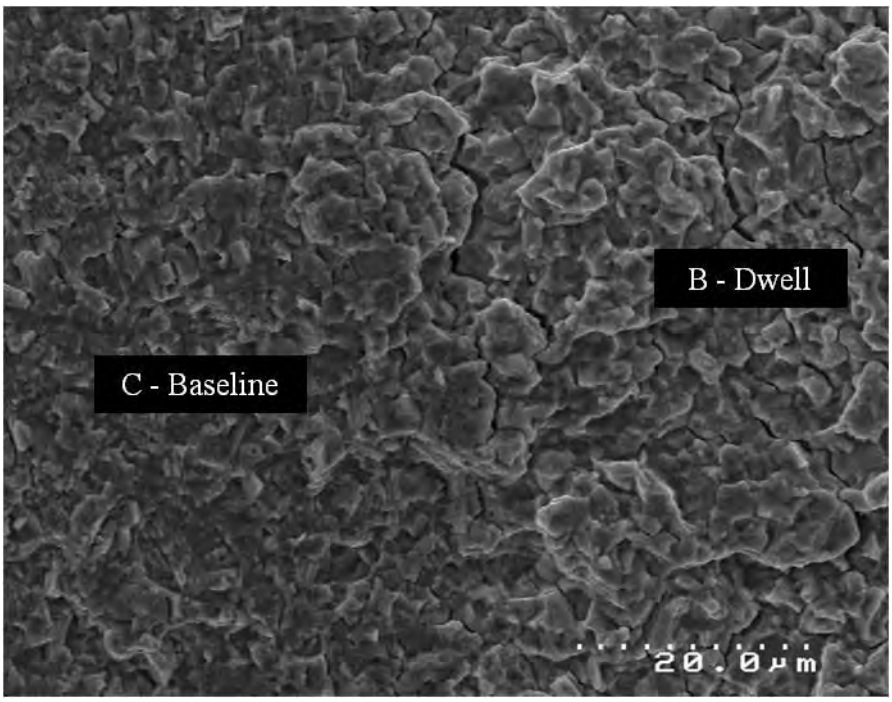
RR1000 Cooling Rate Tests






B - Dwell
20.0µm


B - Dwell
C - Baseline
150µm


B - Dwell
C - Baseline
20.0µm

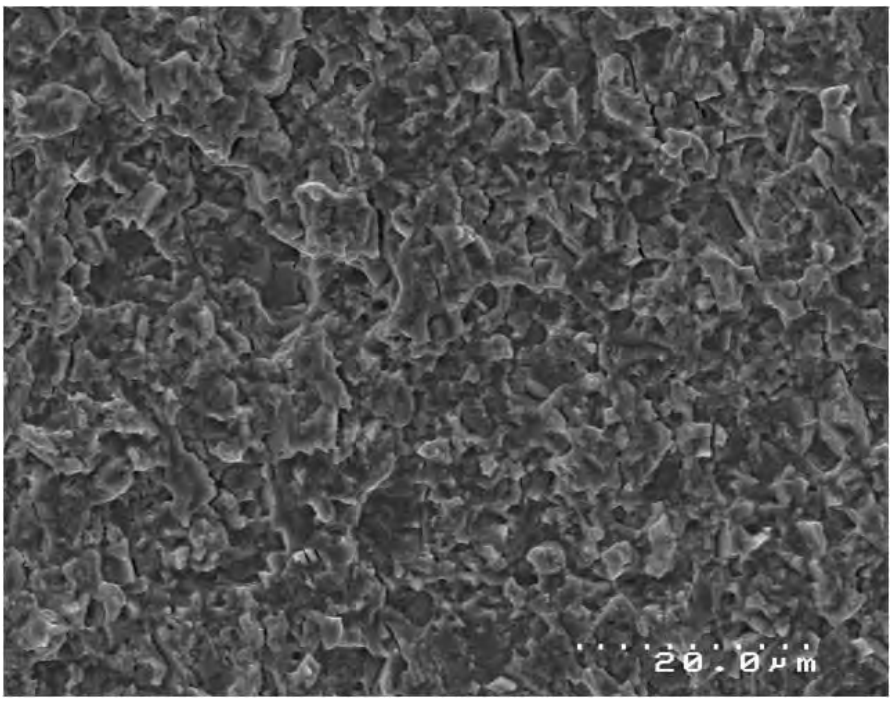
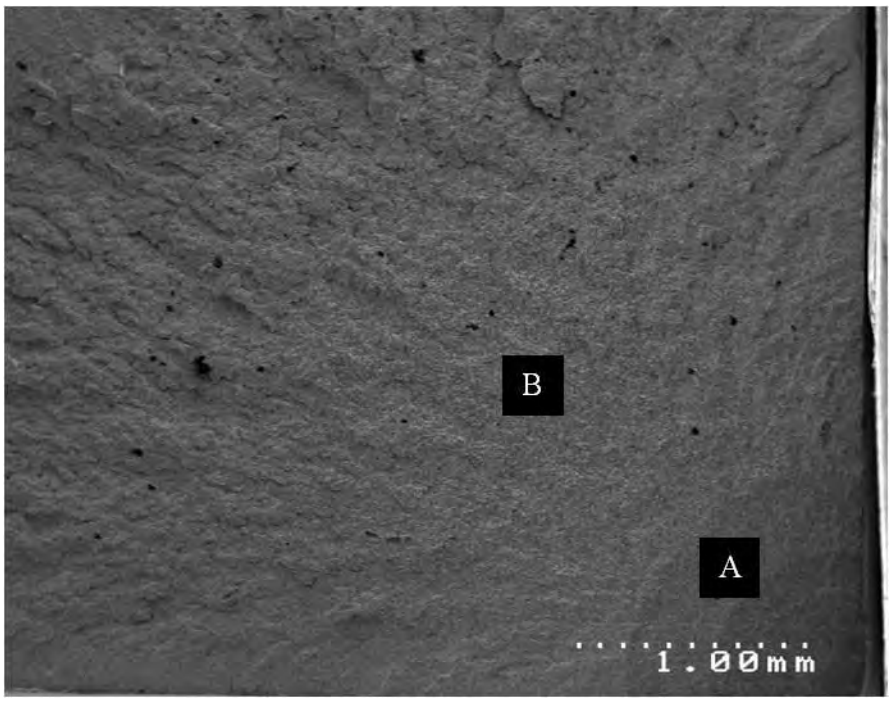
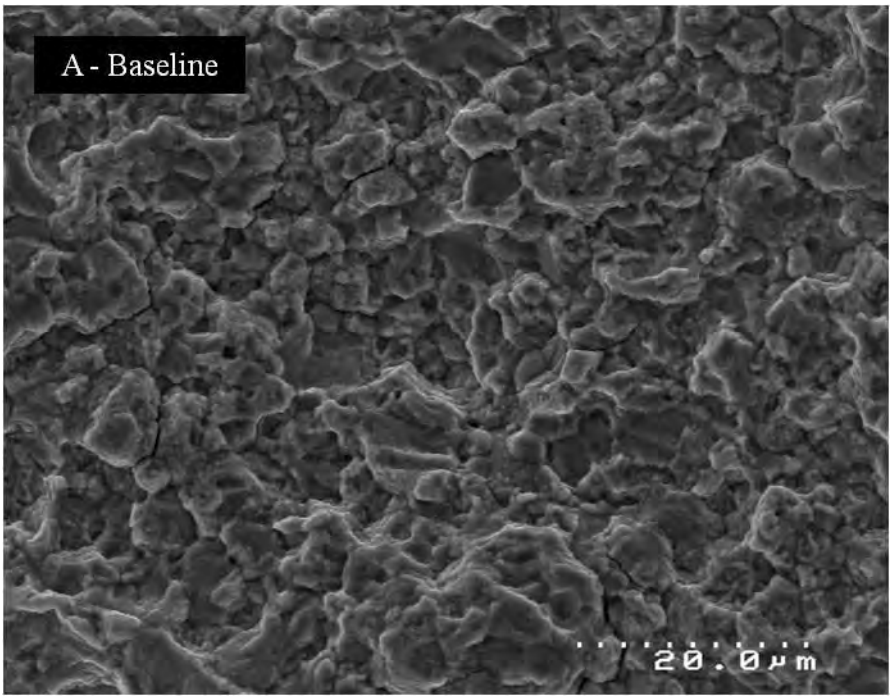


Figure A-90: Showing fractographs of fine-grained RR1000 test piece CX001; tested at 650°C in air, with a dwell load of 12 kN (on a test piece 5 x 5 mm in gauge cross section), and a dwell time of 3,600 seconds. Note that this test piece has been purposefully cooled relatively slowly from the maximum heat treatment temperature (~0.1°C/s) and the morphology of the γ' phase has been significantly affected (reported in section 4.2.2.4 and discussed in section 5.2.4). Each image shows the crack propagating from top right to bottom left. Bands labelled A and C are baseline (1-1-1-1) regions, and the band labelled B represents the dwell region. Note also that at a ΔK of around 22.5 MPa√m, dwell cycles were first applied but the crack did not propagate (beyond a small amount) – hence the band on the lower magnification image during the baseline segment. Higher magnification images are taken at points relating to the following crack growth driving forces (ΔK): A: ~13 MPa√m; B: ~29 MPa√m; C: ~41 MPa√m


B
A
1.00mm


A - Baseline
20.0µm

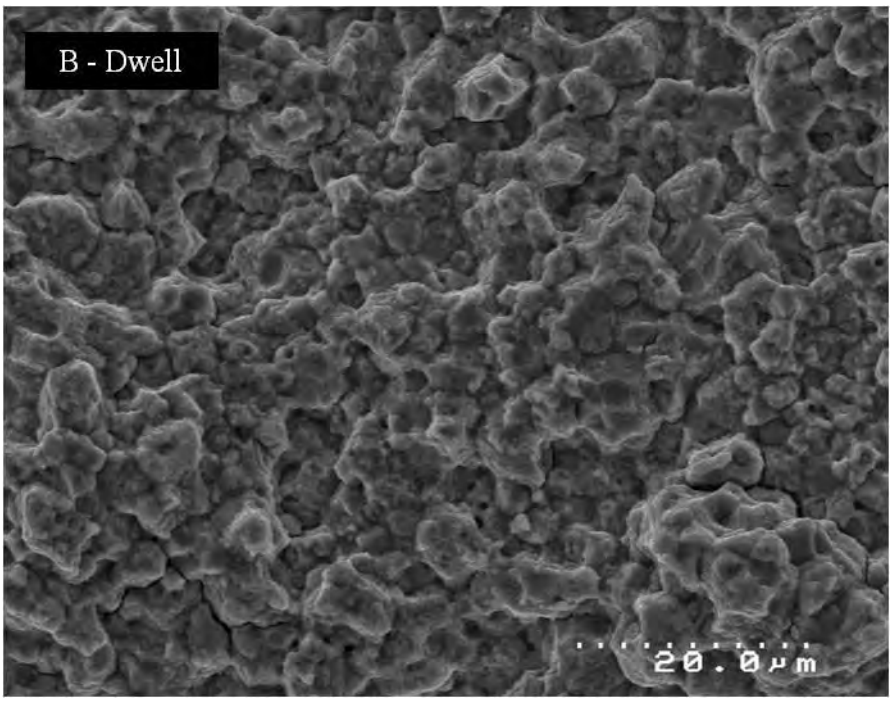


Figure A-91: Showing fractographs of fine-grained RR1000 test piece CX005; tested at 650°C in air, with a dwell load of 12 kN (on a test piece 5 x 5 mm in gauge cross section), and a dwell time of 3,600 seconds. Note that this test piece has been purposefully cooled relatively quickly from the maximum heat treatment temperature (~5°C/s) and the morphology of the γ' phase has been significantly affected (reported in section 4.2.2.4 and discussed in section 5.2.4). Each image shows the crack propagating from bottom right to top left. The band labelled A represents the baseline (1-1-1-1) region, and the band labelled B represents the dwell region. Higher magnification images are taken at points relating to the following crack growth driving forces (ΔK): A: ~13 MPa√m; B: ~22 MPa√m

8 References

1. Reed, R.C., *The superalloys : fundamentals and applications*2006, Cambridge, UK ; New York: Cambridge University Press. xiv, 372 p.

2. Sourmail, T., *Coatings for turbine blades.* 2006.

3. Jain, S., B. Ewing, and C. Yin, *The Development of Improved Performance PM UDIMET 720 Turbine Disks.* Pollock TM, Kissinger RD, Bowan RR, et al, Superalloys, Warrendale, PA: The Minerals, Metals and Materials Society (TMS), 2000: p. 785-794.

4. Mitchell, R., et al., *Process development and microstructure and mechanical property evaluation of a dual microstructure heat treated advanced nickel disc alloy.* TMS Superalloys, 2008: p. 347-356.

5. Moran, M.J., Shapiro, H. N., BMoran, M. J., Shapiro, H. N., Boettner. D. D., Bailey, M., oettner. D. D., Bailey, M., , *Fundamentals of engineering thermodynamics*, ed. L. Ralls2011, United States of America Don Fowley

6. Pineau, A. and S.D. Antolovich, *High temperature fatigue of nickel-base superalloys – A review with special emphasis on deformation modes and oxidation.* Engineering Failure Analysis, 2009. **16**(8): p. 2668-2697.

7. Evans, H., *Unit Five, Stress Concentration Features* Advanced Faligue Life Prediction Correlations 2010: p. 1.

8. Winstone, M. and J. Brooks, *Advanced high temperature materials: Aeroengine fatigue.* Ciência & Tecnologia dos Materiais, 2008. **20**(1-2): p. 15-24.

9. Bhadeshia, H.K.D.H. *Nickel Based Superalloys. Section: Turbine Discs*. 2008; Available from: http://www.msm.cam.ac.uk/phase-trans/2003/Superalloys/superalloys.html.

10. Superalloys, I., *CT Sims, NS Stoloff, and WC Hagel, eds.* John ments. That is, alloy A can be used when low density is Wiley & Sons, New York, NY, 1987: p. 551.

11. Jackson, M.P. and R.C. Reed, *Heat treatment of UDIMET 720Li: the effect of microstructure on properties.* Materials Science and Engineering: A, 1999. **259**(1): p. 85-97.

12. Flower, H.M., *High performance materials in aerospace*1995: Chapman & Hall London.

13. Durand-Charre, M., *The microstructure of superalloys*1998: CRC.

14. Yoon, K.E., et al., *Nanoscale studies of the chemistry of a René N6 superalloy.* Interface Science, 2001. **9**(3): p. 249-255.

15. Fu, C.L., et al., *On the diffusion of alloying elements in the nickel-base superalloys.* Superalloys, 2004. **2004**: p. 867-876.

16. Furrer, D. and H. Fecht, *Ni-based superalloys for turbine discs.* JOM Journal of the Minerals, Metals and Materials Society, 1999. **51**(1): p. 14-17.

17. Donachie, M.J. and S.J. Donachie, *Superalloys: a technical guide*2002: ASM International (OH).

18. Hardy, M.C., et al., *Developing damage tolerance and creep resistance in a high strength nickel alloy for disc applications*. Superalloys 2004, ed. K.A.P.T.M.H.H.H.T.E.R.R.C.S.J.J. Green and S. Walston2004. 83-90.

19. Radis, R., et al., *Multimodal size distributions of γ′ precipitates during continuous cooling of UDIMET 720 Li.* Acta Materialia, 2009. **57**(19): p. 5739-5747.

20. Sczerzenie, F., et al. *Superalloys 1984*. in *Proc. 5th Int. Symp. on Superalloys, TMS-AIME, Warrendale, PA*. 1984.

21. Dieter, G.E., *Mechanical metallurgy*. 3rd ed. McGraw-Hill series in materials science and engineering1986, New York: McGraw-Hill. xxiii, 751 p.

22. Chang, K.M., M. Henry, and M. Benz, *Metallurgical control of fatigue crack propagation in superalloys.* JOM Journal of the Minerals, Metals and Materials Society, 1990. **42**(12): p. 29-35.

23. Ewalds, H.L. and R.J.H. Wanhill, *Fracture mechanics*1984: Edward Arnold.

24. Paris, P.C. and F. Erdogan, *A critical analysis of crack propagation laws.* 1997.

25. Irwin, G.R., *Analysis of stresses and strains near the end of a crack traversing a plate.* J. appl. Mech., 1957.

26. LexTech. *Damage Tolerant Design Handbook.* 2011; Available from: http://www.afgrow.net/applications/DTDHandbook/sections/page2_2_4.aspx.

27. Crompton, J. and J. Martin, *Crack growth in a single crystal superalloy at elevated temperature.* Metallurgical and Materials Transactions A, 1984. **15**(9): p. 1711-1719.

28. Luo, J. and P. Bowen, *Small and long fatigue crack growth behaviour of a PM Ni-based superalloy, Udimet 720.* International Journal of Fatigue, 2004. **26**(2): p. 113-124.

29. Pang, H.T. and P.A.S. Reed, *Microstructure effects on high temperature fatigue crack initiation and short crack growth in turbine disc nickel-base superalloy Udimet 720Li.* Materials Science and Engineering: A, 2007. **448**(1–2): p. 67-79.

30. Onofrio, G., G.A. Osinkolu, and M. Marchionni, *Fatigue crack growth of UDIMET 720 Li superalloy at elevated temperature.* International Journal of Fatigue, 2001. **23**(10): p. 887-895.

31. Onofrio, G., *Effects of loading waveform on fatigue crack growth of Udimet 720 Li superalloy.* International Journal of Fatigue, 2004. **26**(3): p. 203-209.

32. Callister, W.D. and D.G. Rethwisch, *Fundamentals of materials science and engineering: an integrated approach*2011: Wiley.

33. Coffin Jr, L., *Fatigue at high temperature.* Fatigue at elevated temperatures, ASTM STP, 1973. **520**: p. 5-34.

34. Marchionni, M., G.A. Osinkolu, and G. Onofrio, *High temperature low cycle fatigue behaviour of UDIMET 720 Li superalloy.* International Journal of Fatigue, 2002. **24**(12): p. 1261-1267.

35. Osinkolu, G.A., G. Onofrio, and M. Marchionni, *Fatigue crack growth in polycrystalline IN 718 superalloy.* Materials Science and Engineering: A, 2003. **356**(1-2): p. 425-433.

36. Krupp, U., et al., *Oxygen-induced intergranular fracture of the nickel-base alloy IN718 during mechanical loading at high temperatures.* Materials Research, 2004. **7**(1): p. 35-41.

37. Krupp, U., et al., *Brittle intergranular fracture of a Ni-base superalloy at high temperatures by dynamic embrittlement.* Materials Science and Engineering: A, 2004. **387-389**: p. 409-413.

38. Andrieu, E., et al., *Intergranular crack tip oxidation mechanism in a nickel-based superalloy.* Materials Science and Engineering: A, 1992. **154**(1): p. 21-28.

39. Bricknell, R.H., *The Mechanism of Cavity Formation During High Temperature Oxidation of Nickel.* Acta Metallurgica, 1981. **30**: p. 257-264.

40. Knowles, D. and D. Hunt, *The influence of microstructure and environment on the crack growth behavior of powder metallurgy nickel superalloy RR1000.* Metallurgical and Materials Transactions A, 2002. **33**(10): p. 3165-3172.

41. Turan, D., D. Hunt, and D.M. Knowles, *Dwell time effect on fatigue crack growth of RR1000 superalloy.* Materials Science and Technology, 2007. **23**(2): p. 183-188.

42. Molins, R., et al., *Oxidation effects on the fatigue crack growth behaviour of alloy 718 at high temperature.* Acta Materialia, 1997. **45**(2): p. 663-674.

43. Krupp, U., *Dynamic Embrittlement—Time–dependent Quasi–brittle Intergranular Fracture at High Temperatures.* International materials reviews, 2005. **50**(2): p. 83-97.

44. McMahon, C.J., *Comments on "Identification of SAGBO-induced damage zone ahead of crack tip to characterize sustained loading crack growth in alloy 783".* Scripta Materialia, 2006. **54**(2): p. 305-307.

45. Ma, L. and K.-M. Chang, *Identification of SAGBO-induced damage zone ahead of crack tip to characterize sustained loading crack growth in alloy 783.* Scripta Materialia, 2003. **48**(9): p. 1271-1276.

46. Ma, L., X. Liu, and K.-M. Chang, *Reply to comment on "Identification of SAGBO-induced damage zone ahead of crack tip to characterize sustained loading crack growth in alloy 783".* Scripta Materialia, 2006. **54**(2): p. 309-311.

47. Pfaendtner, J.A. and C.J. McMahon Jr, *Oxygen-induced intergranular cracking of a Ni-base alloy at elevated temperatures—an example of dynamic embrittlement.* Acta Materialia, 2001. **49**(16): p. 3369-3377.

48. Lyons, J.S., A.P. Reynolds, and J.D. Clawson, *Effect of aluminide particle distribution on the high temperature crack growth characteristics of a Co-Ni-Fe superalloy.* Scripta Materialia, 1997. **37**(7).

49. Evans, H., H. Li, and P. Bowen, *A Mechanism for Stress-Aided Grain Boundary Oxidation Ahead of Cracks.* Scripta Materialia, 2013.

50. Kitaguchi, H., et al., *Oxidation ahead of a crack tip in an advanced Ni-based superalloy.* Acta Materialia, 2013. **61**(6): p. 1968-1981.

51. Gayda, J. and R. Miner, *Fatigue crack initiation and propagation in several nickel-base superalloys at 650 C.* International Journal of Fatigue, 1983. **5**(3): p. 135-143.

52. Sharma, S.C. *Strength of Materials, Lecture 12*. 2013; Available from: http://nptel.iitm.ac.in/courses/Webcourse-contents/IIT-ROORKEE/strength%20of%20materials/lects%20&%20picts/image/lect12/lecture12.htm.

53. Andrade, E.N.C., *On the viscous flow in metals, and allied phenomena.* Proceedings of the Royal Society of London. Series A, 1910. **84**(567): p. 1-12.

54. Nabarro, F.R.N., *Report of a Conference on the Strength of Solids.* The Physical Society, London, 1948. **75**.

55. Herring, C., *Diffusional viscosity of a polycrystalline solid.* Journal of Applied Physics, 1950. **21**(5): p. 437-445.

56. Coble, R., *A model for boundary diffusion controlled creep in polycrystalline materials.* Journal of Applied Physics, 1963. **34**(6): p. 1679-1682.

57. Saxena, A., D. Hall, and D. McDowell, *Assessment of deflection rate partitioning for analyzing creep crack growth data.* Engineering fracture mechanics, 1999. **62**(1): p. 111-122.

58. Knowles, D. and D. Skelton, *High temperature fatigue of a polycrystalline nickel base superalloy.* Materials Science and Technology, 2001. **17**(11): p. 1403-1412.

59. Skelton, D. and D. Knowles. *Creep fatigue of turbine disc alloys*. in *Fatigue'99: Seventh International Fatigue Congress*. 1999.

60. Saxena, A., *A model for predicting the environment enhanced fatigue crack growth behavior at high temperature.* Thermal and Environmental Effects in Fatigue: Research-Design Interface, CE Jaske, SJ Hudak, and ME Mayfield, eds., ASME PVP, 1983. **71**: p. 171-84.

61. von Mises, R., *Mechanik der festen Körper im plastisch deformablen Zustand.* Göttin. Nachr. Math. Phys, 1913. **1**: p. 582-592.

62. Tresca, M.H., *On further applications of the flow of solids.* Proceedings of the Institution of Mechanical Engineers, 1878. **29**(1): p. 301-345.

63. Mroz, Z. and N.C. Lind, *Simplified theories of cyclic plasticity.* Acta Mechanica, 1975. **22**(1): p. 131-152.

64. Prandtl, L. *Spannungsverteilung in plastischen Körpern*. in *Proceedings of the 1st International Congress on Applied Mechanics, Delft*. 1924.

65. Maitland, T. and S. Sitzman, *Electron backscatter diffraction (EBSD) technique and materials characterization examples*. Vol. 14. 2007: Springer Berlin.

66. Shin, C. and N. Fleck, *Overload retardation in a structural steel.* Fatigue & Fracture of Engineering Materials & Structures, 2007. **9**(5): p. 379-393.

67. Kruch, S., P. Prigent, and J.L. Chaboche, *A fracture mechanics based fatigue-creep-environment crack growth model for high temperature.* International Journal of Pressure Vessels and Piping, 1994. **59**(1–3): p. 141-148.

68. Christensen, R., *Metal fatigue.* M cGraw—H ill, New york, 1959.

69. Jones, R.E., *Fatigue crack growth retardation after single-cycle peak overload in Ti-6Al-4V titanium alloy.* Engineering fracture mechanics, 1973. **5**(3): p. 585-604.

70. Schijve, J. and D. Broek, *Crack propagation: the results of a test programme based on a gust spectrum with variable amplitude loading.* Aircraft Engineering and Aerospace Technology, 1962. **34**(11): p. 314-316.

71. Suresh, S., *Micromechanisms of fatigue crack growth retardation following overloads.* Engineering fracture mechanics, 1983. **18**(3): p. 577-593.

72. Elbert, W. *The significance of fatigue crack closure*. in *Damage Tolerance in Aircraft Structures: A Symposium Presented at the Seventy-Third Annual Meeting American Society for Testing and Materials, Toronto, Ontario, Canada, 21-26 June 1970*. 1971. ASTM International.

73. Ponnelle, S., B. Brethes, and A. Pineau, *High temperature fatigue crack growth rate in inconel 718: Dwell effect annihilations.* European Structural Integrity Society, 2002. **29**: p. 257-266.

74. Matsuoka, S. and K. Tanaka, *Delayed retardation phenomenon of fatigue crack growth resulting from a single application of overload.* Engineering fracture mechanics, 1978. **10**(3): p. 515-525.

75. Wheeler, O., *Spectrum loading and crack growth.* Journal of Basic Engineering, 1972. **94**: p. 181.

76. Sheu, B., P. Song, and S. Hwang, *Shaping exponent in Wheeler model under a single overload.* Engineering fracture mechanics, 1995. **51**(1): p. 135-143.

77. Song, P.S., B.C. Sheu, and L. Chang, *A Modified Wheeler Model to Improve Predictions of Crack Growth Following a Single Overload.* JSME International Journal Series A, 2001. **44**(1): p. 117-122.

78. Yichi, L. and L. Kangxian, *A new model for fatigue crack growth after a single overload.* Engineering fracture mechanics, 1993. **46**(5): p. 849-856.

79. Preuss, M., et al., *Inertia welding nickel-based superalloy: Part I. Metallurgical characterization.* Metallurgical and Materials Transactions A, 2002. **33**(10): p. 3215-3225.

80. Pickard, A., *The application of 3-dimensional finite element methods to fracture mechanics and fatigue life prediction.* Engineering Materials Advisory Services Ltd, 339 Halesowen Rd, Cradley Heath, Warley, West Midlands B 64 6 PH, UK, 1986. 180, 1986.

81. Huang, Z.W., et al., *Inertia Friction Welding Dissimilar Nickel-Based Superalloys Alloy 720Li to IN718.* Metallurgical and Materials Transactions A, 2007. **38**(7): p. 1608-1620.

82. Chakrabarti, D., C. Davis, and M. Strangwood, *Characterisation of bimodal grain structures in HSLA steels.* Materials Characterization, 2007. **58**(5): p. 423-438.

83. Williams, S. and L.-B. Lim, *Inclusion of crack retardation effects in time dependent coponent crack growth calculations* 2010(1).

84. Antolovich, A.P.a.S.D., *High temperature fatigue of nickel-base superalloys - A review with special emphasis on deformation modes and oxidation.* Engineering Failure Analysis, 2009. **16**(8).

85. Bache, M.R., et al., *Environment and time dependent effects on the fatigue response of an advanced nickel based superalloy.* International Journal of Fatigue, 2009. **31**(11–12): p. 1719-1723.

86. Evans, W., J. Jones, and S. Williams, *The interactions between fatigue, creep and environmental damage in Ti 6246 and Udimet 720Li.* International Journal of Fatigue, 2005. **27**(10-12): p. 1473-1484.

87. Evans, W.J., *Time dependent effects in fatigue of titanium and nickel alloys.* Fatigue & Fracture of Engineering Materials & Structures, 2004. **27**(7): p. 543-557.

88. Ghonem, H., T. Nicholas, and A. Pineau, *Elevated temperature fatigue crack growth in alloy 718 - Part 1: Effects of mechanical variables.* Fatigue & Fracture of Engineering Materials & Structures, 1993. **16**(5): p. 565-576.

89. Ghonem, H. and D. Zheng, *Depth of intergranular oxygen diffusion during environment-dependent fatigue crack growth in alloy 718.* Materials Science and Engineering: A, 1992. **150**(2): p. 151-160.

90. J. Tong, S.D., J. Byrne, M. B. Henderson, M. C. Hardy, *Creep, fatigue and oxidation in crack growth in advanced nickel base superalloys.* International Journal of Fatigue, 2001. **23**: p. 897-902.

91. Diboine, A. and A. Pineau, *Creep crack initiation and growth in inconel 718 alloy at 650°C.* Fatigue & Fracture of Engineering Materials & Structures, 1987. **10**(2): p. 141-151.

92. Sherby, O.D. and E.M. Taleff, *Influence of grain size, solute atoms and second-phase particles on creep behavior of polycrystalline solids.* Materials Science and Engineering: A, 2002. **322**(1): p. 89-99.

93. Pencea, I., et al. *New approach for measuring the surface tension of SnAgCu305 molten alloy*. in *Design and Technology in Electronic Packaging (SIITME), 2012 IEEE 18th International Symposium for*. 2012. IEEE.

94. Ellingham, H., *Reducibility of oxides and sulfides in metallurgical processes.* J Soc Chem Ind, 1944. **63**: p. 125-133.

95. Stevens, N., *Personal Communication.* 2009.

96. Simpson, C., *Personal Communication* 2013.

97. Williams, S. and L.-B. Lim, *A user guide for an improved method to analyse and post-process a large number of SC03 models with the aim to establish the material time dependent crack retardation parameters.* 2011.